Thornton Tomasetti

Arecibo Telescope Collapse

Forensic Investigation

Thornton Tomasetti **NN20209**

Prepared For

Arecibo Observatory, operated by **Florida Space Institute**, **University of Central Florida** under cooperative agreement with the **National Science Foundation**

Prepared By

John Abruzzo, P.E., S.E.
Liling Cao, Ph.D., P.E.
Pierre Ghisbain, Ph.D., P.E.

Thornton Tomasetti, Inc.
120 Broadway
New York, NY 10271
+1.212.367.3000
www.ThorntonTomasetti.com

July 25, 2022

Preface

After a first cable failed on the Arecibo Telescope on August 10, 2020, we (Thornton Tomasetti) were engaged by the University of Central Florida (UCF) to be the Engineer of Record for the necessary repairs to stabilize the structure. As preparations were being made for the repairs, a second cable failed on November 6, 2020. On November 19, 2020, the National Science Foundation (NSF) adopted our recommendation to decommission the telescope. The telescope collapsed on its own when additional cables failed on December 1, 2020. We were subsequently retained to perform a forensic investigation of the cable failures and telescope collapse.

We performed the investigation in collaboration with Socotec (formerly Lucius Pitkin), who analyzed and tested samples of the telescope's cables and socket connections in their Brooklyn, NY laboratory. We also worked with Socotec and Lehigh University's Fritz Laboratory to perform a full-scale load test of one of the sockets. Neutron radiography of some of the sockets was performed by Dr. Adrian Brügger of Columbia University in collaboration with the Oak Ridge National Laboratory. Langan provided geotechnical consulting services to support our analysis of the telescope's response to earthquakes.

Before the collapse, UCF retained Wiss, Janney, Elstner Associates (WJE) to investigate the first cable failure and inform the repair plan. The socket connection and matching cable end where the first failure occurred were analyzed by WJE in collaboration with the NASA Engineering and Safety Center (NESC). We reviewed WJE's report,[1] which includes the NESC report, and used some of the reported results as additional data to support our investigation.

Unless otherwise noted, the figures in this report and attached appendices were produced by Thornton Tomasetti on behalf of NSF.

[1] Wiss, Janney, Elstner Associates (WJE). *Auxiliary Main Cable Socket Failure Investigation.* June 21, 2021. Draft report provided by WJE.

Executive Summary

Completed in 1963, the Arecibo Telescope was the largest radio telescope in the world until 2016. The radio feeds of the telescope were located on a steel platform weighing approximately 1.8 million pounds and suspended 500 feet above ground from three concrete towers with more than four miles of steel cables. The cables were arranged in parallel clusters of four or five from tower top to platform and tower top to ground respectively. The telescope was modified in the 1990s to allow the installation of the Gregorian dome and accommodate the increased weight of the platform. At that time, additional cables were installed as single elements from platform to tower to ground. Each cable was a single strand comprising more than 100 high-strength steel wires arranged in concentric layers around a core.

The telescope collapsed on December 1, 2020, after the progressive failure of support cables over a four-month period. The cable failures leading to the collapse occurred at cable ends, where cables are connected to supports with zinc-filled spelter sockets. A first and second socket failed on August 10 and November 6, 2020, respectively, and a third socket failure triggered the collapse on December 1, 2020. All of these failures occurred during fair weather and under normal environmental conditions.

Between February 2021 and May 2022, we investigated the collapse by recovering and testing samples of the cables and sockets, reviewing design documents and maintenance records, and performing a variety of analyses. Our investigation considered the entirety of the telescope's structure, with a particular focus on the cable sockets since they were ultimately the structure's weak point.

We first reviewed the structural design documents for the original construction of the telescope completed in 1963 and the two major upgrades completed in 1974 and 1997. By design, the forces in the cable system were on the higher end of what is typically seen in cable-supported structures, although the expected capacities were still twice those forces. While the telescope was designed to resist loads from hurricanes, it was already highly stressed under its own weight.

We also reviewed the structural inspection and maintenance records produced over the 57 years of the telescope's life. Although the structure was generally well maintained, several conditions were observed on the cable system over time, such as paint degradation, moisture intrusion, vibrations, and individual wire breaks. These conditions were generally addressed adequately and did not significantly contribute to the collapse. In a 2003 inspection, the telescope's Engineer of Record observed that cables had slipped out of their sockets by as much as one-half of an inch and attributed the slips to have occurred during the fabrication or testing of the cables. A later report in 2011 noted that the cable slips remained unchanged from 2003. To our knowledge, the Observatory staff was not instructed to monitor cable slips, nor were they provided with a limit on acceptable cable slip. After Hurricane Maria in 2017, the Observatory staff observed and recorded cable slips of more than one inch on two of the sockets. There is no documentation to show whether these cable slips increased during the hurricane, and to our knowledge they were not identified as an immediate structural integrity issue.

We performed a laboratory analysis of cable and socket samples recovered from the collapsed structure. The results confirm that the cable system met the design specifications on material strength and composition, and was in good condition. We reviewed the analysis performed by Wiss, Janney, Elstner

Associates (WJE) and the NASA Engineering and Safety Center (NESC) of the first socket that failed,[2] and dissected five additional sockets including the second socket that failed and the socket exhibiting the largest cable slip. In the failed and distressed sockets, the zinc casting that holds the cable in the socket experienced significant material flow, allowing the cable to slip. The zinc's mechanical properties showed considerable variability between sockets and within each socket.

We performed an analysis of the telescope structure to determine the forces in the cable system under various conditions, including normal telescope operation and extreme environmental events such as windstorms and earthquakes. The results confirm that the cable system was highly stressed under its own weight, with cable tensions generally consistent with the design documents. Two recent extreme events – Hurricane Maria in 2017 and the January 2020 earthquake sequence – were specifically analyzed and estimated to have temporarily increased the cable tensions by up to 15 percent. This increase could have exacerbated the cable slip in some of the sockets. We analyzed the impact of the first two cable failures on the remaining cables. The first cable to fail was installed in the 1990s and, since it was an isolated cable, its tension could not be redistributed to adjacent parallel cables. Instead, the first cable failure impacted the cable tensions throughout the structure and resulted in a rotation of the telescope's platform.

We studied the sockets to determine why and how some of the sockets exhibited large cable slips and failed while other sockets of identical design and loaded with comparable cable tensions did not. The socket strength analysis involved calculations, finite element analysis, and a full-scale load test to failure. The analysis concludes that the long-term strength of a socket depends on how the cable wires are splayed out in the zinc during socketing. Zinc slowly flows under shear stress when the splayed-out wires, which are typically the two outer layers of the cable, cannot alone resist the cable tension. This condition exists when the wires are insufficiently splayed out for the given cable tension. In this condition, the socket is bound to fail because the zinc will continue to flow until the cable pulls out of the socket entirely. The failure will occur after some time depending on the cable tension and the splayed-out wire geometry, and will be preceded by visible cable slip. Proof-loading of the cable by loading over a period of minutes or hours is not sufficient to assure long-term adequacy of sockets.

From the above reviews and analyses, our investigation concludes that the progressive cable failures and eventual collapse of the Arecibo Telescope were caused by a combination of five factors: (1) the manual and inconsistent splay of the wires during cable socketing, (2) the design of the cable system with relatively low safety factors, (3) the occurrence of extreme environmental events such as hurricanes and earthquakes, (4) the non-replacement, repair or bypass of the sockets where large cable slips were observed, and (5) the addition of auxiliary cables as isolated cables.

More studies are required to characterize the relationship between cable safety factor, geometry of wire splay, and zinc properties to determine the service life of cable-socket assemblies. In the meantime, the risk of socket failure can be mitigated by controlling the factors that contributed to the failure of the telescope's sockets: (1) controlling the number and geometry of splayed-out wires during cable socketing, (2 and 3) designing cable systems with larger safety factors under gravity and transient loads,

[2] Wiss, Janney, Elstner Associates (WJE). *Auxiliary Main Cable Socket Failure Investigation.* June 21, 2021. Draft report provided by WJE.

(4) monitoring the cable slip and slip rate after cable installation, and (5) designing cable systems with multiple adjacent cables on each span.

Our analysis indicates that the excessive cable slips and eventual cable failures would not have occurred if the cable system had been designed with a safety factor of at least 3.0 under gravity loads, and we recommend using a safety factor of at least 4.0 under transient loads. When monitoring cable sockets after installation, limiting the allowable cable slip to one-sixth of the cable diameter as recommended by AASHTO[3] is a reasonable criterion and would have triggered the bypass or replacement of the first socket that failed.

[3] American Association of State Highway and Transportation Officials (AASHTO). AASHTO M 277-06. Standard Specification for Wire Rope and Sockets for Movable Bridges. 2019.

Table of Contents

List of Appendices

1.0 Introduction

The Arecibo Telescope (the telescope) was a radio telescope located at the Arecibo Observatory (AO) in Arecibo, Puerto Rico. The telescope collapsed on December 1, 2020, after 57 years of service. The collapse occurred after two structural cables failed in August and November 2020. In February 2021, we were retained by the University of Central Florida, who operates the Observatory on behalf of the National Science Foundation through a cooperative agreement, to investigate the causes of the cable failures and telescope collapse.

Our investigation encompasses the review of relevant documents, such as design drawings, historical and monitoring data, and field observations made over the life of the structure and during its progressive failure in 2020. We also reviewed the reports on the first cable failure by Wiss, Janney, Elstner Associates (WJE)[4] and the NASA Engineering and Safety Center (NESC).[5] The WJE report includes the NESC report, and therefore our references to the WJE report also refer to the NESC report. As a second focus of the investigation, we recovered failed and intact elements from the collapsed structure and performed a set of laboratory studies and tests. Finally, we performed a set of analyses using computer models of the full telescope structure and some of its components.

The two cable failures that occurred before the collapse and the third cable failure that triggered the collapse all happened near or within zinc-filled spelter sockets at cable ends. No cable failed away from a socket prior to collapse. Each failure involved both the rupture of some of the cable's wires and a deformation of the socket's zinc, and is therefore the failure of a cable-socket assembly. While the terms *cable failure* and *socket failure* are used in this report for the sake of concision, they always refer to the failure of a cable-socket assembly.

This report is organized into three main sections: Background (section 2.0), Observations (section 3.0), and Analysis (section 4.0). The Background section describes the telescope and cable system, and summarizes the structure's history including construction, maintenance, environmental and operational loads, and cable failures leading up to the collapse. The Observations section presents the evidence relevant to cable and socket condition and behavior observed in the field before and after the first cable failure, and in the laboratory after the collapse. The results of two sets of analyses are presented in the Analysis section: a global analysis of the telescope structure to determine the forces experienced by the cables and sockets over time, and a local analysis of zinc-filled spelter sockets to identify the factors that contributed to the failure of some of the telescope's sockets. Lastly, the report provides a brief discussion (section 5.0) of the above information and findings, as well as recommendations (section 6.0) for future work.

This report is intended to provide a brief overview of the investigation and concisely describe the results of many hours of work. More detailed descriptions and explanations of the steps and processes are provided in the attached appendices. In addition to this report, WJE and NESC provided an excellent report on the first socket failure. Much of the work was being performed in parallel, but independently from each other to a large extent.

---

[4] Wiss, Janney, Elstner Associates (WJE). *Auxiliary Main Cable Socket Failure Investigation.* June 21, 2021. Draft report provided by WJE.

[5] NASA Engineering and Safety Center (NESC). *Arecibo Observatory Auxiliary M4N Socket termination Failure Investigation.* NASA/TM-20210017934. NESC-RP-20-01585. June 2021.

2.0 Background

2.1 Telescope Overview and History

The Arecibo Telescope was the largest single-aperture radio telescope in the world when it was constructed in 1963, and remained so until 2016. The primary reflector of the telescope was a fixed spherical dish suspended just above the ground and 1,000 feet in diameter (Figure 1). The radio feeds of the telescope were located 500 feet above the primary reflector on a suspended structure (Figure 2) that was connected to three concrete towers with steel cables. The suspended structure had several moveable parts, which allowed one to position the radio feeds and conduct other experiments. AO is owned by the US National Science Foundation (NSF) and was managed by Cornell University from its opening to 2011. Management was transferred to a consortium led by SRI International in 2011, and to another consortium led by the University of Central Florida in 2018.

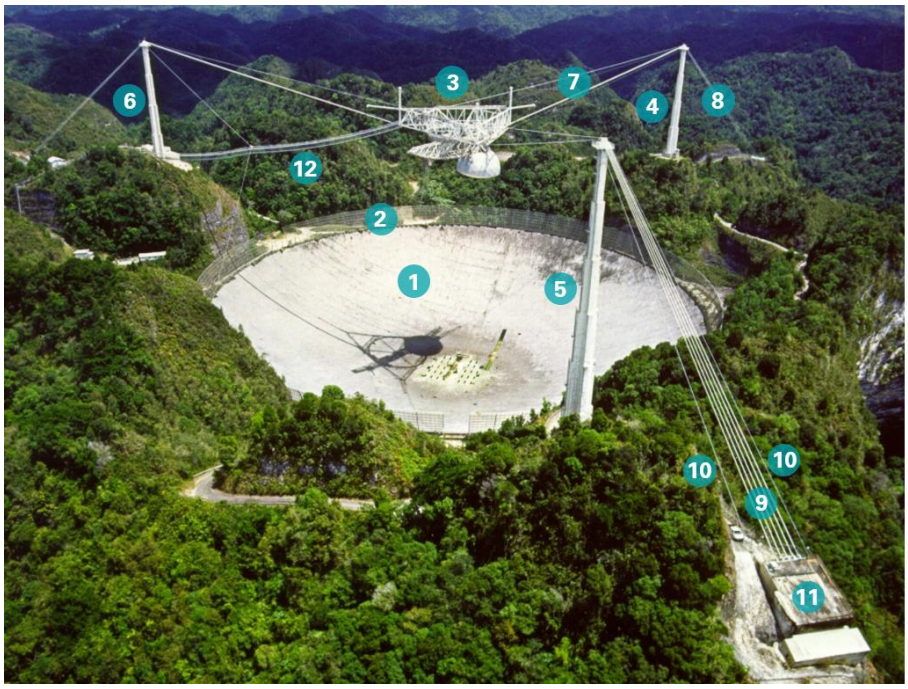

1 Primary reflector
2 Ground screen
3 Suspended structure
4 Tower 4
5 Tower 8
6 Tower 12
7 Tower 4 mains
8 Tower 4 backstays
9 Tower 8 original backstays
10 Tower 8 auxiliary backstays
11 Backstay anchorage
12 Waveguide

Figure 1: Overview of telescope structure after second upgrade *(photo: NSF).*

The original telescope was completed in 1963. The suspended structure was supported with 12 main cables (original mains) – four running in parallel from each tower top. The towers were tied to the ground with 15 backstay cables (original backstays) – five running in parallel from each tower top. The suspended structure was also tied directly to the ground with six inclined tiedowns. These tiedowns were modified in 1974 during a first upgrade of the telescope (Figure 3), with no significant change to the tension in the other cables.

During the second upgrade of the telescope (Figure 3) completed in 1997, the weight of the suspended structure was increased by 40 percent with the addition of the Gregorian and other structural changes. To support the weight increase, six additional main cables (auxiliary mains) and six additional backstay cables (auxiliary backstays) were added to the cable system. Each auxiliary main and backstay was an isolated cable and did not run in parallel with other cables. The inclined tiedowns were replaced with vertical tiedowns equipped with linear actuators (jacks) to minimize the elevation fluctuation of the

suspended structure during day-night temperature cycles. The structure was not significantly modified after the second upgrade. Additional information on the structure's history is provided in Appendix C.

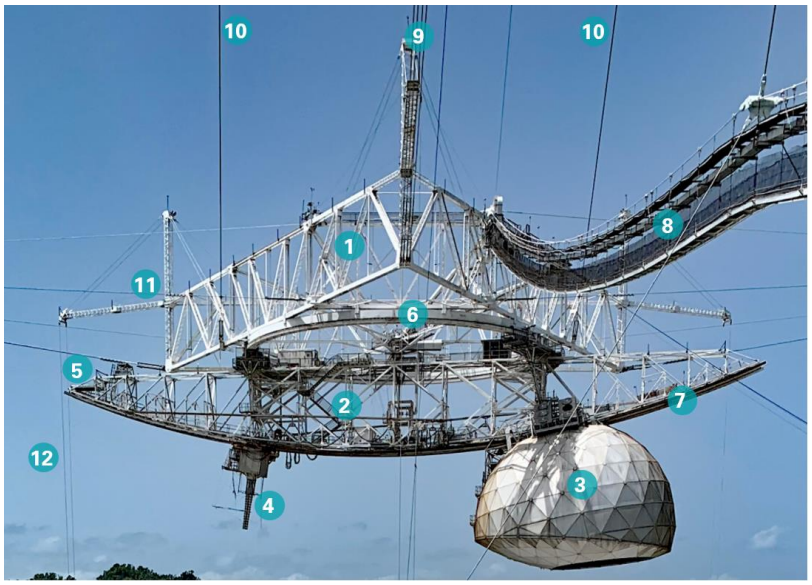

1 Platform
2 Azimuth arm
3 Gregorian
4 Line feed
5 Counterwight
6 Ring girder
7 Azimuth tracks
8 Waveguide
9 Original mains
10 Auxiliary mains
11 Outrigger
12 Tiedowns

Figure 2: Main components of telescope suspended structure after second upgrade
(photo: Mario Roberto Duran Ortiz, Wikipedia - CC BY-SA 4.0).

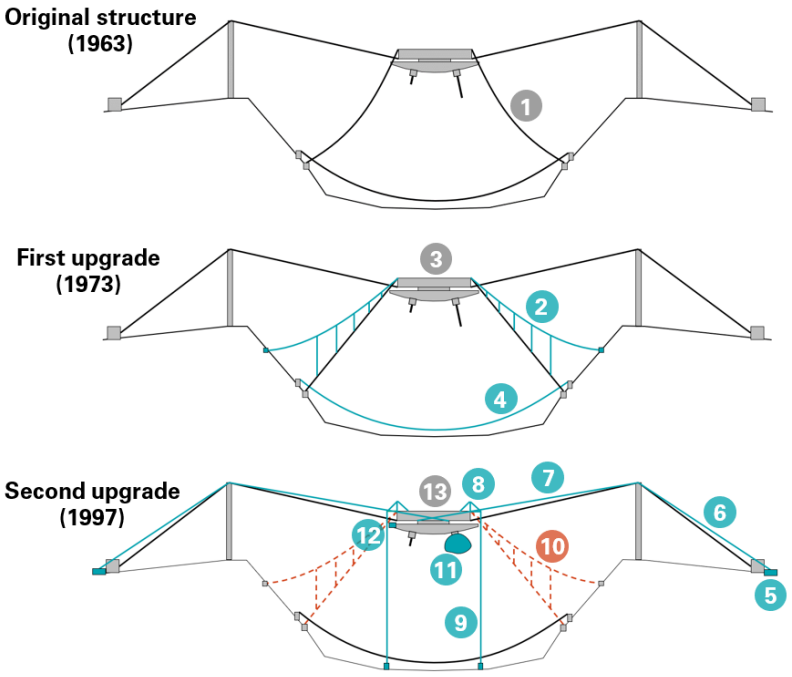

1 Inclined tiedowns sagging under self-weight
2 New carrier cables and hangers removing sag from tiedowns
3 New equipment on suspended structure
4 New primary reflector surface
5 New anchorages for auxiliary backstays
6 New auxiliary backstays
7 New auxiliary mains
8 New tiedown outriggers
9 New vertical tiedowns
10 Removed inclined tiedowns
11 New Gregorian replacing second carriage house
12 New counterweight
13 New equipment and reinforcement on suspended structure

Figure 3: Major structural upgrades of the telescope.

2.2 Cable System Design and Construction

The *cable system* of the telescope consisted of the main and backstay cables supporting the suspended structure above the reflector, and the cable-socket assemblies at the cable ends. The cables were anchored into the sockets, which in turn were connected to the platform, towers, and backstay anchorages. The loads acting on the telescope structure (gravity, wind, earthquakes, etc.) induced stresses in the cables, and the resultant of the stresses over a cable's section is referred to as the cable's *tension* in this report.

2.2.1 Cables and Sockets

After the second upgrade, the telescope structure included more than four miles of steel cables. Each cable was a single strand made of 126 to 216 galvanized steel wires arranged in concentric layers (Figure 4). The wires were woven helicoidally, and the pitch of the helix alternated between layers. The cable diameter, number of wires and wire diameter varied between cable types (Table 1).

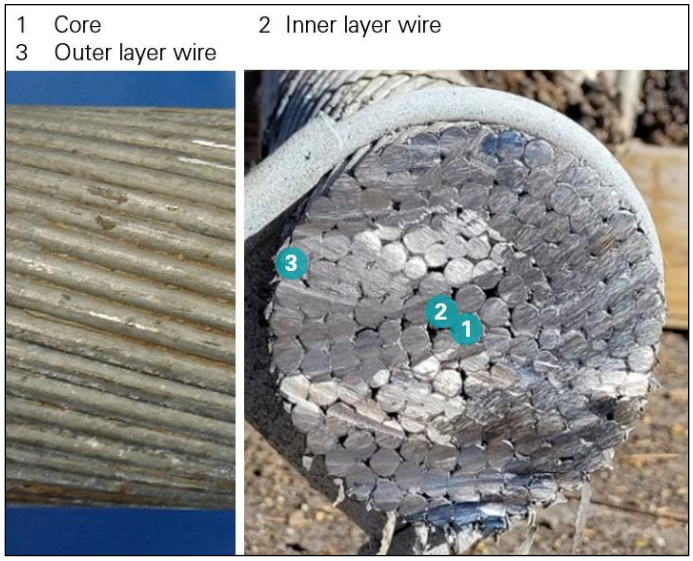

Figure 4: Side and section views of an auxiliary backstay cable.

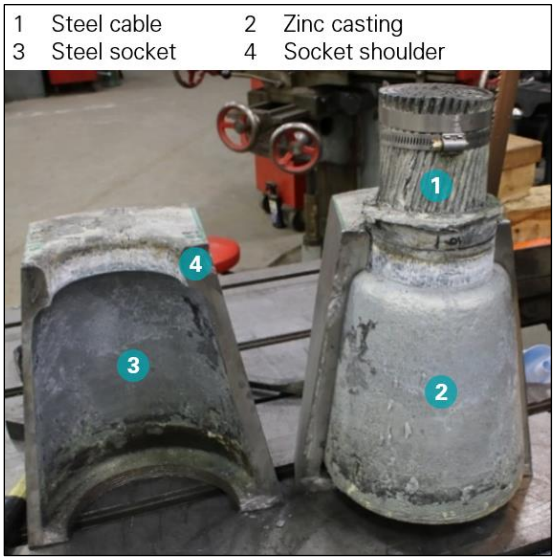

Figure 5: Zinc casting of auxiliary backstay socket B4N_G *(photo: Socotec).*

Table 1: Main and backstay cable properties

	Original Mains	Original Backstays	Auxiliary Mains	Auxiliary Backstays
Cable Diameter	3"	3 1/4"	3 1/4"	3 5/8"
Number of Wires	168	216	126	142 (+23)
Wire Diameter	13/64"	13/64"	1/4"	1/4" (3/16")
Minimum Breaking Strength[A]	1,044 kip	1,212 kip	1,314 kip	1,614 kip
Number of Cables	12	15	6	6

[A] 1 kip = 1,000 pounds

A key property of each cable type is its *Minimum Breaking Strength* (Table 1). Structural cables are fabricated to meet the requirements of a standard, such as ASTM A586[6] for the telescope's auxiliary cables. A standard provides several manufacturing specifications, one of which is a Minimum Breaking Strength. A brand new cable is not expected to fail under any tension lower than its Minimum Breaking Strength. The actual breaking strength of a cable is in fact expected to be somewhat higher than the Minimum Breaking Strength when the cable is new, but it may be lower when the cable is damaged or corroded. The Minimum Breaking Strength is therefore a reference value used to design cable systems, but it is not predictive of the actual breaking strength of a particular cable after a given time in service.

The cables of the telescope were terminated with zinc-filled spelter sockets at both ends (Figure 5, Figure 6). A spelter socket is a steel block with a cone-shaped cavity where the cable is inserted (Figure 6-1) and the cable's wires are spread, splayed or broomed out (Figure 6-2) before the cavity is filled with molten zinc (Figure 6-3). The zinc bonds to the wires and becomes a solid conical block after solidifying, which prevents the cable from exiting the socket, thereby anchoring the cable in the socket. The cable-socket assembly is typically pre-stretched prior to installation, causing the zinc block to seat into the socket and resulting in a little extrusion of the zinc, which is referred to as cable slip (Figure 6-5). Spelter sockets can be connected to supporting structures in a variety of ways, and three types of socket-to-structure connections were used in the telescope (Figure 7). Despite the exterior differences, the internal cable-to-socket connection was similar for all of the telescope's sockets. Most of the telescope's sockets, including socket B4N_G shown in Figure 5, featured a shoulder that breaks the cone's slope near the front of the socket.

Cable manufacturers typically verify through testing that the cable-socket assembly is stronger than the connected cable. In other words, the cable-socket assembly is not expected to fail before the cable. Samples of the auxiliary main and backstay cables were tested in 1993 before the second upgrade of the telescope. For both samples, the first wire ruptures occurred several feet away from the sockets and under a load higher than the cable's Minimum Breaking Strength.

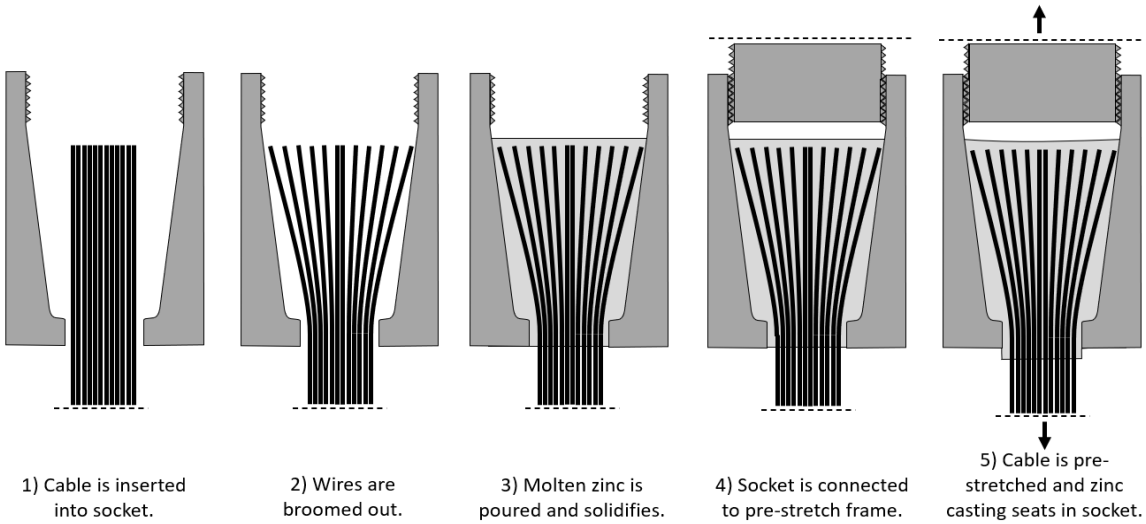

Figure 6: Cable socketing and pre-stretching process.

[6] American Society for Testing and Materials (ASTM). *ASTM A586-18. Standard Specification for Metallic-Coated Parallel and Helical Steel Wire Structural Strand.* 2018.

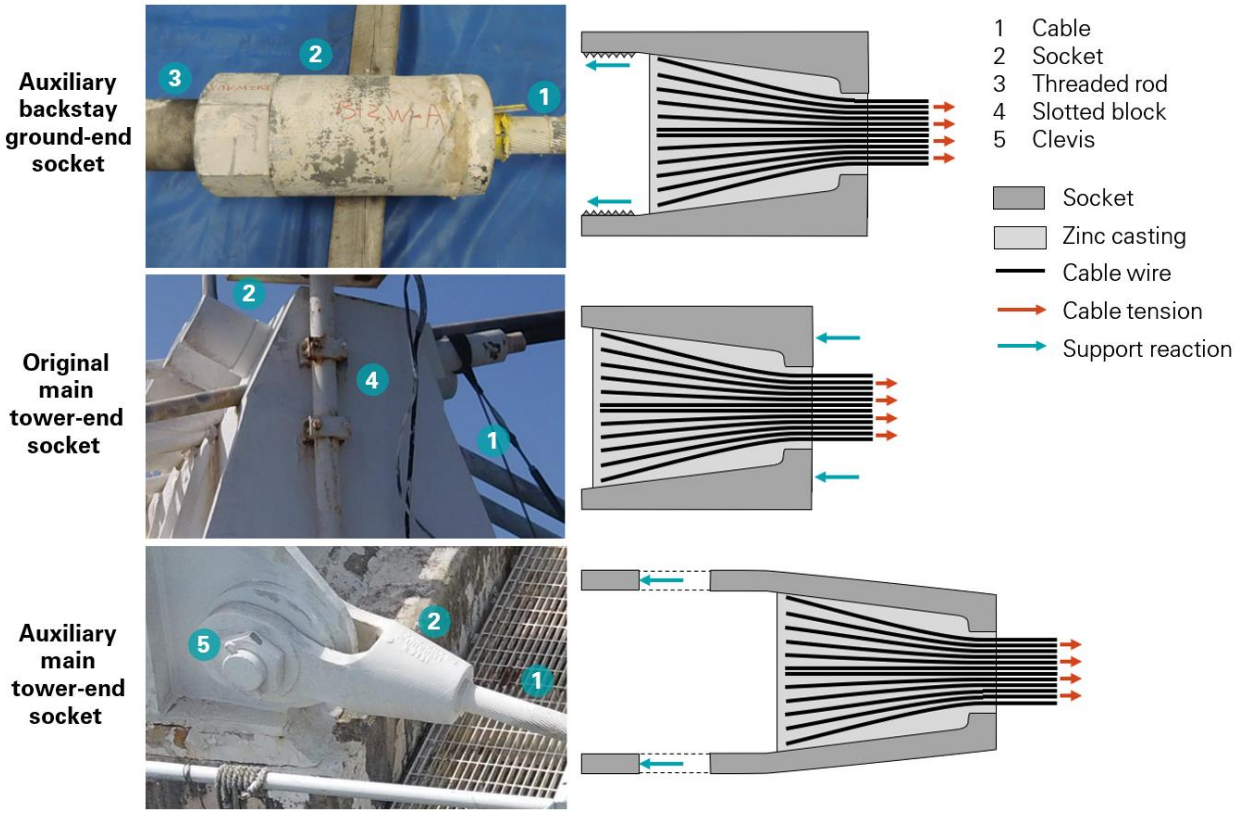

Figure 7: Three zinc-filled spelter socket designs used in the telescope
(top photo: Socotec; middle and bottom photos: NAIC Arecibo Observatory, a facility of the NSF).

2.2.2 Safety Factors

When selecting a cable type and proportioning a cable's diameter, the designer uses a *safety factor* to ensure that the actual breaking strength of the cable is beyond the expected cable tension and reduce the risk of failure to an acceptably low probability. Throughout this report, the safety factor is notional and defined as the cable's Minimum Breaking Strength divided by the cable's actual tension. For a given cable, this safety factor only varies with the cable's tension: if the tension increases due to environmental or situational conditions, the safety factor decreases. While the true safety factor also decreases when a cable is damaged, it is not used in this report as the condition of each cable in-place is not precisely known.

Several structural design standards prescribe a minimum safety factor to be used when designing cable systems, and the prescribed safety factor varies between standards. Standards commonly used nowadays include ASCE-19,[7] which prescribes a safety factor of 2.2 for cables used in building structures, and AASHTO LRFD-8,[8] which prescribes a safety factor of up to 4 for bridge cables. A

[7] American Society of Civil Engineers (ASCE). *ASCE 19-16. Structural Applications of Steel Cables for Buildings*. 2016.

[8] American Association of State Highway and Transportation Officials (AASHTO). *AASHTO LRFD-8. Bridge Design Specifications*. 8th edition. 2017.

precursor of ASCE-19 was AISI,[9] which was first released shortly after the telescope's original construction and prescribed a safety factor of 2.5.

The drawings for the original (1963) and the upgraded (1997) telescope structure specify the Minimum Breaking Strength and expected cable tensions (Figure 8). The average safety factor in the original cable system is approximately 2 under the self-weight of the telescope, and 1.67 considering a 140-mph wind speed in addition to self-weight (Table 2). The second upgrade of the telescope (1997) considered a reduced wind speed of 110 mph for the cable system design, and required the tiedowns be partially released before the occurrence of major windstorms to reduce the cable tensions. As a result, the second upgrade of the telescope increased the average safety factor to 2.25 under self-weight, and 2.15 during the design windstorm (Table 2). As a point of reference, we define the term *design tensions* as those in Table 2, which were extracted from the design documents shown in Figure 8.

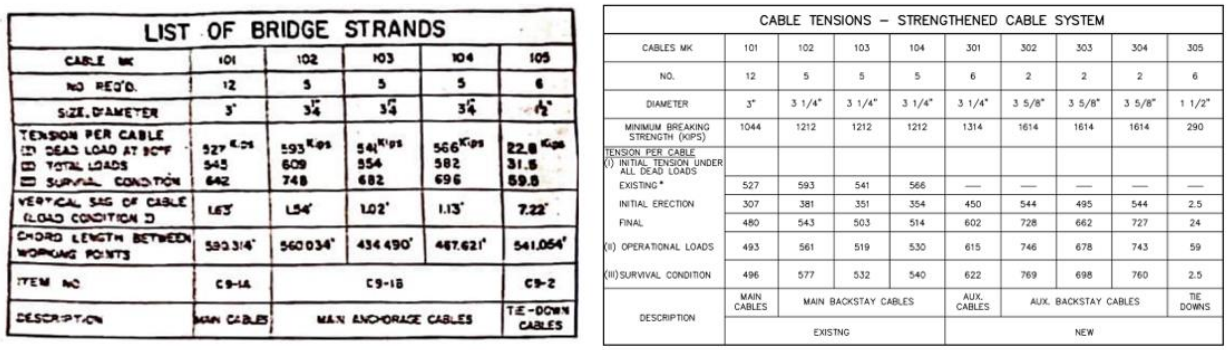

LIST OF BRIDGE STRANDS

CABLE MK	101	102	103	104	105
NO REQ'D.	12	5	5	5	6
SIZE, DIAMETER	3"	3 1/4"	3 1/4"	3 1/4"	1 1/2"
TENSION PER CABLE (1) DEAD LOAD AT 80°F	527 Kips	593 Kips	541 Kips	566 Kips	22.8 Kips
(2) TOTAL LOADS	545	609	554	582	31.5
(3) SURVIVAL CONDITION	642	748	682	696	59.8
VERTICAL SAG OF CABLE (LOAD CONDITION 2)	1.65'	1.54'	1.02'	1.13'	7.22'
CHORD LENGTH BETWEEN WORKING POINTS	593.314'	560.034'	434.490'	487.621'	541.054'
ITEM NO	C9-1A	C9-1B			C9-2
DESCRIPTION	MAIN CABLES	MAIN ANCHORAGE CABLES			TIE-DOWN CABLES

CABLE TENSIONS – STRENGTHENED CABLE SYSTEM

CABLES MK	101	102	103	104	301	302	303	304	305
NO.	12	5	5	5	6	2	2	2	6
DIAMETER	3"	3 1/4"	3 1/4"	3 1/4"	3 1/4"	3 5/8"	3 5/8"	3 5/8"	1 1/2"
MINIMUM BREAKING STRENGTH (KIPS)	1044	1212	1212	1212	1314	1614	1614	1614	290
TENSION PER CABLE (I) INITIAL TENSION UNDER ALL DEAD LOADS									
EXISTING *	527	593	541	566	—	—	—	—	—
INITIAL ERECTION	307	381	351	354	450	544	495	544	2.5
FINAL	480	543	503	514	602	728	662	727	24
(II) OPERATIONAL LOADS	493	561	519	530	615	746	678	743	59
(III) SURVIVAL CONDITION	496	577	532	540	622	769	698	760	2.5
DESCRIPTION	MAIN CABLES	MAIN BACKSTAY CABLES			AUX. CABLES	AUX. BACKSTAY CABLES			TIE DOWNS
	EXISTNG				NEW				

Figure 8: Cable tension tables provided in original (left) and second upgrade (right) structural drawings
(images: structural drawings, courtesy of NAIC Arecibo Observatory, a facility of the NSF).

Table 2: Cable design tensions and safety factors

		Minimum Breaking Strength [kip]	Design Tension in Original Structure [kip (SF)][D]		Design Tension after Second Upgrade [kip (SF)][D]	
			Self-Weight Only	Self-Weight + Max. Wind Load	Self-Weight Only	Self-Weight + Max. Wind Load
Original Cables[B]	**Mains**	1,044	527 (1.98)	642 (1.63)	480 (2.18)	496 (2.10)
	T4 Backstays	1,212	593 (2.04)	748 (1.62)	543 (2.23)	577 (2.10)
	T8 Backstays	1,212	541 (2.24)	682 (1.78)	503 (2.41)	532 (2.28)
	T12 Backstays	1,212	566 (2.14)	696 (1.74)	514 (2.36)	540 (2.24)
	Average[A]		(2.07)	(1.67)	(2.26)	(2.16)
Auxiliary Cables[C]	**Mains**	1,314	-	-	602 (2.18)	622 (2.11)
	T4 Backstays	1,614	-	-	728 (2.22)	769 (2.10)
	T8 Backstays	1,614	-	-	662 (2.44)	698 (2.31)
	T12 Backstays	1,614	-	-	727 (2.22)	760 (2.12)
	Average[A]	-	-	-	(2.24)	(2.15)

[A] Average weighted by number of cables.
[B] Minimum Breaking Strengths reported are based on ASTM A586.
[C] Minimum Breaking Strengths reported are as indicated in drawings for second upgrade.
[D] 1 kip = 1,000 pounds, SF = safety factor.

[9] American Iron and Steel Institute (AISI). *Tentative Criteria for Structural Applications of Steel Cables for Buildings*. 1966.

2.2.3 Installation and Tensioning

The original cables of the telescope were laid out as groups of parallel cables: groups of four cables for the mains, and groups of five cables for the backstays. The cables in one group are spaced approximately one foot apart and share the load from tower or platform equally. This is confirmed by noting equal sag in the cables.

We were unable to find any detailed record of the cable tensioning operations during the original construction and the second upgrade, but the general methods are known. During construction, the platform was lifted in place with temporary cables before installing and tensioning the permanent cables. During the second upgrade, the new auxiliary cables were tensioned gradually as load was added to the suspended structure. It is therefore unlikely that the permanent cables experienced tensions significantly higher than the design tensions (Table 2) during construction. Surveys performed between 1972 and 2016 confirm that under self-weight, the actual cable tensions were consistent with the design tensions. Additional details on the construction and upgrade sequences are provided in Appendix C.

2.3 Cable System Maintenance

Throughout the life of the telescope, the condition of the cable system and the maintenance operations were recorded locally by the AO staff. Occasional structural inspections were also performed by the Engineer of Record Amman & Whitney (AW) between 1972 and 2011. The available information is generally less comprehensive and detailed after the second upgrade in 1997, and the scope of the inspections performed by AW was reduced. Details of the cable system's condition and maintenance history are provided in Appendix D.

Paint Condition

The cables were painted to prevent corrosion, and the paint was well-maintained before the second upgrade in 1997. After the upgrade, AW reported in 2003 and 2011 that the paint on the original cables was in poor condition, with corrosion of the steel wires at some locations. No record of a comprehensive re-painting of the original cables was found after the second upgrade.

Moisture Exclusion System

In the late 1960s, AO observed that the cables were not fully airtight in the transition zone between cable and socket, and determined that this could lead to corrosion within the cable due to moist air intrusion and condensation. In 1972, a system of sleeves, air compressors and dryers was installed at the lower end of the cables to circulate dry air through the cables and prevent accumulation of moisture (Figure 9). The same moisture exclusion system was installed on the auxiliary cables during the second upgrade in 1997. While the system appeared to be functional, condensation was occasionally reported in some of the dry air sleeves between 2002 and 2011. We also observed water accumulation in some of the dry air sleeves during our site visits before and after the collapse.

Vibrations

The cables of the telescope experienced wind-induced vibrations immediately after construction in 1964. Stockbridge dampers (Figure 10) were installed to mitigate the vibrations and appear to have been effective, even though vibrations continued to be reported between 1970 and 2011. The vibrations were

reported as "slight to moderate"[10] and seem to have occurred relatively infrequently and only under specific wind conditions.

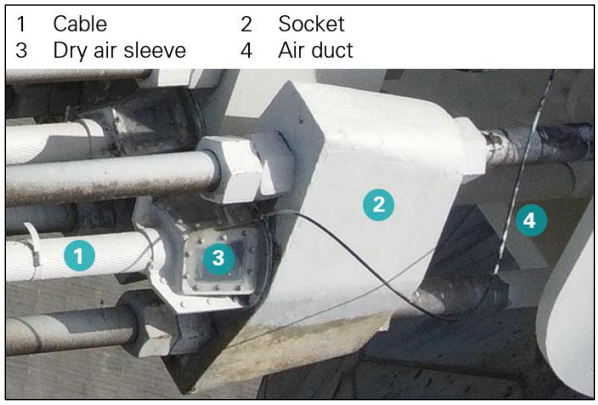

Figure 9: Dry air sleeve on M8-1_P socket
(photo: NAIC Arecibo Observatory, a facility of the NSF).

Figure 10: Stockbridge dampers on original M4 cables
(photo: NAIC Arecibo Observatory, a facility of the NSF).

Repairs and Modifications

Apart from the second upgrade, three significant changes were made to the cable system. In 1981, one of the original backstays of Tower 12 was replaced after six wire breaks were discovered in the cable over time. Then in 1997, a threaded rod connecting the platform-end socket of cable M8-4 was accidentally damaged while implementing the second upgrade of the telescope. A structural bypass was installed to catch the socket should the damaged rod fail (Figure 11). In 2014, a splice near the tower end of the same M8-4 cable was bypassed after multiple wire breaks were discovered during an inspection (Figure 12).

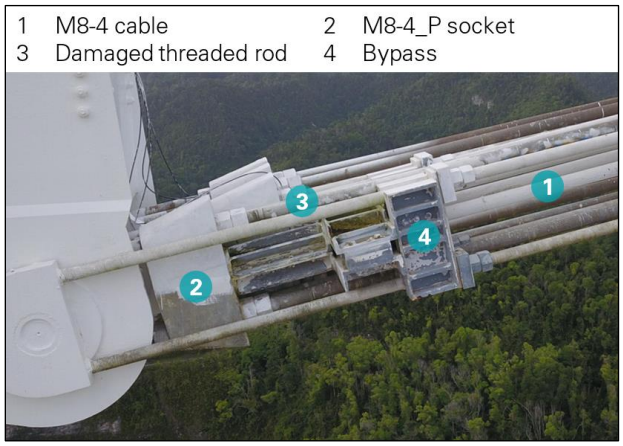

Figure 11: Damaged rod bypass at platform end of cable M8-4
(photo: NAIC Arecibo Observatory, a facility of the NSF).

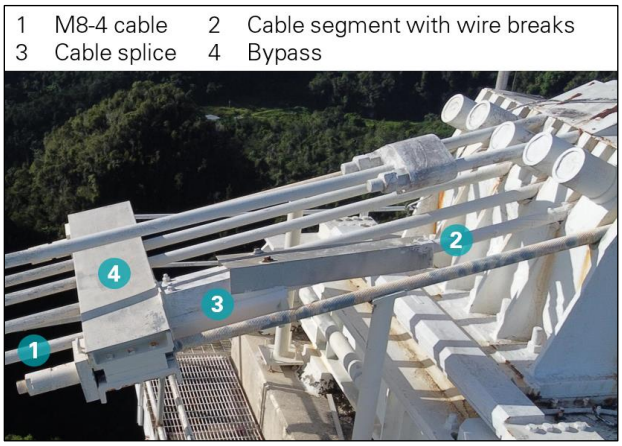

Figure 12: Cable splice bypass near tower end of cable M8-4
(photo: NAIC Arecibo Observatory, a facility of the NSF).

[10] Ammann & Whitney. *Arecibo Radio Telescope Structural Condition Survey.* 2011. Report retrieved from Cornell University archives.

2.4 Load Effects on Cable System

2.4.1 Typical Conditions

In normal operating conditions, the telescope structure was subjected to significant load effects from three sources: its own weight, the movement of the azimuth arm, line feed and Gregorian during operation, and the day-night temperature cycles.

Suspended Structure Weight

The weight of the suspended structure increased significantly during the second upgrade in 1997, but it also varied before and after the upgrade as modifications were made to the structure and its equipment (Table 3). Details on the suspended structure's weight are provided in Appendix C.

Table 3: Suspended structure weight

Year	Structure Configuration	Source	Suspended Structure Weight
1963	Original	Original structural drawings	1,220 kip
1995	Original	Cable tensioning sequence for second upgrade	1,225 kip
1997	Upgraded	Cable sag survey after second upgrade	1,789 kip
2020	Upgraded	Cable sag survey after first cable failure	1,825 kip

Telescope Operation

The operation of the telescope changed the distribution of cable tensions. As shown in Figure 13, the suspended structure of the upgraded telescope consisted of a fixed platform supporting a moving azimuth arm, Gregorian and line feed. When the telescope was operating, the azimuth arm rotated about the center of the platform, while the Gregorian and line feed slid along the bottom of the azimuth arm. These displacements shifted the position of the structure's center of mass, which was balanced by changes in cable tensions. A sample of a weekly data log recording the positions of the azimuth arm, Gregorian and line feed is shown in Figure 14. The first half of the week is representative of the most common operating mode of the telescope, with the azimuth arm and Gregorian moving slowly and completing a few cycles per day. The second half of the week is representative of another operating mode of the telescope, where the Gregorian and line feed are fixed while the azimuth arm spins rapidly and continuously, with approximately four revolutions per hour. The Gregorian was installed during the second upgrade of the telescope to replace a carriage house, which was significantly lighter than the Gregorian. As a result, the operation of the telescope had a more significant impact on the cable forces in the upgraded structure than in the original structure.

Temperature Effects

The fluctuations in air temperature and solar radiation caused the materials of the telescope's structure to expand and contract, which affected the cable tensions. The ambient air temperature was recorded by a weather station located on the telescope's platform. The data indicates an average day-night temperature range of 12.3°F with no significant changes between seasons. In addition, after the first cable failure in 2020, six auxiliary cable sockets were instrumented by WJE with temperature sensors. We monitored the data and measured an average daily temperature range of 14.8°F on the steel surfaces. Details are provided in Appendix I.

The drop in temperature at night caused the telescope's cables to contract and the platform to rise as a result. The accuracy of the telescope's observations was affected by changes in platform elevation. To mitigate these fluctuations, the upgraded structure was equipped with an active tiedown system where electro-mechanical jacks pulled on the tiedowns at night to counter the rise and keep the platform at a constant elevation (Figure 15). A log of the tiedown forces since 2004 indicates that the total tiedown force increased by an average of 60 kip at night under the combined effect of temperature and jack pull-down, which increased the tensions in the entire cable system. The original structure was only equipped with passive tiedown cables, and therefore the impact of day-night cycles on the cable tensions was less significant.

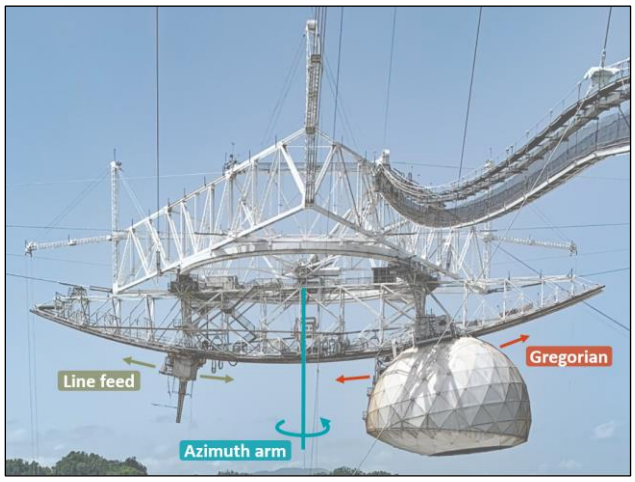

Figure 13: Moveable parts of suspended structure
(photo: Mario Roberto Duran Ortiz, Wikipedia - CC By-SA 4.0).

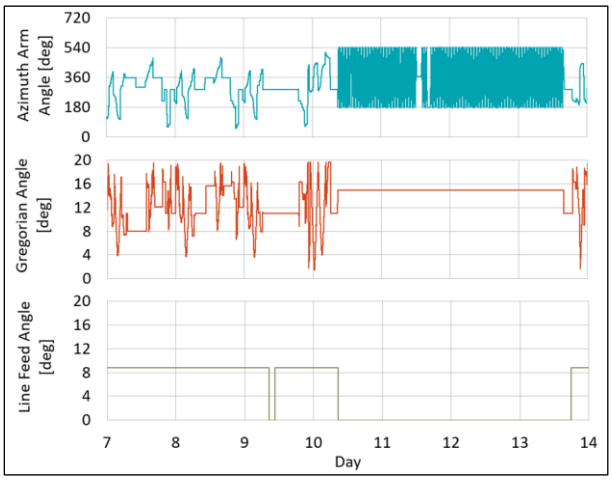

Figure 14: Positions of azimuth arm, Gregorian and line feed during one week of telescope operation (December 7, 2012 to December 14, 2012).

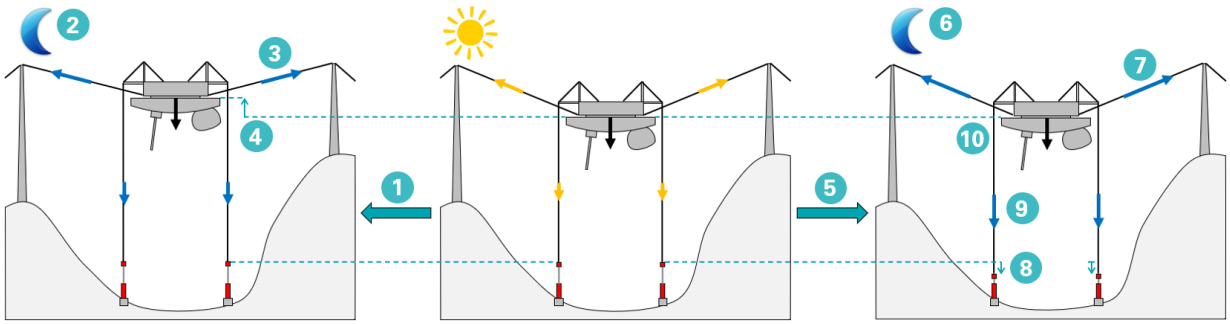

1 Day-night change without tiedown jacking
2 Air temperature drops by 12.3°F
3 Cable tensions increase
4 Platform rises

5 Day-night change with tiedown jacking
6 Air temperature drops by 12.3°F
7 Cable tensions increase
8 Tiedown jacks pull down
9 Total tiedown tension increases by 60 kip
10 Platform stays at same elevation

Figure 15: Tiedown jacks mitigating the impact of day-night temperature cycles on platform elevation in upgraded structure.

2.4.2 Extreme Environmental Events

The Island of Puerto Rico is often subjected to earthquakes and severe windstorms, including hurricanes. These extreme events induced transient loads on the telescope that affected the cable forces.

Windstorms

Tropical storms and hurricanes regularly impact Puerto Rico and introduced high sustained and fluctuating wind loads onto the telescope structure. Hurricane wind speeds were considered in the design of the telescope, with a design wind speed of 140 mph for the original structure and 110 mph for the first and second upgrades. The lower wind speed of 110 mph was determined by AW, the engineer for both upgrades, as corresponding to a 100-year return period. We did not find any document providing the basis for the original wind speed of 140 mph. A wind tunnel study was performed before the second upgrade, with the scope limited to determining the pressures on the Gregorian dome.

The instantaneous wind speed and direction were monitored continuously and logged every second by the weather station on the telescope's platform. In the data log from 2005 to 2020, the highest instantaneous wind speed was 108 mph and occurred during Hurricane Maria on September 20, 2017 (Figure 16). AO did not experience the highest reported wind speed of the hurricane due to its inland location and mountainous terrain. The tiedown forces were also recorded continuously, and the data indicates that the suspended structure responded dynamically during strong wind events.

Earthquakes

Puerto Rico experiences frequent earthquakes due to its location between the North American and Caribbean tectonic plates. AO is equipped with a seismic monitoring station located on a hill of similar topography and geology as the hills where the telescope's towers and cable anchorages are built. The ground accelerations recorded at the station were therefore also experienced by the towers and anchors. Since the telescope's completion in 1963, more than 200 earthquakes of moment magnitude greater than 4.5 occurred within 200 km (125 miles) of AO, including a significant event of moment magnitude 6.4 on January 7, 2020 recorded by the station (Figure 17).

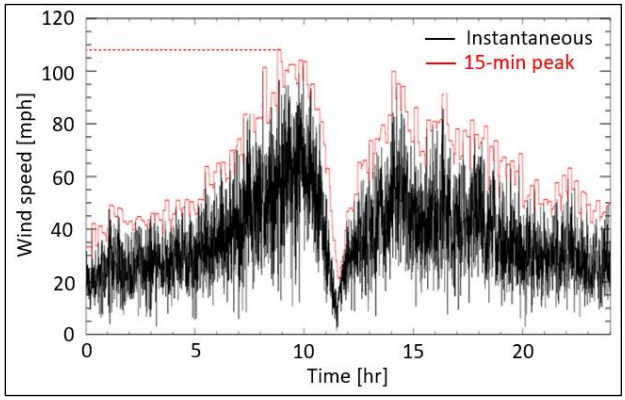

Figure 16: Wind speed recorded on telescope platform during Hurricane Maria on September 20, 2017.

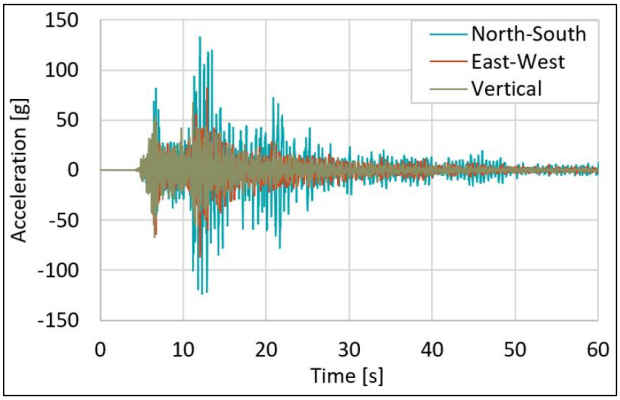

Figure 17: Ground accelerations recorded at AO during M6.4 earthquake on January 7, 2020.

2.5 Cable Failures and Collapse Sequence

At 2:36 AM local time on August 10, 2020, cable M4N pulled out of its socket at the top of Tower 4 (Figure 18). This first failure occurred as the telescope was operating normally, with the azimuth arm rotating with respect to the platform and the Gregorian shifting along the bottom of the azimuth arm. There were no particularly strong winds or any significant earthquake during that night. The telescope continued to operate (azimuth arm and Gregorian movement) for approximately 20 minutes after the cable failure, before being stopped by the operator. Several wire breaks were observed three days later in adjacent cables at the top of Tower 4, and likely occurred when M4N failed (details in Section 3.2.1).

On August 11, 2020, the AO staff placed the telescope in the stowed position. This operation involves moving the azimuth arm and Gregorian into predefined positions and locking them with pins, as was typically done before the arrival of significant windstorms. To reduce the forces in the remaining support cables, the jacks at the base of the tiedowns were fully extended. The azimuth arm, Gregorian and tiedown jacks were not moved again after August 11, 2020.

At approximately 10 PM local time on November 6, 2020, cable M4-4 failed at its socket at the top of Tower 4. This occurred in the absence of high winds and seismic activity. This second cable failure caused new wire breaks at the top of tower 4 (details in Section 3.2.1). In the three weeks following the second cable failure, multiple additional wire breaks occurred in the remaining main cables at the top of Tower 4 (details in Section 3.2.1).

At 7:54 AM local time on December 1, 2020, cable M4-2 failed at its socket at the top of Tower 4, once again without any significant wind or seismic activity. This third cable failure was immediately followed by the failure of the remaining two original mains at the top of Tower 4, initiating the fall of the suspended structure. The suspended structure swung down while still connected to Tower 8 and Tower 12, and impacted a cliff face between these two towers. During the fall, the azimuth arm detached from the platform and fell through the reflector. Finally, the top of the three towers broke off and fell (Figure 19).

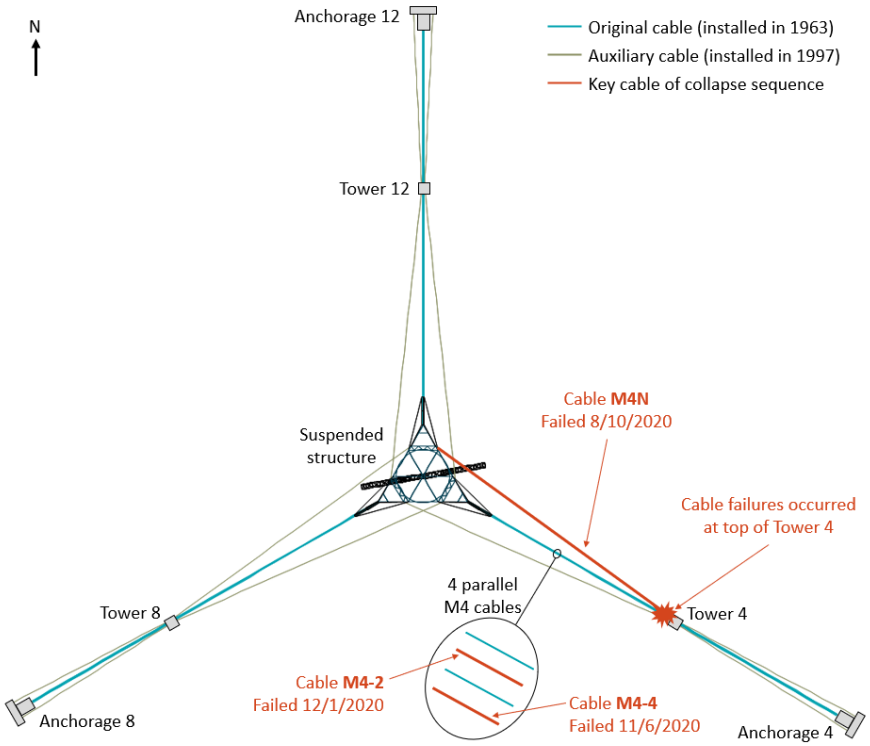

Figure 18: Cable failure locations.

Figure 19: Telescope collapse sequence, looking south.
(Still images of collapse video by NAIC Arecibo Observatory, a facility of the NSF. Intermediate still images are in provided Appendix E.)

3.0 Observations

While the cable system was designed with safety factors greater than 2, the telescope collapsed after the failure of several cable-socket assemblies. The focus of our investigation is therefore to understand the causes and mechanisms of these assembly failures. The failure investigation is performed based on three data sets: the telescope's maintenance and inspection records, the observations made between the first cable failure and the collapse, and the results of laboratory tests performed after the collapse.

3.1 Field Observations Prior to First Cable Failure

The information retrieved from the maintenance and inspection documents relevant to the socket's behavior and failures is summarized in the following, and more details are provided in Appendix D.

3.1.1 Wire Breaks

Each main and backstay cable is made of 126 to 216 steel wires, and individual broken wires were occasionally discovered near the cable ends throughout the structure's life (Figure 20). A total of 40 wire breaks had been reported before 2020 (Figure 22). No more than three wire breaks were reported at each cable end, with two exceptions: six breaks at the bottom of a backstay cable, which was subsequently replaced, and 12 breaks near a cable splice (Figure 21), which was subsequently bypassed. Only the breaks that occurred in the outer layer of wires were visible and therefore counted.

Figure 20: Single wire break observed at ground end of cable B4-1 on 12/12/1996
(photo: NAIC Arecibo Observatory, a facility of the NSF).

Figure 21: Multiple wire breaks observed at splice near tower end of cable M8-4 on 1/14/2014
(photo: NAIC Arecibo Observatory, a facility of the NSF).

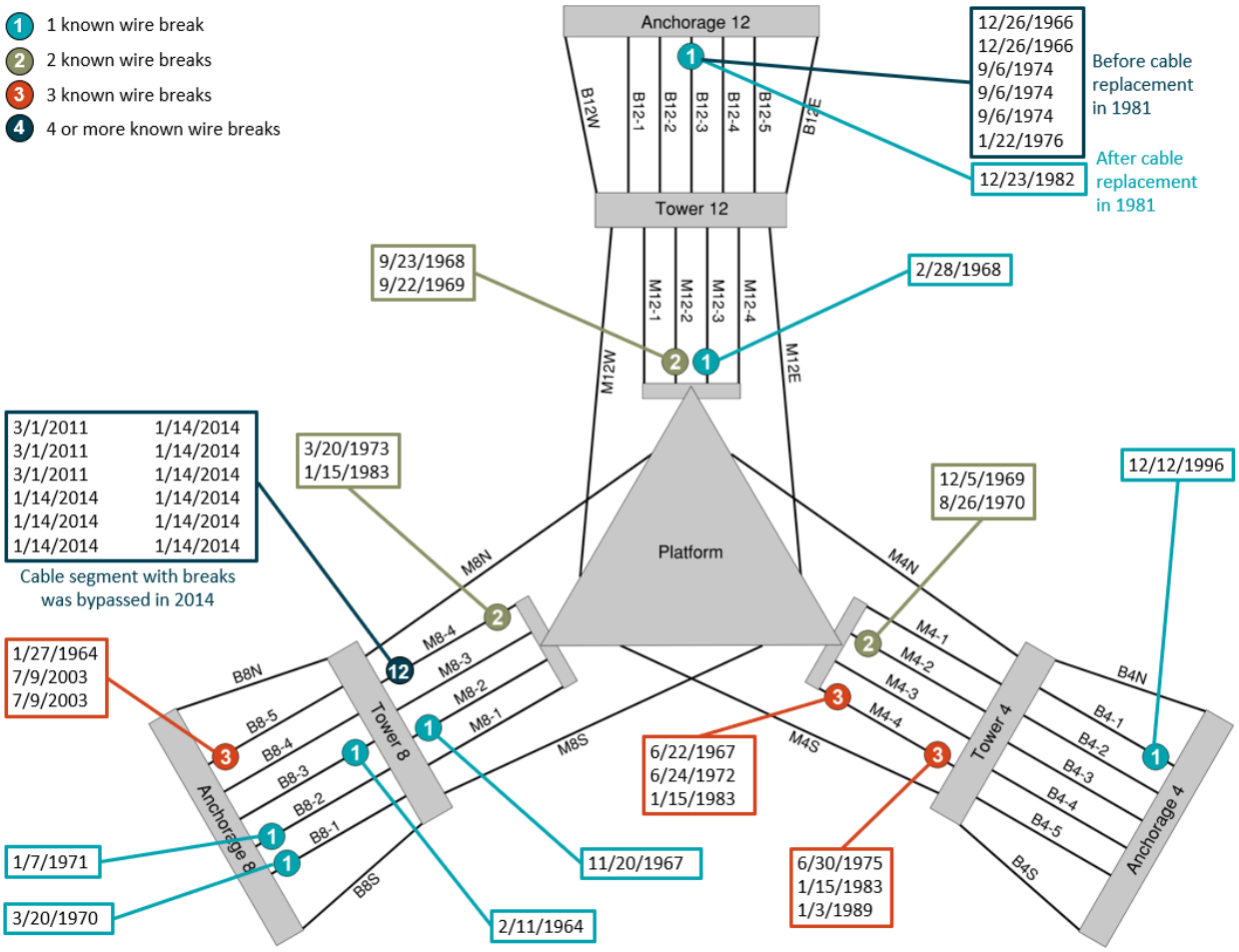

Figure 22: Wire break locations and report dates.

3.1.2 Cable Slips

It is not unusual for a cable to slightly displace out of a spelter socket when it is loaded as the zinc casting seats within the socket's cone. This cable slip is expected to remain relatively small and is exhibited by an extrusion of the zinc casting outside of the socket. For reference, one standard that addresses cable slip at spelter sockets is AASHTO M 277-06,[11] which limits the slip to one-sixth of the cable diameter when proof-loaded to 80 percent of the cable's Minimum Breaking Strength. For the telescope's main and backstay cables, this limit corresponds to a maximum slip between 0.5 and 0.6 inch.

Before failing on August 10, 2020, the end of cable M4N had slipped by more than one inch outside its socket at the top of Tower 4 (Figure 23). This slip is approximately one-third of the cable's diameter, and twice the AASHTO limit.

[11] American Association of State Highway and Transportation Officials (AASHTO). *AASHTO M 277-06. Standard Specification for Wire Rope and Sockets for Movable Bridges*. 2019.

Cable slips were observed but not consistently monitored and reported before August 2020. AW indicate in their inspection reports from 2003 and 2011 that they observed slips of up to 0.5 inch at the auxiliary cable sockets. It is not clear how many locations were inspected. Before the first cable failure, the AO staff observed significantly greater slips than reported by AW on at least two sockets: a 1.125-inch slip at the tower end of M4N (February 2019, Figure 23), and a 1.5-inch slip at the ground end of B12W (May 2018, Figure 24).

The cable slips were measured on all of the auxiliary cable sockets after the telescope's collapse, except for the first socket to fail (Figure 25). There is no consistent correlation between the cable slips and safety factors, which indicates that the cable slip at a socket does not only depend on the cable tension. The safety factors in Figure 25 are based on the actual cable tensions under gravity loads, determined through analysis (section 4.1.2).

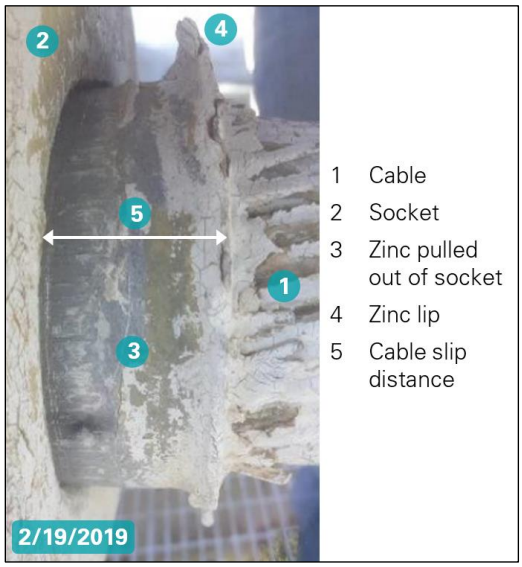

Figure 23: Last known cable slip (1.125 inch) at socket M4N_T, where first cable failure occurred *(photo: NAIC Arecibo Observatory, a facility of the NSF).*

Figure 24: Cable slip increase measured at socket B12W_G *(photos: NAIC Arecibo Observatory, a facility of the NSF).*

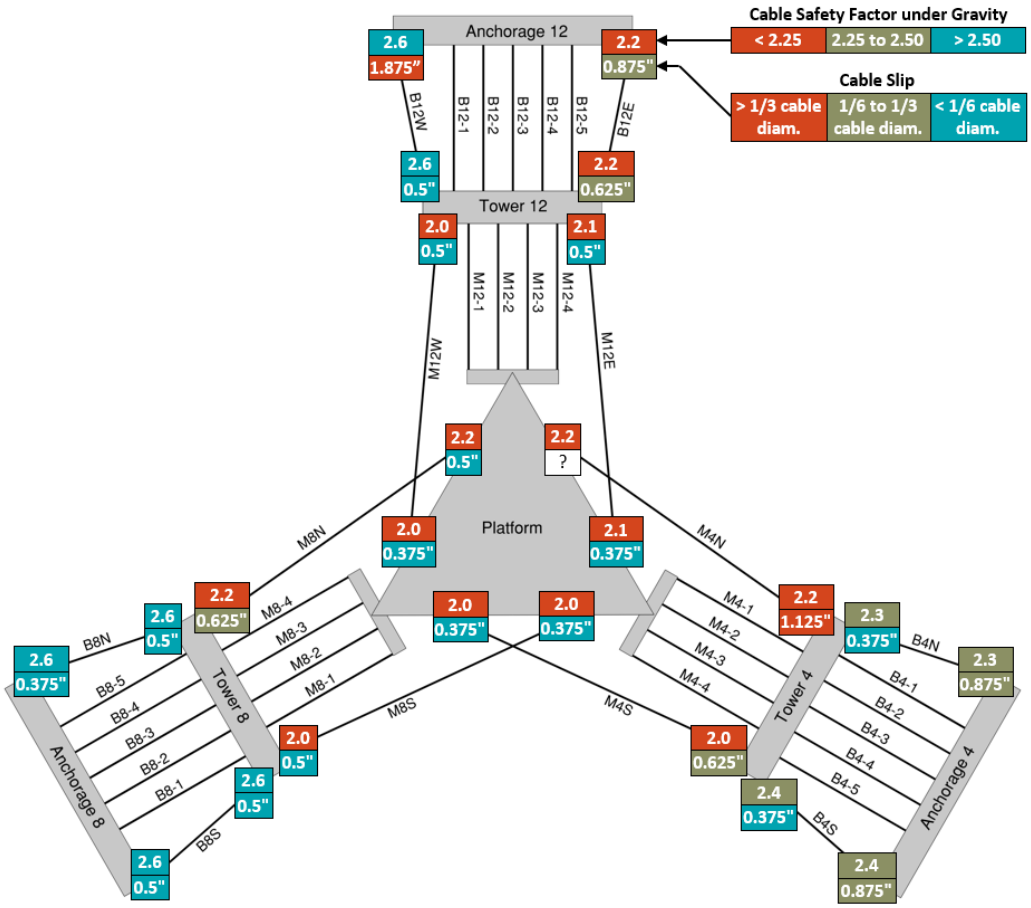

Figure 25: Cable safety factors and measured cable slips on auxiliary cable sockets.

3.2 Field Observations Between First Cable Failure and Collapse

After the first cable failure on August 10, 2020, the cable system was frequently inspected by AO until the collapse of the telescope on December 1, 2020. The inspections were visual and performed using drones to keep personnel at a safe distance from the damaged structure. While the cable ends at all three towers and three platform corners were regularly inspected, damage was only observed in the original main cables connecting to Tower 4 (M4 cables) and their sockets. Visible damage includes wire breaks, socket deformation, and full cable failures. The observed damage is summarized in this section, with additional details provided in Appendix E. The wire breaks counted in this section only include the breaks in the outer layer of wires, as breaks in the inner layers, if any, are not visible.

3.2.1 First Cable Failure

Based on the AO inspection records, the M4 cables had experienced eight wire breaks before the M4N failure (first cable failure): three breaks at each end of M4-4, and two breaks at the tower end of M4-2. The last of these wire breaks was reported in 1989.

The M4N failure caused four new wire breaks in M4-4 (Figure 26). Drone photos taken shortly after the failure show a significant deformation of the zinc casting of the M4-2 socket (Figure 26), although it is not known whether this deformation occurred before or during the M4N failure. The cracks and dip on the

casting's back surface indicate that a cylindrical casting core, whose diameter is approximately equal to the cable diameter, had moved within the socket.

In the three months between the M4N and M4-4 cable failures, the only visible changes are two new wire breaks, at the tower ends of M4-1 and M4-2.

The cable slips were measured at the tower and ground ends of the auxiliary cables after the first cable failure, and at the platform ends after the collapse (Figure 25). One-third of the cable slips exceeded the AASHTO limit of one-sixth of the cable diameter. The maximum cable slip was observed at the ground end of B12W, and had increased from 1.5 inches in May 2018 to over 1.75 inches in September 2020 (Figure 24).

1 Cable M4-1
2 Cable M4-2
3 Cable M4-3
4 Cable M4-4
5 Failed M4N_T socket
6 Chipped paint due to four wire breaks
7 Anchor block at top of Tower 4

8 Socket M4-1_T
9 Socket M4-2_T
10 Socket M4-3_T
11 Socket M4-4_T
12 Crack at back of M4-2_T zinc casting

Figure 26: Damage on original M4 cables at top of Tower 4 after first cable failure
(photos: NAIC Arecibo Observatory, a facility of the NSF).

3.2.2 Second Cable Failure

The failure of M4-4 on November 6, 2020 caused multiple new wire breaks in the remaining M4 cables: three breaks at the tower end of M4-1, a break at the tower end on M4-2, and four breaks at the platform end of M4-2. No change was observed on the other sockets. The breaks were documented shortly after the cable failure.

In the three weeks following the M4-4 failure, seven and five additional wires breaks were observed at the tower end of M4-1 and M4-2, respectively (Figure 27). The zinc casting of the M4-2 socket continued to deform with signs of crack movement at the back face of the casting (Figure 28).

1 Four wire breaks in M4-1
2 Two wire breaks in M4-2

3 11 wire breaks in M4-1
4 Seven wire breaks in M4-2

Figure 27: Wire break development after second cable failure
(photos: NAIC Arecibo Observatory, a facility of the NSF).

1 Failed end of M4-4 cable
2 Crack at back of M4-2_T zinc casting sealed before M4-4 failure

3 New crack at back of M4-2_T zinc casting due to further casting deformation

Figure 28: Evidence of socket casting core displacement after second cable failure
(photos: NAIC Arecibo Observatory, a facility of the NSF).

3.2.3 Third Cable Failure and Telescope Collapse

On December 1, 2020, the telescope collapsed immediately after the failure of cable M4-2 at the top of Tower 4, which was captured on a drone video (Figure 29). The video shows a wire break on M4-2, followed by the entire cable failure three seconds later and the failure of the remaining two M4 cables immediately after. After loss of support from Tower 4, the platform swung down away from Tower 4 and crashed into a cliff face between Tower 8 and Tower 12.

1 New wire break in M4-2
2 Complete failure of M4-2
3 Complete failure of M4-1
4 Complete failure of M4-3

Figure 29: Progressive failure of original main cables at top of Tower 4.
(still images of drone video by NAIC Arecibo Observatory, a facility of the NSF. Intermediate still images are provided in Appendix E.)

3.3 Post-Collapse Laboratory Study

Socket M4N_T, where the first cable failure occurred, was recovered on September 23, 2020 and sent to Kennedy Space Center for analysis by NESC in collaboration with WJE. The cable end that slipped out of M4N_T was recovered after the collapse in December 2020 and provided to NESC-WJE as well. The results of the M4N_T failure investigation are provided in WJE's report dated June 21, 2021.[12]

Additional sockets and cable samples were recovered from the site between December 2020 and July 2021. We worked with Socotec to perform a series of laboratory analyses and a full-scale load test. The laboratory observations are summarized in the following, and more details are provided in Appendix L through Appendix O.

3.3.1 Cable System General Condition

The original (1964) and auxiliary (1997) cables were in good general condition when the telescope collapsed. Several cable segments were taken apart to observe the condition of the inner layers of wires. As shown in Figure 30, moderate corrosion of the wires' galvanizing zinc and superficial corrosion of the wires' base steel was observed at some discrete locations. The remaining weight of galvanizing zinc was measured on wires taken from the outer layers of three original cables. After 57 years of service, more than 80 percent of the tested wires still had more galvanizing zinc than required for new Class A wires

[12] Wiss, Janney, Elstner Associates (WJE). *Auxiliary Main Cable Socket Failure Investigation*. June 21, 2021. Draft report provided by WJE.

per the standard applicable to the telescope's auxiliary cables.[13] Three fractured wires due to the development of stress-corrosion cracks were discovered in the inner layers of one cable sample.

Setting aside the cable slips and casting deformations, the original and auxiliary cable sockets were in good condition. Corrosion was observed on the zinc casting surfaces that were not in tight contact with the socket's steel, but this corrosion had no impact on the socket's strength.

Additional details on the cable and socket general conditions are provided in Appendices L and M.

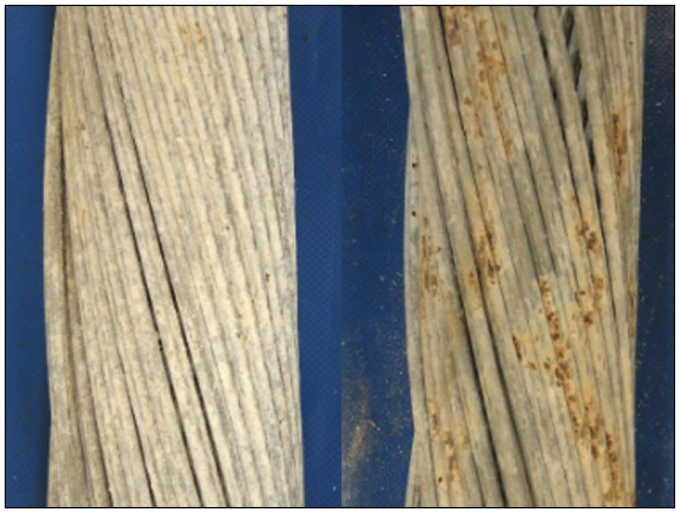

Figure 30: Oxidation of galvanizing zinc (left) and wire steel (right) in second wire layer of an original M4 cable *(photos: Socotec).*

Figure 31: Surface corrosion of B12W_G socket casting *(photo: Socotec).*

3.3.2 Wire and Zinc Properties

The auxiliary cables were specified by the design drawings to meet the ASTM A586 standard.[13] While no standard was specified for the original cables, they were required to have the same strength as prescribed in ASTM A586. Wire specimens taken from three original cables were tested to failure, and all specimens met the mechanical properties of ASTM A586 (160 ksi yield stress, 220 ksi ultimate stress, and four percent elongation in 10 inches). A 15-foot segment of auxiliary backstay cable was also load-tested, and the cable was able to carry a tension higher than the cable's Minimum Breaking Strength, which corresponds to the ultimate stress requirement of ASTM A586. The wire and cable tests are respectively detailed in Appendix L and Appendix N.

Zinc samples were taken from one original socket and three auxiliary sockets for chemical composition and tensile load testing. Three samples, including one from an original socket and two from auxiliary sockets, were evaluated for chemical composition. All three samples met the 99.5 pure zinc requirement of the ASTM B6 standard[14] prescribed for the original socket castings. Tensile tests were performed on 10 zinc coupons, and the ultimate tensile stress ranges from 3 ksi to 12 ksi depending on the coupon

[13] American Society for Testing and Materials (ASTM). *ASTM A586-18. Standard Specification for Metallic-Coated Parallel and Helical Steel Wire Structural Strand.* 2018.

[14] American Society for Testing and Materials (ASTM). *ASTM B6-18. Standard Specification for Zinc.* 2018.

locations. The coupons extracted near the front of the casting (smaller diameter end) had a higher ultimate tensile stress than the coupons taken near the back of the casting (larger diameter end). This is consistent with the distribution of grain sizes in the casting. A smaller grain size was observed at the front of the sockets and is likely due to faster cooling of the zinc during the socketing process. In the casting of an auxiliary socket, it was also observed that the galvanizing zinc had not been removed from the wires prior to socketing. Details of the tests performed on the zinc castings are provided in Appendix M.

3.3.3 Socket Wire Broom Geometry

During socketing, the cable's wires are spread out inside the socket to form a broom before pouring zinc. The casting of socket M4-4_T (second cable failure) and four auxiliary sockets (M8N_T, B4N_G, B4S_G, B12W_G) that exhibited different degrees of cable slip were cut in the transverse direction to observe the wire broom. As shown in Figure 32, the wire brooms are irregular, and differences in wire distribution between the center and perimeter of the casting can be observed. Additional observations and results on the wire broom geometry are provided in Appendix M.

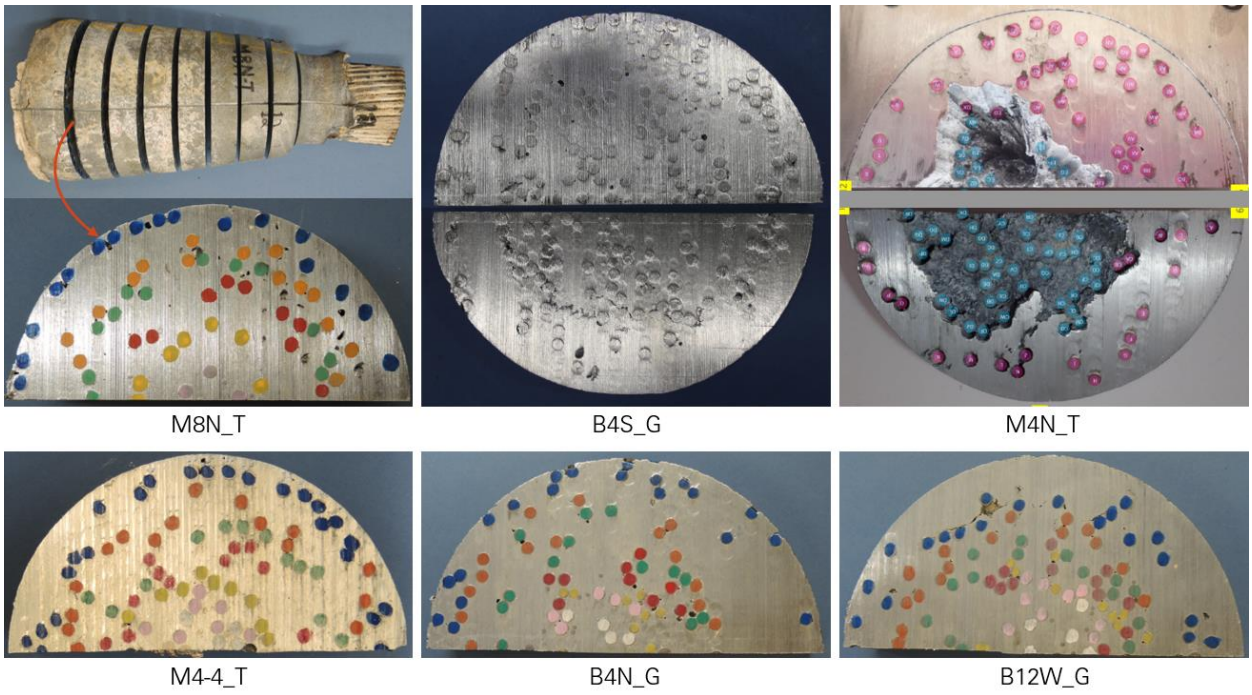

Figure 32: Wire distribution at back of socket castings *(M4N_T photos: WJE[15]; other photos: Socotec).*

3.3.4 Socket Failure Mechanism

The zinc casting of sockets that failed or experienced significant cable slips were cut open longitudinally, and three key features were observed (Figure 33). First, a displaced inner core was observed within the casting of every socket. This core is shaded in Figure 33 for illustration and can be approximated as a cylindrical volume centered on the socket's axis and with a diameter equal to the smaller diameter of the

[15] Wiss, Janney, Elstner Associates (WJE). *Auxiliary Main Cable Socket Failure Investigation.* June 21, 2021. Draft report provided by WJE.

socket's cavity. Second, ruptured outer wires were observed in the sockets that failed. And third, outer wires were observed to have slipped within the zinc outside of the displaced core in the socket that exhibited the largest cable slip but did not fail (B12W_G).

The surfaces of the longitudinal cuts of the socket's castings were macro-etched to observe the grain structure. Elongated deformation of the zinc grains was observed between wires near the surface of the displaced casting core (Figure 34).

The inner core and the inner wires completely pulled out of the first socket that failed (M4N_T). In the second socket that failed (M4-4_T), the core remained in the socket after shifting significantly and the remaining wires ruptured outside of the core. As a result, the two failed sockets look different yet both failures started inside the socket with a displacement of the core and the rupture of outer wires (Figure 35).

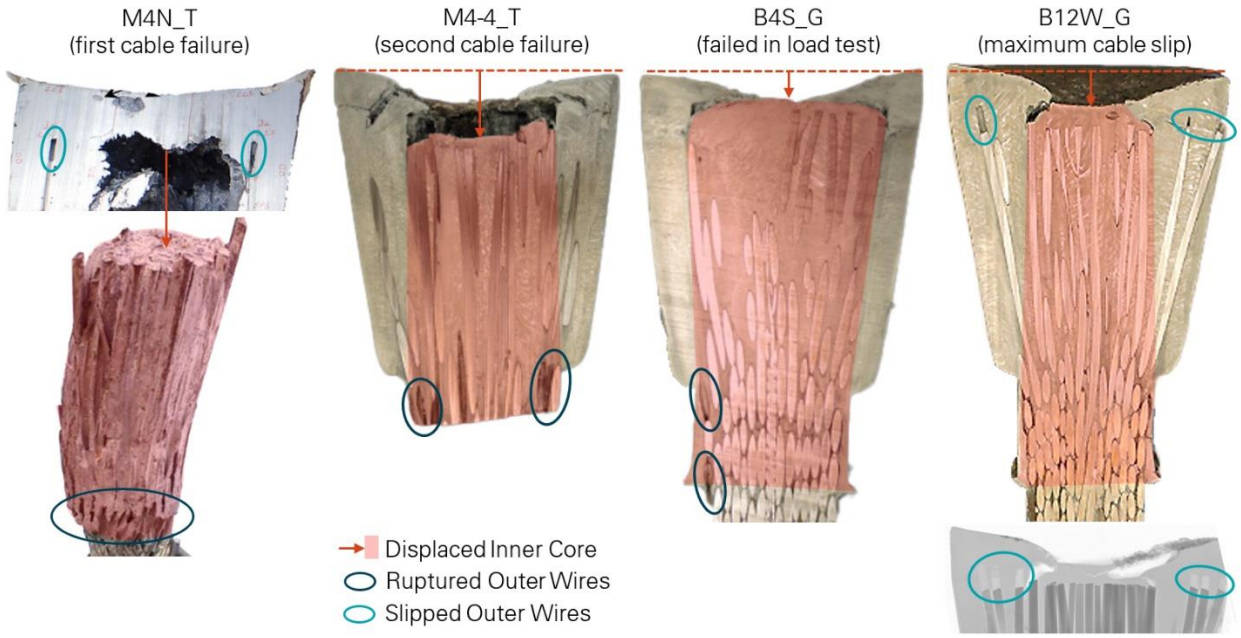

Figure 33: Observations in distressed sockets *(M4N_T photos: WJE[16]; B12W_G radiograph: Adrian Brügger, Columbia University - Oak Ridge National Laboratory; other photos: Socotec).*

[16] Wiss, Janney, Elstner Associates (WJE). *Auxiliary Main Cable Socket Failure Investigation.* June 21, 2021. Draft report provided by WJE.

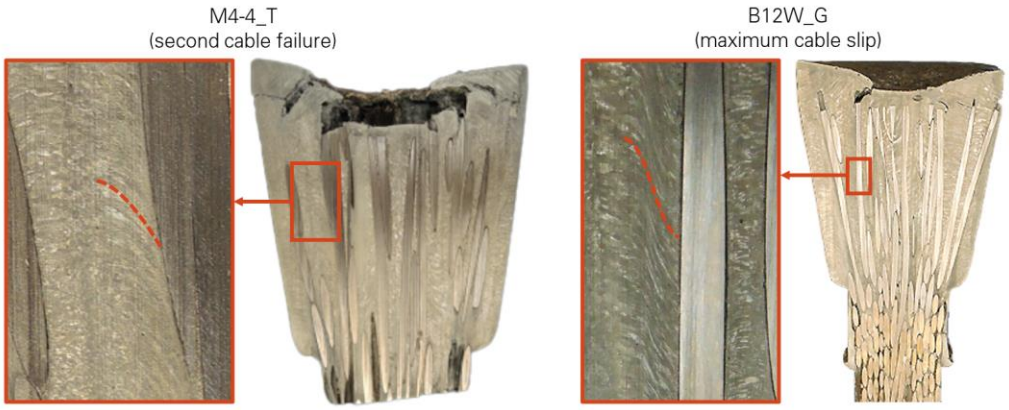

Figure 34: Evidence of grain flow near surface of displaced core in socket zinc casting *(photos: Socotec).*

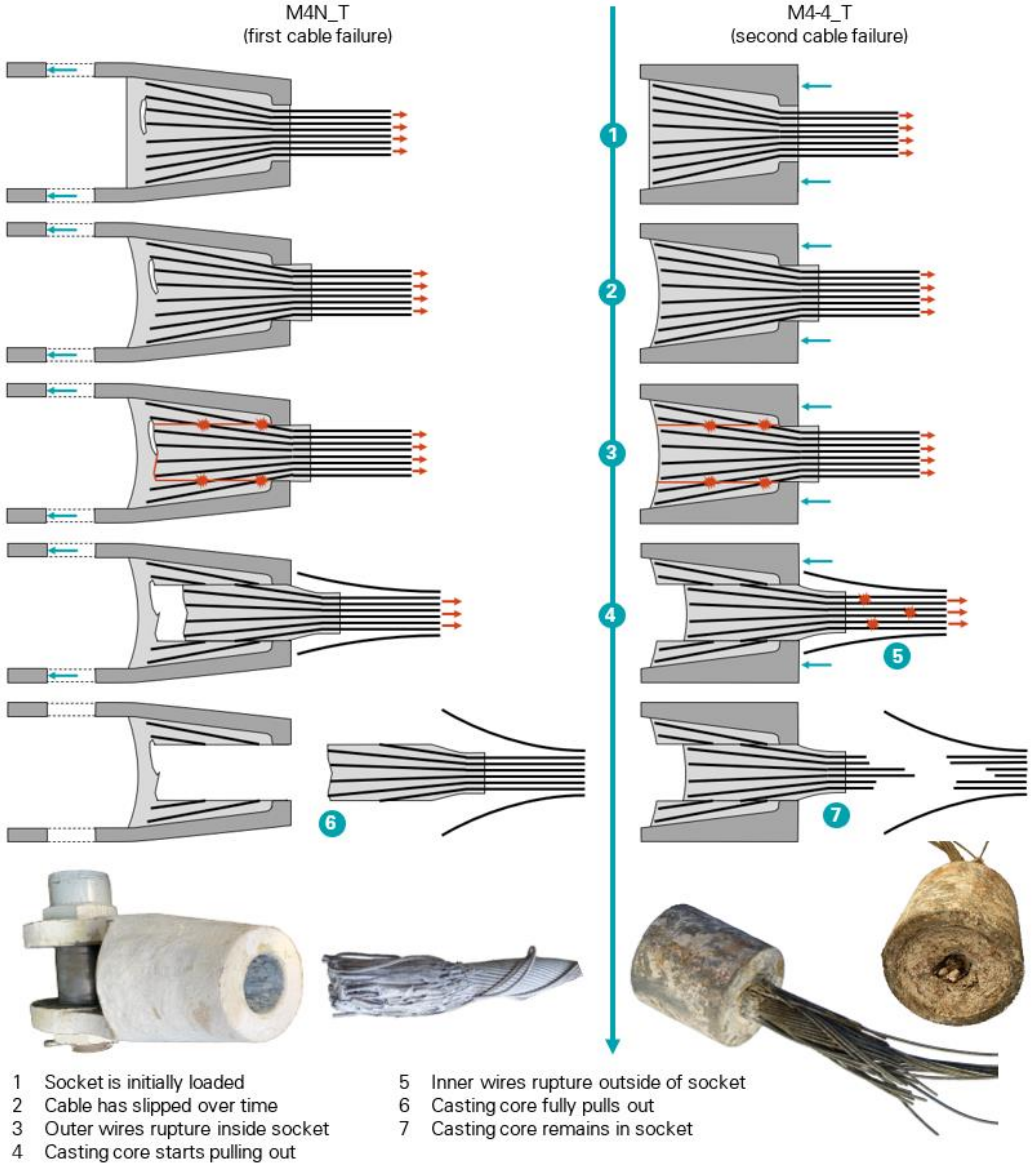

Figure 35: First two socket failures
(M4N_T socket photo: NAIC Arecibo Observatory, a facility of the NSF; M4-4_T photos: Socotec).

4.0 Analysis

A set of analyses was performed on mathematical and digital models of the telescope and sockets to interpret the field and laboratory observations and further investigate the socket failures. The forces in the sockets during telescope operation and extreme environmental events, such as hurricanes and earthquakes, were determined first. The sockets' behavior and failures under those forces were then analyzed.

4.1 Socket Force Analysis

The forces in the telescope's sockets were determined through analysis of the entire telescope structure under a variety of loads representing the telescope's typical conditions and extreme environmental events. The objective was to determine the maximum forces that the cable sockets experienced in each condition, along with the amplitude and frequency of the force cycles.

4.1.1 Method and Assumptions

The cable tensions were determined using finite element (FE) analysis models of the original and upgraded telescope structure (Figure 36). The models include the telescope's suspended structure, towers, waveguide, and the main, backstay and tiedown cables. The Gregorian and line feed(s) are modeled as loads on the suspended structure, and the cables are modeled as special tension-only elements that capture the cable's sag and associated stiffness reduction. The cable properties are modeled per the ASTM A586 standard prescribed for the telescope's cables. For the towers, the concrete properties are based on test results of concrete cores taken from the towers after the collapse. Additional information on the analysis models is provided in Appendix F.

The sockets transfer the cable tensions to the telescope's platform, towers, and anchorages. The socket forces are therefore equal to the cable tensions obtained from the FE models. Since the main and backstay cables are inclined, the tension is slightly different at the two ends of each cable. However, because the cables are highly tensioned, the relative difference in tension between the ends of any cable is less than two percent. This difference is considered by reporting the average cable tension over the length of the cable.

No design capacity is known for the sockets of the telescope. Spelter sockets are typically expected to develop the full Minimum Breaking Strength of the connected cables based on proof load tests by the cable manufacturers. As a measure of the stress level in a cable and the connected socket, the cable's safety factor (SF) is used in our analysis. As noted earlier, the safety factor is defined as the ratio of the cable's Minimum Breaking Strength to the cable's actual tension. The normalized stress range (NSR) is used to evaluate how much a cable's tension fluctuates under operational loads and temperature, wind, and seismic effects. The normalized stress range is defined as the ratio of the cable's peak-to-peak tension change to the cable's Minimum Breaking Strength.

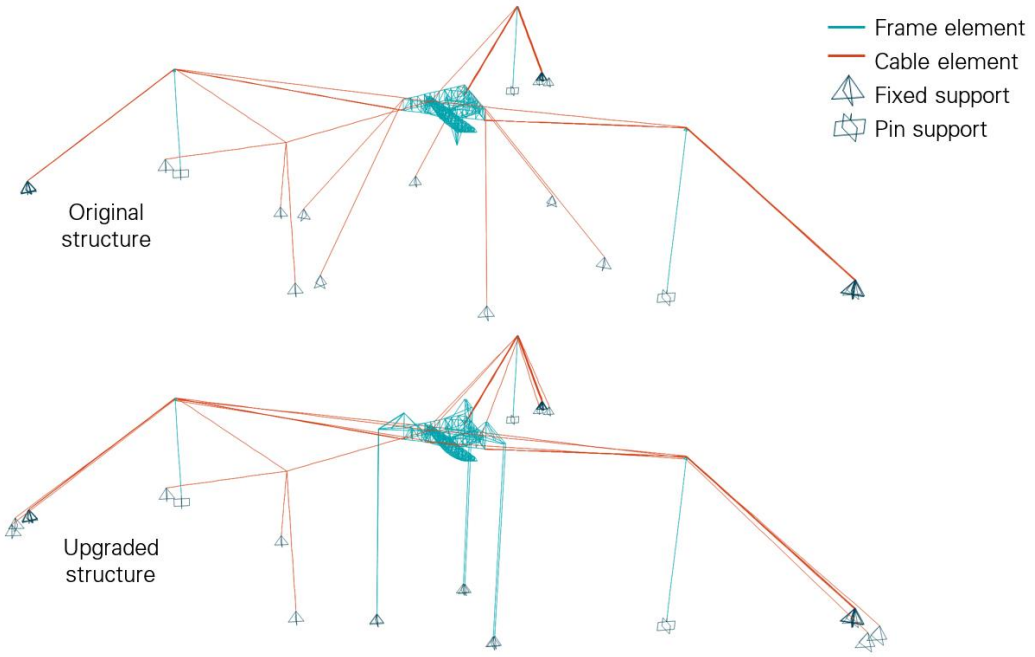

Figure 36: FE models of original and upgraded telescope structure.

4.1.2 Analysis of Typical Conditions

For the majority of its lifetime, the telescope was primarily subjected to three load effects: its own weight, the movement of the azimuth arm, Gregorian and line feed(s) during operation, and the day-night temperature cycle.

Telescope Weight

The weight of the original and upgraded structures, respectively 1,225 kip and 1,825 kip, is considered in the analyses. Before applying any additional load (seismic, wind, etc.), the FE model is initialized in a baseline state where the cable tensions under the structure's weight are known. For the original structure, the baseline tensions are the cable tensions determined by AW before the second upgrade. To determine the baseline tensions in the upgraded structure, we used the cable sag survey performed in August 2020 after the first cable failure, and we removed the effect of the cable failure through analysis. This process is detailed in Appendix G.

Telescope Operation

To simulate the movement of the azimuth arm, Gregorian and line feed during operation of the upgraded telescope, we applied moving loads on the fixed platform in the FE model. The maximum changes in cable tension due to telescope operation were determined by simulating a full rotation of the azimuth arm with the Gregorian fully extended out and the line feed pointing straight down, which maximizes the load imbalance on the fixed platform. Results are shown in Figure 37 for representative auxiliary cables, and the largest normalized stress range due to telescope operation is 3.8 percent. We also simulated multiple days of actual telescope operation based on logs of the azimuth arm, Gregorian and line feed positions. From the simulation results, the number and magnitude of the cable tension cycles were determined statistically. The number of cycles is in the order of five cycles per day during standard

telescope operation, and 90 cycles per day when the telescope is used for atmospheric studies. In both cases, the maximum normalized stress range is less than four percent. The telescope operation analysis is detailed in Appendix H.

Temperature Cycles

On an average night, the total tension in the tiedowns of the upgraded structure increases by 60 kip as jacks pull down on the tiedowns to keep the platform at a constant elevation (Figure 38). From the FE model, we determined that the platform elevation remains constant under the additional tiedown tension if the temperature of the platform and cables decreases by 15.8°F. This result is consistent with the 12.3°F average day-night temperature difference measured in the air on the telescope's platform. The combined effect of the additional tiedown tension and temperature drop is a three percent increase in the main and backstay cable tensions. We applied the same 15.8°F temperature drop to the FE model of the original structure, and observed a 2.5 percent increase in cable tensions. For both structures, these fluctuations correspond to normalized stress ranges of less than two percent. The temperature analysis is detailed in in Appendix I.

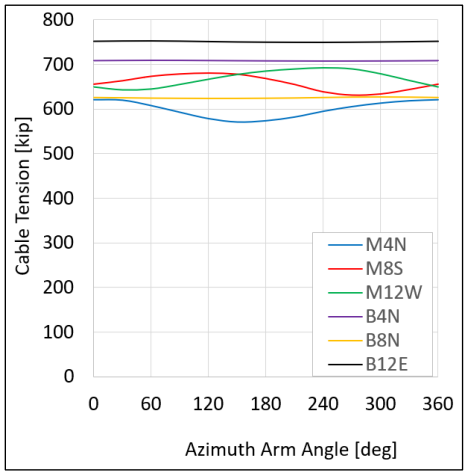

Figure 37: Tension in representative auxiliary cables during full revolution of azimuth arm with Gregorian fully extended out.

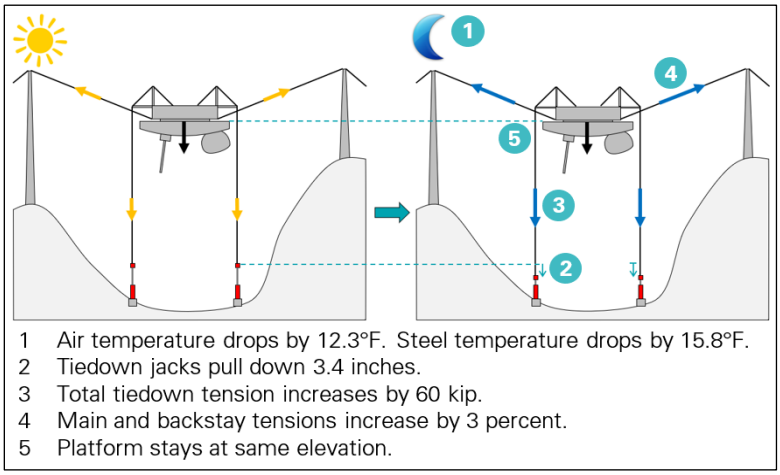

Figure 38: Impact of average day-night temperature cycle on upgraded telescope structure.

4.1.3 Analysis of Extreme Environmental Events

The loads induced by windstorms and earthquakes are transient, and their effect on the telescope was determined through dynamic analysis in the FE models. The telescope's structure tends to respond dynamically according to its fundamental modes of vibration, which combine movement of the platform and bending of the towers. The first modal period is 2.3 seconds for the original structure, and 3.0 or 4.5 seconds for the upgraded structure depending on whether the tiedowns are taut or released. We considered a damping ratio of one percent for the structure's global modes, which we estimated from the vibrations recorded in the tiedown tensions during the first cable failure. The structure's modal properties are detailed in Appendix F.

Windstorms

To determine the sustained and turbulent loads induced by wind on the telescope's platform, we performed a series of computational fluid dynamics (CFD) analyses (Figure 39). The results were then calibrated with actual wind speed time histories recorded on the platform, and applied to the FE models of the telescope. Through this process, we simulated the structure's response to 2.5 hours of typical ambient wind, and to the 2.5 hours leading up to the peak of Hurricane Maria.

Ambient wind causes a normalized stress range of less than one percent in the cables, with approximately 28,000 cycles per day. In the wind conditions of Hurricane Maria, the most significant wind gusts result in a normalized stress range of up to four percent in the original structure, and eight percent in the upgraded structure. The impact is more significant in the upgraded structure primarily because of the down-drag wind force acting on the Gregorian. The impact of Hurricane Maria on some of the cables of the upgraded structure is shown in Figure 40. The wind analysis is detailed in Appendix J.

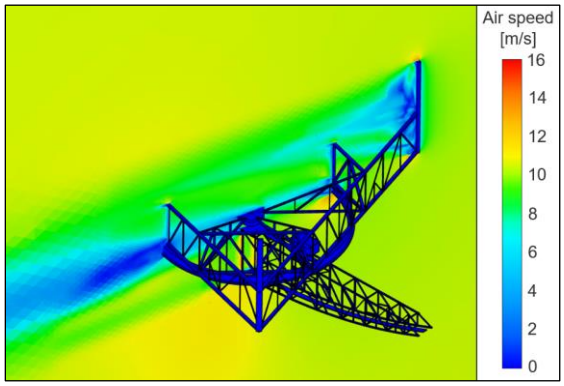

Figure 39: Computational fluid dynamics analysis of platform for 10 meter per second (22.4 mph) wind.

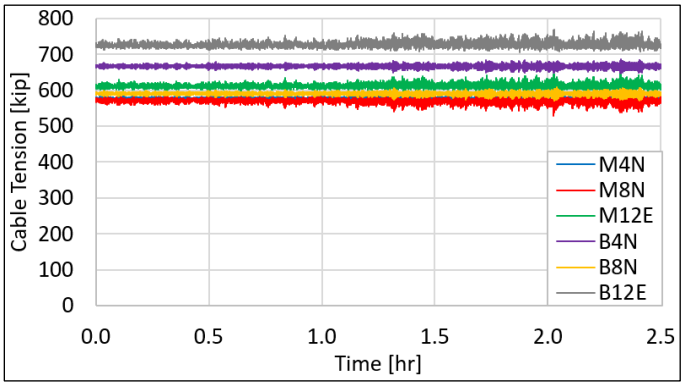

Figure 40: Tension in representative auxiliary cables during peak of Hurricane Maria.

Earthquakes

To evaluate the potential impact of seismic activity on the cable tensions, we analyzed the telescope's response to two significant earthquakes that occurred in January 2020 and the ground accelerations of which were recorded at the Observatory. The response spectrum for the larger earthquake, of moment magnitude 6.4, is shown in Figure 41. The response spectrum indicates that the earthquake primarily affects stiffer structures with periods shorter than one second, while the telescope's first global modes have periods greater than two seconds. In the FE models, we applied the recorded ground accelerations with a time delay between the different towers and cable anchorages based on the estimated shear wave velocity at the site. Considering both earthquakes and a range of shear wave velocities, the maximum normalized stress range is eight percent in the original structure and five percent in the upgraded structure. The impact of the larger earthquake on some of the cables of the upgraded structure is shown in Figure 42. The earthquake analysis is detailed in Appendix K.

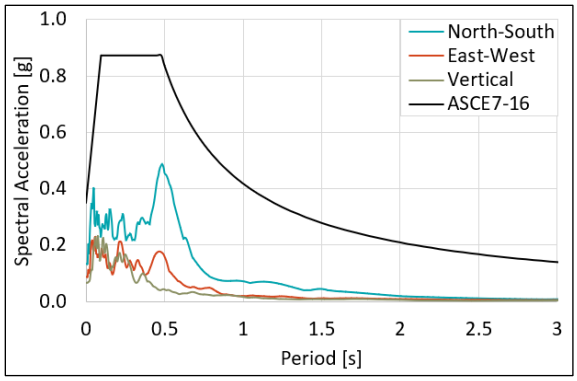

Figure 41: Response spectra of ground accelerations measured at AO during January 7, 2020, M6.4 earthquake, compared to design response spectrum.

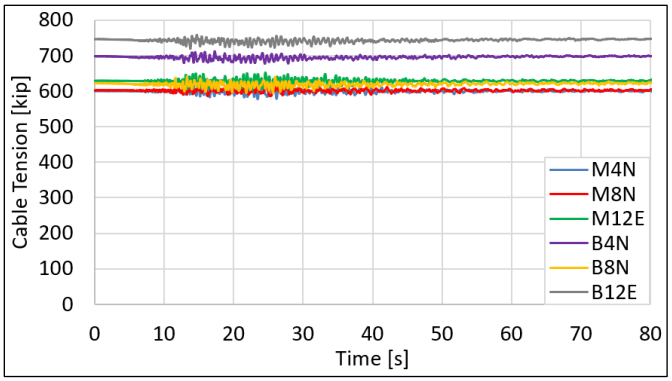

Figure 42: Tension in representative auxiliary cables during January 7, 2020, M6.4 earthquake

4.1.4 Analysis of Cable Failure Events

The two cable failures that occurred before the collapse caused tension redistribution among the remaining cables. We performed an analysis of the cable tensions throughout the 2020 events, and the results for the main cables are summarized in Figure 43 (cable tensions) and Figure 44 (cable safety factors).

The cable tensions were first measured on site by surveying the cable sags when the telescope was stowed after the first cable failure (M4N). Starting from these known tensions in the FE model, we simulated the cable failures and telescope movements that occurred before and after the sag survey.

By comparing the position of the platform before and after the first cable failure (M4N), we determined that cable M4N carried a tension of 600 kip when it failed. This corresponds to a safety factor of 2.2. The M4N failure had a significant impact on the four original M4 cables, decreasing their safety factor from 2.0 to 1.6. After one of these cables failed (M4-4), the safety factor of the remaining three M4 cables dropped to 1.3. The collapse started with the failure of another M4 cable (M4-2). If the structure had stabilized after this third cable failure, the safety factor in the remaining two M4 cables would have been less than 1.0.

The M4N failure had a more significant impact on the redistribution of cable tensions than the M4-4 failure. Since M4N was an isolated cable, its failure resulted in an imbalance in the suspended structure. The suspended structure rotated to reach a new balance state resulting in increased and decreased tensions in the rest of the cable system. M4-4 ran in parallel with three other original M4 cables. As a result, when M4-4 failed, its tension was primarily redistributed to the three other M4 cables.

The impact of the 2020 events on the cable tensions is detailed in Appendix G.

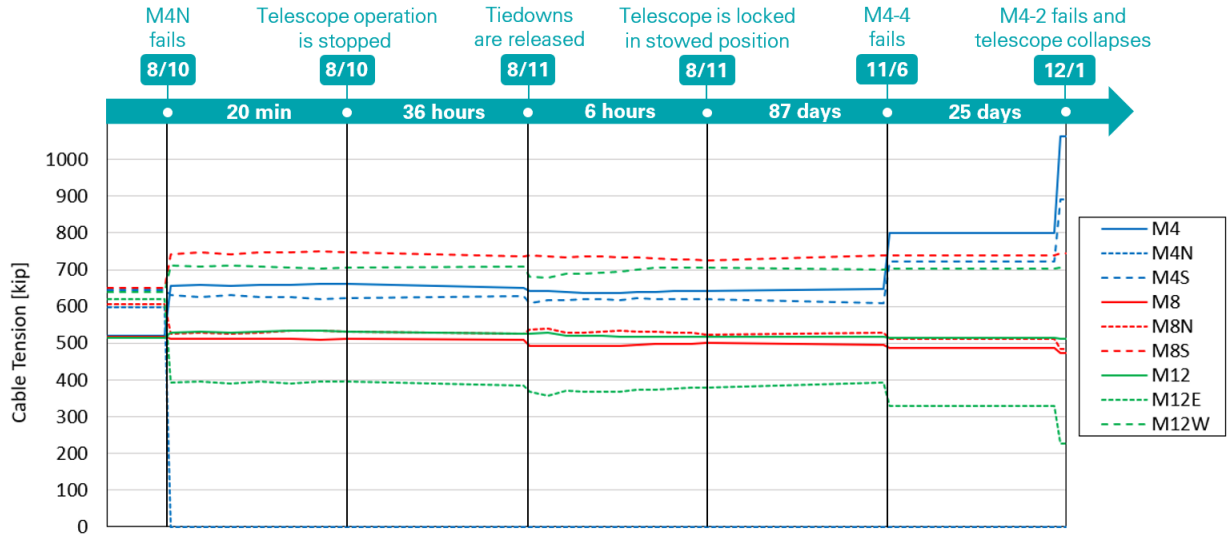

Figure 43: Tension in main cables between first cable failure and collapse.

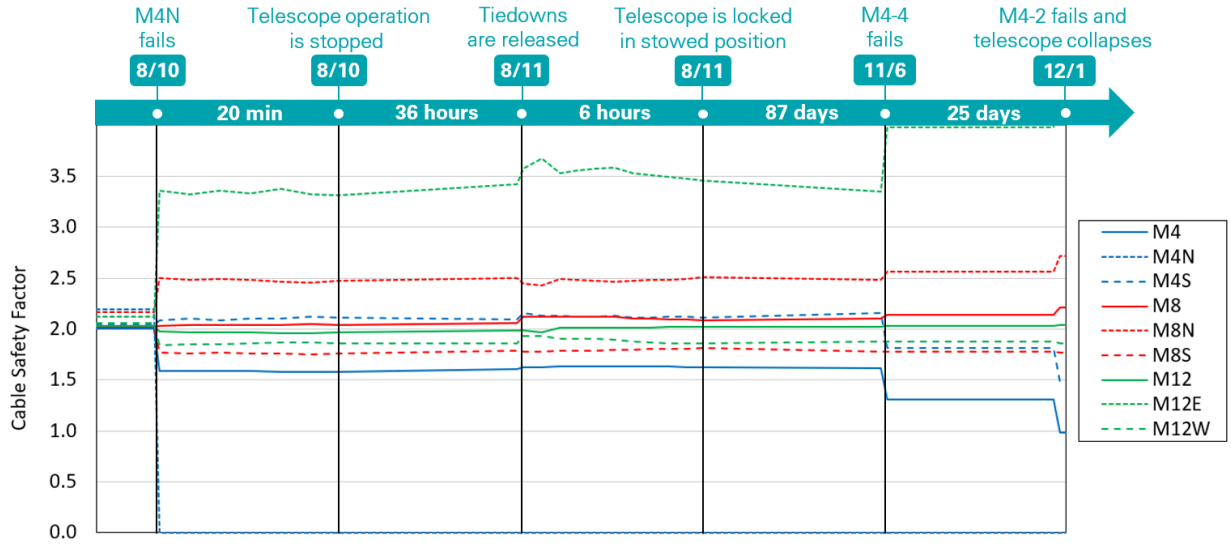

Figure 44: Safety factor in main cables between first cable failure and collapse.

4.1.5 Summary

The safety factors and normalized stress ranges under different loading conditions are summarized in Table 4 for the cables that failed prior to collapse (M4, M4N), the cable where the maximum slip was observed at a socket (B12W), and the average of all mains and backstays. For transient loading conditions (telescope operation, Hurricane Maria, and 2020 earthquakes), the safety factor is calculated based upon the maximum cable tension experienced. Every loading condition includes the weight of the telescope.

The results show that before and after the second upgrade, the safety factors were not significantly affected by the telescope operation or the wind and seismic events. The cable failures in 2020 reduced the safety factors in the M4 cables from 2.1 to as low as 1.3 because the tension in the remaining cables

increased after the first two cables failed. The safety factor in cable B12W, whose ground-end socket exhibited the largest cable slip, was 17 percent higher than that in the average backstay. The normalized stress ranges during transient loading conditions are under seven percent, which is not large enough to cause a fatigue issue.

Table 4: Minimum safety factor (SF) and normalized stress range (NSR) in selected cables and on average over all main and backstay cables

		Cable M4[A]		Cable M4N[B]		Cable B12W[C]		Average Main		Average Backstay	
		SF	NSR	SF	NSR	SF	NSR	SF	NSR	SF	NSR
Before Second Upgrade	Telescope Stowed	2.1	-	-	-	-	-	2.1	-	2.3	-
	Temperature Cycle	2.1	1.2%	-	-	-	-	2.1	1.2%	2.3	1.1%
	Telescope Operation	2.1	0.0%	-	-	-	-	2.1	0.0%	2.3	0.0%
	Hurricane Maria[D]	1.9	4.0%	-	-	-	-	1.9	4.1%	2.1	3.7%
	2020 Earthquakes[D]	2.0	2.6%	-	-	-	-	2.0	4.4%	2.2	5.0%
	Worst Combination[E]	1.9	-	-	-	-	-	1.9	-	2.1	-
After Second Upgrade	Telescope Stowed	2.0	-	2.2	-	2.6	-	2.0	-	2.2	-
	Temperature Cycle	1.9	1.6%	2.2	1.2%	2.5	1.2%	2.0	1.5%	2.2	1.3%
	Telescope Operation	1.9	1.9%	2.1	3.8%	2.6	0.2%	1.9	2.5%	2.2	0.1%
	Hurricane Maria	1.9	6.0%	2.1	4.9%	2.5	3.8%	1.9	6.5%	2.1	5.0%
	2020 Earthquakes	1.9	3.9%	2.1	3.4%	2.5	2.8%	1.9	3.8%	2.1	2.9%
	Worst Combination[E]	1.8	-	2.0	-	2.4	-	1.8	-	2.0	-
After First Cable Failure	After M4N Failure	1.6	-	-	-	2.7	-	2.0	-	2.3	-
	After M4-4 Failure	1.3	-	-	-	2.7	-	2.0	-	2.3	-
	After M4-2 Failure[F]	1.0	-	-	-	2.7	-	2.2	-	2.4	-

[A] M4 is a set of four cables including M4-4 (second cable to fail) and M4-2 (third cable to fail, triggering collapse).
[B] Cable M4N is the first cable to fail.
[C] The largest cable slip was observed at the ground-end socket of cable B12W.
[D] This event occurred after the second upgrade but is used as representative extreme event for analysis.
[E] Worst case between (operation + earthquake) and Hurricane Maria.
In both cases, the temperature is assumed to be 10°F lower than the daytime average.
[F] Static analysis, assuming that structure stabilized after M4-2 failure.

4.2 Socket Strength Analysis

Three of the telescope's sockets failed and other sockets showed significant cable slip while the tension in the connected cables was less than their Minimum Breaking Strength. We investigated the cable slips and socket failures through calculations, finite element analysis, and a full-scale load test to failure. The socket behavior inferred from our investigation is presented first, followed by the supporting analyses.

4.2.1 Socket Behavior

In a zinc-filled spelter socket, the cable tension is transferred to the socket through a zinc casting. In the telescope's sockets that failed or exhibited the largest cable slip, we observed the displacement of a cylindrical *core* within the casting. If we consider the forces acting on this core (Figure 45), the cable tension is resisted by shear stress on the core surface and/or tension in the wires that cross through the

core surface. These wires are referred to as the *crossing wires*, and are typically part of the outer layers of the cable.

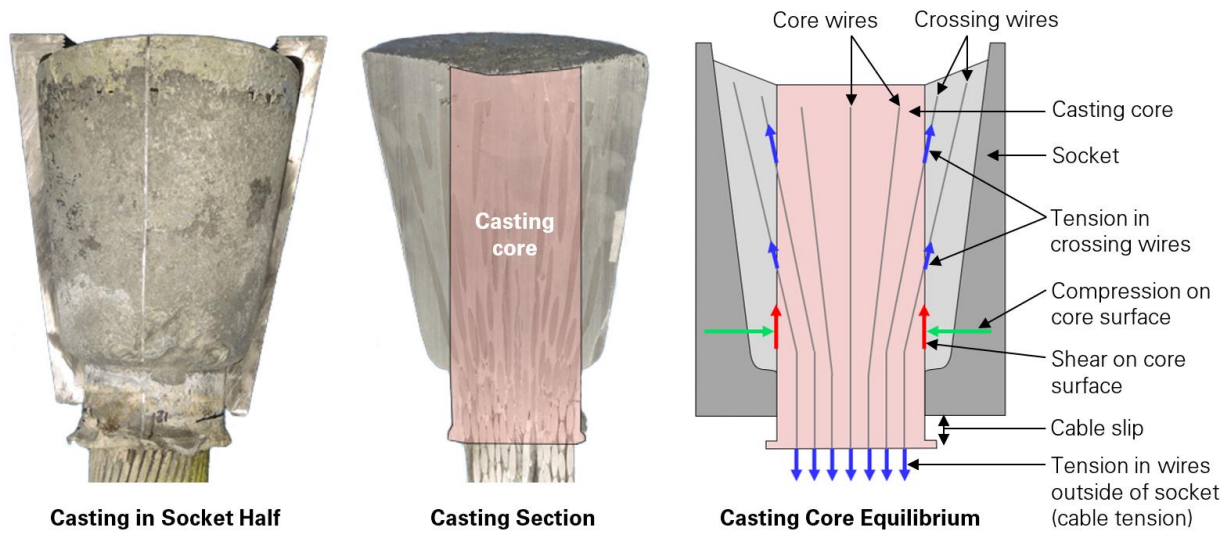

Figure 45: Equilibrium of socket casting core *(photos: Socotec).*

The cable slips observed on the telescope's sockets are the result of two mechanisms. First, the pre-stretching and/or initial loading of the cable caused the zinc casting to shift and deform to become tightly wedged into the socket. This is expected to occur in any zinc-filled spelter socket, and to result in a relatively small cable slip (up to one sixth of the cable diameter per AASHTO[17]). In the telescope's sockets that were cut open, we observed that the cable slip had increased due to a displacement of the casting's core. This second mechanism caused the large cable slips observed on the telescope's sockets, and is the focus of our analysis.

For the core to displace within the casting, a compatible shear movement must occur between the core and the rest of the casting. This movement may occur through plastic deformation or creep of the zinc near the core surface, which we refer to as *zinc flow*. Zinc flow can only occur if a shear stress is acting on the core surface. In other words, the core cannot displace when the full cable tension is resisted by the crossing wires, such that there is no shear stress on the core surface.

A key parameter affecting the cable slip is therefore the wire broom geometry, which includes the number of crossing wires, their length outside of the core, and their orientation with respect to the core surface. If a cable was not broomed out, the cable tension could only be resisted in shear on the core surface (Figure 46). This would result in rapid zinc flow, zinc shear failure and/or cable slip from the zinc. In any case, the cable would slip out of the socket under any substantial tension. Conversely, when the cable is broomed out, the crossing wires stretch and pick up more tension as the cable slips due to zinc flow (Figure 47). The increased tension in the crossing wires decreases the shear stress on the core, which slows down and effectively stops the zinc flow and cable slip. This, however, is only possible if the crossing wires have a sufficient capacity collectively to resist the full cable tension.

[17] American Association of State Highway and Transportation Officials (AASHTO). *AASHTO M 277-06. Standard Specification for Wire Rope and Sockets for Movable Bridges*. 2019.

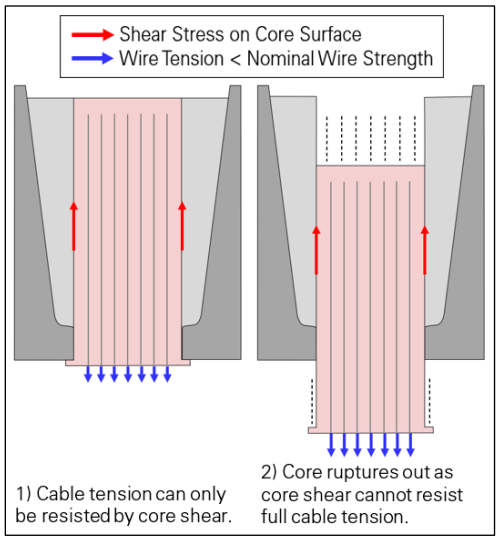

Figure 46: Case 0 – Core rupture in absence of wire broom.

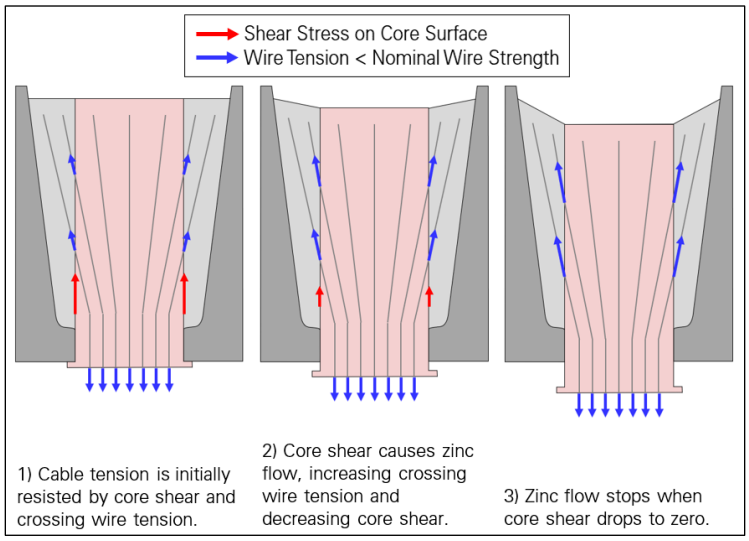

Figure 47: Case 1 – Limited cable slip when crossing wires can resist full cable tension.

The tensile behavior of a steel wire is elastoplastic and simplified as elastic-perfectly plastic in the following to describe socket behavior. The maximum tension that a wire can resist before yielding and eventually rupturing is referred to as the *nominal wire strength*. A crossing wire is considered *fully developed* if its bond and friction with the zinc outside of the core is sufficient to resist the nominal wire strength without slipping. Conversely, a crossing wire that slips outside the core under a tension lower than the nominal wire strength is considered *partially developed*.

A socket where the crossing wires cannot resist the full cable tension is bound to fail, and the socket's failure mode depends on whether the crossing wires are fully or partially developed. If the crossing wires are fully developed (Figure 48), they continue to stretch near the core surface as the zinc continues to flow. Some of the wires rupture when they reach their ultimate tensile strain, which increases core shear and accelerates zinc flow, leading to more wire ruptures and, eventually, to *core rupture*. If the crossing wires are partially developed, they can slip in parallel with the core instead of rupturing, leading to *core flow-out* (Figure 49). In this case, the cable continues to gradually slip out of the socket. Complete slip-out or rupture of the core will eventually occur as the contact length between cable and socket decreases and/or the zinc's strain becomes too large. Macroscopically, the socket failure is more brittle when the crossing wires are fully developed, and more ductile when the crossing wires are partially developed. Actual sockets may include both fully and partially developed crossing wires and therefore exhibit intermediate behaviors and failure modes (Figure 50).

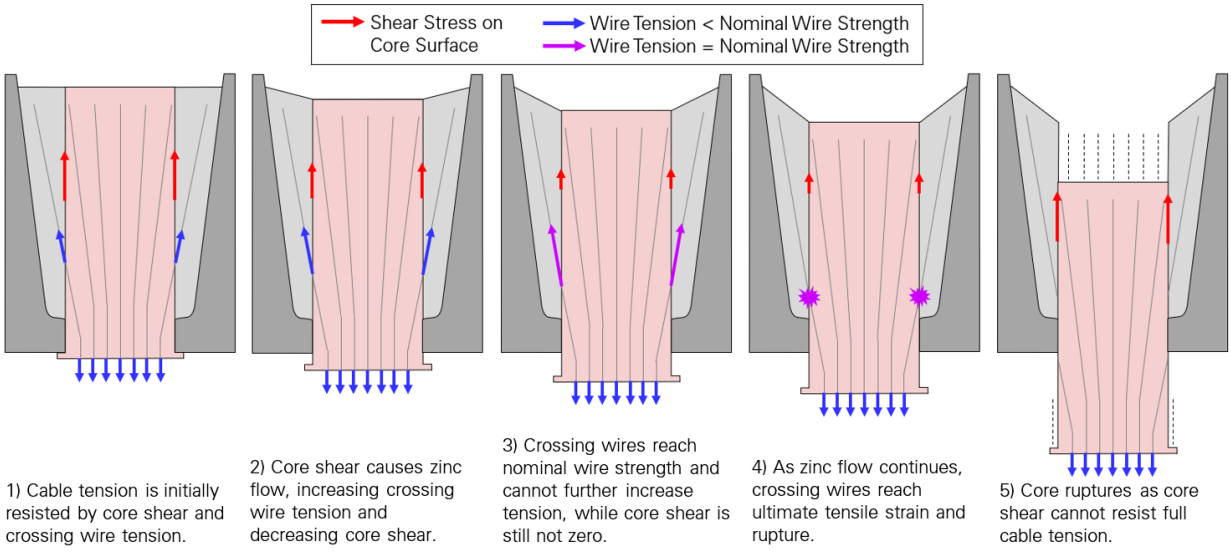

Figure 48: Case 2 – Core rupture when crossing wires cannot resist full cable tension and are fully developed.

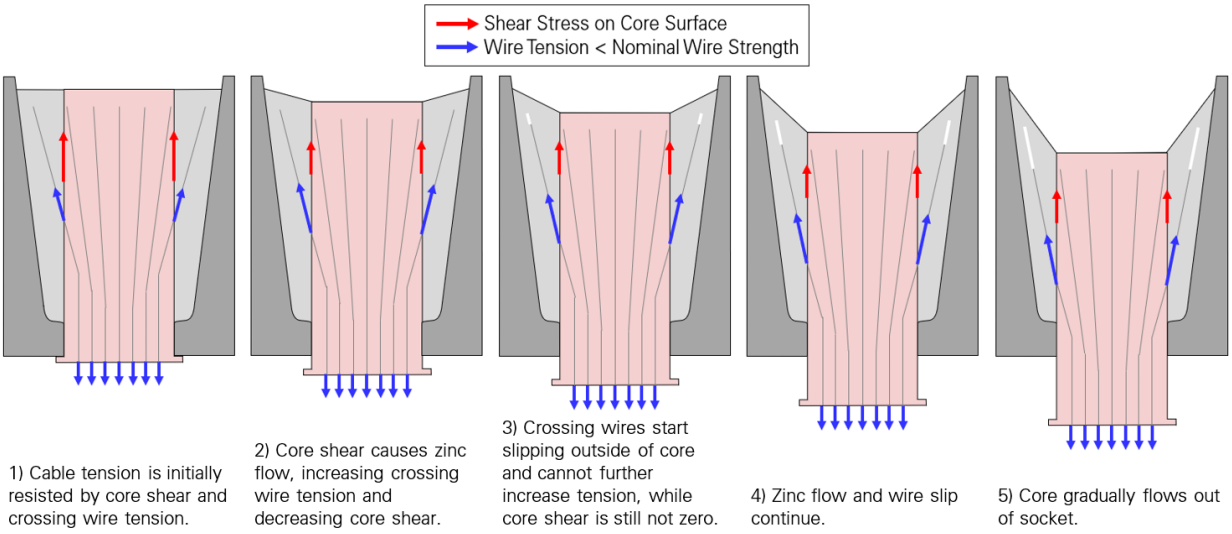

Figure 49: Case 3 – Core flow-out when crossing wires cannot resist full cable tension and are partially developed.

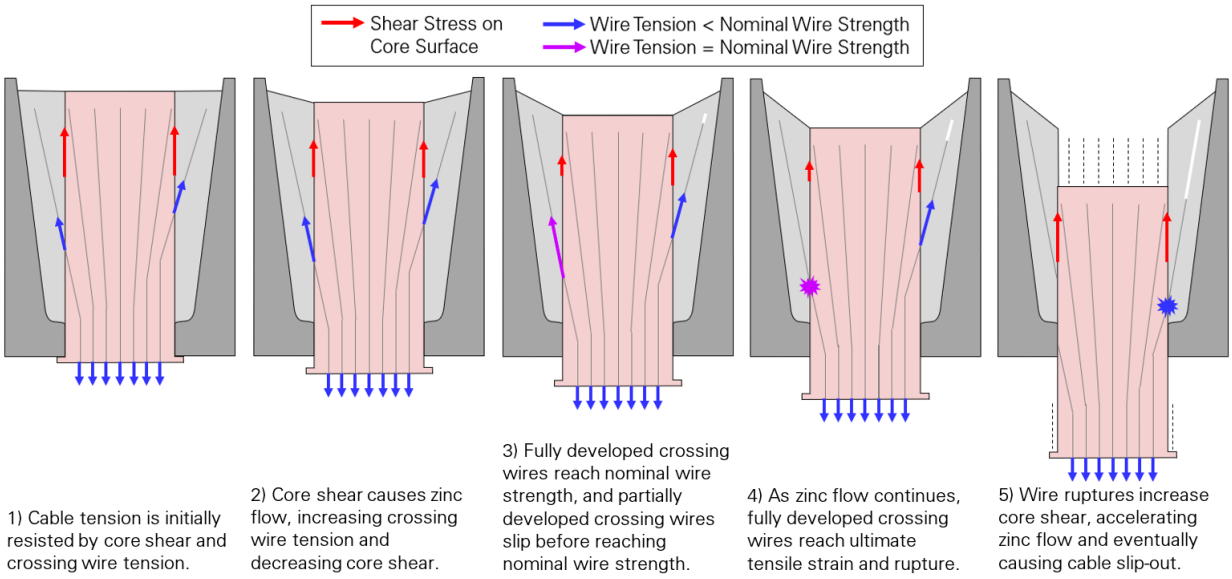

Figure 50: Case 4 – Socket failure when crossing wires cannot resist full cable tension and include both fully and partially developed wires.

4.2.2 Finite Element Analysis

The socket behavior presented above is consistent with the results of a series of analyses performed on finite element (FE) models of zinc-filled spelter sockets. The models and results are summarized in the following, and detailed in Appendix P.

Model

The baseline FE model represents an auxiliary backstay ground-end socket with a uniform wire broom, where the wires are evenly spaced in the radial and circumferential directions (Figure 51). Such wire broom has a 60-degree axisymmetry, and therefore the model is limited to a 60-degree wedge with appropriate boundary conditions. The zinc casting can overcome friction and slip on the surface of the socket cavity. The zinc is modeled as an elastoplastic material based on laboratory tensile test results, and assigned a creep behavior allowing the material to continue to deform under sustained tensile or shear stress. The wires' steel is also modeled as an elastoplastic material based on the laboratory tensile test results. The wires are tied to the zinc, i.e. wire slip within the zinc is not modeled.

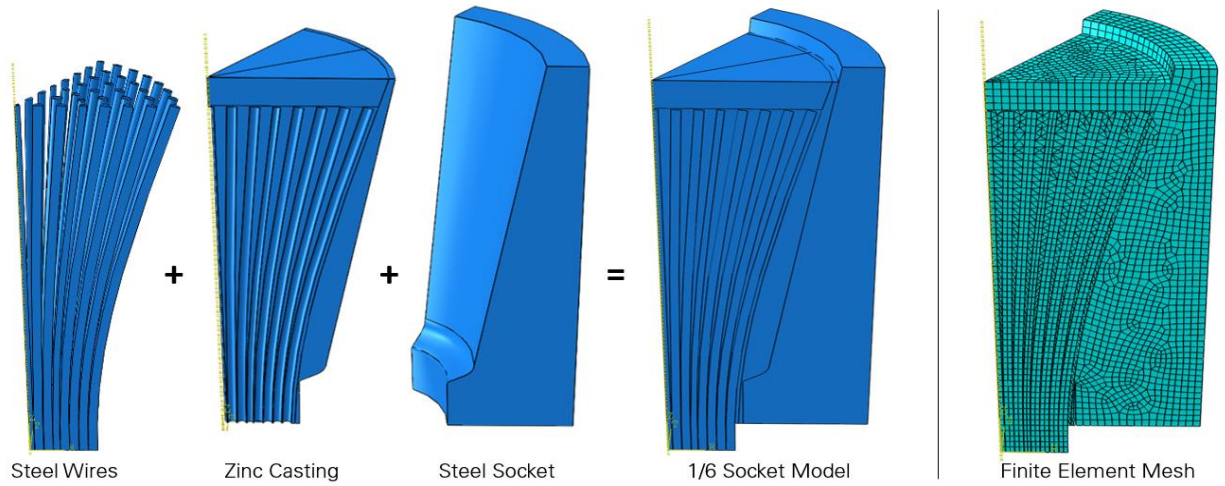

Figure 51: Baseline FE model of auxiliary backstay ground-end socket.

Effect of Socket Shoulder

The baseline model represents a socket whose design includes a shoulder, like all of the telescope's sockets that failed or exhibited large cable slips. To study the effect of the shoulder on socket behavior, a FE model was constructed by removing the shoulder from the baseline model. After loading both models to half of the cable's breaking strength, the load was held to allow the zinc to flow.

The initial loading causes higher shear stress at the front of the zinc casting, as the load is partially resisted in bearing on the shoulder (Figure 52). However, after one year of zinc flow, the shear stress distribution is similar in the castings with and without a shoulder. The wire stresses are also similar in the two models.

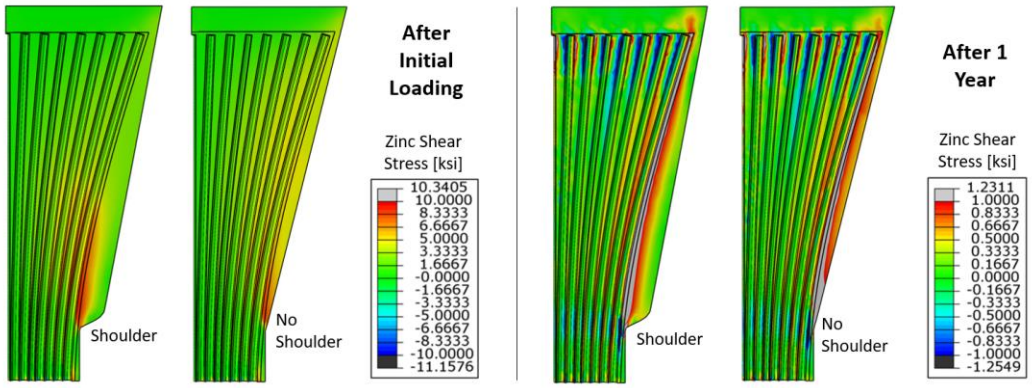

Figure 52: Shear stress in zinc casting with and without shoulder.

Impact of Wire Broom

Additional FE models were derived from the baseline model to study the impact of wire broom geometry on socket behavior. These include models where only one, two and three layers of wires are broomed out, and a model where the wire broom is uniform but narrower than in the baseline model (Figure 53).

The models were loaded to half of the cable's breaking strength, and the load was held while simulating 25 years of zinc flow.

In the cable modeled with the socket, the two outermost wire layers account for 48 percent of the cable's section area. Those two layers are therefore sufficient to resist most or all of the applied load, which is 50 percent of the cable's minimum breaking strength. With that in mind, the FE analysis results (Figure 53, Figure 54) are consistent with the socket behavior previously introduced (Figure 47 vs. Figure 48, pages 34 to 35): if the full cable tension can be resisted by the broomed-out wires (uniform, three-layer and two-layer brooms), zinc flow stops and the socket does not fail and shows limited cable slip. In contrast, if the broomed-out wires cannot resist the full cable tension (one-layer broom), zinc flow and cable slip continue over time and eventually cause the socket to fail. As wire slip within the zinc was not modeled, the wires and the core ruptured in the FE model.

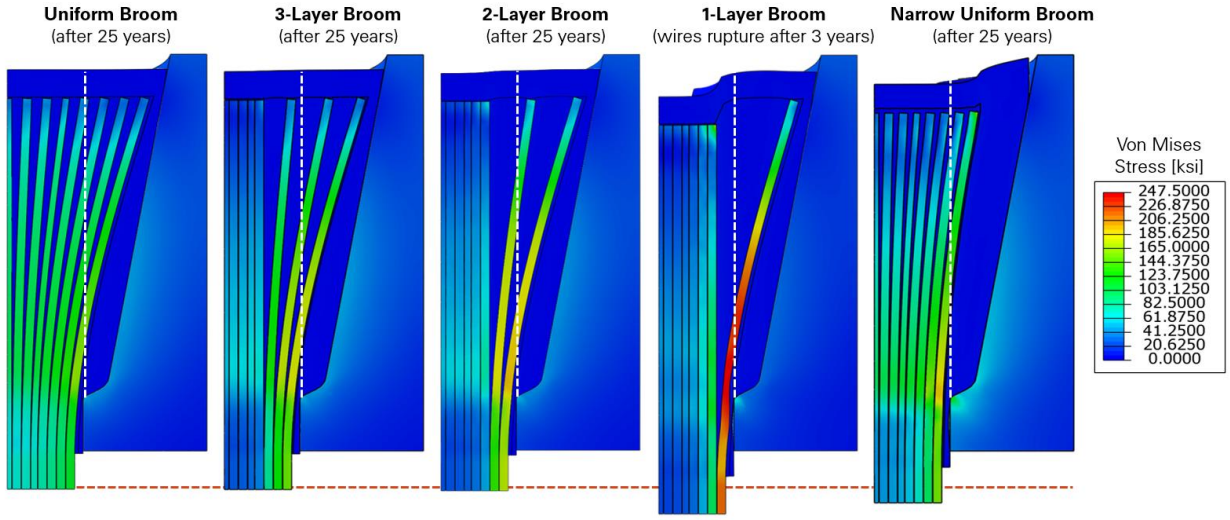

Figure 53: Cable slip and wire stress for different idealized wire brooms after 25 years of zinc flow.

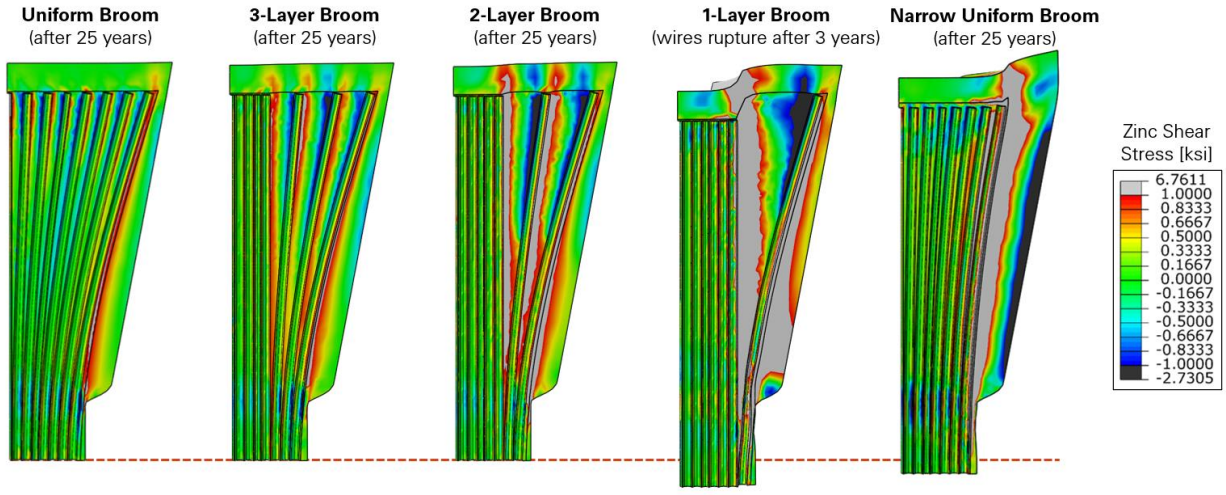

Figure 54: Zinc shear stress for different idealized wire brooms after 25 years of zinc flow.

4.2.3 Socket Load Test to Failure

The recovered ground-end auxiliary backstay socket B4S_G was load-tested to failure at Lehigh University's Fritz Laboratory. The purpose of the test was to observe and measure the behavior of the cable-socket assembly under constant and cyclic loads, and to observe the socket's failure mode.

Socket B4S_G was recovered from the collapsed telescope with 15 feet of cable attached. The socket was generally in good condition, had no visible wire breaks, and exhibited an intermediate cable slip of 0.875 inch. The free end of the cable was cast in a new zinc-filled spelter socket, and the specimen was installed in a test frame (Figure 55).

Over the course of four days, the specimen was initially loaded and held at 100, 125 and 150 percent of the cable's service load of 675 kip for 20 hours, and a series of load cycles was applied at each load level (Figure 57). After unloading to half the service load, the load was increased until seven outer wires ruptured in socket B4S_G (Figure 56) and the specimen was unable to carry more load. The maximum tension reached was two percent greater than the cable's Minimum Breaking Strength, such that the cable still met its design strength requirement after 25 years of service. No wire ruptures were observed at the new socket end.

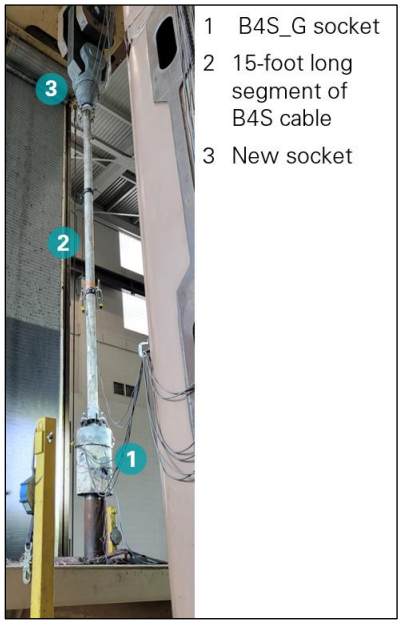

Figure 55: Socket and cable specimen in load testing machine.

Figure 56: Failed wires in B4S_G socket at end of load test.

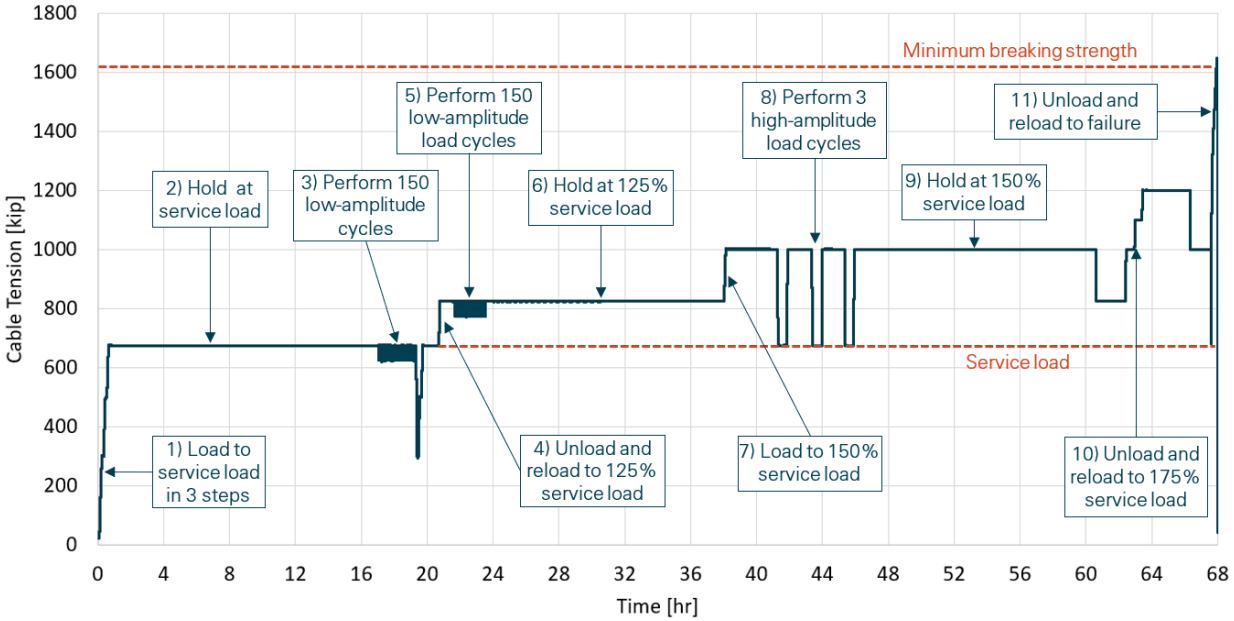

Figure 57: Loading time history of B4S_G socket test.

The zinc flow is non-recoverable, as was observed in the socket load test. The cable slip was monitored throughout the test with four displacement sensors at each socket (Figure 59). Plastic flow occurred in both sockets over the course of each hold, and the flow rate increased with the load. The cable slips resulting from the plastic flow were different between the new and existing sockets, although the cable tension was the same in both sockets. During the initial loading, the cable slip was more than 10 times larger at the new socket (0.35 inch) than at B4S_G (0.03 inch). This is due to the zinc casting of the new socket being wedged into the socket for the first time to achieve load transfer. When the load was increased to the next two levels, the additional cable slip remained larger in the new socket but the difference with B4S_G was less significant. For each load level, the cable continued to slip at both sockets while the load was held constant. This is evidence of time-dependent deformations occurring in the zinc castings. During the final loading to failure, the cable slip increased more at B4S_G (0.40 inch) than the new socket (0.27 inch). Considering the pre-existing slip of B4S_G (0.875 inch), the total cable slip at the end of the test was 1.375 inch at B4S_G, and 0.85 inch at the new socket. This is consistent with the socket behavior previously introduced (Figure 48 page 35), where a socket exhibits significant cable slip before failing. In addition, the total slip of 1.375 inch is relatively close to the last known slip of 1.125 inch at the first telescope socket that failed (M4N_T). The slip rate increased substantially in B4S_G once the cable tension exceeded 75 percent of the Minimum Breaking Strength, and it was clear that the cable was pulling from the socket.

The stress in several outer wires near both sockets was monitored throughout the test with strain gages, while the average cable stress is known from the applied load (Figure 60). Under each increased load, the stress in the outer wires increased disproportionately more than in the inner wires. The outer wire stress is higher than the average cable stress at both sockets, and the difference is generally consistent with the measured cable slip. This is consistent with the socket behavior previously introduced (Figure 47 to Figure 50, pages 34 to 36), where the cable slip causes the tension to increase in the outer wires.

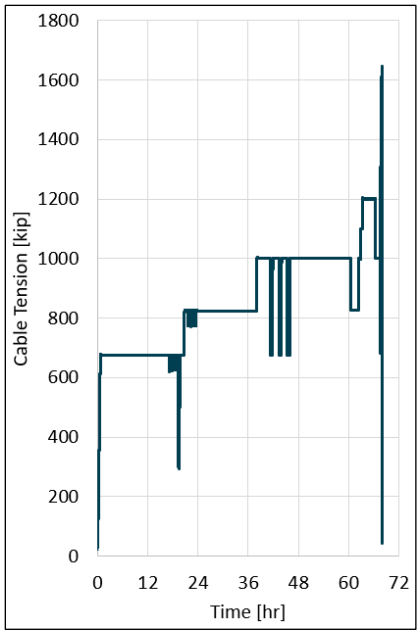

Figure 58: Loading time history.

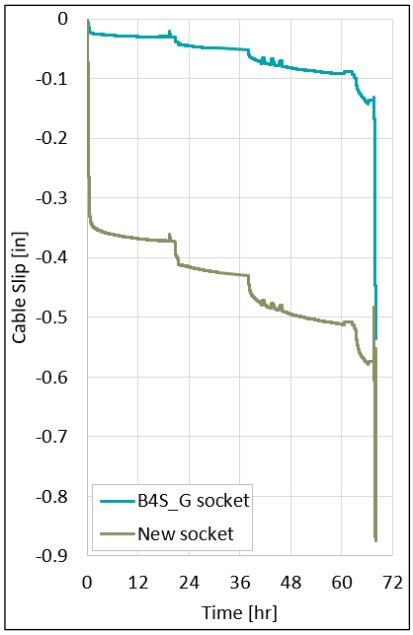

Figure 59: Average cable slip per socket.

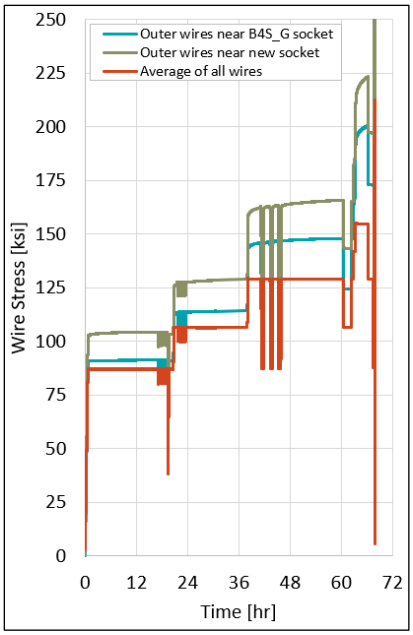

Figure 60: Outer wire stress vs. average cable stress.

4.2.4 Socket Calculations

The socket behavior presented above is consistent with the results of a mathematical model that we developed and applied to the telescope's sockets cut open in laboratories. The model and results are summarized in the following, and additional details are provided in Appendix O.

Model

The proposed mathematical model considers the equilibrium of the socket casting's core (Figure 45 page 33) and calculates the maximum resistance to the cable tension that can be developed in shear on the core surface and in tension in the crossing wires.

The maximum shear resistance is determined according to Mohr-Coulomb theory, based on the cohesion of the zinc material and friction on the core surface. Friction is due to the radial compressive stress induced by squeezing the casting into the cone-shaped socket cavity.

The maximum tensile resistance that a crossing wire can provide is the minimum of the nominal wire strength (fully developed wires) and the wire's slip capacity with respect to the zinc outside the core (partially developed wires). The nominal wire strength is calculated as the average of the yield and ultimate tensile strengths measured on 12 wires taken from the telescope's cables. The wire slip capacity is determined according to Mohr-Coulomb theory, based on the bond strength between wire and zinc, and friction on the wire surface.

Wire Broom Geometry

The wire broom geometry must be known to calculate the capacity of the crossing wires. The wire broom geometry was revealed from transverse cuts in the casting of six telescope sockets (Figure 61,

Figure 62), which include three failed sockets and three other sockets exhibiting different cable slips. The wire broom geometry of socket M4N_T (first cable failure) is provided in WJE's investigation report,[18] and the other five sockets were cut open at Socotec's laboratory.

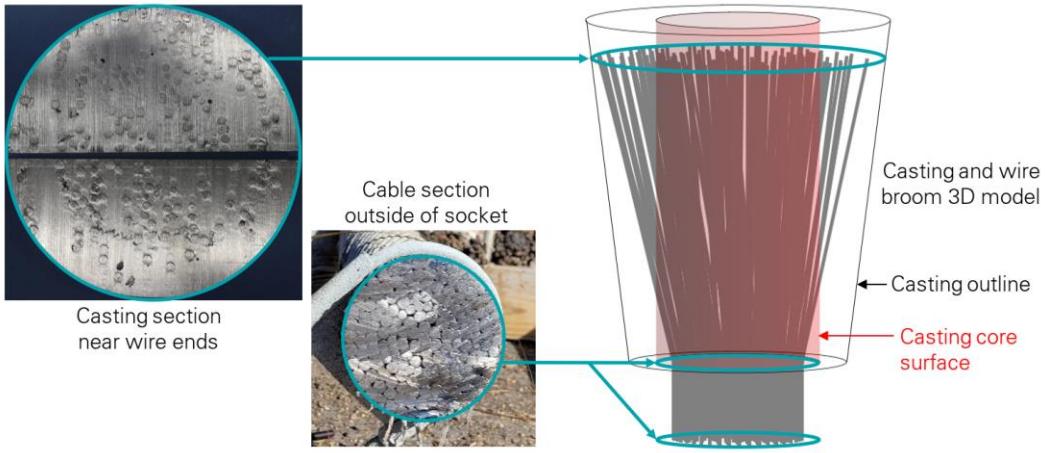

Figure 61: Construction of broom geometry from cable and casting sections *(casting section photo: Socotec).*

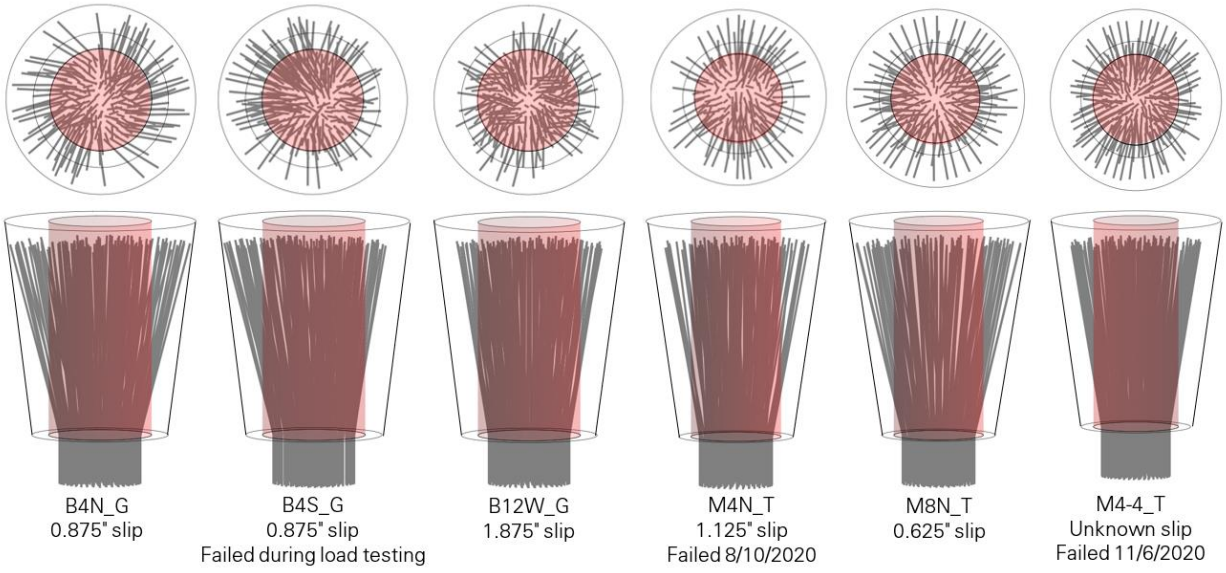

Figure 62: Wire broom geometries considered.

[18] Wiss, Janney, Elstner Associates (WJE). *Auxiliary Main Cable Socket Failure Investigation*. June 21, 2021. Draft report provided by WJE.

To characterize the broom geometry, we define a wire's *brooming ratio* as the wire's distance to the central axis (r) divided by the casting's radius (d) in the plane containing the wire ends (Figure 63). For the five auxiliary sockets considered, the cable slip decreases as the average brooming ratio increases (Figure 64). This result is a first general correlation between wire broom and cable slip, which was further investigated.

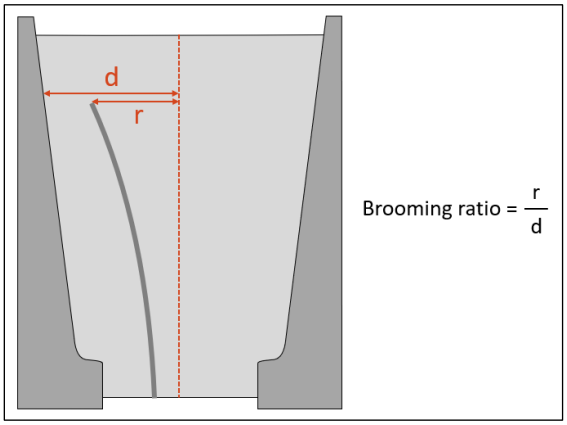

Figure 63: Definition of brooming ratio.

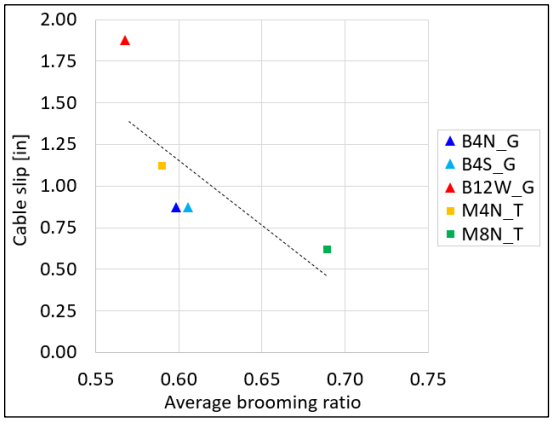

Figure 64: Cable slip vs. average brooming ratio for five auxiliary sockets.

Wire Broom Effect on Cable Slip

For the six sockets of known wire broom geometry, we calculated the minimum shear stress that would be needed on the core surface to resist the cable tension when the crossing wires are loaded to their capacity (Table 5).

Table 5: Required core shear, cable slip and safety factors in sockets considered

		Before M4N Failure						After M4N Failure
		M4-4_T	**M8N_T**	**B4S_G**	**B4N_G**	**M4N_T**	**B12W_G**	**M4-4_T**
Cable Slip [in]		Unknown	0.625	0.875	0.875	1.125	1.875	Visible
Under Gravity Loads	**Cable Tension [kip]**	534	602	665	698	600	624	646
	Crossing Wires Capacity [kip]	565	752	659	671	554	561	581
	Shear Stress Needed on Core [ksi]	0	0	0.05	0.22	0.43	0.52	0.70
	Cable Safety Factor	2.0	2.2	2.4	2.3	2.2	2.6	1.6
Maximum During Hurricane Maria	**Cable Tension [kip]**	543	636	687	721	631	647	-
	Crossing Wires Capacity [kip]	567	761	662	674	558	565	-
	Shear Stress Needed on Core [ksi]	0	0	0.20	0.39	0.69	0.67	-
	Shear Stress Increase vs. Gravity	-	-	+283%	+73%	+58%	+29%	-
	Cable Safety Factor	1.9	2.1	2.3	2.2	2.1	2.5	-
Min. Cable Safety Factor to Not Need Shear Stress on Core		1.8	1.7	2.5	2.4	2.4	3.0	1.8

Under gravity loads, the cable slip increases with the shear stress needed for the five auxiliary sockets (Figure 65 left). In addition, when the first cable failed, the shear stress needed in socket M4-4_T increased from zero to the largest stress (0.7 ksi) among all considered sockets as the M4 cables experienced a 30 percent increase in tension. Socket M4-4_T failed three months later, and fracture

planes were observed around the casting core in the recovered socket. Core movement was also visible on the back of the M4-4_T casting after the first cable failure.

The shear stress needed on the core surface was also calculated for the maximum cable tensions experienced during Hurricane Maria. For the sockets that already relied on the shear stress under gravity loads, the required shear stress increased significantly during the hurricane.

These results are consistent with the socket behavior previously introduced (Figure 47 vs. Figure 48, Figure 49 and Figure 50, pages 34 to 36): the cable slip is driven by the need to transfer the cable tension out of the casting core in shear due to insufficient capacity of the crossing wires.

Wire Broom Effect on Socket Failure

A socket can include both fully developed crossing wires (wires rupture before slipping) and partially developed crossing wires (wires slip before rupturing). A socket's *wire development ratio* is defined as the fraction of crossing wires that are fully developed. The wire development ratio is therefore a measure of the general tendency for the crossing wires to slip (low ratio) or fracture (high ratio) in a given socket. For the six sockets of known wire broom geometry, the wire development ratio was calculated under the socket's service load and failure load, if applicable (Table 6). The wire development ratio increases with load because the load-induced confinement stress in the casting governs how much friction can be developed between wire and zinc to resist wire slip.

Table 6: Wire development ratio in sockets considered

	Gravity Loads Before M4N Failure						Gravity Loads After M4N Failure	End of Load Test
	M4-4_T	**M8N_T**	**B4S_G**	**B4N_G**	**M4N_T**	**B12W_G**	**M4-4_T**	**B4S_G**
Cable Slip [in]	Unknown	0.625	0.875	0.875	1.125	1.875	Visible	1.375
Wire Development Ratio	58%	43%	47%	60%	59%	38%	65%	66%
Socket Failure Mode	None	None	None	None	Core Rupture	Core Flow-out	Core Rupture	Core Rupture

Four of the six sockets that were analyzed failed or were in the process of failing. The failures of sockets M4N_T and M4-4_T occurred in the field and involved the rupture of multiple outer wires and a significant shift or complete pull-out of the core, which corresponds to core rupture (Figure 48, page 35). The load test of socket B4S_G was stopped after seven outer wires ruptured, indicating that the socket was on the brink of core rupture. Finally, socket B12W_G experienced a very large cable slip as its crossing wires slipped without fracturing, which corresponds to core flow-out (Figure 49 page 35).

The three sockets exhibiting core rupture had a larger wire development ratio (59 to 66 percent) than the socket exhibiting core flow-out (38 percent) (Table 6, Figure 65 right, and Figure 66). This result is consistent with the socket behavior previously introduced (Figure 48 vs. Figure 49, page 35): fully developed wires lead to core fracture, while partially developed wires lead to core flow-out.

Figure 65 summarizes the observed socket behavior: if shear stress is needed on the core surface to resist the full cable tension, the zinc flows and causes cable slip over time. When the cable slip becomes too large, the socket fails in core rupture or core flow-out depending on whether the crossing wires are primarily fully developed or partially developed.

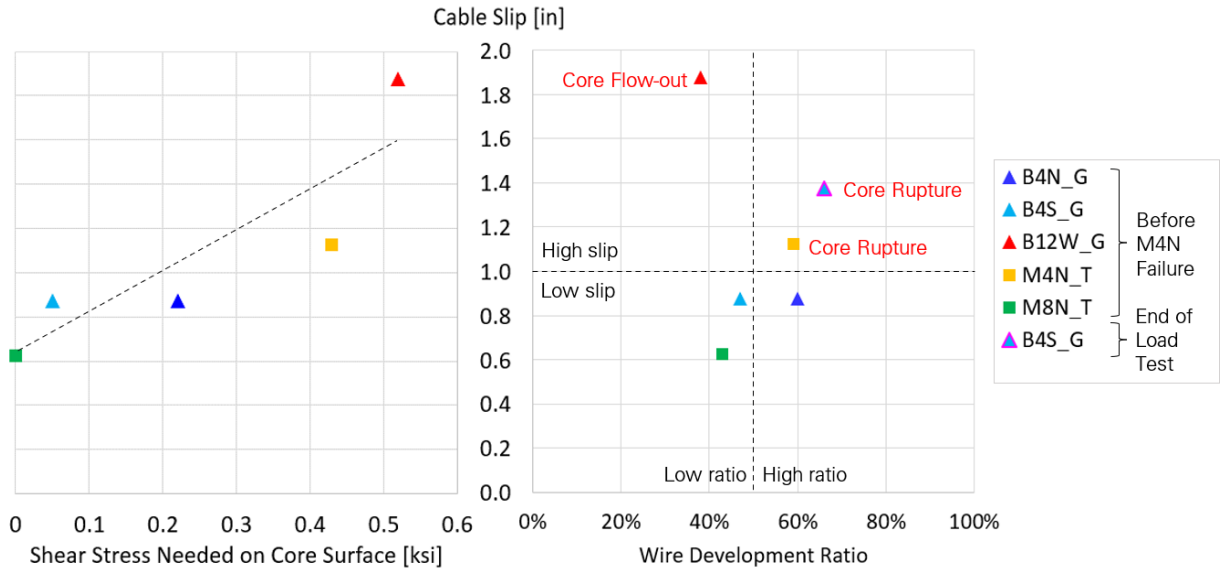

Figure 65: Correlation between core shear stress, wire development ratio, cable slip, and socket failure.

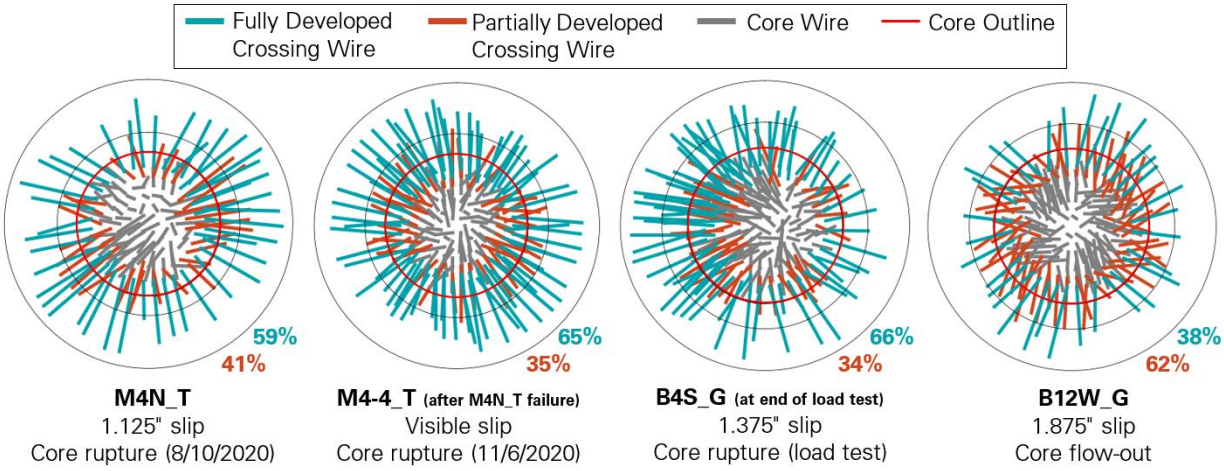

Figure 66: Fully and partially developed crossing wires in failed and failing sockets.

5.0 Discussion

The Arecibo Telescope collapsed after three cables at the top of Tower 4 failed progressively in 2020. It started from the failure of auxiliary main cable M4N on August 10, 2020, followed by the failure of original main cable M4-4 on November 6, 2020, and the failure of original main cable M4-2 on December 1, 2020, which immediately triggered failure of M4-1 and M4-3, allowing the platform to fall. The first three cable failures all occurred within the cable-socket assemblies at Tower 4 and involved the rupture of outer wires inside the socket and a significant deformation or complete pull-out of part of the socket's zinc casting. These failures are therefore referred to herein as *socket failures*.

The degradation of the cable wires over their 57-year life span did not contribute to the socket failures. Issues relating to paint conditions, infrequent cable vibrations, and the moisture exclusion system were observed occasionally during inspections, some of which were remediated prior to 2020. Local corrosion was observed in some individual wires, but there was no widespread corrosion throughout the cable system. Stress corrosion cracks and pitting were not predominant in the collected wire samples. A total of 22 wire breaks were reported before the first cable failure (not including the breaks that had occurred in the replaced cable B12-3 and at the by-passed splice of cable M8-4). The number of broken wires was less than one percent of the total number of wires in the cable system. All but three of these wire breaks occurred prior to the installation of the Gregorian. No wire breaks were reported in cable M4N prior to failure in 2020. The socket failures must, therefore, be attributed to some other mechanism.

The mechanism of zinc flow as presented in Section 4.2.4 explains a high variation of socket behavior observed among the cable sockets. A total of 78 sockets were installed to anchor the cable ends to their supports, including 54 sockets for the original cables and 24 sockets for the auxiliary cables. Prior to the first cable failure, eight auxiliary cable sockets, which is one-third of the auxiliary cable system, exhibited excessive cable slips larger than one-sixth of the cable diameter under sustained tension in a range of 40 to 50 percent of the cables' Minimum Breaking Strengths. The original cable sockets exhibited less significant cable slip even though they were in service approximately twice as long. When the telescope collapsed, three out of 78 sockets (M4N_T, M4-4_T and M4-2_T) had failed by core rupture after exhibiting cable slips of approximately one inch, and one socket (B12W_G) was failing by core flow-out and exhibited a cable slip of almost two inches. All of the telescope's cables had a similar safety factor (between 1.9 and 2.6) under sustained loads, were connected to sockets of similar internal design, and were socketed with a process that did not significantly change between the 1960s (original cables) and the 1990s (auxiliary cables). Yet, the amount of cable slip and the type of failure mode was different between the sockets. The variation of socket behavior is attributed to the variation of wire brooming.

The sockets were zinc-filled spelter sockets. All of the sockets were fabricated by splaying out the ends of the cable wires to form a broom inside the socket cavity and pouring molten zinc to create a cone-shaped casting in the socket. As the wires were bent and splayed manually during brooming, they were not evenly distributed in the radial and circumferential directions. The wire broom geometry is then unique to each socket. This is evident in the range of brooming ratios observed in the sockets that were examined in the laboratory. The zinc used as filling material between the wires and the socket wall was 99.5 percent pure. Pure zinc is a soft and low-strength metal compared to steel. When highly stressed through shear and compression due to confinement at the front of the socket, the zinc deforms plastically and will exhibit considerable ductility. Zinc also exhibits creep at room temperature, at a rate that follows a power law of the sustained stress. Flow of zinc through plastic deformation and creep can result in large deformations, which were clearly visible in the sockets that were cut open.

The capacity of zinc-filled spelter sockets is dependent upon the total strength of splayed wires in the socket. The model presented in Section 4.2 predicts the failure mechanism of the wires and zinc core within the socket based on the collected data from field assessment and laboratory examination. The socket's *long term capacity* is defined as the maximum force that can be resisted by the socket without relying on shear in the zinc. If a sufficient number of wires are splayed out of the zinc casting core, shear in the zinc is minimal and the long-term socket slip is negligible. But if the number of wires splayed out of the core is insufficient, a cascading mechanism forms between splayed wires and zinc core which results in a limited life span of the socket. The socket life span is a function of rate of zinc flow. Zinc flow increases exponentially with the magnitude of the shear stress around the core. Zinc flow results in a gradual slip of the inner wires out of the socket, increasing the tension in the splayed-out wires until they slip or rupture. This creates a cascading effect, and eventually enough wires will slip or rupture to allow the core and inner wires to pull out of the socket.

This phenomenon occurred in several sockets (M4N_T, M4-4_T, M4-2_T and B12W_G) prior to collapse in 2020. The first socket that failed in August 2020 (M4N_T) had exhibited an excessive cable slip of 1.125 inch at an increased slip rate a year and a half before failing. The second socket (M4-4_T) failed three months later, and the third socket (M4-2_T) failed another three weeks later. B12W_G had exhibited a considerable amount of slip prior to failure. For all these sockets, deformation, craters and/or cracks observed at the back of the socket's zinc casting indicated continued zinc flow at an accelerated rate prior to failure.

The sockets of the telescope were in a state of high sustained stress during their life spans. Therefore, for the flow not to occur, the wire brooming becomes critical. A summary of some of the brooming metrics identified in Appendix O is presented in Table 7. Socket B12W_G has a very low wire development ratio, indicating that many of the wires splayed out of the core slip rather than rupture. Since the wires were not rupturing, there would be no redistribution of wire tensions but slip would continue since the zinc shear stress was high as indicated by the low actual-to-minimum safety factor ratio. Socket M4N_T has a high wire development ratio. Therefore, the outer wires would tend to rupture rather than slip. The rupture of wires would cause an increase in the tension in the remaining wires, increasing the zinc shear stress and accelerating the zinc flow. The process continues until there is insufficient shear strength to retain the core and the plug pulls from the socket. Of the sockets opened in the laboratory, the sockets that did not fail (and were not in the process of failing) had a safety factor of at least 95 percent of the minimum safety factor where no shear stress occurs on the core surface. The other four sockets (M4N_T, B12W_G, M4-4_T after M4N_T failure, and B4S_G in the load test) had a safety factor of less than 95 percent of the minimum (as seen in row 6 of Table 7) and failed by core rupture or by core flow-out. In our analysis of the sockets studied in the laboratory, we estimated that the sockets would not have experienced any large cable slips or have failed if their cables had been designed with a minimum safety factor of 3.0. More data is needed to develop an upper bound of safety factor which will provide essentially an infinite life to the sockets. Additionally, more data is needed to develop a relationship between safety factor, quality of brooming, and service life.

Table 7: Summary of socket properties and behavior

	Gravity Loads Before M4N Failure						Gravity Loads After M4N Failure	End of Load Test
	M4-4_T	**M8N_T**	**B4S_G**	**B4N_G**	**M4N_T**	**B12W_G**	**M4-4_T**	**B4S_G**
Cable Slip [in]	Unknown	0.625	0.875	0.875	1.125	1.875	Visible	1.375
Wire Brooming Ratio[A]	61%	69%	61%	60%	59%	57%	61%	61%
Wire Development Ratio[B]	58%	43%	47%	60%	59%	38%	65%	66%
Min. Cable Safety Factor to Not Need Core Shear	1.8	1.7	2.5	2.4	2.4	3.0	1.8	2.5
Actual Cable Safety Factor	2.0	2.2	2.4	2.3	2.2	2.6	1.6	0.98
Actual/Min. Safety Factor	1.11	1.29	0.96	0.96	0.92	0.87	0.89	0.39
Socket Failure Mode	None	None	None	None	Core Rupture	Core Flow-out	Core Rupture	Core Rupture

[A] Quantifies the width of the wire broom (would be 100% if all wire ends were touching the socket's steel).
[B] Fraction of crossing wires that are fully developed. Quantifies the crossing wire's tendency to rupture vs slip (would be 100% if all crossing wires ruptured before slipping).

In the discussion above, the cable force was assumed constant. While hurricanes and earthquakes increased the cable tensions by no more than 15 percent, the model predicts that the resulting tension from the load fluctuation is large enough to increase the shear demand on the core by 30 percent on socket B12W_G and 60 percent on socket M4N_T (Table 5). Given the high level of shear stress already in the zinc core from sustained gravity load, we expect this stress increase, while transient, may have a significant effect on the life span of these sockets. This is very similar to the prediction of fatigue life of components where the accumulated damage of many cycles needs to be considered. Understanding the effect of the accumulation of damage to the sockets can be further studied by a controlled test program using a sufficient number of samples to accommodate the necessary variables. Until then, using a higher safety factor for the sustained load is a conservative design approach to keep the cable wires at a relatively low state of stress and thus minimize zinc flow.

6.0 Conclusions and Recommendations

The progressive cable failures and eventual collapse of the Arecibo Telescope were caused by a combination of factors that impacted the forces and long-term capacities of zinc-filled spelter sockets. Our investigation identified five key factors, which are summarized in the following. Relevant recommendations to mitigate the risk and consequences of socket failure are also provided.

- The wire broom geometry determines the socket's long-term capacity, which is the force that can be resisted by the socket without relying on shear stress in the zinc. Shear stress causes zinc flow, which can lead to large cable slip and socket failure. The telescope's cables were socketed following typical practice, where the cable wires are splayed manually to form a broom before casting the zinc. Due to the manual brooming process, the long-term socket capacity varied between sockets. Zinc-filled spelter sockets with more consistent long-term capacities could be obtained by specifying and controlling the shape of the wire broom during socketing. Proof-loading the cable by testing over a short period is insufficient to assure the long-term capacity of sockets.

- A sufficient safety factor is required to ensure that the socket force is less than the socket long-term capacity. The telescope's cable system was designed with relatively low safety factors under the structure's own weight. The cables were therefore highly stressed over the entire life of the telescope, and not only during extreme environmental events such as hurricanes and earthquakes. This allowed zinc flow to occur over a long period of time in some of the sockets. While the cable system was designed with safety factors between 2.0 and 2.4 under the structure's own weight, those safety factors were not sufficient to prevent long-term zinc flow in sockets with narrow wire brooms. Our analysis indicates that a safety factor of 3.0 under gravity loads would have been needed to prevent long-term zinc flow in the sockets.

- The hurricanes and earthquakes that regularly impact Puerto Rico increased the cable tensions and further lowered the cable safety factors temporarily. We estimated that the cable tensions increased by up to 15 percent. However, this moderate increase was sufficient to develop or increase the shear stress in some of the sockets' zinc and therefore exacerbate zinc flow. Whether zinc flow can occur rapidly during transient high loads would need further investigation. Until this is better understood, a safety factor of 4.0 should be used for the worst loading condition, even if it is transient.

- It is now clear from our study that excessive cable slip occurs in zinc-filled spelter sockets due to zinc flow and is a sign of upcoming failure through core rupture or core flow-out. Excessive cable slip was observed on the first socket that failed at least a year and a half before failure, but was not identified as an immediate structural concern. Monitoring the cable slip and slip rate is a reasonable method to determine if a socket is failing, and the limit of one-sixth of the cable diameter appears to be a reasonable threshold for slip monitoring based on what was observed on the telescope's sockets. Cable slip can cause the rupture of individual outer wires before complete socket failure. A socket exhibiting outer wire ruptures should therefore be closely inspected and monitored for cable slip. However, monitoring wire ruptures is not sufficient to determine if a socket is failing.

- The first socket failure occurred at the end of an isolated cable (M4N), whose tension could not be redistributed to adjacent cables. Instead, this first failure resulted in a rotation of the platform and tension changes throughout the cable system. Designing cluster cable systems with multiple adjacent cables on each span provides redundancy. In the event of a cable failure, the remaining adjacent cables can sustain the increased load for a period of time, allowing and easing the replacement of the failed cable or cables.

More studies are required to characterize the relationship between cable safety factor, quality of brooming, and socket service life. In the meantime, cables terminated with zinc-filled spelter sockets should be designed with a safety factor of at least 3.0 under gravity loads, and at least 4.0 under transient loading conditions. A safe cable system can still be designed with a lower safety factor, such as the 2.2 safety factor prescribed in ASCE 19.[19] However, in that case, the sockets should be inspected regularly to measure cable slip. A socket should be replaced or bypassed when excessive cable slip indicates that zinc flow continues to occur over time. Limiting the allowable cable slip to one-sixth of the cable diameter is reasonable until further studies are performed.

7.0 Acknowledgments

We would like to thank the staff at the Arecibo Observatory, the University of Central Florida, and the National Science Foundation for their assistance in this investigation. We also would like to thank Cornell University for providing access to the Arecibo Observatory archives in the Rare and Manuscript Collections.

[19] American Society of Civil Engineers (ASCE). *ASCE 19-16. Structural Applications of Steel Cables for Buildings*. 2016.

Appendix A
Telescope Description and Nomenclature

1.0 Introduction

This appendix discusses the terminology used throughout this report to identify each part of the telescope, and in particular the cables and cable sockets that are the primary focus of the forensic investigation. This appendix also outlines some of the key dimensions and properties of the telescope structure.

2.0 Telescope

The telescope was the largest instrument at the Arecibo Observatory and the largest single-aperture radio telescope in the world until 2016. The main components of the telescope are shown in Figure 1 and Figure 2, and its dimensions are shown in Figure 3.

The **primary reflector** is a 1,000-foot-diameter spherical cap built in a natural sinkhole and supported by a cable net system. The surface of the primary reflector is comprised of approximately 40,000 perforated aluminum panels.

Located along the perimeter of the primary reflector is a **ground screen** – a 50-foot-tall wire mesh barrier that mitigates radio interference between the telescope and the surrounding terrain.

The radio feeds of the telescope are mounted on a **suspended structure** located approximately 500 feet above the center of the primary reflector. This structure is further described in section 3.0 of this appendix.

Supporting the suspended structure are three concrete **towers** on three hills surrounding the primary reflector. The towers are numbered 4, 8 and 12, as if located at 4 o'clock, 8 o'clock and 12 o'clock on a clock dial where 12 o'clock is north. This 4-8-12 system is also used for the cable and anchors connected to each tower.

The main cables, also simply referred to as the **mains**, support the suspended structure from the top of the towers. The mains include the original mains and auxiliary mains, which were installed during construction and the second upgrade of the telescope, respectively. The mains are further described in section 4.0 of this appendix, and their socket connections in section 5.0.

The top of the towers are tied back to the ground with backstay cables, also simply referred to as **backstays**. Like the mains, the backstays include the original backstays and auxiliary backstays, and are further described in sections 4.0 and 5.0 of this appendix.

At ground level, the backstays are connected to concrete **anchorages** located in the hills further back from the primary reflector.

The **waveguide** is a pedestrian bridge providing access to the suspended structure from the base of tower 12, and also carrying power and radio waves to the instruments on the suspended structure (hence the term waveguide). The waveguide is supported from the top of the three towers with its own system of cables, and is structurally independent from the suspended structure.

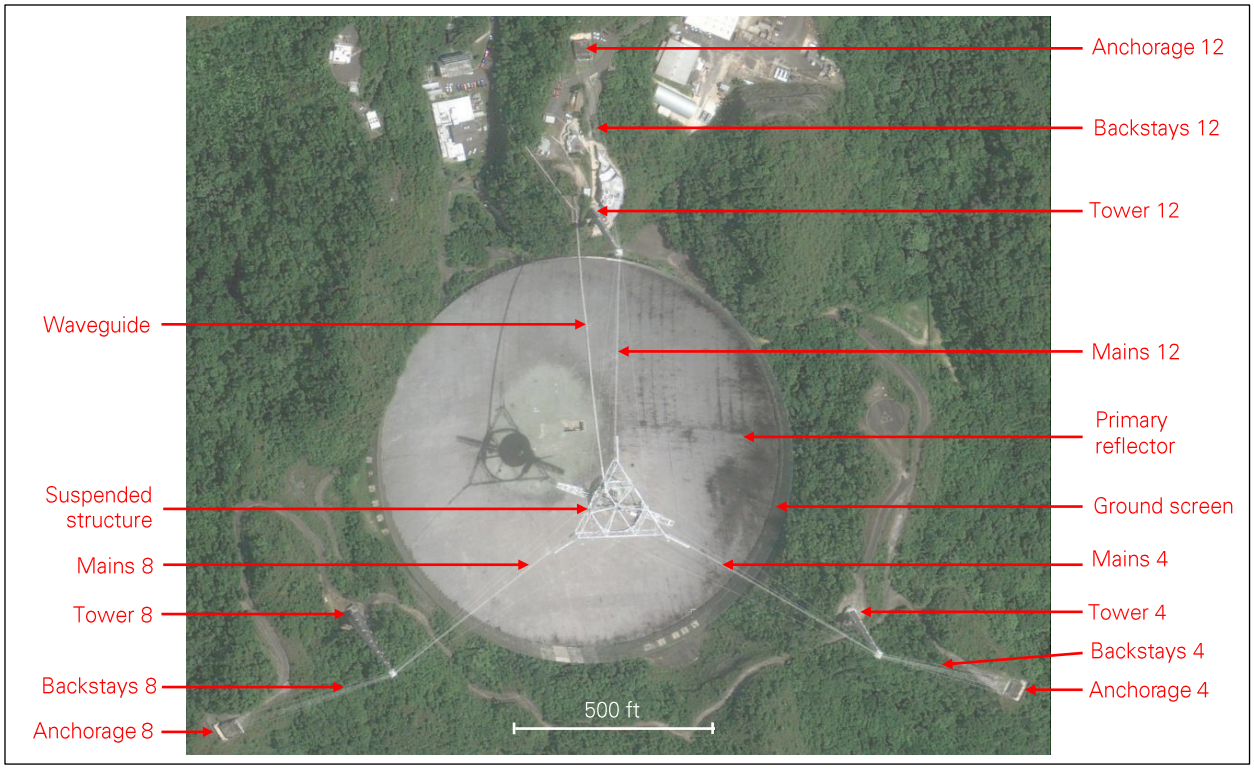

Figure 1: Main components of upgraded telescope *(photo: NSF).*

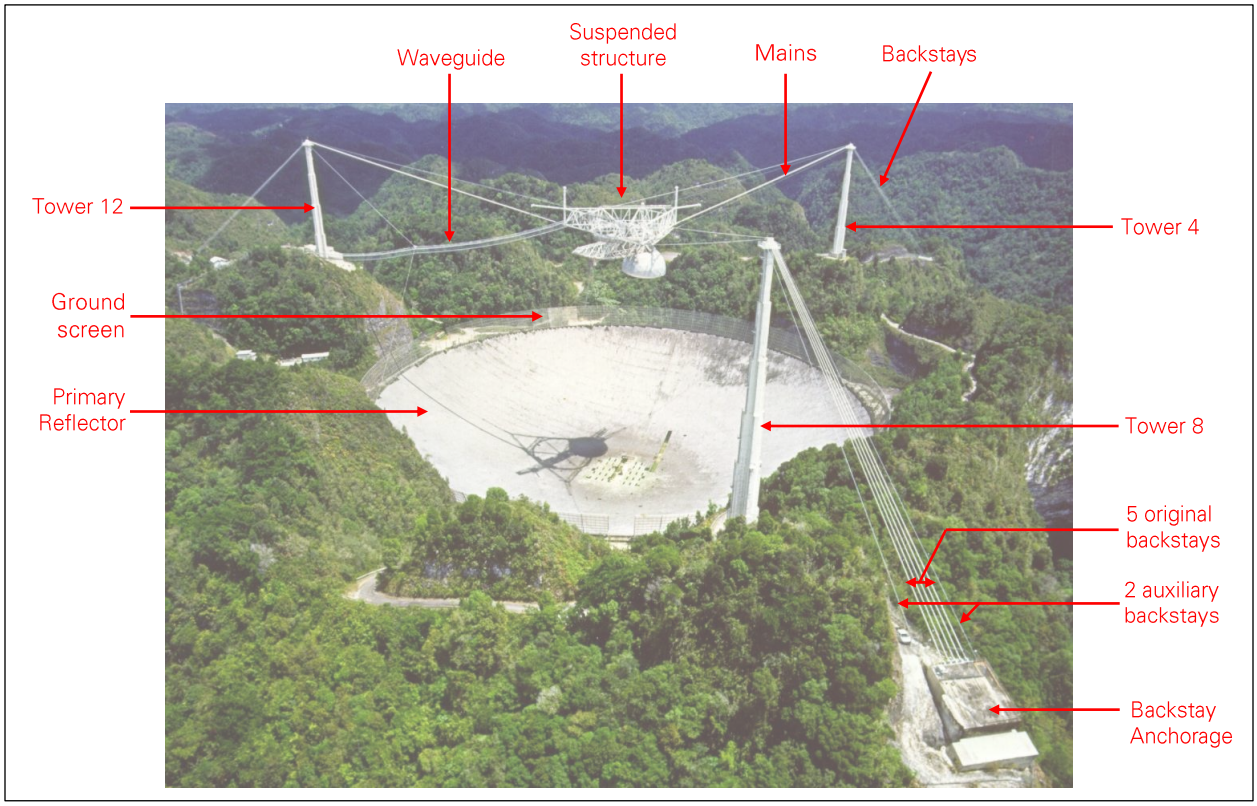

Figure 2: Main components of upgraded telescope *(photo: NSF).*

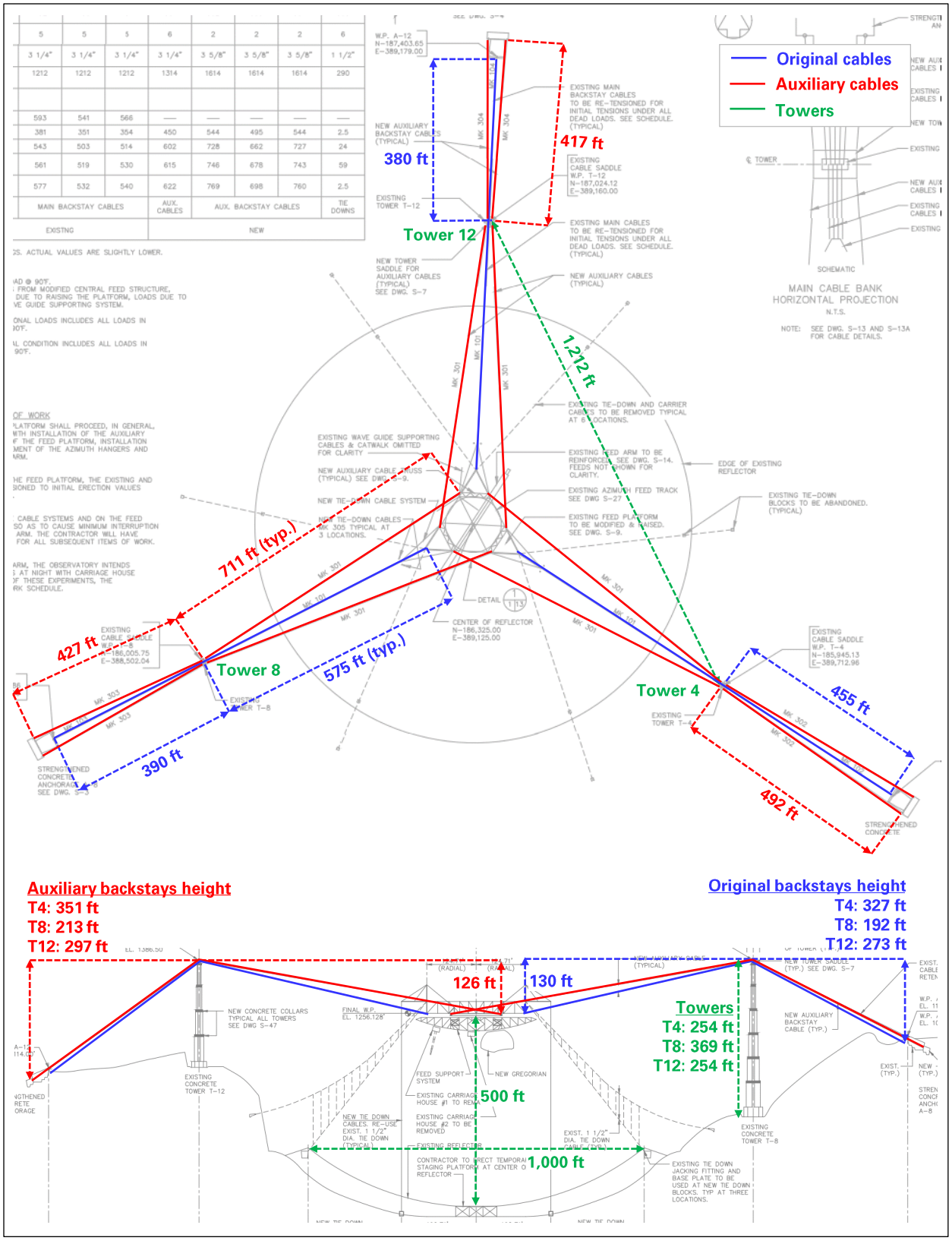

Figure 3: Dimensions of upgraded telescope
(background images: structural drawings, courtesy of NAIC Arecibo Observatory, a facility of the NSF).

3.0 Suspended Structure

The suspended structure supports the radio feeds of the telescope approximately 500 feet above the primary reflector, with moving parts that can change the position of the feeds and steer the telescope, while the primary reflector remains fixed on the ground. This section describes the main components of the suspended structure. Further information on the history, weight and typical movement of these components is provided in Appendix C and H.

The suspended structure and supported equipment were modified over the years. Before the second upgrade completed in 1997, the general configuration was as shown in Figure 4 and is described below.

As the upper part of the suspended structure, the platform consists of several steel trusses (Figure 6) and is a triangular structure supported by four cables (original mains) at each corner. The platform is fixed in space, except for the slight movement induced by environmental loads such as temperature and wind. The bottom of the platform supports the **ring girder**, which is a circular track allowing the rotation of the azimuth arm below.

As a bow-shaped truss structure suspended from the platform, the **azimuth arm** can rotate about a vertical axis passing through the center of the platform, and is supported by trolleys whose wheels sit on the ring girder. The pivot point at the center of the platform prevents the azimuth arm from moving laterally from the center, but does not carry any of the azimuth arm's weight.

The bottom of the azimuth arm supports two parallel **azimuth tracks**. In the original structure, two **carriage houses** were suspended from the azimuth arm, each supported by trolleys whose wheels sat on the azimuth tracks, allowing movement along the bottom of the azimuth arm. The carriage houses supported the radio feeds of the telescope, and one of these was removed as part of the second upgrade.

Each corner of the platform was connected to the ground with two **inclined tiedowns,** which were also removed as part of the second upgrade.

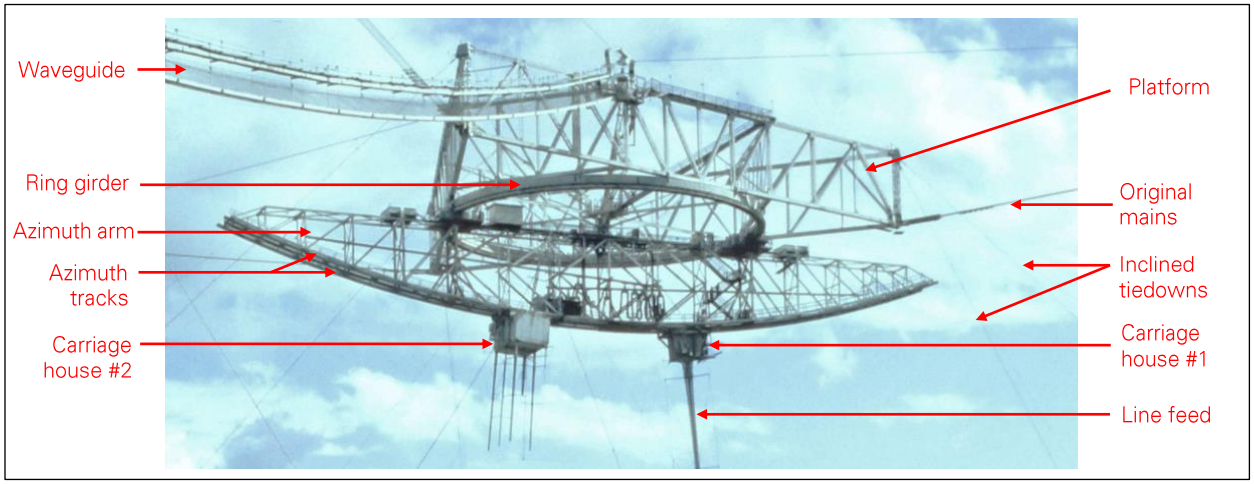

Figure 4: Original suspended structure in 1982 *(photo: Manfred Niermann, Wikipedia - CC BY-SA 4.0).*

Major modifications to the suspended structure were made during the second upgrade of the telescope, which was completed in 1997. The upgraded suspended structure is shown in Figure 5, and the principal changes made to the original structure are described below.

One of the carriage houses was removed from the azimuth arm and replaced with the **Gregorian**, a dome-shaped enclosure that contains telescope feeds and secondary and tertiary reflectors. Like the removed carriage house, the Gregorian is supported by trolleys whose wheels sit on the azimuth tracks, allowing movement along the bottom of the azimuth arm. Because the Gregorian is heavier than the remaining carriage house, which supports the **line feed**, a **counterweight** was installed on the azimuth arm. The counterweight is a fixed tray loaded with lead bricks and pellets.

The six inclined tiedowns were removed and replaced with three **vertical tiedowns**, each of which consists of two cables. An **outrigger** was added at each corner of the platform in order to keep the tiedowns clear of the azimuth arm. Two additional cables (auxiliary mains) were installed between each tower and the platform, and between each tower and its anchor on the ground.

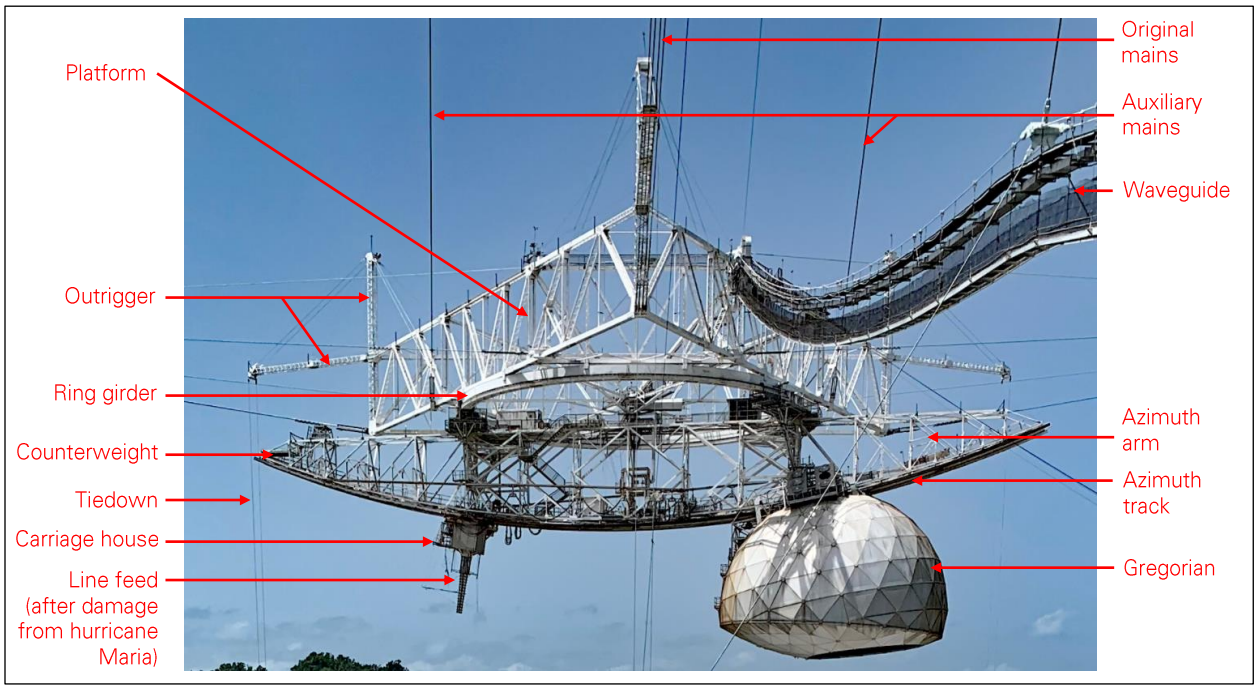

Figure 5: Upgraded suspended structure in 2019 *(photo: Mario Roberto Durán Ortiz, Wikipedia - CC BY-SA 4.0).*

The general dimensions and truss nomenclature for the suspended structure are shown in Figure 6.

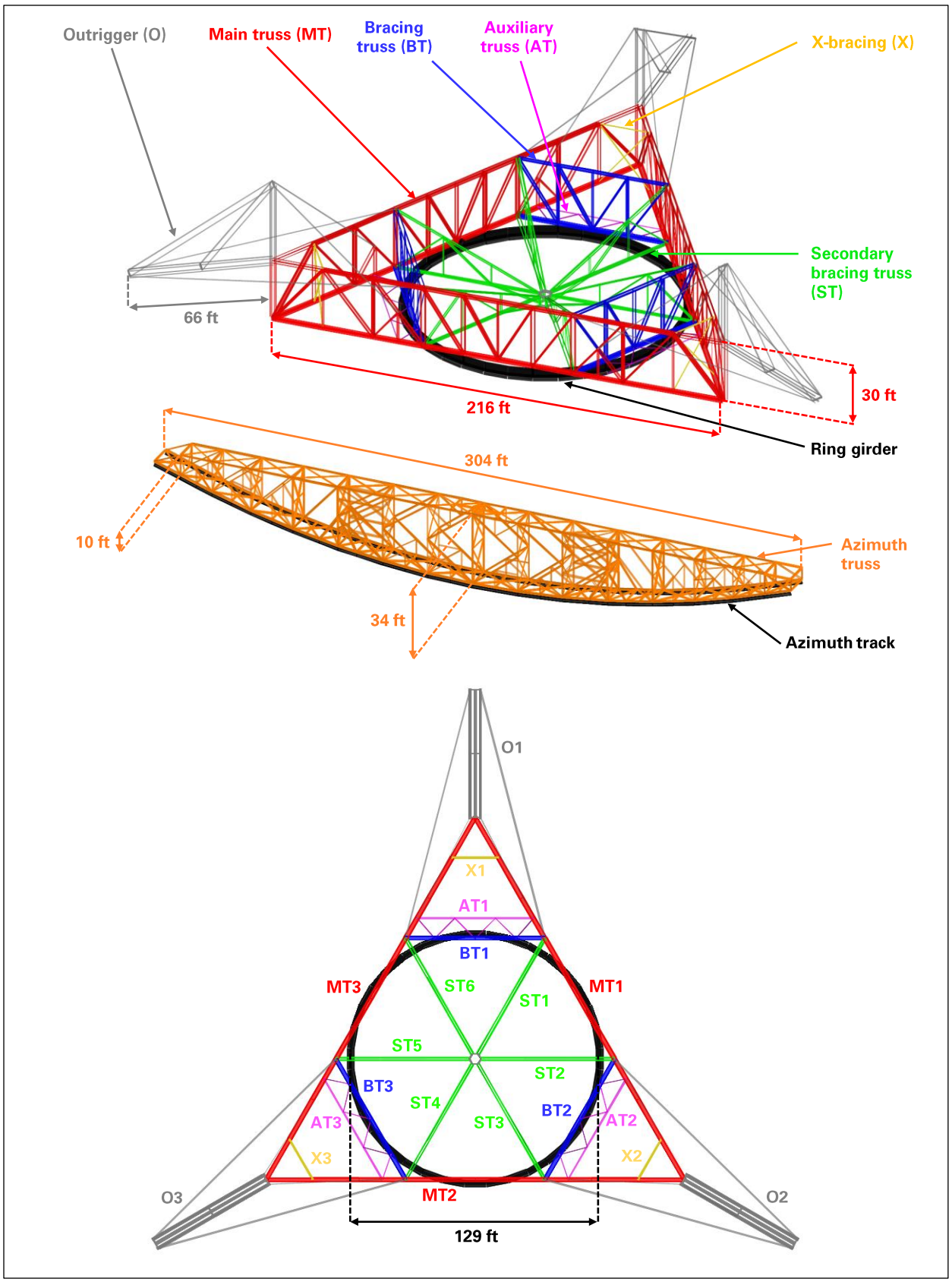

Figure 6: Truss nomenclature and dimensions of upgraded suspended structure.

4.0 Cables

The telescope structure includes three types of cables: the mains between towers and platform, the backstays between towers and ground, and the tiedowns between platform and ground. A cable is considered **original** if it was installed during construction of the telescope (with the exception of B12-3, replaced in 1981 but still considered original), and **auxiliary** if it was installed during the second upgrade, completed in 1997. Each cable is assigned a unique ID, as shown in Figure 7.

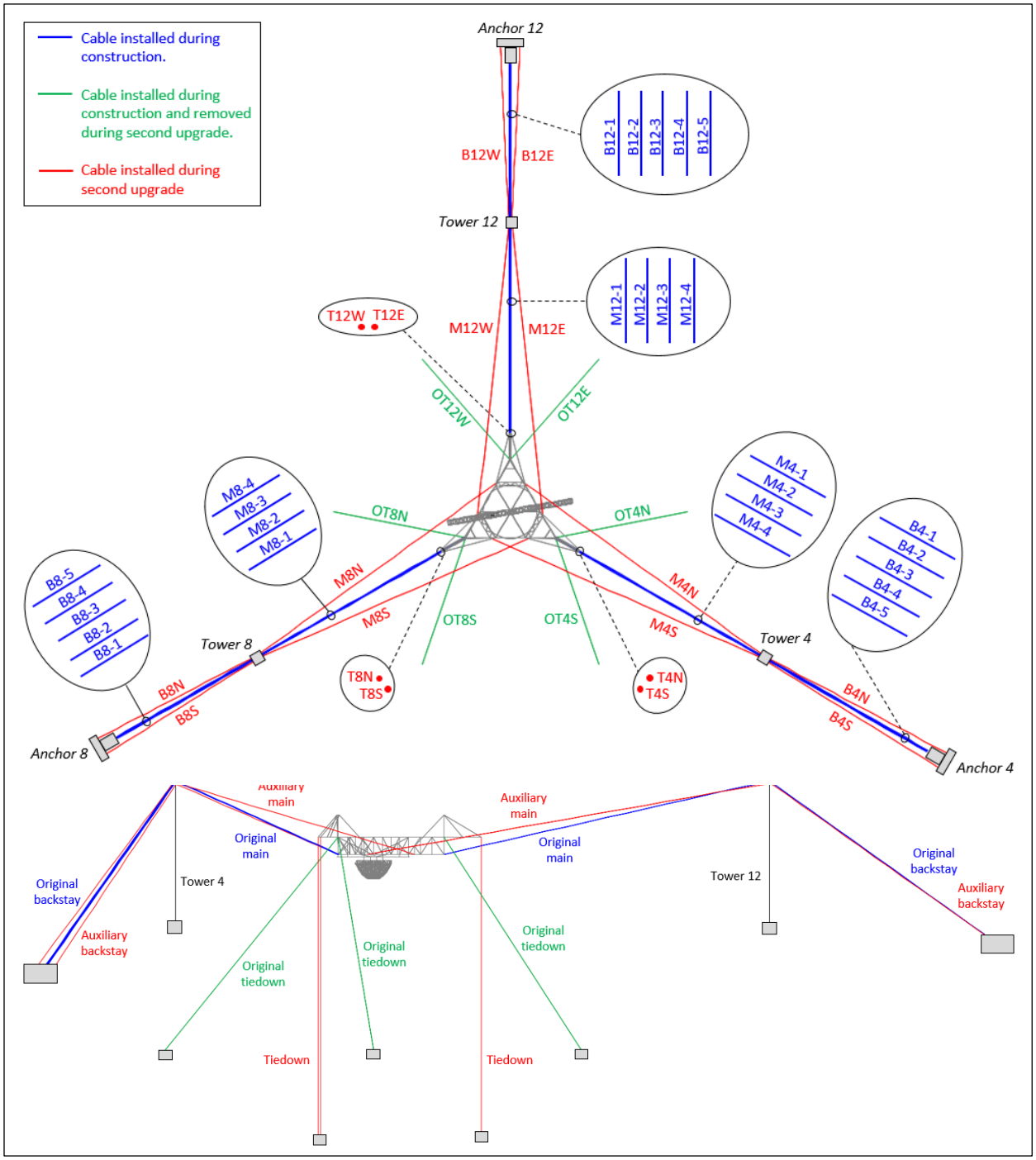

Figure 7: Cable nomenclature and IDs.

Each telescope **cable** is a single **strand** of galvanized steel **wires**. While we primarily use the term cable, the term strand is used in some of the documents that we reviewed, and the two terms are considered synonymous in this report.

As shown in Figure 8, the steel wires of a cable are arranged in concentric **layers**. The innermost layer is referred to as the **core** and may be comprised of a single wire or several smaller wires. The wires are woven helicoidally, in alternating helix direction between adjacent layers.

There are five different cable sections among the mains and backstays of the telescope. Photographs and key properties of each section are shown in Figure 9.

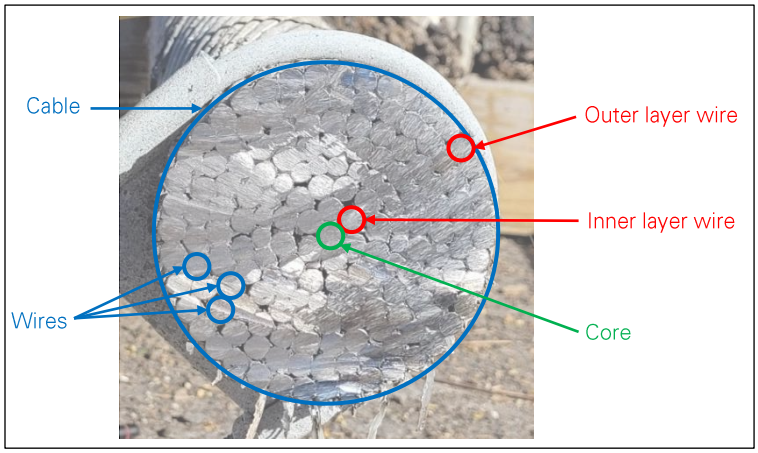

Figure 8: Cable and wire nomenclature, shown on an auxiliary backstay section.

Original main
Cable diameter = 3 in
Wire diameter = 13/64 in
Number of wires = 168
Linear weight[1] = 19 lbf/ft
Min. breaking strength[2] = 1,044 kip

Auxiliary main
Cable diameter = 3 1/4 in
Wire diameter = 1/4 in
Number of wires = 126
Linear weight[1] = 22 lbf/ft
Min. breaking strength[2] = 1,314 kip

Original backstay
Cable diameter = 3 1/4 in
Wire diameter = 13/64 in
Number of wires = 216
Linear weight[1] = 22 lbf/ft
Min. breaking strength[2] = 1,212 kip

Replacement B12-3
Cable diameter = 3 1/4 in
Wire diameter = 1/4 in
Number of wires = 126
Linear weight[1] = 22 lbf/ft
Min. breaking strength[3] = 1,314 kip

Auxiliary backstay
Cable diameter = 3 5/8 in
142 wires of 1/4 in diameter
23 wires of 3/16 in diameter
Linear weight[1] = 28 lbf/ft
Min. breaking strength[2] = 1,614 kip

[1] Typical linear weight per ASTM A586.
[2] Per 1992 structural drawings for second upgrade.
[3] Assumed identical to auxiliary mains.

Figure 9: Cable properties.

5.0 Cable Sockets

The mains and backstays are connected to the platform, towers, and anchors with spelter sockets. As shown in Figure 10, each socket is uniquely identified with the letter P (platform), T (tower) or G (ground) appended to the corresponding cable ID.

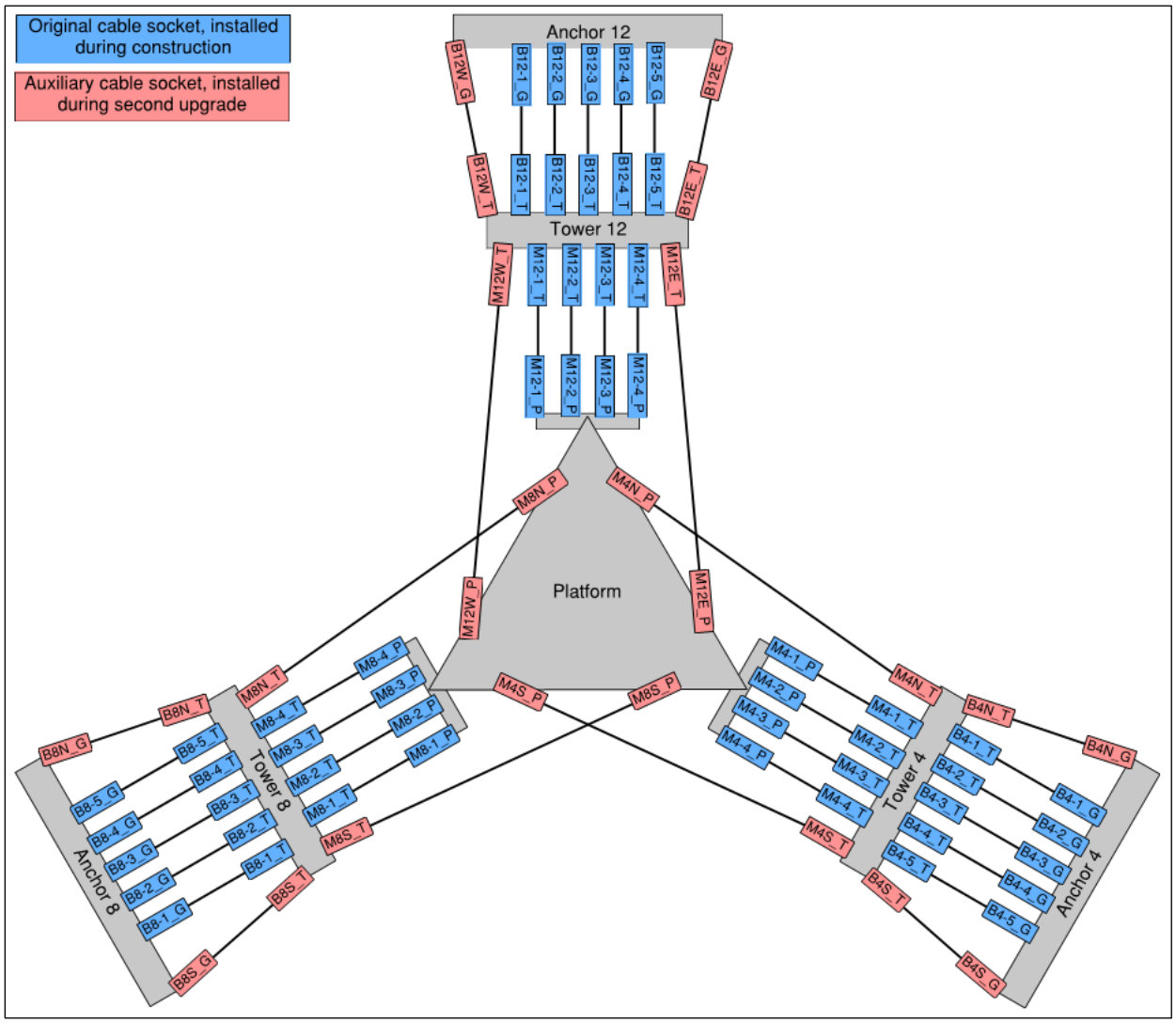

Figure 10: Socket IDs.

The terminology used to describe spelter sockets in this report is illustrated in Figure 11. Each socket is a steel block with a cone-shaped **cavity**, and the cables enter the socket through its **front** end. The other end of the socket is referred to as the **back** and is connected to the supporting structure, which may be the platform, a tower, or an anchor.

In the cone-shaped cavity of the steel block, a **zinc casting** fills the gaps between the broomed-out wires of the cable. The some of the telescope's sockets feature a **shoulder** at the front, which is a step in the diameter of the socket's cavity.

For this investigation, we define the **cable slip** as the distance between the front end of the steel block and the front edge of the zinc casting around the cable. This is the distance by which the cable has displaced with respect to the socket since the casting was poured.

Figure 11: Spelter socket nomenclature, shown on socket B4N_G cut open at Socotec's laboratory *(photo: Socotec).*

6.0 Organizations

The organizations referred to in this report are listed in Table 1.

Table 1: List of relevant organizations.

Name	Acronym used in this report	Involvement with the Arecibo Telescope
Ammann & Whitney	AW	Ammann & Whitney (AW) was a structural engineering consulting firm based in New York, NY. AW was the Structural Engineer of Record for the first and second upgrades of the Arecibo Telescope, as well as smaller structural modifications. AW also performed several structural inspections of the Telescope. AW merged with Louis Berger in 2016.
Bethlehem Steel		Bethlehem Steel was a steelmaking company based in Bethlehem, PA. Bethlehem Steel fabricated the steel members of the suspended structure and all of cable sockets of the Arecibo Telescope.
Comsat RSI	RSI	Comsat RSI was a satellite antenna manufacturer and was the prime contractor for the second upgrade of the Arecibo Telescope.
Cornell University	CU	Cornell University managed and operated the Arecibo Observatory from 1963 to 2011.
Elgood-Mayo Corp.		Elgood-Mayo was a subcontractor of Comsat RSI for second upgrade of the Arecibo Telescope. Elgood-Mayo was responsible for tensioning the structure's cables.
Louis Berger		Louis Berger is an engineering consulting firm based in Morristown, NJ. In 2016 Louis Berger merged with AW, which was regularly used as Engineering of Record for structural work on the Arecibo Telescope. In 2018, Louis Berger was acquired by WSP.
National Astronomy and Ionosphere Center	NAIC	Other name of the Arecibo Observatory.
Praeger-Kavanagh		Praeger-Kavanagh was an engineering consulting firm based in New York, NY. Praeger-Kavanagh was the engineer for the original structural of the Arecibo Telescope.
SRI International		SRI International in a nonprofit scientific research institute based in Menlo Park, CA. SRI International managed and operated the Arecibo Observatory from 2011 to 2018.
Temcor		Temcor was the engineer and manufacturer of the Gregorian dome for the second upgrade of the Arecibo Telescope. Temcor is now part of CST.
University of Central Florida	UCF	The University of Central Florida leads a consortium (with Universidad Metropolitana in San Juan and Yang Enterprises) that has been managing and operating the Arecibo Observatory since 2018.
Von Seb		Von Seb was the architect of the original Arecibo Telescope.
Williamsport Wirerope Works	WWW	Former name of Wirerope Works
Wirerope Works		Wirerope Works is a fabricator of steel cables (wire ropes and single strands) based in Williamsport, PA. Wirerope Works fabricated and socketed the auxiliary cables of the Arecibo Telescope. Wirerope Works also socketed the free end of the cable recovered from the collapsed telescope for load testing.
WSP	WSP	WSP is an engineering consulting firm based in Canada. In 2018, WSP acquired Louis Berger, who had previously merged with the Arecibo Telescope's Engineer of Record Amman & Whitney.

Appendix B
Documents and Data Reviewed

1.0 Introduction

Our investigation of the telescope's collapse partially relies on documents and data produced throughout the structure's history.

A primary source of documents is Cornell University's Rare and Manuscript Collections, which we refer to as the CU Archives. CU managed the Arecibo Observatory (AO) from 1969 to 2011, and their archives contain a large volume of documents including reports, contracts, drawings, meeting minutes and correspondence. As shown in Figure 1, the second upgrade of the telescope is particularly well documented. The documents reviewed are listed in Section 2.0 below, and the correspondence reviewed is listed in Section 3.0.

Most of the other documents used in our investigation were provided directly by AO and the University of Central Florida (UCF), who currently manages AO. These include documents produced after the end of the CU era in 2011, and some information that was only available on site such as maintenance records and monitoring data. The main documents and data sets provided by AO and UCF are listed in Section 4.0 below.

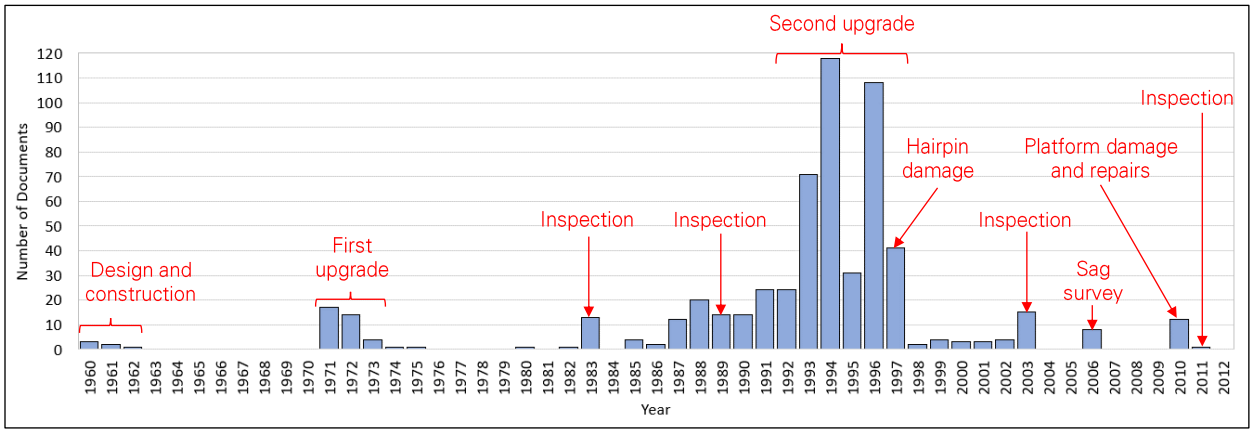

Figure 1: Production dates of reviewed documents retrieved from the CU Archives.

2.0 CU Archives Documents

Table 1: Reviewed documents retrieved from CU Archives.

Date	Title	Author Organization(s)	Contents	Type
1/1/1960	Original Tower Drawings	Von Seb, Inc	Original tower and backstay anchor structural drawings. Tower design is sloped, not stepped.	Drawings
7/19/1960	Boring Log	CU	Boring log from original construction with notes from Bill McGuire.	Report
12/1/1960	Cable and Anchorage Metalwork, Central Feed Structure	Von Seb Inc	Structural drawings of original telescope structure. Includes platform, cables and waveguide. Does not include towers or backstay anchors.	Drawings
6/28/1961	Tower and Backstay anchor structural drawings	Von Seb Inc, Garcia Commercial Inc	Final tower and backstay anchor structural drawings. This is the stepped tower design.	Drawings
7/5/1961	Platform Truss Details	Bethlehem Steel Company	Blueprints of platform and azimuth steel members and connections.	Drawings
1/1/1962	Telescope construction photos	AO	Telescope construction photos.	Media

Table 1: Reviewed documents retrieved from CU Archives.

Date	Title	Author Organization(s)	Contents	Type
1/1/1971	Wind Tunnel Tests of the New Reflector Surface Proposed for the Arecibo Radar Telescope	Sage Action Inc	Results of wind tunnel test of new reflector surface for first telescope upgrade. Performed by Sage Action at Cornell, and Boundary Layer Wind Tunnel Lab at University of Western Ontario.	Report
9/17/1971	Arecibo Proposers Meeting with LTV Electrosystems	US Court Reporters	Meeting minutes of meeting between people from Cornell, LTVE, DBA Service, Bookhaven National Lab were present. LTVE responds to questions from NAIC.	Report
1/1/1972	Upgrade Drawings	AW	Drawings for 1st upgrade. Date is estimated.	Drawings
2/1/1972	Cornell-AW Agreement	CU	Engineering services agreement between Cornell, NAIC, and Amman & Whitney for upgrading the antenna feed positioning and tracking capabilities of Arecibo.	Admin.
2/1/1972	Summary of Modifications	AW	Summary of required modifications for 1st upgrade.	Report
2/28/1972	Arecibo Transmitter Engineering Report [incomplete]	Raytheon	Excerpts from report include table of contents, mechanical design and weight summary, and high-power dummy load design considerations.	Report
2/28/1972	Conceptual Design of a High-Power S-Band Radar Transmitter [incomplete]	Continental Electronics	Includes introduction and weight estimates on catwalk, Azimuth arm, carriage house.	Report
5/8/1972	Engineering Services Agreement - NAIC Upgrading project	CU	Contract between CU and AW to perform condition assessment of telescope structure and study feasibility of the first upgrade.	Admin.
7/15/1972	Arecibo Reflector Upgrading - Project Schedule	LTV	Construction schedule for telescope first upgrade.	Admin.
8/5/1972	Engineering Service Agreements - NAIC Upgrading Project	CU	Contract for AW to (1) evaluate the condition of the structure and (2) perform feasibility study of an upgrade.	Admin.
8/15/1972	Feasibility Study and Concept Development for Upgrading of Suspended Antenna Structure	AW	Report by AW on feasibility of an upgrade. Includes information about design basis and wind loads.	Report
8/15/1972	Results of survey of suspended structure and reflector cable anchorages.	AW	Survey data for platform and reflector anchorages.	Report
9/15/1972	Report on Inspection of cable System	AW	Inspection reports, including count of wire breaks on all cables.	Report
10/20/1972	Tiedown Cable System Anchorages	AW	Drawings for new anchorage tiedowns along with elevation vs. distance plots relative to the existing anchorages	Drawings
10/20/1972	Tie-down Cable System Plan, Elevation and Cable Details	AW	Drawings of tiedown system as modified by 1st upgrade. Mentions 110mph as survival wind speed.	Drawings
2/14/1973	Supplemental Agreement No. 5	CU, E-Systems Garland Division, AW	Agreement between Cornell and LTVE. Includes exhibits: Technical provisions for tie-down cable system, Results of Survey of suspended Structure and Reflector Cable Anchorages, Increase in contract price.	Admin.
3/22/1973	Test report on Hanger G2	AW	Weld testing report on weld on Hanger G2.	Report
9/25/1973	A&W On-Site Trip Report	AW	Notes from trip whose purpose was on-site review and coordination of the design drawing for the upgrade of the elevation railway.	Report
10/9/1973	Invitation for Bids - Site Work, Special Tasks	Continental Electronics	Continental Electronics is the contractor and is asking for bids to be its subcontractor for 6 different tasks.	Admin.
10/18/1974	The Upgraded Arecibo Observatory	Science	6-page paper on the first upgrade of the telescope.	Article
6/15/1975	Instructions, Arecibo Superstructure Analysis Program for use on IBM System/370 (Model 168) Computer at Cornell	CU	Instructions to use a dedicated computer program to analyze the telescope structure.	Report
11/1/1980	Gregorian feed concepts for the Arecibo Telescope	CU	Paper that presents conceptual designs for the Gregorian feed systems in the search for optimum designs.	Report
8/8/1983	Preliminary Cable grip design and quote	Lucker Manufacturing	Quote for a cable grip with capacity of 300 kip.	Admin.

Table 1: Reviewed documents retrieved from CU Archives.

Date	Title	Author Organization(s)	Contents	Type
8/8/1983	Summary of wire break and structural history up to 1983	AW	Part of a report containing map of wire breaks and discovery dates up to 1983. Confirms that all of the breaks are near a socket.	Report
5/9/1985	Radome Pressure Dist. Calculations	NAIC	Calculations of wind pressure on radome surface.	Calcs.
7/30/1985	Radome Wind Tunnel Study Contract (University of Western Ontario & Cornell University)	NAIC	Contract between NAIC and the University of Western Ontario to perform a wind tunnel test in preparation for the addition of a radome on the platform.	Admin.
1/1/1986	Condition of Steel Cable After Period of Service	CU	Paper by CU professors S.L. Phoenix, H.H. Johnson and Bill McGuire. Talks specifically about Arecibo Observatory, and B12-3 cable replaced in 1981 due to wire breaks. Also discusses cable sockets.	Article
11/25/1986	Subcontract Between Cornell and Pratt	CU, Pratt	Subcontract between Cornell and Pratt for Pratt to study seismic effects on the supporting towers.	Admin.
11/9/1988	Inspection "mini physical" scope and cost	AW	Scope and cost of inspection to be performed by AW.	Admin.
12/5/1988	Draft of Engineering service inspection agreement (AW & NAIC)	NAIC	Draft of agreement between NAIC and AW for AW to perform inspection of structure.	Admin.
5/1/1989	Mini Inspection Results	AW	1989 inspection results.	Report
7/1/1989	Report on the Project of Earthquake Related Upgrading of Tower 8 Support at the Arecibo Observatory	Dr. Mikolaj Wegrzyn	Report on upgrading the Tower 8 foundations for seismic reasons.	Report
1/3/1990	Arecibo Upgrade Study	TIW Systems	Report of third party review of preliminary design for the Gregorian upgrade. Mentions good condition of structure.	Report
1/3/1990	NAIC Gregorian Upgrade Drawings	AW	Structural drawings for Gregorian upgrade. Include platform reinforcement, new cables, and changes to backstay anchors and tower tops.	Drawings
9/16/1990	Upgrading Organization Chart	NAIC	Upgrade Planning/Design task group organizational chart and roster.	Admin.
10/2/1990	Proposed organization hierarchy and roles for upgrade	NAIC	Proposed organization charts for upgrade project.	Admin.
10/26/1990	Algorithm and Sample Calcs for Hagen's Geometry	NAIC	Sample calculation to convert six ranging measurements into pointing directions.	Calcs.
12/9/1990	Azimuth Rail Shimming Curve for Lifted Platform	NAIC	Analysis of azimuth rail shimming after the platform has been elevated.	Calcs.
1/17/1991	Revised Photogrammetric Survey Agreement	NAIC	Follow-up to phone call about revisions made to SRMC's proposal.	Admin.
8/19/1991	Proposal for Stress Analysis of the Ring-Girder Hangers at the Arecibo Observatory	Fracture Analysis Consultants Inc	Proposal for FE analysis of current and proposed hangers supporting the ring girder. File also includes related paperwork and correspondence.	Admin.
11/21/1991	Transmittal of Owner/Engineer Agreement between CU and AW	CU	Contract between CU and AW for Gregorian upgrade engineering. Includes NSF's authorization. Details scope of AW's work.	Admin.
1/1/1992	1992 Estimated Design Weight - Gregorian Weight	Unknown	Gregorian dome weight breakdown.	Data
1/1/1992	AO Upgrade Rigging Scheme	Canron	Plan view drawings of the post-Gregorian-upgrade site.	Drawings
1/14/1992	Gregorian Structural System Calculations 02141992	Research Engineers Inc.	STAAD model output includes node displacements, member forces, etc.	Calcs.
1/27/1992	Anchor Cable 8-2 Report	NAIC	Report about observed protuberances on backstay B8-2. Includes sag survey data. Includes note about previous survey error.	Report
2/10/1992	Gregorian Structural System Calculations 02101992	Research Engineers Inc.	STAAD model output includes node displacements, member forces, etc.	Calcs.
3/12/1992	Platform Average Elevation @ Corner of WP for 90°F	NAIC	Plot of average platform elevation between 1974 and 1992.	Data

Table 1: Reviewed documents retrieved from CU Archives.

Date	Title	Author Organization(s)	Contents	Type
4/30/1992	1992 Upgrading Platform Maintenance Report	NAIC	Upgrading platform maintenance report.	Report
6/26/1992	Tensioning of Cable System	AW	Jack set-up to tension auxiliary backstays at ground end.	Drawings
7/1/1992	Auxiliary cable fabrication requirements	NAIC	Requirements for fabrication of auxiliary cables.	Admin.
7/1/1992	Technical Specifications and List of Drawings for Gregorian Upgrading	AW	Specifications and a list of gradings for the 1992 Gregorian upgrade.	Drawings
7/22/1992	Final Report of Structural Analysis of the Existing and Proposed Hangers for the Arecibo Ring Girder	Fracture Analysis Consultants, Inc	Report on FE analysis of existing and proposed ring girder hangers.	Report
9/21/1992	SETI Project	Geotec	Report on geotechnical investigation for SETI project.	Report
10/1/1992	Addendum No. 1 to Specifications for Gregorian Upgrading	AW	Revisions to the specifications for Gregorian Upgrading.	Admin.
1/11/1993	Cable Tensioning Sequence	NAIC	Cable tensioning sequence for Gregorian upgrade. Includes description of steps and weight increase. Overrides previously defined tensioning sequences.	Report
1/11/1993	Cable Tensioning Sequence	AW	Revised cable tensioning procedure.	Procedure
6/14/1993	Design Pressure Coefficients for Spherical Domes	TEMCOR / West Wind Laboratory	Report on wind tunnel tests of lon-span domes. This is a generic test of domes, not specifically of Arecibo's Gregorian dome.	Report
7/9/1993	Submittal of Welding Certifications and Mill Certifications.	RSI	Mill certifications from Bethlehem Steel.	Report
8/5/1993	Wind Tunnel Testing of Dome	RSI	Proposal to perform wind tunnel test of Gregorian dome.	Admin.
8/10/1993	Measurement of the Structural Response of a New Ring-Girder Hanger at the Arecibo Observatory	Fracture Analysis Consultants Inc	Report on in-situ strain gage analysis of the new ring girder hangers.	Report
8/17/1993	Modulus and Ultimate Strength Testing of Six Structural Strands	Williamsport Wirerope Works Inc	Results of strength and stiffness tests of cables for 2nd upgrade, performed at Leghigh University.	Report
9/3/1993	Anchor Dimensions	RSI	Discussion of the dimensions of the aux. backstay anchors, which impacts the length that the cables must be cut at.	Drawings
9/28/1993	Cable Raw Material Certification and Strength Test Results	RSI	Mill certifications and strength test results for auxiliary cables.	Report
10/8/1993	Various mill certifications and steel test reports	Tubular Steel Inc	Mill certificates.	Report
10/17/1993	Revised Cable Length Calculations and Revised Drawings	RSI	Sketches showing aux. cable dimensions based on later survey data.	Drawings
11/11/1993	Various mill certifications and steel test reports	Multiple steel fabricators	Mill Certifications and other test reports.	Report
12/1/1993	Wind study of Arecibo Radio Observatory	West Wind Laboratory	Report on wind tunnel test of Gregorian.	Report
1/26/1994	Waveguide Moment Calc	NAIC	Calc of moment introduced by thermal expansion of the waveguide and its effect on the moment on the joint.	Calcs.
2/9/1994	Transmitter Room Floor Deflections	NAIC	Calc that analyzes the deflection of the transmitter room floor due to load included by transmitter installation and its potential effects on the integrity of the torque tube.	Calcs.
2/14/1994	Borehole logs	Geotec	Bore logs near backstay anchors made in preparation for Gregorian upgrade.	Report
3/25/1994	Feed Platform Erection Plan - Phase 2	RSI	Plan to install X Bracing, Replace the center bearing, and replace some of the bolts.	Procedure

Table 1: Reviewed documents retrieved from CU Archives.

Date	Title	Author Organization(s)	Contents	Type
4/11/1994	Submittal of Plan for the Removal of the Tie Down Cables.	RSI	Plan to remove existing tiedowns.	Procedure
4/14/1994	Arecibo Factory Inspection/Test Submittal Report	RSI	Mill Certifications and other test reports.	Report
4/15/1994	Arecibo Factory Inspection/Test Submittal Report	RSI	Mill certifications.	Report
4/15/1994	Arecibo Factory Inspection/Test Submittal Report	RSI	Mill Certifications and other test reports. Test reports and manufacture of C's Bolts, Nuts and Washers.	Report
4/15/1994	Secondary Submittal of Plan for the Removal of the Tiedown Cables.	RSI	Revised plan to remove existing tiedowns.	Procedure
5/23/1994	Additional Loading of Anchor Blocks by Gregorian Antenna	Geotec	Report on backstay anchor capacity to support additional load from Gregorian upgrade.	Report
6/6/1994	Cable Joint and Saddle Gap	NAIC	Photo and sketch of gap raising future corrosion concerns.	Report
7/5/1994	Feed Platform Erection Plan - Phase 2. Revision A.	RSI	Plan for implementing platform upgrades (cross-bracing, bolt replacement, center bearing installation).	Procedure
7/5/1994	Feed Platform Erection Plan, Revision A	RSI	Plan to implement platform modifications as part of the second upgrade.	Procedure
7/13/1994	AO Upgrade - Structural Upgrade Rigging Schematic	North American Tower King	Rigging drawing for installing the aux. cables.	Drawings
8/3/1994	[8-3-1994] Submittal of Procedure, Cable Tension Monitoring	RSI	Plan for monitoring the cable tensioning procedure. Includes details of the procedure.	Procedure
8/7/1994	Cable Installation and Tensioning Work Plan	RSI	Detailed procedure for aux. cables installation.	Procedure
8/18/1994	Feed Platform Erection Plan - Phase 2. Revision B.	RSI	Revised plan for implementing platform upgrades (cross-bracing, bolt replacement, center bearing installation).	Procedure
8/18/1994	Feed Platform Erection Plan, Revision B	RSI	Revised plan to install X Bracing, Replace the center bearing, and replace some of the bolts.	Procedure
8/24/1994	Cable Installation and Tensioning Work Plan, Rev A	RSI	Detailed procedure for aux. cables installation.	Procedure
9/6/1994	Platform Main Truss reinforcement installations	NAIC	Report that platform reinforcement installation is complete.	Report
9/21/1994	Auxiliary Cable detail structural drawings	RSI	Structural drawings of auxiliary cables and associated hardware (sockets, threaded rods).	Drawings
10/7/1994	Visitor Center for the Arecibo Observatory	Geotec	Report on geotechnical investigation at location of Visitor Center.	Report
11/1/1994	Waveguide modified supports	NAIC	Sketches of modified supports for the waveguide.	Drawings
12/15/1994	Change Order Reference [15-Dec-1994]	CU, RSI	Change orders for Gregorian construction. Supporting information mentions design wind speed and subsequent Gregorian design changes.	Admin.
12/26/1994	Unbalanced Moment, Feed Arm Active Control, Tie Downs	AW	Calculations on feed arm unbalance and tiedown tensions.	Calcs.
1/30/1995	Tower Deflection Monitoring Log	RSI	Tower deflection monitoring log for a few days in January 1995.	Data
8/30/1995	Tower Deflection report	RSI	Plots of tower deflection vs time	Report
10/1/1995	Gregorian Dome Weight	Unknown	Detailed breakdown of Gregorian dome weight.	Data
10/6/1995	Tie Down Jack Design	NAIC	Drawings of power lines and supports for tiedown jacks.	Drawings
10/13/1995	Platform Tie Down Jack	NAIC	Drawings of tiedown jacks.	Drawings
10/30/1995	Update to Permitted Zenith Angle Combinations	NAIC	Provide acceptable combinations of zenith angles for the Gregorian and Line Feed, after Joe Vellozzi increased the allowable unbalance moment on the azimuth.	Calcs.
11/10/1995	Dome Weight, Permitted Zenith Angle, Tie Down Tensions	NAIC	Includes: Gregorian Dome Weight estimate; Electronics Shelter Drawings; Memo "Permitted Zenith Angle Combinations"; Memo Required Tie-down Tensions.	Calcs.

Table 1: Reviewed documents retrieved from CU Archives.

Date	Title	Author Organization(s)	Contents	Type
11/17/1995	Cable Installation and Tensioning Work Plan	RSI	Procedure to install and tension the aux. cables.	Procedure
12/14/1995	Intermediate Tensioning and Tower Deflection Report	RSI	Cable tensioning and tower deflection intermediate report.	Report
1/1/1996	The second Arecibo upgrade	IEEE	6-page paper on the Gregorian upgrade.	Article
3/14/1996	Aux Cable Tensioning	AW	Alternate cable tensioning procedure.	Procedure
4/9/1996	Platform Height Change during dome liftoff on 3 April 1996	NAIC	Monitoring data for platform height as Gregorian upgrade is being implemented.	Report
4/9/1996	Technical Report - Second Intermediate Tensioning	RSI	Report of 2nd intermediate cable tensioning. Includes cable forces and tower deflection measurements.	Report
5/23/1996	Report - 3rd Intermediate Tensioning	RSI	Detailed report on 3rd intermediate tensioning of the cables. Includes cable force measurements.	Report
6/4/1996	Backstay and Main Cables Catenary Sag	NAIC	Sag survey of Tower 4 and 12 cables.	Data
6/4/1996	Tower Deflection after cast tension of auxiliary main cables	NAIC	Sketch and tower deflection measurements.	Data
6/6/1996	A-12 backstay catenary resurvey	NAIC	Results of Tower 12 catenary sag survey.	Report
7/17/1996	Bill McGuire - Proposed Consulting Agreement	NAIC	Proposal to hire Bill McGuire as consultant on cable issues during the Gregorian upgrade.	Admin.
8/15/1996	Optical Lab Project	Geotec	Report on geotechnical investigation at location of Optical Lab.	Report
9/19/1996	Arecibo Observatory - Cable Tension Inconsistencies	NAIC	Report on 1st, 2nd and 3rd intermediate tensioning steps, and cable tension inconsistencies observed.	Report
9/23/1996	Cable Tension Inconsistencies	RSI	Report on difficulties in measuring cable tension during jacking, and inconsistencies in results. Includes summary of previous measurements, and recommendations.	Report
10/28/1996	Joe Vellozzi Draft Procedure, final backstay tensioning	NAIC	Procedure to finish tensioning the backstays.	Procedure
11/14/1996	Feed Platform Weight Audit	RSI	Feed platform weight audit 6/14/1996-11/14/1996	Data
11/14/1996	RSI Platform Weight Data	RSI	RSI Platform Weight Data 6/14/1996-11/14/1996	Data
12/12/1996	(12-12-96) Anchor Cable Broken Wire	NAIC	Photos of a broken wire at Tower 4 backstay anchor.	Media
12/12/1996	Tower Deflection Monitoring Procedure	RSI	Procedure for monitoring the deflection of towers. Includes a log from 1994-1996.	Procedure
2/5/1997	Map of cuts in damaged hairpin	NAIC	Map of cuts in damaged hairpin.	Data
2/6/1997	Arecibo Hairpin Material Property Analysis	LPI	LPI proposal to perform material testing on hairpin.	Admin.
2/6/1997	Hairpin details, damage and updated arrangements	AW, NAIC	Sketches and notes on hairpin damage.	Drawings
2/15/1997	Dome Weight Calibration	AW	Calcs and correspondence about the effect of dead load cable tensions on the deflection and tilt of the gregorian dome.	Calcs.
2/15/1997	Photos (hairpin)	Unknown	Photos of damaged hairpin rod and related laboratory tests.	Media
2/21/1997	Tensioning results from 2-21-97	NAIC	Status report on tensioning activities.	Report
2/25/1997	Evaluation of 3in Diameter Rod - Arecibo Hairpin	LPI	LPI report on testing of damaged hairpin rod.	Report
2/25/1997	Evaluation of 3-in Diameter Rod - Arecibo Hairpin	LPI	LPI test results for hairpin.	Report
2/25/1997	Take-up at T4	NAIC	Comparison of planned vs actual platform position. Includes monitoring data.	Data
3/3/1997	A Proposal to NAIC for Fracture and Fatigue Analyses of a Damaged Hairpin Rod at Arecibo.	Fracture Analysis Consultants	Proposal to analyze damaged hairpin. Scope includes analysis and testing.	Admin.

Table 1: Reviewed documents retrieved from CU Archives.

Date	Title	Author Organization(s)	Contents	Type
3/3/1997	Fracture and Fatigue Analyses of a Damaged Hairpin Rod at Arecibo	Fracture Analysis Consultants, Inc	Report on analysis and monitoring of damaged hairpin.	Report
3/31/1997	Upgrade Weight Tracking	NAIC	Document tracking weight of the platform from 1993 through 3/31/97	Data
4/5/1997	Aux Hairpin Details	AW	Sketches of auxiliary cable hairpin.	Drawings
5/2/1997	Damage to T8 hairpin	RSI	Notice form RSI to Cornell that they will be seeking compensation from Cornell for the extra effort cause by the hairpin damage.	Admin.
6/19/1997	Some facts (and a little history) about Arecibo	Cornell Chronicle	Summary of Arecibo's history, including both upgrades.	Article
9/25/1998	Hurricane George	NAIC	Report on damage sustained by Hurricane George. Mentions 1/16" movement at sockets.	Report
1/25/1999	Seismic Risk Survey, Arecibo Observatory	EQE International	Proposal to perform a seismic risk assessment.	Admin.
8/15/1999	Analysis of survey data taken in June 1999	CU	Analysis of survey of secondary reflector.	Report
10/1/1999	Seismic Risk Survey NAIC Arecibo Observatory	EQE International	Report on seismic risk. Partly based on the review of a 1986 report by Pratt University.	Report
3/15/2000	Main Cable Data (length, weight, angles)	AW	Cable force calculation from cable sag.	Calcs.
12/4/2000	Visitor Center at Arecibo Radio Observatory	Geotec	Report on geotechnical investigation at location of Visitor Center.	Report
12/8/2000	Administration Building at Radio Observatory	Geotec	Report on geotechnical investigation at location of Administration Building.	Report
1/8/2001	North V.S.Q. Building at Arecibo Observatory	Geotec	Report on geotechnical investigation at location of Visiting Scientists Quarters.	Report
2/15/2001	Gregorian Antenna Feed Module Weight Survey	NAIC	Weight of some equipment in the Gregorian. Total is 24 kip.	Data
1/1/2002	The National Astronomy and Ionosphere Center's Arecibo Observatory in Puerto Rico	Single Dish Radio Astronomy	24-page paper on the history of Arecibo Observatory up to 2002.	Article
10/29/2002	Evaluation of Fracture Bolt - Arecibo antenna	LPI	Analysis and testing of a broken bolt.	Report
2/27/2003	Gregorian weight measurements 1998, 2003	NAIC	Results of Gregorian weight measurements performed in 1998 and 2003. Trolley weight is shown separately.	Data
3/27/2003	Weight added to Gregorian by Maintenance Department since December 1993	NAIC	List and weight of items added to the Gregorian between 1993 and 2003. Total is 12 kip.	Data
5/13/2003	Condition Assessment of Radio Telescope - Arecibo Observatory	LPI	Report on assessment of anchor bolts.	Report
5/15/2003	Arecibo telescope Structural Condition Survey 2003	AW	AW report on structural condition survey.	Report
5/28/2003	Suspended Structure Weight Measurement	AW	Sag survey and derived cable forces and platform weight.	Report
7/15/2003	Dome Weight with Jacks	NAIC	Jack pressures during dome weight measurement.	Data
12/4/2003	Arecibo Telescope Structural Review	CU	List of items requiring remedial action, based on AW structural review. Includes condensation in Tower 4 backstay socket boxes.	Report
12/5/2003	Arecibo Telescope Structural Review	NAIC	List of deficiencies identified by the AW 2003 survey.	Report
12/5/2003	Feed Support System Balancing Requirements and Use Limitations	AO	List of constraints and allowances for the feed system and azimuth arm weight and positioning	Calcs.
8/29/2006	Suspended Platform Weight ad Main Cable Tensions from Measured Sags	AW	Results of 2006 sag survey, including cable tensions and platform weight. Also includes platform weight from 2003 and 1992 sag surveys.	Report

Table 1: Reviewed documents retrieved from CU Archives.

Date	Title	Author Organization(s)	Contents	Type
2/1/2010	Report on the Geotechnical Investigation At the Proposed Site for the New Arecibo Observatory Reference Antenna	Sierra Geotechnical Group	Report on geotechnical investigation at location of Reference Antenna.	Report
2/3/2010	Photos (slipped bolts, buckled lacing)	NAIC	3 photos showing slipped bolts and buckled lacing.	Media
2/16/2010	Proposed Repair Procedure	AW	Procedure and drawings to repair damaged member/connection.	Drawings
3/15/2010	Report on the Geotechnical Investigation At the Proposed Site for the HF Antennas	Sierra Geotechnical Group	Report on geotechnical investigation at center of reflector in preparation for installing the 6 HF antennas.	Report
4/6/2010	P-886 soil sample HF Antennas Boring Location	Sierra Geotechnical Group	Boring locations for geotechnical investigation at center of reflector, in preparation for installing the 6 HF antennas.	Drawings
9/8/2010	Proposed reinforcement drawing, 2010 updates	AW	Structural drawings for the reinforcement of 4 platform members.	Drawings
9/8/2010	Proposed Reinforcement Sequence	AW	Order in which 4 platform members are to be reinforced and required azimuth and Gregorian position at each step.	Drawings
3/15/2011	Arecibo Telescope Structural Condition Survey 2011	AW	Full report on condition survey. Includes photographs, drawings with observation locations, and LPI test reports.	Report

3.0 CU Archives Correspondence

Table 2: Reviewed correspondence retrieved from CU Archives.

Start Date	End Date	Instances	Author organization(s)	Subject
3/1/1971	11/18/1971	15	CU, LTV Electro Systems	Pre-Contract Correspondence
9/1/1972	-	1	CU	NAIC Upgrading Project – Comments on A&W Design
12/23/1982	-	1	Bethlehem Steel, CU	Confirmation of Cable Testing
1/10/1983	-	1	CU	Comments on AW Condition Survey Report
1/19/1983	-	1	CU, National Steel Erectors Corp.	Response to cable installation and wire breaking inquiry
4/1/1983	4/22/1983	2	NAIC	Feedback on AW condition assessment report
4/6/1983	-	2	NAIC, William McGuire	Feed Support System Correspondence
7/27/1983	-	1	NAIC, RSI	Testing for Structural Strand
8/8/1983	-	1	CU	Recommended engineering tests and companies for second telescope upgrade
8/8/1983	-	1	CU, Lucker Manufacturing	Proposed Cable Grip - Lucker Manufacturing
8/9/1983	-	1	United States Steel Corp, William McGuire	Strand Testing Correspondence and Meeting Minutes
8/19/1983	-	1	NAIC	Tower Top - Main Cable No. 4
9/30/1985	11/6/1985	2	CU, NAIC	Radome Wind Tunnel Study
4/1/1987	12/3/1987	12	AW, CU, Metropolitan Soils and Engineering Materials Laboratory, Inc., NAIC	Review of Geotec Subsoil Exploration Report
4/5/1988	-	2	NAIC, William McGuire	Cable deterioration concerns article
9/12/1988	9/25/1988	3	AW, NAIC	A12-3 slackening after 1981 installation
11/9/1988	11/21/1988	2	AW, NAIC	Suspended Structure "mini physical"
11/22/1988	-	1	AW, CU	Proposal to increase AW inspection scope to include NDT of welds
12/10/1988	12/16/1988	10	AW, CU, NAIC	Monitoring the Embedded Backstay Cables, mini physical, testing
1/11/1989	-	10	NAIC	Main Cable M4-4 Wire Broken
1/20/1989	-	1	CU, NAIC	Request for CU Facilities and Business VP to be a part of condition survey results conversation

Table 2: Reviewed correspondence retrieved from CU Archives.

Start Date	End Date	Instances	Author organization(s)	Subject
1/24/1989	-	1	AW, NAIC	Cracks in azimuth ring girder hangers
2/12/1990	-	3	NAIC, Planning/Design Task Group	Meetings #1-3 Minutes, Appendices
10/2/1990	-	1	NAIC, NSF	Proposed organization hierarchy and roles for upgrade
10/15/1990	-	1	NAIC	Platform Lift Discussion
12/7/1990	12/9/1990	3	NAIC, Planning/Design Task Group	Review of separate carriage house and feed system, Azimuth Rail, Carriage House Layout
1/16/1991	1/17/1991	4	NAIC, Southern Resource Matting Corporation	Photogrammetric Survey SRMC
2/11/1991	-	10	NAIC, Planning/Design Task Group, Composite Engineers	Meetings #4-9 Minutes, Appendices
7/16/1991	-	1	AW, NAIC	Platform Balancing Requirements and Use Limitations
8/27/1991	10/9/1991	3	Cirrus Consulting, NAIC	Arecibo Antenna Analysis
10/8/1991	-	1	Antenne-Kildal, NAIC	Synthesis of Gregorian Arecibo Feed
10/17/1991	-	1	NAIC	Report on NAIC Interaction with Scientific Technical Upgrading
10/18/1991	-	1	NAIC	Memorandum Ground Screen Configuration
1/12/1992	-	6	NAIC, Planning/Design Task Group	Meetings #10-14 Minutes, Appendices
2/18/1992	-	1	AW, NAIC	Necessary tiedown arrangement for structural and Gregorian considerations
5/11/1992	8/13/1992	2	AW, NAIC	Presentation/comments on AW 95% completed detailed design work
7/1/1992	-	1	AW	Confirmation of vertical tiedown outrigger stability
7/1/1992	-	1	AW, RSI	Design Wind Speed, Gregorian Dome
1/11/1993	-	1	Wire Rope Industries of Canada, Ltd	Prestretching Procedure
1/19/1993	-	6	NAIC	Meeting #15-20 Minutes, Appendices
2/4/1993	-	1	AW, NAIC	Proposed steel collars and new tower saddles, exceptions to cable specifications
5/6/1993	-	1	NAIC	Site Map Database
6/1/1993	-	4	AW, RSI	Anchor Bolt Alignment, Cables, Working Slab on Main anchors, Structural Cable Information
6/1/1993	-	2	RSI, Williamsport Wirerope Works	Elevated strength cable design and testing, Discussion of auxiliary cable testing loads and schedules
6/14/1993	-	1	RSI, Temcor, West Wind Laboratory	Design Pressure Coefficients for Spherical Domes
6/29/1993	7/1/1993	2	AW, NAIC	Anchor A8, Newly Discovered Shelf, Testing of Structural Strands
7/9/1993	-	6	AW, NAIC, RSI	Cable Length / Survey Data, Testing, Cable Joint, Anchor Dimensions
10/1/1993	1/1/1994	9	AW, NAIC, RSI	Gregorian Wind Tunnel Tests
10/1/1993	10/1/1996	24	Continental Electronics Corporation, NAIC, RSI, Temcor	Weight correspondences (43 pages)
10/17/1993	-	1	AW, RSI	Revised Cable Length Calculations and Revised Drawings
1/1/1994	-	2	Hart Consultant Group, Temcor, WWL	Design Wind Speed, Gregorian Dome Upgrading
1/4/1994	-	1	NAIC	WWL wind Tunnel test comments
2/2/1994	-	1	CU	Arecibo seismic upgrade comments
2/7/1994	-	1	RSI, Temcor	Dome design per clearance, deflection, and wind speed
2/17/1994	-	1	CU, NAIC	Earthquake design magnitude
2/26/1994	-	1	NAIC, William McGuire Consulting Structural Engineer	ASCE 7-95 Wind Loads
2/28/1994	-	1	NAIC	WR-2100 layout for 430 MHz Transmitter in Gregorian

Table 2: Reviewed correspondence retrieved from CU Archives.

Start Date	End Date	Instances	Author organization(s)	Subject
3/1/1994	-	2	AW, NAIC, RSI	Dome design wind speed clarifications
3/3/1994	-	1	CU, RSI	Arecibo Gregorian Upgrading Project
3/17/1994	-	1	NAIC	430 MHz Waveguide
4/1/1994	-	3	NAIC, RSI	Submittals of Plan for the Removal of the Tie Down Cables
4/7/1994	-	1	NAIC	Comments on Platform Erection Plan, Phase 2
5/1/1994	-	2	NAIC	430 MHz Waveguide
5/1/1994	8/1/1995	4	NAIC	Azimuth Feed Arm Center Bearing
5/4/1994	-	12	NAIC	Platform Main Truss Reinforcement Installations, Platform Erection Plan
5/18/1994	1/6/1994	3	AW, NAIC	Cable Joint Weldment Rat Hole Memo #4, Cable Joint and Saddle Gap
6/1/1994	4/1/1997	22	AW, NAIC, RSI	Cable Drape for Gregorian, Field issues
6/21/1994	-	1	AW, RSI	Main Aux Cables
6/21/1994	-	1	NAIC	Weldment #06 on RSI Drawing 15040
6/23/1994	-	6	NAIC	Auxiliary Main Cable Joints - Clip Angle Hole Reaming
7/5/1994	-	1	NAIC	Thoughts about the 430 MHz System in the Gregorian
7/19/1994	-	1	RSI, NATK	Review of Procedure
8/22/1994	8/29/1994	2	NAIC	Cable Installation and Tensioning Work Plan procedure comments
8/26/1994	-	1	AW, NAIC	Waveguide Realignment Detail
9/1/1994	4/1/1997	17	AW, NAIC	Tiedown Information
9/13/1994	-	1	NAIC	Exist Main Cable Adjustment
9/22/1994	-	1	NAIC, RSI	Cable Tension Monitoring Procedure
11/1/1994	-	1	NAIC	Waveguide modified supports
11/3/1994	-	1	NAIC	Additional Spacers on the Cable Fittings at the Tower Saddle
2/3/1995	-	11	AW, NAIC, RSI	Cable tensioning procedure, monitoring, comments
2/20/1995	-	1	NAIC	430 MHz Transmitter
2/23/1995	-	1	NAIC	A.O. Existing Jack Equipment
2/27/1995	-	1	AW, NAIC	Platform Weight
3/7/1995	-	1	AW, NAIC, RSI	Chafing Plate Rework
5/18/1995	-	1	NAIC	WR-2100 for Upgrade
10/6/1995	-	1	NAIC, RSI	First Intermediate cable tensioning
10/11/1995	-	3	AW, NAIC	Permitted Zenith Angle Combinations, Dome Weight, Tie Down Tensions
10/20/1995	10/23/1995	2	NAIC, RSI	Cable tensioning, shims
1/12/1996	-	1	NAIC, RSI	Tower Deflection
1/25/1996	-	1	NAIC	Updated weight tracking sheets
1/25/1996	-	2	NAIC, RSI	Relief from Backup Cable Tensioning Monitoring
2/2/1996	-	1	NAIC	430 MHz System
2/3/1996	-	3	NAIC	430 MHz Switch
2/8/1996	-	1	NAIC	Carriage House 1
2/8/1996	-	1	NAIC, RSI	Feed System Weight for Intermediate Tension
2/14/1996	-	1	NAIC, RSI	Intermediate Cable Tensioning #2
3/4/1996	-	3	NAIC	Platform Elevation
3/13/1996	-	1	AW, NAIC	Aux Cable Creep
3/14/1996	-	1	NAIC, RSI	Update of Dome Weight Estimate
3/27/1996	-	1	AW, NAIC	Final Cable Adjustments
4/17/1996	-	1	Elgood-Mayo, NAIC	Request for budget estimates for maintenance due to anticipated cable creep
4/29/1996	4/30/1996	5	AW, NAIC, RSI	2nd/3rd intermediate tensioning
4/30/1996	-	1	NAIC, RSI	Chairs for monitoring existing backstay

Table 2: Reviewed correspondence retrieved from CU Archives.

Start Date	End Date	Instances	Author organization(s)	Subject
5/1/1996	-	1	NAIC	Tensioning – 3-inch rise after backstay tensioning
5/1/1996	5/2/1996	2	NAIC	Platform Height, 15 March - 15 May 1996
5/2/1996	-	1	NAIC	Dome lift line winch tension
5/6/1996	-	2	AW, NAIC	Main Cables/Anchors 4 and 12, Catenary measurement, backstays, aux mains
5/7/1996	5/8/1996	7	AW, NAIC, RSI	3rd Intermediate Tensioning, cable geometry/force calculations
5/7/1996	-	1	NAIC, RSI	Main aux cables additional jacking requirements
5/9/1996	-	1	NAIC, RSI	Work stopped on upgrade
5/9/1996	-	1	NAIC, RSI	Data on Hydraulic Cylinders
5/22/1996	-	1	NAIC	Platform Weight sheets - updated
6/1/1996	-	5	AW, NAIC, RSI	Monitoring of A12 backstays
6/6/1996	-	1	AW, NAIC	Platform Position Before and After Intermediate Tensioning
6/12/1996	-	1	AW, NAIC	Cable sags/tensions
6/26/1996	-	1	AW, NAIC	Cable Tension Summary
6/28/1996	-	1	NAIC	Cable Sag Survey
7/6/1996	-	1	NAIC	Weight Sheets
7/8/1996	-	1	William McGuire Consulting Structural Engineer, Construction Technology Laboratory	Cable tension measurement technique discussion
7/30/1996	-	1	NAIC, RSI	Cable Tension Verification with Sag Measurement
8/7/1996	8/12/1996	2	AW, NAIC, RSI, Temcor	Dome Correspondence
9/18/1996	-	10	AW, CEC, NAIC, RSI	Waveguide Correspondence
10/2/1996	-	1	Elgood-Mayo, RSI	Measurement accuracy and recalibration
10/11/1996	-	3	NAIC	A4,8,12 Cable oscillation period measurements
10/15/1996	-	1	AW, NAIC	Final Cable Tensioning and Raising of Platform
10/18/1996	-	1	AW, NAIC	Ballast Platform Weight
10/22/1996	-	1	NAIC, William McGuire Consulting Structural Engineer	Idea to install strain gages on aux backstays to monitor forces
10/23/1996	-	2	AW, NAIC, RSI	Tensioning and tiedown installation schedule clarification
10/30/1996	-	1	AW, NAIC	Jacking Testing Scheme
10/30/1996	-	1	NAIC, RSI	Weight addition/removal, context unspecified
11/1/1996	11/9/1996	2	AW, NAIC	A-4 Cable Catenary Sag
11/1/1996	1/1/1997	13	AW, NAIC, RSI	Final backstay tensioning (procedure, final measurements)
1/24/1997	1/31/1997	2	AW, NAIC	Platform Elevation Survey Following Tensioning at Corner 4, Cable U bolt cut on Main 8-4
1/25/1997	1/26/1997	2	AW, NAIC	Monitor tension, Final jacking tensions per cable
2/1/1997	-	10	NAIC, RSI	Final tensioning at all towers
2/2/1997	2/14/1997	6	Anthony Ingraffea Consulting Structural Engineer, AW, LPI, NAIC, RSI	Damage to T8 Hairpin, Summary, Testing, Examination
2/2/1997	-	1	AW, NAIC	Send 12" samples to LPI
2/15/1997	-	1	AW, NAIC	Dome Weight Calibration
2/17/1997	-	1	NAIC	Load Cell
2/18/1997	-	1	CU, RSI	Your Letter of February 5, 1997
3/10/1997	-	1	NAIC	Hairpin nuts
5/2/1997	-	1	NAIC, RSI	Damage to T8 hairpin
11/6/1998	-	1	AW, NAIC	Cable Tensions
1/12/1999	-	1	NAIC, EQE International	NAIC's request for a proposal to perform seismic risk assessment
11/14/2001	-	1	AW, CU	Gregorian Trolleys

Table 2: Reviewed correspondence retrieved from CU Archives.

Start Date	End Date	Instances	Author organization(s)	Subject
1/24/2002	-	1	NAIC	Dome Feed Module Load
9/18/2002	-	1	AW, NAIC	Shim Block Bolts
3/28/2003	-	1	NAIC	Dome Weight
5/12/2003	-	1	NAIC	Broken Wires in Cables
5/26/2003	-	1	AW, NAIC	Dome Weight from Platform Corner Displacement
7/23/2003	7/24/2003	2	NAIC	Anchor 8 Broken Wire, Gregorian Dome Weight
12/11/2003	-	1	NAIC, William McGuire Consulting Structural Engineer	Comments on azimuth drive/feed arm system
3/17/2006	-	2	NAIC	Catenary Survey
6/6/2006	-	1	CU, NAIC	T4 Auxiliary cable force discrepancy
7/21/2006	8/29/2006	2	AW, CU	Suspended Catwalk System Limiting Weight Study
8/31/2006	9/1/2006	2	CU, NAIC	Cable Reactions on Towers
2/11/2010	-	1	AW, NAIC	Notes on proposed connection repair
2/14/2010	-	1	AW, CU, NAIC	Arecibo Repair
4/20/2010	-	2	AW, CU, NAIC	Meeting
11/29/2010	-	1	William McGuire	Questions and Suggestions for Studies and Action Concerning Arecibo

4.0 Documents and Data Provided by AO and UCF

Table 3: Reviewed documents and data provided by AO and UCF.

Start Date	End Date	Title	Author Organization	Contents	Type
1/1/1969	12/31/1989	Quarterly Maintenance Reports	AO	Quarterly report describing the telescope's condition and maintenance performed.	Maintenance Records
1/1/1997	12/31/2017	Maintenance cards	AO	Logs of maintenance performed on the telescope.	Maintenance Records
1/1/2004	12/1/2020	Wind speed data	AO	Wind speed and direction recorded at platform weather station.	Data
6/1/2004	8/10/2020	Telescope operation data	AO	Azimuth, Gregorian and line feed angles and tiedown forces vs. time.	Data
1/14/2014	-	M8-4 splice photos	AO	Photos of broken wires in M8-4 splice box.	Media
3/11/2014	-	Earthquake Damage to Main Support Cable M8-4	AW	Report on M8-4 splice bypass	Report
4/24/2017	-	Arecibo Observatory – Main Cable Tensions and Suspended Platform Weight from LIDAR Measured Cable Sags	Louis Berger	2016 Sag Survey	Report
1/1/2018	12/1/2020	Maintenance Logs	AO	Logs of maintenance performed on the telescope.	Maintenance Records
8/10/2020	-	Platform position data	AO	Platform corner elevation and platform rotation before and after M4N failure.	Data
8/11/2020	11/30/2020	Drone inspection photos	AO	Drone inspection photos of cables and sockets near the towers and platforms, performed regularly after the first cable failure.	Media
9/1/2020	-	Cable sag survey	AO	Laser scans of the telescope's cables performed after the first cable failure.	Data

Appendix C
Telescope Structure and Cable System History

1.0 Introduction

After the original structure of the Arecibo Telescope was completed in 1963, the structure was modified several times over its 57-year lifespan before collapsing in 2020. In addition to occasional changes, repairs, and reinforcements, two major upgrades were completed in 1974 and 1997.

This appendix traces the structure's history, with a focus on the events that affected the cable tension, including a significant modification of the cable system during the second upgrade and several changes in the weight of the suspended structure over time. The structure also experienced numerous wind storms and earthquakes, and the impact of these events on the cable tensions are covered in Appendix J and Appendix K. The evolution of the condition of the cable system is detailed in Appendix D.

2.0 Construction

The Arecibo Telescope was constructed over three years from 1960 to 1963. The site was selected for its topography, with a natural sinkhole large enough to fit the 1,000-foot-diameter reflector with minimal excavation work (Figure 1). The three towers needed to support the telescope's feeds 500 feet above the reflector were built on hills surrounding the sinkhole (Figure 2, Figure 3), reducing the tower height required. The platform was first assembled at the bottom of the sinkhole and lifted into place using temporary cables supported by the towers (Figure 4). The permanent cables between the towers and platform were then installed and tensioned. We found no record of the specific cable tensioning procedure used at the time, but the general method indicates that during construction the original cables did not experience tensions greater than the final tensions. Finally, the ring girder and the azimuth arm were hoisted up from the platform (Figure 5) and connected to complete the suspended structure (Figure 6). The telescope became operational in November 1963.

The design cable tensions in the newly-constructed telescope are provided in the original structural drawings by Praeger-Kavanagh (Figure 7) for several load cases. These include a baseline case where the structure only supports its own weight, unaffected by exterior conditions or events, and an ultimate case where the structure has cooled down by 20°F and resists 140 mph winds. The cable tensions in these two cases are compared to the minimum breaking strength of the cables in Table 1. The average safety factor (SF) is 2.07 in the baseline case and 1.67 in the ultimate case.

To determine the design weight of the suspended structure, we calculated the vertical reactions at the platform end of the mains and tiedowns. With the calculations based on standard catenary equations and the known cable weight, endpoint coordinates and baseline tensions, the suspended structure weight is estimated to be 1,220 kilopound (kip).

The backstays were surveyed in 1972 in preparation for the first upgrade of the telescope and, as shown in Table 1, the measured backstay tensions were within three percent of the design tensions. While we did not find any similar survey results for the main cables, the close agreement of the design and surveyed backstay tensions suggests that in 1972, the other cable tensions and the suspended structure's weight were likely close to the design values provided in the original structural drawings.

Figure 1: Telescope site during partial excavation of hills around the natural sinkhole in December 1960
(photo: NAIC Arecibo Observatory, a facility of the NSF).

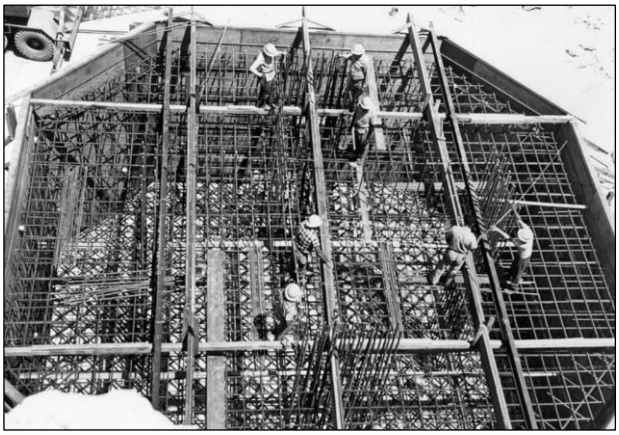

Figure 2: Reinforcement being laid out in the pedestal of Tower 12 in April 1961
(photo: NAIC Arecibo Observatory, a facility of the NSF).

Figure 3: Temporary cable system, later used to lift the platform in September 1962
(photo: NAIC Arecibo Observatory, a facility of the NSF).

Figure 4: Platform being lifted into place in October 1962
(photo: NAIC Arecibo Observatory, a facility of the NSF).

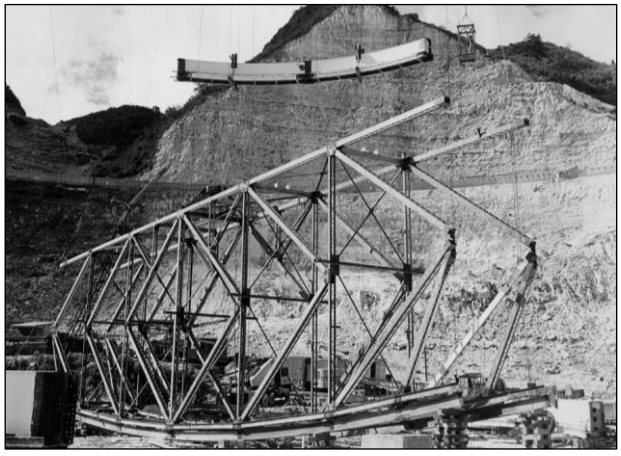

Figure 5: Ring girder segment being lifted to the platform while the azimuth arm is being assembled in December 1962
(photo: NAIC Arecibo Observatory, a facility of the NSF).

Figure 6: Original telescope structure essentially complete in August 1963
(photo: NAIC Arecibo Observatory, a facility of the NSF).

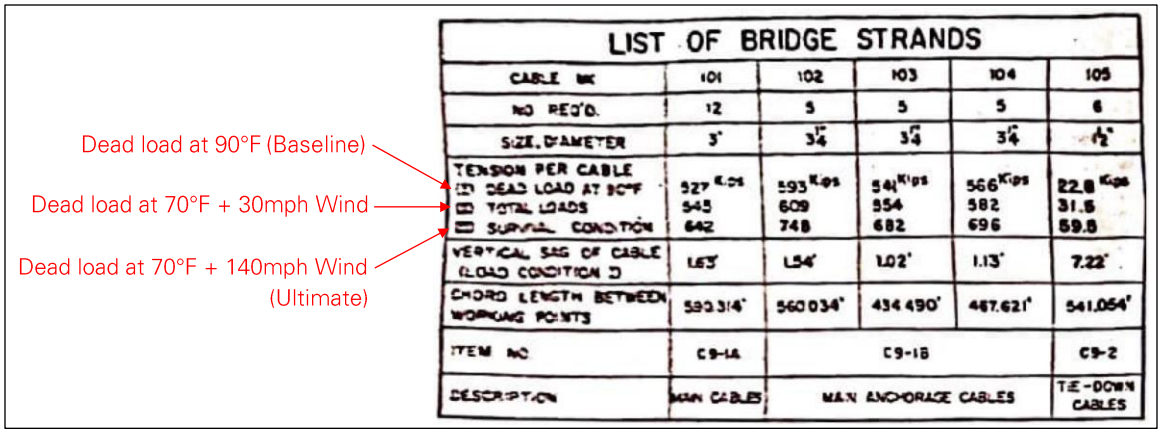

Figure 7: Design cable tensions in original structural drawings
(image: structural drawings, courtesy of NAIC Arecibo Observatory, a facility of the NSF).

Table 1: Design and measured cable tensions and safety factors (SF) before first upgrade.

		Mains	Tower 4 Backstays	Tower 8 Backstays	Tower 12 Backstays	Average[C]
1960 Design Drawings[A]	**Minimum Breaking Strength [kip]**	1,044	1,212	1,212	1,212	-
	Baseline Tension [kip] (SF)	527 (1.98)	593 (2.04)	541 (2.24)	566 (2.14)	(2.07)
	Ultimate Tension [kip] (SF)	642 (1.63)	748 (1.62)	682 (1.78)	696 (1.74)	(1.67)
	Ultimate / Baseline	1.22	1.26	1.26	1.23	1.24
1972 Survey[B]	**Average Tension [kip] (SF)**	-	590 (2.05)	523 (2.32)	556 (2.18)	(2.18)
	Maximum Tension [kip] (SF)	-	658 (1.84)	558 (2.17)	577 (2.10)	-
	Tension Coefficient of Variation	-	7.1%	4.1%	2.7%	-
	Survey Average / Design Baseline	-	1.00	0.97	0.98	0.98

[A] Praeger-Kavanagh. Structural drawings for original telescope. December 1, 1960. Drawings provided by Arecibo Observatory.
[B] Ammann & Whitney. *Results of Survey of Suspended Structure and Reflector Cable Anchorages*. August 1972. Report retrieved from Cornell University archives.
[C] Average weighted by number of cables.

3.0 First Upgrade

The first major upgrade of the telescope was completed in 1974. The most significant change consisted in covering the primary reflector with aluminum panels to improve the accuracy of the reflector surface (Figure 8), which had no impact on the telescope's superstructure.

The cable system of the superstructure was also modified (Figure 9). The original cable system included six inclined tiedowns connecting the platform to the ground and providing torsional stiffness to the suspended structure. The tiedowns had to be sufficiently pre-tensioned (23 kip at 90°F per the original structural drawings) to minimize sag and provide the required stiffness. As part of the first upgrade, a carrier cable with a set of hangers was installed directly over each tiedown to support it from above, eliminating tiedown sag. As a result, the tiedown stiffness was increased without increasing the pre-tension, which was in fact decreased, down to 8 kip at 90°F per the structural drawings of the first upgrade (Figure 10). This modified tiedown system was designed by Ammann & Whitney (AW).

The first upgrade also added 30 kip of new equipment[1] to the suspended structure, increasing its total weight to 1,250 kip. However, the reduction in tiedown pre-tension adequately compensated for the weight increase, so that the net effect of the first upgrade was a slight reduction in the main cable tensions (Table 2). We estimated the reduction to be 1.4 percent.

Figure 8: Aluminum panels being installed on the primary reflector during the first upgrade *(photo: NAIC Arecibo Observatory, a facility of the NSF).*

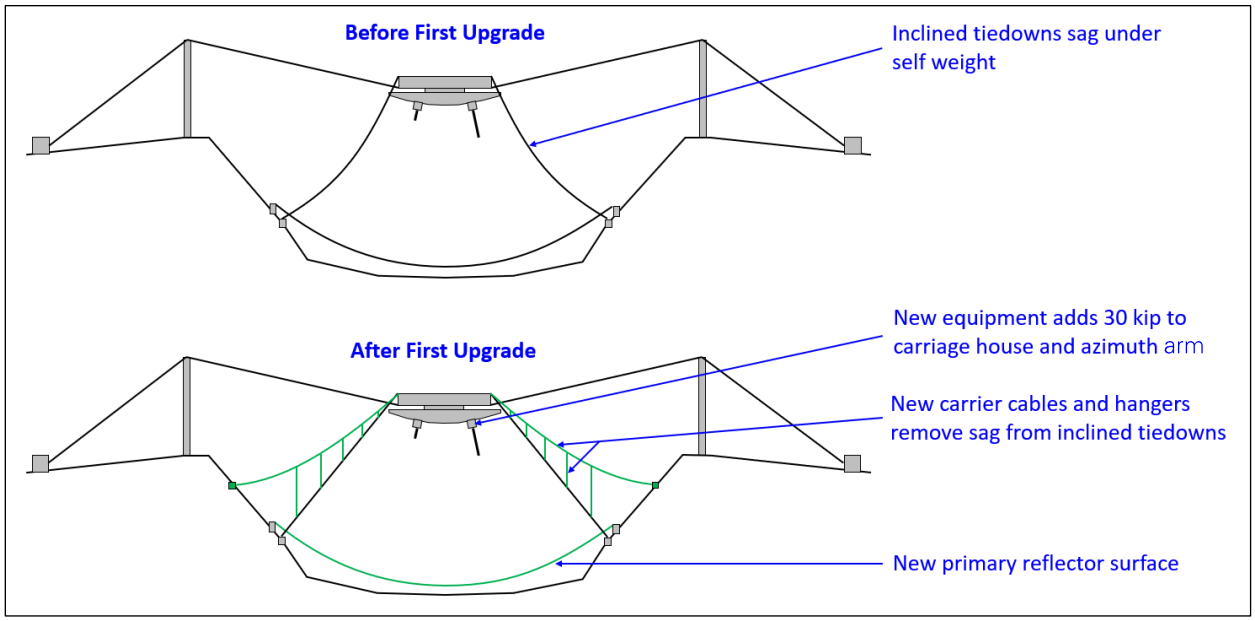

Figure 9: First upgrade of telescope structure.

[1] Lalonde, L.M. "The Upgraded Arecibo Observatory". *Science*. Vol 186. October 18, 1974.

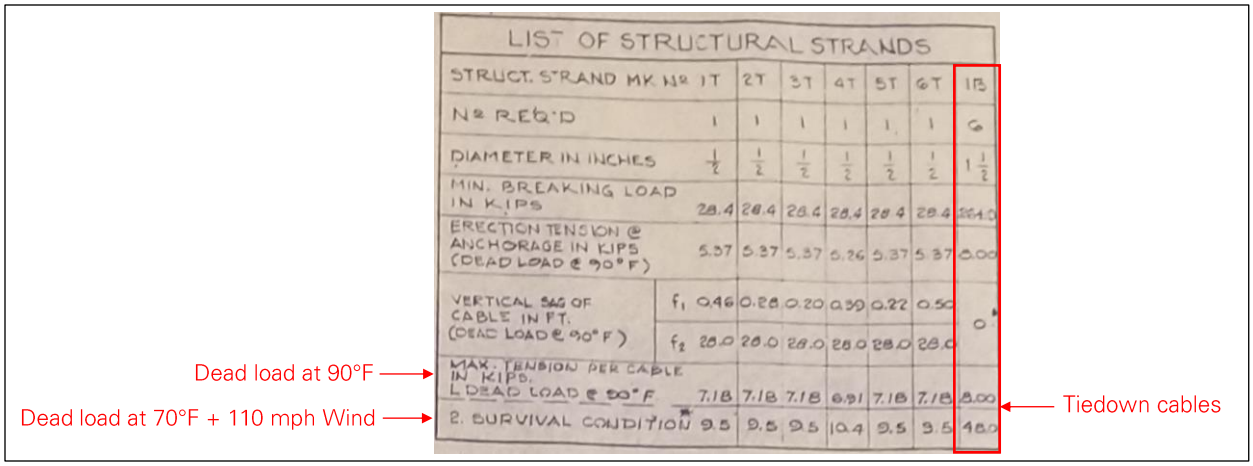

Figure 10: Tiedown tensions in structural drawings for first upgrade
(image: structural drawings, courtesy of NAIC Arecibo Observatory, a facility of the NSF).

Table 2: Impact of first upgrade on main cable tensions. Tiedown and carrier cable tensions are for dead load at 90°F.

	Before First Upgrade	After First Upgrade	Relative Change
Suspended Structure Weight [kip]	1,220	1,250	+2.5%
Tiedown Average Tension [kip]	22.8	8	-64.9%
6 Tiedowns Total Vertical Pull on Platform [kip]	111	37	-66.7%
Carrier Cable Average Tension [kip]	-	5.5	-
6 Carrier Cables Total Vertical Pull on Platform [kip]	-	26	-
Total Vertical Force Resisted by Main Cables [kip]	1,331	1,313	-1.4%

4.0 Between Upgrades

The telescope structure did not change significantly between the two major upgrades, although the weight of the suspended structure likely varied as equipment and instruments were added and removed over time. We estimated its weight to be 1,250 kip after the first upgrade (section 0 above), while the cable tensioning sequence for the second upgrade started with a weight of 1,300 kip (section 5.0 below). This 50-kip discrepancy may reflect an actual weight increase between the upgrades, but could also be due to differences in calculation assumptions between the two upgrades. In any case, 50 kip is less than five percent of the suspended structure's weight.

One noteworthy event between the two upgrades is the replacement of a backstay cable in September 1981. After discovering a sixth broken wire at the ground end of cable B12-3, Arecibo Observatory (AO) had the cable replaced to prevent further wire breaks and potential cable failure. The cable end and socket with the broken wires were analyzed at Cornell University (Figure 11), with the findings presented in a paper by Phoenix, Johnson, and McGuire.[2] In 1988, AO determined that the replacement cable had

[2] Phoenix, S.L., Johnson, H.H., and McGuire, W. "Condition of Steel Cable after Period of Service". *Journal of Structural Engineering.* 112(6). 1986.

lost approximately 10 percent of its tension,[3] which according to AW was due to regular cable relaxation after installation, and caused only a 2.5 percent tension increase in the other four backstays of Tower 12.

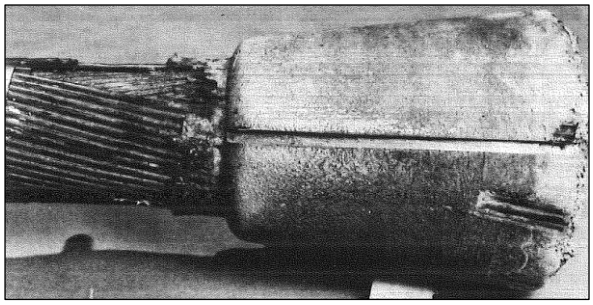

Figure 11: Zinc casting at ground end of cable B12-3 replaced in 1981 *(photo: Phoenix, Johnson, and McGuire[4]).*

5.0 Second Upgrade

The second major upgrade of the telescope, undertaken between 1995 and 1997, significantly modified the suspended structure and cable system (Figure 12). The primary purpose of the upgrade was to replace one of the carriage houses and line feeds with a Gregorian dome (Figure 13), henceforth referred to as the Gregorian. The Gregorian is an enclosure containing new instruments that added capabilities to the telescope (secondary and tertiary reflectors and new radio feeds). The Gregorian, however, is more than five times heavier than the removed carriage house (200 kip v. 35 kip), so to mitigate the imbalance on the suspended structure, a counterweight was added at the tip of the azimuth arm opposite the Gregorian. In addition, the steel trusses of the platform and azimuth arm had to be reinforced to accommodate the new loads, further increasing the suspended structure's weight. Finally, the inclined tiedowns and carrier cables were removed and replaced with vertical tiedowns, which required the addition of outriggers at the platform corners so that the new vertical tiedowns were kept clear of the azimuth arm rotation.

[3] Joe Vellozzi (Ammann & Whitney). Letter to Jose Maldonado (Arecibo Observatory). September 27, 1988. Correspondence retrieved from Cornell University archives.

[4] Phoenix, S.L., Johnson, H.H., and McGuire, W. "Condition of Steel Cable after Period of Service". *Journal of Structural Engineering.* 112(6). 1986.

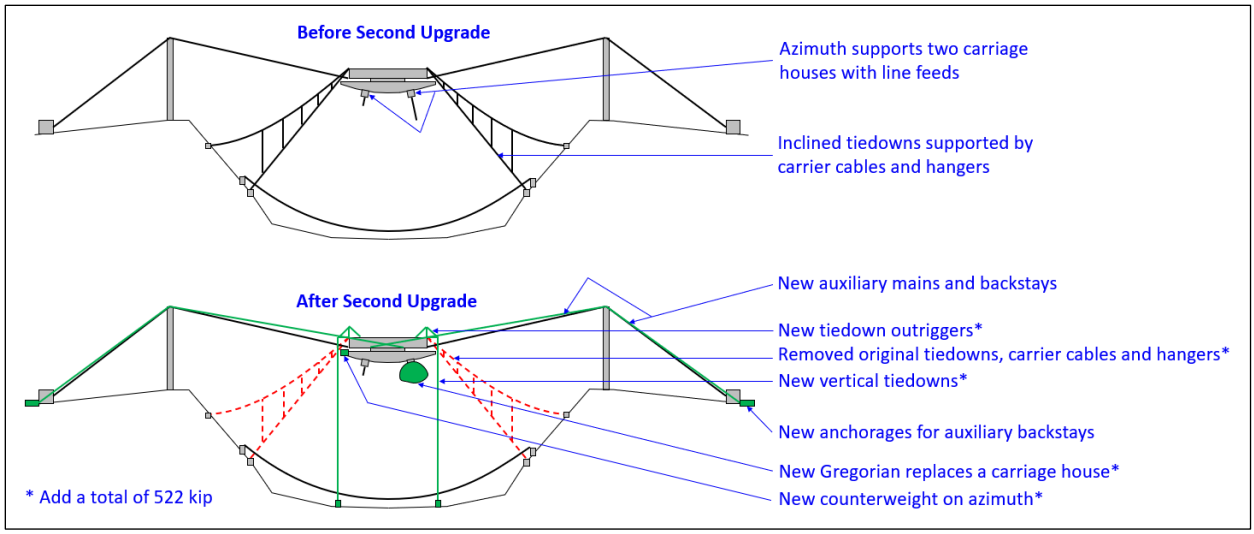

Figure 12: Second upgrade of telescope structure.

Figure 13: Gregorian being lifted into place during second upgrade
(photo: NAIC Arecibo Observatory, a facility of the NSF).

AW provided the structural design of the second upgrade, and Table 3 provides a breakdown of the changes to the suspended structure's weight and tiedown tensions specified in AW's structural drawings. The total weight of the suspended structure was increased by 522 kip, a 42 percent addition over the estimated weight of 1,250 kip before the upgrade. After adding the contribution of the tiedown tensions, the total vertical load resisted by the main cables increased by up to 616 kip. The new tiedowns were expected to be released in advance of major wind events (*storm condition* in Table 3) to reduce the vertical load on the main cables.

Table 3: Suspended structure weight and tiedown tension changes in second upgrade.
Adapted from structural drawings for second upgrade.

	Suspended Structure Weight Change [kip]	Tiedown Total Vertical Force Change [kip]	Change in Total Vertical Force Resisted by Main Cables [kip]
Platform Reinforcement	+70	-	+70
New Tiedown and Outrigger System	+48	-	+48
Changes to Ring Girder and Azimuth Arm Trolleys	+78	-	+78
Azimuth Arm Reinforcement and Add'l Equipment	+135	-	+135
Carriage House Removal	-33	-	-33
New Gregorian	+170	-	+170
New Counterweight and Framing	+54	-	+54
Inclined Tiedowns and Carrier Cables Removal	-	-50	-50
New Tiedowns (Storm Condition)	-	+144 (+15)	+144 (+15)
Total (Storm Condition)	+522	+94 (-35)	+616 (+487)

To accommodate the increased load, 12 cables were added to the structure. These new cables are referred to as auxiliary cables. At each of the three towers, two auxiliary cables were added between the tower and the platform (auxiliary mains), and two were added between the tower and the ground (auxiliary backstays). Each auxiliary cable is larger in diameter and designed to carry more tension than the corresponding original cable. The design cable tensions for several load cases are provided in the structural drawings (Figure 14), including a baseline case (dead load only) and an ultimate case (maximum wind). The baseline and ultimate cable tensions before and after the upgrade are summarized in Table 4, with the corresponding safety factors. The upgrade increased the safety factor in the original cables, on average from 2.07 to 2.26 in the baseline case, and from 1.67 to 2.16 in the ultimate case. For the auxiliary cables, the average safety factor was 2.24 in the baseline case and 2.15 in the ultimate case. The safety factors were therefore essentially identical for the original and auxiliary cables after the upgrade.

On average over all of the cables, the ultimate tension was only 5 percent higher than the baseline tension after the upgrade, while the difference was 24 percent before the upgrade. There are two reasons for this discrepancy. First, the design of the upgraded structure assumes that the new tiedowns will be released in advance of a significant wind event, so that the main and backstay tensions are reduced before the arrival of the ultimate wind load. Second, according to the structural drawings, the design wind speed for the upgraded structure was 100 mph, while the original structure was based on a design wind speed of 140 mph. The design wind speed is further discussed in Appendix J.

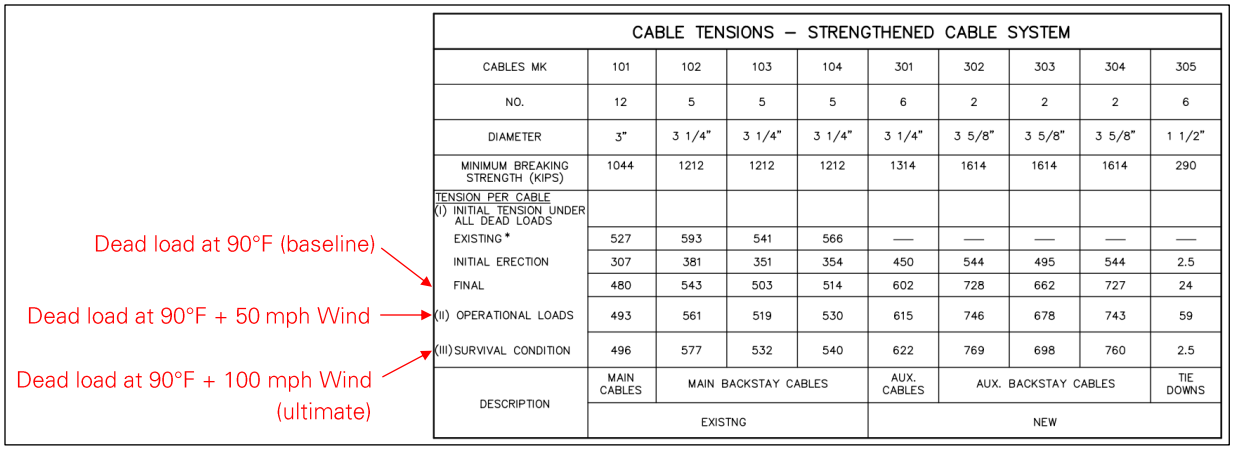

CABLE TENSIONS – STRENGTHENED CABLE SYSTEM

CABLES MK	101	102	103	104	301	302	303	304	305
NO.	12	5	5	5	6	2	2	2	6
DIAMETER	3"	3 1/4"	3 1/4"	3 1/4"	3 1/4"	3 5/8"	3 5/8"	3 5/8"	1 1/2"
MINIMUM BREAKING STRENGTH (KIPS)	1044	1212	1212	1212	1314	1614	1614	1614	290
TENSION PER CABLE (I) INITIAL TENSION UNDER ALL DEAD LOADS									
EXISTING *	527	593	541	566	—	—	—	—	—
INITIAL ERECTION	307	381	351	354	450	544	495	544	2.5
FINAL	480	543	503	514	602	728	662	727	24
(II) OPERATIONAL LOADS	493	561	519	530	615	746	678	743	59
(III) SURVIVAL CONDITION	496	577	532	540	622	769	698	760	2.5
DESCRIPTION	MAIN CABLES	MAIN BACKSTAY CABLES			AUX. CABLES	AUX. BACKSTAY CABLES			TIE DOWNS
	EXISTNG				NEW				

Figure 14: Cable tensions in structural drawings for second upgrade
(image: structural drawings, courtesy of NAIC Arecibo Observatory, a facility of the NSF).

Table 4: Impact of second upgrade on cable tensions.

		Minimum Breaking Strength [kip]	Baseline		Ultimate		Ultimate / Baseline	
			Before 2nd Upgrade [kip (SF)]	After 2nd Upgrade [kip (SF)]	Before 2nd Upgrade [kip (SF)]	After 2nd Upgrade [kip (SF)]	Before 2nd Upgrade	After 2nd Upgrade
Original Cables	**Mains**	1,044	527 (1.98)	480 (2.18)	642 (1.63)	496 (2.10)	1.22	1.03
	T4 Backstays	1,212	593 (2.04)	543 (2.23)	748 (1.62)	577 (2.10)	1.26	1.06
	T8 Backstays	1,212	541 (2.24)	503 (2.41)	682 (1.78)	532 (2.28)	1.26	1.06
	T12 Backstays	1,212	566 (2.14)	514 (2.36)	696 (1.74)	540 (2.24)	1.23	1.05
	Average[A]	-	(2.07)	(2.26)	(1.67)	(2.16)	1.24	1.05
Auxiliary Cables	**Mains**	1,314	-	602 (2.18)	-	622 (2.11)	-	1.03
	T4 Backstays	1,614	-	728 (2.22)	-	769 (2.10)	-	1.06
	T8 Backstays	1,614	-	662 (2.44)	-	698 (2.31)	-	1.05
	T12 Backstays	1,614	-	727 (2.22)	-	760 (2.12)	-	1.05
	Average[A]	-	-	(2.24)	-	(2.15)	-	1.04

[A] Average weighted by number of cables.

The second upgrade was implemented by gradually tensioning the new auxiliary cables as weight was added to the suspended structure. In a final step, the original mains were tensioned with the auxiliary cables to raise the suspended structure by 2 feet. Our review of the correspondence between the different parties involved (in particular, AO, AW, and the primary contractor Comsat RSI) indicates that the specific sequence of cable tensioning and weight increase was changed during the project. The final sequence is described in a March 14, 1996 letter by AW,[5] and shown in Figure 15. We observe that the original cables did not exceed their pre-upgrade tension throughout the sequence, as the auxiliary cables were tensioned before each weight increase. Similarly, the auxiliary cables did not exceed their final post-upgrade tension at any point during the sequence. The total weight added to the suspended structure per the final sequence is 489 kip, which is 6 percent less than the 522 kip budgeted in the structural drawings.

[5] Jow Vellozzi (Ammann & Whitney). Letter to Kurt Samuelson (Arecibo Observatory). March 14, 1996. Correspondence retrieved from Cornell University archives.

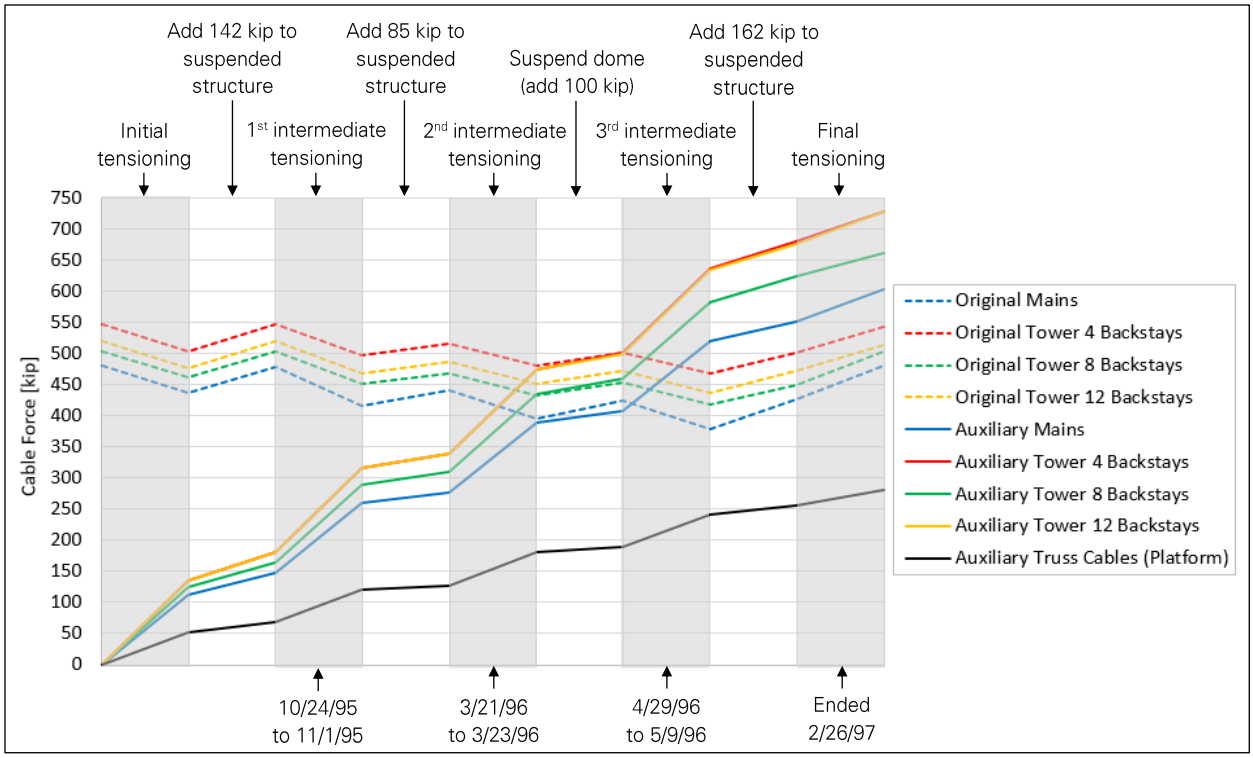

Figure 15: Cable tensioning sequence per AW's 3/14/1996 memorandum.

According to RSI's reports on the first,[6] second,[7] and third[8] intermediate tensioning steps, difficulties in confirming the cable tensions were encountered several times during the project. Those issues are summarized in a report by NAIC,[9] who also retained a consultant (William McGuire) to review the circumstances. Our review of the different reports and associated correspondence found no evidence that any cable tension significantly exceeded the final design tension during the tensioning procedure. The cable tensioning operations were completed on 2/26/1997.[10]

On 1/31/1997, a threaded rod connecting the socket of cable M8-4 to the platform was damaged as contractors were cutting a nut that prevented the installation of a jack required for a cable tensioning operation[11] (Figure 16). The damage consisted of several cuts on the surface of the rod (Figure 17), raising concerns about potential crack propagation through the rod. Fracture Analysis Consultants

[6] Comsat RSI. *Intermediate Tensioning and Tower Deflection Report*. December 14, 1995. Report retrieved from Cornell University archives.

[7] Comsat RSI. *2nd Intermediate Tensioning*. April 9, 1996. Report retrieved from Cornell University archives.

[8] Comsat RSI. *3rd Intermediate Tensioning*. May 23, 1996. Report retrieved from Cornell University Archives.

[9] Arecibo Observatory. *Cable Tension Inconsistencies*. September 19, 1996. Report retrieved from Cornell University archives.

[10] Kurt Samuelson (Arecibo Observatory). Letter to Steve Young (Comsat RSI). February 26, 1997. Correspondence retrieved from Cornell University archives.

[11] Jose Maldonado (Arecibo Observatory). Letter to Kurt Samuelson (Arecibo Observatory). January 31, 1997. Correspondence retrieved from Cornell University archives.

analyzed the damage and a rod sample, and concluded that the rod remained fit for service[12]. However, a structural bypass was installed to catch the socket in the event that the damaged threaded rod fails.

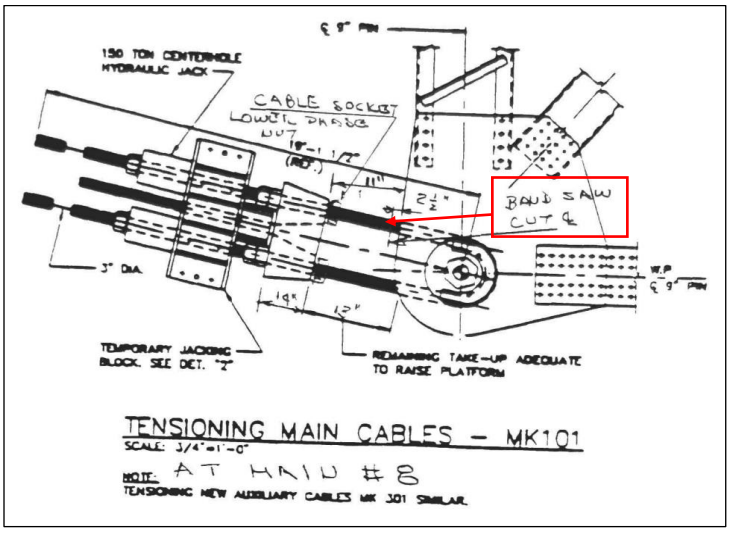

Figure 16: Location of threaded rod damage on M8-4 connection to platform *(image: NAIC Arecibo Observatory, a facility of the NSF[11]).*

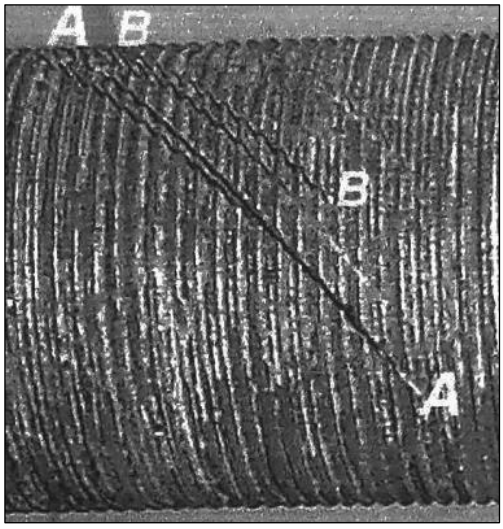

Figure 17: Cuts in M8-4 hairpin *(photo: Fracture Analysis Consultants[12]).*

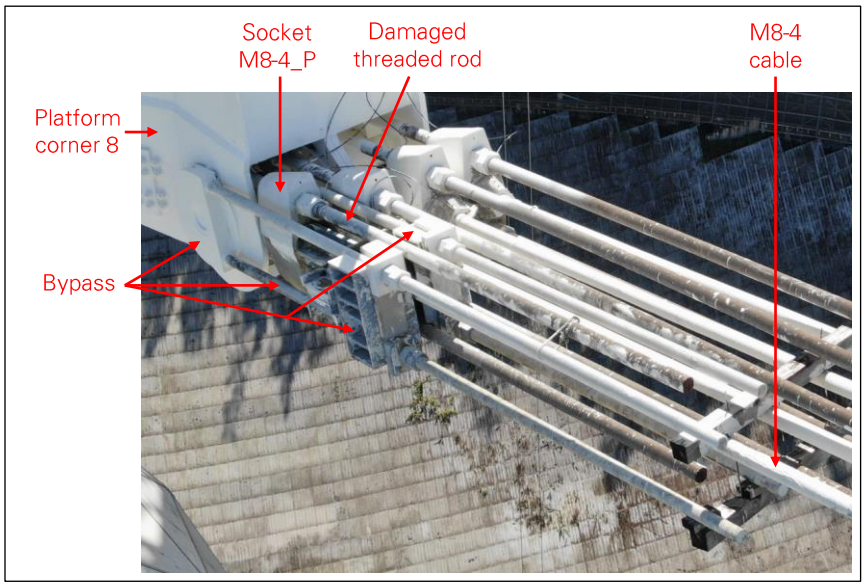

Figure 18: Bypass on socket M8-4_P *(photo: NAIC Arecibo Observatory, a facility of the NSF).*

[12] Fracture Analysis Consultants, Inc. *Fracture and Fatigue Analyses of Damaged Hairpin Rod at Arecibo*. March 3, 1997. Report retrieved from Cornell University archives.

6.0 After Second Upgrade

On 2/3/2010, local damage was discovered on a diagonal truss member of the platform (Figure 19), near the east backstay of the corner 12 tiedown outrigger. After re-analysis of the structure, AW prescribed the reinforcement of the damaged member and 23 other platform truss members, adding 14 kip of steel to the platform.

Puerto Rico was hit by an earthquake of magnitude 6.4 on 1/13/2014, and the next day the AO staff discovered several broken wires near the splice in cable M8-4. Cable M8-4 had been spliced near the top of Tower 8 during construction of the telescope in the 1960s, possibly because it was fabricated too short. After inspecting the splice, AW determined that the short segment of cable between the splice and the tower had at least 12 broken wires and was at risk of failing. AW designed a bypass system that connects the splice to the tower with a beam and a pair of threaded rods, which was installed in March 2014[13] (Figure 20). AW described the bypass as a temporary solution and recommended that the M8-4 cable be replaced. Preparations to replace M8-4 were being made when the M4N cable failed in August 2020.

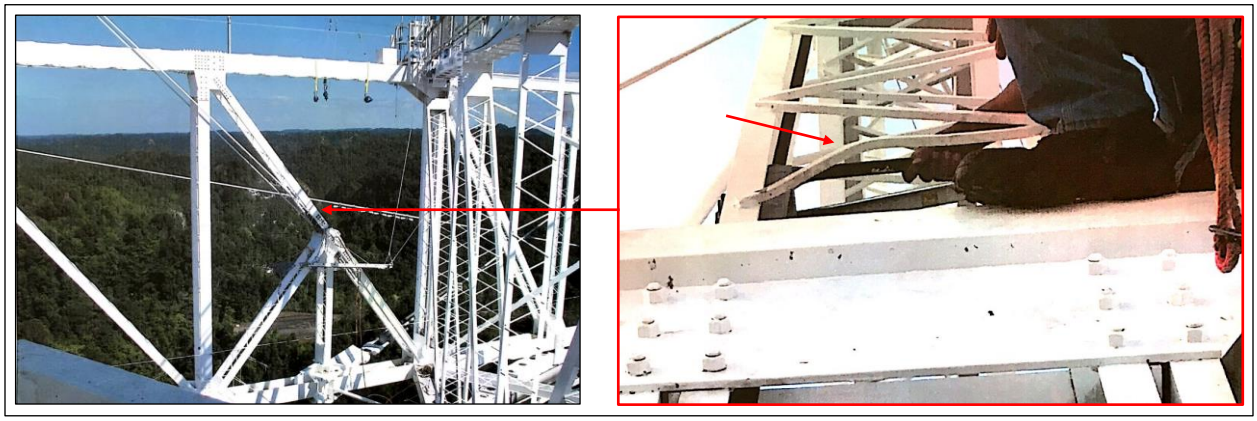

Figure 19: Damaged truss member lacing near outrigger 12 east backstay connection to platform on February 5, 2010. *(photos: NAIC Arecibo Observatory, a facility of the NSF).*

[13] Joel Stahmer (Ammann & Whitney). Letter to R. Kerr (Arecibo Observatory). March 11, 2017.

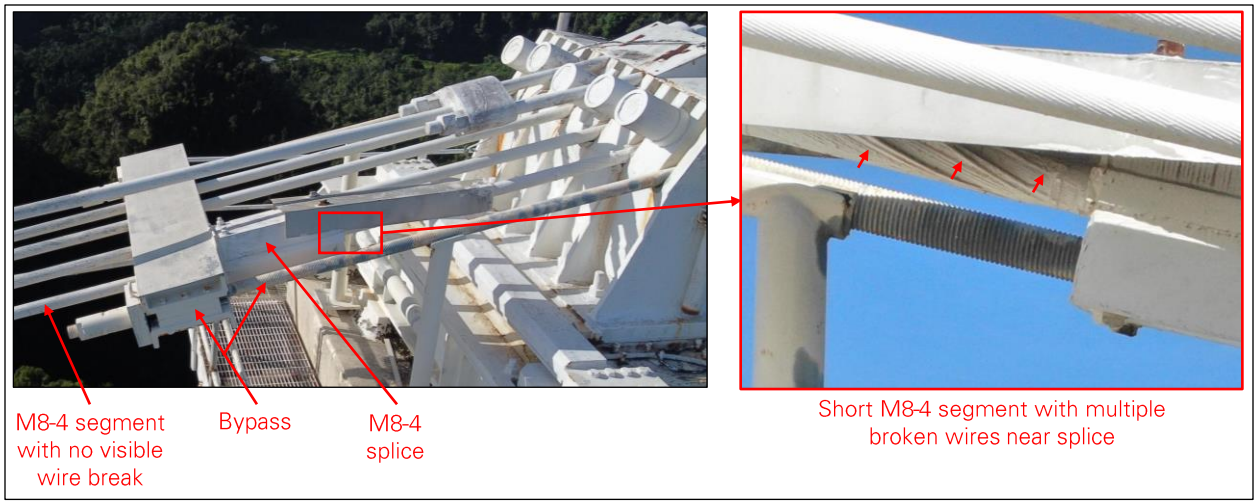

Figure 20: M8-4 splice bypass *(photos: NAIC Arecibo Observatory, a facility of the NSF).*

The cable system was surveyed several times after the second upgrade. In our review of the documents provided by AO and retrieved from the Cornell University Archives, we identified three of those surveys with complete data for the main cables. The surveys were performed in 2003,[14] 2006,[15] and 2016,[16] and the results are summarized in Table 5. The cable tensions are affected by temperature, telescope position, and tiedown tensions, but from the survey reports we could not always verify these parameters when each cable was surveyed. The results of the different surveys are nonetheless generally consistent with the cable tensions and suspended structure weight expected after the second upgrade.

Table 5: Main cable tensions and suspended structure weight surveyed after second upgrade.

	Design (End of 2nd Upgrade in 1997)	2003 Survey[14]	2006 Survey[15]	2016 Survey[16]	Survey Average	Survey Coefficient of Variation	Survey Average / Design
M4 Tension [kip]	480	510	481	498	496	2.4%	1.03
M4N Tension [kip]	602	654	631	566	617	6.0%	1.02
M4S Tension [kip]	602	582	577	634	598	4.3%	0.99
M8 Tension [kip]	480	509	516	490	505	2.2%	1.05
M8N Tension [kip]	602	654	666	625	648	2.7%	1.08
M8S Tension [kip]	602	642	647	594	628	3.8%	1.04
M12 Tension [kip]	480	496	491	449	479	4.4%	1.00
M12E Tension [kip]	602	599	600	576	592	1.9%	0.98
M12W Tension [kip]	602	634	593	572	600	4.3%	1.00
Suspended Structure Weight [kip]	1,789	1,798	1,798	1,748	1,781	1.3%	1.00

[14] Ammann & Whitney. *Suspended Platform Weight and Cable Tensions from Measured Cable Sags*. May 28, 2003. Report retrieved from Cornell University archives.

[15] Ammann & Whitney. *Suspended Platform Weight and Cable Tensions from Measured Sags.* August 29, 2006. Report retrieved from Cornell University archives.

[16] Louis Berger. *Main Cable Tensions and Suspended Platform Weight from LIDAR Measured Cable Sags*. April 24, 2017. Report provided by Arecibo Observatory.

Appendix D
Cable System Condition History

1.0 Introduction

The Arecibo Telescope collapsed after several cables failed at the top of Tower 4. The cable system had been inspected and maintained several times over the 57-year lifespan of the structure, with broken wires discovered on some of the cables and movement observed at some of the auxiliary cable sockets. The cable system had also been upgraded with vibration dampers and a moisture control system.

This appendix reviews the history of the cable system's condition as depicted in documents provided by Arecibo Observatory (AO) and retrieved from the Cornell University (CU) archives. As shown in Figure 1, these documents include AO's regular maintenance records (Figure 2, Figure 3) and reports from occasional inspections performed by AO or the Engineer of Record, Ammann & Whitney (AW).

This appendix focuses on the telescope's cables and cable sockets and does not address the condition of the suspended structure, towers, or primary reflector. Each aspect of the cable system's condition (paint, wire breaks, socket slip, moisture exclusion, and vibration) is considered in a separate section.

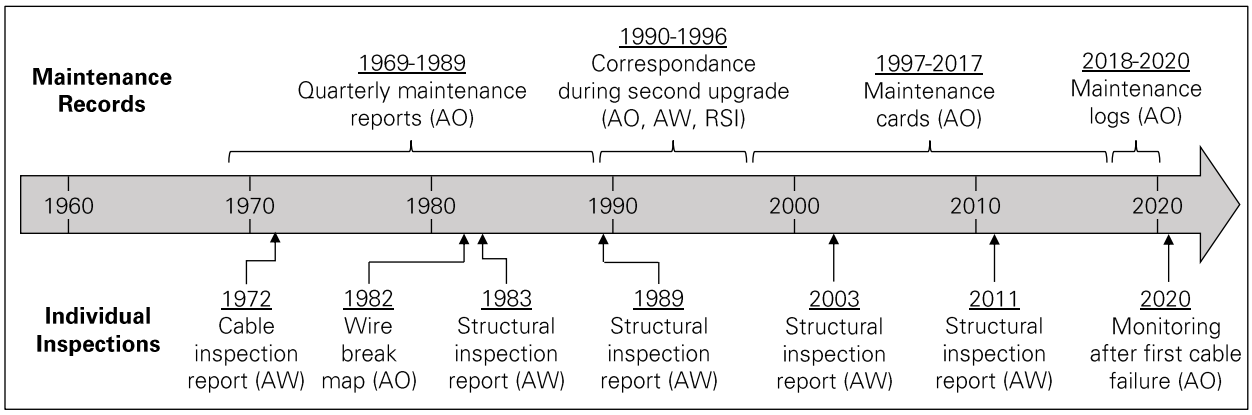

Figure 1: Primary documents reviewed relevant to condition of cable system.

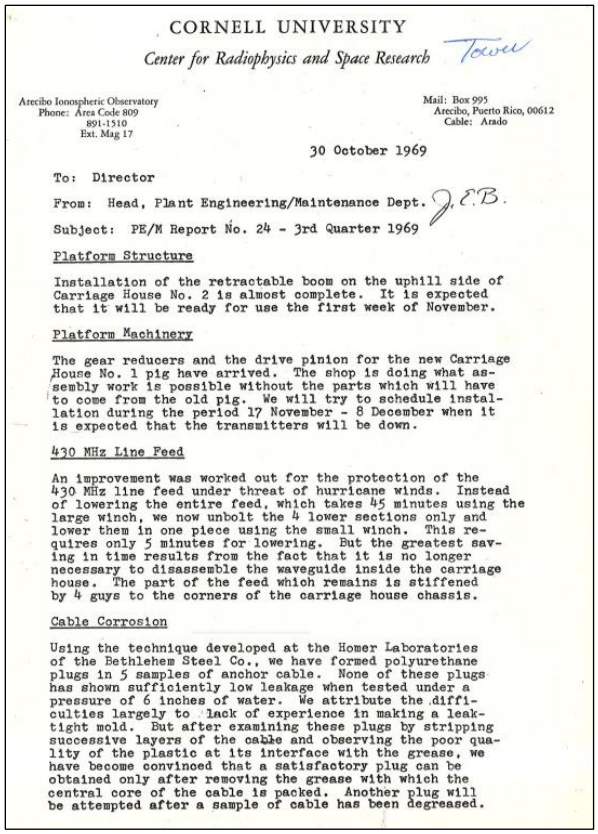

CORNELL UNIVERSITY

Center for Radiophysics and Space Research Tower

Arecibo Ionospheric Observatory
Phone: Area Code 809
891-1510
Ext. Mag 17

Mail: Box 995
Arecibo, Puerto Rico, 00612
Cable: Arado

30 October 1969

To: Director

From: Head, Plant Engineering/Maintenance Dept. J.E.B.

Subject: PE/M Report No. 24 - 3rd Quarter 1969

Platform Structure

Installation of the retractable boom on the uphill side of Carriage House No. 2 is almost complete. It is expected that it will be ready for use the first week of November.

Platform Machinery

The gear reducers and the drive pinion for the new Carriage House No. 1 pig have arrived. The shop is doing what assembly work is possible without the parts which will have to come from the old pig. We will try to schedule installation during the period 17 November - 8 December when it is expected that the transmitters will be down.

430 MHz Line Feed

An improvement was worked out for the protection of the 430 MHz line feed under threat of hurricane winds. Instead of lowering the entire feed, which takes 45 minutes using the large winch, we now unbolt the 4 lower sections only and lower them in one piece using the small winch. This requires only 5 minutes for lowering. But the greatest saving in time results from the fact that it is no longer necessary to disassemble the waveguide inside the carriage house. The part of the feed which remains is stiffened by 4 guys to the corners of the carriage house chassis.

Cable Corrosion

Using the technique developed at the Homer Laboratories of the Bethlehem Steel Co., we have formed polyurethane plugs in 5 samples of anchor cable. None of these plugs has shown sufficiently low leakage when tested under a pressure of 6 inches of water. We attribute the difficulties largely to lack of experience in making a leak-tight mold. But after examining these plugs by stripping successive layers of the cable and observing the poor quality of the plastic at its interface with the grease, we have become convinced that a satisfactory plug can be obtained only after removing the grease with which the central core of the cable is packed. Another plug will be attempted after a sample of cable has been degreased.

Figure 2: Example of first page of quarterly inspection and maintenance report produced from 1969 to 1989 *(courtesy of NAIC Arecibo Observatory, a facility of the NSF).*

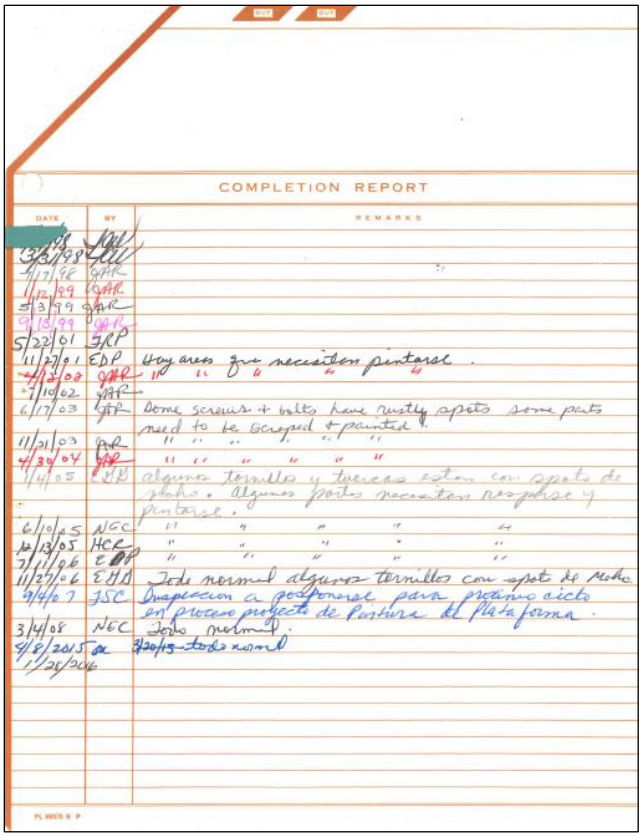

COMPLETION REPORT

DATE	BY	REMARKS
3/3/98	[illegible]	
4/17/98	GAR	
1/12/99	GAR	
5/3/99	GAR	
9/13/99	GAR	
5/22/01	JRP	
11/27/01	EDP	Hay areas que necesitan pintarse.
4/23/02	GAR	" " " " " "
7/10/02	GAR	
6/17/03	GAR	Dome screws + bolts have rusty spots some parts need to be scraped + painted.
11/21/03	GAR	" " " " " "
4/30/04	GAR	" " " " " "
1/14/05	EDP	algunos tornillos y tuercas estan con spots de oxido. Algunas partes necesitan ser pulidas y pintarse.
6/10/05	NEC	" " " " " "
12/13/05	HCR	" " " " " "
7/[illegible]/06	EDP	" " " " " "
11/27/06	EDP	Todo normal algunos tornillos con spot de oxido
9/4/07	JSC	Inspeccion a posponerse para proximo ciclo en proceso proyecto de Pintura de Plataforma.
3/4/08	NEC	Todo normal.
4/8/2015	ac	7/20/15 todo normal
1/21/2016		

Figure 3: Example of maintenance card system used from 1997 to 2017 *(courtesy of NAIC Arecibo Observatory, a facility of the NSF).*

2.0 Cable Paint

The telescope's cables are made of galvanized steel wires, which were painted to protect against corrosion. The paint's anti-corrosive role is two-fold: it covers the surface of the outer wires to protect them from corrosion, and it seals any gap between the outer wires to prevent water from seeping into the cable and corroding the inner wires.

AO's maintenance records indicate that the original cables (installed in 1963) were fully repainted between 1973 and 1974, and again between 1984 and 1988, while the auxiliary cables (installed in 1995) were fully repainted in 2003.

The condition of the cable paint was reviewed by AW during each inspection of the structure, and their conclusions are summarized in Table 1. The paint appears to have remained in good condition from the telescope's construction to its second upgrade, which is consistent with AO's maintenance records indicating that the cables were repainted at least twice during that period. However, during the first inspection after the second upgrade in 2003, AW noted that the paint on the original cables had deteriorated (Figure 4) to the point that the cables had started to corrode. After the next inspection in 2011, AW reported that the condition of the original cables remained unchanged, and it is unknown whether the cables had been repainted between the two inspections. The paint on the auxiliary cables appears to have remained in good condition after their installation during the second upgrade.

Table 1: Cable paint condition as described in inspection reports.

Source	Quotes	Notes
1972 cable inspection report[A]	"In general, the cables were found to be in good condition."	
1983 structural inspection report[B]	"The white exterior paint is kept in excellent condition."	
1989 structural inspection report[C]	"Examination of the cables at the end sockets and with binoculars over the central portion disclosed no changes from the last inspection (1982)."	
2003 structural inspection report[D]	Original backstays: "The paint exhibits varying degrees of peeling, cracking, flaking and discoloration … Exposed individual wires are visible at many locations where the paint has deteriorated … The galvanizing on the wires has begun to oxidize in some locations, initiating the first phase of rusting of the wire … The paint condition of the backstays is rated as poor." Auxiliary backstays: "The paint on the auxiliary backstays remains flexible and in good condition overall … The paint condition of the auxiliary backstays is rated as good." Auxiliary mains: "The paint condition of the auxiliary main cables is rated as good." Recommendation: "The [original] backstay cables and the [original] main cables should be cleaned, inspected for wire breaks, and painted along their entire lengths."	The cables were subject to close-up inspection at the cable ends, and inspected with binoculars from the ground, the platform and the top of Tower 4 and Tower 12.
2011 structural inspection report[E]	Original backstays: "The backstay paint condition was rated as poor by the 2003 survey and there is no change in status." Auxiliary backstays: "The paint condition on the auxiliary cables was rated as good in the 2003 survey, and there is no change in status." Original mains: "The main cable paint condition was rated as poor in the 2003 survey, and there is no change in status." Auxiliary mains: "The paint condition of the auxiliary main cables was rated as good in the 2003 report and there is no change in status." Recommendation: "As a priority, all of the original project cables should be painted."	The cables were subject to close-up inspection at the cable ends, and inspected with binoculars from the ground, the platform and the top of the towers.

[A] Ammann & Whitney. *Report on Inspection of Cable System*. September 1972. Report retrieved from Cornell University archives.
[B] 1983. Report retrieved from Cornell University archives.
[C] Ammann & Whitney. *Arecibo Mini Inspection*. May 1989. Report retrieved from Cornell University archives.
[D] Ammann & Whitney. *Structural Condition Survey 2003*. May 2003. Report retrieved from Cornell University archives.
[E] Ammann & Whitney. *Structural Condition Survey 2011*. March 2011. Report retrieved from Cornell University archives.

Figure 4: Original backstay B12-5 near anchor in 2003. Clamps and missing paint indicate a broken wire. Paint is also cracked between other wires *(photo: Ammann & Whitney[1]).*

Figure 5: Paint deterioration on original mains at top of Tower 12 in 2011 *(photo: Ammann & Whitney[2]).*

3.0 Cable Internal Moisture

AO's maintenance records indicate that by the late 1960s, a water intrusion problem had been identified in the structure's cables. It was observed that the cable ends near the sockets were not fully airtight, allowing moist air and rainwater to enter the cable and corrode the wires from the inside. Several attempts to seal the cable ends with polyurethane plugs were made in 1969 and 1970, but this method was eventually abandoned because the plastic material failed to fully penetrate and bond to the cable.

As an alternative to sealing off the cable ends, AO implemented a moisture exclusion system that pushed dry air into the cable. As shown in Figure 6, the lower end of each cable was encased in an airtight sleeve just outside the cable socket, so dry air could be pushed into the sleeve and forced to enter the cable through the gaps between the wires near the socket. According to experiments

[1] Ammann & Whitney. *Structural Condition Survey 2003.* May 2003. Report retrieved from Cornell University archives.
[2] Ammann & Whitney. *Structural Condition Survey 2011.* March 2011. Report retrieved from Cornell University archives.

conducted in 1971, a pressure of one pound per square inch in the sleeve at the bottom of a cable was sufficient to cause airflow inside the cable and detect air escaping at the top of the cable.

Dry air sleeves were installed on the original cables in 1972. The system was later improved by adding moisture detectors in 1976 and replacing the sleeves in 1983 with larger windows to facilitate visual inspections. Despite occasional issues with the air compressors and dryers, the system appeared to function satisfactorily[3] through the 1980s and 1990s, and the auxiliary cables installed in 1995 were also equipped with similar dry air sleeves.

The maintenance and inspection documents include several reports, beginning in 2002, of condensation inside the dry air sleeves of some of the auxiliary cables (Figure 7 and Figure 8). The cause, extent and duration of the problem are not precisely known, although it affected backstays and main cables and persisted until at least 2011.

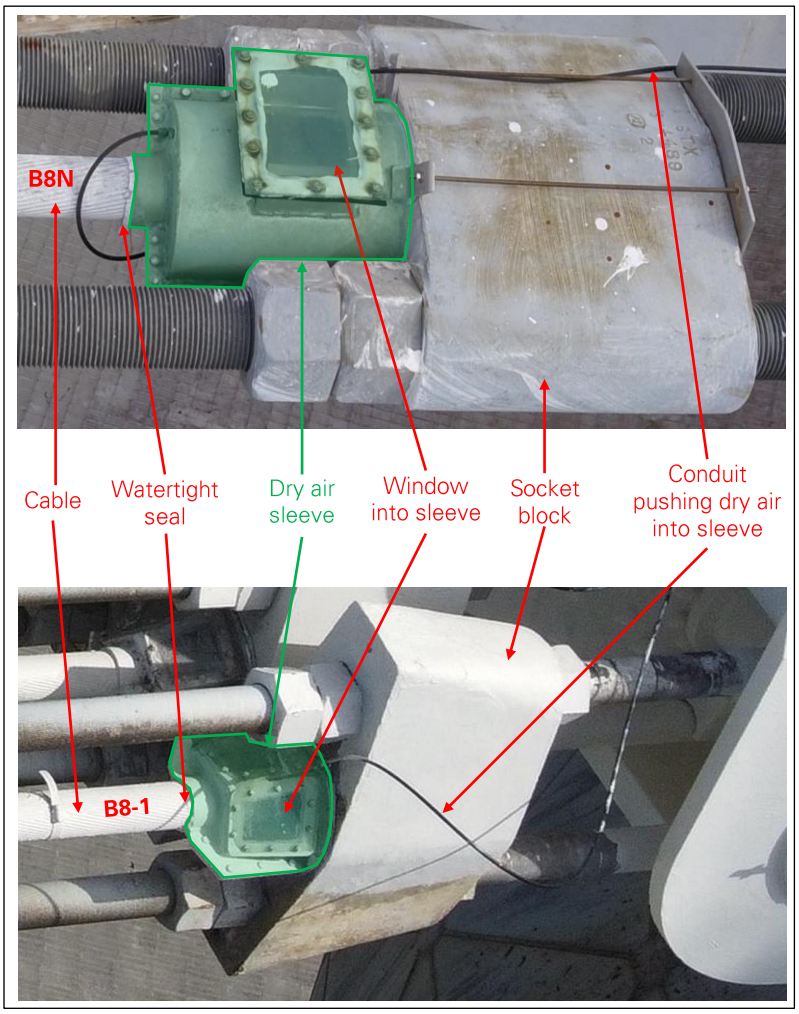

Figure 6: Moisture exclusion system on auxiliary main (B8N, top) and original main (B8-1, bottom) sockets in 2020 *(photos: NAIC Arecibo Observatory, a facility of the NSF).*

[3] Tor Hagfors (Arecibo Observatory). Letter to William McGuire (Cornell University). April 5, 1988. Correspondence retrieved from Cornell University archives.

Figure 7: Condensation inside dry air sleeve of cable B4S (left) compared to typical condition of dry air sleeves (right) in 2003 *(photos: Amman & Whitney[4]).*

Figure 8: Condensation inside dry air sleeve on cable M4N in 2011 *(photos: Amman & Whitney[5]).*

4.0 Wire Breaks

Each cable of the Arecibo Telescope consists of a single strand of galvanized steel wires, with between 126 and 216 wires per cable depending on the cable and wire diameters.

It is not uncommon for individual wires to break in structural cables, even when the overall cable tension is less than the cable's minimum breaking strength. Wire breaks may be due to local propagation of cracks, corrosion, or friction between adjacent wires or with other surfaces. When a wire breaks, its tension gets redistributed to the remaining wires of the cable, generating a slight stress increase on each wire. A wire break in the outer layer of a strand can be detected visually through paint damage, loose

[4] Ammann & Whitney. *Structural Condition Survey 2003.* May 2003. Report retrieved from Cornell University archives.
[5] Ammann & Whitney. *Structural Condition Survey 2011.* March 2011. Report retrieved from Cornell University archives.

wire ends and/or high wires (a wire bulging out of the strand). A wire break inside the strand is usually not visible from the outside and can only be detected with an x-ray.

The AO maintenance records include reports of wire breaks discovered by the AO staff over time. As no x-ray reports were found about the wire breaks, we assume that the reported wire breaks only occurred in the cables' outer layer. In this appendix, these breaks are referred to as the *known wire breaks*, since other wires may have broken inside the cables and not been visible.

A map of the wire breaks discovered up to 1983 was published in a paper by Phoenix, Johnson and McGuire (Figure 9), with the map showing 20 known wire breaks. Six of these breaks were located at the ground end of cable B12-3, leading AO to replace that cable in 1981 as a precaution (Appendix C). According to the AO maintenance records and correspondence, eight additional wire breaks were discovered between 1982 and 2003 (Figure 10). The only new breaks on record after 2003 are located near the M8-4 cable splice: AW observed three breaks during a 2011 inspection, and nine additional breaks when re-inspecting the structure after a significant earthquake in January 2014 (Figure 11). As a precaution, a bypass was installed over the segment of cable with 12 breaks (Appendix C).

Overall, a total of 40 wire breaks had been reported in the cable system before the first cable failure on August 10, 2020. This is only 0.6 percent of the total number of wires in the telescope's cables. The number of breaks drops to 22 or 0.3 percent of the wires when excluding the B12-3 cable that was replaced and the M8-4 cable segment that was bypassed. Every known wire break is located near a socket at a cable end.

After discovering a wire break, the AO staff typically installed clamps on the cable to keep the broken wire in place. These clamps and the broken wires they hold remain visible after the cable is repainted (Figure 12). The numerous drone photos taken in 2020 after the first cable failure show evidence of past wire breaks at locations generally consistent with the breaks reported in the AO records. Past wire breaks could not be precisely counted from the drone photos, as some of the clamps appear to have been installed preventively while other clamps appear to have been removed or to have fallen from the cables.

The known wire breaks before the first cable failure are mapped in Figure 13, and the number of known breaks over time is plotted in Figure 14. A map of the cable clamps and clamp marks observed in 2020 is also presented in Figure 15.

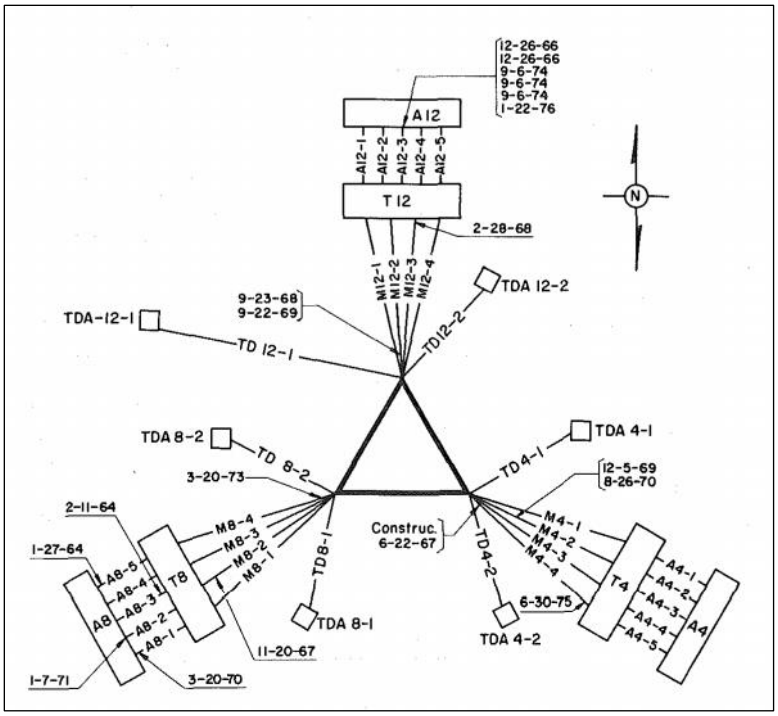

Figure 9: 1986 map of wire breaks *(image: Phoenix, Johnson, and McGuire[6]).*

Figure 10: Wire break at ground end on B4-1 discovered on December 12, 1996
(photo: NAIC Arecibo Observatory, a facility of the NSF).

[6] Phoenix, S.L., Johnson, H.H., and McGuire, W. "Condition of Steel Cable after Period of Service". *Journal of Structural Engineering*. 112(6). 1986.

Figure 11: Multiple wire breaks near M8-4 splice discovered on January 14, 2014
(photo: NAIC Arecibo Observatory, a facility of the NSF).

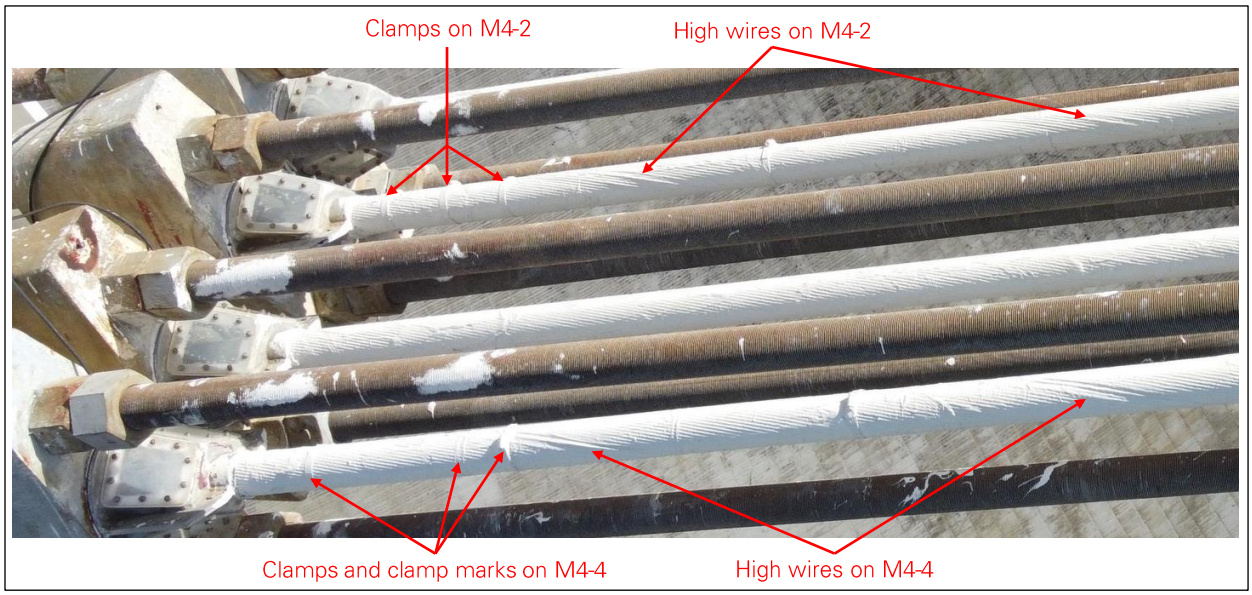

Figure 12: Evidence of past wire breaks at platform end of M4 cables
(photo: NAIC Arecibo Observatory, a facility of the NSF).

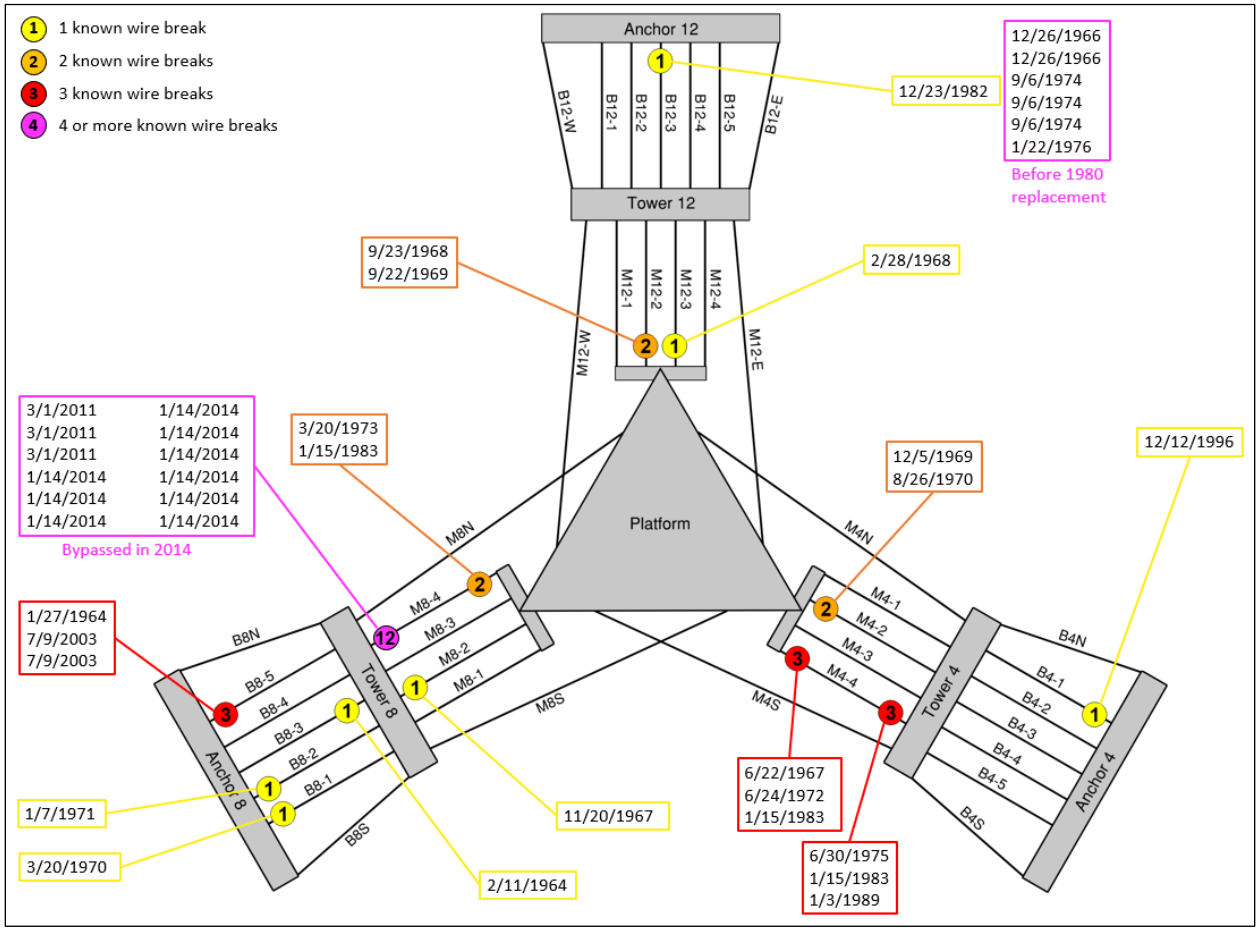

Figure 13: Known wire break locations and discovery dates before first cable failure.

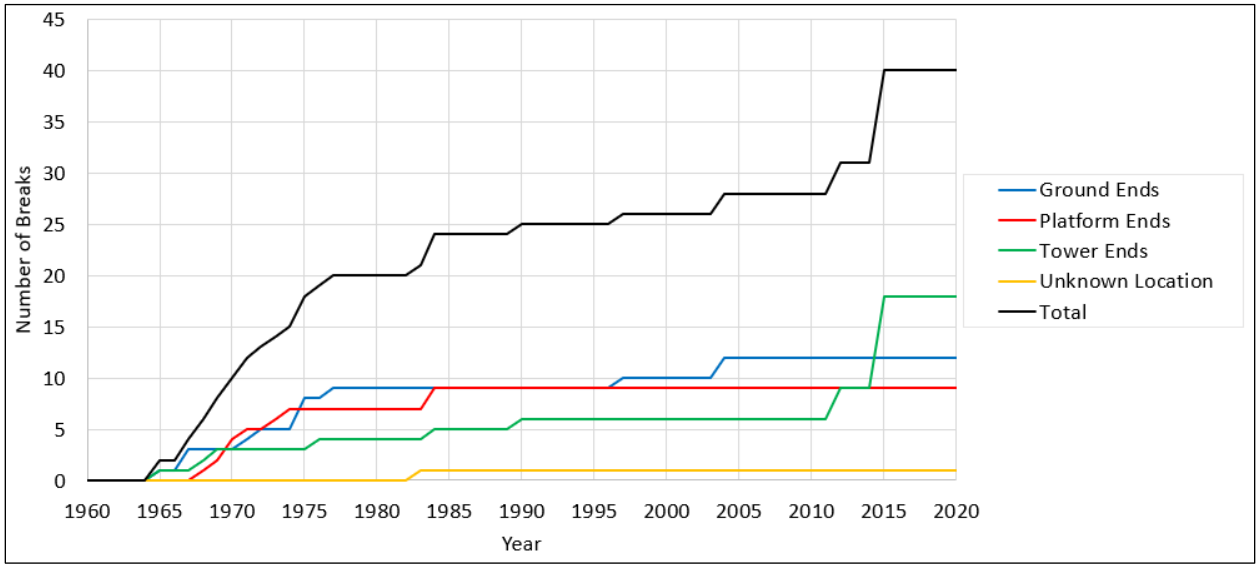

Figure 14: Count of known wire breaks up to first cable failure.

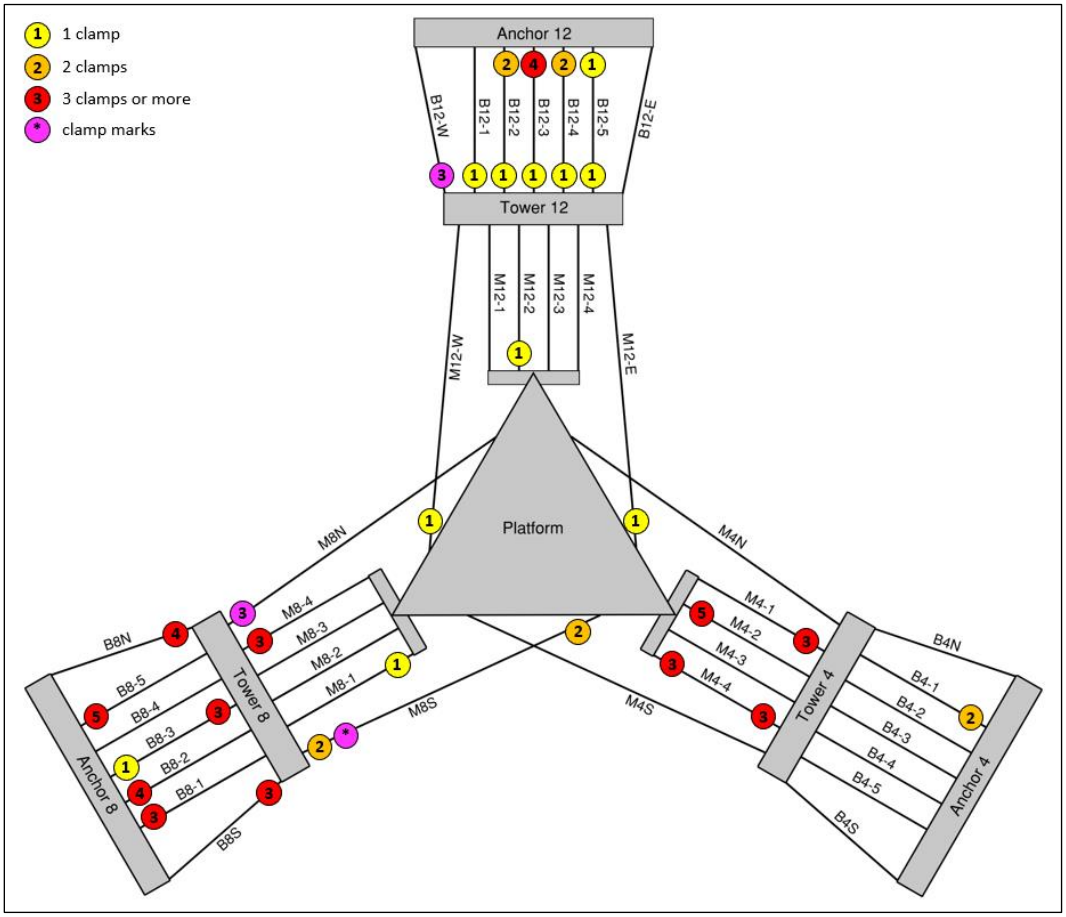

Figure 15: Cable clamps and clamp marks observed after first cable failure.

5.0 Cable Slip

In this report, the *cable slip* refers to the distance that a cable end shifted with respect to its socket. In zinc-filled spelter sockets, the cable slip is typically measurable as the length of zinc extruded out of the socket (Figure 16).

Before breaking free on August 8, 2020, the end of cable M4N at the top of Tower 4 had slipped by more than one inch from its socket. This one-inch slip is approximately one-third of the cable's diameter and significantly more than typically observed in structural cables terminated with zinc-filled spelter sockets. We reviewed the telescope's maintenance and inspection records, as well as photographs, provided by AO to determine the history, extent, and severity of cable slip in the telescope structure. The available information is presented in this section.

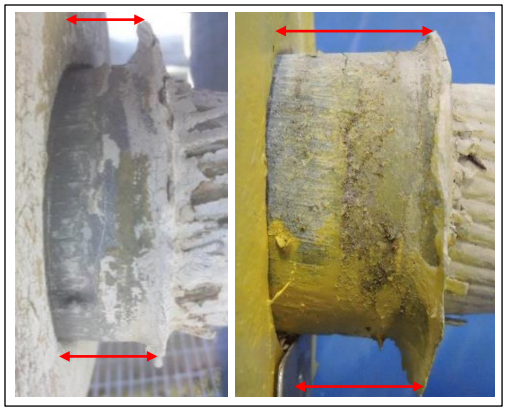

Figure 16: Cable slip at socket M4N_T (left) and B12W_G (right)
(photos: NAIC Arecibo Observatory, a facility of the NSF).

5.1 Inspection Reports

The structure's inspection reports (Table 2) only mention cable slip for the auxiliary cables, installed in 1995. A post-hurricane inspection performed by the AO staff in 1998 reported a 1/16-inch displacement at the auxiliary cable sockets, although it is not clear whether this refers to cable slip or some other type of displacement. AW reported a cable slip of up to ½ inch at all of the auxiliary cable sockets after their 2003 inspection, and no measurable change after their 2011 inspection.

Table 2: Auxiliary cable end slip conditions as described in inspection reports.

Source	Quotes
1998 post-hurricane damage assessment[A]	"In general, new cable connection at socket shows some displacement toward the inside of the socket in the order of 1/16"."
2003 structural inspection report[B]	Auxiliary backstays: "At the faces of the auxiliary backstays the zinc has separated away from the leading edge of the socket by up to ½". This condition was observed at all of the sockets for the auxiliary backstay cables and appears to have occurred during the fabricating or testing phase of the cable assemblies." Auxiliary mains: "As at the auxiliary backstays, the cast zinc has separated away from the leading edge of the sockets by up to ½". This condition was observed at the auxiliary cables."
2011 structural inspection report[C]	Auxiliary backstays: "The end socket ½" cast zinc leading edge separation was observed at all cables but has not measurably increased since reported in the 2003 survey." Auxiliary mains: "As noted in the 2003 report, the cast zinc has separated away from the leading edge of all the sockets by up to ½", a condition that remains unchanged."

[A] Arecibo Observatory. *Hurricane George*. September 25, 1998. Report retrieved from Cornell University archives.
[B] Ammann & Whitney. *Structural Condition Survey 2003*. May 2003. Report retrieved from Cornell University archives.
[C] Ammann & Whitney. *Structural Condition Survey 2011*. March 2011. Report retrieved from Cornell University archives.

5.2 Cable Slips Before Collapse

A map of the auxiliary cable slips at the time of collapse is provided in Figure 17. To determine the cable slips, we reviewed photographs taken in 2020 before the collapse and, when possible, took measurements on the sockets recovered after the collapse. The collapse does not appear to have significantly increased any of the cable slips.

The map indicates the ratio of the cable slip to the cable diameter, and sockets are flagged when this ratio is greater than one sixth. The one-sixth limit is based on the AASHTO M277[7] standard for testing wire ropes used in moveable bridges. Because the telescope's auxiliary cables had been loaded for 25 years when the structure collapsed and may therefore have experienced long-term creep effects that do not occur during short load tests, the comparison of the Arecibo cable slips to the one sixth limit is for reference only.

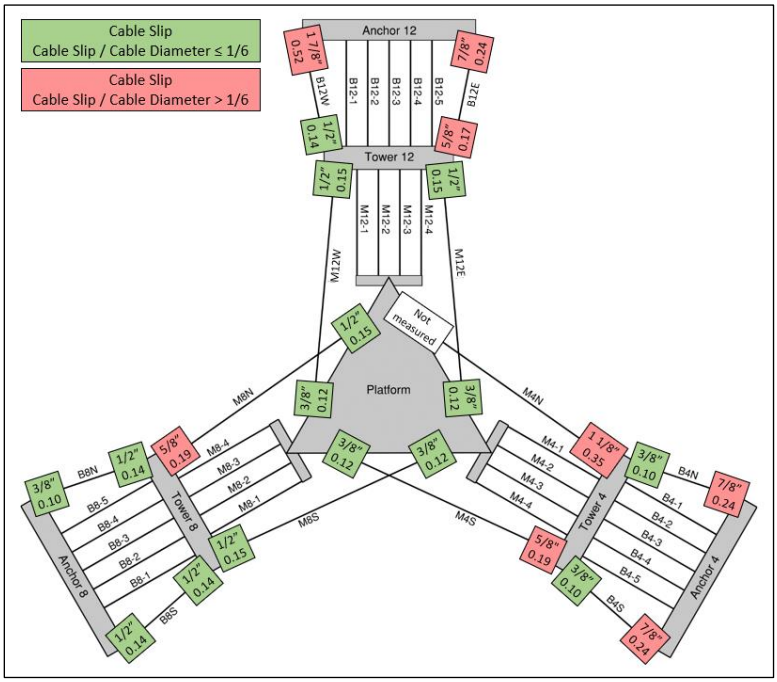

Figure 17: Cable slip at auxiliary sockets before collapse.

5.3 Photographs

The key available photographs of cable slip are compiled in this section, and include the latest drone photographs of the tower ends before collapse, as well as post-collapse photographs of the ground ends. A representative photograph is also provided for each time a cable end was photo-recorded up close by AO or WJE before the collapse.

[7] American Association of State Highway and Transportation Officials (AASHTO). *AASHTO M 277-06. Standard Specification for Wire Rope and Sockets for Movable Bridges*. 2019.

5.3.1 Auxiliary Main Tower-End Sockets

Socket M4N_T

Figure 18: Cable slip at socket M4N_T. As seen from the north side (left) and measured on north (top right) and south (bottom right) sides of socket *(photos: NAIC Arecibo Observatory, a facility of the NSF).*

Socket M4S_T

Figure 19: Cable slip at socket M4S_T
(photo: Ammann & Whitney[8]).

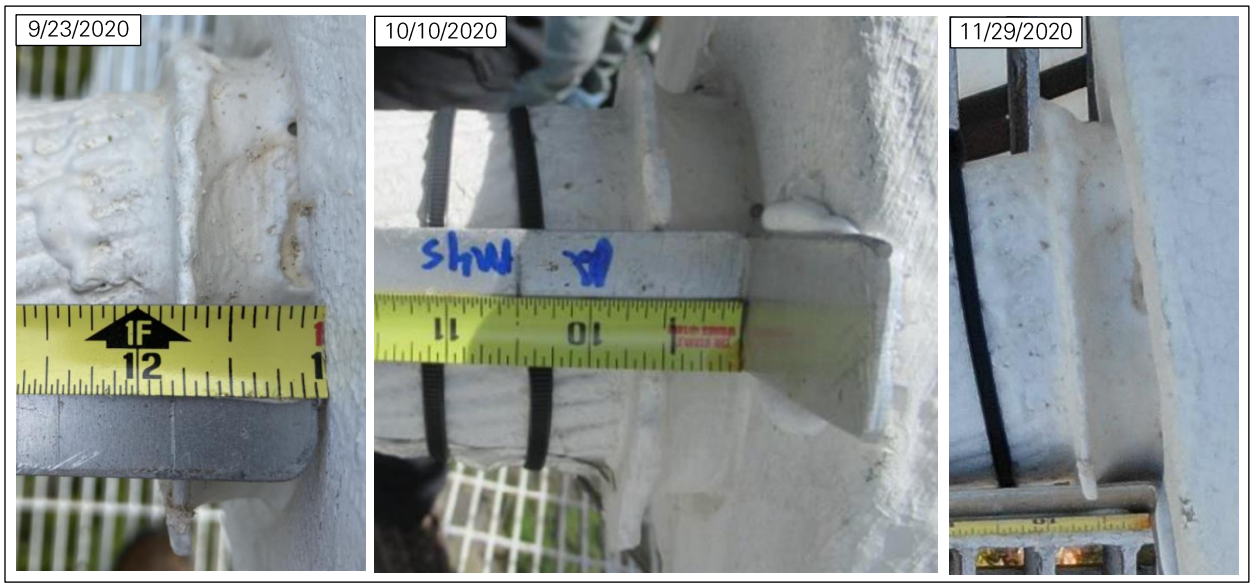

Figure 20: Cable slip at socket M4S_T
(left and center photos: WJE[9]; right photo: NAIC Arecibo Observatory, a facility of the NSF).

[8] Ammann & Whitney. *Structural Condition Survey 2003.* May 2003. Report retrieved from Cornell University archives.
[9] Wiss, Janney, Elstner Associates (WJE). *Auxiliary Main Cable Socket Failure Investigation.* June 21, 2021. Draft report provided by WJE.

Socket M8N_T

Figure 21: Cable slip at socket M8N_T
(left and center photos: NAIC Arecibo Observatory, a facility of the NSF).

Socket M8S_T

Figure 22: Cable slip at socket M8S_T
(left photo: WJE[10]; center photo: NAIC Arecibo Observatory, a facility of the NSF).

[10] Wiss, Janney, Elstner Associates (WJE). *Auxiliary Main Cable Socket Failure Investigation.* June 21, 2021. Draft report provided by WJE.

Socket M12E_T

Figure 23: Cable slip at socket M12E_T
(photos: NAIC Arecibo Observatory, a facility of the NSF).

Figure 24: Cable slip at socket M12E_T
(left and center photos: WJE[11]; right photo: NAIC Arecibo Observatory, a facility of the NSF).

[11] Wiss, Janney, Elstner Associates (WJE). *Auxiliary Main Cable Socket Failure Investigation.* June 21, 2021. Draft report provided by WJE.

Socket M12W_T

Figure 25: Cable slip at socket M12W_T
(left photo: NAIC Arecibo Observatory, a facility of the NSF; right photo: WJE[12]).

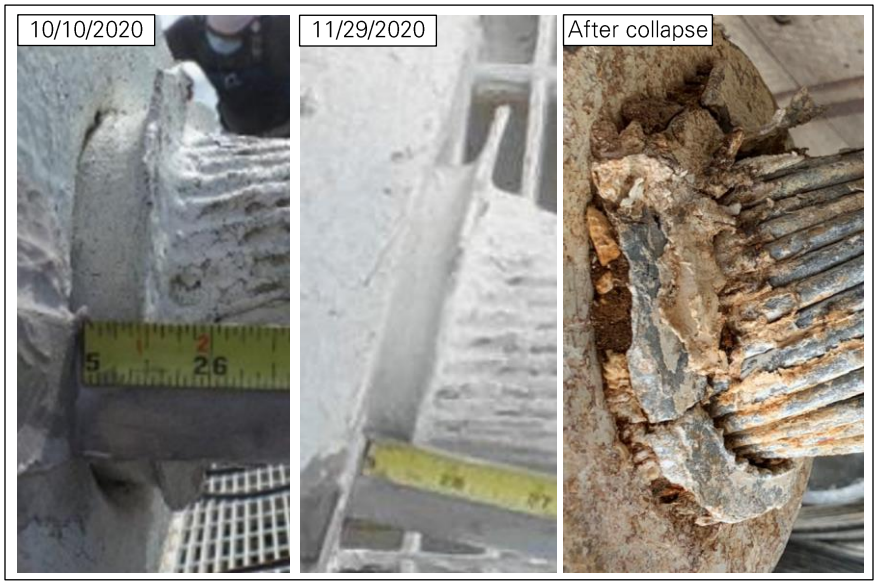

Figure 26: Cable slip at socket M12W_T
(left photo: WJE[12]; center photo: NAIC Arecibo Observatory, a facility of the NSF).

[12] Wiss, Janney, Elstner Associates (WJE). *Auxiliary Main Cable Socket Failure Investigation.* June 21, 2021. Draft report provided by WJE.

5.3.2 Auxiliary Main Platform-End Sockets

Socket M4S_P

Figure 27: Cable slip at socket M4S_P.

Socket M8N_P

Figure 28: Cable slip at socket M8N_P.

Socket M8S_P

Figure 29: Cable slip at socket M8S_P.

Socket M12E_P

Figure 30: Cable slip at socket M12E_P.

Socket M12W_P

Figure 31: Cable slip at socket M12W_P.

5.3.3 Auxiliary Backstay Tower-end Sockets

Socket B4N_T

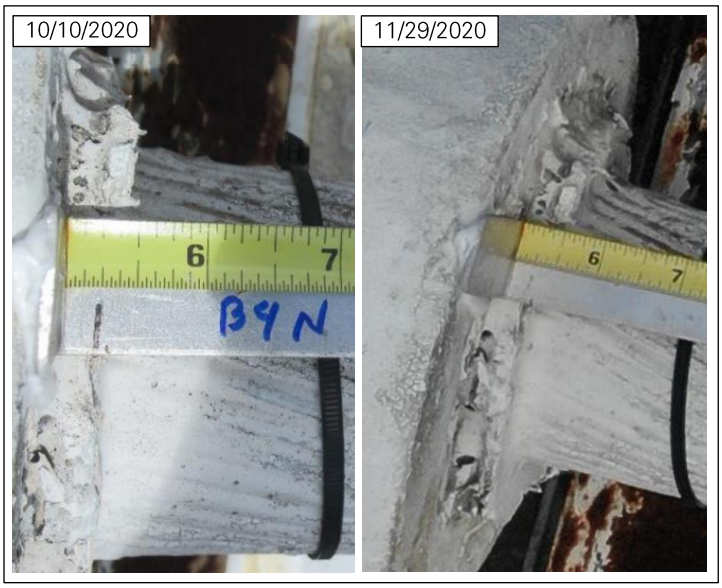

Figure 32: Cable slip at socket B4N_T
(left photo: WJE[13]; right photo: NAIC Arecibo Observatory, a facility of the NSF).

Socket B4S_T

Figure 33: Cable slip at socket B4S_T
(left and right photos: NAIC Arecibo Observatory, a facility of the NSF; center photo: WJE[13]).

[13] Wiss, Janney, Elstner Associates (WJE). *Auxiliary Main Cable Socket Failure Investigation.* June 21, 2021. Draft report provided by WJE.

Socket B8N_T

Figure 34: Cable slip at socket B8N_T
(photos: NAIC Arecibo Observatory, a facility of the NSF).

Socket B8S_T

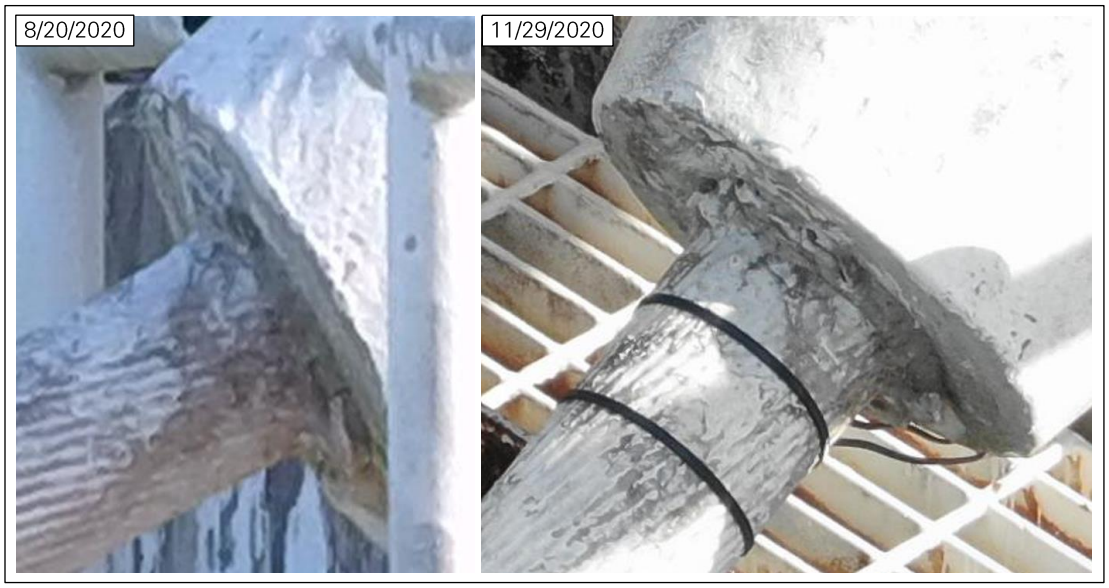

Figure 35: Cable slip at socket B8S_T
(photos: NAIC Arecibo Observatory, a facility of the NSF).

Socket B12E_T

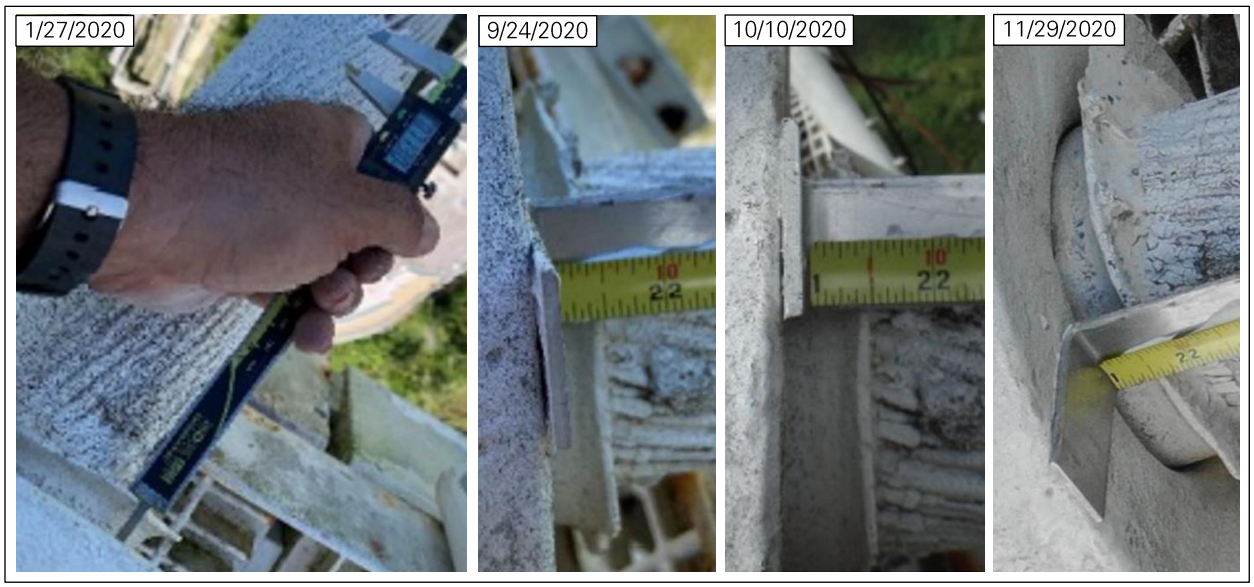

Figure 36: Cable slip at socket B12E_T
(left and right photos: NAIC Arecibo Observatory, a facility of the NSF; center photos: WJE[14]).

Socket B12W_T

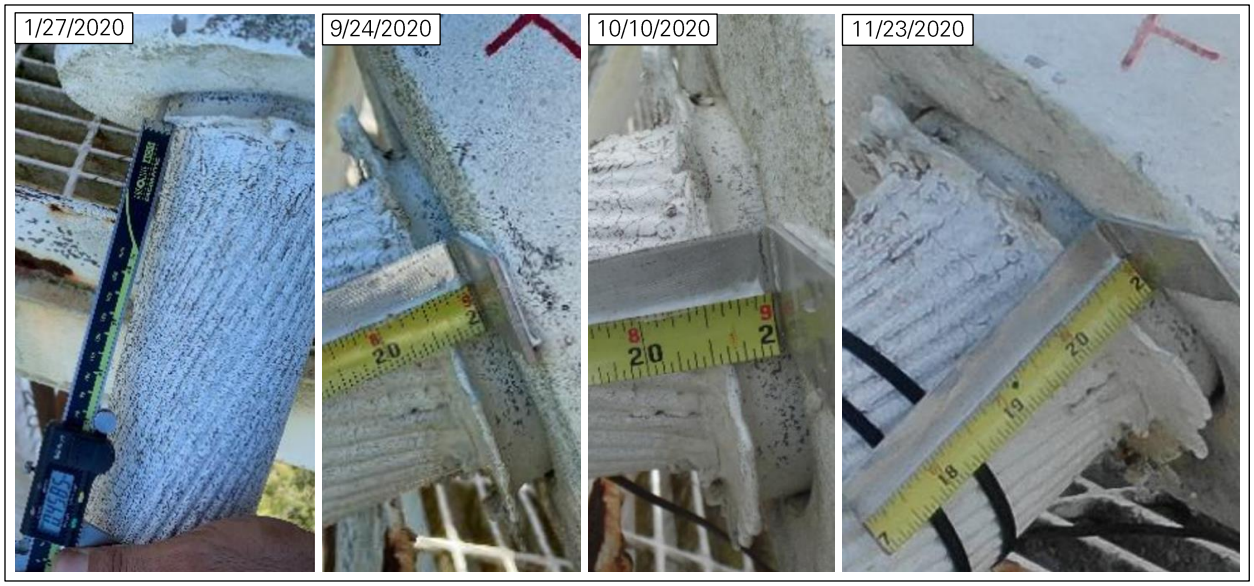

Figure 37: Cable slip at socket B12W_T
(left and right photos: NAIC Arecibo Observatory, a facility of the NSF; center photos: WJE[14]).

[14] Wiss, Janney, Elstner Associates (WJE). *Auxiliary Main Cable Socket Failure Investigation.* June 21, 2021. Draft report provided by WJE.

5.3.4 Auxiliary Backstay Ground-end Sockets

Socket B4N_G

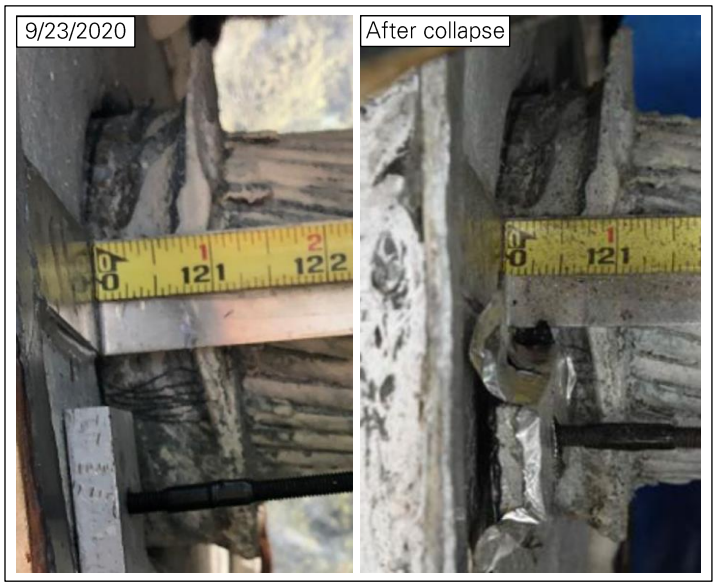

Figure 38: Cable slip at socket B4N_G
(left photo: WJE[15]).

Socket B4S_G

Figure 39: Cable slip at socket B4S_G.

[15] Wiss, Janney, Elstner Associates (WJE). *Auxiliary Main Cable Socket Failure Investigation.* June 21, 2021. Draft report provided by WJE.

Socket B8N_G

Figure 40: Cable slip at socket B8N_G.

Socket B8S_G

Figure 41: Cable slip at socket B8S_G.

Socket B12E_G

Figure 42: Cable slip at socket B12E_G.

Socket B12W_G

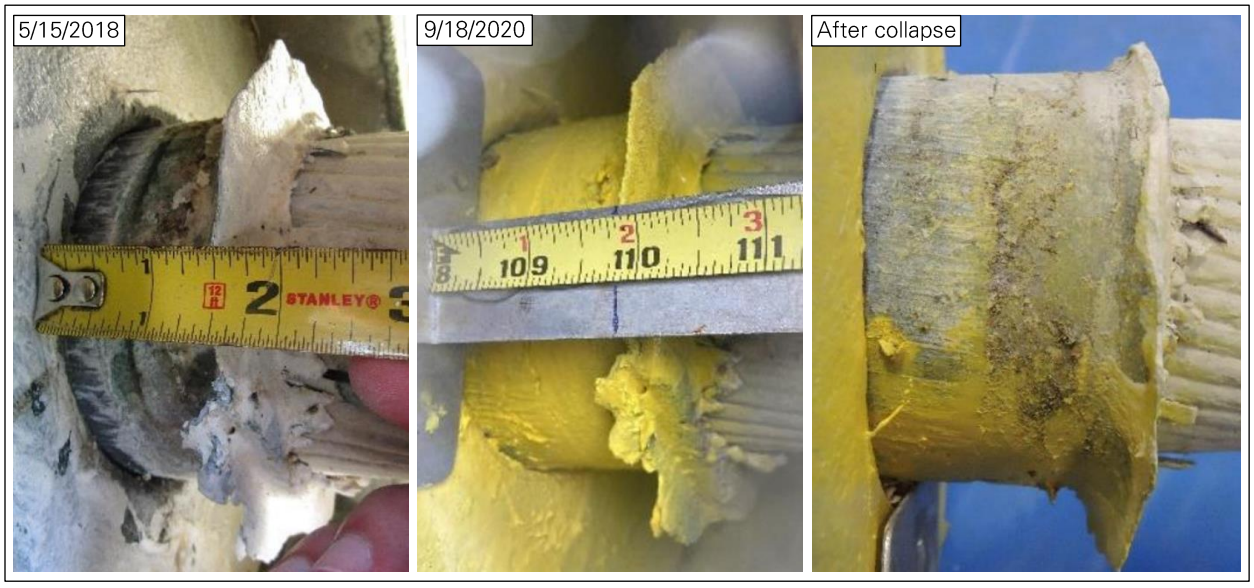

Figure 43: Cable at socket B12W_G
(left and center photos: NAIC Arecibo Observatory, a facility of the NSF).

6.0 Cable Vibrations

The main and backstay cables began experiencing wind-induced vibrations immediately after construction of the telescope in 1963, and Stockbridge dampers (Figure 44) were then installed to mitigate the vibrations.[16] As shown in Table 3, cable vibrations continued to be reported throughout the lifespan of the telescope, which led to upgrades and adjustments of the dampers. While we have not seen any data on the amplitude of the cable movement, AW did not consider that the vibrations were a concern from a structural standpoint. The vibrations also appear to have been relatively infrequent and may have occurred only under specific wind conditions. Finally, the initial installation and later adjustments of the damper system appear to have been effective.

Table 3: Cable vibrations mentioned in maintenance and inspection reports.

Source	Quotes
1970 maintenance report[A]	"While the dampers have been highly effective in reducing vibration of the cables, these vibrations still do occasionally occur. Since the installation of the dampers, there have been 2 or 3 guards' reports of vibrations. It is certain that the vibrations die out quickly after the excitation ceases."
1975 maintenance report[B]	"Main cable and anchor cable dampers were repositioned as specified by Ammann & Whitney."
1979 maintenance report[C]	"Vibration dampers were installed on the main platform suspension cables at tower four as recommended by Ammann & Whitney … Since the dampers were installed on 23 February, the cables have vibrated only once."
1983 structural inspection report[D]	"Stockbridge dampers were installed to minimize aeolian vibrations which, although never severe, had been observed." "Any evidence of vibration is reported."
1989 structural inspection report[E]	"There is still an ongoing vibration of the main cables which seems to be worse in the afternoon when the wind is choppy compared to the early morning hours." "Cable spacers made of energy absorptive material should be designed and installed on the main and backstay cables at third points. This should reduce the amplitude of the galloping vibrations."
2011 structural inspection report[F]	"From the top of T12, main cables M12-3 and M12-4 exhibited a slight to moderate amplitude of wind induced vibration. " "Auxiliary backstay A4 South and A12 West exhibited a slight wind induced vibration." "Cable dampers should be installed at Tower 12 for cables M12-3 and M12-4 and Anchorage A4 for cable M4S AUX."

[A] Arecibo Observatory. Quarterly maintenance report. April 1, 1970. Report provided by Arecibo Observatory.
[B] Arecibo Observatory. Quarterly maintenance report. December 8, 1975. Report provided by Arecibo Observatory.
[C] Arecibo Observatory. Quarterly maintenance report. May 2, 1979. Report provided by Arecibo Observatory.
[D] 1983. Report retrieved from Cornell University archives.
[E] Ammann & Whitney. *Arecibo Mini Inspection*. May 1989. Report retrieved from Cornell University archives.
[F] Ammann & Whitney. *Structural Condition Survey 2011*. March 2011. Report retrieved from Cornell University archives.

[16] Phoenix, S.L., Johnson, H.H., and McGuire, W. "Condition of Steel Cable after Period of Service". *Journal of Structural Engineering*. 112(6). 1986.

Figure 44: Stockbridge dampers near top (left) and bottom (right) of original M4 cables in 2020
(photos: NAIC Arecibo Observatory, a facility of the NSF).

Appendix E
Cable Failures and Telescope Collapse

1.0 Introduction

After a first cable failed on August 10, 2020, the cable system was frequently inspected by the Arecibo Observatory (AO) staff until the collapse on December 1, 2020. Those inspections were visual and mostly performed with drones to keep personnel at a safe distance from the damaged structure. This appendix compiles some of the inspection photos and still images of videos provided by AO to show the visible damage that developed in the cable system between first cable failure and collapse. The appendix is limited to observations. We relied on these observations to perform an analysis of the cable failures, which is presented in Appendix O.

The structural damage observed between the cable failure and collapse consists of cable wire breaks, cable socket deformation, and full cable failures. Damage was only observed among the original main cables supporting the telescope's platform from Tower 4 (the M4 cables), and most of the damage occurred near the top of Tower 4 (Figure 1).

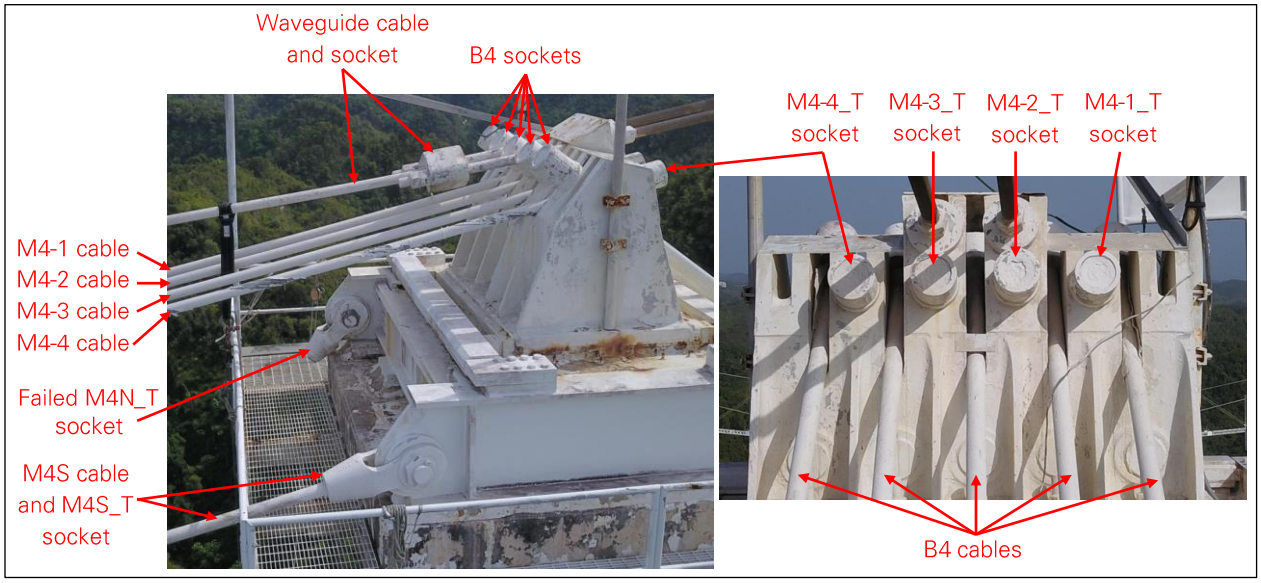

Figure 1: Cables and sockets at top of Tower 4 after M4N failure, looking northeast (left) and northwest (right) *(photos: NAIC Arecibo Observatory, a facility of the NSF).*

Each of the M4 cables is a single strand of 168 steel wires, and in some of the cables multiple wires fractured before the entire cable failed. From the drone photos, we determined the number of wire breaks by counting the wires visibly loose and based on the paint damage on the cable surface. Only the wire breaks in the outer layer of the cable are counted, as any wire break in the inner layers would not be visible on the drone photos.

2.0 Before M4N Failure

According to the AO inspection records, a total of eight wire breaks were observed on the M4-2 and M4-4 cables between 1967 and 1989 (Table 1). Drone photos taken after the M4N failure (Figure 2, Figure 3) are consistent with those records, as they show protruding wires and/or clamps on the two cables. The clamps were likely installed to keep the broken wires tight with the rest of the cable. However, we noted

that clamps had been installed at the tower end of the M4-1 cable (Figure 3), while there is no record of any wire break at that location (Table 1).

Table 1: Wire breaks in Tower 4 original main cables on record before M4N failure.

	M4-1	M4-2	M4-3	M4-4
Tower End	none	none	none	6/30/1975 1/15/1983 1/3/1989
Platform End	none	12/5/1969 8/26/1970	none	6/22/1967 6/24/1972 1/15/1983

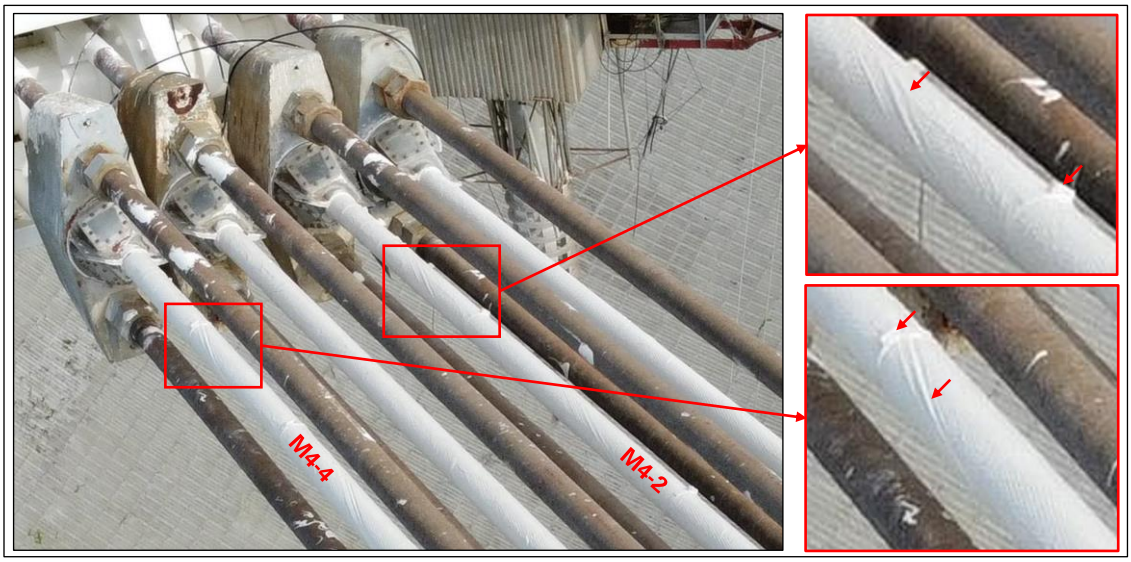

Figure 2: Clamps and evidence of previous wire breaks on M4-2 and M4-4 near platform
(photo: NAIC Arecibo Observatory, a facility of the NSF).

Figure 3: Clamps on M4-1 and M4-2 near Tower 4, likely installed after previous wire breaks. The paint damage on M4-4 corresponds to fresh wire breaks following the M4N failure.
(Photo: NAIC Arecibo Observatory, a facility of the NSF.)

3.0 M4N Failure

Cable M4N pulled out of its socket at the top of Tower 4 on August 10, 2020. This section describes the damage discovered in the other cables over the next few days.

3.1 Wire Breaks

Shortly after the M4N failure, four wire breaks were observed in M4-4 near Tower 4 (Figure 4). No wire break was observed in any other M4 cable or near the platform (Figure 5).

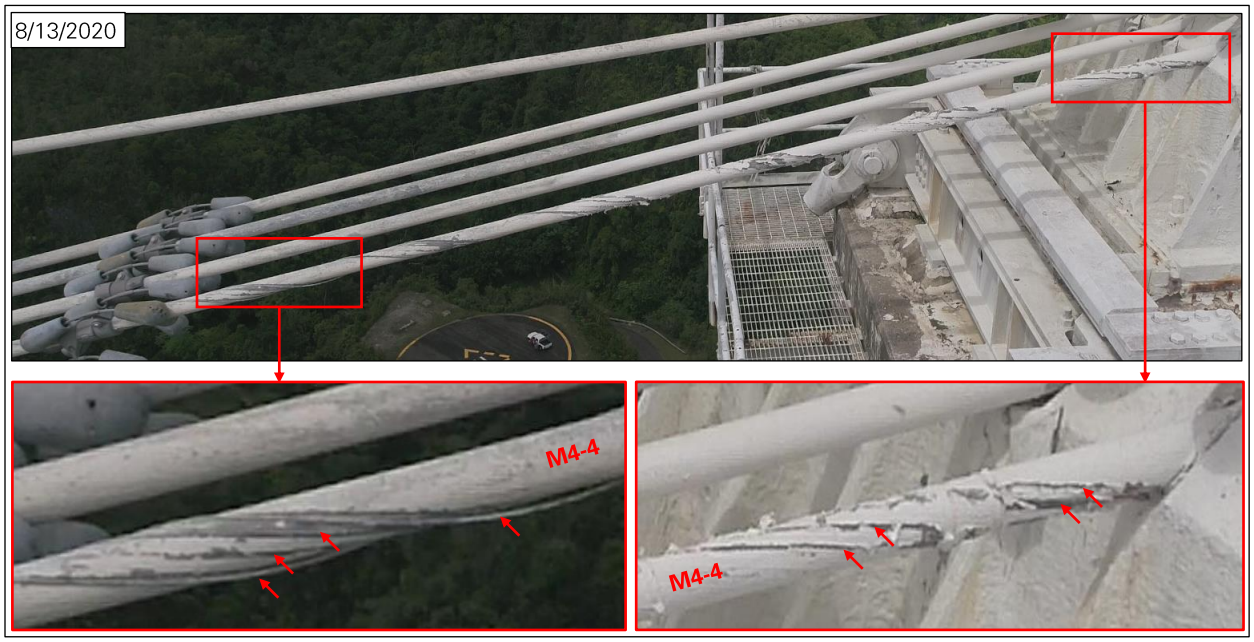

Figure 4: M4 cables near Tower 4 on August 13, 2020. Four wires are broken in M4-4, and no wire is broken in the other three cables. *(Photo: NAIC Arecibo Observatory, a facility of the NSF.)*

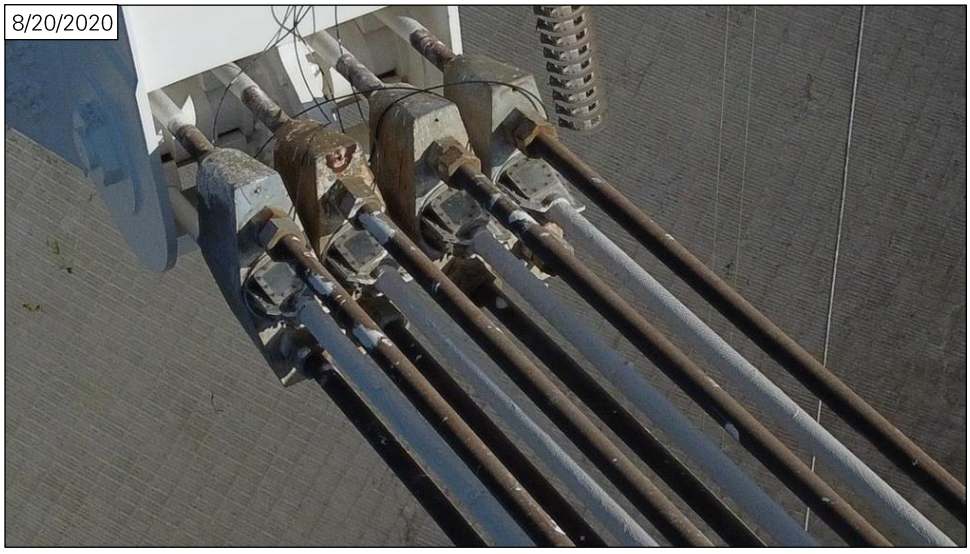

Figure 5: M4 cable near platform on August 20, 2020. No wire is broken.
(Photo: NAIC Arecibo Observatory, a facility of the NSF.)

3.2 Socket Condition

The back end of the M4 sockets at Tower 4 is shown in Figure 6 after the M4N failure. On socket M4-2_T, a circular crack is visible on the surface of the zinc casting, and the central part of the casting has moved inwards. On socket M4-4_T, the surface of the casting also appears to be deformed with the central part moving inwards, but to a lesser extent than for M4-2_T. It is unknown whether these deformations occurred before or during the M4N failure.

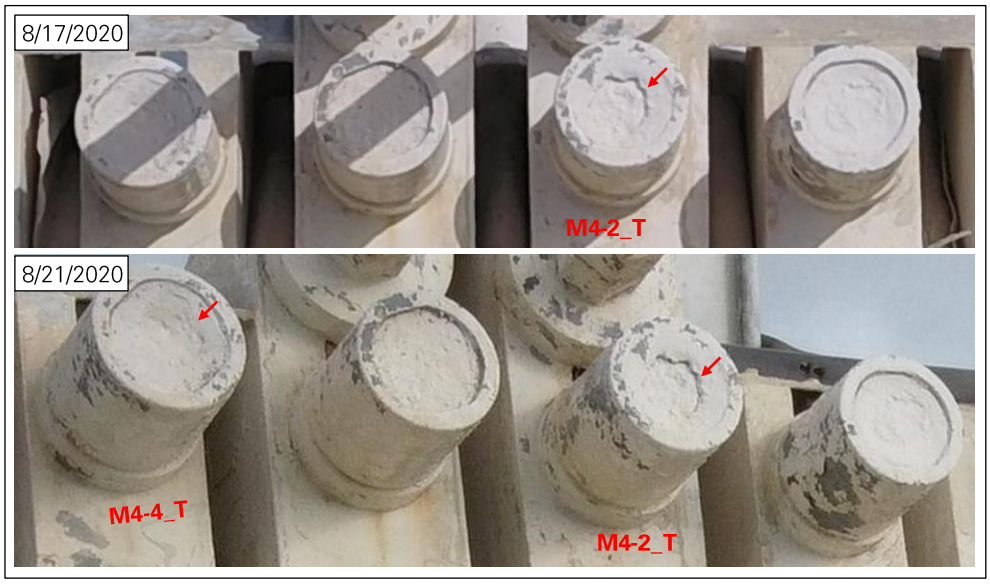

Figure 6: M4 sockets at Tower 4 after M4N failure
(photos: NAIC Arecibo Observatory, a facility of the NSF).

4.0 Between M4N and M4-4 Failure

AO inspected the structure on a regular basis in the three-month period between the M4N failure on August 10, 2020, and the M4-4 failure on November 6, 2020

4.1 Wire Breaks

The failed M4N_T socket was removed from the top of Tower 4 on September 23, 2020 for forensic analysis. During the operation, AO took close-up photographs of the M4 cables. The photographs show four broken wires on M4-4 (Figure 7), and one broken wire on M4-1 (Figure 8). The M4 cables were then repainted at the top of Tower 4 (Figure 9).

A new wire break was discovered on M4-2 on October 15, 2020 (Figure 10), and new paint damage was observed on M4-4 on October 19, 2020 (Figure 11). This paint damage, however, appears to be due to the movement of wires already broken. No more changes were observed by 10/30/2020 (Figure 12, Figure 13), which is a week before the failure of M4-4.

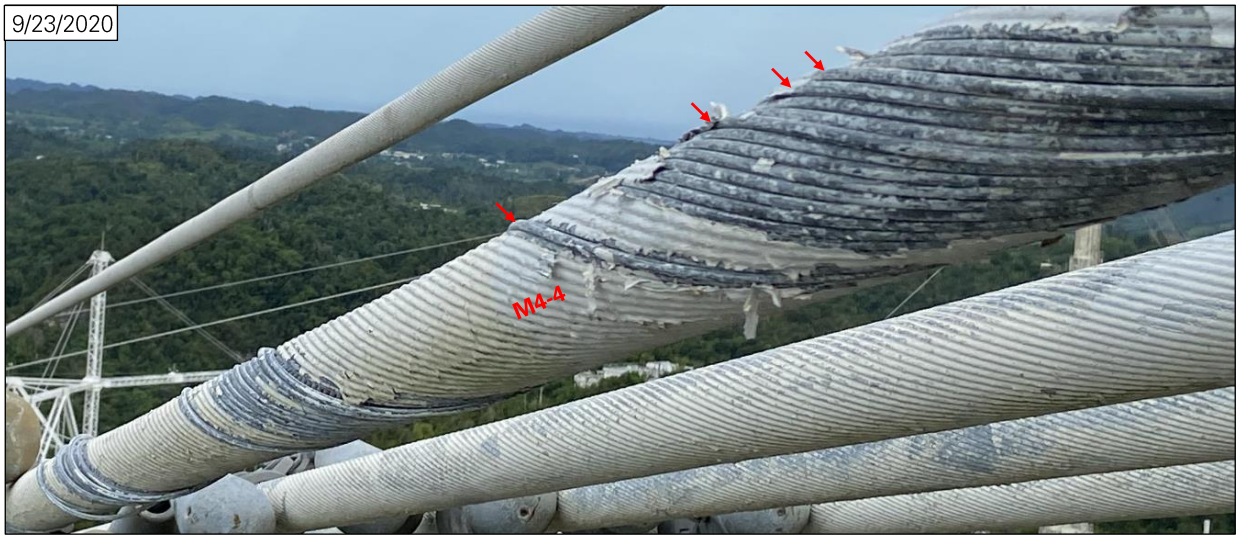

Figure 7: Close-up view of M4-4 near Tower 4 on September 23, 2020. Four wires are broken.
(Photo: NAIC Arecibo Observatory, a facility of the NSF.)

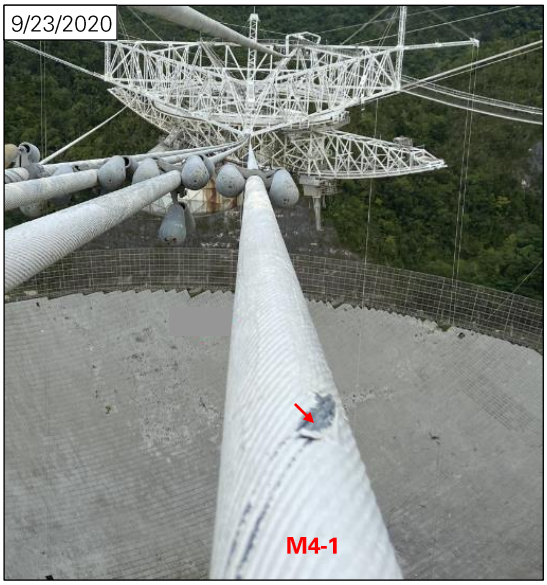

Figure 8: Close-up view of M4-1 near Tower 4 on September 23, 2020. A wire is broken.
(Photo: NAIC Arecibo Observatory, a facility of the NSF.)

Figure 9: M4 cables freshly repainted near Tower 4 on October 1, 2020
(photo: NAIC Arecibo Observatory, a facility of the NSF).

Figure 10: New wire break in M4-2 on October 15, 2020
(photos: NAIC Arecibo Observatory, a facility of the NSF).

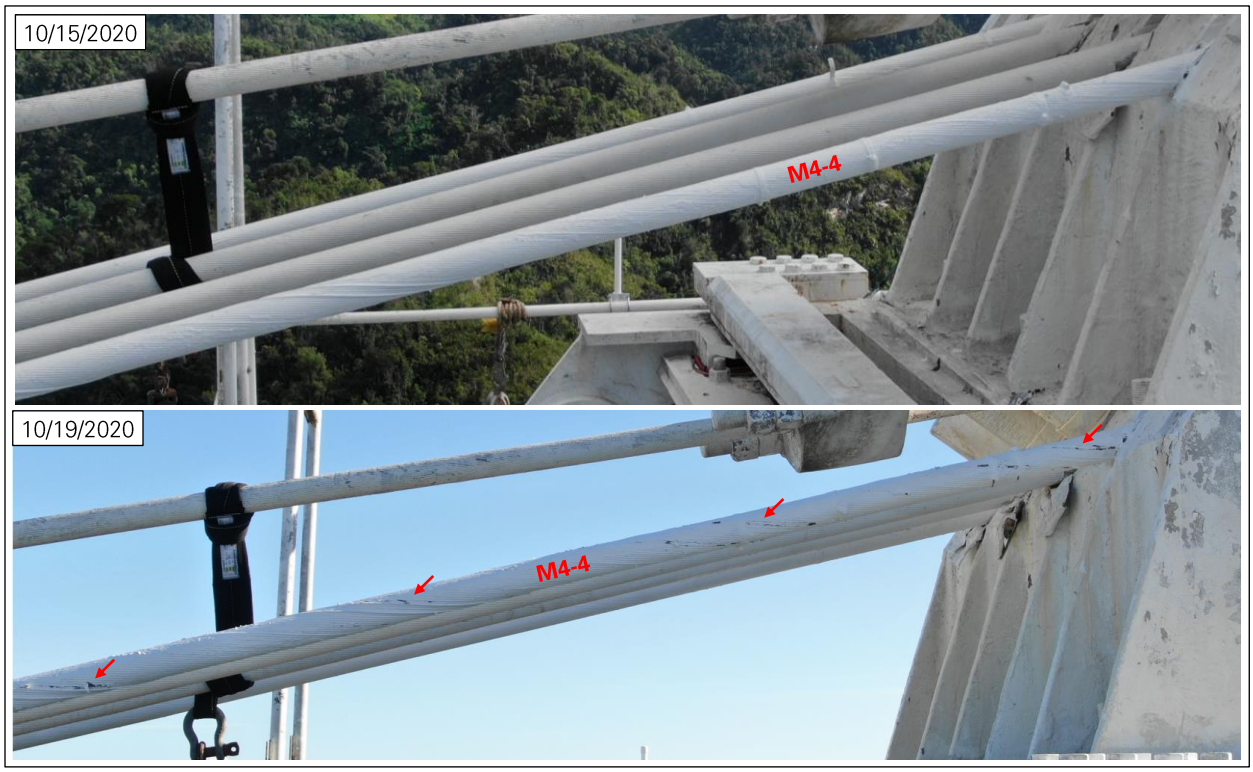

Figure 11: Broken wire movement in M4-4 on October 19, 2020
(photos: NAIC Arecibo Observatory, a facility of the NSF).

Figure 12: M4 cables near Tower 4 on October 30, 2020. No significant change is visible since October 19, 2020.
(Photo: NAIC Arecibo Observatory, a facility of the NSF.)

Figure 13: M4 cables near platform on October 30, 2020. No wire is broken.
(Photo: NAIC Arecibo Observatory, a facility of the NSF.)

4.2 Socket Condition

The crack in the zinc casting at the back of socket M4-2_T was sealed by October 1, 2020 (Figure 14). No significant change was observed on the sockets in October 2020 (Figure 15).

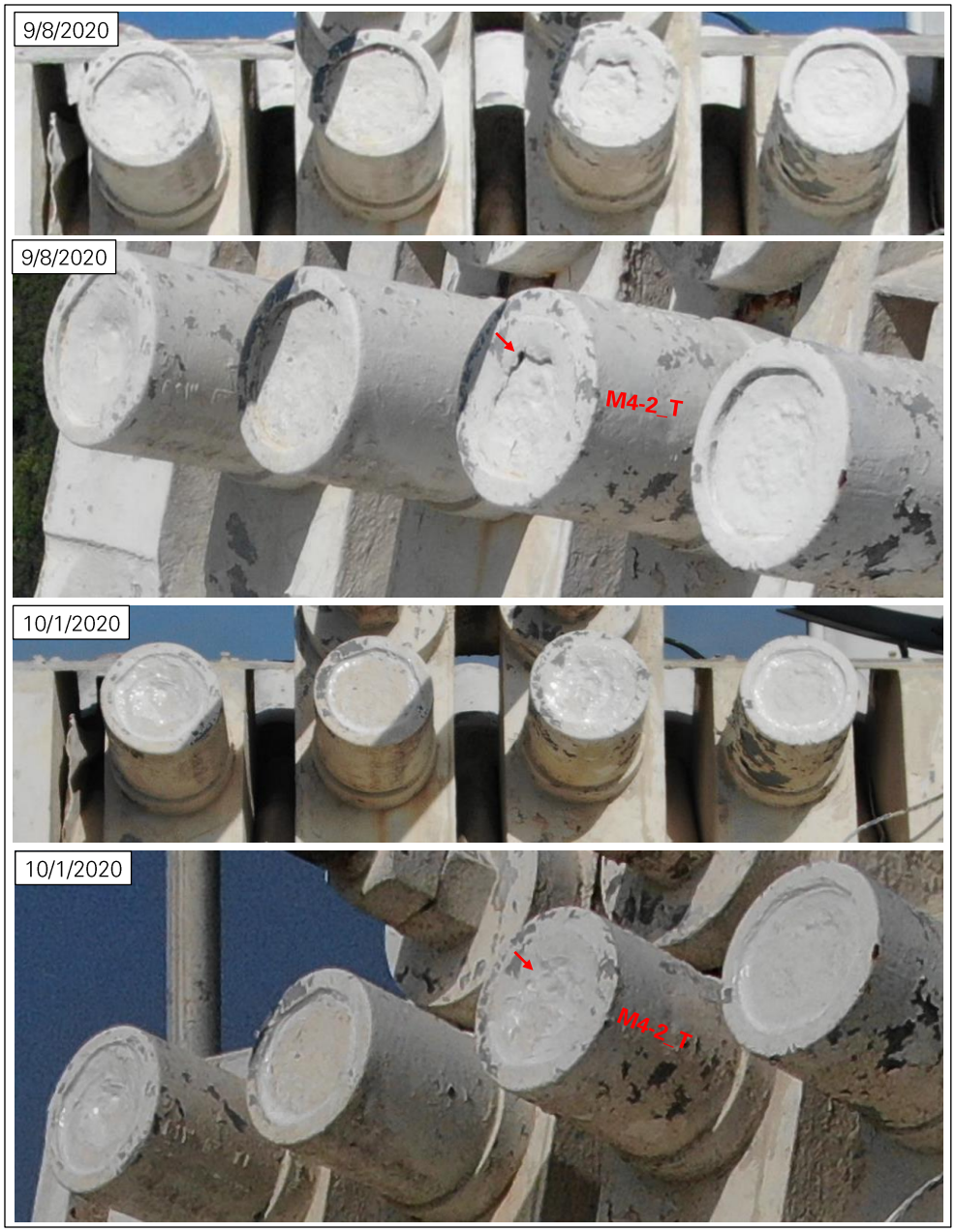

Figure 14: Sealant added at back of M4 sockets at Tower 4 by October 1, 2020
(photos: NAIC Arecibo Observatory, a facility of the NSF).

Figure 15: M4 sockets at Tower 4 on October 30, 2020. No significant change is visible since October 1, 2020.
(Photo: NAIC Arecibo Observatory, a facility of the NSF.)

5.0 M4-4 Failure

Cable M4-4 failed on November 6, 2020. This section describes the damage observed in the other M4 cables on the day of failure and the day after.

5.1 Wire Breaks

Shortly after the M4-4 failure, three new wire breaks were observed in M4-1 and a new wire break was observed in M4-2 near Tower 4 (Figure 16). Four wire breaks were also observed in M4-2 near the platform (Figure 17).

Figure 16: M4 cables near Tower 4 on November 6, 2020, with three new wire breaks in M4-1 and a new wire break in M4-2
(photos: NAIC Arecibo Observatory, a facility of the NSF).

Figure 17: M4 cables near platform on November 7, 2020. Four adjacent wires are broken in M4-2.
(Photos: NAIC Arecibo Observatory, a facility of the NSF.)

5.2 Socket Condition

The zinc casting of socket M4-4_T experienced significant deformation during the M4-4 failure or in the week preceding it, with the central part of the casting moving inwards (Figure 18). The M4-4 failure did not cause any visible change in the other three sockets (Figure 18).

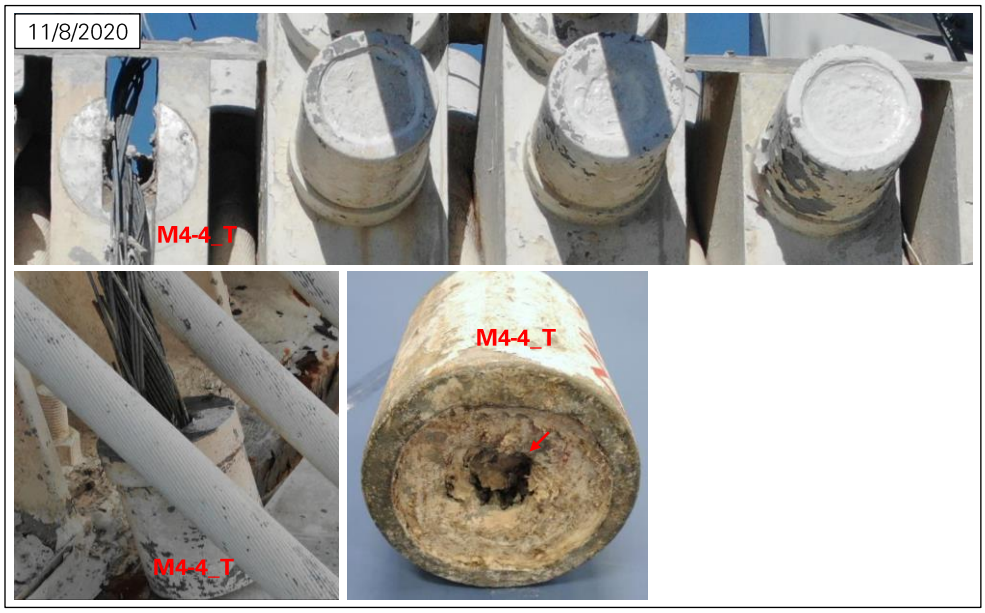

Figure 18: M4 sockets at Tower 4 on November 8, 2020, and socket M4-4_T as recovered after collapse
(top and bottom left photos: NAIC Arecibo Observatory, a facility of the NSF; bottom center photo: Socotec).

6.0 Between M4-4 Failure and Collapse

After the M4-4 failure, the remaining M4 cables were inspected at least once a day until the telescope collapsed.

6.1 Wire Breaks

Between the M4-4 failure and the collapse, seven and five new wire breaks were observed in the M4-1 and M4-2 cables respectively near Tower 4. The new wire breaks are shown in Figure 19 through Figure 27. No new wire break was observed in the M4 cables near the platform (Figure 28).

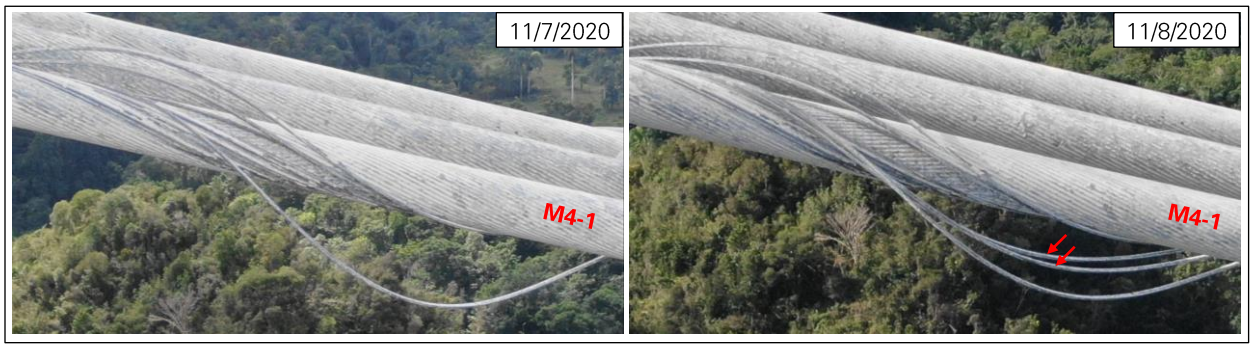

Figure 19: Two new wire breaks in M4-1 on November 8, 2020
(photos: NAIC Arecibo Observatory, a facility of the NSF).

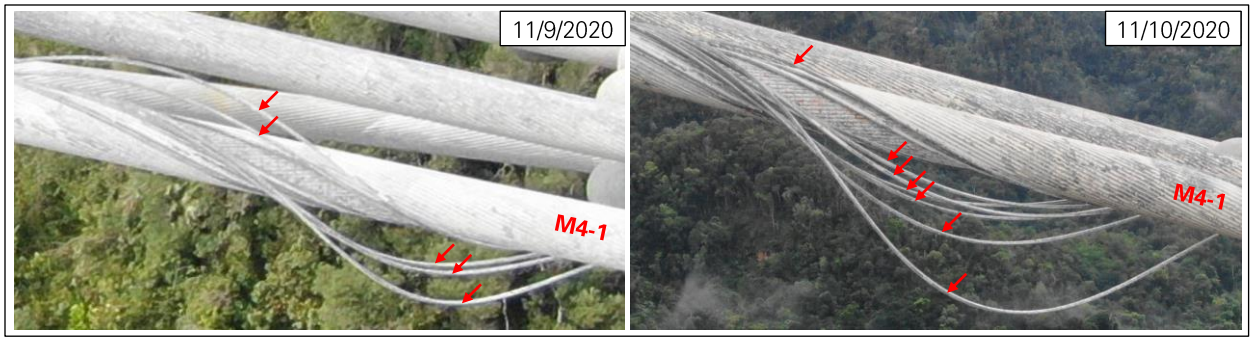

Figure 20: Two new wire breaks in M4-1 on November 10, 2020
(photos: NAIC Arecibo Observatory, a facility of the NSF).

Figure 21: New wire break in M4-2 on November 11, 2020. The break occurred away from the socket.
(Photos: NAIC Arecibo Observatory, a facility of the NSF.)

Figure 22: New wire break in M4-1 on November 13, 2020
(photos: NAIC Arecibo Observatory, a facility of the NSF).

Figure 23: New wire break in M4-2 on November 20, 2020
(photos: NAIC Arecibo Observatory, a facility of the NSF).

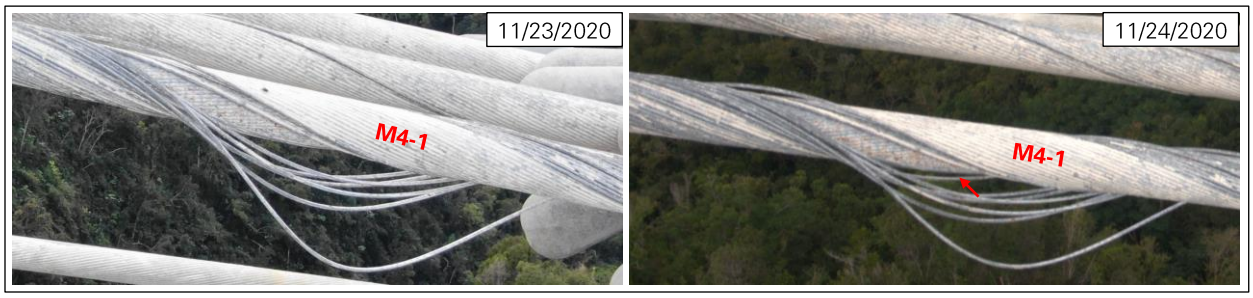

Figure 24: New wire break in M4-1 on November 20, 2020
(photos: NAIC Arecibo Observatory, a facility of the NSF).

Figure 25: New wire break in M4-1 on November 26, 2020
(photos: NAIC Arecibo Observatory, a facility of the NSF).

Figure 26: New wire break in M4-2 on November 29, 2020
(photos: NAIC Arecibo Observatory, a facility of the NSF).

Figure 27: Two new wire breaks in M4-2 on December 1, 2020
(photos: NAIC Arecibo Observatory, a facility of the NSF).

Figure 28: M4 cables near platform on November 28, 2020, with no visible change since November 7, 2020
(photos: NAIC Arecibo Observatory, a facility of the NSF).

The evolution of the number of wire breaks observed in the M4 cables near Tower 4 after the first cable failure is shown in Figure 29.

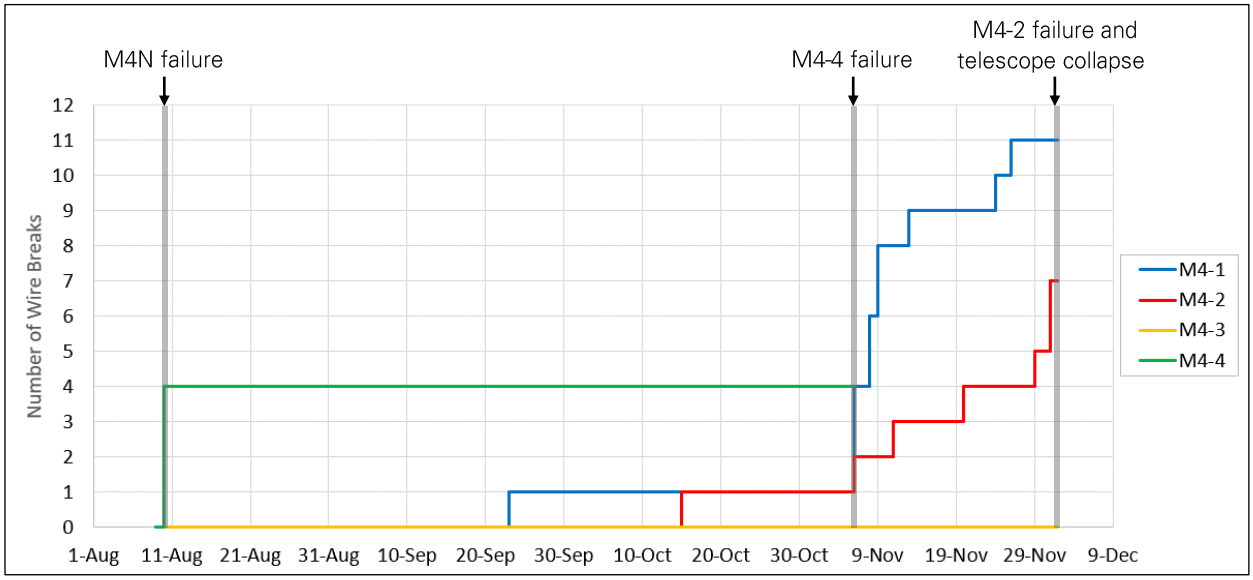

Figure 29: Count of wire breaks in M4 cables near Tower 4 between M4N failure and collapse.

6.2 Socket Condition

The central part of the zinc casting of socket M4-2_T moved inwards after the M4-4 failure. As shown in Figure 30, a crack developed in the sealant that had been installed between the M4N and M4-4 failures.

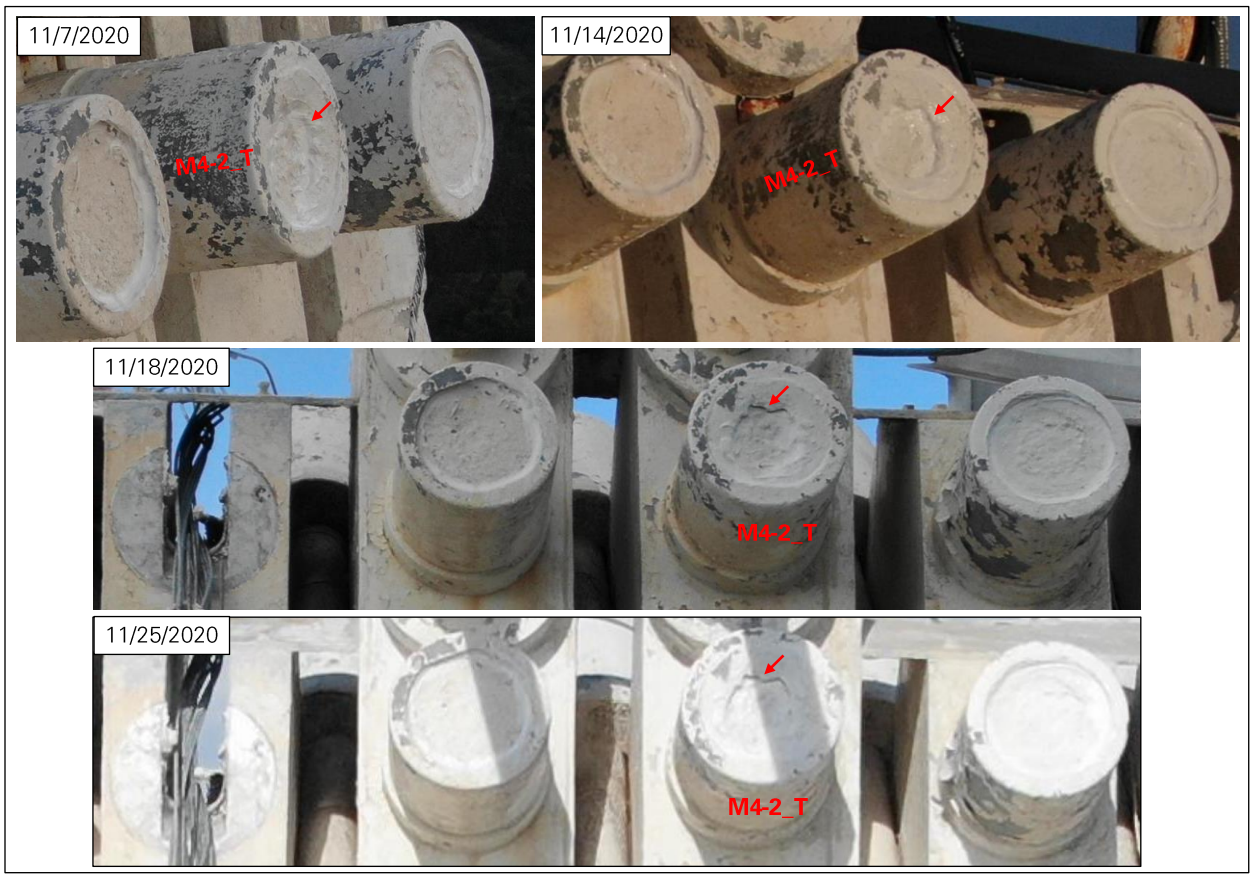

Figure 30: M4 sockets at Tower 4 after M4-4 failure. On socket M4-2, the central part of the zinc casting appears to move inwards, resulting in a new sealant crack. (Photos: *NAIC Arecibo Observatory, a facility of the NSF.)*

7.0 Collapse

The telescope collapsed on December 1, 2020, immediately after the failure of cable M4-2 at the top of Tower 4. This section describes the cable failure and the telescope collapse sequence as captured on video.

7.1 Top of Tower 4

The AO staff was performing a drone inspection of the top of Tower 4 when cable M4-2 failed and triggered the collapse of the telescope. Key frames of the video recorded by the drone are compiled on Figure 31 through Figure 33.

The M4-2 socket recovered after the collapse is shown in Figure 34. The central part of the zinc casting moved further inwards since the last known photo (November 25, 2020, Figure 30). This movement may have occurred suddenly when M4-2 failed.

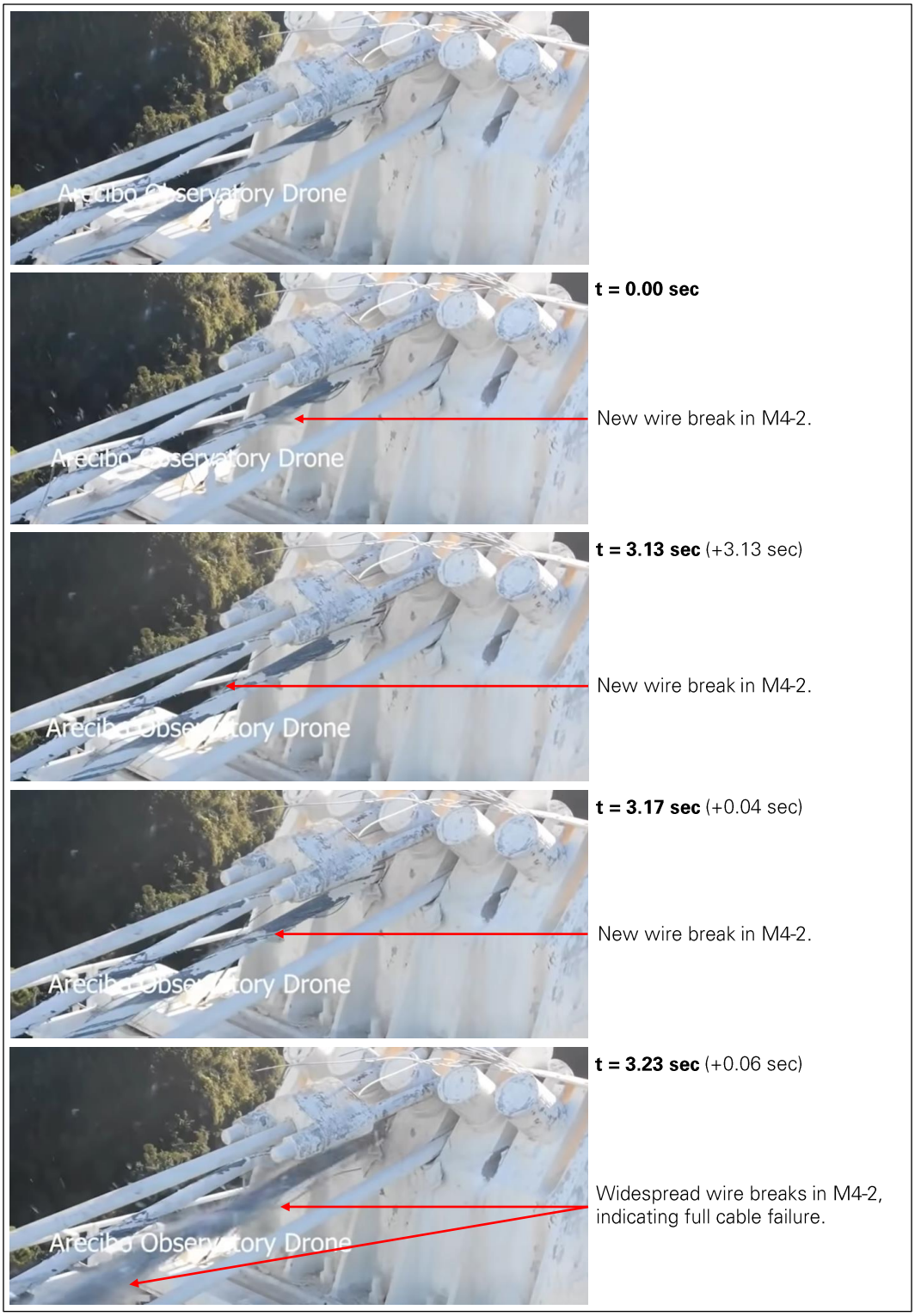

Figure 31: Still images of drone video of top of Tower 4 during telescope collapse: seconds 0.00 to 3.23 *(video: NAIC Arecibo Observatory, a facility of the NSF).*

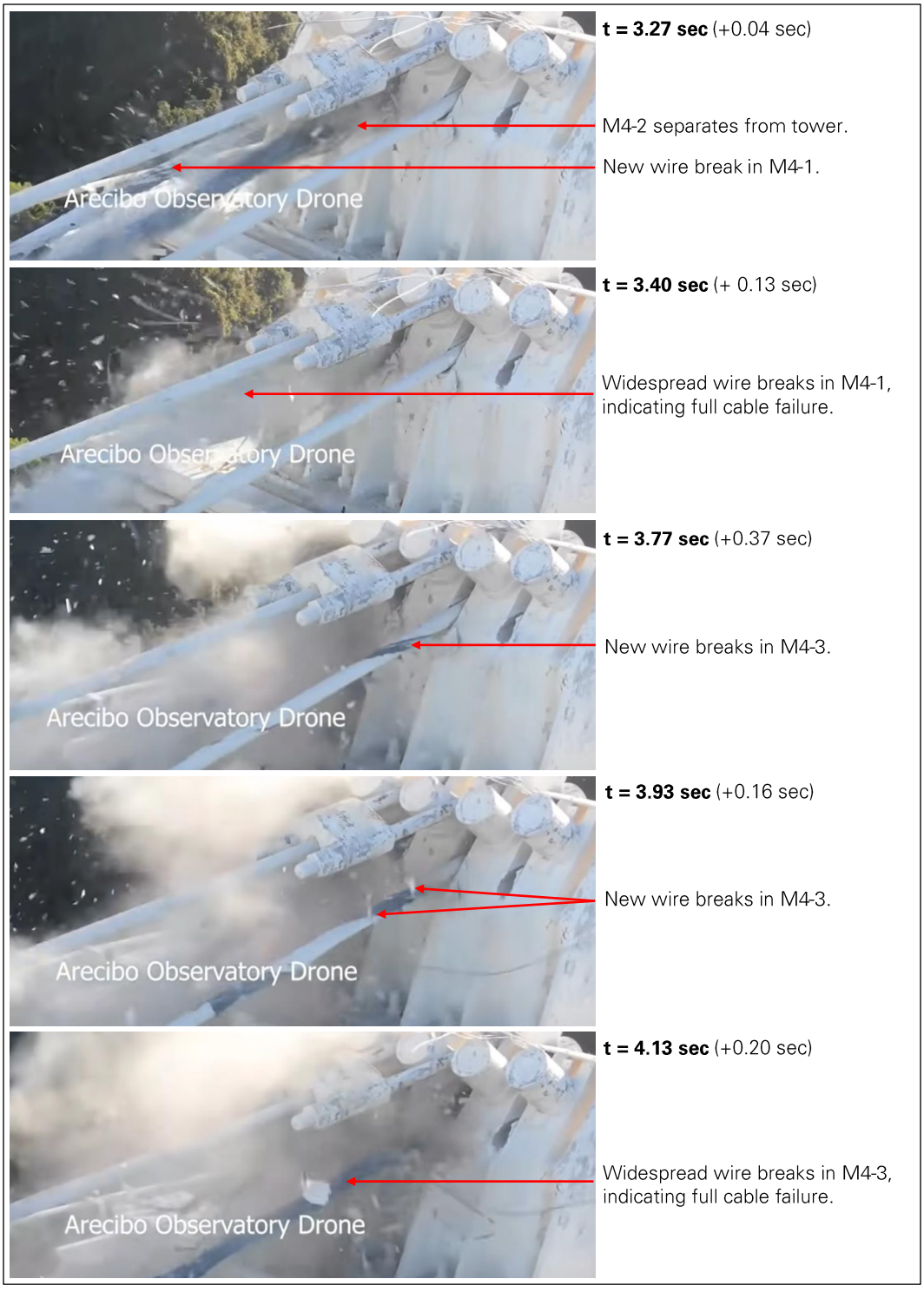

Figure 32: Still images of drone video of top of Tower 4 during telescope collapse: seconds 3.27 to 4.13 *(video: NAIC Arecibo Observatory, a facility of the NSF).*

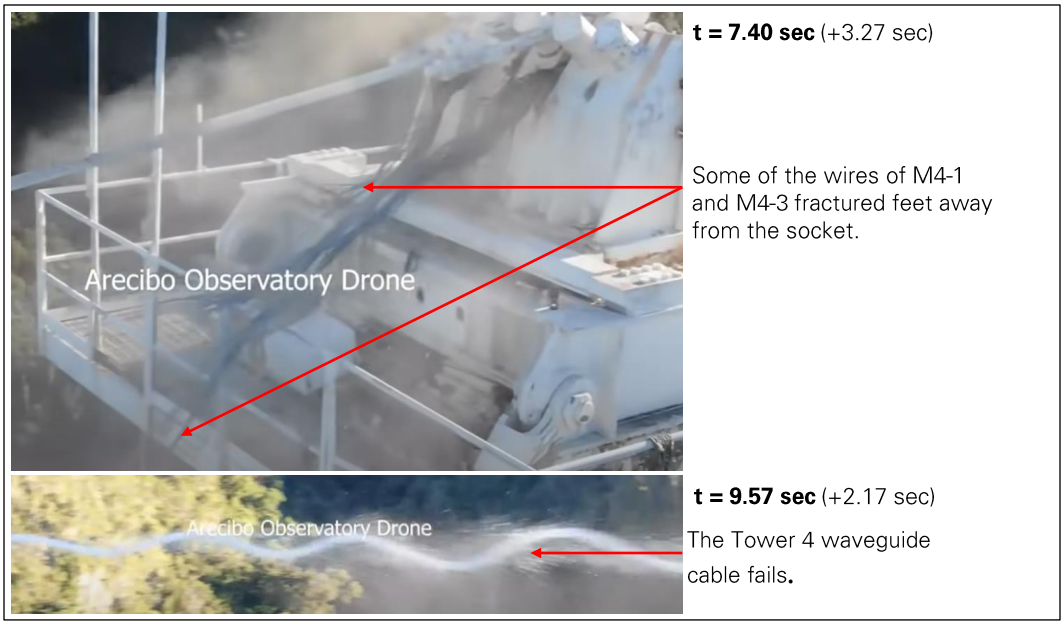

Figure 33: Still images of drone video of top of Tower 4 during telescope collapse: seconds 3.27 to 9.57 *(video: NAIC Arecibo Observatory, a facility of the NSF).*

Figure 34: Socket M4-2_T recovered after collapse.

7.2 Overall Structure

At the time of the collapse, a camera set up in the telescope's control room was recording the suspended structure. The collapse lasted approximately 15 seconds, between the M4-2 failure and the landing of the last cables and tower tops. Still images of the collapse video at one second intervals are shown in Figure 35 through Figure 40.

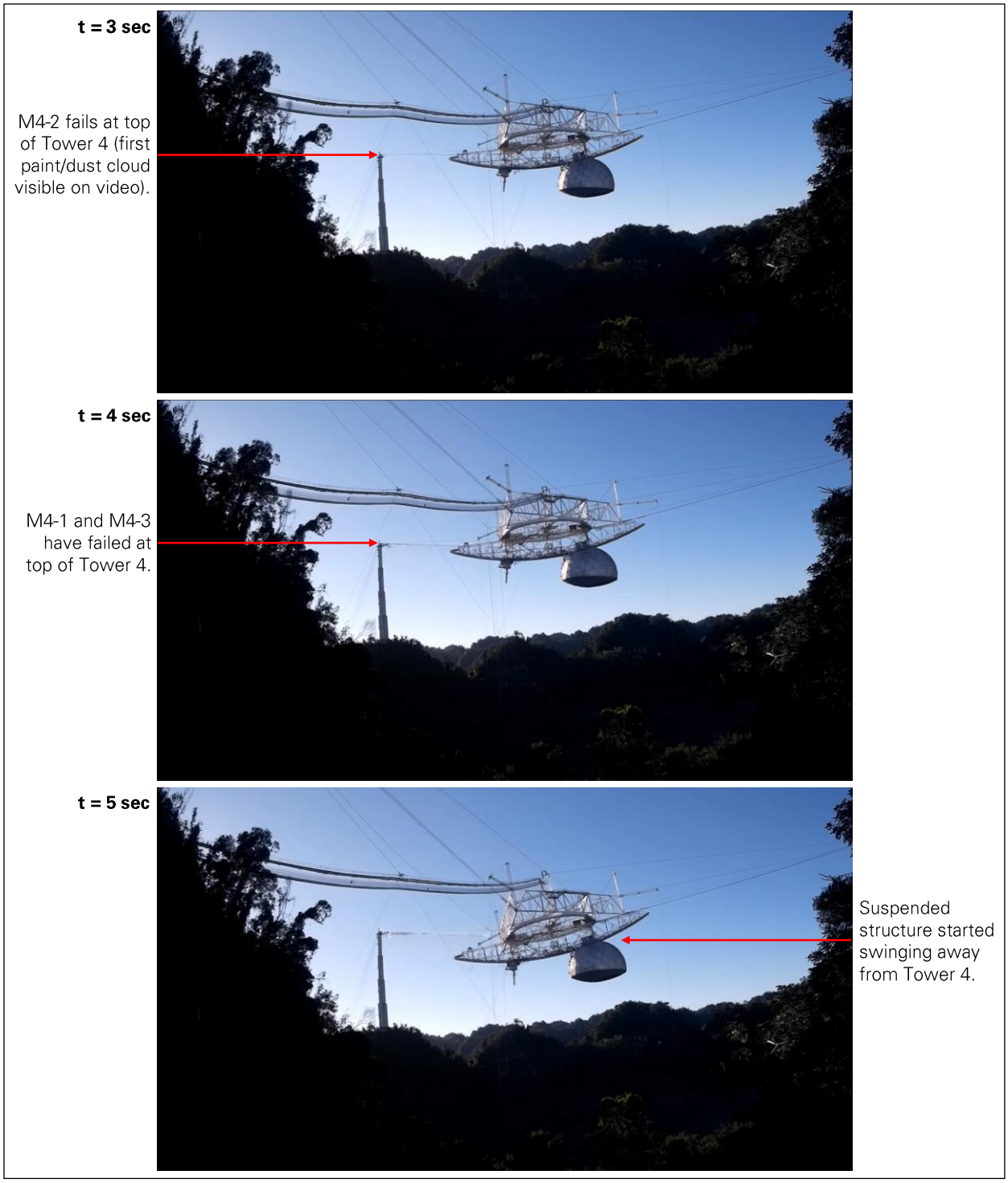

Figure 35: Still images of telescope collapse video: seconds 3 to 5
(video: NAIC Arecibo Observatory, a facility of the NSF).

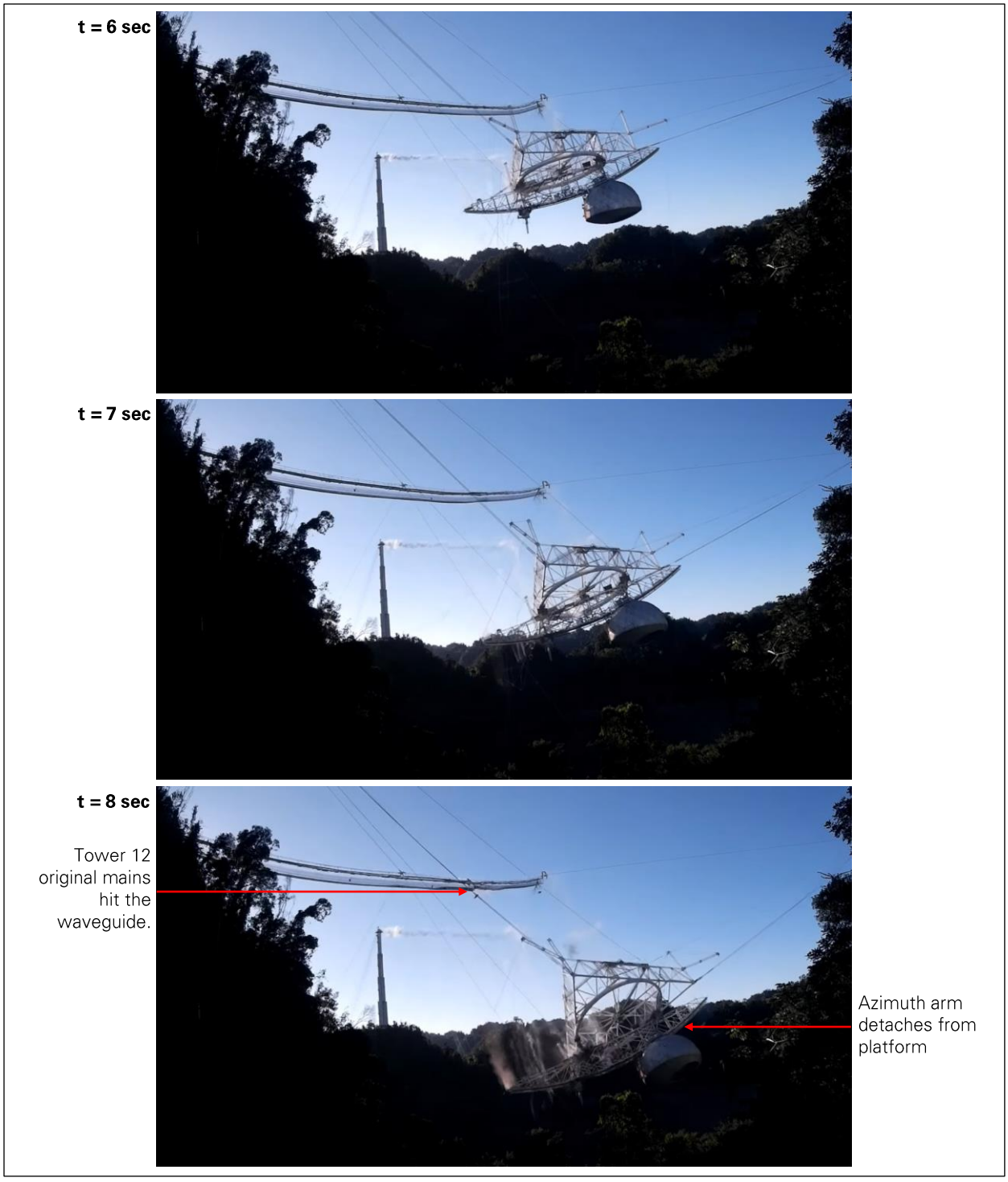

Figure 36: Still images of telescope collapse video: seconds 6 to 8
(video: NAIC Arecibo Observatory, a facility of the NSF).

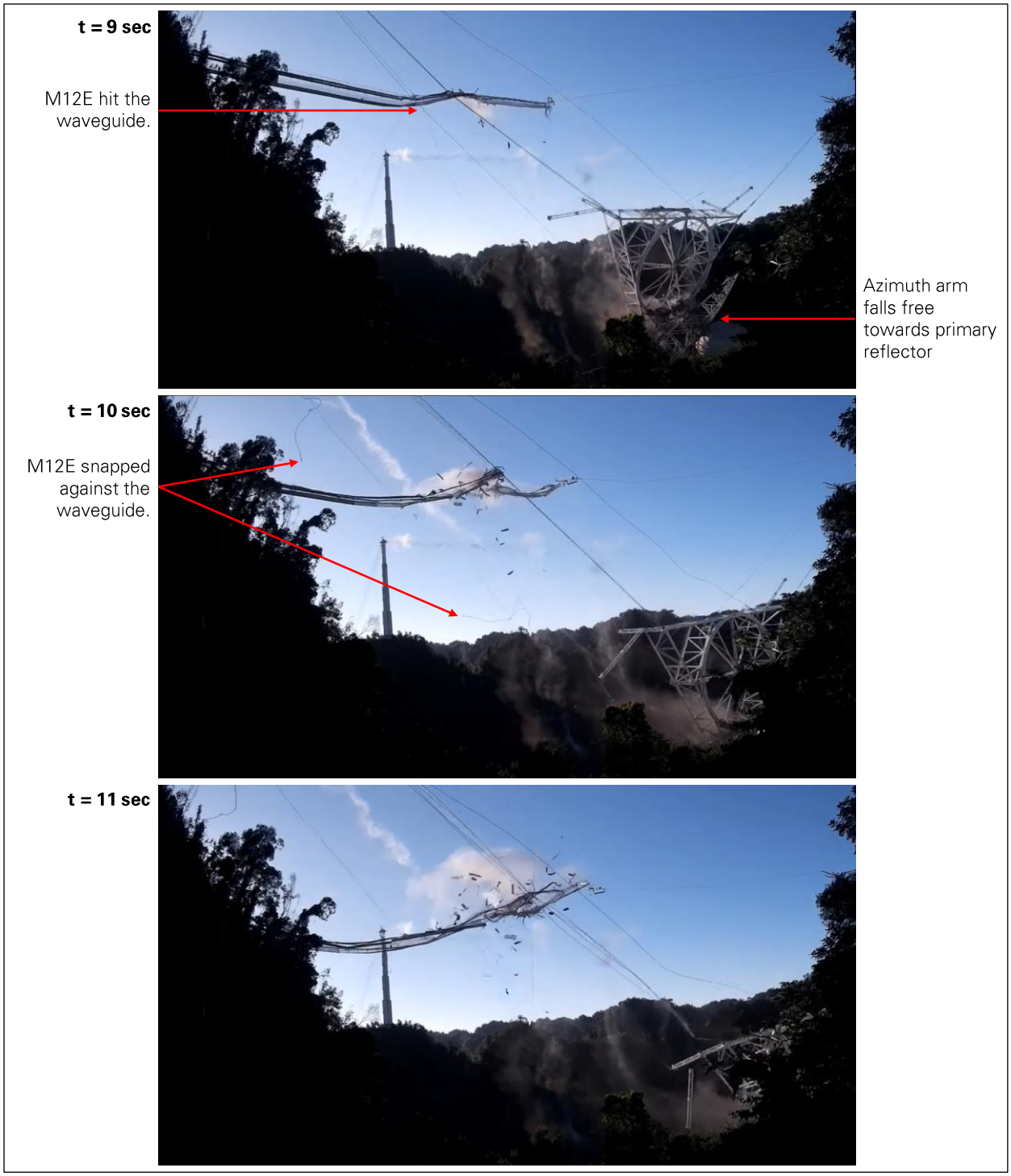

Figure 37: Still images of telescope collapse video: seconds 9 to 11
(video: NAIC Arecibo Observatory, a facility of the NSF).

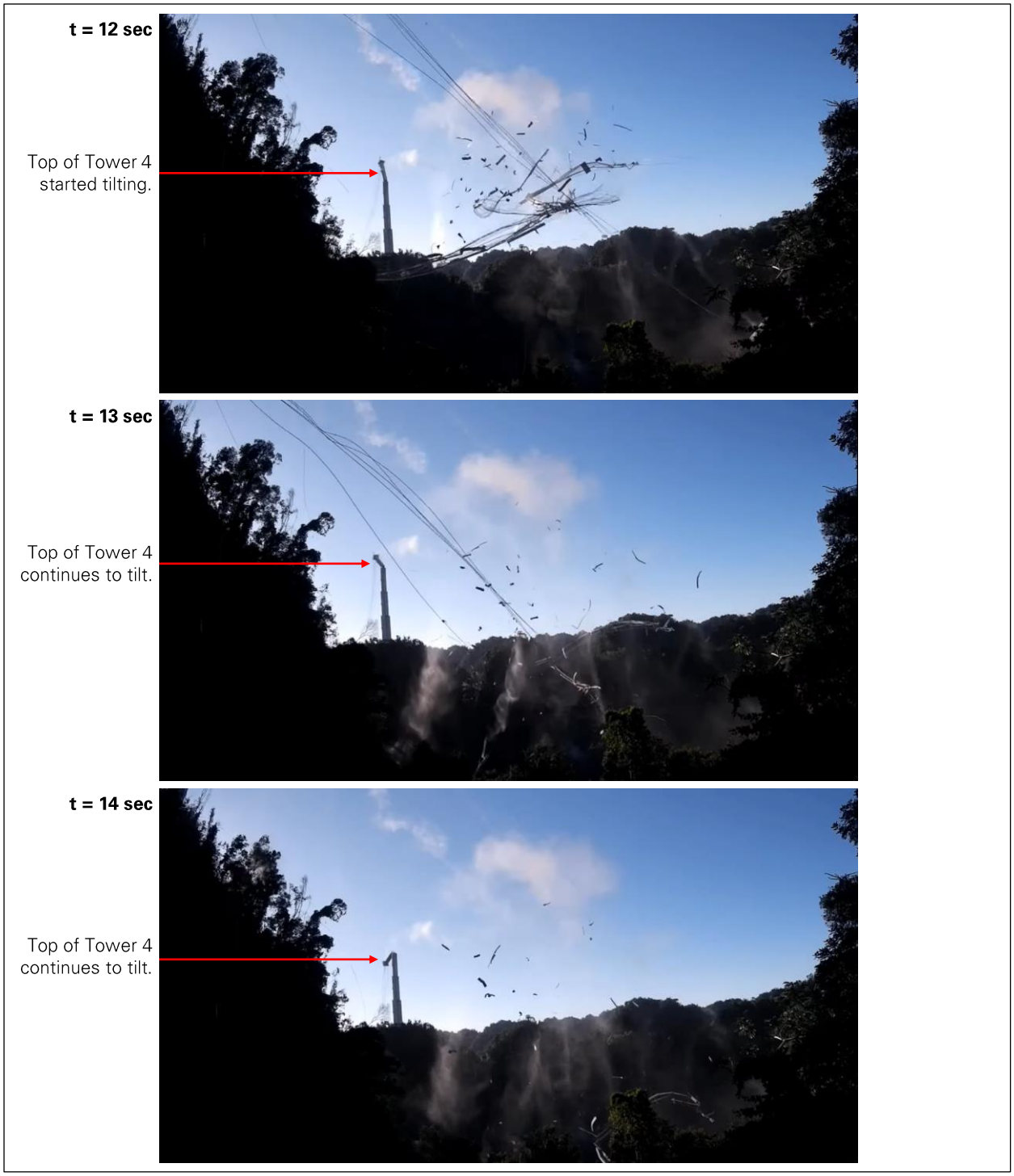

Figure 38: Still images of telescope collapse video: seconds 12 to 14
(video: NAIC Arecibo Observatory, a facility of the NSF).

Figure 39: Still images of telescope collapse video: seconds 15 to 17
(video: NAIC Arecibo Observatory, a facility of the NSF).

Figure 40: Still images of telescope collapse video: seconds 18 to 19
(video: NAIC Arecibo Observatory, a facility of the NSF).

Appendix F
Structural Analysis Models

1.0 Introduction

To investigate the cable failures and eventual collapse of the telescope, it is necessary to determine how the cable tensions varied over time when the telescope was operating and subject to environmental loads such as temperature, wind, and earthquakes. To perform this analysis, we constructed finite element analysis (FEA) models of the original and upgraded telescope structures. Analysis was primarily performed in the FEA program SAP2000, and some analyses were repeated in the FEA program Abaqus for validation. All of the FEA models used are based on similar assumptions and are of similar scope and level of detail.

The assumptions made in the FEA models are presented in this appendix. The general structural behavior of the telescope, as determined from the models, is also presented. The models were then used to determine the cable tensions under a variety of loads, and these results are presented in Appendix G, H, I, J and K.

2.0 Modeling Assumptions

The assumptions below were used to build the telescope models in both FEA programs.

2.1 Elements and Boundary Conditions

The FEA models are built to represent the superstructure of the telescope, which includes the towers, suspended structure, mains, backstays, tiedowns and waveguide. The telescope's primary reflector and ground screen are structurally independent of the superstructure and are not included in these analysis models. Distinct models were built to analyze the original structure (Figure 1) and the upgraded structure (Figure 2).

The **towers** are modeled as frame elements, which capture axial, shear, bending and torsional deformations, as well as P-delta effects in nonlinear analyses. The stepped shape of the towers is modeled using several frame elements of different cross-sections. The bottom of each tower is assumed to be fully fixed and located at the elevation of the top of the tower pedestal.

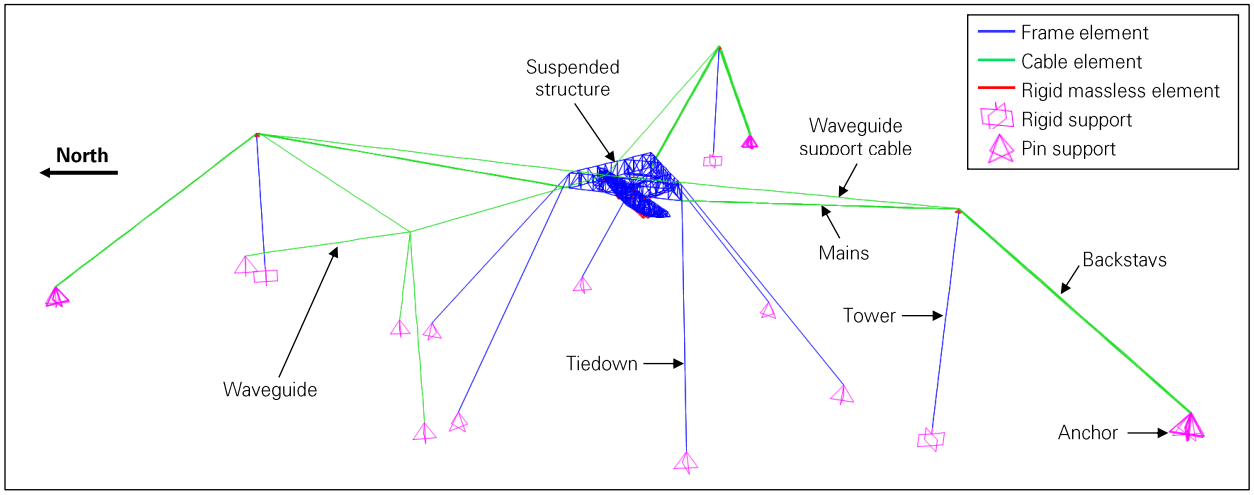

Figure 1: Finite element model of original structure.

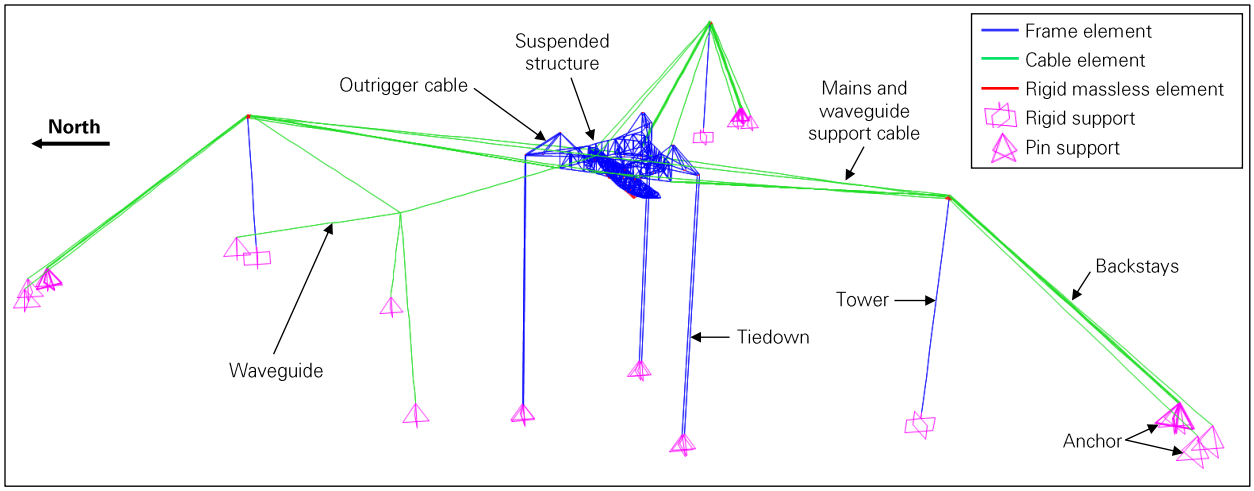

Figure 2: Finite element model of upgraded structure.

The platform and azimuth arm trusses of the **suspended structure** are also modeled as frame elements. These truss members are built up from standard steel channels and angles with lacing. We assume that the lacing is rigid, such that the channels and angles act compositely. Because the azimuth arm is modeled in the stowed position, which the telescope was locked in before high wind events, we apply wind loads directly to the azimuth arm in our wind analyses (Appendix J). To model other positions of the azimuth arm during telescope operation, the azimuth arm elements can be removed from the model and replaced with equivalent gravity loads that act directly on the platform (Appendix H). The steel cables in the outriggers of the upgraded platform are short in length and tensioned adequately such that their sags are negligible. These cable elements are therefore also modeled as frame elements.

The **Gregorian** and **line feed(s)** are not primary structural elements, and they are not modeled as finite elements in the suspended structure. Their weight is applied to the azimuth arm in accordance with their positions.

The **mains and backstays** are modeled as cable elements, whose behavior take into account the cable sag. Although the cable elements used in the SAP2000 and Abaqus models do not have identical assumptions, both versions of those elements are adequate for the analysis of the telescope structure. This is further discussed in sections 3.0 and 4.0 below. The **waveguide**, waveguide support cables and waveguide tiedowns are also modeled as cable elements.

Even though the **tiedowns** of the suspended structure are steel cables, these cables are modeled as frame elements because their sag is negligible: the tiedowns of the upgraded structure are vertical, while the tiedowns of the original structure were inclined but supported by carrier cables. Carrier cables were only installed during the first upgrade in 1974. Since this first upgrade did not significantly impact the telescope's structural behavior, the pre-1974 structure is not modeled in our analysis.

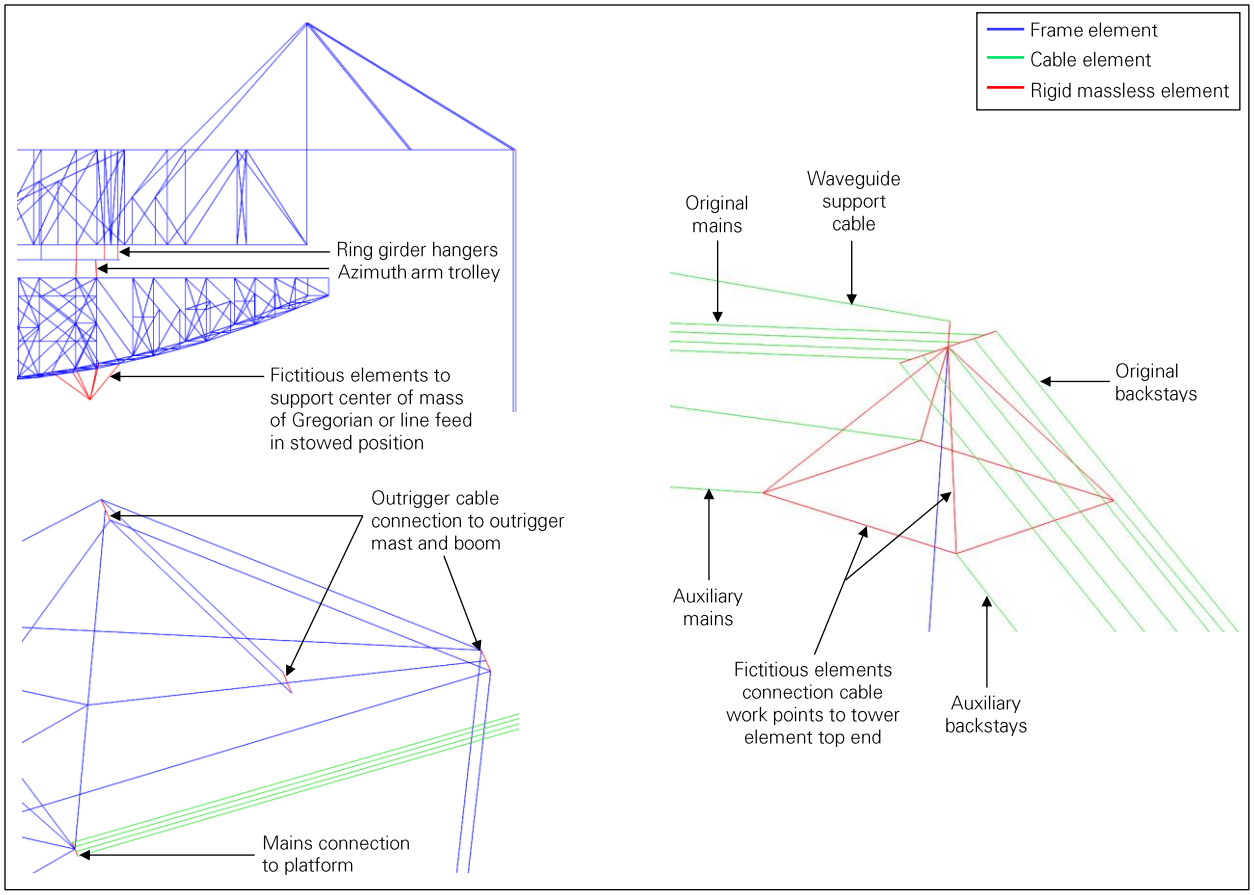

Figure 3: Use of rigid massless elements.

As shown in Figure 3, some of the frame and cable elements are connected in the model with rigid massless elements. Rigid massless elements are used to model some of the cable connections to the towers and the platform, so that each cable element starts and ends at the work point of the actual cable. Rigid massless elements are also used to model the ring girder hangers and azimuth arm trolleys due to their rigidity and short length. Finally, rigid massless elements are used to add a node at the actual center of mass of the Gregorian and line feed(s) in each model, so that the mass distribution of the suspended structure can be accurately modeled in dynamic analyses.

2.2 Concrete Properties

The weight and stiffness of the concrete towers contribute the dynamic properties of the structure. The towers were built in the early 1960s and are made of normal-weight reinforced concrete, which we assume to weigh 150 pounds per cubic foot (pcf).

After the collapse of the telescope, concrete cores were taken at multiple points on the towers while installing scaffolding, and the cores were tested for strength, with the test results presented in Table 1. The average strength varies from 5.71 kilopound per square inch (ksi) to 6.43 ksi between the towers. Based on these results, we assume a uniform concrete strength of 6 ksi for the structural analysis

model. From this assumed strength, the Young's modulus is estimated at 4,415 ksi, per the ACI 318-14 standard.[1]

Table 1: Concrete strength test results.

	Tower 4	Tower 8	Tower 12
Number of Tests	3	33	8
Average Strength [ksi]	6.36	5.71	6.43
Strength Standard Deviation [ksi]	1.36	1.38	0.56
Strength Coefficient of Variation	21%	24%	9%

Our analyses of the structure's response to hurricanes (Appendix J) and earthquakes (Appendix K) indicate that most of the tower concrete did not experience any tension large enough to cause cracking. The concrete stiffness is therefore not reduced in the models.

2.3 Cable Properties

The cable properties are critical parameters in the structural analysis of the telescope. For instance, the cable mechanical properties affect how multiple cables share the environmental loads acting on the suspended structure, and the cable weight is key to the calculation of cable tensions from the results of the sag surveys.

Per the structural drawings for the second upgrade of the telescope (1992), the auxiliary cables met the ASTM A586[2] standard, which specifies the metallic area, Young's modulus, and linear weight for any cable diameter. Samples of the auxiliary cables were also tested at Lehigh University before installation (1993). The original construction drawings (1960) do not specify a standard for the original cables, but they require a minimum wire tensile strength of 220 ksi, consistent with the ASTM A586 standard. The original and auxiliary cables are also of similar fabrication, with galvanized steel wires arranged in alternating helicoid layers to form a single strand.

We considered both the ASTM A586 standard and the 1993 Lehigh tests to select cable properties for the models. For the sake of consistency, we calculated the cable properties from the nominal cable diameter using the same equations and assumptions for every cable, and we verified that the results were consistent with the ASTM A586 and Lehigh test values. This process is summarized in Table 2, which compiles the ASTM values, the Lehigh values (when available), and the values used in the models. Table 2 also provides the coefficient of variation (CV) between the different values: the CV does not exceed five percent, which is satisfactory since a five percent difference in any cable property would not significantly impact the cable and telescope behavior under load.

The **metallic area** of a cable section is modeled as 75 percent of the nominal area, which is directly calculated from the nominal diameter.

The **effective Young's modulus** of the wires is assumed to be 25,500 ksi, which is the average of the two values measured in the Lehigh tests. This is lower than Young's modulus of solid steel (typically

[1] American Concrete Institute. *ACI 318-14. Building Code Requirements for Structural Concrete*, 2014.
[2] American Society for Testing and Materials. *ASTM A586-18. Standard Specification for Metallic-Coated Parallel and Helical Steel Wire Structural Strand*. 2018.

29,000 ksi) because of the helical arrangement of the wires and the softer galvanizing zinc around each wire, though it is higher than the minimum of 23,000 ksi required per ASTM.

The **axial rigidity** of a cable is the product of the effective Young's modulus and the metallic area.

The **linear weight** of a cable is modeled as 79 percent of the weight of a solid steel rod of nominal cable diameter, considering a steel weight density of 490 pcf.

The **minimum breaking strength** has not been calculated but is taken directly from the second upgrade structural drawings, which provide the minimum breaking strength of the new auxiliary cables to be installed during the upgrade, as well as the existing original cables. The actual breaking strength of the auxiliary cables tested at Lehigh in 1993 was measured five to eight percent higher than the minimum specified breaking strength.

Table 2: Selection of cable properties for analysis models. The values used in the models are in **bold**.

	Source	Original Mains	Original Backstays	Auxiliary Mains	Auxiliary Backstays
Nominal Diameter [in]	-	3	3-1/4	3-1/4	3-5/8
Nominal Area [in²]	-	7.07	8.30	8.30	10.32
Metallic Area [in²]	ASTM A586	5.4	6.3	6.3	7.9
	1993 Lehigh tests	-	-	6.23	7.65
	Modeled = 0.75 x (nominal area)	**5.30**	**6.22**	**6.22**	**7.74**
	CV	1%	1%	1%	1%
Effective Young's Modulus [ksi]	ASTM A586 (minimum)	23,000	23,000	23,000	23,000
	1993 Lehigh tests	-	-	25,000	25,900
	Modeled = 25,500 ksi	**25,500**	**25,500**	**25,500**	**25,500**
	CV	5%	5%	4%	5%
Axial Rigidity [kip]	ASTM A586	124,200	144,900	144,900	181,700
	1993 Lehigh tests	-	-	155,638	198,115
	Modeled = 0.75 x (nominal area) x (25,500 ksi)	**135,187**	**158,657**	**158,657**	**197,382**
	CV	4%	5%	4%	4%
Linear Weight [lbf/ft]	ASTM A586	19.00	22.00	22.00	28.00
	1993 Lehigh tests	-	-	21.18	26.03
	Modeled = 0.79 x (nominal area) x (490 pcf)	**18.91**	**22.19**	**22.19**	**27.60**
	CV	0%	0%	2%	3%
Minimum Breaking Strength [kip]	1992 upgrade drawings	1,044	1,212	1,314	1,614
	1993 Lehigh tests	-	-	1,414	1,687
	Considered = 1992 upgrade drawings	**1,044**	**1,212**	**1,314**	**1,614**
	CV	0%	0%	3%	2%

2.4 Baseline Cable Tensions

Models are used to perform multiple static and dynamic analyses to determine how cable tensions vary during telescope operation and under environmental loads. Before running any analysis, a model is initialized in a baseline state where the cable tensions are known.

For the original structure, the baseline cable tensions are those determined by Ammann & Whitney before the second upgrade of the telescope. These tensions are specified at the start of the cable jacking sequence for the second upgrade, with the original tiedowns already removed from the structure.

For the upgraded structure, the baseline cable tensions are those in effect when the telescope is in the stowed position, with the tiedowns slack before the first cable failure. To determine these tensions, we began with the August 2020 sag survey that provides reliable values for the cable tensions after the first cable failure, and we removed the effect of the cable failure through analysis. This process is detailed in Appendix G.

The baseline cable tensions for the original and upgraded structures are shown in Figure 4. In both cases, the telescope is stowed, and the tiedowns are slack or removed. The complete baseline states of the models are summarized in section 2.7.

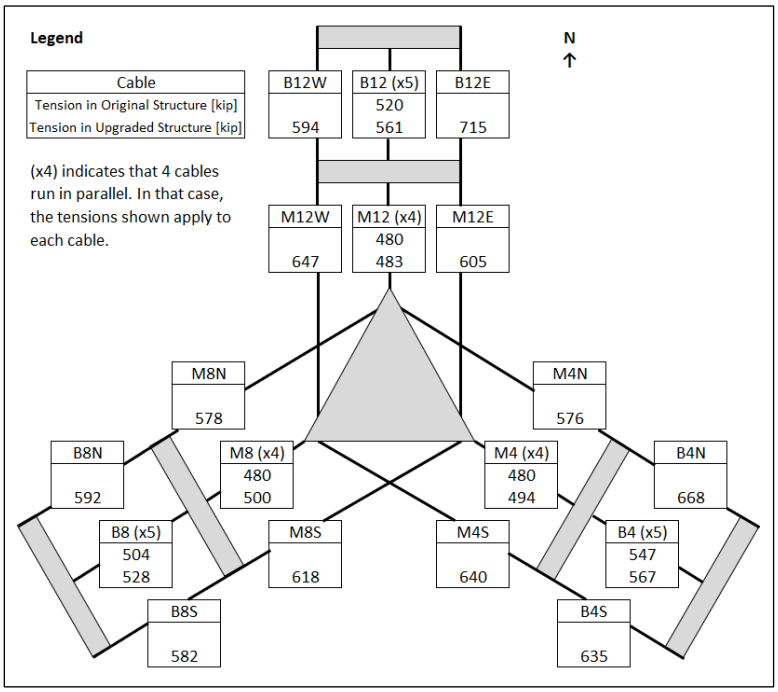

Figure 4: Baseline cable tensions (stowed position and slack tiedowns) in original and upgraded structures.

2.5 Suspended Structure Weight

The weight of the suspended structure changed over time as new equipment was added to the telescope, particularly during the second upgrade with the addition of the Gregorian, counterweight, tiedown outriggers and steel reinforcement. We determined the total weight of the suspended structure at two points in time from the baseline cable tensions described above: from the known cable weights, dimensions and tensions, we calculated the vertical reaction at the platform end of each main cable and added them up to obtain the weight of the suspended structure. The parameters and results of this calculation are shown in Table 3. We calculated a total weight of 1,225 kilopound (kip) for the original structure and 1,825 kip for the upgraded structure. The weight difference (600 kip) is consistent with the 615 kip weight increase indicated in the structural drawings for the second upgrade.

Table 3: Suspended structure total weight calculation from baseline cable tensions.

Main Cable(s)	Qty.	Linear Weight [lbf/ft]	Horiz. Length [ft]	Original Structure				Upgraded Structure			
				Vert. Length [ft]	Horiz. Force [kip]	Average Tension [kip]	Vert. Force on Platform [kip]	Vert. Length [ft]	Horiz. Force [kip]	Average Tension [kip]	Vert. Force on Platform [kip]
M4	4	18.91	575	132	468	480	102	130	482	494	104
M4N	1	22.19	711	-	-	-	-	126	568	576	92
M4S	1	22.19	711	-	-	-	-	126	630	640	103
M8	4	18.91	575	132	468	480	102	130	488	500	105
M8N	1	22.19	711	-	-	-	-	126	569	578	92
M8S	1	22.19	711	-	-	-	-	126	608	618	99
M12	4	18.91	575	132	468	480	102	130	471	483	101
M12E	1	22.19	711	-	-	-	-	126	596	605	97
M12W	1	22.19	711	-	-	-	-	126	638	647	105
Total	-	-	-	-	-	-	1,225	-	-	-	1,825

In the structural analysis models, the weight of the suspended structure is broken down as shown in Table 4 and illustrated in Figure 5 and Figure 6.

The weight for the structural steel of the platform and azimuth arm is estimated to be 1,085 kip by applying a factor of 1.5 to the weight of the frame elements. This factor is estimated from typical member and connection designs to account for the weight of member lacing and connections, which are not explicitly modeled. Some of the platform and azimuth arm members were reinforced during the second upgrade and, for the sake of simplicity, the properties of these reinforced members are used in all the models. Even though the weight of the structural steel is slightly overestimated in the models of the original structure, it does not significantly impact the analysis because the total weight of the suspended structure is correctly modeled by adjusting the superimposed dead load.

The weight of the Gregorian, line feed and/or second carriage house is modeled as concentrated loads at the center of mass of the respective objects. As shown in Figure 5 and Figure 6, rigid massless elements are used to tie each center of mass to the azimuth arm. The counterweight is assumed to be evenly shared by the four azimuth arm work points that support the actual counterweight tray.

Finally, a superimposed dead load is calculated to obtain the total weight determined from the baseline cable tensions. This dead load is evenly distributed between the work points of the middle span of the

azimuth arm, as this is where most of the telescope's additional equipment (electrical, mechanical, catwalks, etc.) is located.

Table 4: Suspended structure weight breakdown in FE models.

	Weight in Model of Original Structure [kip]	Weight in Model of Upgraded Structure [kip]
Platform + Azimuth Arm Structural Steel	1,085	1,085
Outriggers + Slack Tiedowns	-	51
Line Feed	35	35
Second Carriage House	35	-
Gregorian	-	200
Counterweight	-	45
Superimposed Dead Load	70	410
Total	1,225	1,825

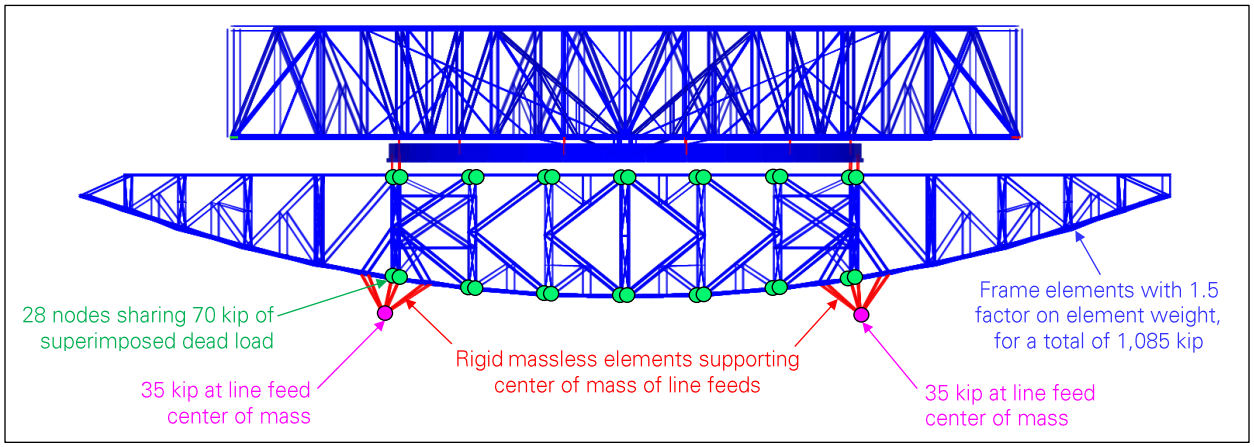

Figure 5: Weight distribution in FEA model of original suspended structure.

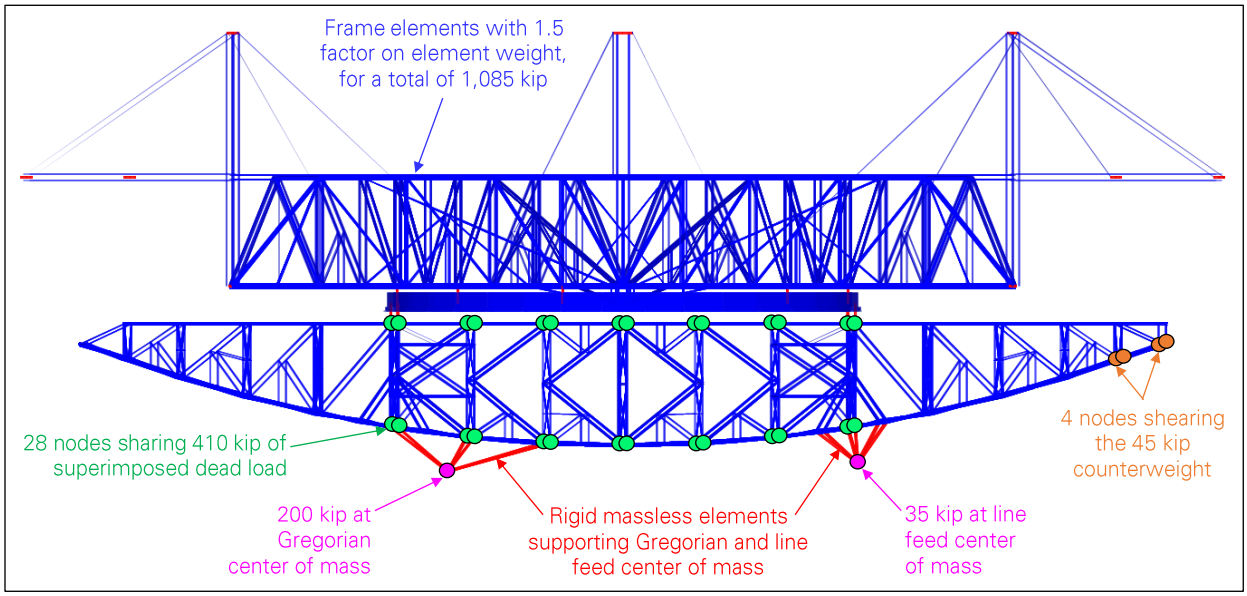

Figure 6: Weight distribution in FEA model of upgraded suspended structure.

2.6 Damping

The global vibration modes of the telescope involve movement of the towers and the suspended structure (section 6.0 below). The structure does not include an engineered damping system to mitigate global vibrations that may be induced by dynamic environmental loads such as wind and earthquakes. The mains and backstays are equipped with Stockbridge dampers (Figure 7), but these dampers are specifically tuned to mitigate cable vibrations and do not act on the global movement of the structure. As a result, the global vibrations are only controlled by the telescope structure's intrinsic damping, which is due to several phenomena, such as friction in the bolted steel connections of the platform, between the layers of cable wires, or within the reinforced concrete of the towers.

Figure 7: Stockbridge dampers on Tower 4 original mains.

The amount of intrinsic damping in a structure depends on factors such as material, design, age, and condition, and it typically increases with vibration amplitude and frequency – all of which make intrinsic damping difficult to calculate. Alternatively, it must be measured or estimated from experience. As an order of magnitude, the intrinsic damping ratio is typically between one and two percent in steel structures, and between two and five percent in reinforced concrete structures. Since the structure of the Arecibo telescope is unique and is composed of both steel and concrete, its intrinsic damping ratio would be expected to be in a range between one and five percent.

Although we did not find any record of damping measurements for the telescope structure, damping can be estimated from the tiedown tensions recorded during the first cable failure on August 10, 2020. The tiedowns were equipped with load cells, and the tiedown tensions were logged every second. The tiedown tension data shows that the sudden release of the M4N cable tension acted as an impulsive load on the structure and triggered global vibrations that gradually diminished over several minutes due to damping. Because the tiedowns of the upgraded telescope are vertical cables between the platform corners and the ground, the tiedown tensions are proportional to the vertical movement of the platform corners. As shown in section 6.0 below, the first global dynamic mode of the structure involves such movement.

Each of the three platform corners had two tiedown cables, and each tiedown cable tension was measured independently. Platform corner 12 dropped approximately two feet when the M4N cable failed, causing its tiedown cables to become slack, while the tiedown cables at platform corners 4 and 8 remained taut (Figure 8). The tiedown cable tensions after failure are shown in Figure 9. The tensions

were recorded once every second, with the periods of the vertical vibration of the platform expected to be in the order of three seconds (section 6.0 below). As a result, the vibration cycles are visible in the recorded cable tensions, but the peak cable tensions are not captured for every cycle. As shown in Figure 9, by fitting a logarithmic decrement to each recorded cable tension to estimate damping, we obtain a damping ratio of 1.0 percent from the corner 4 tiedown cables and 1.4 percent from the corner 8 tiedown cables. Based on these results, we assumed a damping ratio of one percent for every global vibration mode of the telescope structure in our dynamic analyses.

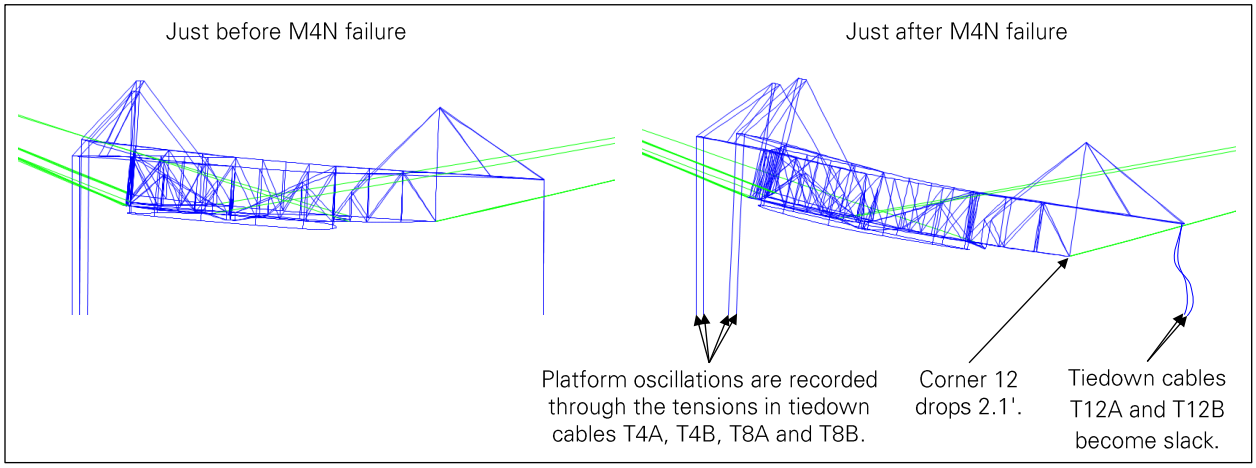

Figure 8: Platform response to M4N failure (looking west, displacements magnified x10).

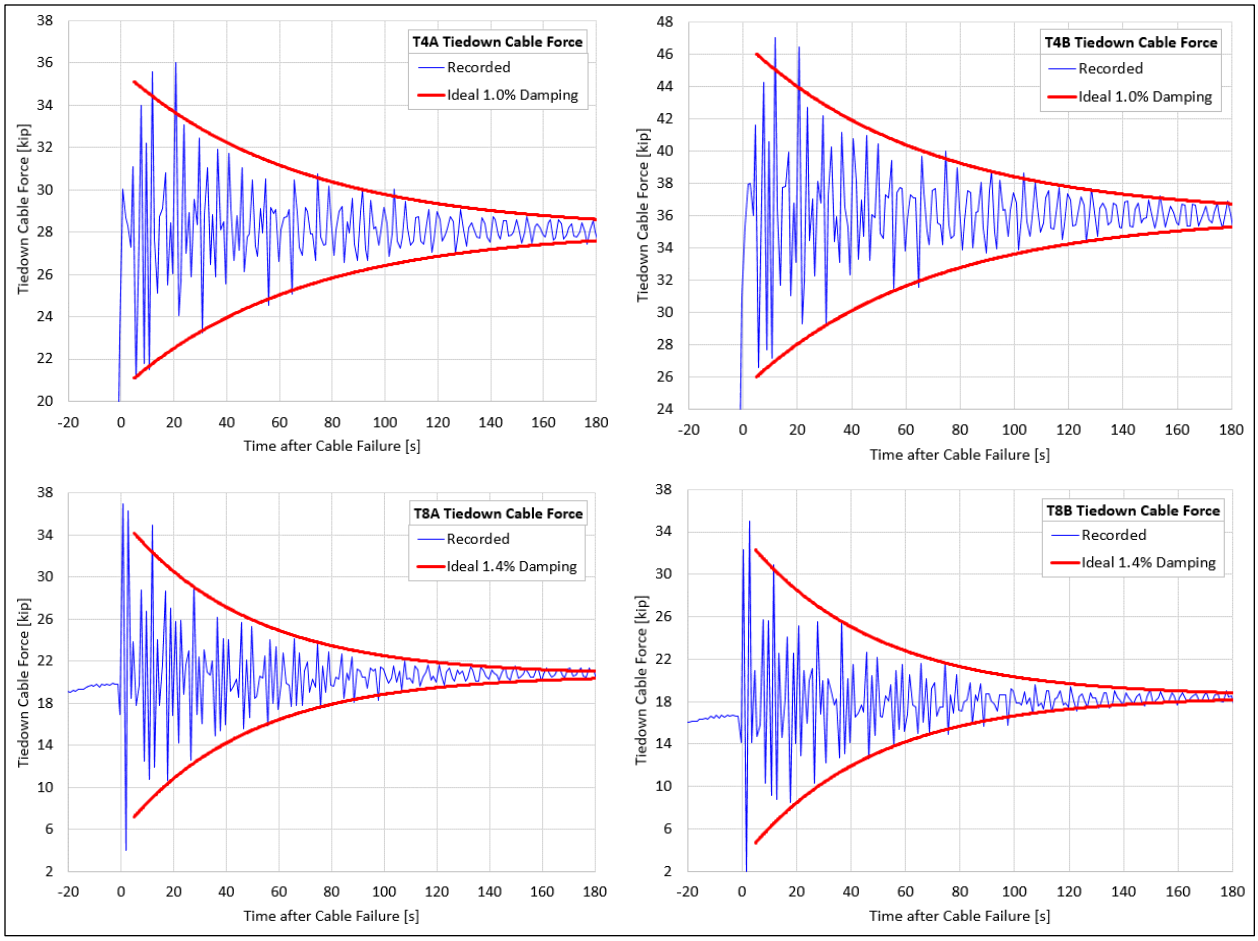

Figure 9: Damping measurement from tiedown tensions during first cable failure.

2.7 Summary of Model Baseline States

Before performing any analysis, the original and upgraded telescope models are initialized in the baseline states summarized in Table 5. Starting from a baseline state, analyses were performed by adding and/or tensioning the tiedowns, applying environmental loads, or moving the azimuth arm, Gregorian and/or line feeds. These analyses are presented in Appendix G, H, I, J and K.

Table 5: Summary of FE model baseline states.

	Original Structure	Upgraded Structure
Suspended Structure Weight	1,225 kip	1,825 kip
Cable Tensions	Specified at start of cable jacking sequence for second upgrade.	Determined through analysis from August 2020 cable sag survey.
Telescope Position	Stowed	Stowed
Tiedowns	Removed	Slack
Damping Ratio	1%	1%

3.0 SAP2000 Models

SAP2000 is a finite element analysis program developed by Computers and Structures and commonly used for structural analysis in the industry. SAP2000 is particularly effective at analyzing structures made of discrete slender members, such as building frames and steel bridges, and can account for geometric nonlinearities, including large structural deformations and member P-delta effects.

The towers and suspended structure are modeled with SAP2000's *frame* element, which captures axial, shear, bending and torsional stresses and strains. The mains and backstays are modeled with SAP2000's *cable* element. It is a nonlinear element that captures the changing direction of the tension with the cable curvature, and considers the cable stiffness reduction due to sag. The behaviors of the frame and cable elements are compared in Figure 10.

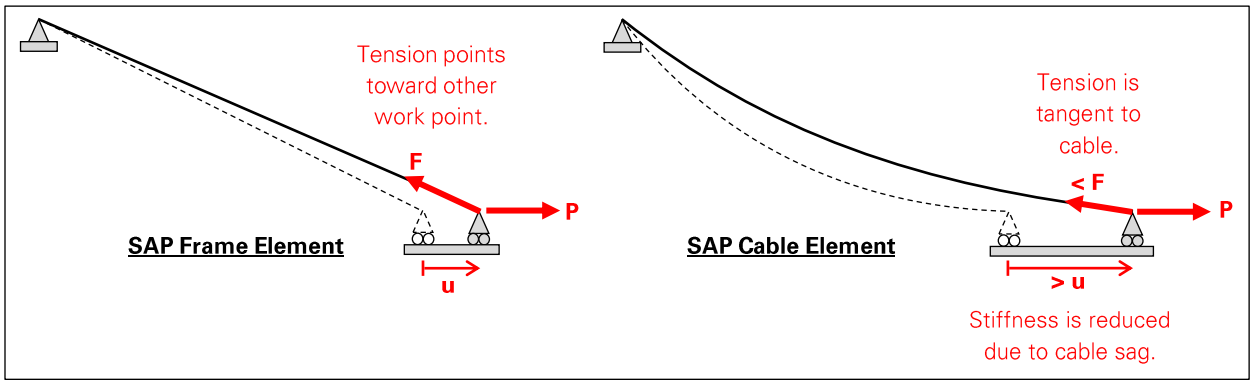

Figure 10: Frame vs. cable element for cable modeling in SAP2000.

SAP2000 is efficient to set up and run a large number of analyses in a given model, which facilitates the telescope analysis for different positions of the azimuth arm, Gregorian and/or line feed(s), with wind or earthquakes of different magnitude coming from different directions. For this purpose, we used SAP2000 models as the main production models for the analysis of the Arecibo structure. Every cable tension analysis presented in this report was performed using a SAP2000 model. As detailed below in section 4.0, some of the analyses were replicated in Abaqus to verify the SAP2000 results.

Overviews of the SAP2000 models were previously shown in Figure 1 and Figure 2.

4.0 Abaqus Models

Abaqus is a general-purpose finite element analysis program developed by Dassault Systems, which is commonly used in the industry and academia for a variety of applications far beyond the analysis of structures. As a top-of-the-line finite element analysis program with a strong validation record, Abaqus can access an extensive library of elements and material models to analyze a broad range of problems for structural analysis.

The telescope towers and suspended structure are modeled with Abaqus' *B31* element – a standard 2-node linear element with essentially the same behavior characteristics as SAP2000's *frame* element. The mains and backstays are modeled with Abaqus' *B31H* element, which accounts for the changing direction of the tension with the cable curvature, but not for the cable stiffness reduction due to sag (Figure 11).

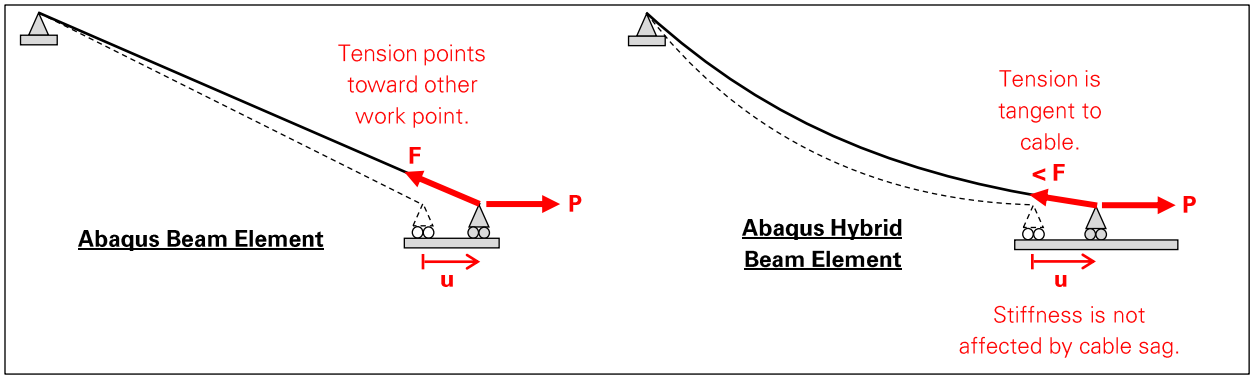

Figure 11: Beam vs. hybrid beam element for cable modeling in Abaqus.

The telescope's cable stiffness reduction due to cable sag is detailed in Table 6. The maximum reduction of 1.7 percent has a minimal impact on the results and conclusions of any cable tension analysis, so Abaqus' *B31H* element is appropriate for modeling the telescope cables.

We used the Abaqus models as validation models for the primary analysis work performed in SAP2000.

Table 6: Cable axial stiffness reduction due to sag.

Cable	Axial Stiffness Neglecting Sag [kip/in]	Original Structure			Upgraded Structure		
		Average Tension [kip]	Axial Stiffness Considering Sag [kip/in]	Axial Stiffness Relative Change due to Sag	Average Tension [kip]	Axial Stiffness Considering Sag [kip/in]	Axial Stiffness Relative Change due to Sag
M4	19.10	480	18.87	-1.2%	494	18.89	-1.1%
M4N	18.32	-	-	-	576	18.01	-1.7%
M4S	18.32	-	-	-	640	18.10	-1.2%
M8	19.10	480	18.87	-1.2%	500	18.90	-1.1%
M8N	18.32	-	-	-	578	18.02	-1.7%
M8S	18.32	-	-	-	618	18.07	-1.4%
M12	19.10	480	18.87	-1.2%	483	18.87	-1.2%
M12E	18.32	-	-	-	605	18.06	-1.5%
M12W	18.32	-	-	-	647	18.10	-1.2%
B4	23.61	547	23.42	-0.8%	567	23.44	-0.7%
B4N	27.23	-	-	-	668	26.96	-1.0%
B4S	27.23	-	-	-	635	26.92	-1.2%
B8	30.43	504	30.20	-0.8%	528	30.23	-0.7%
B8N	34.47	-	-	-	592	34.10	-1.1%
B8S	34.47	-	-	-	582	34.08	-1.1%
B12	28.27	520	28.09	-0.7%	561	28.12	-0.5%
B12E	32.14	-	-	-	715	31.95	-0.6%
B12W	32.14	-	-	-	594	31.81	-1.0%

5.0 Global Mass and Stiffness

The suspended structure is flexible and its deformation under load is captured in the structural analysis models, with each steel member modeled as a flexible frame element. To perform order-of-magnitude calculations or validate complex analysis results, however, it can also be useful to consider the suspended structure as a rigid body that can move and rotate in three directions under the effect of loads (Figure 12), based on its mass and the stiffness provided by the supporting towers and cables. The relevant mass and stiffness properties are summarized in Table 7 and Table 8. The mass properties were determined analytically from the position and properties of the steel members and adding the contributions of the SDL, Gregorian, line feed(s) and/or counterweight. The moment of inertia about each axis assumes that the axis passes through the center of mass of the suspended structure. To determine the stiffness properties, we applied unit loads to the suspended structure and calculated its global displacement and rotation from the deflections observed at the three bottom corners of the platform. This was done without making the suspended structure rigid in the model, and with the azimuth arm, Gregorian and/or line feed(s) in stowed position.

General observations are as follows:

- The auxiliary cables, added during the second upgrade, increase the horizontal stiffness (translation in both horizontal directions) by 30 percent and the torsional stiffness (rotation about vertical axis) by 360 percent.
- The vertical stiffness (translation in vertical direction) of the upgraded structure is 250 percent greater when the tiedowns are taut than when they are slack.
- Despite having more support cables and vertical tiedowns, the upgraded structure has a slightly lower vertical stiffness (translation in vertical direction) than the original structure. This is because the tiedowns of the upgraded structure are connected to the platform through outriggers that add flexibility to the tiedown system.
- Most of the tilt stiffness (rotational stiffness about both horizontal axes) is provided by the tiedowns, as shown by the relatively low tilt stiffness values for the upgraded structure with tiedowns slack.

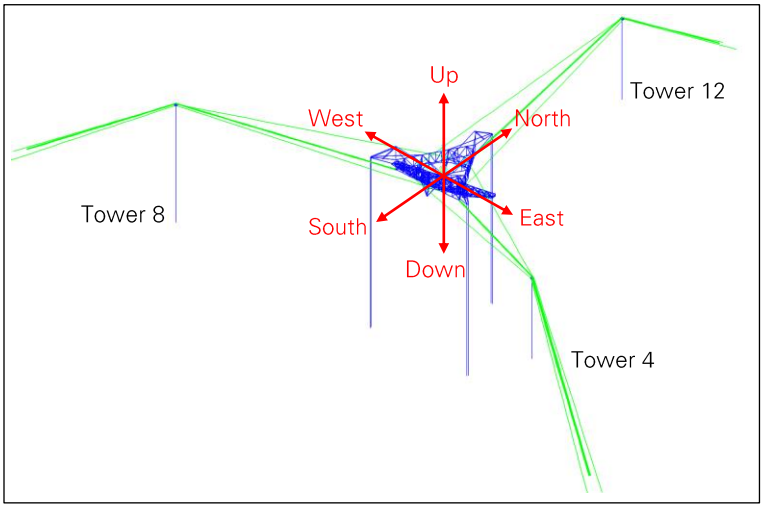

Figure 12: Suspended structure axes.

Table 7: Global mass properties of suspended structure, in stowed position.

		Original Structure	Upgraded Structure
Weight [kip]		1,225	1,825
Mass [kip·s²/ft]		38.0	56.7
Moment of inertia [kip·ft·s²/deg]	**North-South Axis**	2,674	4,177
	East-West Axis	1,640	2,193
	Vertical Axis	3,677	5,078

Table 8: Global stiffness properties of suspended structure.

		Original Structure	Upgraded Structure with Tiedowns Slack	Upgraded Structure with Tiedowns Taut
Translational stiffness [kip/ft]	**North-South Axis**	897	1,173	1,175
	East-West Axis	898	1,177	1,179
	Vertical Axis	340	119	297
Rotational stiffness [kip·ft/deg]	**North-South Axis**	64,342	22,414	79,251
	East-West Axis	64,399	22,904	79,767
	Vertical Axis	36,802	133,214	136,640

6.0 Dynamic Modes

The dynamic modes of a structure describe how the structure tends to vibrate in response to dynamic loads. The actual response of the structure may follow one or just a few modes when the load remains close to periodic over a long period of time, but the superposition of many modes may occur when the load is more random. In any case, knowing the dynamic modes is useful for interpreting and verifying the results of dynamic analysis. Prior to performing the wind and seismic analyses presented in Appendix J and K, we determined the modes of the telescope from the SAP2000 and Abaqus models.

The modes of the original and upgraded structures are discussed in this section. For the upgraded structure, we consider cases where the tiedowns are tensioned or slack, since tiedowns were partially or fully loosened before windstorms. All of the modes assume that the telescope is in the pre-storm stowed position. In the figures showing the mode shapes, we have highlighted the greatest displacements for each mode. For practical purposes, only the modes with a period greater than 1 second are shown in this appendix.

General observations about the modes are as follows:

- Most of the modes involve bending of one or several towers. The towers are therefore integral to dynamic analysis, and cannot be considered as fixed supports for the suspended structure.
- Multiple modes involve the rotation of the suspended structure about a vertical axis, or about an axis parallel or perpendicular to the azimuth arm. These modes are partially driven by the masses of the Gregorian and line feed(s) being at a distance from the axis of rotation, and therefore these modes depend on the position of the azimuth arm, Gregorian, and line feed(s). All of the modes illustrated below assume that the telescope is stowed, but we expect that modes of similar periods and shapes would be obtained for other configurations of the telescope.

6.1 Original Structure

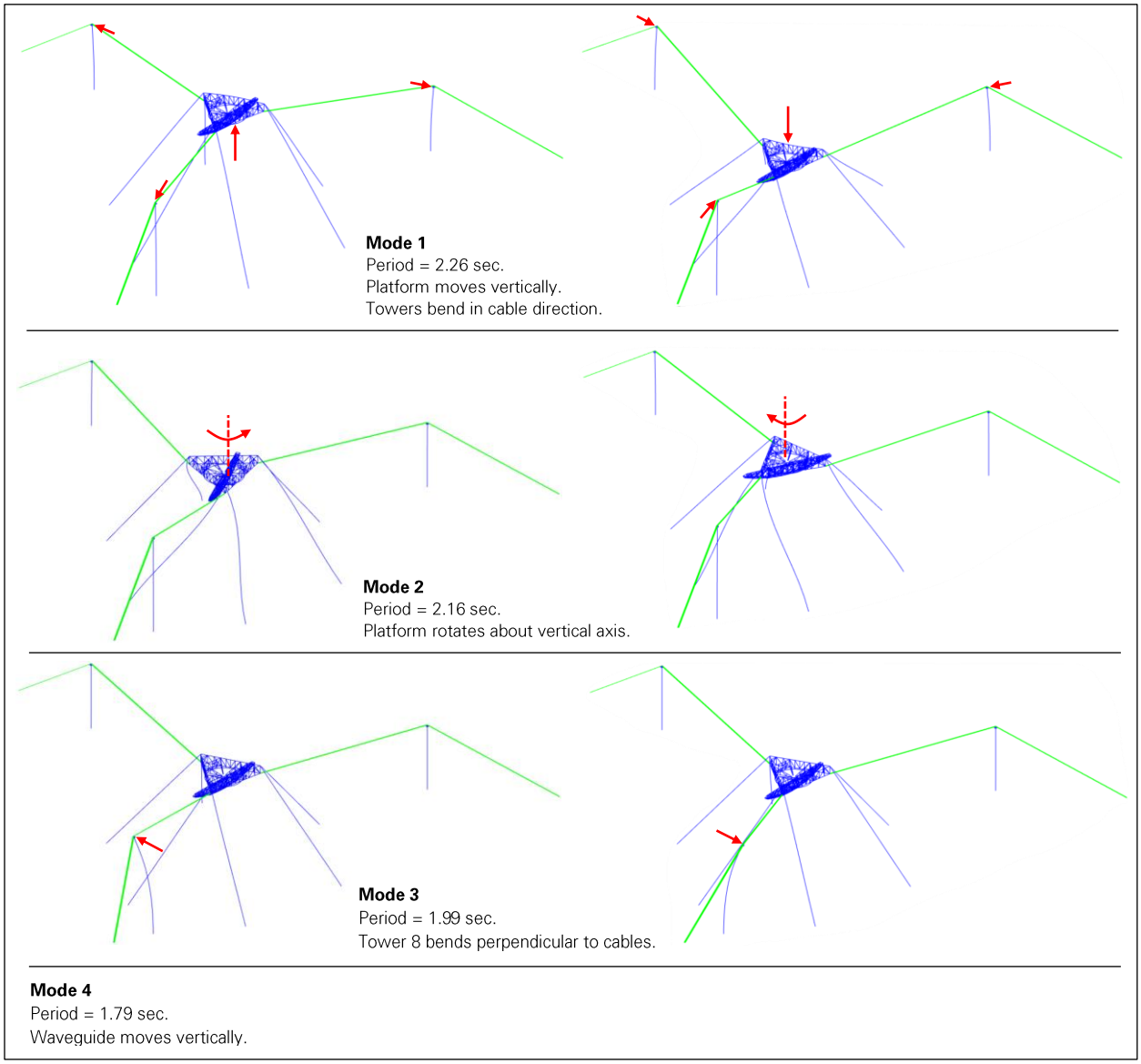

Figure 13: Vibration modes 1-4 of original structure.

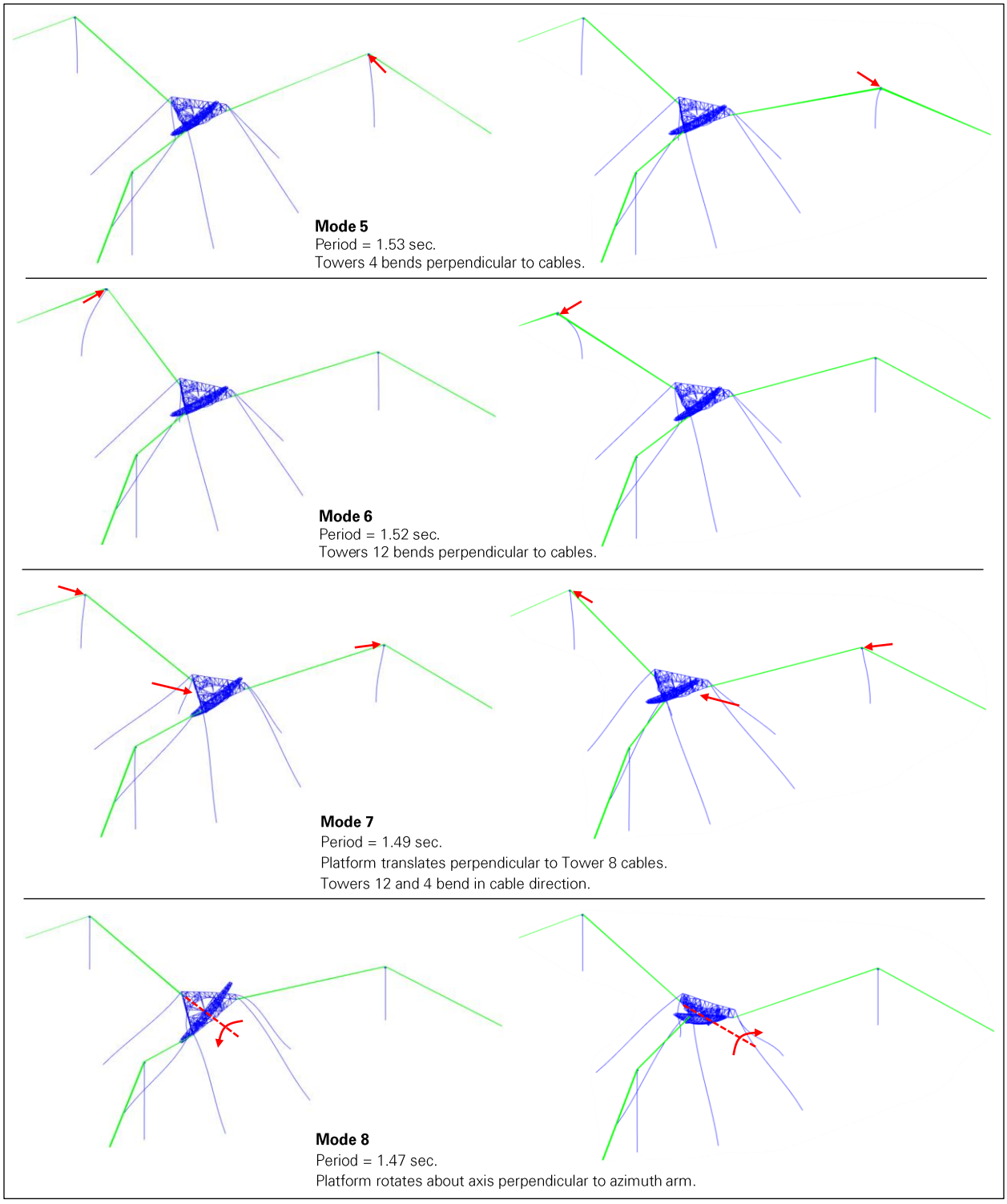

Figure 14: Vibration modes 5-8 of original structure.

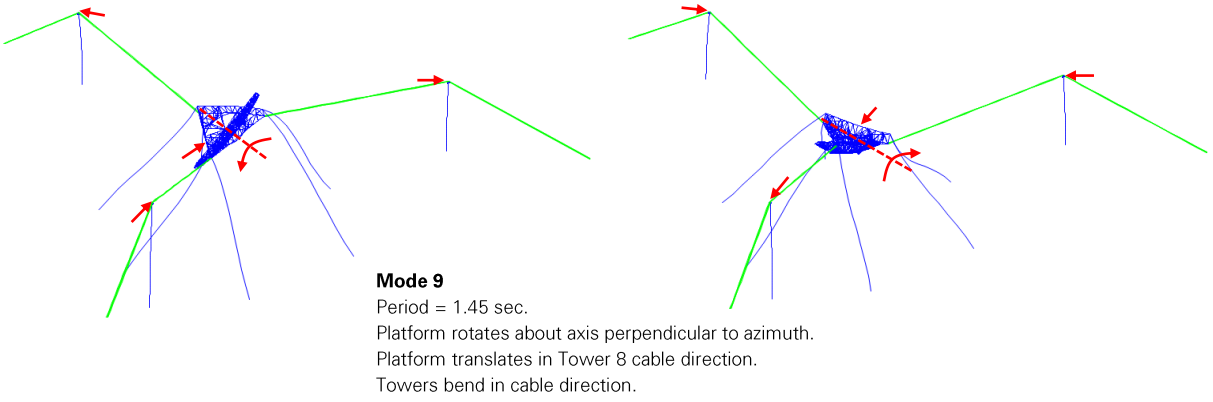

Mode 9
Period = 1.45 sec.
Platform rotates about axis perpendicular to azimuth.
Platform translates in Tower 8 cable direction.
Towers bend in cable direction.

Mode 10
Period = 1.25 sec.
Waveguide moves horizontally.

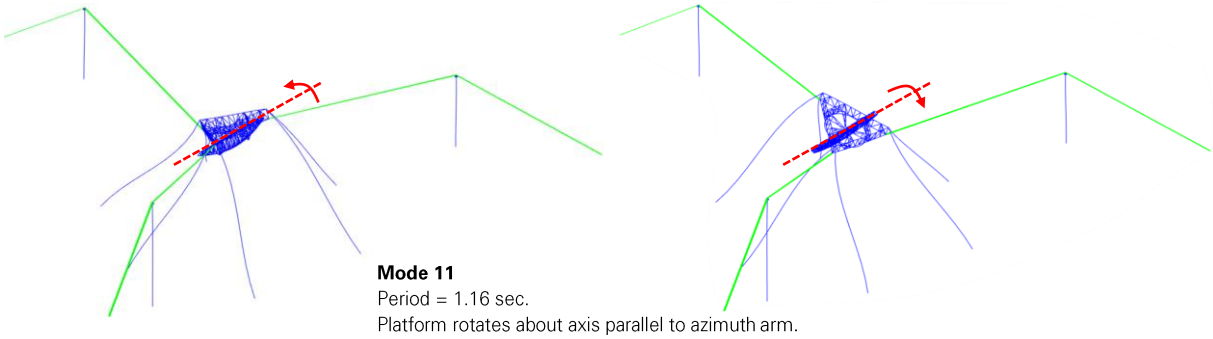

Mode 11
Period = 1.16 sec.
Platform rotates about axis parallel to azimuth arm.

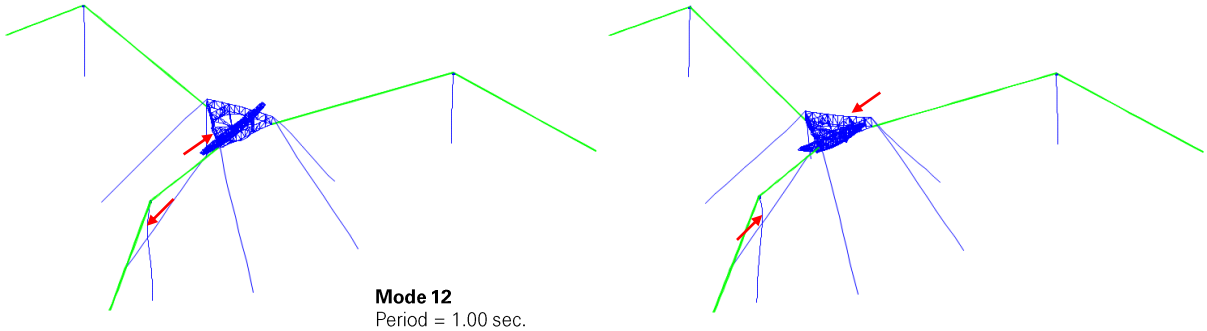

Mode 12
Period = 1.00 sec.
Platform translates parallel to M8 Cables.
Tower 8 sees 2nd mode bending in cable direction.

Figure 15: Vibration modes 9-12 of original structure.

6.2 Upgraded Structure

6.2.1 Tiedowns Tensioned

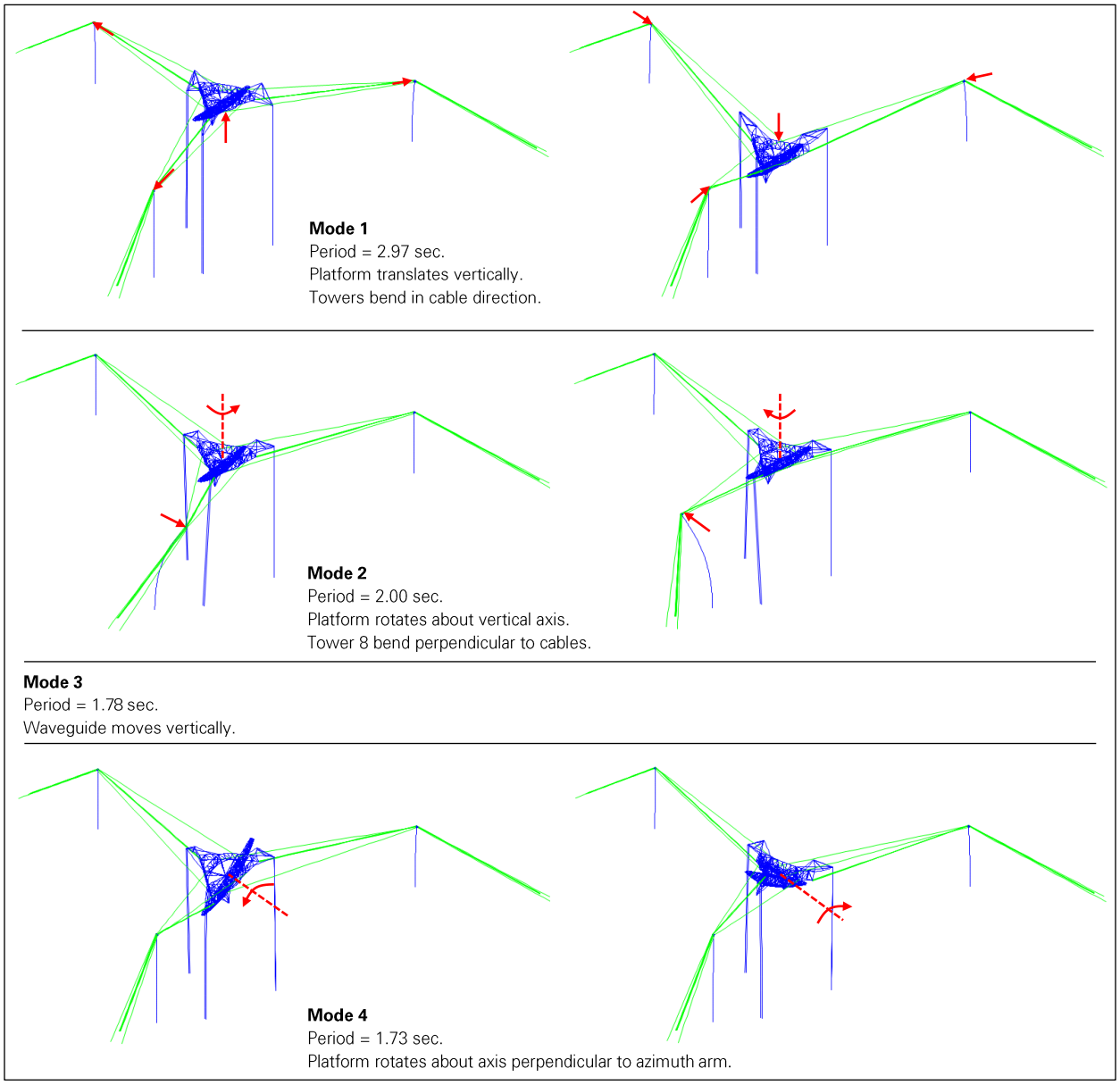

Figure 16: Vibration modes 1-4 of upgraded structure with tiedowns tensioned.

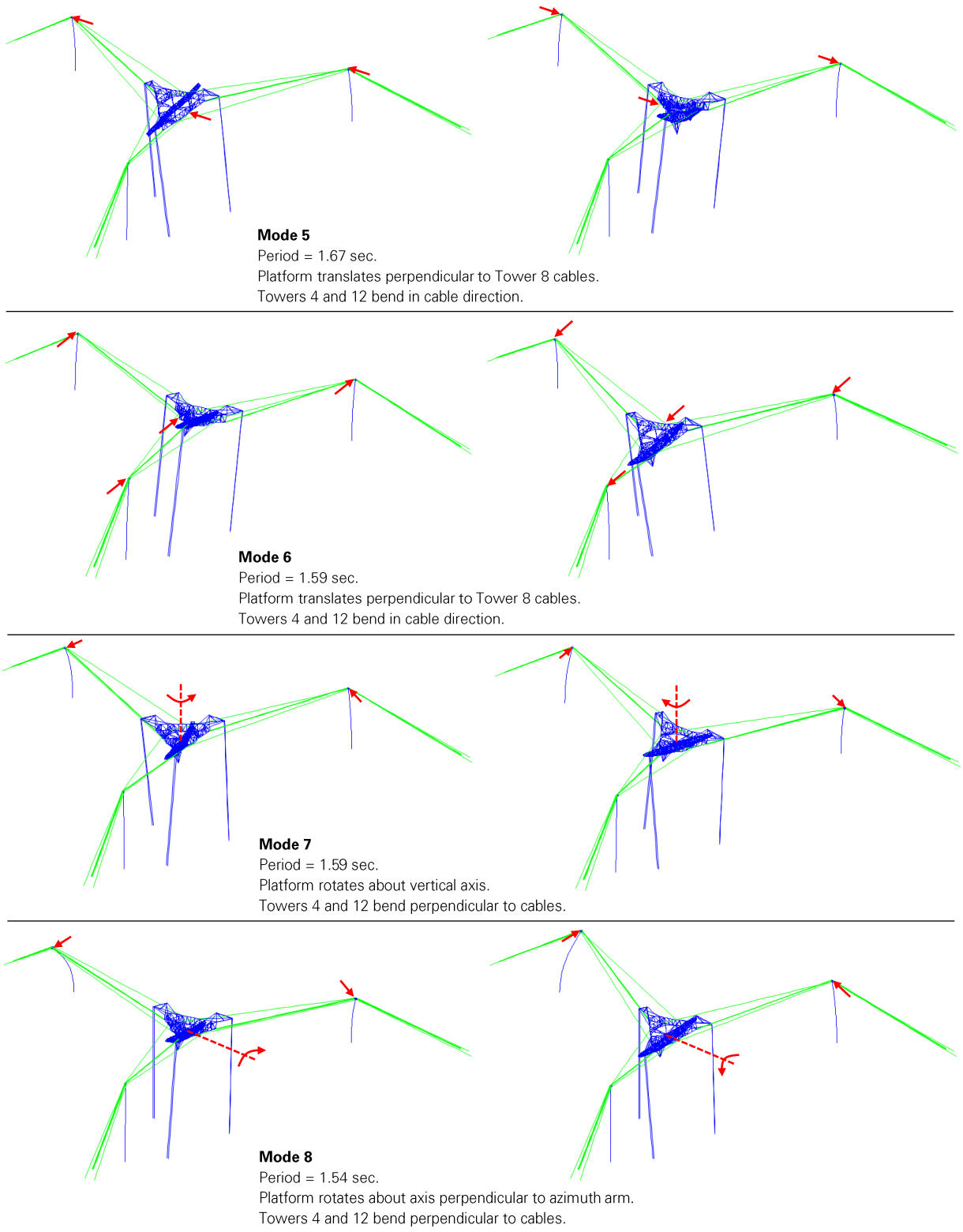

Figure 17: Vibration modes 5-8 of upgraded structure with tiedowns tensioned.

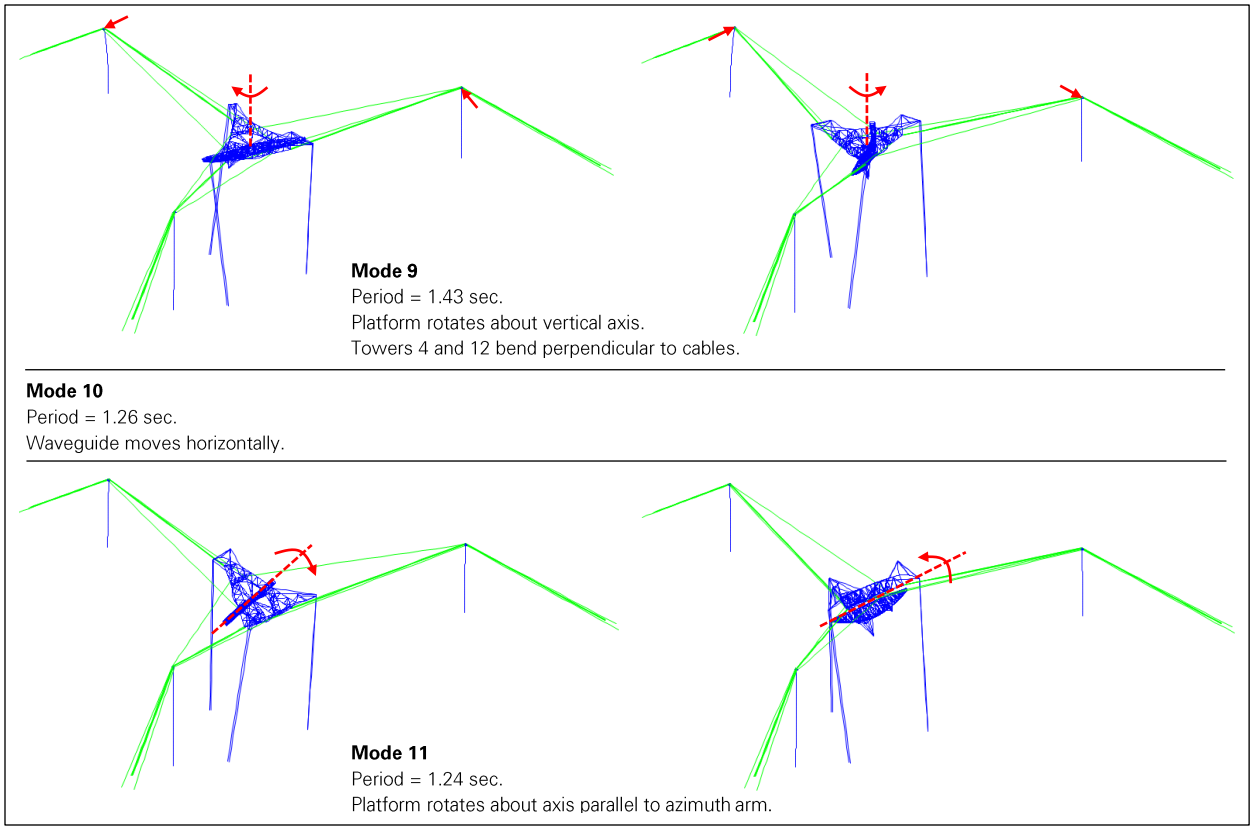

Figure 18: Vibration modes 9-11 of upgraded structure with tiedowns tensioned.

6.2.2 Tiedowns Slack

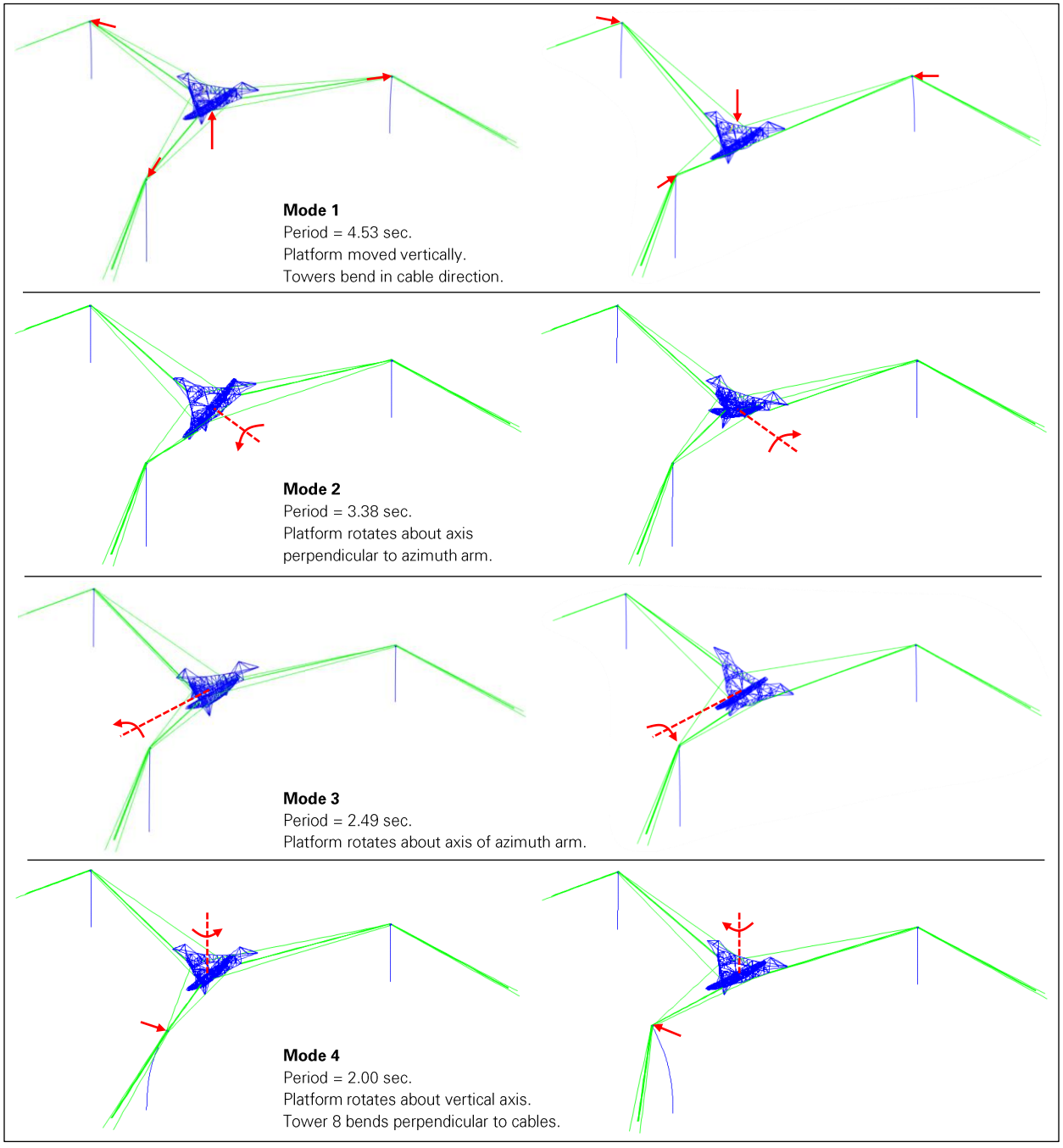

Figure 19: Vibration modes 1-4 of upgraded structure with tiedowns slack.

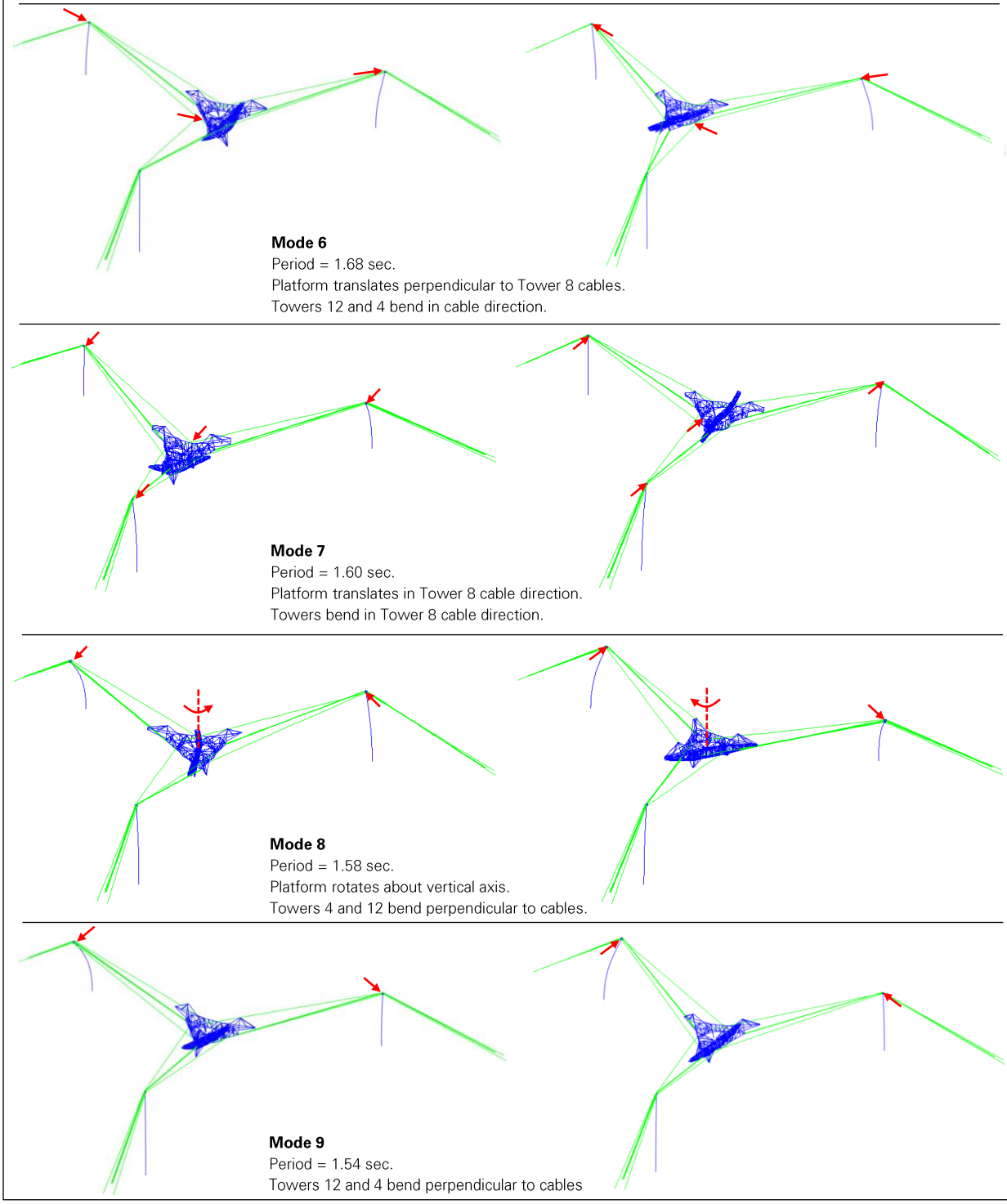

Figure 20: Vibration modes 5-9 of upgraded structure with tiedowns slack.

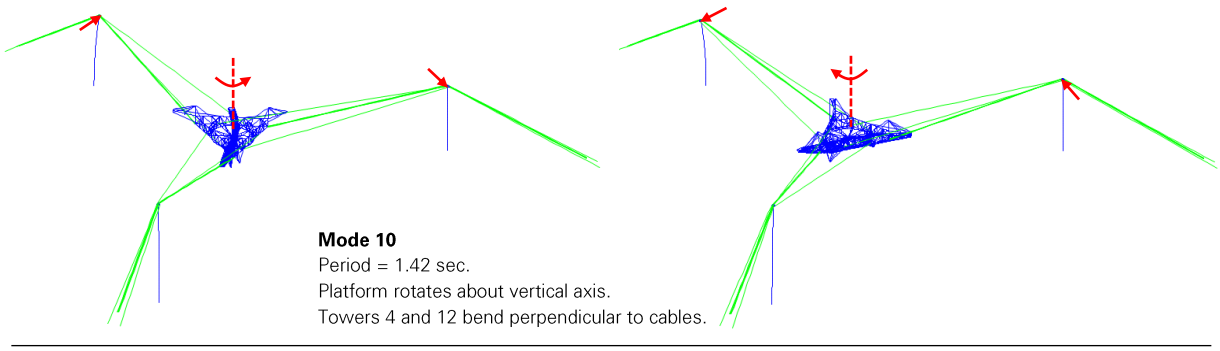

Mode 10
Period = 1.42 sec.
Platform rotates about vertical axis.
Towers 4 and 12 bend perpendicular to cables.

Mode 11
Period = 1.20 sec.
Waveguide moves horizontally.

Figure 21: Vibration modes 10-11 of upgraded structure with tiedowns slack.

Appendix G
Cable Tensions during 2020 Events

1.0 Introduction

In the second half of 2020, the telescope experienced two cable failures approximately three months apart, and eventually collapsed three weeks after the second failure (Table 1). Between the two cable failures, the azimuth arm and Gregorian were moved to the stowed position, and the tiedowns were partially released to reduce the stress on the remaining cables, which were also surveyed to determine their current tensions. This appendix presents our analysis of the cable tensions in 2020, from the first cable failure to the structure's collapse.

Table 1: Timeline of 2020 cable failures and collapse.

Date	Event
8/10/2020	M4N fails during telescope operation. Telescope operation continues for 20 minutes before telescope is stopped.
8/11/2020	Azimuth arm and Gregorian are moved to stowed position. Tiedowns are released as much as possible.
8/28/2020 – 9/4/2020	Cable shapes are surveyed.
11/6/2020	M4-4 fails.
12/1/2020	M4-2 fails and triggers collapse of telescope.

2.0 August 2020 Sag Survey

After the first cable failure, the remaining cables were surveyed to determine the tension in each cable. The objectives at the time were to evaluate the stability of the structure and to assess potential repair options. We relied on the sag survey to calibrate our structural analysis models of the upgraded structure (Appendix F), since the survey provides a complete set of cable tensions (except for the failed cable M4N) at a specific time and for a known configuration of the telescope. Calibrating the models with measured tensions is important because the cable system is statically indeterminate.

2.1 Laser Scans

The sag survey consists of several laser scans performed by Arecibo Observatory (AO) between August 28 and September 4, 2020, after the telescope was placed in the stowed position and the tiedowns partially released following the first cable failure. The scans were performed on a few different days but within the same week and always at daytime. Based on our analysis of the effect of temperature on the cable tensions (Appendix I), the tension change that a cable may have experienced between scans is negligible compared to the actual cable tension. Collectively, the scans are therefore considered to be a single consistent survey of the cable system.

Each scan focuses on either the mains (Figure 1) or backstays (Figure 2) of a given tower. The scan data is a point cloud, with millions of points recreating the cable surfaces in three dimensions. Each scan was captured with the scanner set up at a fixed position. The scanner's accuracy decreases with distance, generating noisier data for the cable surfaces located further away from the scanner (Figure 3). When selecting points to measure the cable sag, we avoided the noisier surfaces when possible, and otherwise selected average points within the noise consistently along the cable.

Figure 1: Tower 8 mains in August 2020 laser scan.

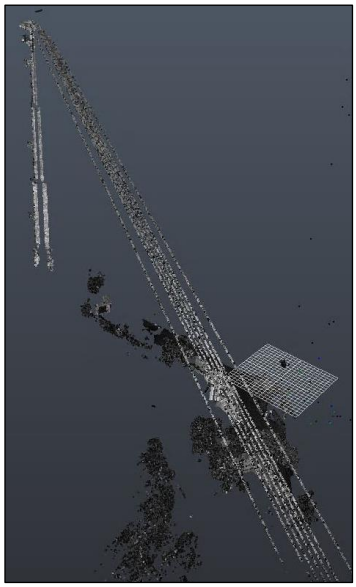

Figure 2: Tower 12 backstays in August 2020 laser scan.

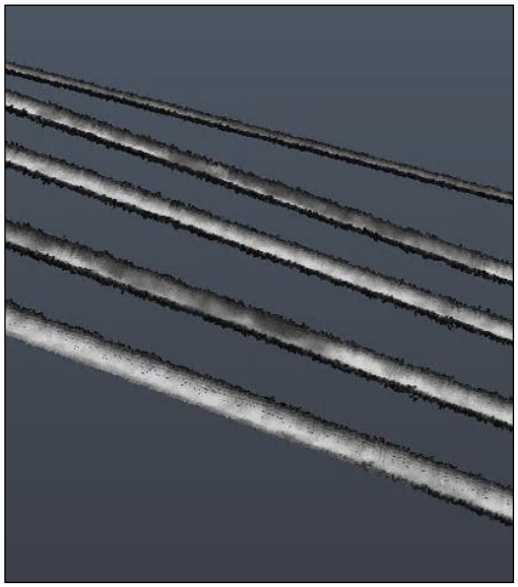

Figure 3: Tower 12 mains in August 2020 laser scan.

2.2 Cable Tensions

The only transverse load on any main or backstay is the cable's own weight, except for the Stockbridge vibration dampers. However, the dampers are relatively light and located near the ends of the cable, so their impact on the cable shape is negligible. Under its own weight, a cable assumes a catenary shape that is a function of the cable's weight and the horizontal component of the cable tension. Because this horizontal force is constant along the cable, by extracting the catenary shape from the sag survey and with the cable's weight known, we can calculate the horizontal force. The vertical force and the tension (axial force) can then be derived geometrically from the horizontal force and cable shape.

The procedure to determine a cable tension from the sag survey is illustrated in Figure 4. We first select approximately 10 points along the cable from the laser scan data, covering as much cable length as possible while staying away from the cable ends where data tends to be sparse or noisier. The missing or noisy data near the cable ends is due to the vibration dampers, obstruction from the terrain, and/or distance from the scanner. We then fit a catenary shape to the selected points, using the equation and parameters provided in Table 2. The only unknown parameter is the horizontal cable force, which is adjusted until the catenary best fits the selected points. The average distance between the selected points and the best-fit catenary is less than 0.25 inch for the mains and backstays, and less than 0.50 inch for the waveguide cables. Once the horizontal force in the cable is determined, the vertical reactions at both cable ends and the average tension (axial force) in the cable can be calculated, as shown in Table 2.

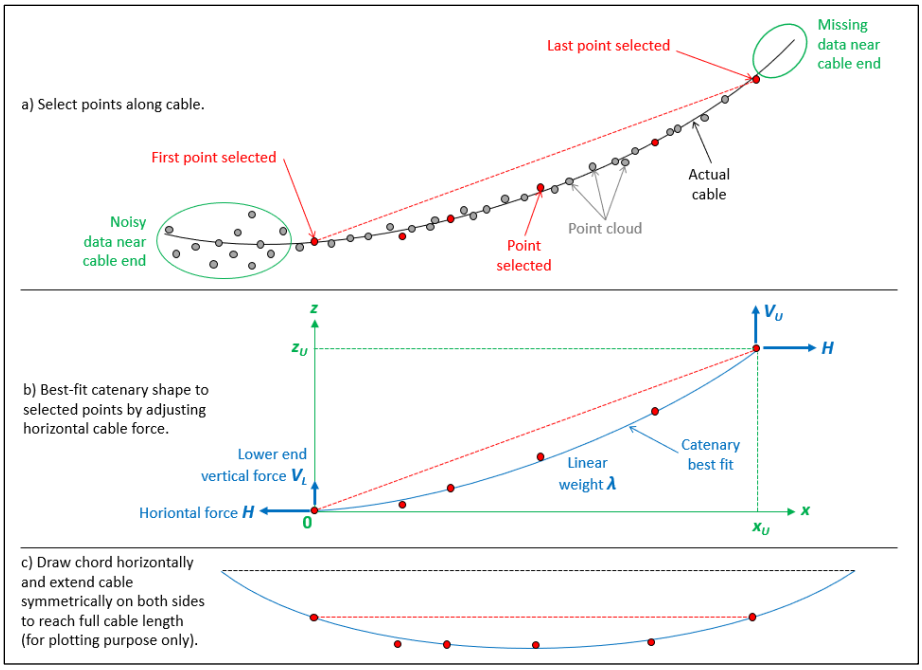

Figure 4: Sag measurement on laser scan data.

Table 2: Equations for catenary shape fitting and cable tension calculations.

Cable properties	H = horizontal force λ = linear weight (Table 3) x_u = horizontal length (Figure 4.b) z_u = vertical length (Figure 4.b)
Catenary shape	$z = z_0 + a\cosh\left(\frac{x-x_0}{a}\right)$
Catenary shape parameters	$a = \frac{H}{\lambda}$ $\quad x_0 = \frac{1}{2}\left(x_u - 2a\,sinh\left(\frac{z_u}{2a\,sinh\left(\frac{x_u}{2a}\right)}\right)\right)$ $\quad z_0 = -a\,cosh\left(\frac{x_0}{a}\right)$
Lower end vertical force	$V_L = sinh\left(-\frac{x_0}{a}\right)$
Upper end vertical force	$V_U = sinh\left(\frac{x_u-x_0}{a}\right)$
Average tension (axial force)	$F = \frac{1}{2}\left(\sqrt{H^2 + {V_L}^2} + \sqrt{H^2 + {V_U}^2}\right)$

The selected points, fitted catenary, and average tension are shown in Figure 5 through Figure 9 for every cable analyzed. At each tower, to significant shape difference was observed among the four original mains and among the five original backstays. As a result, we analyzed a single cable from each set and considered the calculated cable tension applicable to every cable of the set. The assumptions and results of the cable tension calculations are provided in Table 3, Table 4 and Table 5.

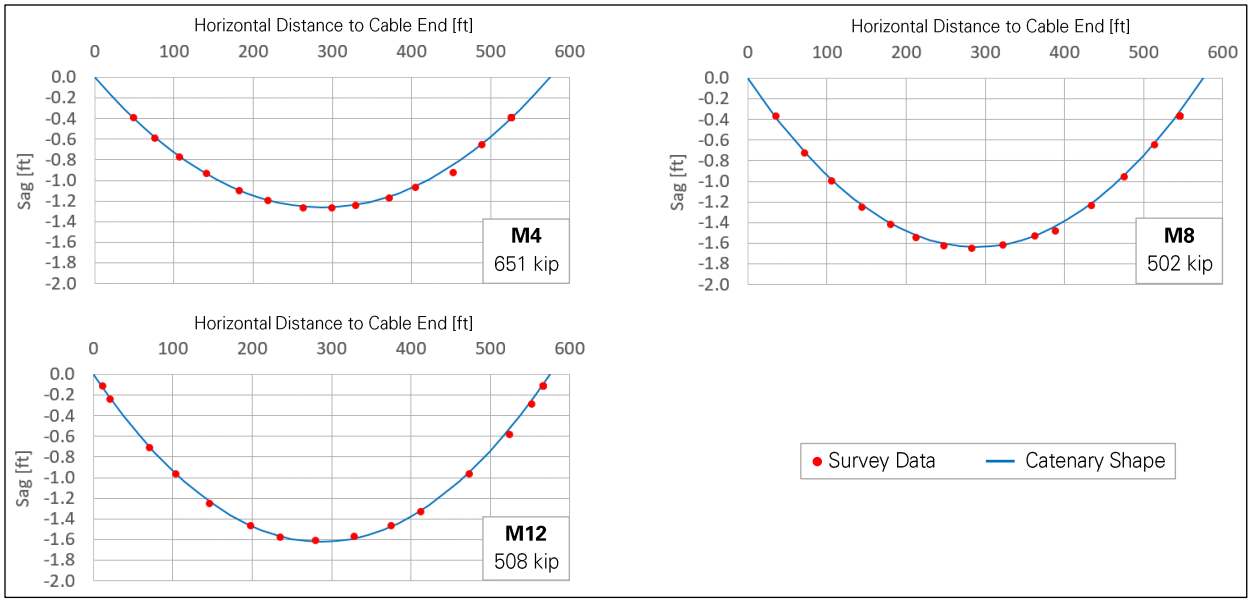

Figure 5: Catenary shape fitting on sag survey data for original main cables.

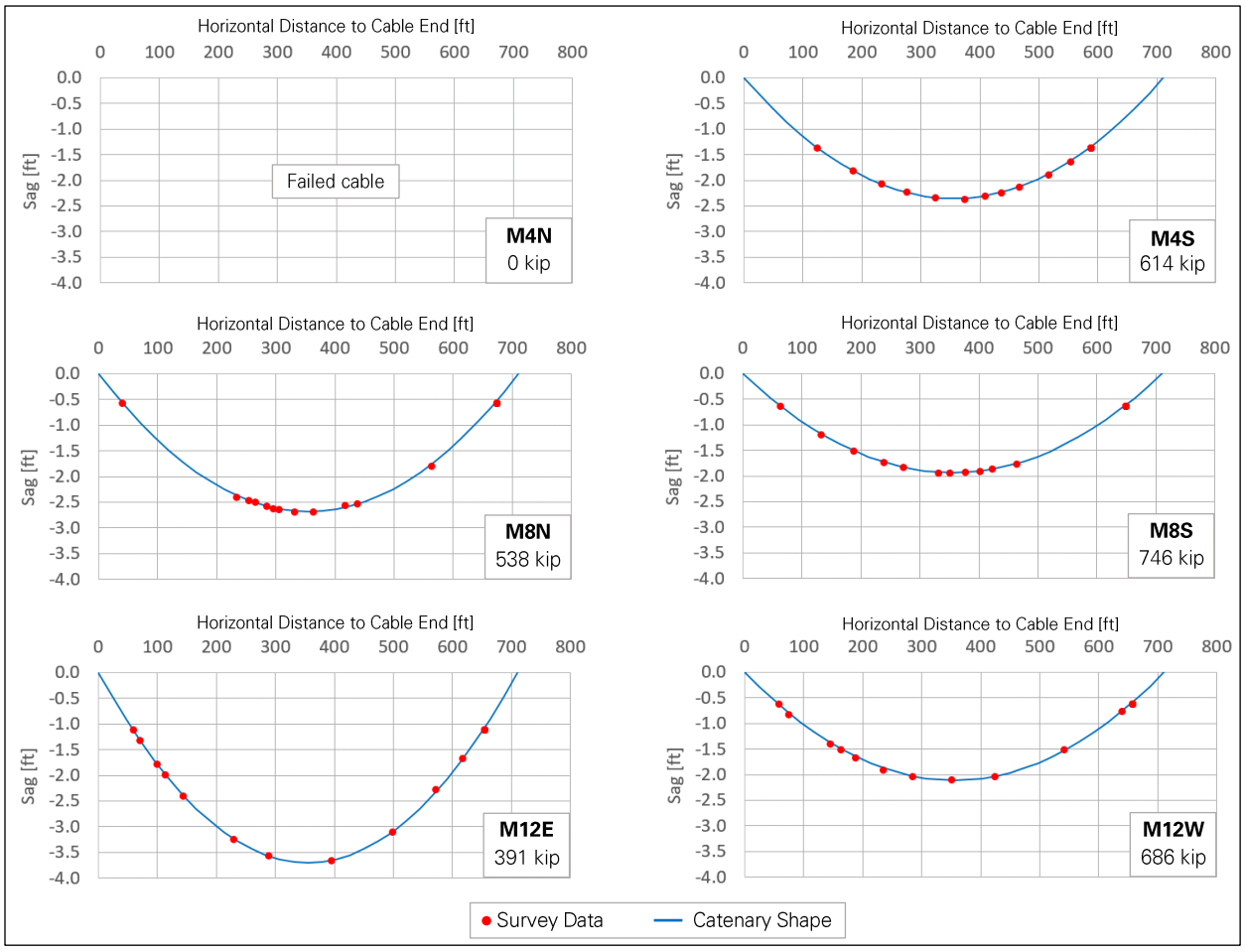

Figure 6: Catenary shape fitting on sag survey data for auxiliary main cables.

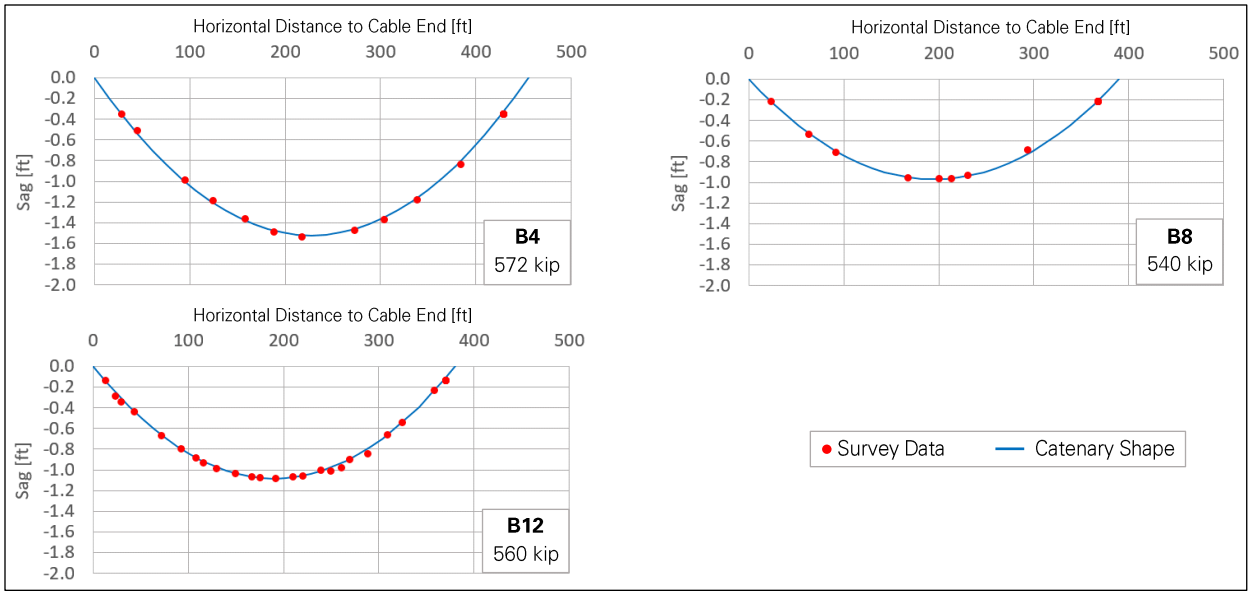

Figure 7: Catenary shape fitting on sag survey data for original backstay cables.

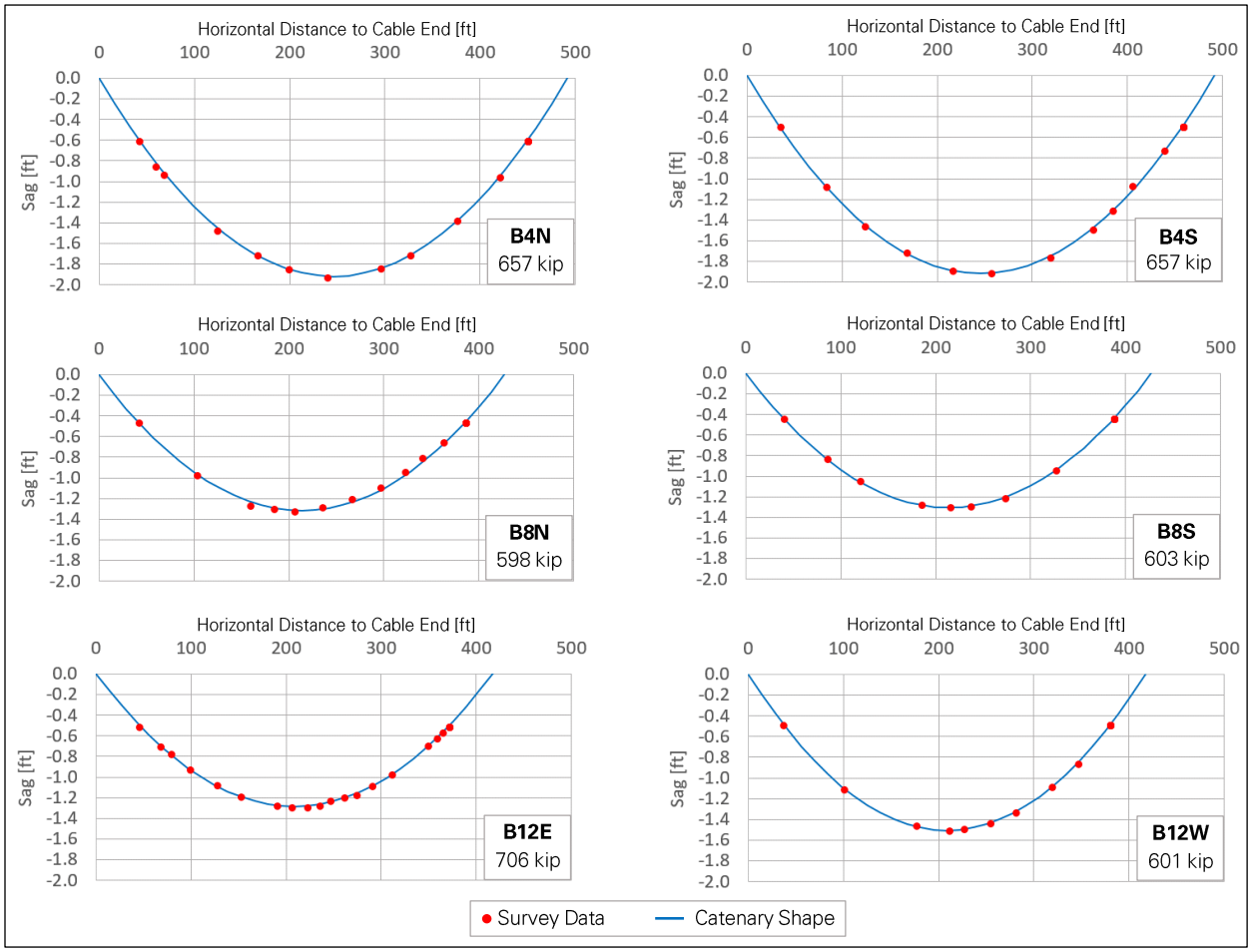

Figure 8: Catenary shape fitting on sag survey data for auxiliary backstay cables.

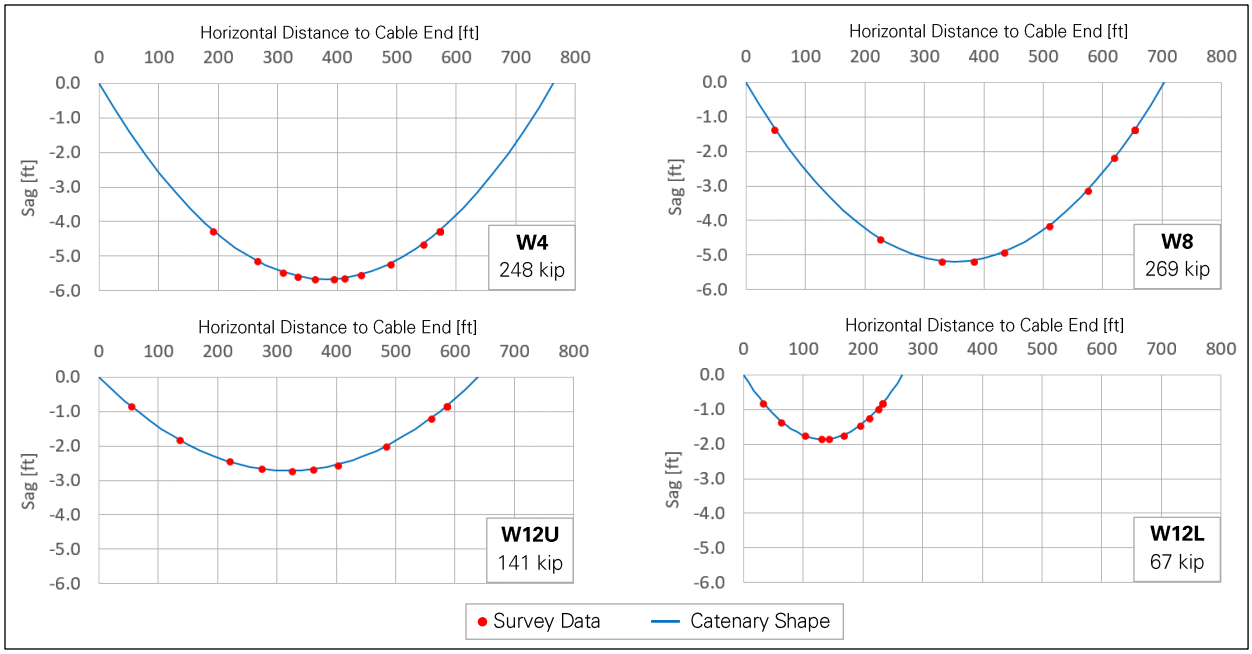

Figure 9: Catenary shape fitting on sag survey data for waveguide cables.

The suspended structure stabilized after the first cable failure, and therefore the resultant of the cable tensions acting on the platform must be zero in both horizontal directions. However, when summing up the horizontal forces derived from the sag survey, we obtain resultants of 72 kilopound (kip) and 15 kip in the south and west directions, respectively. This imbalance is small considering that each of the main cables carries several hundred kip, and may be due to temperature differences between the laser scans or noise in the laser scan data. Rather than introducing this imbalance in the structural analysis models, we applied small correction factors to the measured cable tensions until the horizontal resultant on the suspended structure was exactly zero. Correction factors were only applied to the main cables, and the same factor was applied to every main cable connected to a given tower. As shown in Table 3, the correction factors change the cable tensions by less than 1.5 percent (factors are between 0.985 and 1.015).

Table 3: Sag survey results and correction for main cables.

Cable	Qty.	Linear Weight [lbf/ft]	Distance Between Work Points			August 2020 Sag Survey		Force Correction Factor	Corrected Forces		
			North [ft]	West [ft]	Up [ft]	Sag [ft]	Avg. Tension [kip]		Avg. Tension [kip]	Horizontal [kip]	Vertical at Platform [kip]
M4	4	18.9	288	498	-130	1.26	651	0.991	645	629	137
M4N	1	22.2	418	575	-126	-	-	-	-	-	-
M4S	1	22.2	289	649	-126	2.35	614	0.991	609	599	98
M8	4	18.9	288	-498	-130	1.64	502	0.986	495	483	104
M8N	1	22.2	418	-575	-126	2.68	538	0.986	531	522	84
M8S	1	22.2	289	-649	-126	1.94	746	0.986	736	724	120
M12	4	18.9	-575	0	-130	1.62	508	1.012	514	501	108
M12E	1	22.2	-707	-74	-126	3.70	391	1.012	396	390	61
M12W	1	22.2	-707	74	-126	2.11	686	1.012	694	683	113

Table 4: Sag survey results for backstay cables.

Cable	Qty.	Linear Weight [lbf/ft]	Distance Between Work Points			August 2020 Sag Survey		
			North [ft]	West [ft]	Up [ft]	Sag [ft]	Avg. Tension [kip]	Horizontal Force [kip]
B4	5	22.2	-228	-394	-327	1.52	572	465
B4N	1	27.6	-232	-433	-351	1.92	657	535
B4S	1	27.6	-259	-418	-351	1.92	657	535
B8	5	22.2	-195	338	-192	0.97	540	485
B8N	1	27.6	-198	378	-213	1.32	598	535
B8S	1	27.6	-229	361	-213	1.30	603	540
B12	5	22.2	380	0	-273	1.08	560	455
B12E	1	27.6	417	-20	-297	1.28	706	575
B12W	1	27.6	416	20	-297	1.51	601	490

Table 5: Sag survey results for waveguide cables.

Cable	Qty.	Linear Weight [lbf/ft]	Distance Between Work Points			August 2020 Sag Survey		
			North [ft]	West [ft]	Up [ft]	Sag [ft]	Avg. Tension [kip]	Horizontal Force [kip]
W4	1	18.9	412	642	-91	5.66	248	246
W8	1	22.2	412	-570	-91	5.19	269	267
W12U	1	7.4	-638	36	-91	2.72	141	140
W12L	1	9.5	-263	42	-185	1.86	67	55

The resultant of the cable tensions on the suspended structure and three towers are shown in Table 6, before and after correction. At the top of the towers, the horizontal force is not zero, but less than 100 kip. This slight imbalance, compared to the magnitude of the cable tensions, can be explained by the M4N cable failure and the towers' ability to carry horizontal loads to the ground in bending. The final set of cable tensions derived from the sag survey is summarized in Figure 10.

Table 6: Resultant of cable tensions on suspended structure and towers.

Location	Direction	Resultant Force Before Correction of Main Tensions [kip]	Resultant Force After Correction of Main Tensions [kip]
Suspended structure	North	**-72**	**0**
	West	**15**	**0**
	Up	1,879	1,871
Top of Tower 4	Cable direction	-7	-36
	Perp. to cable direction	52	51
	Up	1,421	1,419
Top of Tower 8	Cable direction	-15	-61
	Perp. to cable direction	6	6
	Up	1,191	1,186
Top of Tower 12	Cable direction	-111	-74
	Perp. to cable direction	-43	-43
	Up	1,487	1,491

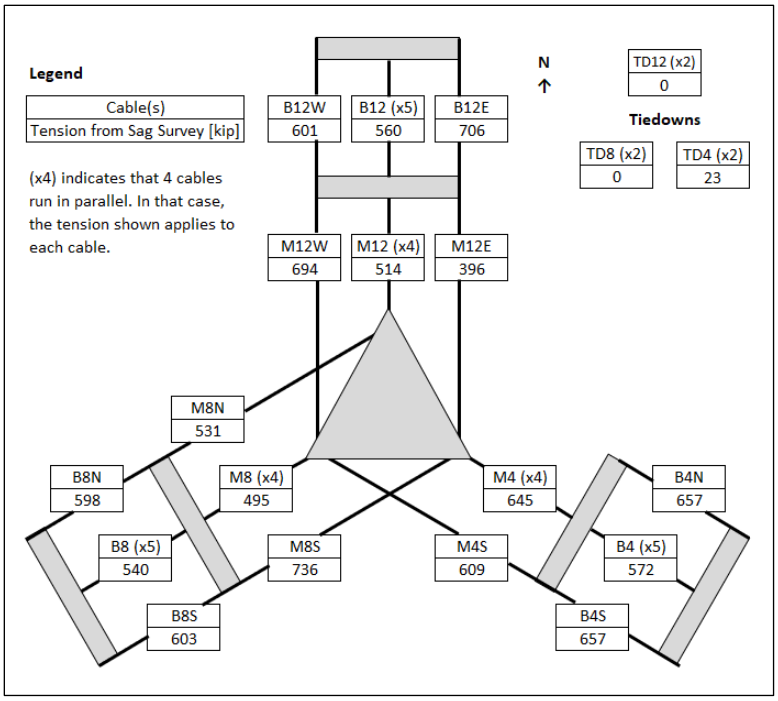

Figure 10: Cable tensions derived from August 2020 sag survey.

2.3 Suspended Structure Weight

The results of the sag survey indicate that the main cables carry a total vertical force of 1,871 kip (Table 6), which is balanced by the weight of the suspended structure and the tiedown tensions. The tiedown monitoring data provided by AO indicates that when the sag survey was performed, the average tension at daytime was 45 kip in tiedown 4, and zero in tiedowns 8 and 12. Tiedowns 8 and 12 were slack, as tiedown 12 became slack when the first cable failed, and tiedown 8 was released the next day to reduce the stress on the remaining cables. Tiedown 4 was also released as much as the jacking system would allow, but could not be fully slackened since the corresponding platform corner had shifted up after the cable failure. Considering the 45 kip tiedown tension, the weight of the suspended structure is 1,871 - 45 = 1,826 kip (Figure 11). The weight distribution between the steel trusses, the Gregorian and the line feed is detailed in Appendix F.

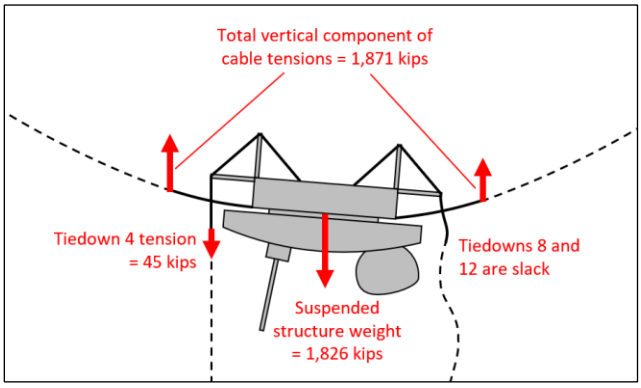

Figure 11: Suspended structure equilibrium during sag survey.

3.0 Cable Tensions before First Cable Failure

The August 2020 sag survey (section 2.0 above) provides a reliable measurement of the cable tensions after the failure of cable M4N (first cable failure). Starting from these known tensions, we performed a series of analyses to determine the cable tensions before failure, and in particular the tension in M4N when it failed.

Since cable M4N is connected to the east side of the platform near corner 12, its failure caused corner 12 to drop down and move west. During telescope operation, the platform corner positions were continuously monitored with laser rangers to adjust the tiedown tensions in order to keep the platform at a constant elevation through the day-night temperature cycles. Plots of the laser ranger data before and after the M4N failure were provided by AO and are shown in Figure 12. The plots show the elevation of the three platform corners and the rotation of the platform about three orthogonal axes. The fluctuations before failure are due to the telescope's operation since the tiedowns compensated for temperature effects. After failure, the fluctuations are due to temperature since the telescope and tiedown jacks were no longer operating. Table 7 summarizes the average elevations and rotations before failure, and the nighttime elevations and rotations after failure. We considered the nighttime values after failure because they are more consistent between days than the daytime values.

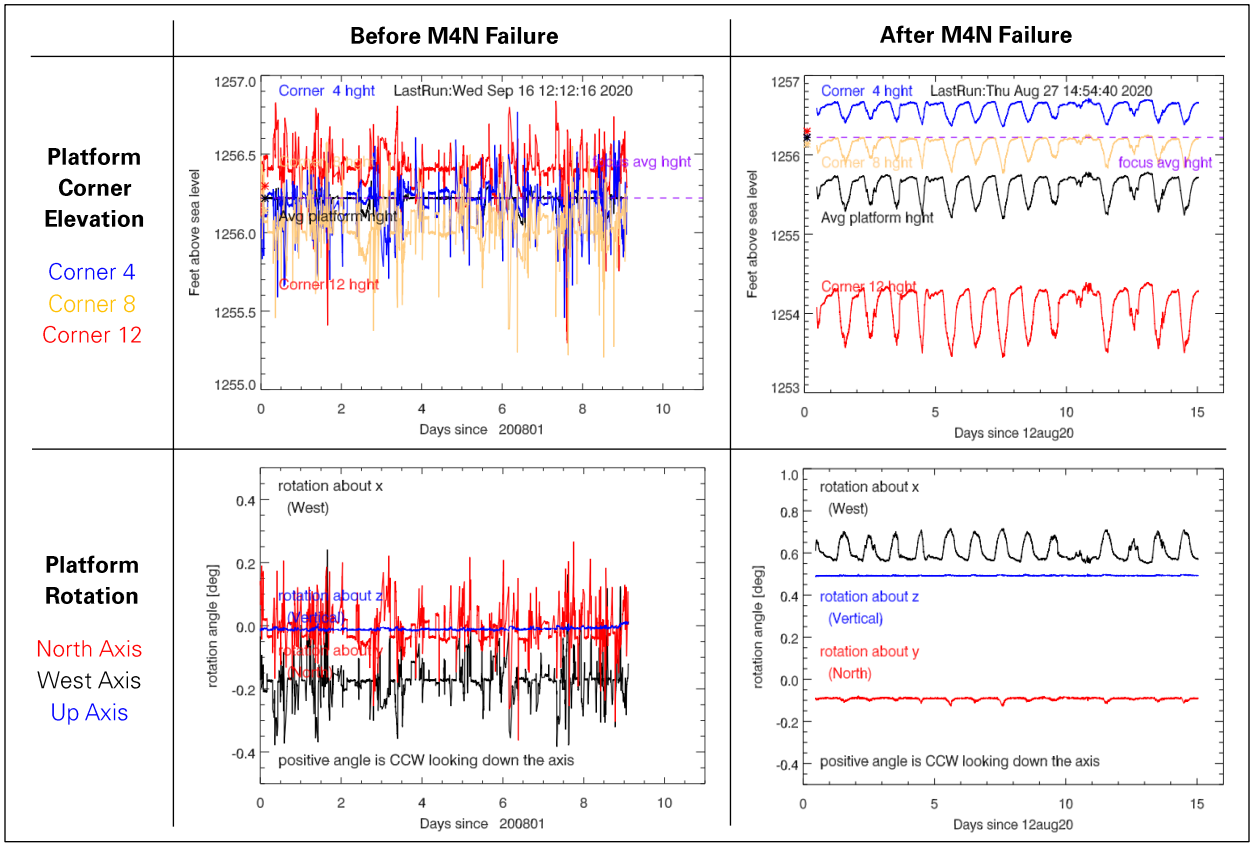

Figure 12: Platform corner elevation and rotation before and after M4N failure
(images: NAIC Arecibo Observatory, a facility of the NSF).

Table 7: Effect of M4N failure on platform position based on monitoring data.

	Average Before M4N Failure	Nighttime Average in Stowed Position After M4N Failure	Difference
Corner 4 Elevation [ft]	1256.1	1256.7	+0.6
Corner 8 Elevation [ft]	1256.1	1256.2	+0.1
Corner 12 Elevation [ft]	1256.4	1254.3	-2.1
Rotation about North Axis [deg]	-0.02	-0.09	-0.07
Rotation about West Axis [deg]	-0.17	0.56	+0.73
Rotation about Up Axis [deg]	-0.01	0.49	+0.50

To determine the cable tensions before the M4N failure, we performed a series of analyses on the telescope model. Each analysis involves four steps representing different states of the structure in reverse chronological order. The parameters of each step are detailed in Table 8 and rely on the telescope monitoring data provided by AO and shown in Figure 17 (section 4.0 below).

In Step 1, the model is set up to match the state of the structure during the August 2020 sag survey, with M4N removed from the model and the other cable tensions as determined from the survey (section 2.0 above). Step 2 increases the tiedown tensions to represent the nighttime condition, as the sag surveys were performed at daytime. In Step 3, the azimuth arm and Gregorian are moved to the position they were in when M4N failed, and the M4N cable is added back to the model and tensioned to an assumed value, which represents the state of the structure just before the M4N failure. Finally, in Step 4, the azimuth arm and Gregorian are moved back to the stowed position, and the tiedowns are fully released. This represents a baseline state of the structure before the M4N failure, which we will use as a starting point for the analysis of the upgraded structure under environmental and operation loads (Appendix H, I, J and K).

Steps 3 and 4 were repeated with increasing values of the M4N tension assumed at the time of failure, from 400 kip to 800 kip in 25 kip increments. After each analysis with a different M4N tension, we output the change in corner elevation and platform rotation from Step 3 to Step 2, as illustrated in Figure 13. For these analyses, we modeled the azimuth arm as loads on the platform's ring girder and varied these loads to represent different positions of the azimuth arm and Gregorian.

Table 8: Analysis steps to determine cable tensions before failure M4N failure.

Step	1	2	3	4
State	Telescope stowed after M4N failure, daytime	Telescope stowed after M4N failure, nighttime	Just before M4N failure	Baseline = telescope stowed before M4N failure, tiedowns slack
Azimuth Arm Angle [deg]	258	258	30.0	258
Gregorian Angle [deg]	8.5	8.5	10.7	8.5
Line Feed Angle [deg]	8.8	8.8	8.8	8.8
Tiedown 4 Tension [kip]	45	50	37	0
Tiedown 8 Tension [kip]	0 (slack)	10	35	0
Tiedown 12 Tension [kip]	0 (slack)	0 (slack)	20	0
M4N Tension	0 (failed)	0 (failed)	Assumed	Determined through analysis continuing from Step 3
Other Cable Tensions	Derived from August 2020 sag survey	Determined through analysis continuing from Step 1	Determined through analysis continuing from Step 2	Determined through analysis continuing from Step 3

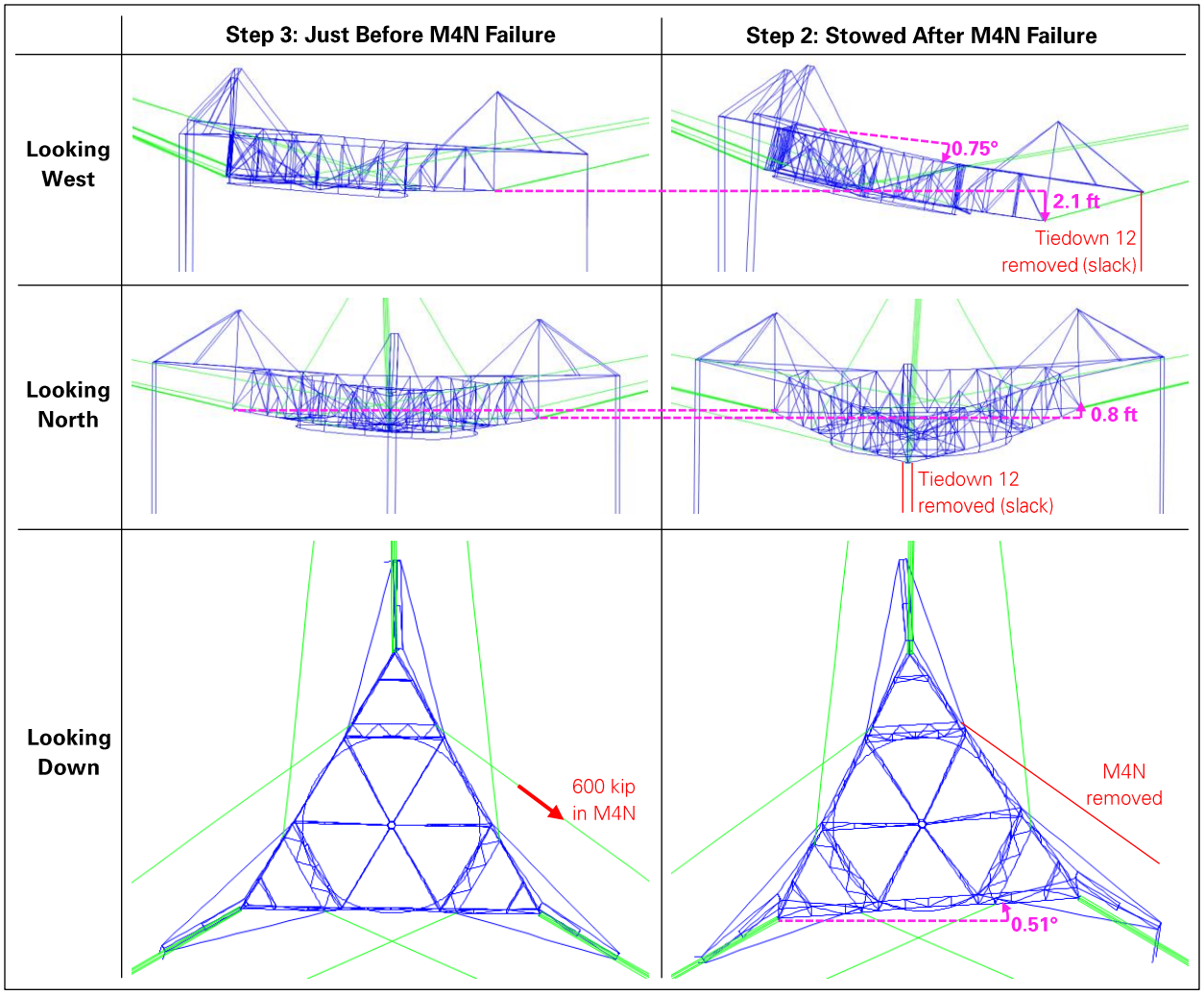

Figure 13: Analysis of platform response to M4N failure assuming M4N carries 600 kip at failure time. (Displacements magnified x10. Azimuth arm, Gregorian and line feed modeled as loads on ring girder.)

The results of the series of analyses are plotted in Figure 14 and compared to the monitoring data. The more significant changes observed in the monitoring data after the M4N failure are the rotation about the vertical axis (0.5 degree) and the drop of Corner 12 (2.1 feet), which results in a rotation about the west axis (0.73 degree). On the other hand, the rotation about the north axis (0.07 degree) and the vertical movement of Corner 4 (0.6 foot) and Corner 8 (0.1 foot) are less significant. For the three more significant parameters, the model matches the monitoring data when the M4N tension is between 580 kip and 600 kip at the time of failure.

Based on these results, we assume that M4N carried a tension of 600 kip when it failed. The complete set of cable tensions at the time of the M4N failure is provided in Figure 15 and compared to each cable's minimum breaking strength. The 600 kip in M4N are 46 percent of the cable's minimum breaking strength.

The cable tensions when the telescope is stowed with tiedowns released before the M4N failure are provided in Figure 16. These are the resultant tensions obtained in Step 4 of the analysis when the M4N tensions in Step 3 is 600 kip. With M4N still connected and the tiedowns released, these tensions correspond to a minimum stress state in the overall cable system.

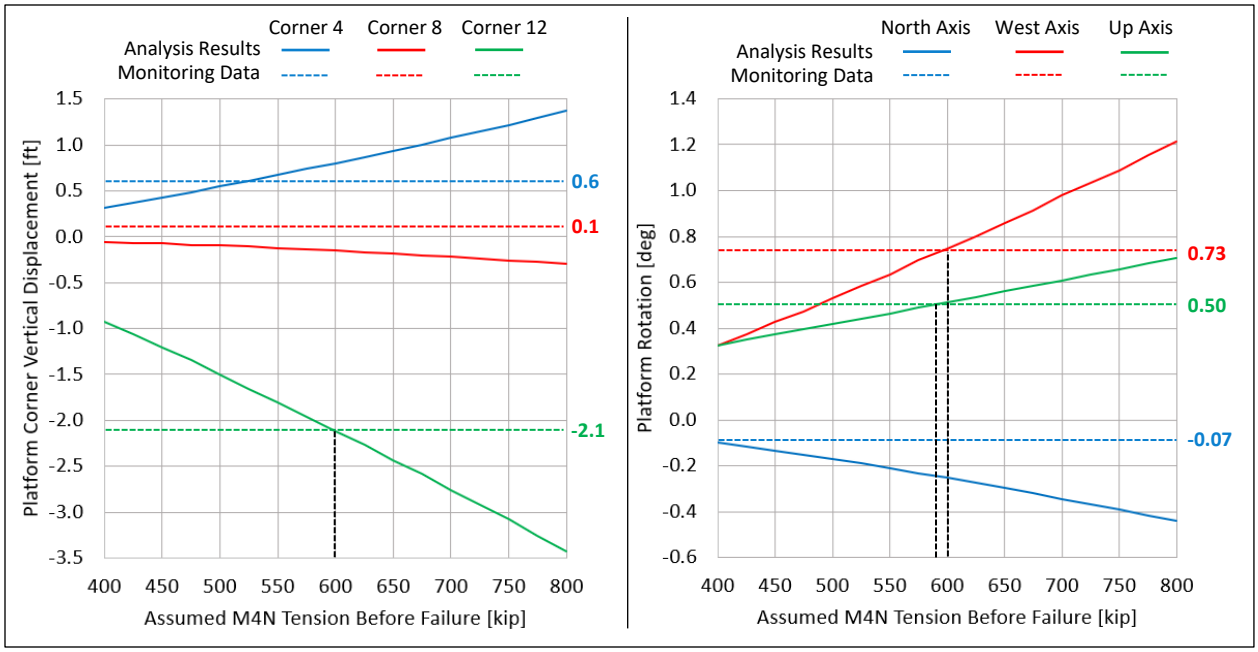

Figure 14: Determination of M4N tension just before failure from analysis results and monitoring data.

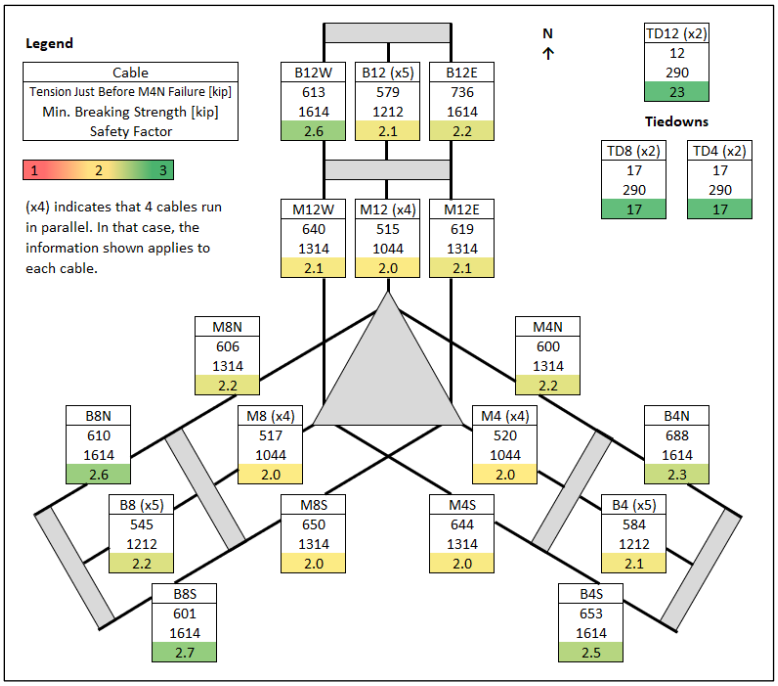

Figure 15: Cable tensions and safety factors just before M4N failure.

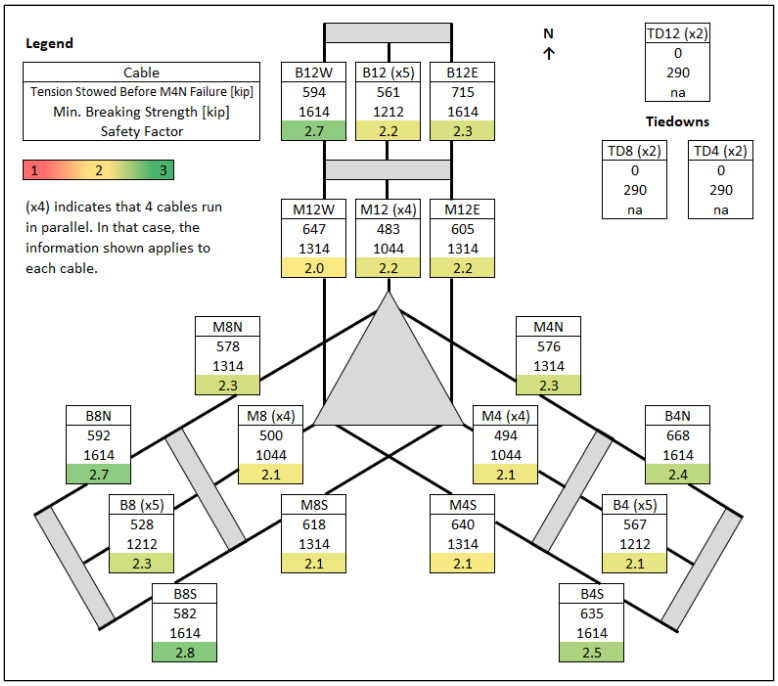

Figure 16: Cable tensions and safety factors with telescope stowed and tiedowns slack before M4N failure.

4.0 Cable Tension History after First Cable Failure

The telescope stopped operating shortly after the M4N failure (first cable failure). Still, the tensions in the cable system continued to change as the telescope was moved to the stowed position, and again when M4-4 failed (second cable failure). We performed an analysis of these events to determine the tensions experienced by each cable between the first cable failure and the collapse of the structure.

4.1 Timeline

The telescope monitoring data provided by AO documents what the structure underwent in the few days following the failure of M4N (Figure 17). Cable M4N failed at 2:35 AM on August 10, 2020, causing Tiedown 12 to go slack while increasing the tension in Tiedown 4. The telescope continued to operate for 20 minutes after the failure, with the azimuth arm rotating by 17 degrees and the Gregorian moving outwards by 2.5 degrees. When telescope operation was stopped after 20 minutes, the Gregorian was still located in the northeast quadrant that cable M4N had contributed support. On August 11, 2020, AO fully extended the jacks at the base of Tiedown 4 and Tiedown 8 to reduce the stress on the remaining cables. Later that day, the azimuth arm and Gregorian were moved to the stowed position. After this move, no adjustment was made to the telescope position until the collapse on December 1, 2020.

As the damaged structure experienced day-night temperature cycles, the tension varied from 40 to 50 kip in Tiedown 4 and from 0 to 10 kip in Tiedown 8, while Tiedown 12 remained slack.

On November 6, 2020, cable M4-4 failed near its tower-end socket. On December 1, 2020, cable M4-2 also failed near its tower-end socket, immediately followed by the remaining M4 cables and triggering the collapse of the telescope.

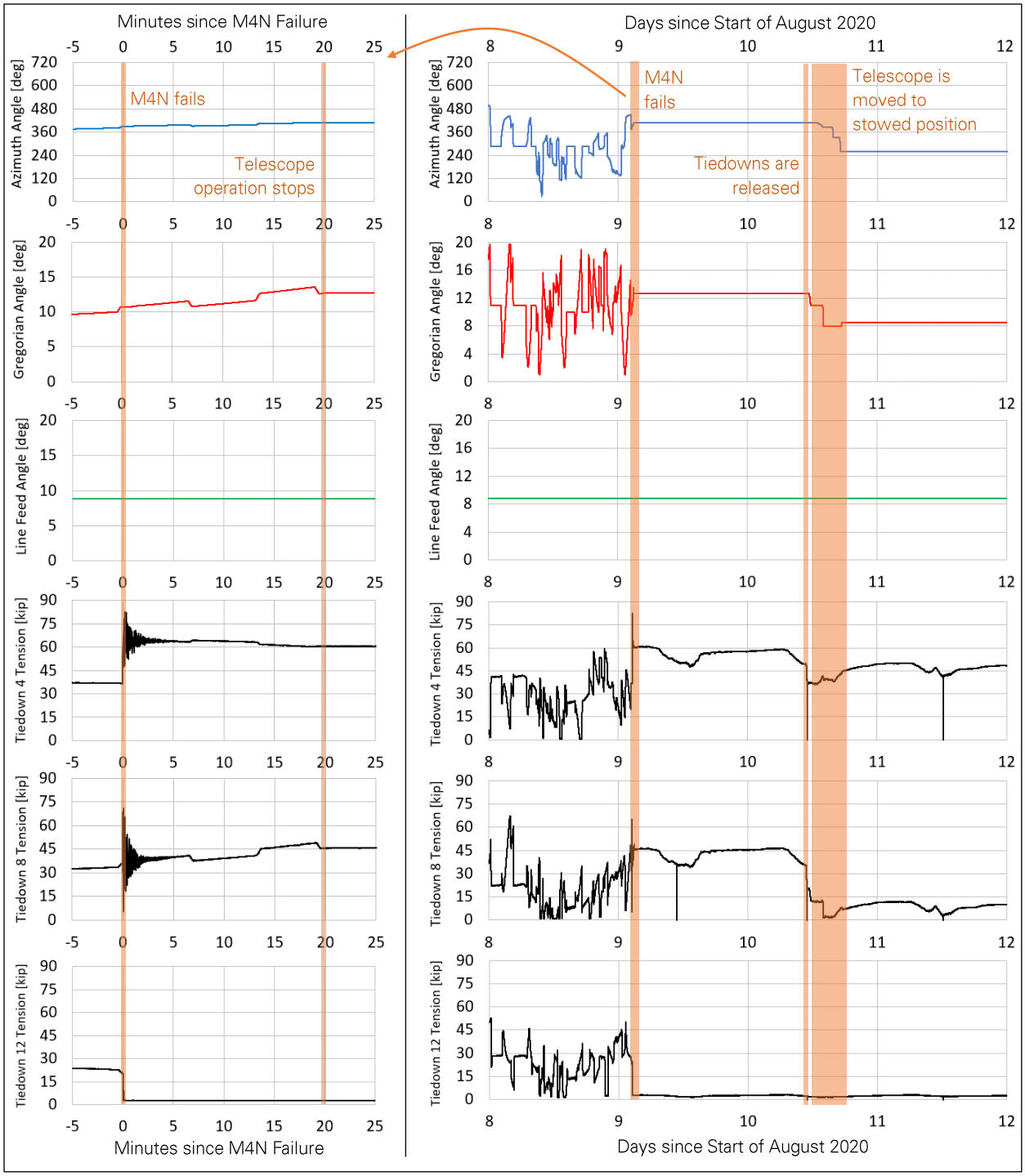

Figure 17: Telescope position and tiedown tensions before and after first cable failure (M4N).

4.2 Analysis

To determine the tensions in the cable system after the first cable failure, we performed a multi-step analysis that simulates the 2020 sequence of events in chronological order. At the start of the analysis, the model is set up to match the state of the structure just before the M4N failure (section 3.0 above). The subsequent steps simulate the M4N failure, the tiedown releases, the azimuth arm and Gregorian movement, and the M4-4 and M4-2 failures. The cable tension results are shown in Figure 18 for the mains and in Figure 19 for the backstays. The last step indicates what the cable tensions would have been if the structure had stabilized after the M4-2 failure on December 1, 2020. In reality the structure was never in that state, as the telescope collapsed immediately after the M4-2 failure.

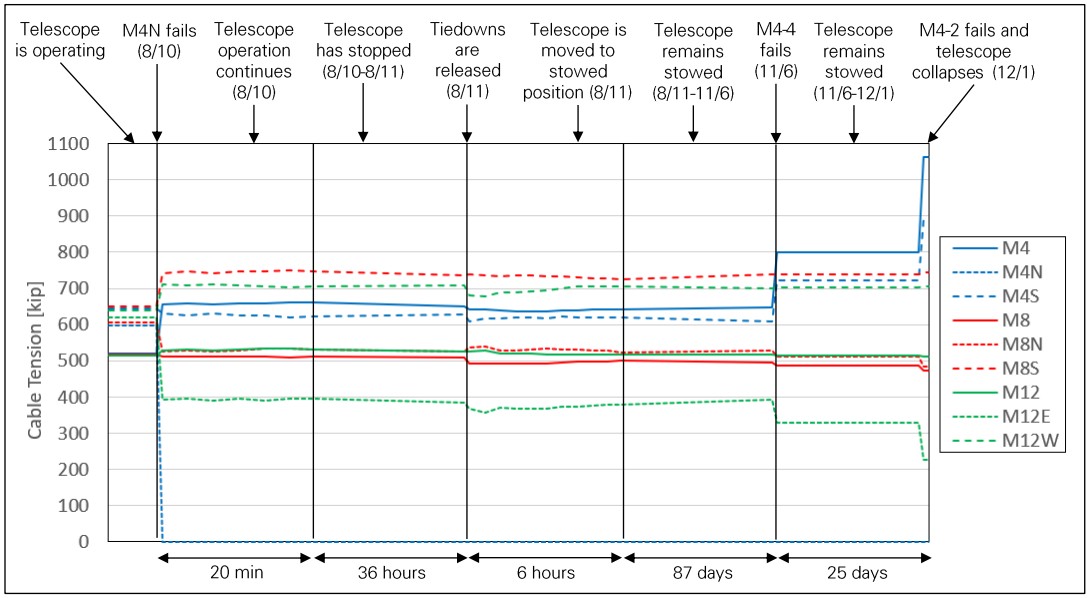

Figure 18: Main cable tensions from M4N failure to collapse.

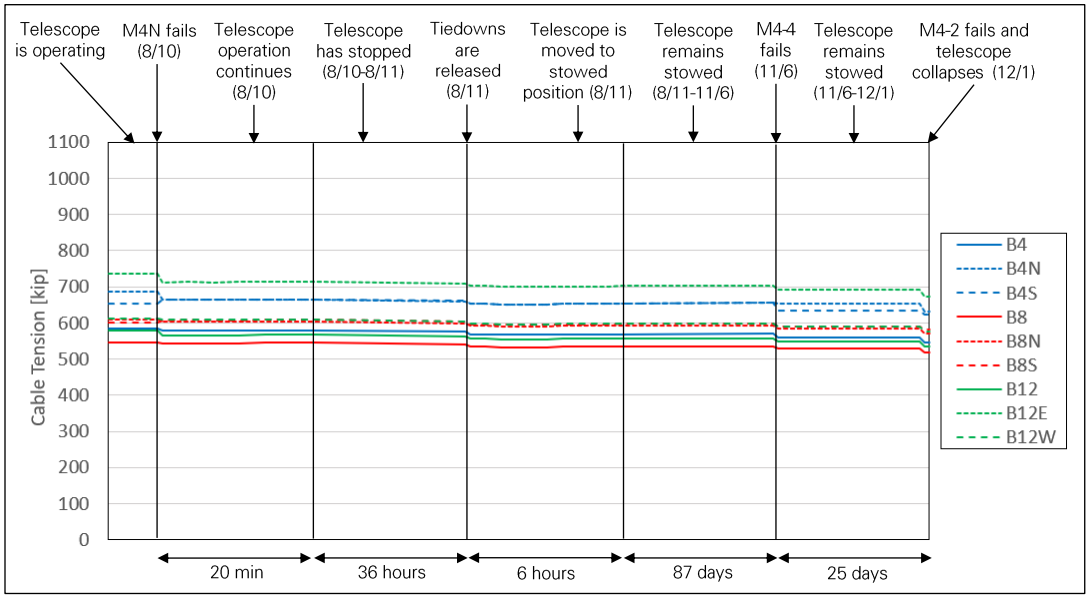

Figure 19: Backstay cable tensions from M4N failure to collapse.

Figure 20 through Figure 25 indicate the cable safety factor during and after each cable failure. The safety factor is the ratio of the cable's minimum breaking strength to the actual cable tension. The tensions during each cable failure are estimated, assuming a dynamic amplification factor of 2.0 due to the sudden cable tension release. The safety factor in the M4 cables was 1.6 and 1.3 after the M4N and M4-4 failures, respectively, and would have been 0.98 if the structure had withstood the M4-2 failure.

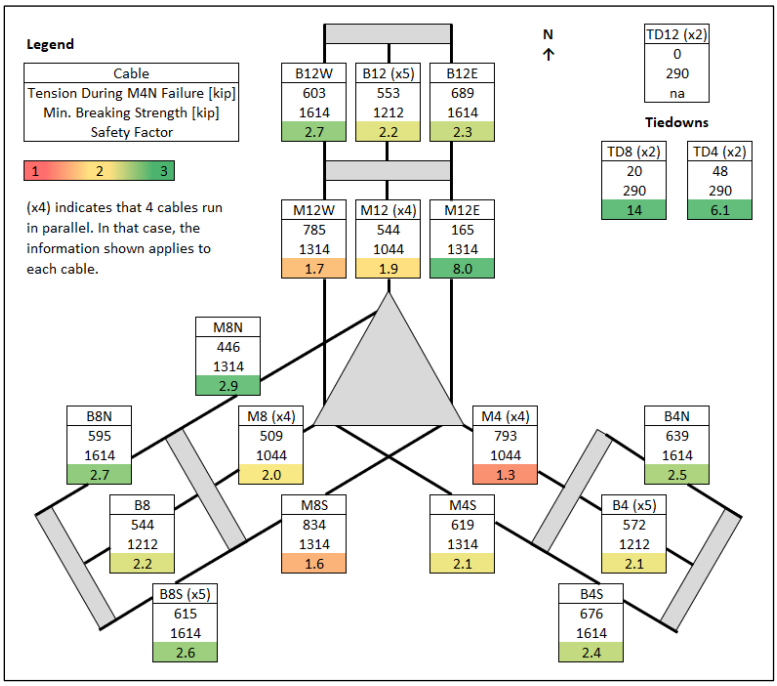

Figure 20: Cable tensions and safety factors during M4N failure, with 2.0 dynamic amplification.

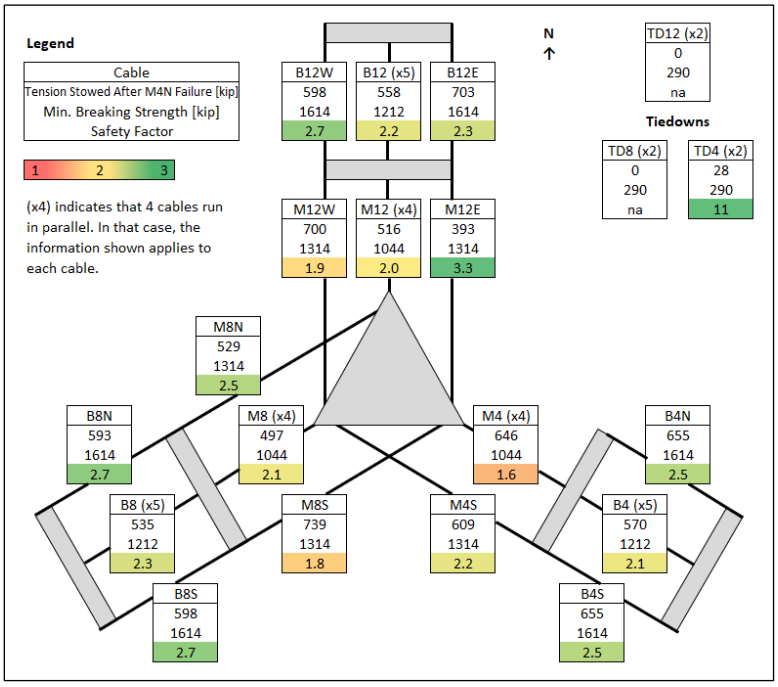

Figure 21: Cable tensions and safety factors when telescope is stowed after M4N failure.

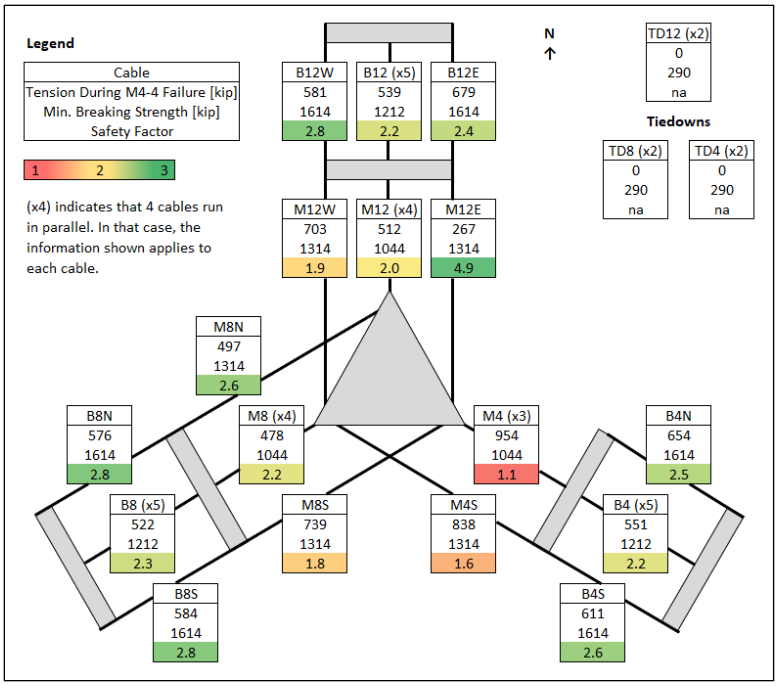

Figure 22: Cable tensions and safety factors during M4-4 failure, with 2.0 dynamic amplification.

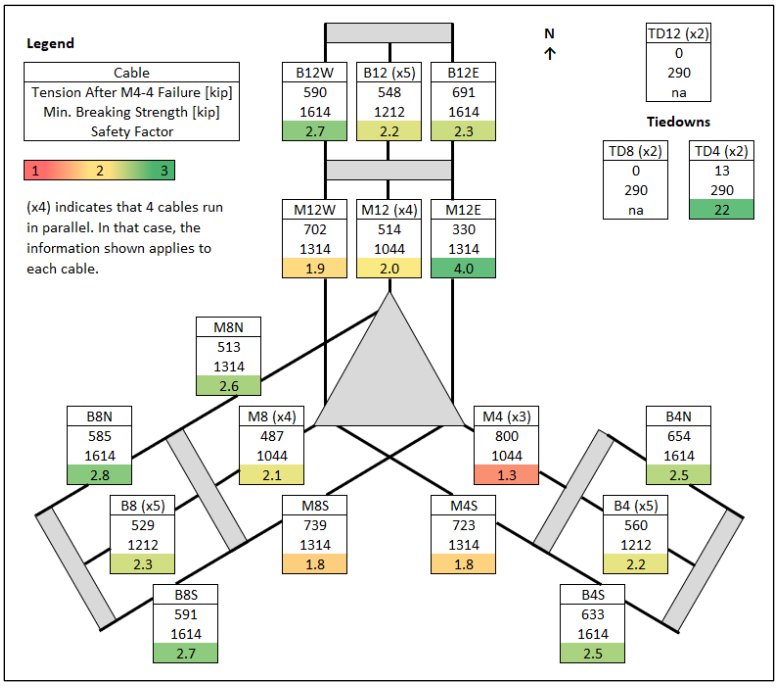

Figure 23: Cable tensions and safety factors after M4-4 failure.

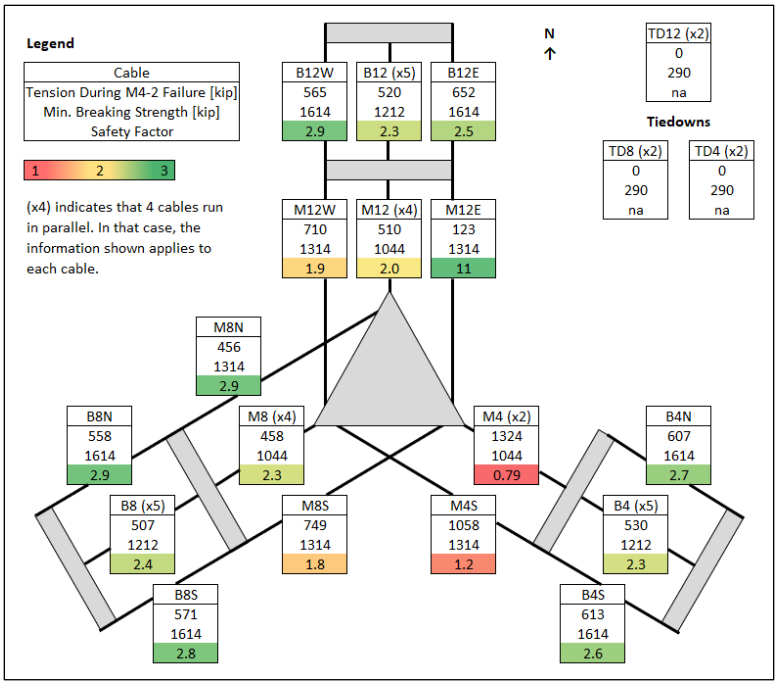

Figure 24: Hypothetical cable tensions and safety factors during M4-2 failure, with 2.0 dynamic amplification.

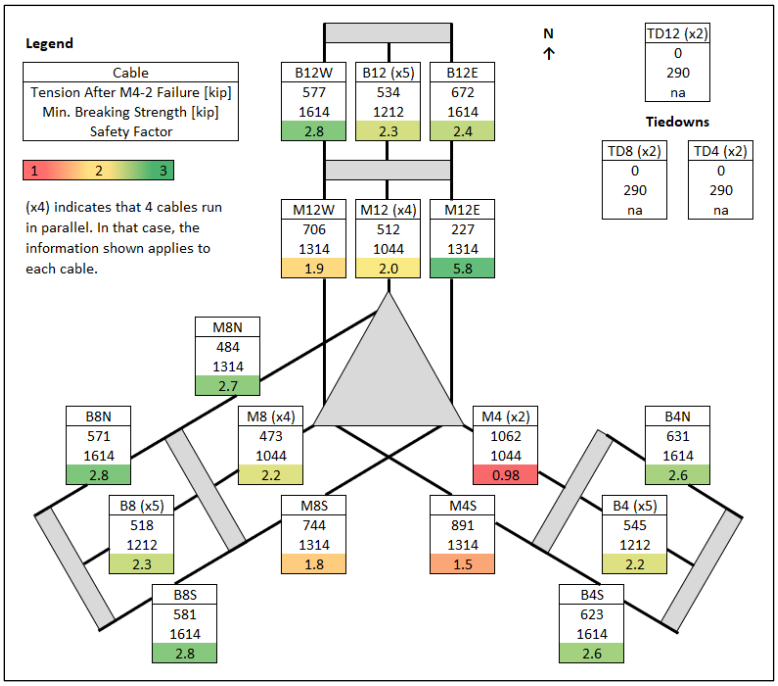

Figure 25: Hypothetical cable tensions and safety factors after M4-2 failure.

Appendix H
Telescope Operation Impact on Cable Tensions

1.0 Introduction

The suspended structure of the Arecibo Telescope consists of a fixed platform supporting several moving parts used to steer the telescope (Figure 1, Figure 2). When the telescope is operating, the displacement of the moving parts shifts the center of mass of the structure, generating tension changes in the cables supporting it. This appendix discusses the effect of telescope operation on the cable tensions.

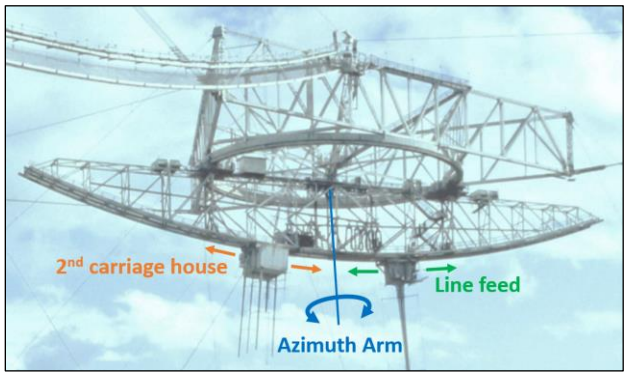

Figure 1: Moving parts of original telescope *(photo: Manfred Niermann, Wikipedia - CC BY-SA 4.0).*

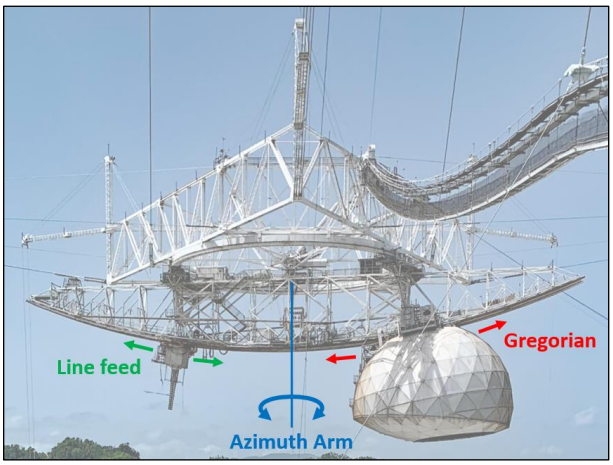

Figure 2: Moving parts of upgraded telescope, shown with line feed damage caused by Hurricane Maria *(photo: Mario Roberto Durán Ortiz, Wikipedia - CC BY-SA 4.0).*

2.0 Background

2.1 Original Structure

The moving parts of the original structure, completed in 1964, consisted of an azimuth arm that could rotate about the platform's central axis, and a line feed and second carriage house that could slide along the bottom of the azimuth arm (Figure 1). The line feed and second carriage house were relatively light compared to the rest of the structure and, as explained to us by the Arecibo Observatory (AO) staff, they were typically positioned symmetrically on both sides of the azimuth arm. As a result, the center of mass of the original structure did not move significantly during telescope operation.

2.2 Upgraded Structure

The second upgrade of the structure was completed in 1997 and, among other changes, replaced the second carriage house with the Gregorian (Figure 2). Weighing 200 kilopound (kip), the Gregorian was significantly heavier than the second carriage house (35 kip). This introduced a load imbalance on the azimuth arm, and to mitigate it a counterweight was added at the tip of the azimuth arm opposite to the Gregorian. However, since the counterweight was fixed while the Gregorian could move, the center of mass of the upgraded structure still moved during telescope operation.

2.2.1 Parameters and Operation Modes

The configuration of the upgraded telescope at any given time is defined by three angular parameters (Figure 3):

- The **azimuth arm angle** is the horizontal angle between the north direction and the longitudinal direction of the azimuth arm. The azimuth arm angle is zero when the span of the azimuth arm that supports the Gregorian points north. The azimuth arm can complete up to two revolutions (720 degrees) in the same direction before turning back.

- The **Gregorian angle** is the angle between the vertical axis of the telescope and a radius of 420 feet passing through the focal point of the Gregorian. The center of mass of the Gregorian is approximately two degrees downhill of the focal point and 430 feet from the center of rotation. The Gregorian angle is zero when positioned at the center of the azimuth arm, and the maximum Gregorian angle of 20 degrees is reached when it is at the tip of the azimuth arm.

- The **line feed angle** is the angle between the vertical axis of the telescope and the axis of the line feed. The line feed angle is zero when the line feed points straight down, and the maximum line feed angle of 20 degrees is reached when the line feed is at the tip of the azimuth arm.

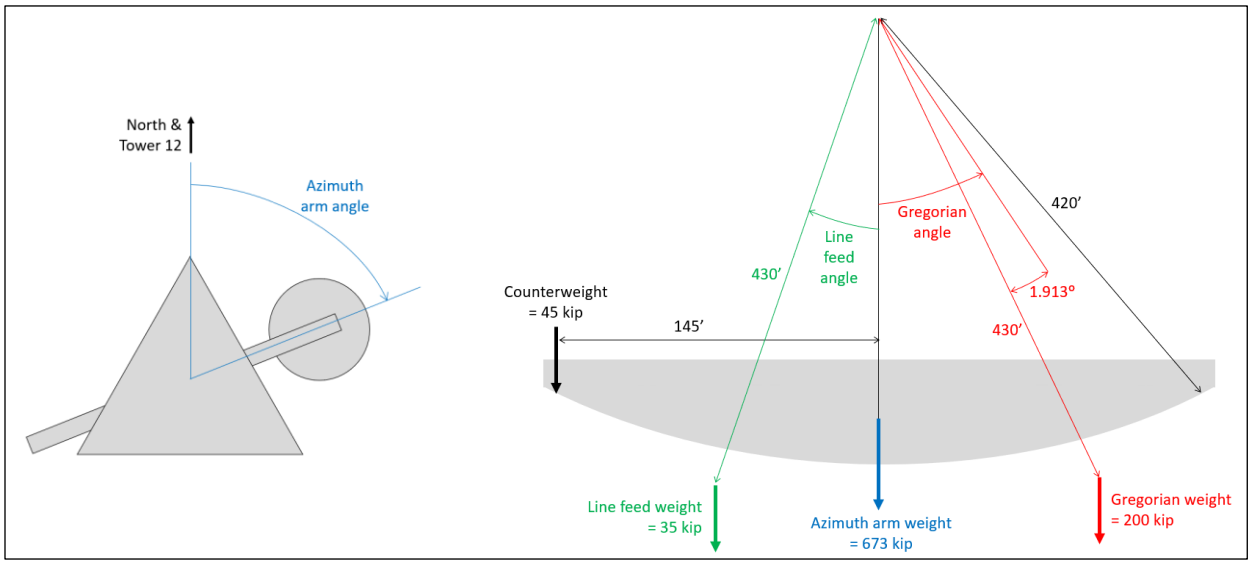

Figure 3: Upgraded telescope parameters and azimuth arm mass distribution.

The corners of the platform are connected to the ground with tiedown cables, and their tensions can be actively controlled with electro-mechanical jacks. However, this system is only used to mitigate the effect of temperature on the average elevation of the suspended structure (Appendix I), and the tiedown jacks are not actively adjusted for changes in the azimuth arm, Gregorian or line feed angles.

Depending on the type of observation or experiment being performed, the telescope operates in one of two general modes:

- In **standard** mode, the azimuth arm, Gregorian and/or line feed move slowly and typically complete less than 10 cycles per day. The standard mode is, for example, used to track a moving object that the telescope is observing.

- In **atmospheric** mode, the azimuth arm rotates more rapidly, at a rate of up to four revolutions per hour, with the Gregorian and line feed fixed at a given angle. This mode is used for studies of the Earth's atmosphere.

Before and during high wind events, the telescope is placed in a predetermined stowed position, which corresponds to an azimuth arm angle of 258 degrees, a Gregorian angle of 8.5 degrees, and a line feed angle of 8.9 degrees. Pins are then inserted between the fixed platform and the moving parts for the duration of the wind event.

2.2.2 Operation Data

A telescope operation data log was provided by AO. Covering the period from June 2004 to August 2020, the log includes the azimuth arm, Gregorian and line feed angles as well as the tension in each tiedown, all recorded every second. One week of data is shown in Figure 4 as an example, where the difference between the standard and atmospheric modes is clearly visible. The data log indicates that over the past 16 years, the telescope was operating in standard mode for approximately 85 percent of the time and in atmospheric mode for approximately five percent of the time, while for the remaining 10 percent of the time the telescope was not operating.

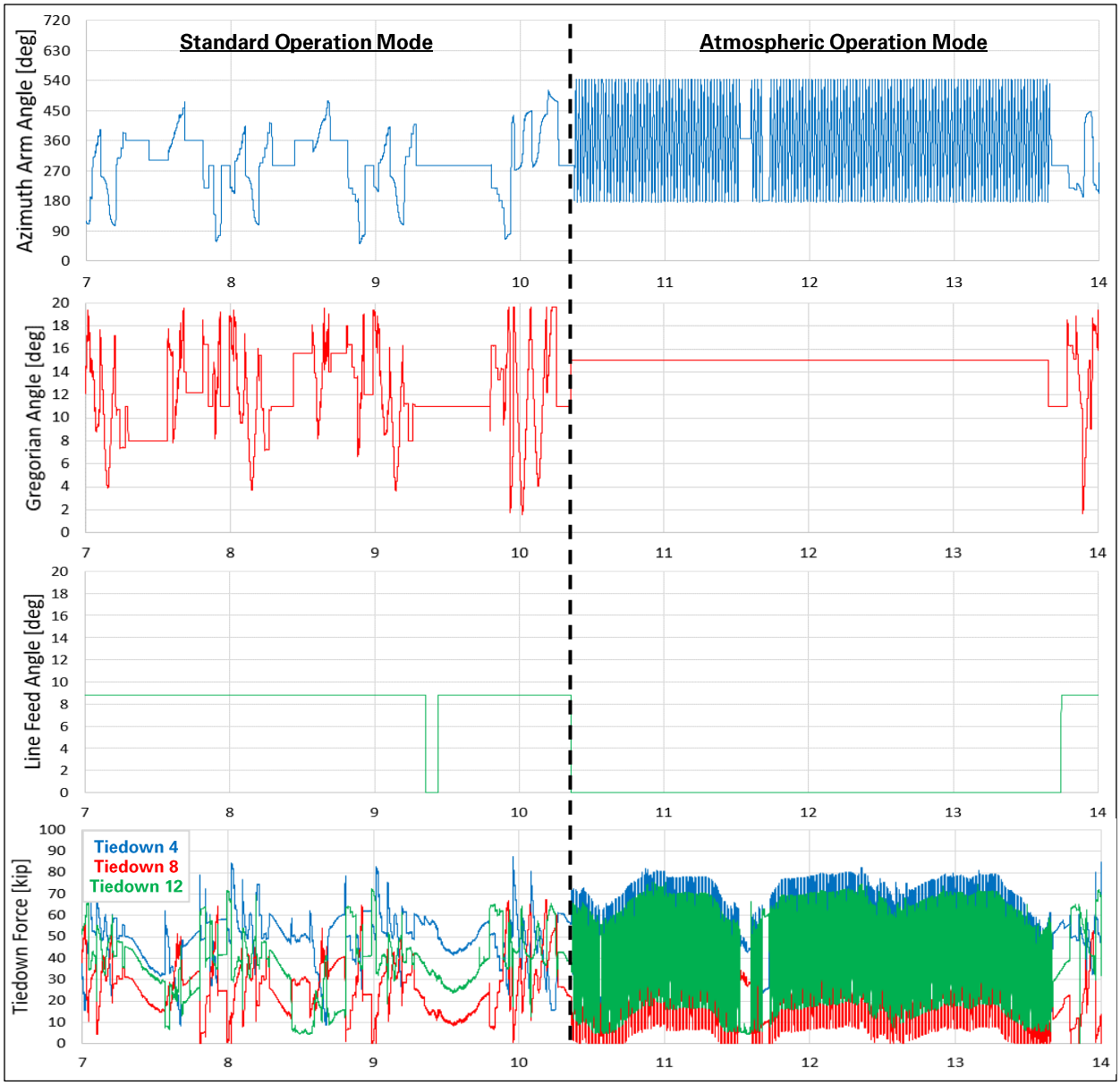

Figure 4: One week of telescope operation data (12/7/2012 to 12/14/2012).

3.0 Analysis Method

We performed a structural analysis of the telescope during operation to determine the maximum tensions and the number of tension cycles experienced by the cable system. The models used for this analysis is detailed in Appendix F.

3.1 Load Application to Model

The combined weight of the moving parts is transferred to the fixed platform at two points where the azimuth arm is suspended from the ring girder. The position of these two points on the ring girder depends on the orientation of the azimuth arm, while the distribution of the suspended weight between the two points depends on the positions of the other moving parts (line feed and Gregorian or second

carriage house). To analyze multiple configurations of the telescope, we removed the azimuth arm from the analysis model and replaced it with a pair of loads applied directly to the ring girder (Figure 5). The position and magnitude of each load could then be modified as needed to represent different positions of the moving parts.

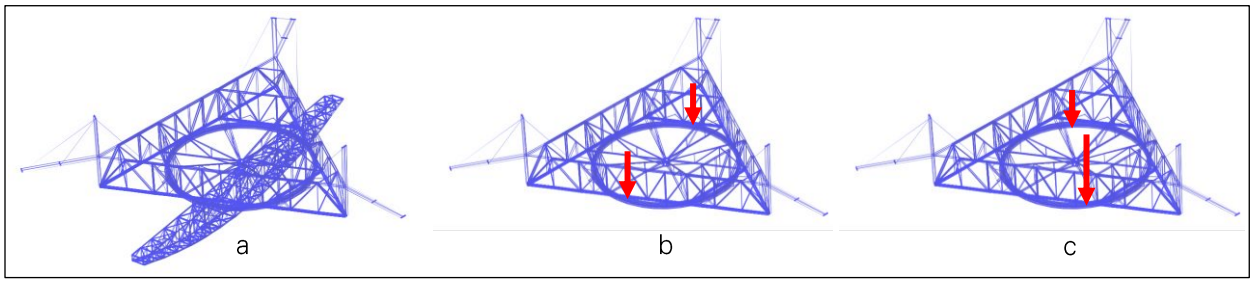

Figure 5: Modeling of telescope operation loads. (a) The azimuth arm is initially modeled as elements in the stowed position. (b) The azimuth arm elements are removed and replaced with loads on the ring girder. (c) The loads on the ring girder are moved and adjusted to represent movement of the moving parts.

3.2 Original Structure

In the original structure, the total weight of the azimuth arm, line feed and second carriage house is approximately 400 kilopound (kip). Since the line feed and second carriage house are relatively light and move symmetrically, the azimuth arm remains essentially balanced during telescope operation. In the analysis model, the total weight of the moving parts is therefore always transferred to the ring girder as two equal loads of 200 kip.

We simulated a full revolution of the azimuth arm while monitoring the change in cable tensions. The model was initialized so that the tiedown tensions are equal when the azimuth arm is stowed. As shown below in section 4.1, the results indicate that the rotation of the azimuth arm had a negligible impact on the cable tensions, and therefore no further analysis was performed on the original structure.

3.3 Upgraded Structure

The azimuth arm of the upgraded structure supports a 200-kip Gregorian on one side and a 35-kip line feed on the other. Part of the line feed fell off during Hurricane Maria in 2017, but the undamaged line feed weight of 35 kip is considered in our analyses. To reduce the weight imbalance on the azimuth arm, a 45-kip counterweight was installed at the tip of the azimuth arm opposite the Gregorian (Figure 3), with the counterweight fixed on the azimuth arm so that the azimuth arm is essentially balanced when the Gregorian and line feed are in stowed position. For other positions of the Gregorian and line feed, the azimuth arm is not balanced and transfers a moment to the platform, in addition to a total weight of 953 kip. The azimuth arm imbalance moment is shown in Table 1 for key configurations of the telescope.

To determine the minimum and maximum tensions that each cable can experience during telescope operation, we first simulated a full revolution of the azimuth arm with the maximum azimuth arm imbalance moment.

Table 1: Azimuth arm imbalance moment for key telescope configurations.

Telescope Configuration	Gregorian Angle [deg]	Line Feed Angle [deg]	Azimuth Arm Imbalance Moment [kip·ft]	Azimuth Arm Weight Eccentricity [ft]
Maximum imbalance towards line feed	0	20.0	-14,540	-15.3
Stowed	8.5	8.8	1,000	1.1
Typical atmospheric mode	15.0	0	12,950	13.6
Typical standard mode	20.0	8.8	17,860	18.8
Maximum imbalance towards Gregorian	20.0	0	20,180	21.2

Then, to determine the amplitude and number of tension cycles actually experienced by the cables over time, we simulated four 10-day periods of actual telescope operation as recorded in the data log. Three of the 10-day periods were selected to represent the standard mode of operation, and the fourth 10-day period was selected to represent the atmospheric mode. Figure 6 to Figure 9 show the azimuth arm, Gregorian and line feed angles and the calculated azimuth arm imbalance moment for the four 10-day periods. The maximum azimuth arm imbalance moment is 17,860 kip·ft, which corresponds to a fully-extended Gregorian and a stowed line feed.

Prior to each analysis, we initialized the model so that the tiedown tensions are equal when the telescope is stowed.

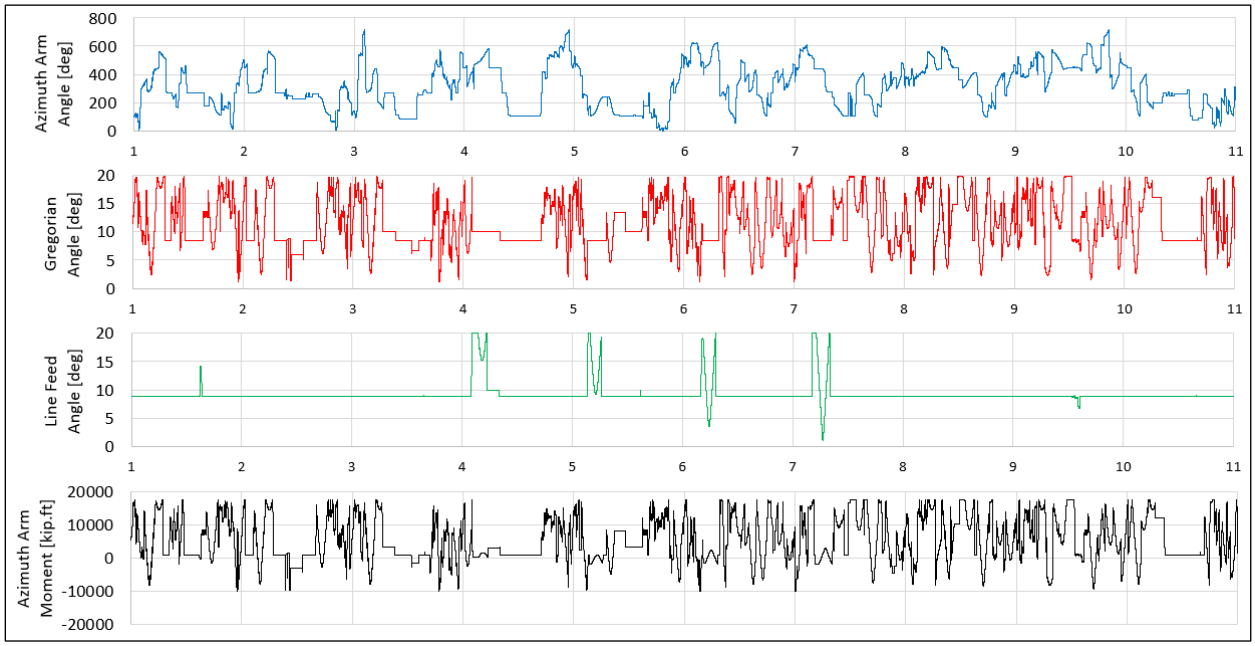

Figure 6: Ten days of telescope standard operation data (August 1-11, 2004).

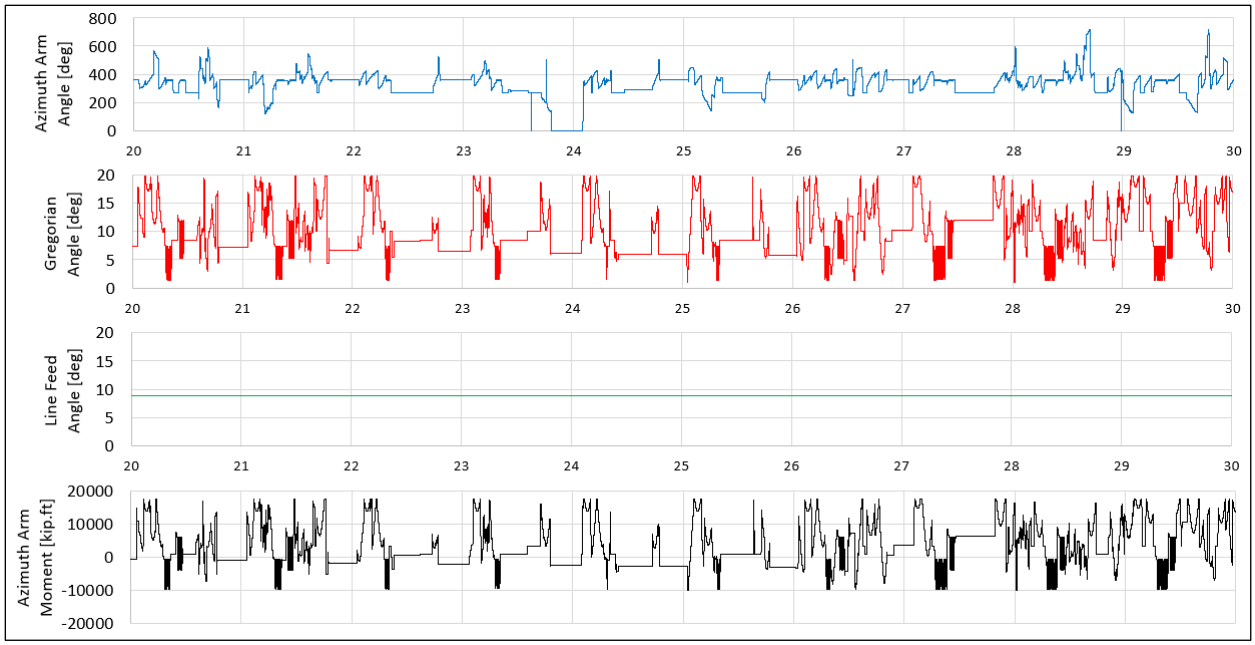

Figure 7: Ten days of telescope standard operation data (May 20-30, 2005).

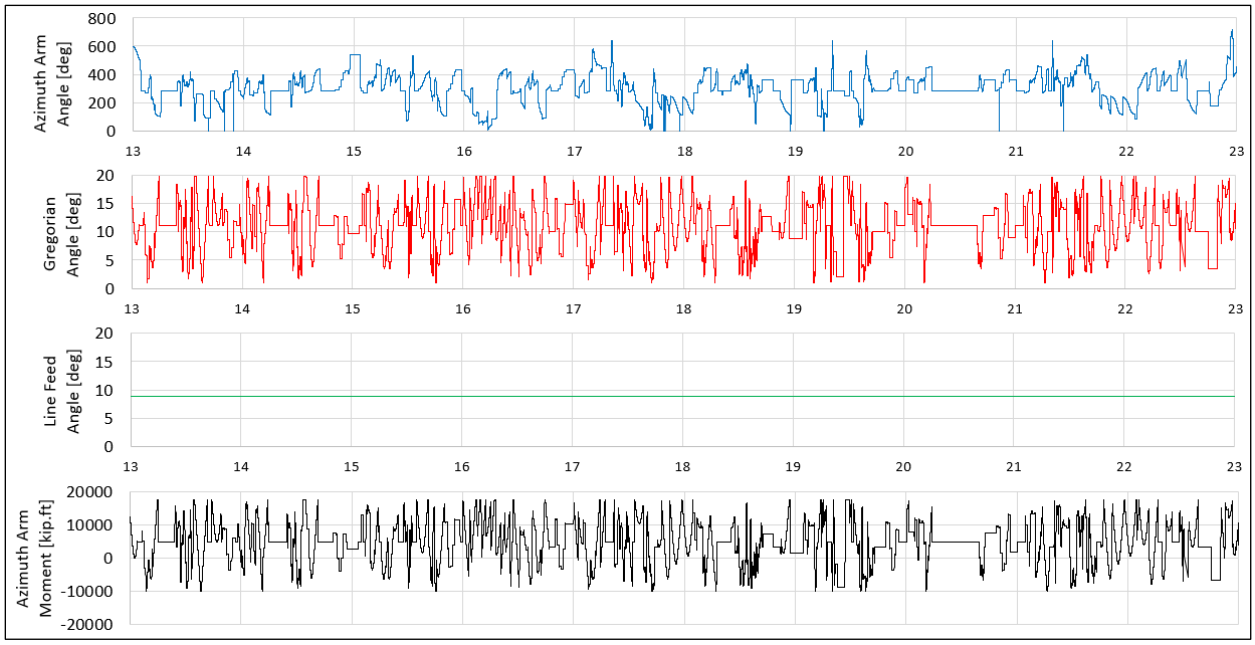

Figure 8: Ten days of telescope standard operation data (May 13-23, 2020).

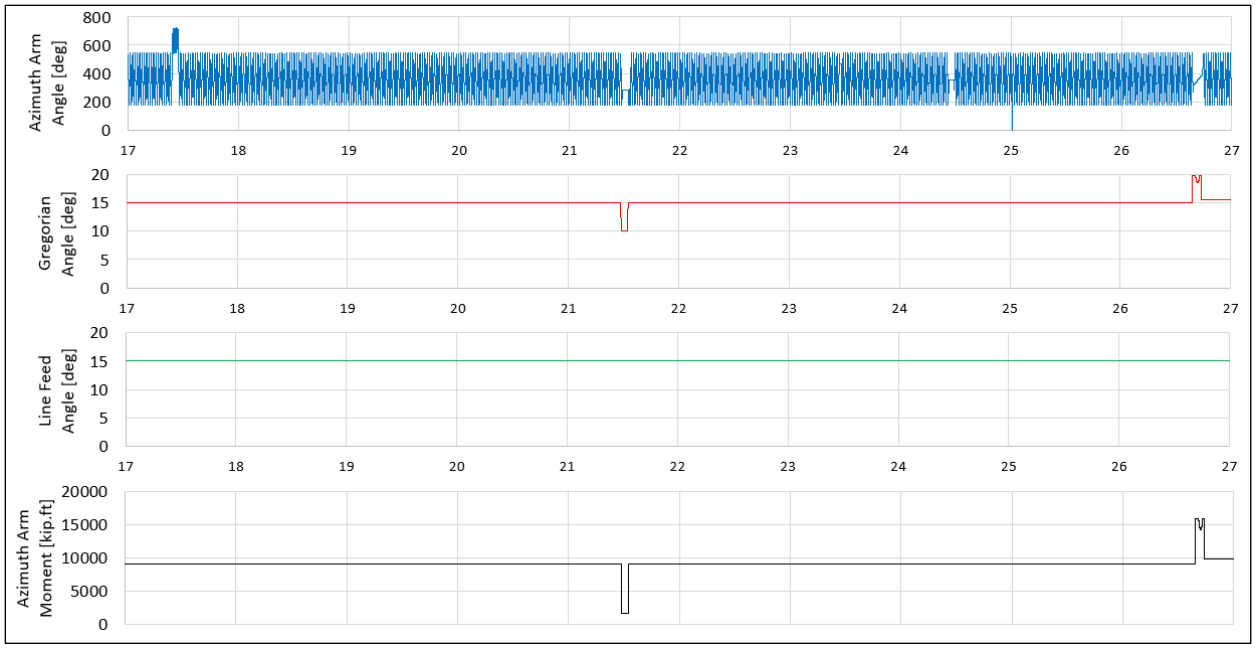

Figure 9: Ten days of telescope atmospheric operation data (January 17-27, 2008).

4.0 Cable Tension Results

4.1 Original Structure

We analyzed the operation of the original structure by simulating a complete revolution of the balanced azimuth arm. As shown in Figure 10, the tensions in the main cables and backstays remain essentially constant for any azimuth arm orientation. This is because the center of mass of the azimuth arm remains centered on the platform. Figure 11 shows the tensions in the six original tiedowns, which vary by up to one kip as the azimuth arm rotates. The minimum safety factors in the cables and tiedowns during telescope operation are provided in Figure 12. The safety factor is calculated by dividing the cable's minimum breaking strength by the cable's maximum actual tension.

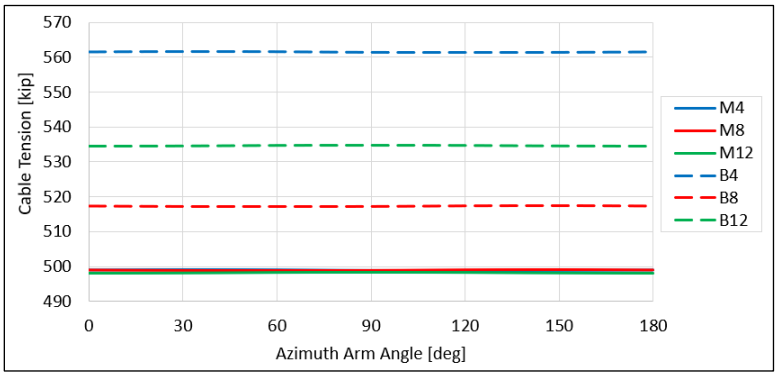

Figure 10: Tension in main and backstay cables for full revolution of azimuth arm in original structure.

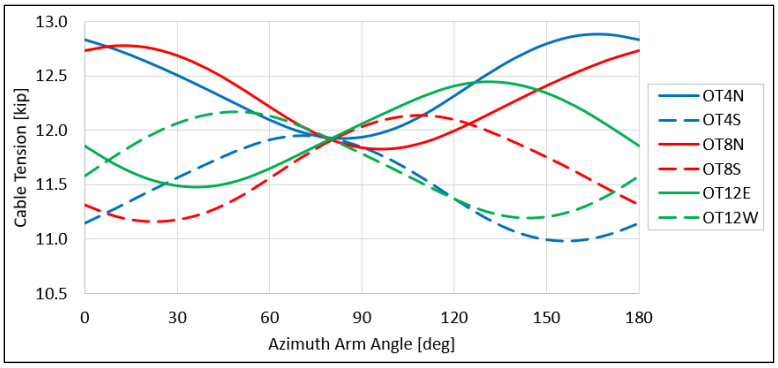

Figure 11: Tension in tiedown cables for full revolution of azimuth arm in original structure.

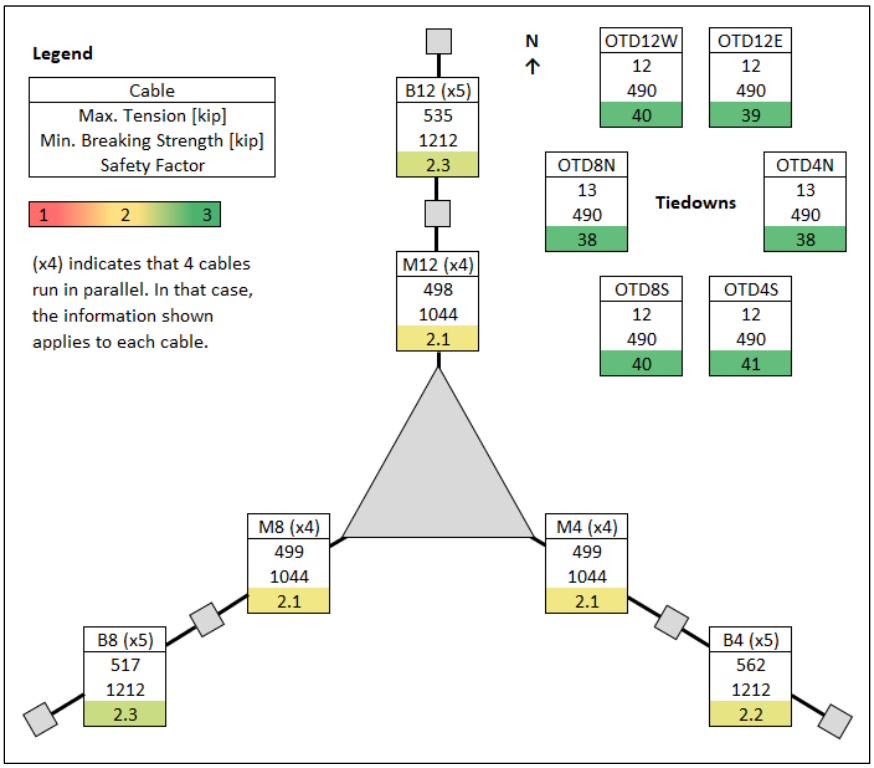

Figure 12: Minimum safety factor in cables for full revolution of azimuth arm in original structure.

4.2 Upgraded Structure

We first analyzed the operation of the upgraded structure by simulating a complete revolution of the azimuth arm with the maximum azimuth arm imbalance. During the azimuth arm revolution, each cable experiences a tension cycle. The tension range (peak-to-peak) is approximately 20 kip in the original main cables, and 50 kip in the auxiliary main cables (Figure 13). The tension range is negligible in the backstays (Figure 14), and 55 kip in the tiedowns (Figure 15). The corresponding cable safety factors and normalized stress ranges are shown in Figure 16 and Figure 17. The normalized stress range is calculated by dividing the cable's tension range by the cable's minimum breaking strength.

In a second analysis, we simulated three 10-day periods of telescope operation in standard mode. From the cable tension time history results, we counted the daily average number of tension cycles using the rainflow method. The results are compiled in Table 2, where the magnitude of a tension cycle is

expressed as a normalized stress range. The magnitude and number of cycles are low from a fatigue perspective, with only eight cycles per day producing a normalized stress range of at least one percent in the auxiliary main cables, and only three cycles per day in the original main cables.

Finally, we simulated a 10-day period of telescope operation in atmospheric mode, and again counted the number of cable tension cycles, with the results summarized in Table 3. In this case, the only tension cycles causing a normalized stress range greater than one percent are in the auxiliary main cables, with approximately 90 cycles per day. This corresponds to the azimuth arm spinning at a rate of 22 degrees per minute, or one revolution every 16 minutes.

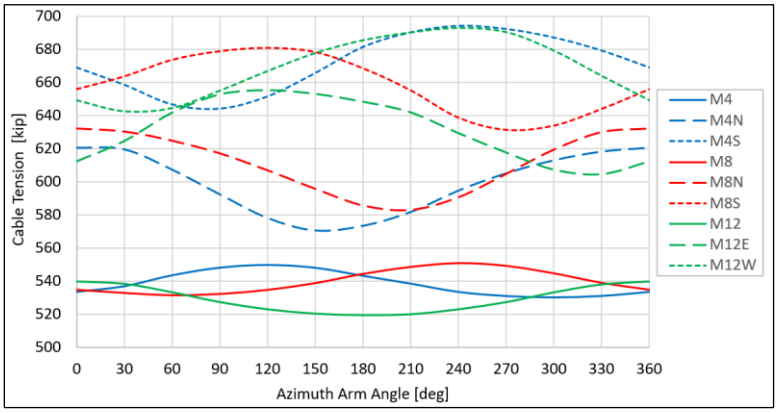

Figure 13: Tension in main cables for full revolution of azimuth arm with maximum azimuth arm imbalance in upgraded structure.

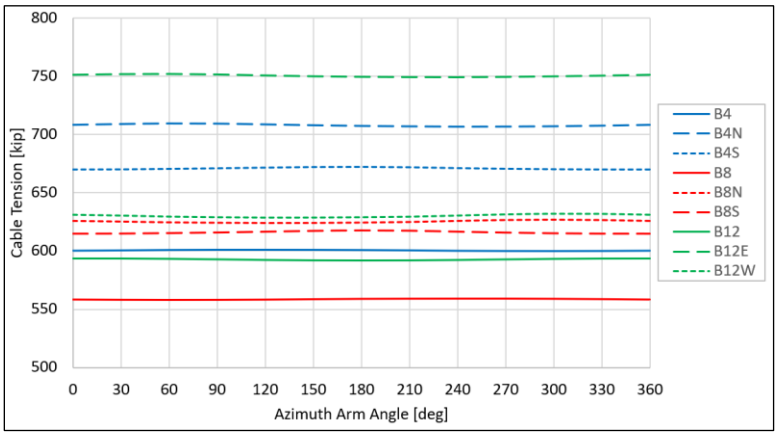

Figure 14: Tension in backstay cables for full revolution of azimuth arm with maximum azimuth arm imbalance in upgraded structure.

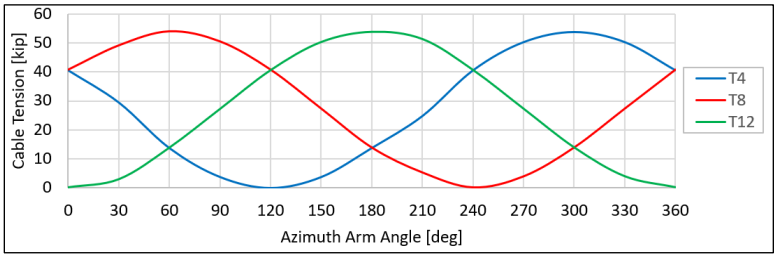

Figure 15: Tension in tiedown cables for full revolution of azimuth arm with maximum azimuth arm imbalance in upgraded structure.

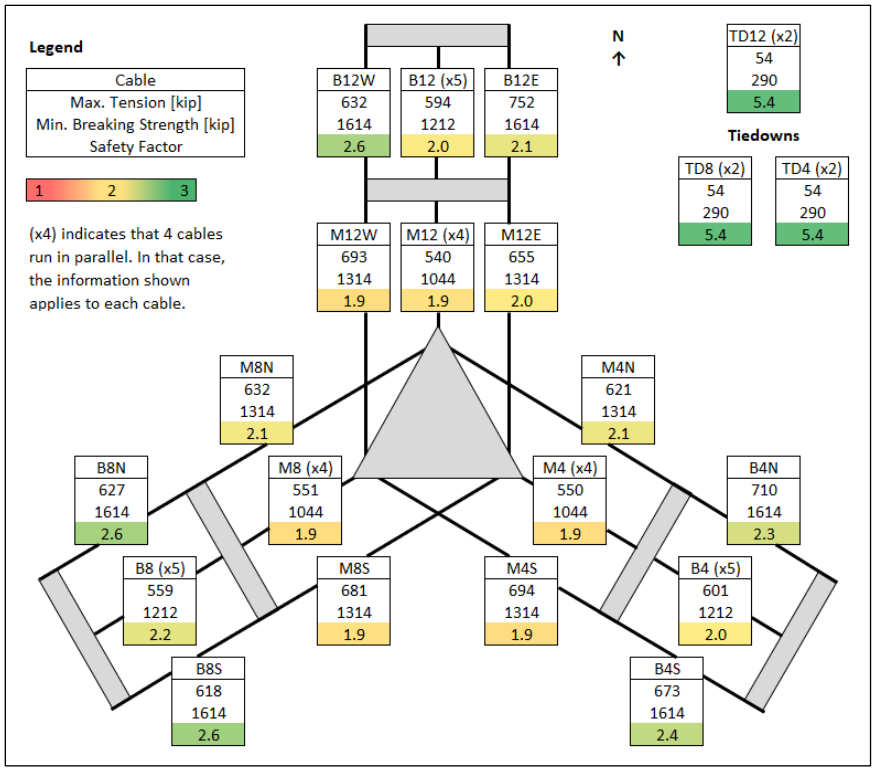

Figure 16: Cable safety factors for full revolution of azimuth arm with maximum azimuth arm imbalance in upgraded structure.

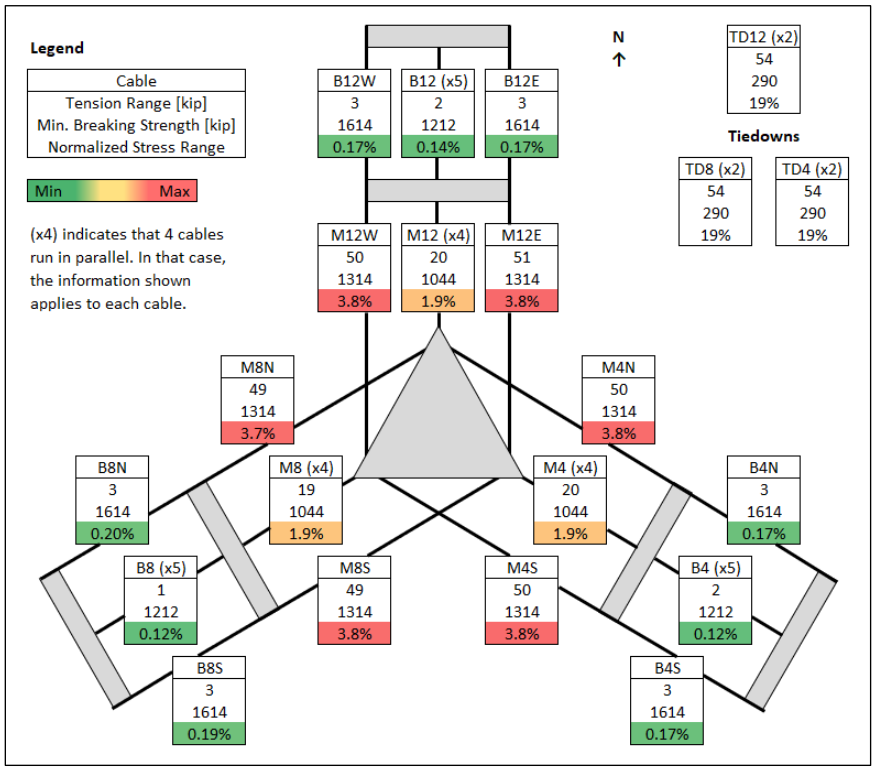

Figure 17: Cable normalized stress range for full revolution of azimuth arm with maximum azimuth arm imbalance in upgraded structure.

Table 2: Average number of cable tension cycles per day during standard telescope operation in upgraded structure.

	Normalized Stress Range (= Tension Range / Minimum Breaking Strength)						
	1-2%	**2-3%**	**3-4%**	**4-5%**	**5-10%**	**10-15%**	**15-20%**
M4	2.8						
M4N	4.4	2.2	0.4				
M4S	5.2	2.3	0.7				
M8	2.8						
M8N	4.7	2.0	0.4				
M8S	5.7	2.1	0.7				
M12	2.4						
M12E	4.8	2.2	0.6				
M12W	5.3	2.2	0.6				
Backstays							
T4	4.7	5.6	2.4	1.6	4.7	2.2	0.4
T8	6.5	4.3	2.3	2.0	4.3	2.1	0.6
T12	4.5	2.4	1.6	3.8	4.4	1.9	0.3

Table 3: Average number of cable tension cycles per day during atmospheric telescope operation in upgraded structure.

	Normalized Stress Range (= Tension Range / Minimum Breaking Strength)					
	1-2%	**2-3%**	**3-4%**	**4-5%**	**5-10%**	**10-15%**
M4	0.1					
M4N	88.5	1.3				
M4S	88.9					
M8	0.1					
M8N	89.5	0.1				
M8S	90.1	0.1				
M12	0.1					
M12E	88.3	1.3				
M12W	88.5	1.2				
Backstays						
T4	0.7	44.4		0.2	89.4	0.1
T8	0.6	44.6	0.1	0.1	89.4	0.1
T12			0.2	0.2	89.5	0.1

Appendix I
Temperature Impact on Cable Tensions

1.0 Introduction

The telescope structure is exposed to the elements and experiences daily fluctuations in air temperature and solar radiation levels. Temperature changes in the steel and concrete cause these materials to expand or contract, affecting the forces in the structure. The steel cables naturally tighten at night as they cool down and slacken during the day as they warm up. In the upgraded structure, the tiedown cable tensions are also actively controlled with jacks to keep the suspended structure at a constant elevation while the temperature varies. This appendix presents our analysis of the effect of the daily temperature cycles on the cable tensions.

2.0 Data

Our analysis relies on three sets of data recorded at the Arecibo Observatory (AO): air temperature, cable socket temperature, and tiedown tensions.

2.1 Air Temperature Data

The air temperature was measured continuously by a weather station located on the suspended structure (Figure 1), and we were provided with the minimum and maximum temperature recorded every day since January 2000. Although we only considered data between January 2005 and December 2015 due to gaps in the data outside that range, we consider those 11 years of data sufficient since the daily temperature cycles are not expected to vary significantly from year to year.

In this appendix, the *daily temperature range* is the difference between the high and low temperatures over a 24-hour period. The distribution of the daily temperature range between 2005 and 2015 is shown in Figure 2. The average range is 12.3°F, with a standard deviation of 3.0°F. Figure 3 shows the average daily low and high temperatures for each month of the year. While the temperatures are approximately 5°F higher in the summer months than in the winter months, the temperature range does not change significantly month to month. Additional air temperature statistics for each month are provided in Table 1.

Figure 1: Location of weather station on suspended structure
(photo: Mario Roberto Duran Ortiz, Wikipedia - CC BY-SA 4.0).

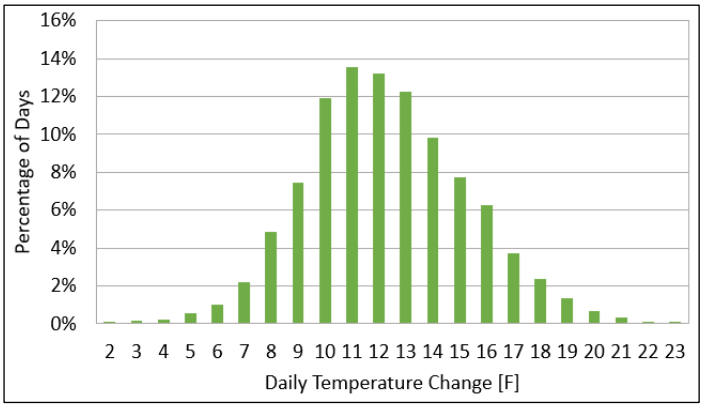

Figure 2: Distribution of daily air temperature ranges (January 1, 2005 to December 31, 2015).

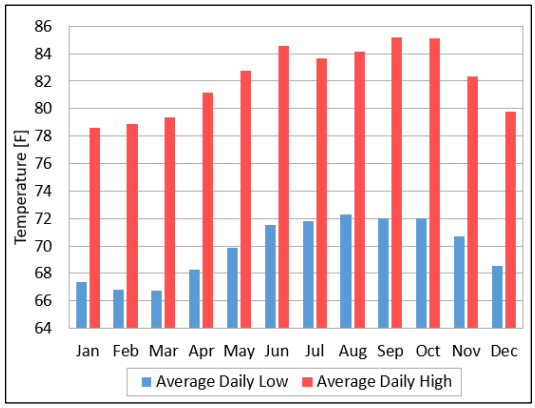

Figure 3: Monthly average of daily low and high air temperatures (January 1, 2005 to December 31, 2015).

Table 1: Daily air temperature range statistics by month (January 1, 2005 to December 31, 2015).

	Jan	Feb	Mar	Apr	May	Jun	Jul	Aug	Sep	Oct	Nov	Dec	Year
Average Daily Low [°F]	67.4	66.8	66.7	68.3	69.9	71.6	71.8	72.3	72.0	72.0	70.7	68.6	69.8
Average Daily High [°F]	78.6	78.9	79.4	81.2	82.7	84.5	83.7	84.1	85.2	85.1	82.3	79.8	82.1
Average Daily Range [°F]	11.2	12.1	12.6	12.9	12.8	13.0	11.9	11.9	13.2	13.0	11.6	11.2	12.3
Daily Range Std. Dev. [°F]	3.3	3.2	3.1	2.9	3.0	2.8	2.6	2.9	3.1	2.7	2.9	2.8	3.0
Daily Range Coef. of Variation	0.29	0.26	0.24	0.22	0.24	0.22	0.22	0.24	0.23	0.20	0.25	0.25	0.24

2.2 Steel Temperature Data

After the first cable socket failure in August 2020, some of the remaining sockets were instrumented by Wiss, Janney, Elstner Associates, Inc. (WJE). For six of the sockets, the instrumentation included a thermocouple that measured the steel temperature on the surface of the socket. A month of data for one of the sockets is shown in Figure 4 as an example.

The average daily low and high surface temperatures for each of the six sockets are shown in Figure 5. The daily low temperature is consistently between 70.5°F and 72.5°F for every socket, while the daily high temperature varies more significantly between sockets, from 83°F to 90°F. The wider range of daily high temperatures may be due to shade, as each socket surface with a thermocouple is shielded from direct sunlight at a different time of the day. Additional statistics on the socket surface temperatures are provided in Table 2. On average over the six sockets, the daily temperature range is 14.8°F, which is 2.5°F higher than the average daily air temperature range, and can be attributed to solar radiation heating up the steel to a temperature higher than that of the air.

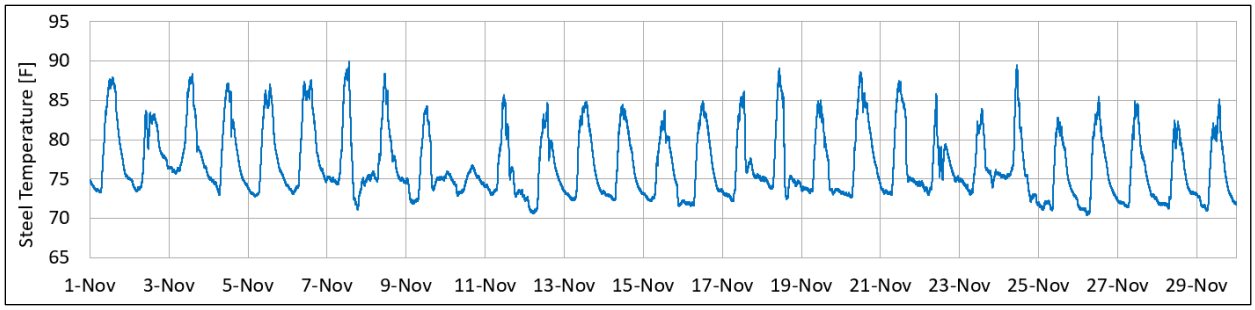

Figure 4: B4N socket surface temperatures recorded in November 2020.

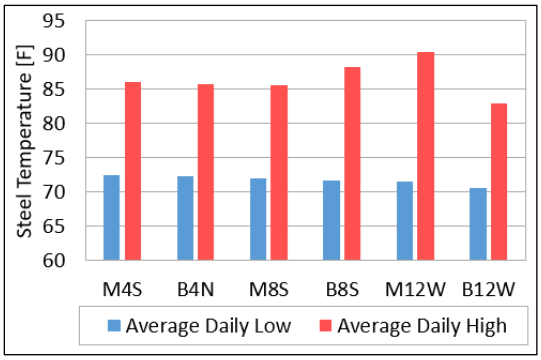

Figure 5: Average daily low and high socket surface temperatures in November 2020.

Table 2: Statistics on socket surface daily temperature range in November 2020.

	M4S	B4N	M8S	B8S	M12W	B12W	Overall
Average Daily Low [°F]	72.5	72.3	71.9	71.6	71.4	70.6	71.7
Average Daily High [°F]	86.1	85.7	85.6	88.2	90.4	83.0	86.5
Average Daily Range [°F]	13.6	13.4	13.7	16.6	18.9	12.4	14.8
Daily Range Std. Dev. [°F]	2.8	2.6	2.6	3.3	3.1	1.9	3.6
Daily Range Coef. of Variation	0.21	0.19	0.19	0.20	0.17	0.15	0.24

2.3 Tiedown Tension Data

The upgraded telescope structure has three vertical tiedowns connecting the platform to the ground below through the primary reflector (Figure 6). Each tiedown consists of two parallel cables tied to the ground with a single electro-mechanical jack (Figure 7). The jacks are used to adjust the tiedown tension so that the platform remains at a constant elevation while the structure undergoes temperature changes. The three jacks are displacement-controlled and share the same displacement at any point in time. The jack displacement adjusted automatically based on the average elevation of the platform, which is measured from the rim road with laser rangers.

Figure 6: Upgraded structure tiedowns *(photo: NSF).*

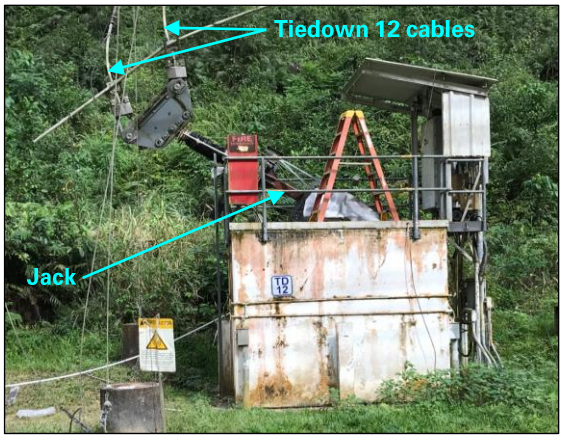

Figure 7: Base of tiedown 12, after telescope collapse.

Each tiedown cable is also equipped with a load cell that measures the cable tension. Cable tensions recorded since 2004 were provided by AO, together with records of the azimuth arm, Gregorian and line feed positions. This data is shown in Figure 8 and Figure 9 for two weeks near the start and end of the data set: the first week of August 2020 (last week of telescope operation, before the first cable failure), and the same week in 2004 (the first year for which tiedown tension data is available). For both weeks, the total tiedown tension (sum of the six tiedown cable tensions) experiences relatively smooth daily cycles compared to the more rapid changes of the azimuth arm, Gregorian and line feed positions, which is consistent with the tiedown jacks being adjusted to compensate only for temperature effects over the course of a day. The total tiedown tension varies between 60 kilopound (kip) and 120 kip in 2004, and between 30 kip and 90 kip in 2020. The overall decrease of 30 kip between 2004 and 2020 may be due to further loads added to the suspended structure or to some relaxation in the cable system supporting the structure. However, in both 2004 and 2020, the total tiedown tension varies by approximately 60 kip each day.

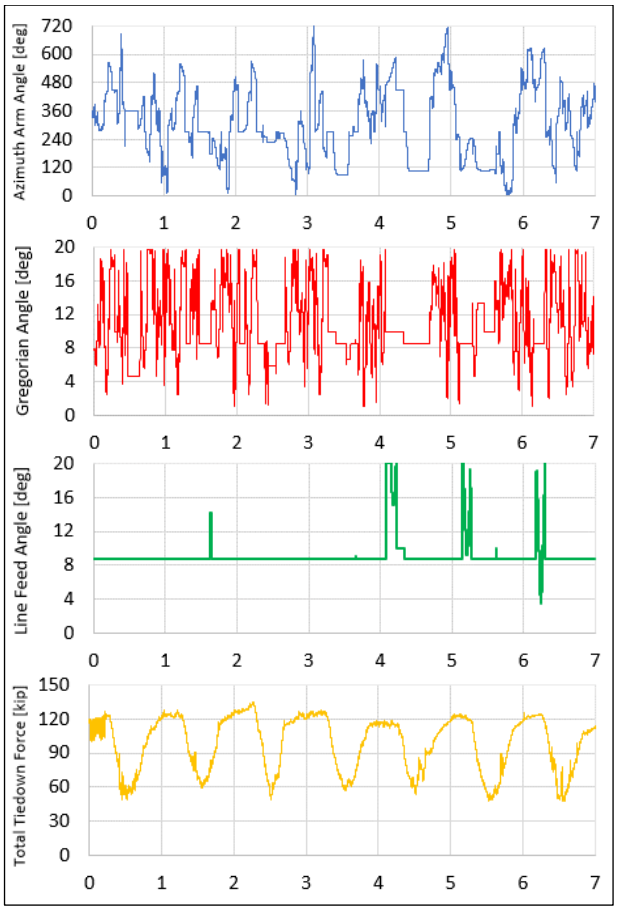

Figure 8: Telescope operation monitoring data for first week of August 2004.

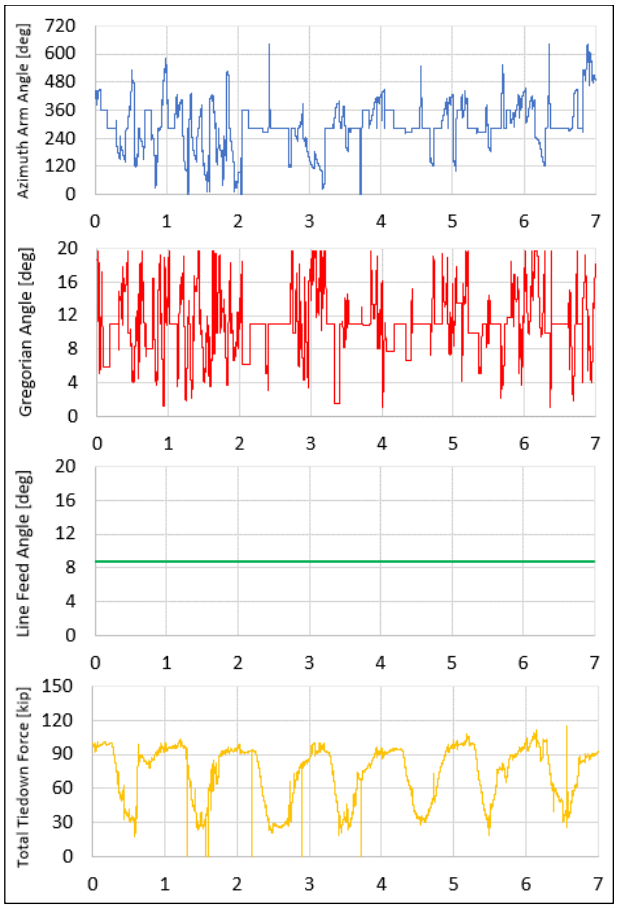

Figure 9: Telescope operation monitoring data for first week of August 2020.

3.0 Analysis

Based on the above data, we performed heat transfer and structural analysis to determine the effect of daily temperature cycles on the cable tensions.

3.1 Concrete Tower Temperature Analysis

No temperature measurements of the concrete towers are available, as far as we know. The towers are made of 6-foot-thick reinforced concrete walls. Since concrete has a relatively low thermal conductivity, most of the tower volume should remain at a constant temperature through the day-night cycle. To verify this, we performed a heat transfer analysis on two tower cross-sections: the top of Tower 4 (smallest tower cross-section) and the bottom of Tower 8 (largest tower cross-section).

The heat transfer analysis was performed in two dimensions, where each tower section is modeled as a single layer of solid elements. The concrete properties considered in the model are summarized in Table 3. To model the daily temperature cycles, we considered a time-dependent adiabatic surface temperature (AST) – the concrete surface temperature when it reaches thermal equilibrium with the environment, accounting for both convective and radiative heat transfers. The AST is assumed to be similar to the temperature measured on the surface of the steel sockets, which varies by 15°F each day

on average (Table 2). For the analysis of the towers, we assumed that the AST varies linearly between 70°F at midnight and 85°F at noon. Convective and radiative heat transfer was modeled between the environment's AST and the concrete surface, and conductive heat transfer was modeled within the concrete. The analysis simulates the temperature cycle over a number of days until a steady state is reached, where the concrete undergoes the same temperature change every day.

The results of the heat transfer analysis are shown in Figure 10 for Tower 4 and Figure 11 for Tower 8. In both cases, the majority of the tower section remains at the same average temperature of 77.5°F, and only the surface of the concrete experiences a temperature cycle. Each day, the average temperature varies by 0.9°F at the top of Tower 4 and by 0.7°F at the bottom of Tower 8. These temperature ranges cause the towers to expand and contract by less than 0.05 inch, which has a negligible impact on the hundreds of feet of cables connected to the towers.

Table 3: Concrete properties for heat transfer analysis.

Thermal conductivity	2.25 W/m/°C
Specific heat	916 J/kg/°C
Mass density	7850 kg/m^3
Surface emissivity	0.9
Convective heat transfer coefficient with air	25 W/m^2/°C
Thermal expansion coefficient	1.0 x 10^{-5}/°C

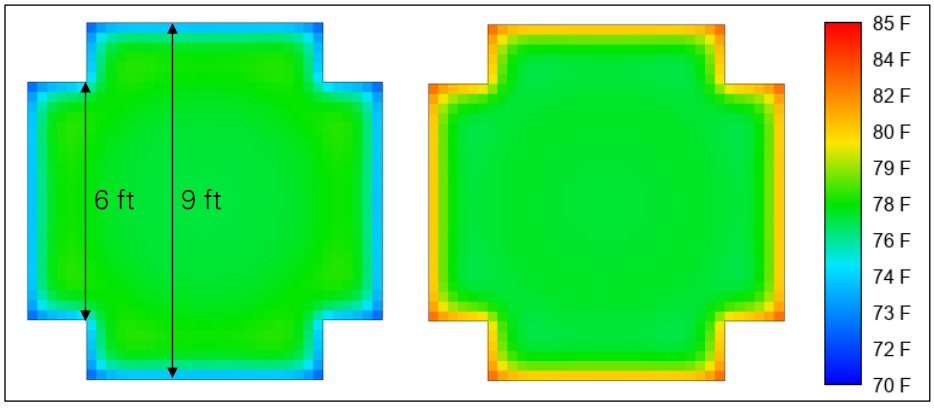

Figure 10: Midnight (left) and noon (right) concrete temperature at top of Tower 4.

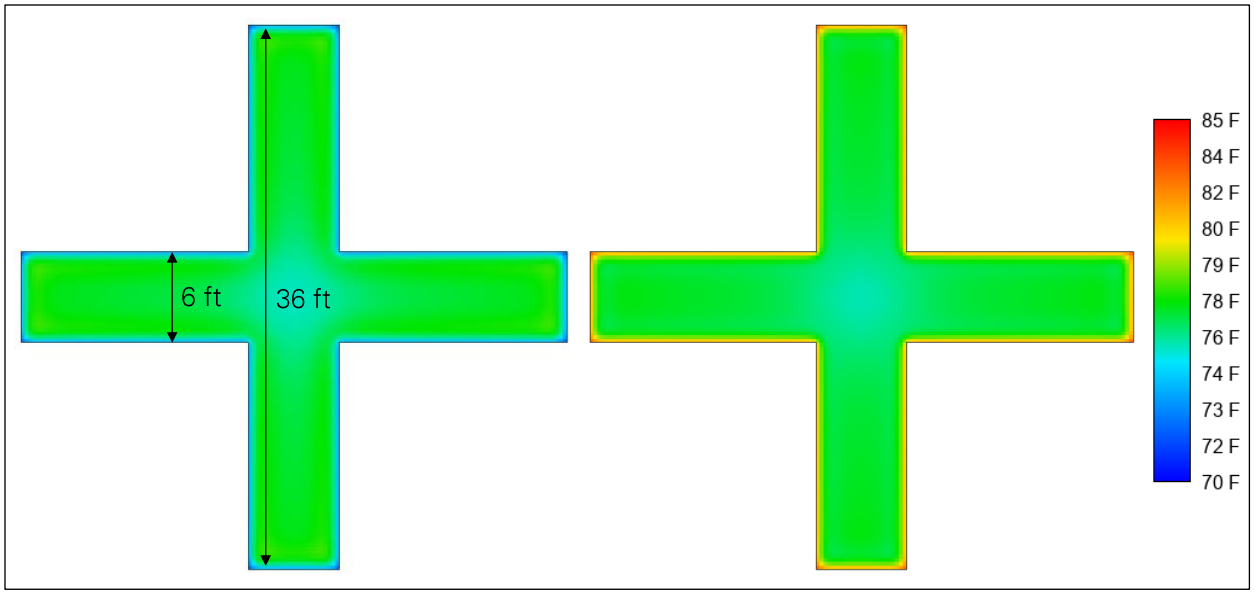

Figure 11: Midnight (left) and noon (right) concrete temperature at bottom of Tower 8.

3.2 Steel Temperature Analysis

The daily temperature range was measured on the surface of six cable sockets in November 2020, with results ranging from 13.4°F to 18.9°F, depending on the socket (section 0 above). As confirmed by these measurements, the daily temperature range is expected to vary locally across the steel structure. For instance, the thicker cables and sockets heat up and cool down more slowly than the lighter steel angles of the platform trusses, and some of the steel surfaces are shielded from direct sunlight more often than others. The steel temperature, however, is not expected to vary significantly between different areas of the telescope, specifically between the cables tied to different towers. This is because the cables and the suspended structure stand higher than the surrounding hills (except for the lower end of the backstays), so that the incident sunlight is uniform over the entire steel structure during most of the day. In addition, the trusses of the suspended structure are too hollow to effectively shield one another from sunlight, and the narrow concrete towers cast only minimal shade on the structure. As a result, to determine the effect of temperature on the cable tensions, we assumed that the entire steel structure experiences the same daily temperature range.

We determined the daily temperature range in the steel from the tiedown tensions of the upgraded structure. The total tiedown tension is known to increase by approximately 60 kip at night as the steel cools down and the tiedown jacks pull down to keep the platform at a constant elevation (section 0 above). Using a finite element model of the telescope structure (Figure 12), we determined the combination of steel temperature drop and jack pull down (two "variables") that results in a 60 kip total tiedown tension increase while keeping the platform elevation constant (two "equations").

The analysis results and the calculation of the daily temperature range in the steel are summarized in Table 4. We first set up the model in a reference state representing the daily high temperature, with the telescope stowed and the tiedowns taut. We then simulated two hypothetical scenarios: a steel temperature drop of 10°F without any jack movement, and a jack pull down of one inch without any steel temperature change. For both scenarios, the model provides the changes in tiedown tension and platform elevation. From these results, we calculated that to increase the tiedown tension by 60 kip

while keeping the platform elevation constant, the steel temperature must decrease by 15.8°F while the jacks must pull down by 3.35 inches.

The average daily temperature range in the steel is therefore 15.8°F, which is consistent with the temperature range of between 13.4°F and 18.9°F measured on the surface of six cable sockets in 2020 (section 0 above). It is also consistent with the average temperature range of 12.3°F in the air (section 2.1 above), as solar radiation heats up the steel to above the air temperature.

The tiedown jacks are not always active, for example when the telescope is not operating. From the previous analysis results, we calculated that without tiedown jacking, the platform rises by two inches at night (Table 4). The typical day-night cycles with and without tiedown jacking are illustrated in Figure 13 and Figure 14.

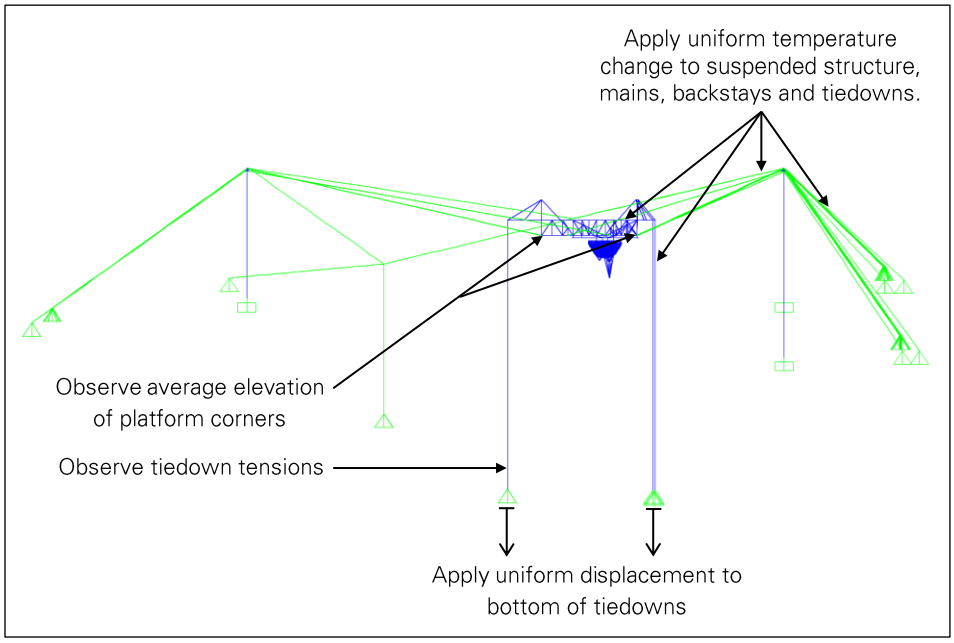

Figure 12: Finite element model (SAP2000) setup for steel temperature analysis.

Table 4: Calculation of steel temperature change from analysis results.

Case	Difference with Reference Case			
	Steel Temperature [°F]	**Tiedown Jack Length [in]**	**Platform Elevation [in]**	**Total Tiedown Tension [kip]**
Reference = Daily high temperature (daytime)	0	0	0	0
Cool down steel by 10°F	- 10	0	+ 1.27	+ 25
Pull down 1 inch on tiedowns	0	-1.00	- 0.60	+ 6
Daily low temperature (nighttime)	- 15.8	- 3.35	**0**	**+ 60**
Daily low temperature without tiedown jacking	- 15.8	0	+ 2.01	+ 40

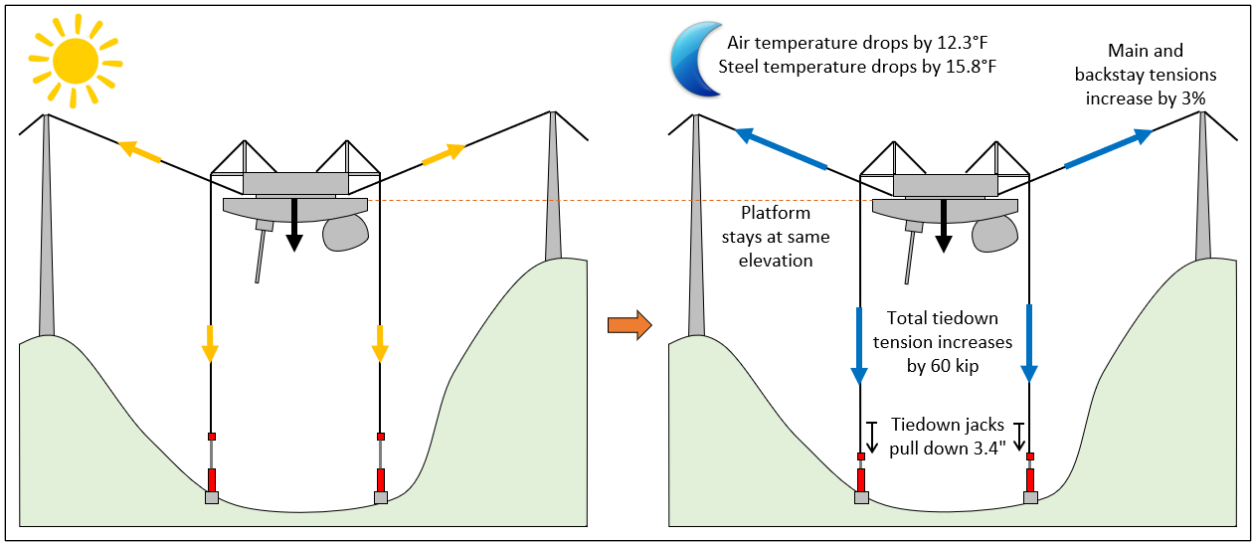

Figure 13: Typical day-night cycle in upgraded structure with tiedown jacking.

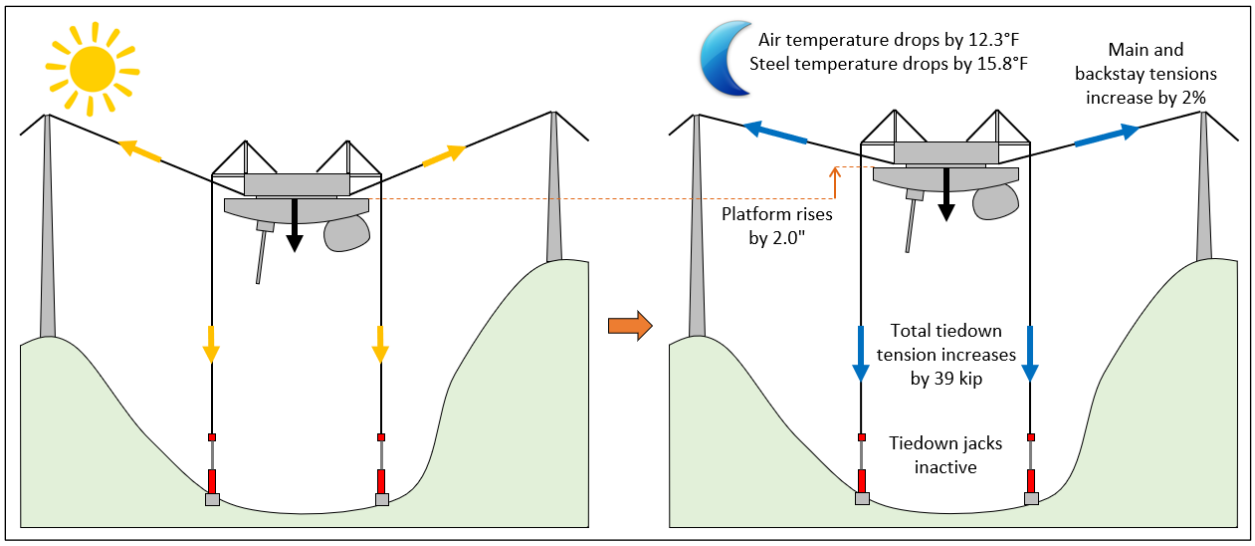

Figure 14: Typical day-night cycle in upgraded structure without tiedown jacking.

3.3 Cable Tension Analysis

To determine the effect of temperature changes on the cable tensions, we simulated a day-night cycle in the models of the original and upgraded structures. In both cases, the steel structure is assumed to cool down uniformly by 15.8°F at night (section 3.2 above) while the temperature of the concrete towers remains constant (section 3.1 above). Both analyses are performed with the telescope in stowed position.

In the original structure, each of the six inclined tiedowns is assumed to carry a tension of 11 kip when the temperature is at its maximum, which is the estimated tiedown tension after the first upgrade of the telescope in 1974. The inclined tiedowns of the original structure are not equipped with jacks and react passively to the temperature change. We applied the 15.8°F temperature drop to the steel in the model, and the cable tension results are presented in section 4.0 below.

In the upgraded structure, each tiedown cable is assumed to carry a tension of 10 kip when the temperature is at its maximum, for a total of 60 kip. This matches the daytime total tiedown tension in the earliest telescope monitoring data available to us (section 0 above). We considered the earliest data because the total tiedown tension decreases over the years. The tiedowns of the upgraded structure are equipped with jacks, and we determined that the jacks pull down by 3.35 inches as the structure cools down to keep the platform elevation constant (section 3.2 above). To simulate the day-night cycle, we applied the temperature drop and jack pull down simultaneously in the model. The cable tension results are presented in section 4.0 below.

4.0 Cable Tension Results

The results presented in this section describe the impact of the typical daily temperature cycle on the cable tensions. These results assume that the telescope does not move and experiences no other environmental loads.

4.1 Original Structure

In the original structure, the main and backstay tensions vary by approximately 2.5 percent during the daily temperature cycle (Figure 15), while the normalized stress range (ratio of cable tension change to cable minimum breaking strength) is approximately one percent (Figure 16). From a material fatigue perspective, these tension fluctuations are minimal.

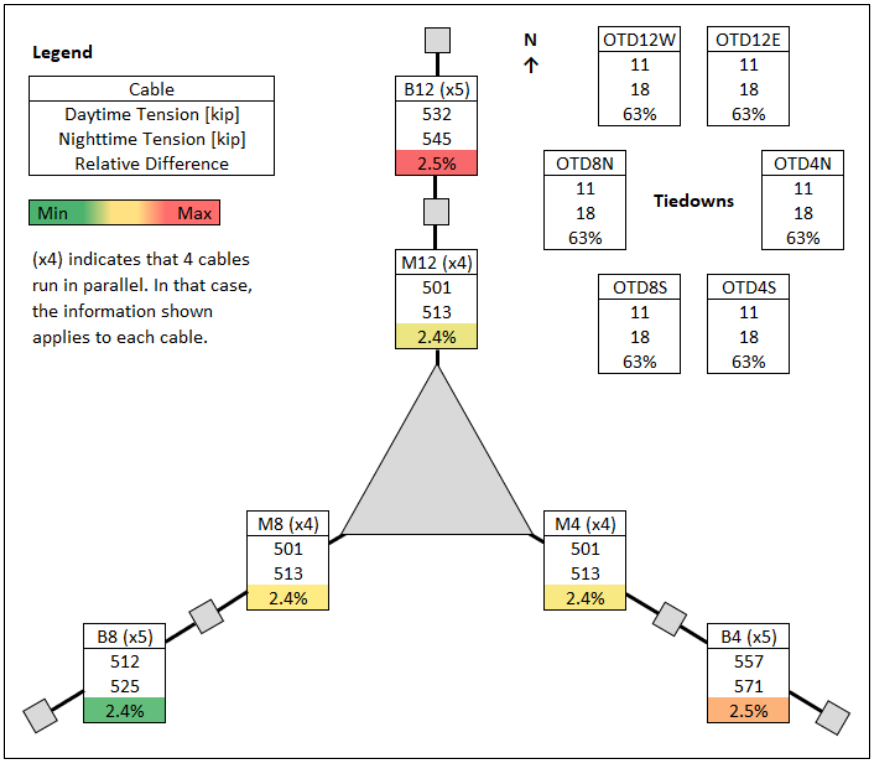

Figure 15: Cable tension change due to daily temperature cycle in original structure.

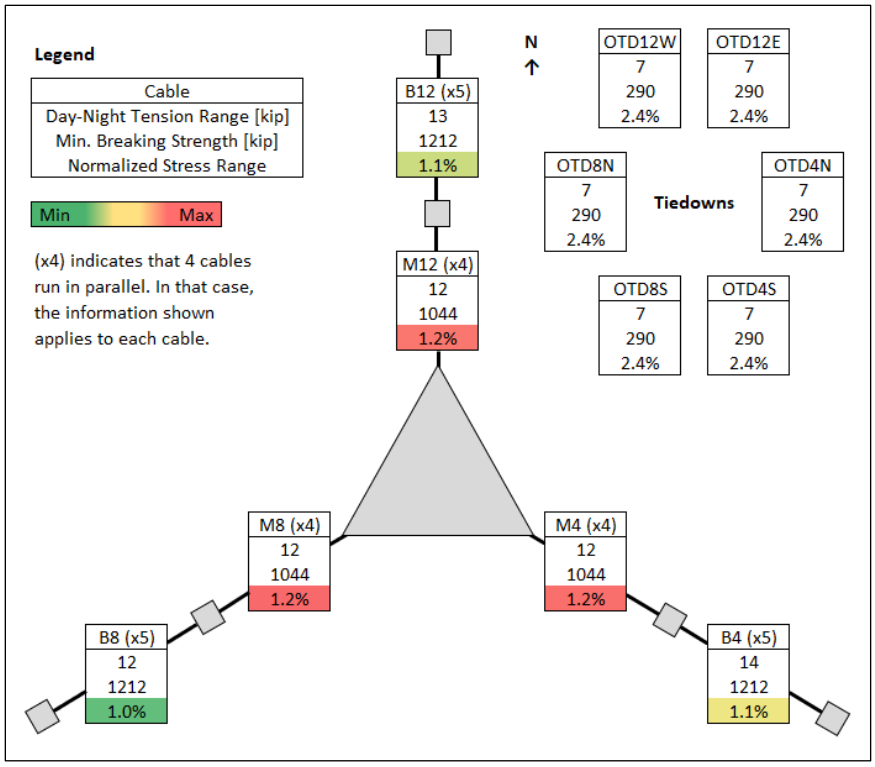

Figure 16: Cable normalized stress range due to daily temperature cycle in original structure.

4.2 Upgraded Structure

In the upgraded structure, the main and backstay tensions vary by approximately three percent during the daily temperature cycle (Figure 17), and the normalized stress range varies between one and two percent (Figure 18). While still low from a material fatigue perspective, the cable tension fluctuations are wider in the upgraded structure than in the original structure due to the tiedown jacks, which increase the tiedown tensions at night beyond the effect of the steel cooling down.

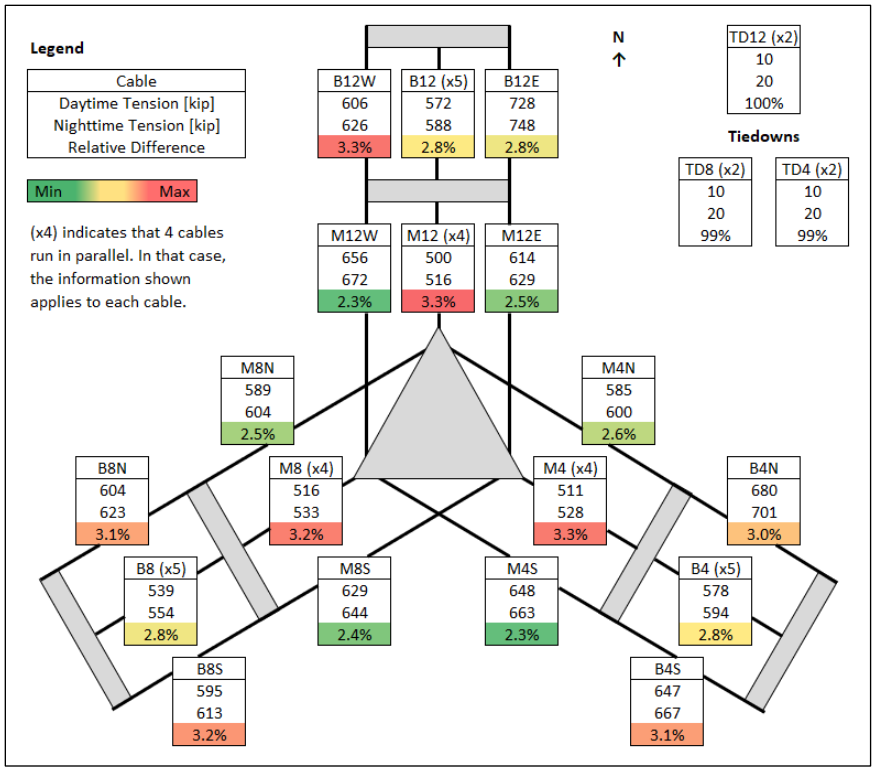

Figure 17: Cable tension change due to daily temperature cycle in upgraded structure.

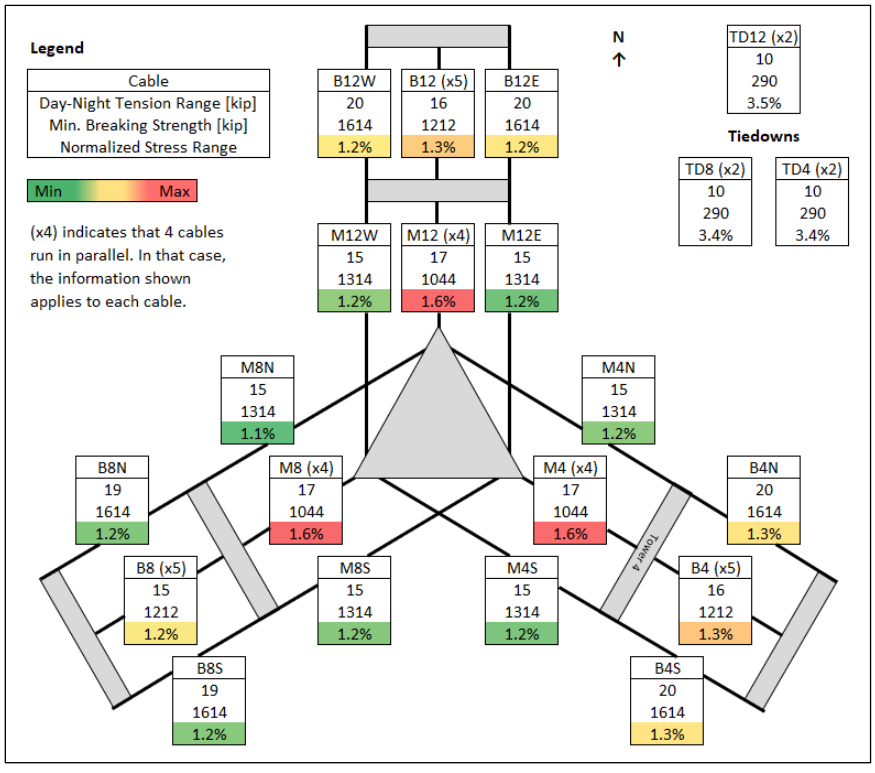

Figure 18: Cable normalized stress range due to daily temperature cycle in upgraded structure.

Appendix J
Wind Impact on Cable Tensions

1.0 Introduction

Tropical storms and hurricanes regularly impact the island of Puerto Rico in the summer months, which can subject the telescope to high sustained and fluctuating wind loads. Our analysis of the wind loads effects on the telescope's cable system is presented in this appendix.

The highest instantaneous wind speed ever recorded at Arecibo Observatory is 110 mph and occurred as the eye of Hurricane Maria approached the site on September 20, 2017. While the hurricane caused widespread destruction in Puerto Rico, the only significant damage reported on the telescope was a failure of the line feed (Figure 1). However, because of the relatively short time between Hurricane Maria and the telescope's first cable failure (August 10, 2020), it is natural to investigate the storm as a potential factor contributing to the collapse. Hurricane Maria is therefore used as a reference load throughout our analysis of the wind load effects.

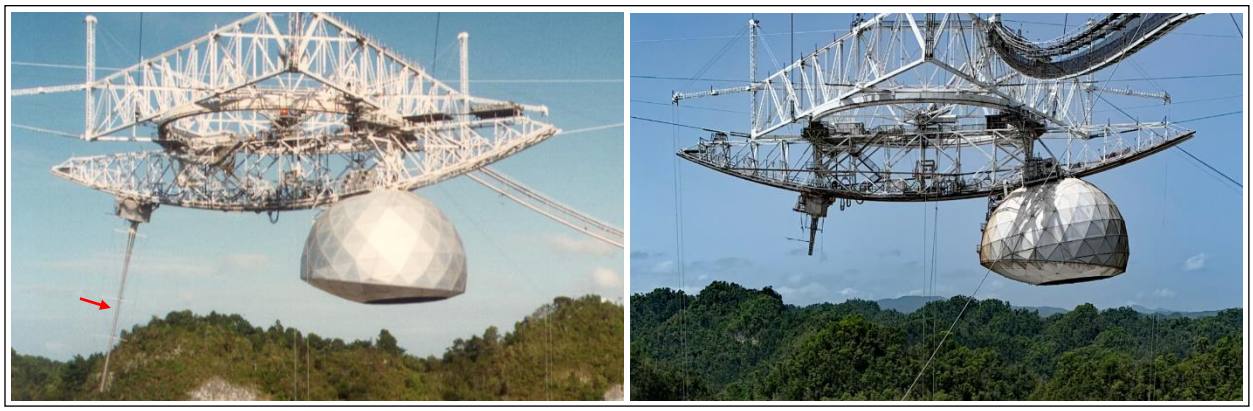

Figure 1: Suspended structure before (left) and after (right) Hurricane Maria, with damage to the line feed
(left photo: NAIC Arecibo Observatory, a facility of the NSF;
right photo: Mario Roberto Duran Ortiz, Wikipedia - CC By-SA 4.0).

2.0 Design Considerations

We reviewed the structural design documents and associated correspondence produced during the construction and upgrades of the telescope. Our findings are summarized in this section.

2.1 Design Wind Speed

The documents we reviewed indicate that different wind speeds were considered for the design of the original structure and the two upgrades.

The structural drawings for the original structure[1] indicate a design wind speed of 140 mph. Before the first upgrade of the telescope, a feasibility study by Ammann & Whitney (AW)[2] determined that the speed of 140 mph corresponds to the 300-year wind event at the telescope's site, and that the 100-year

[1] Praeger-Kavanagh. Structural drawings for original telescope. December 1, 1960. Drawings provided by Arecibo Observatory.

[2] Ammann & Whitney. *Feasibility Study and Concept Development for Upgrading of Suspended Antenna Structure.* August 1972. Report retrieved from Cornell University archives.

wind speed is only 114 mph. AW's structural drawings for the first upgrade[3] indicate a design wind speed of 110 mph, suggesting that the 100-year wind event was selected as design event.

Before the second upgrade of the telescope, the design wind speed was discussed between AW (engineer of record), Radiation Systems Inc (RSI, prime contractor for the upgrade), Temcor (engineer for the Gregorian), and West Wind Laboratory (WWL, contracted to perform a wind tunnel study of the Gregorian). AW had specified a wind speed of 100 mph for the design of the second upgrade,[4] but WWL's report on the wind tunnel test of the Gregorian included a recommendation to use a much higher speed of 153 mph.[5] AW increased the design wind speed to 110 mph based on newly available data but dismissed the 153 mph recommendation as too conservative and based on an unsolicited study by WWL.[6] AW also clarified that 110 mph would be used for the global structural design of the upgrade, which includes the calculation of cable tensions, while Temcor may consider a higher wind speed as deemed appropriate for the local design of the Gregorian enclosure. WWL maintained their recommendation of 153 mph but also determined that the Gregorian enclosure should be designed for 123 mph[7] to be consistent with the 110 mph selected by AW for the global structural design. AW confirmed the two speeds of 110 mph and 123 mph for the global and local design of the upgrade respectively[8] and, to our knowledge, the final design was based on those wind speeds.

2.2 Design Wind Load and Cables Tensions

The structural drawings for the original and upgraded structures indicate the maximum cable tensions calculated under dead load and the combination of dead load and design wind load. These tensions are summarized in Table 1, where the relative tension increase due to wind is also calculated. While wind increases the cable tensions by up to 26 percent in the original structure, the increase is less than six percent in the upgraded structure. This difference is due to three factors. First, the design wind speed was lowered from 140 mph to 110 mph between the original design and the second upgrade (section 2.1 above). Then, the second upgrade added 12 cables to the system, such that more cables shared the wind load. And finally, the design of the upgraded structure assumes that the tiedown cables between the platform and the ground are partially released before the arrival of a significant storm, purposefully to reduce the cable tensions.

From the cable tensions provided in the drawings and the known geometry of the cable system, we back-calculated the total design wind load on the suspended structure. The calculation assumes that the maximum tension in a cable occurs when the wind blows in the cable's direction towards the suspended structure (e.g. the maximum tension in the Tower 12 mains occurs when the wind blows south). The

[3] Ammann & Whitney. Structural drawings for first upgrade of telescope. October 20, 1972. Drawings retrieved from Cornell University archives.

[4] Amman & Whitney. Structural drawings for second upgrade of telescope. 1992. Drawings provided by Arecibo Observatory.

[5] West Wind Laboratory, Inc. *Wind Study of Arecibo Radio Observatory.* December 1993. Report retrieved from Cornell University archives.

[6] Joseph Vellozzi (Ammann & Whitney). Letter to William Terry (Radiation Systems Inc). January 18, 1994. Correspondence retrieved from Cornell University archives.

[7] Jon Raggett (West Wind Laboratory, Inc). Letter to Alfonso Lopez (Temcor). January 31, 1994. Correspondence retrieved from Cornell University archives.

[8] Joseph Vellozzi (Ammann & Whitney). Letter to Walter Marusak (Radiation Systems Inc). March 8, 1994. Correspondence retrieved from Cornell University archives.

suspended structure is assumed rigid, and the wind load is assumed horizontal only (no uplift or downdrag). The pre-storm tiedown release is taken into account in the upgraded structure. We determined a total design wind load of 675 kilopound (kip) for the original structure and 444 kip for the upgraded structure (Figure 2).

Before the second upgrade, a wind tunnel study was performed on the Gregorian dome (section 2.3 below). However, we found no record of any wind tunnel study on the steel trusses making up the rest of the suspended structure. Therefore, it is likely that the wind loads on the trusses were determined analytically. This is typically done through some variant of a drag calculation where the wind load is proportional to the square of the wind speed and to the structure's area modified by a drag coefficient. From the design wind speed and load previously determined, we back-calculated the effective product of drag coefficient and surface area (Table 2). We note that this quantity increases by only 7 percent between the original to upgraded structures, even though the Gregorian dome adds significant surface area. This may be explained by the lower drag coefficient of the Gregorian dome compared to steel trusses and possibly the use of different assumptions in the calculation of the load on the steel trusses.

Table 1: Design wind load and cable tensions in structural drawings of original and upgraded telescope.

		Original Structure			Upgraded Structure		
		Dead Load Only [kip]	Dead Load + Design Wind [kip]	Relative Increase due to Wind	Dead Load Only [kip]	Dead Load + Design Wind [kip]	Relative Increase due to Wind
Original Cables	Mains	527	642	+22%	480	496	+3%
	Tower 4 Backstays	593	748	+26%	543	577	+6%
	Tower 8 Backstays	541	682	+26%	503	532	+6%
	Tower 12 Backstays	566	696	+23%	514	540	+5%
Auxiliary Cables	Mains	-	-	-	602	622	+3%
	Tower 4 Backstays	-	-	-	728	769	+6%
	Tower 8 Backstays	-	-	-	662	698	+5%
	Tower 12 Backstays	-	-	-	727	760	+5%

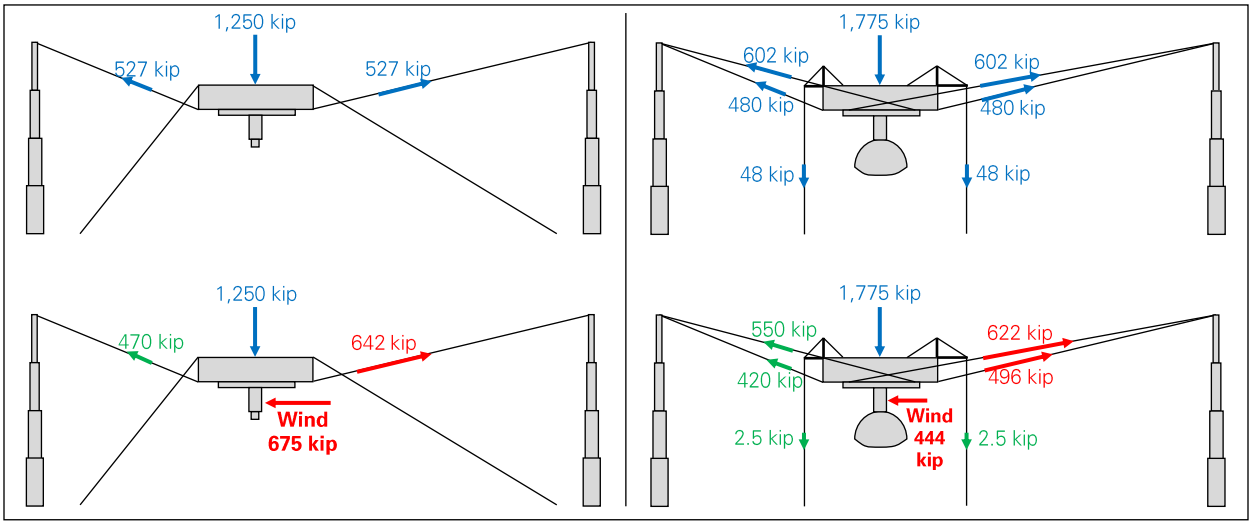

Figure 2: Equilibrium of original (left) and upgraded (right) structures under design wind load and cable tensions.

Table 2: Design wind load information derived from structural drawings.

	Original Structure	Upgraded Structure
Design Wind Speed [mph]	140	110
Design Wind Load [kip]	675	444
Effective Drag Coefficient x Area[A] [ft²]	13,480	14,360

[A] Calculated as F / (0.5 ρ V²) where F is the wind load, ρ the mass density of air and V the wind velocity

2.3 Gregorian Wind Tunnel Test

A wind tunnel study was performed in 1993 as part of the engineering of the telescope's second upgrade. The study was conducted by West Wind Laboratory (WWL). Its objective was to determine the maximum wind pressures on the surface of the Gregorian dome, to be used by Temcor to design the dome enclosure. However, WWL also integrated the wind pressures over the dome's surface to determine the total wind loads on the dome, which are provided in their report. While we could not confirm all of the assumptions and parameters used by WWL, this wind tunnel study remains a valuable data point to compare to our calculations and computational fluid dynamic (CFD) analyses.

The wind tunnel tests relied on a typical method for testing large structures, where the structure's dimensions and the wind speed are both scaled-down. As long as the airflow in the test is still fully turbulent, as is for the full-size structure during a hurricane, the wind forces from the test can be scaled back to the full-size structure. Additional details are provided in section 5.1, where the same method is applied to CFD analysis results.

The tests were performed on a 1:125 scaled model (approximately 2.5 feet) of the suspended structure (Figure 3). While the model also included the platform and azimuth arm, only the Gregorian was equipped with pressure taps. At least three tests were performed with the wind coming from three different directions (Gregorian's front, back, and side). An additional test was performed on a cylinder with a diameter similar to Gregorian's model (Figure 3). The force on the cylinder was found to agree well with the expected drag force on a cylinder in a turbulent regime, confirming that the test regime was fully turbulent.

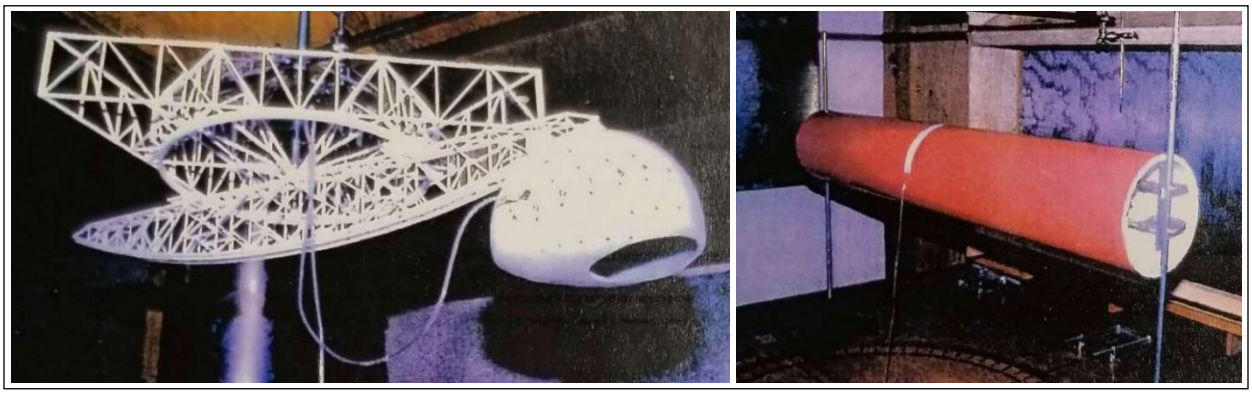

Figure 3: Model of suspended structure (left) and calibration cylinder (right) during 1993 wind tunnel tests. *(photos: West Wind Laboratory).*

The resultant forces on the Gregorian determined from the wind tunnel tests are presented in Figure 4, after scaling to the 110 mph design wind speed. An effective drag coefficient is then calculated in Table 3 for each wind direction.

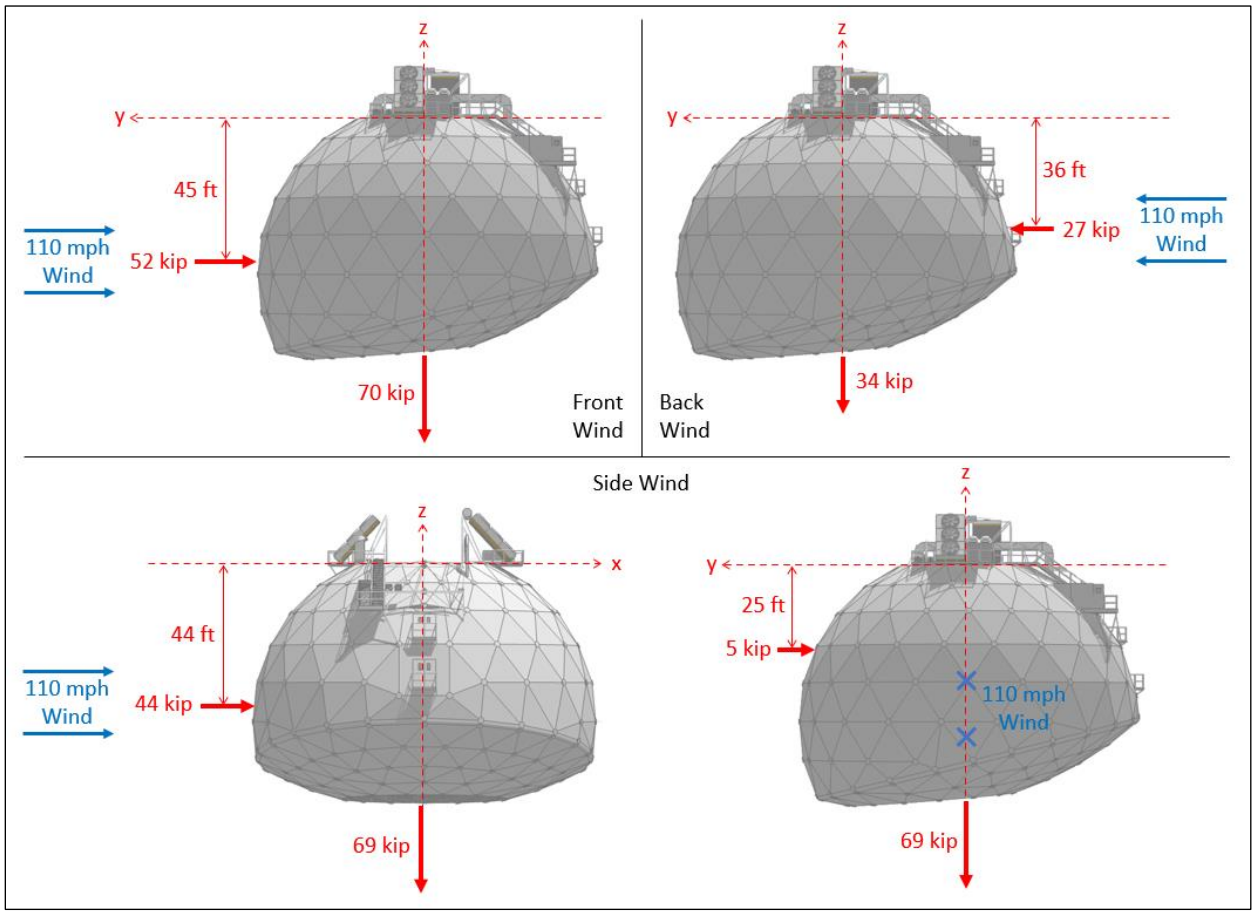

Figure 4: Gregorian wind tunnel test results, scaled to 110 mph wind speed *(images: Sketchup 3D Warehouse).*

Table 3: Gregorian effective drag coefficient calculation from wind tunnel test results.

Wind Speed V [mph]		110		
Air Mass Density ρ [lbf.s^2.ft^{-4}]		0.00238		
Dynamic Wind Pressure P = 0.5 ρ V^2 [psf]		31.0		
Wind Direction		From Front (-y)	From Back (+y)	From Side (±x)
Along Wind	**Wind Load F [kip]**	52	27	44
	Projected Area A [ft2]	3850	3850	3850
	Effective Drag Coefficient C = F / P / A	0.44	0.23	0.37
Cross Wind	**Wind Load [kip]**	0	0	5

3.0 Data

Our analysis of the telescope's response to wind loads relies on two sets of data recorded over time at the Observatory: the wind speed and direction and the telescope's tiedown tensions.

3.1 Wind Speed and Direction

The telescope's platform was equipped with a weather station that measured wind speed and direction, among other meteorological parameters (Figure 5). The wind speed was measured by two independent instruments: an anemometer and a doppler.

The doppler data was plotted by AO for several windstorms, such as Hurricane Maria, as shown in Figure 6. The plots show the wind slowing down to almost zero and reversing direction as the eye of the storm passes over the Observatory. We also note that the maximum instantaneous wind speed recorded during the storm is 108 mph, or two percent less than the second upgrade's design wind speed of 110 mph.

Figure 5: Location of weather station on suspended structure
(photo: Mario Roberto Duran Ortiz, Wikipedia - CC By-SA 4.0).

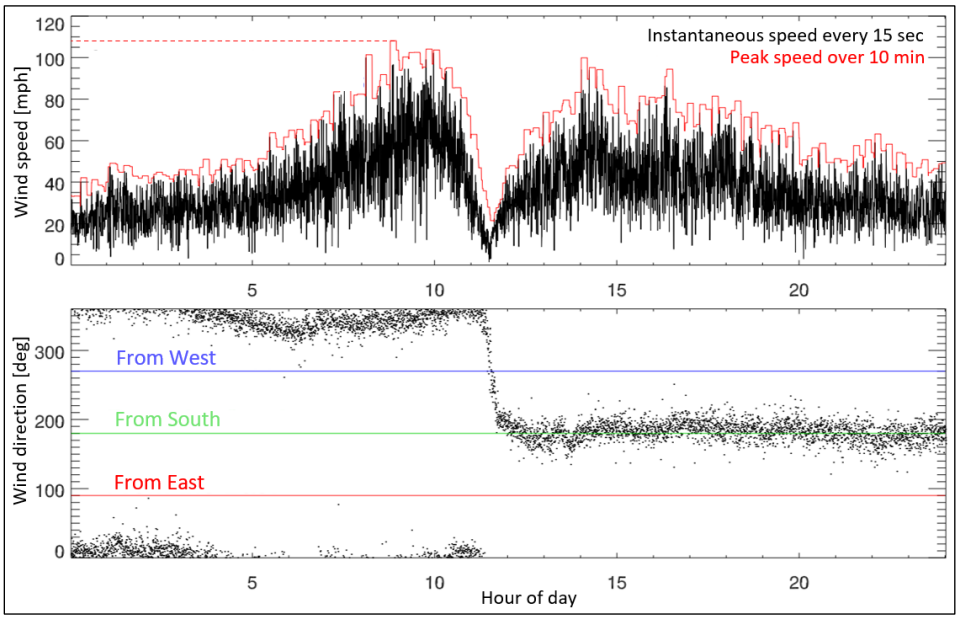

Figure 6: Wind speed and direction on suspended structure on September 20, 2017 as hurricane Maria passes over the Observatory *(images: NAIC Arecibo Observatory, a facility of the NSF).*

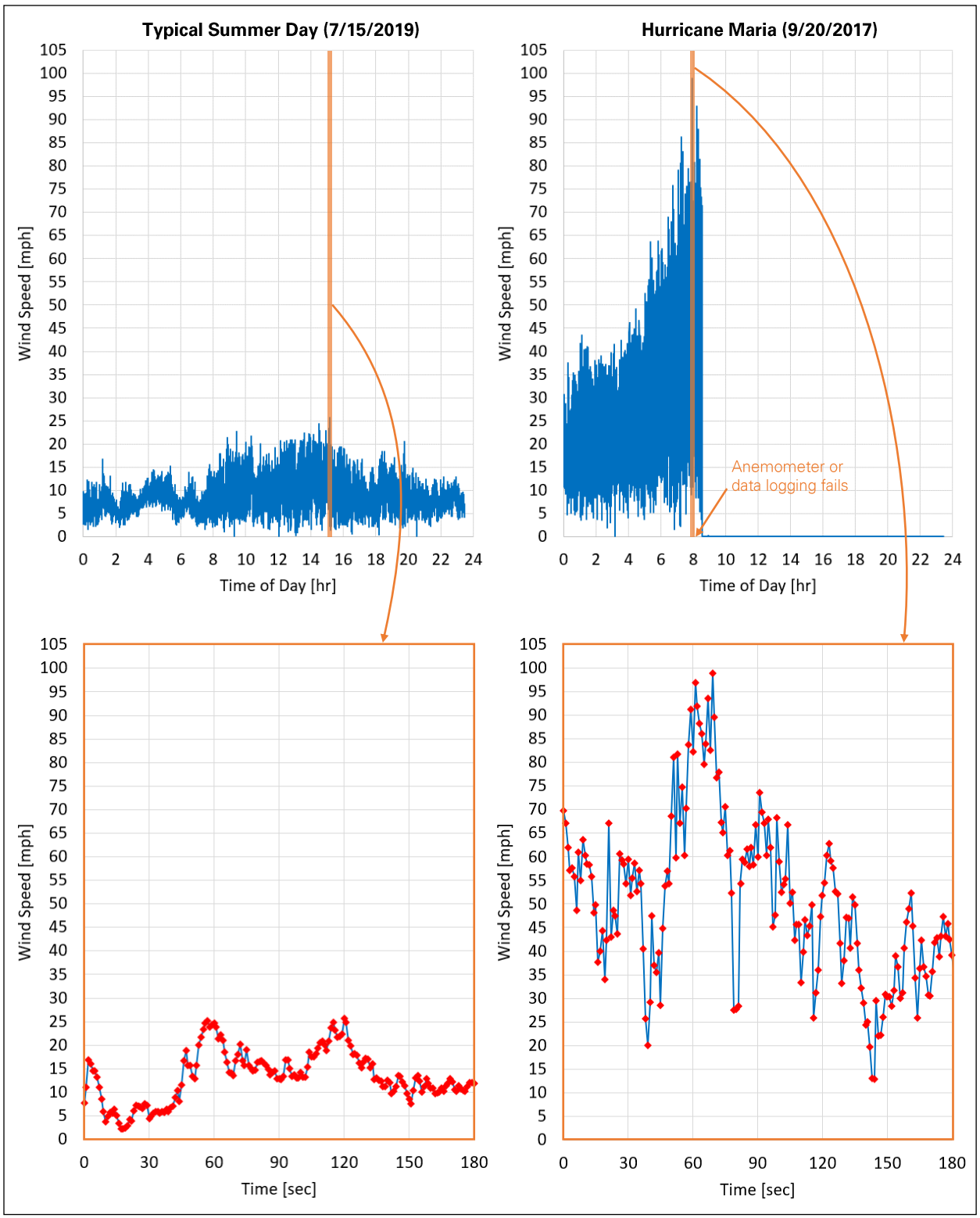

Figure 7: Wind speed recorded at one Hertz on a typical summer day and during Hurricane Maria.

The anemometer data was logged at one-second intervals from 2005 to the collapse in 2020, and the complete data set was provided to us by AO. While the data has gaps, likely due to power outages and equipment malfunctions, it captures several major windstorms and otherwise records the ambient wind on regular days. For two reasons, the anemometer data is particularly valuable to study the suspended structure's dynamic response to wind loads. First, it was measured directly on the suspended structure and therefore does not need to be scaled or modified to account for elevation or topographic effects. And second, it was recorded at shorter time intervals (one second) than the period of the structure's first mode of vibration (approximately three seconds), such that the wind's frequency content that could impact the structure's dynamic response is expected to be reasonably well captured in the data.

Excerpts of the anemometer data are provided in Figure 7 for a typical summer day and on the day of Hurricane Maria. The data for Hurricane Maria stops at 8:30 AM due to power loss or damage to the system.

3.2 Telescope Tiedown Tensions

The three tiedowns of the upgraded structure, which connected the platform to the ground, were equipped with load cells that measured the tiedown tensions continuously. Each tiedown consisted of two parallel cables, and each cable had its own load cell. The tiedown cable tensions were logged at one-second intervals since 2004, and the complete data set was provided to us by AO.

The tiedown tensions can be used to evaluate the vertical movement of the suspended structure during windstorms. While the tiedown tensions are usually affected by the tiedown jacks' action and the daily temperature cycles, the jacks were locked in place during storms and the temperature effects are much slower and easily discernable from wind-induced vibrations. A limitation is that the tiedown jacks were locked in an extended position to decrease the tiedown tensions and stress in the overall cable system. As a result, the tiedown tensions were relatively low during storms, which may affect the accuracy of the load cells.

The tiedown tensions recorded during Hurricane Maria are shown in Figure 8. For tiedowns 8 and 12, the tiedown tension is calculated as the sum of the tensions in the tiedown's pair of load cells. For tiedown 4, the tiedown tension is calculated as twice the tension in one of the load cells, as the other load cell recorded unrealistically high values even before the storm. Finally, the total tiedown tension is also calculated. We observe that the three tiedown tensions are generally synchronized and fluctuate at a three-second period (3 data points per cycle), which is consistent with the period of the suspended structure's first mode of vibration.

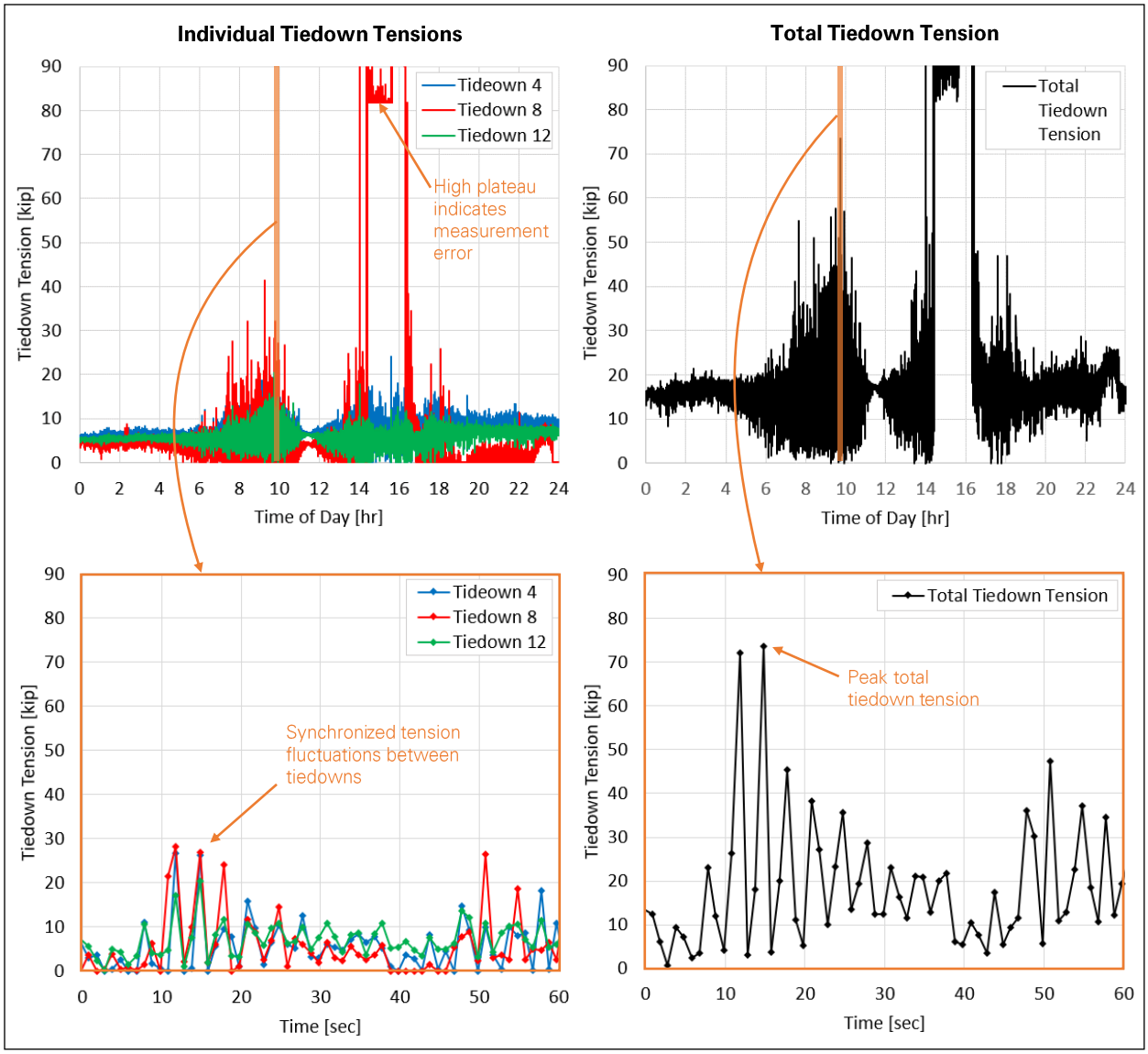

Figure 8: Tiedown tensions recorded during Hurricane Maria.

4.0 Static Wind Load Calculations

As a first analysis, we estimated the wind loads on the upgraded telescope through first-principle and standard structural design calculations. This type of calculation is inherently approximate, and the structure's unique features require making assumptions that increase the uncertainty on the results. Yet, those results remain a valuable basis for validating the more complex analyses presented in the rest of this appendix. All of the calculations presented in this section estimate the static wind load induced by the reference wind speed of 110 mph considered in this study.

4.1 Suspended Structure

4.1.1 Platform and Azimuth Arm

The platform and azimuth arm are three-dimensional truss structures through which wind can flow. Wind can induce significant loads on this type of structure as it passes through several trusses that do not effectively shield one another.

To estimate the wind loads, we first applied two methods provided in the ASCE7-16[9] standard to calculate design wind loads on open structures (*Open Signs and Frames* for the first method, and *Trussed Towers* for the second method). Both methods rely on the structure's *solidity ratio*, which measures how open the structure is. First, the solidity ratio of the platform and azimuth arm are determined, as shown in Figure 9. Each method then provides an empirical formula to calculate an effective drag coefficient from the solidity ratio.

As a third method, we calculated the wind load assuming that the platform and azimuth arm were solid blocks with drag coefficients of 1.0.

All three methods require a dynamic wind pressure, calculated in Table 4 per the ASCE7-16 procedure. The wind load per the three methods is then calculated in Table 5.

Table 4: Calculation of dynamic wind pressure on platform and azimuth arm per ASCE7-16.

Quantity	Calculation or Assumption	Notes
Basic wind speed	V = 110 mph	Reference wind speed in this appendix.
Exposure category	B	
Terrain exposure constants	$\alpha = 7$ $z_g = 1{,}200$ ft	From exposure category.
Ground elevation factor	$K_e = 1.0$	Conservative. Neglects elevation above sea level.
Topographic factor	$K_{zt} = 1.0$	
Wind directionality factor	$K_d = 0.85$	Fixed value for *Open Signs and Frames* and *Trussed Towers* methods
Height above ground	z = 515 ft	Suspended structure average elevation above bottom of reflector
Velocity pressure coefficient	$K_z = 2.01\ (z/z_g)^{(2/\alpha)} = 1.58$	
Velocity pressure	$q_z = 0.00256\ K_z\ K_{zt}\ K_d\ K_e\ V^2 = 41.6$ psf	
Gust factor	G = 1.0	
Dynamic pressure	$q_z\ G = 41.6$ psf	

[9] American Society of Civil Engineers (ASCE). *ASCE 7-16. Minimum Design Loads and Associated Criteria for Buildings and Other Structures.* Chapters 26 and 29. 2016.

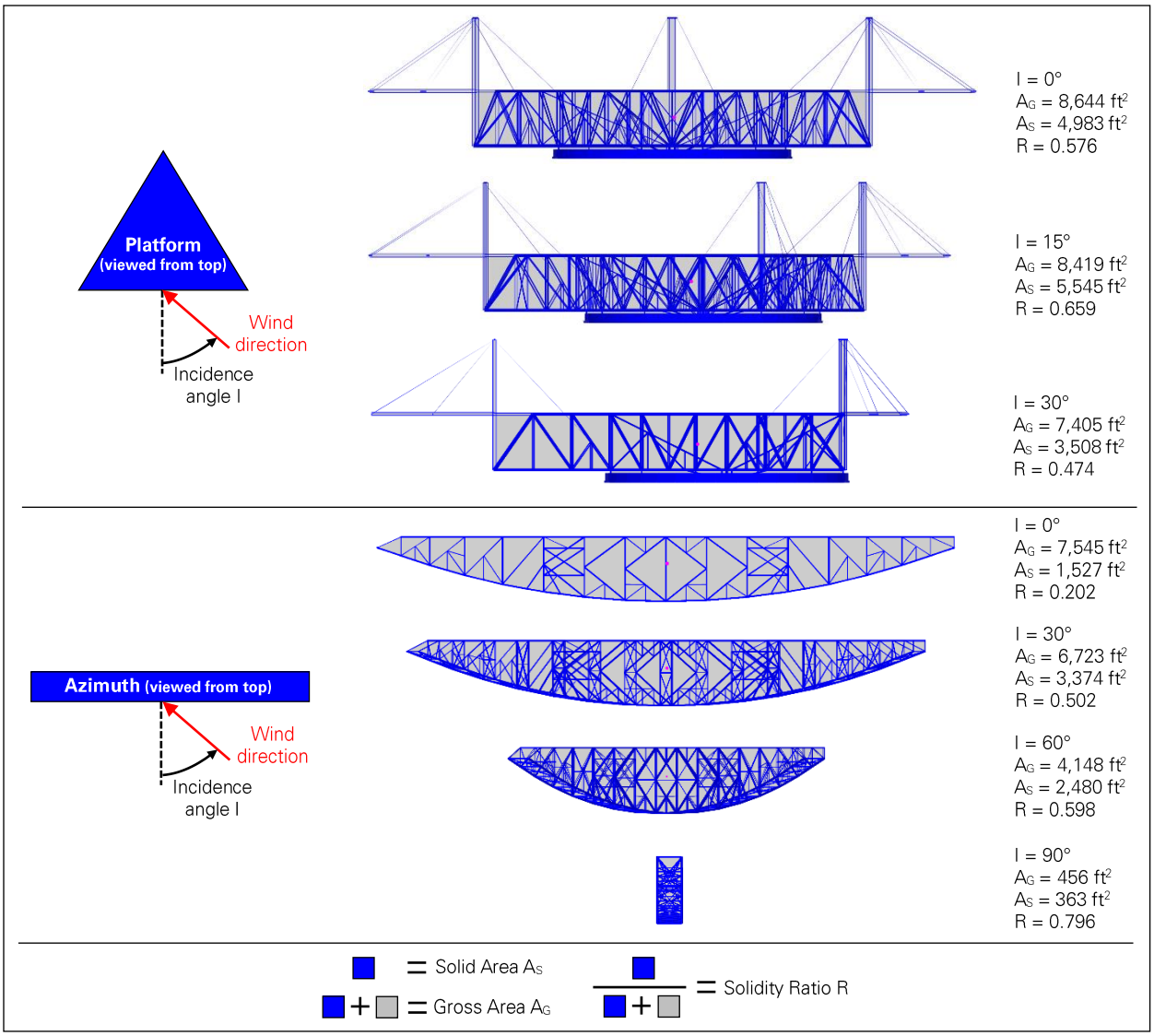

Figure 9: Platform and azimuth arm area properties for wind load calculation.

Table 5: Platform and azimuth arm wind load calculations at 110 mph (q_z G = 41.6 psf).

		Platform			Azimuth Arm			
Properties	**Incidence angle I [deg]**	0	15	30	0	30	60	90
	Gross area A_G [ft²]	8,644	8,419	7,405	7,545	6,723	4,148	456
	Solid area A_S [ft²]	4,983	5,545	3,508	1,527	3,374	2,480	363
	Solidity ratio R = A_S / A_G	0.576	0.659	0.474	0.202	0.502	0.598	0.796
ASCE7 *Open Signs and Frames* method	**Drag coeff.** $C = \begin{cases} 2.0 & R < 0.1 \\ 1.8 & 0.1 < R < 0.3 \\ 1.6 & R > 0.3 \end{cases}$	1.6	1.6	1.6	1.8	1.6	1.6	1.6
	Wind load F = q_z G C A_s [kip]	332	369	234	114	225	165	24
ASCE7 *Trussed Towers* method	**Drag coeff. C = 4 R^2 – 5.9 R + 4**	1.93	1.85	2.10	2.97	2.05	1.90	1.84
	Wind load F = q_z G C A_s [kip]	400	427	307	189	287	196	28
Solid drag method	**Drag coefficient C**	1.0	1.0	1.0	1.0	1.0	1.0	1.0
	Wind load F = q_z G C A_G [kip]	360	350	308	314	280	173	19

4.1.2 Gregorian

The wind load on the Gregorian is estimated through the simple drag force calculation shown in Table 6. Based on the hemispherical shape of the Gregorian dome, a drag coefficient of 0.5 is considered.

Table 6: Gregorian wind load calculation.

Quantity	Calculation or Assumption	Notes
Dynamic wind pressure	q_z G = 41.6 psf	Section 4.1.1 above.
Projected area	A = 3,850 ft^2	Approximately the same for all wind directions
Drag coefficient	C = 0.5	Drag coefficient for a sphere
Wind load	F = q_z G C A = 80 kip	

4.1.3 Total

The wind loads calculated above for the platform, azimuth arm, and Gregorian are combined in Figure 10 to obtain the total load on the suspended structure. The telescope is assumed to be in the stowed position, where the azimuth arm is 12 degrees off of the east-west direction. The total wind load is minimum when the wind is parallel to the azimuth arm. The three calculation methods result in total wind loads within 30 percent of each other for any wind direction.

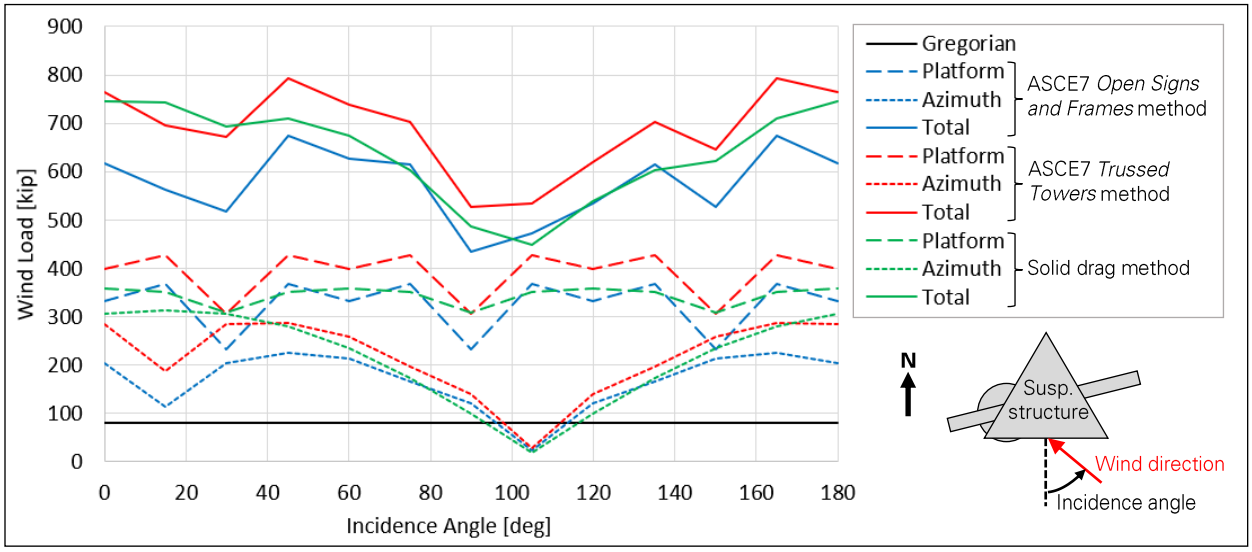

Figure 10: Calculated 110 mph wind load on suspended structure.

4.2 Towers

To estimate the wind load on the telescope's towers, we applied the method provided in ASCE7-16[10] to calculate design wind loads on *Chimneys, Tanks and Similar Structures*. This method is typically used for tall smokestacks, whose aspect ratios are comparable to the Arecibo towers.

The calculation and results are presented in Table 7 and Figure 11, where a different load is calculated for each tower segment based on the segment's width and average elevation. The dynamic wind pressure is calculated with similar parameters as for platform and azimuth arm (section 4.1.1 above): basic wind speed V = 110 mph, terrain exposure constants $\alpha = 7$ and $z_g = 1{,}200$ ft, topographic factor $K_{zt} = 1.0$, wind directionality factor $K_d = 0.9$ (fixed value for the *Chimneys, Tanks and Similar Structures* method), ground elevation factor $K_e = 1.0$ and gust-effect factor G = 1.0. In addition, for square cross-sections and tall aspect ratios, the method prescribes the force coefficient $C_f = 2.0$.

Table 7: 110 mph wind load calculation on towers.

		Tower 4 or 12				Tower 8					
Segment (1 = bottom, 4 or 6 = top)		**1**	**2**	**3**	**4**	**1**	**2**	**3**	**4**	**5**	**6**
Segment width	**w [ft]**	24	18	12	9	36	30	24	18	12	9
Segment height	**h [ft]**	63.4	63.4	63.4	63.4	61.4	61.4	61.4	61.4	61.4	61.4
Segment mid-elevation	**z [ft]**	407	470	533	597	291	352	414	475	536	598
Velocity pressure coefficient	**$K_z = 2.01\ (z/z_g)^{(2/\alpha)}$**	1.48	1.54	1.59	1.65	1.34	1.42	1.48	1.54	1.60	1.65
Velocity pressure	**$q_z = 0.00256\ K_z\ K_{zt}\ K_d\ K_e\ V^2$ [psf]**	41.1	42.9	44.4	45.9	37.4	39.5	41.3	43.0	44.5	45.9
Linear load	**$\lambda = q_z\ G\ C_f\ w$ [kip/ft]**	1.97	1.54	1.07	0.83	2.69	2.37	1.98	1.55	1.07	0.83
Segment load	**$F = \lambda\ h$ [kip]**	125	98	68	52	165	145	122	95	66	51
Tower load	**ΣF [kip]**	343				644					

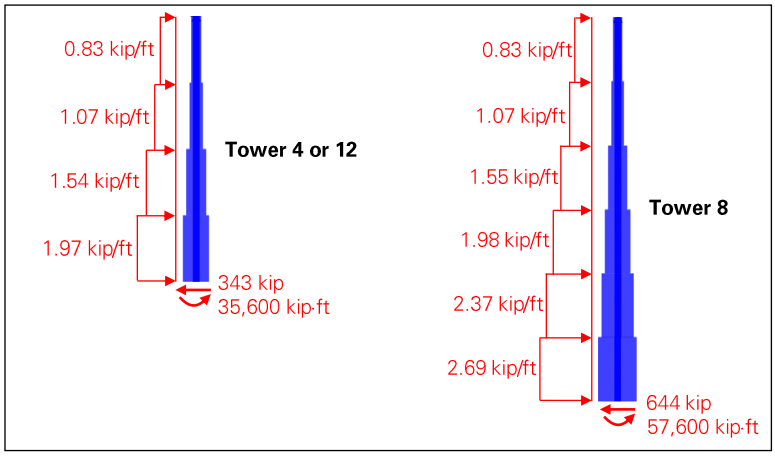

Figure 11: Calculated 110 mph wind load on towers.

[10] American Society of Civil Engineers (ASCE). *ASCE 7-16. Minimum Design Loads and Associated Criteria for Buildings and Other Structures*. Chapters 26 and 29. 2016.

4.3 Cables

The upgraded telescope structure included over four miles of main and backstay cables, which also caught wind. We estimated the wind load acting on the cables through the drag force calculation presented in Table 8. The calculation is simplified by assuming that the dynamic wind pressure at the elevation of the platform, calculated as q_z G = 41.6 psf per ASCE7-16[11] (section 4.1.1 above), applies to the entire length of each cable. The load is calculated for the case where the wind direction is perpendicular to the cable. The air flow is fully turbulent since the Reynolds number for a three-inch diameter cylinder perpendicular to a 110 mph wind is 250,000. In that regime, the drag coefficient of a cylinder can be taken as C = 1.2.

The total wind load on the cable system is shown in Figure 12 for different wind directions, considering the angle between the wind direction and each cable and assuming no shielding between parallel cables. The average total load on the main cables is 90 kip, half of which would be transferred to the suspended structure (45 kip). This is an order of magnitude less than the calculated wind load acting directly on the suspended structure (section 4.1.3 above).

Table 8: 110 mph wind load calculation on individual cables.

		Original	Original Backstays			Auxiliary	Auxiliary Backstays		
		Mains	Tower 4	Tower 8	Tower 12	Mains	Tower 4	Tower 8	Tower 12
Diameter	**D [in]**	3	3.25	3.25	3.25	3.25	3.625	3.625	3.625
Span	**S [ft]**	590	560	434	468	722	604	477	512
Linear Wind Load	**w = q_z G C D [lbf.ft^{-1}]**	12.5	13.5	13.5	13.5	13.5	15.1	15.1	15.1
Total Wind Load	**F = w S [kip]**	7.4	7.6	5.9	6.3	9.8	9.1	7.2	7.7
Linear Weight	**λ [lbf/ft]**	18.9	22.2	22.2	22.2	22.2	27.6	27.6	27.6
Wind-to-Weight Ratio	**w / λ**	0.66	0.61	0.61	0.61	0.61	0.55	0.55	0.55

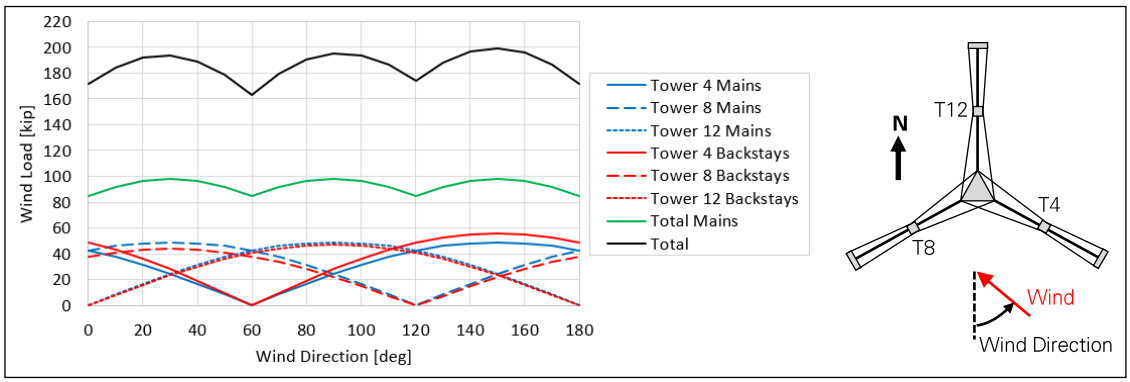

Figure 12: Calculated 110 mph wind load on cables.

The estimated wind load on a cable is of the same order of magnitude as the cable's weight, with ratios between 55 and 66 percent. The cable must therefore stretch and develop additional tension to carry this local wind load, in addition to any change of tension resulting from the global equilibrium of the structure.

[11] American Society of Civil Engineers (ASCE). *ASCE 7-16. Minimum Design Loads and Associated Criteria for Buildings and Other Structures.* Chapters 26 and 29. 2016.

The cable tension increase needed to carry the local wind load is calculated in Table 9. The wind load causes a horizontal deflection of up to 1.2 feet at midspan of the cable, but the corresponding tension increase is less than 0.3 percent of the pre-existing cable tension.

Table 9: Cable wind load effect on cable tensions.

		Original Main	Tower 4 Original Backstay	Auxiliary Main	Tower 4 Auxiliary Main
Length	**L [ft]**	589.877	560.024	721.538	603.972
Axial Rigidity	**EA [kip]**	135,587	158,657	155,638	198,115
Tension Before Wind	**T [kip]**	480.0	543.0	602.0	728.0
Linear Wind Load	**w [lbf/ft]**	12.5	13.5	13.5	15.1
Tension with Wind	**T′ [kip]**	481.3	544.3	603.7	729.3
Length with Wind	$L' = \frac{2T'}{w}\sinh\left(\frac{wS}{2T'}\right)$ **[ft]**	589.883	560.029	721.545	603.976
Check Tension and Length Compatibility	$T' = T + \frac{EA}{L}(L' - L)$ **[kip]**	481.3 (matches)	544.3 (matches)	603.7 (matches)	729.3 (matches)
Relative Tension Increase due to Wind	$\frac{T' - T}{T}$	0.27%	0.24%	0.28%	0.18%
Wind-Induced Horizontal Deflection [ft]	$S = \frac{T'}{w}\left(\cosh\left(\frac{wL}{2T'}\right) - 1\right)$ **[ft]**	1.13	0.97	1.46	0.94

5.0 Computational Fluid Dynamic Analysis

As a second approach to determine the wind loads on the suspended platform, we performed a set of computational fluid dynamic (CFD) analyses. CFD has two benefits over the first-principle and standard design calculations presented above (section 4.0).

First, as a general numerical method, CFD applies to structures of any type and shape, including the telescope's unique suspended structure. By contrast, the standard design calculations use empirical formulas calibrated on typical structures. As a result, they may not be as accurate for unique structures like the telescope, although they can be adapted with conservative assumptions for design purpose as presented above. CFD is however expected to provide a more accurate estimate of the wind loads acting on the telescope's suspended structure.

Second, CFD captures the turbulence of the air flow passing through and around the suspended structure. Turbulence, which includes effects such as vortex shedding, can cause the wind load to fluctuate even when the wind speed is constant. Therefore, the magnitude and frequency of the load fluctuations need to be captured as they may cause vibration and resonance of the suspended structure during windstorms.

5.1 Similitude and Results Scaling

Each of the CFD analyses presented below applies a constant wind speed upstream of the suspended structure. The analysis is then run until the model reaches a quasi-steady state. Because of the turbulent airflow, the forces on the suspended structure may fluctuate with a fixed amplitude and frequency.

The results of a CFD analysis performed at a given wind speed can be scaled to another wind speed, as long as the airflow is fully turbulent for both speeds. The equations relevant to the scaling process are provided in Table 10. First, an airflow is considered fully turbulent if its Reynolds number is greater than

100,000. Then, as long as the airflow remains fully turbulent, the wind pressure is proportional to the square of the wind speed, and the turbulence frequency is proportional to the ratio of the wind speed to the characteristic length. This scaling method is commonly applied to wind tunnel test results to determine the loads due to wind speeds that are too high to be practically achieved in a wind tunnel.

Table 10: Flow similitude and scaling.

	Flow #1 (wind tunnel or CFD)	Flow #2 (actual)
Characteristic Length	L_1	L_2
Fluid Kinematic Velocity	v_1	v_2
Wind Velocity	U_1	U_2
Reynolds Number	$Re_1 = \frac{U_1 L_1}{v_1}$	$Re_2 = \frac{U_2 L_2}{v_2}$
Wind Pressure (scaling also applicable to resultant forces and moments)	p_1	$p_2 = p_1 \left(\frac{U_2}{U_1}\right)^2$ if $Re_1 > 10^5$ and $Re_2 > 10^5$
Wind Turbulence Frequency	f_1	$f_2 = f_1 \left(\frac{U_2 L_1}{U_1 L_2}\right)$ if $Re_1 > 10^5$ and $Re_2 > 10^5$

5.2 CFD Model

We performed the CFD analyses with the PaceFish solver. PaceFish implements a Lattice Boltzmann Method (LBM) on a cartesian structured mesh, and runs analysis on Graphical Processing Units (GPUs) through a cloud service.

The objective of the CFD analysis is to determine the wind loads on the suspended structure. Therefore, as shown in Figure 13, the model does not include the towers and cables. The suspended structure is assumed fixed and rigid and is placed in a computational domain through which the air flow is simulated. Each truss member of the platform and azimuth arm is modeled, in addition to the ring girder and Gregorian dome. However, smaller features such as member lacing, connection plates, or outrigger cables are omitted. These features are too small to be realized within the mesh of the computational domain, which was made just fine enough to provide accurate results for the overall wind load. The suspended structure is modeled with the azimuth arm and Gregorian in the stowed position, as they were during significant windstorms.

Each analysis applies a constant wind speed upstream of the suspended structure. However, the Lattice Boltzmann Method is transient, and therefore each analysis is run until a quasi-steady state is achieved. In that state, the pressures and forces of the structure are either constant or fluctuating with a constant amplitude and frequency due to turbulence. The turbulence model is an Improved Delayed Detached Eddy Simulation (IDDES kw-SST).

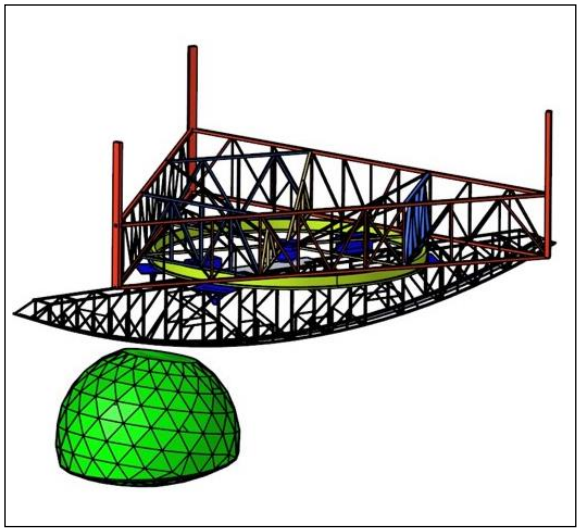

Figure 13: Suspended structure geometry in CFD model.

With the structure modeled at full scale, the CFD analyses are performed at 22.4 mph (10 meter per second, or m/s) wind speed. As shown in Table 11, this wind speed is sufficiently high for the flow to be fully turbulent around the smaller elements of the suspended structure. The results obtained from the CFD analyses at 22.4 mph can therefore be scaled to the actual maximum wind speed of 110 mph (section 5.1 above). Like for an actual wind tunnel test, running the CFD analysis at a lower wind speed is more practical. In addition, a larger mesh size can be used in the computational domain, which can make the analysis orders of magnitude faster to complete.

Table 11: Reynolds numbers of CFD and actual flows on suspended structure (air kinematic viscosity v = 1.61 10^{-4} ft^2/s).

		Platform		Gregorian		Steel Member	
		CFD Model	**Actual**	**CFD Model**	**Actual**	**CFD Model**	**Actual**
Characteristic Length	**L [ft]**	216	216	84	84	1	1
Wind Speed	**[mph]**	22.4	110	22.4	110	22.4	110
	U [m/s]	10	49	10	49	10	49
	[ft/s]	33	161	33	161	33	161
Reynolds Number	$\mathbf{Re = \frac{UL}{v}}$	4.4 10^7	2.2 10^8	1.7 10^7	8.4 10^7	2.0 10^5	1.0 10^6
Fully-Turbulent?	**Re > 10^5?**	yes	yes	yes	yes	yes	yes

5.3 Results

In two separate CFD analyses, a wind speed of 22.4 mph (10 m/s) was applied in two orthogonal directions: north wind (wind blows from north to south) and west wind (west to east).

In each analysis, the CFD solver determines the pressure on the model's surfaces. The pressure is then integrated over the model to obtain the resultant wind loads acting on the structure, which are forces and moments in three directions. Separate integrations are performed for the platform, azimuth arm, and Gregorian to determine the loads on each substructure, as defined in Figure 16. The loads are time-dependent since the analysis is transient. However, they eventually reach a quasi-steady state where each load is either essentially constant, or fluctuates with fixed amplitude and frequency. The air velocity in different planes cutting through the suspended structure is shown in Figure 14 and Figure 15.

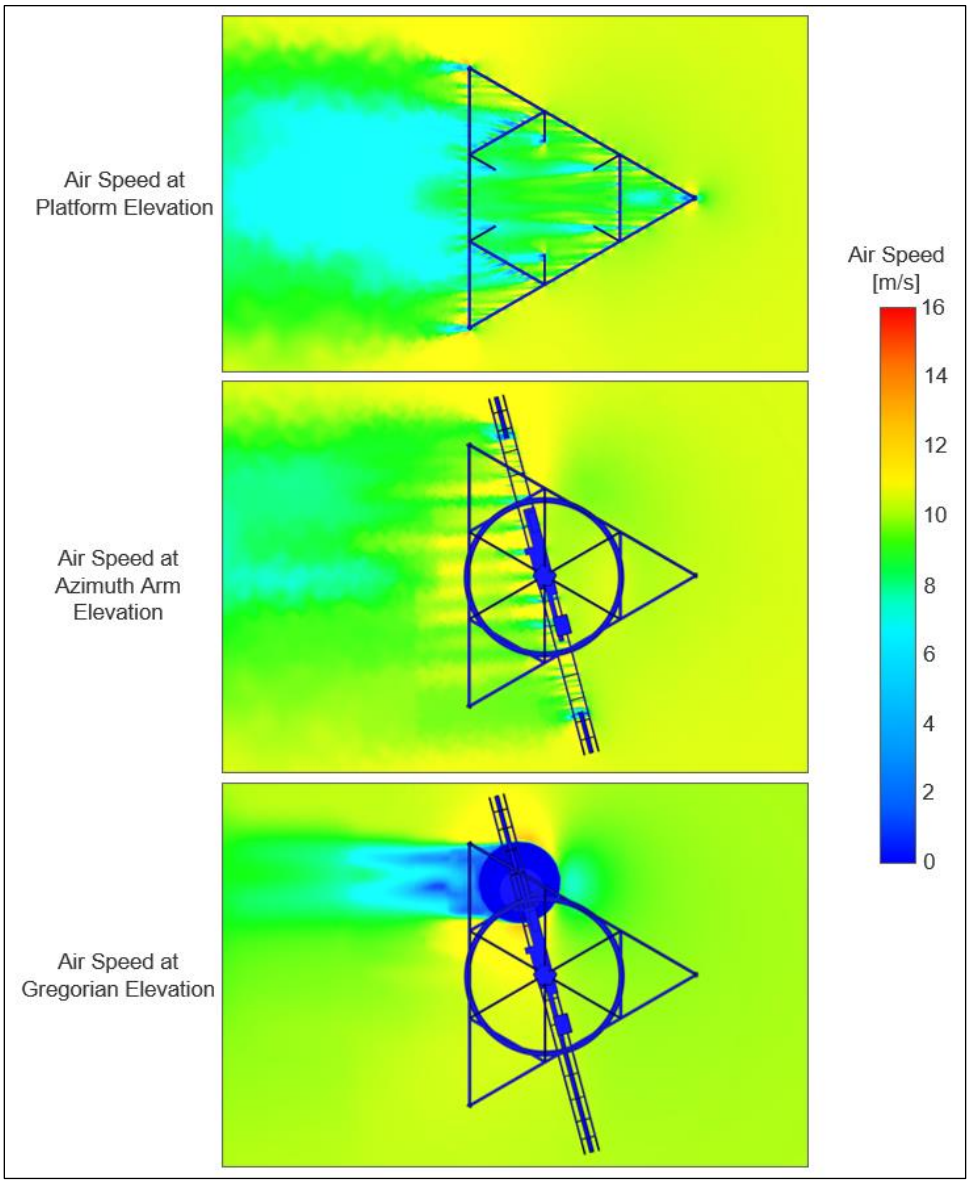

Figure 14: Air velocity around suspended structure in CFD analysis of 22.4 mph (10 m/s) north wind.

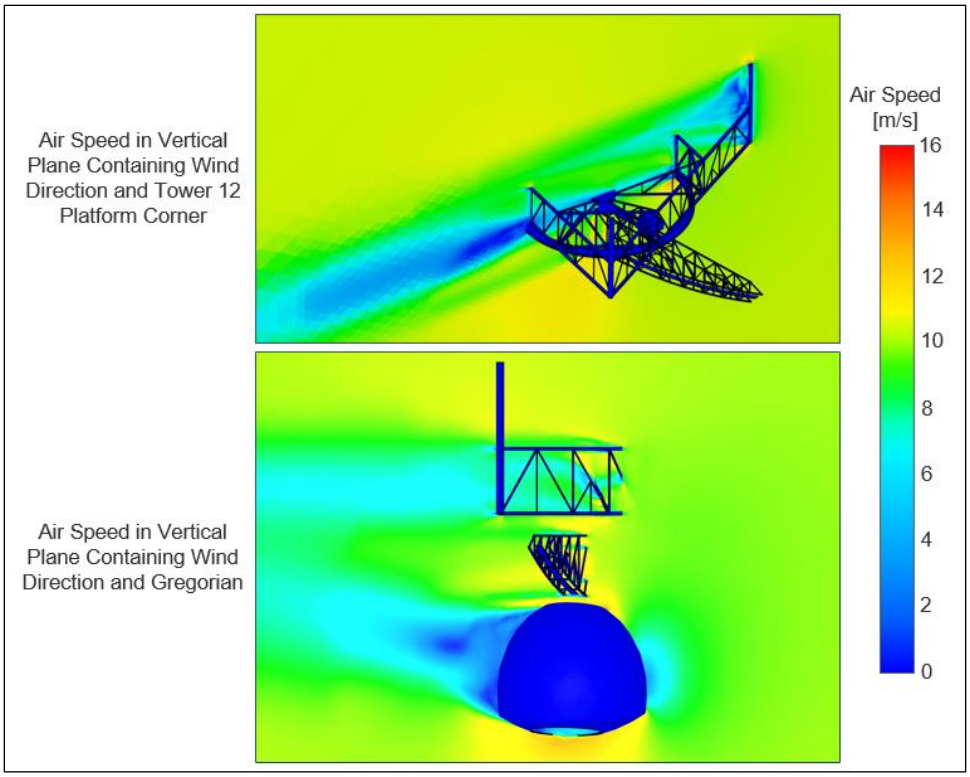

Figure 15: Air velocity around suspended structure in CFD analysis of 22.4 mph (10 m/s) north wind.

The loads on the platform, azimuth arm and Gregorian for 60 seconds of quasi-steady state are shown in Figure 17 (north wind) and Figure 18 (west wind). The average value and the amplitude and frequency of the fluctuation (turbulence) of the loads are summarized in Table 12 (north wind) and Table 13 (west wind). The tables provide these results as retrieved from the CFD model with a 22.4 mph wind and after scaling to the reference wind speed on 110 mph (section 5.1 above). The most significant wind forces are also summarized in Figure 19.

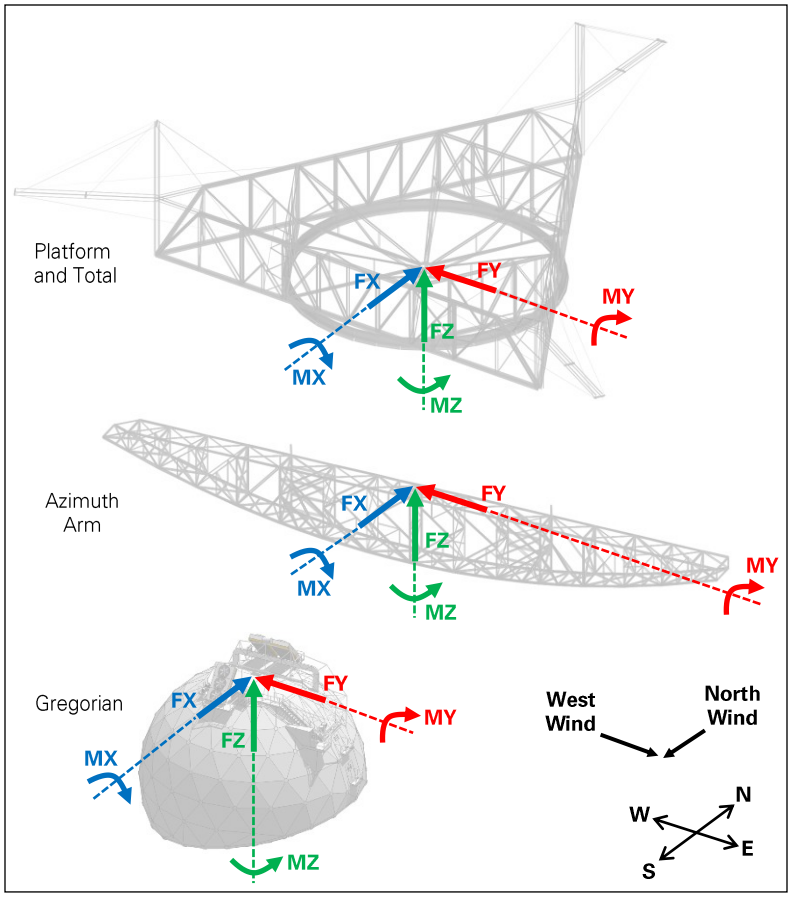

Figure 16: Resultant forces and moments on platform, azimuth arm and Gregorian.

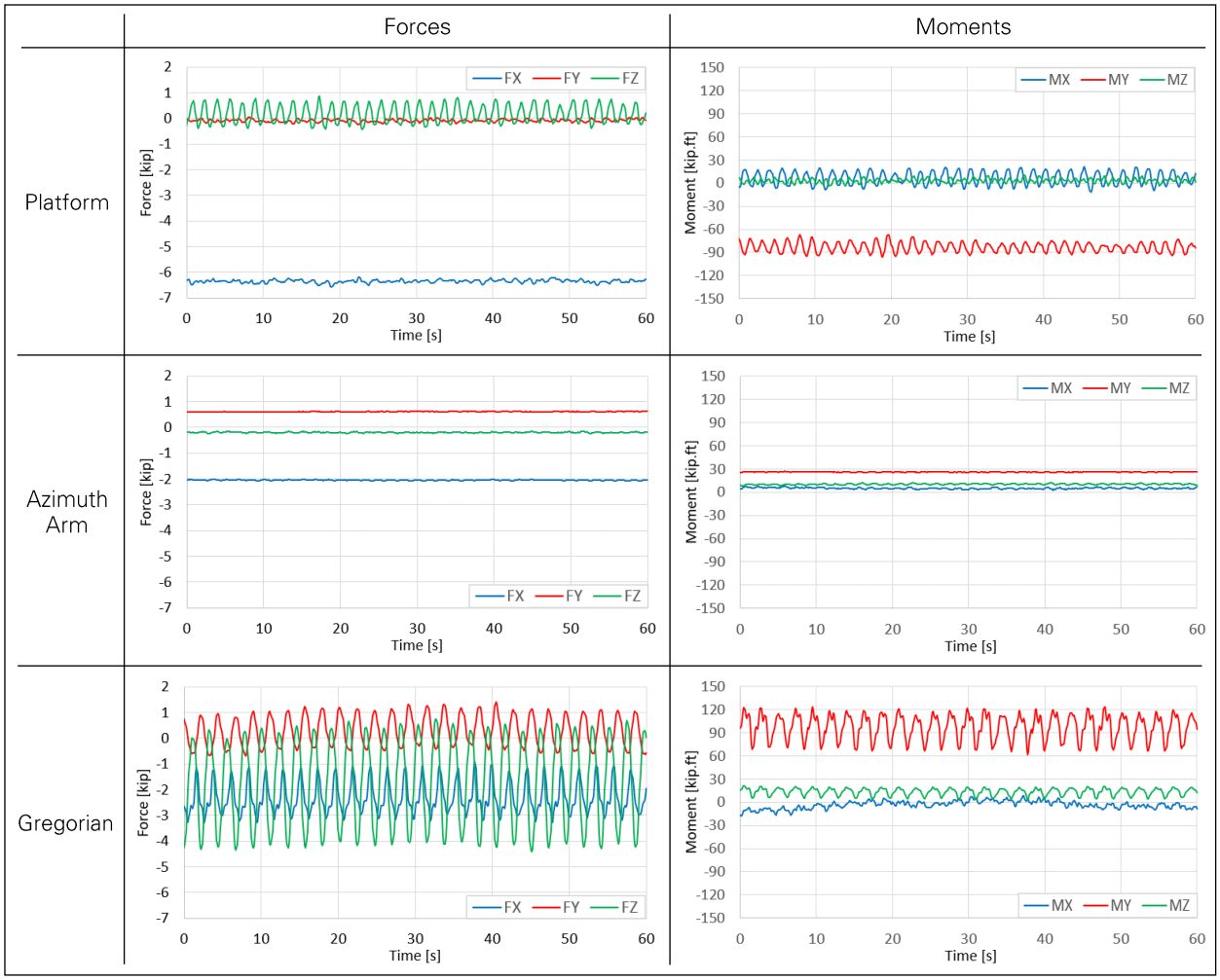

Figure 17: Resultant forces and moments on suspended structure in quasi-steady state for 22.4 mph (10 m/s) north wind.

Table 12: Resultant forces and moments on suspended structure in quasi-steady state for north wind.

		CFD Results (22.4 mph)						Scaled to Reference Wind Speed (110 mph)					
		Average		Turbulence Amplitude		Turbulence Frequency		Average		Turbulence Amplitude		Turbulence Frequency	
		F [kip]	M [kip·ft]	F [kip]	M [kip·ft]	f_F [Hz]	f_M [Hz]	F [kip]	M [kip·ft]	F [kip]	M [kip·ft]	f_F [Hz]	f_M [Hz]
Platform	**X**	-6.4	7.5		12.5		0.61	-155	181		302		3.00
	Y	-0.1	-82.5		7.5		0.61	-2	-1,995		181		3.00
	Z	0.2	5.0	0.5		0.61		5	121	12		3.00	
Azimuth Arm	**X**	-2.0	5.0					-48	121				
	Y	0.6	26.0					15	629				
	Z	-0.2	10.0					-5	242				
Gregorian	**X**	-2.2	-5.0	1.0		0.44		-53	-121	24		2.19	
	Y	0.2	90.0	0.8	25.0	0.44	0.44	5	2,176	19	605	2.19	2.19
	Z	-1.9	12.5	2.3	7.5	0.44	0.44	-46	302	56	181	2.19	2.19
Total	**X**	-10.6	-68.0	1.0	164.8			-256	-1,644	24	3,986		
	Y	0.7	150.9	0.8	64.0			17	3,648	19	1,549		
	Z	-1.9	132.3	2.8	62.8			-46	3,200	68	1,518		

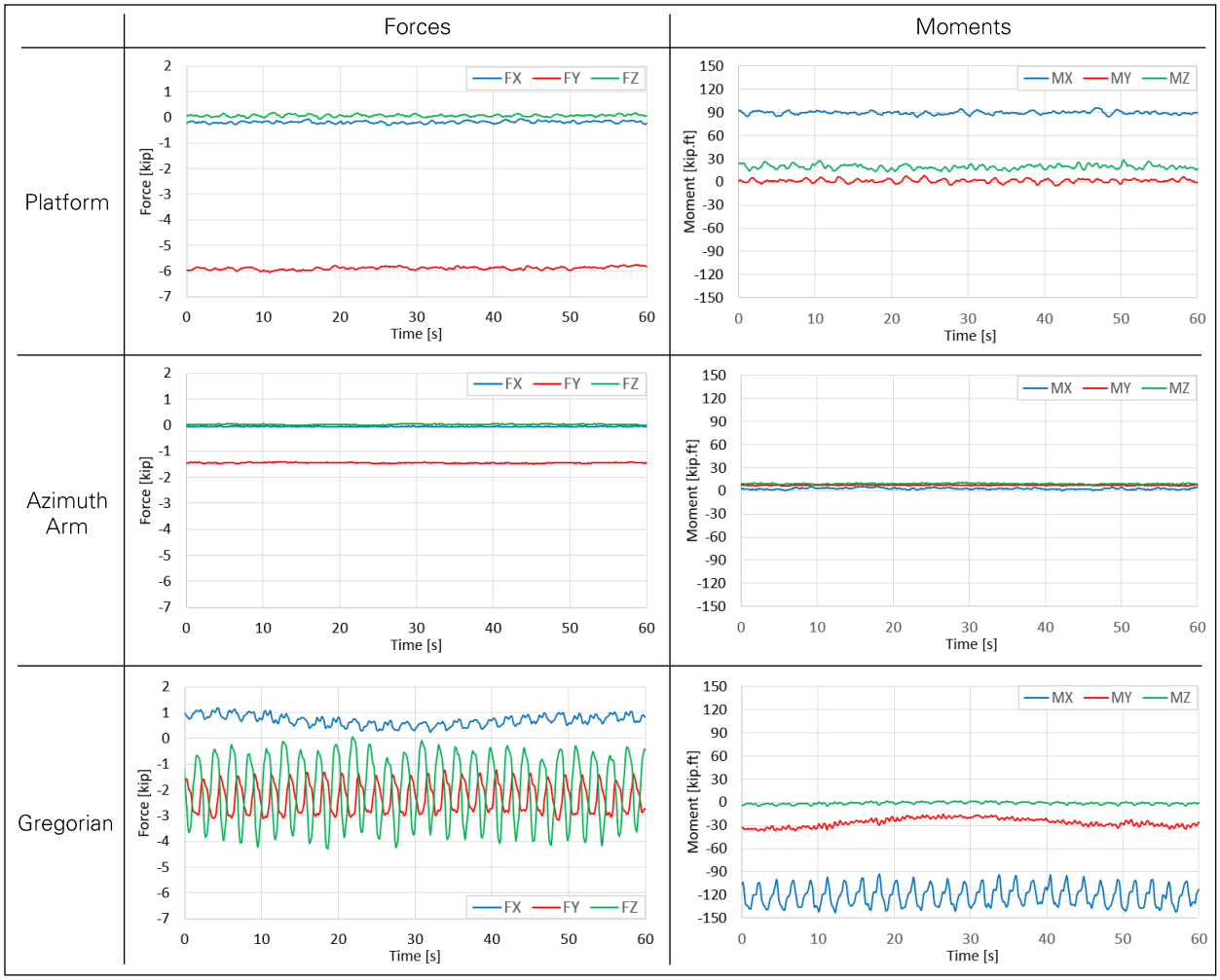

Figure 18: Resultant forces and moments on suspended structure in quasi-steady state for 22.4 mph (10 m/s) west wind.

Table 13: Resultant forces and moments on suspended structure in quasi-steady state for west wind.

		CFD Results (22.4 mph)						Scaled to Reference Wind Speed (110 mph)					
		Average		Turbulence Amplitude		Turbulence Frequency		Average		Turbulence Amplitude		Turbulence Frequency	
		F [kip]	M [kip·ft]	F [kip]	M [kip·ft]	f_F [Hz]	f_M [Hz]	F [kip]	M [kip·ft]	F [kip]	M [kip·ft]	f_F [Hz]	f_M [Hz]
Platform	**X**	-0.2	90.0					-5	2,176				
	Y	-5.9	20.0					-143	484				
	Z	0.1	0.0					2	0				
Azimuth Arm	**X**	-0.1	3.0					-2	73				
	Y	-1.5	7.0					-36	169				
	Z	0.0	9.0					0	218				
Gregorian	**X**	0.8	-120.0	0.2	20.0	0.44	0.44	19	-2,902	5	484	2.19	2.19
	Y	-2.3	-30.0	0.8		0.44		-54	-725	19		2.19	
	Z	-2.2	-2.0	1.7		0.44		-53	-48	41		2.19	
Total	**X**	0.5	-267.0	0.2	143.3			12	-6,457	5	3,465		
	Y	-9.7	-61.7	0.8	4.3			-235	-1,492	19	104		
	Z	-2.1	-12.1	1.7	16.5			-51	-293	41	399		

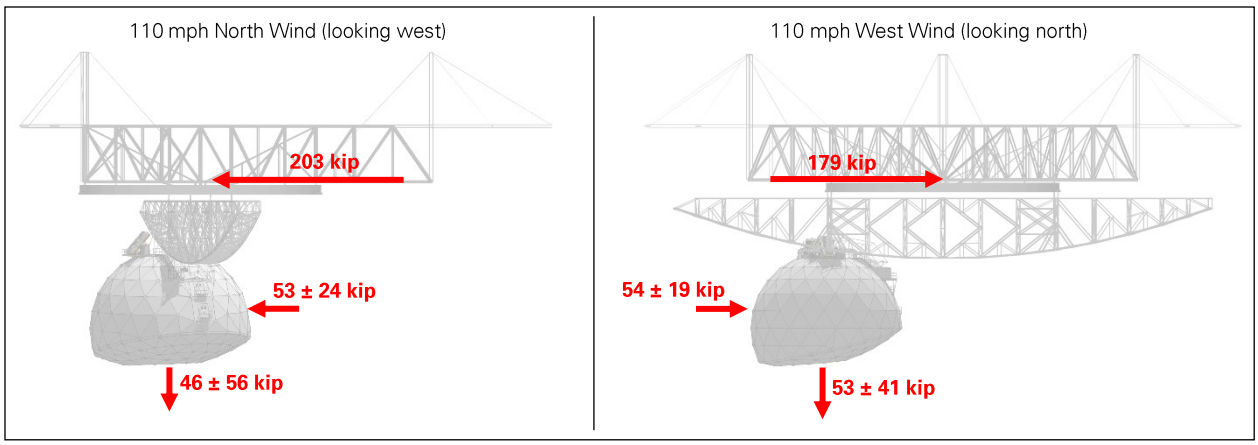

Figure 19: Main wind forces on suspended structure.

5.4 Validation

As a first validation of the CFD model, we compared the results of CFD analysis to the results of the wind tunnel study performed in 1993 (section 2.3 above). The comparison is limited to the loads on the Gregorian since the wind tunnel study does not provide the loads on the platform and azimuth arm. Nevertheless, the wind tunnel tests were performed on a full model of the suspended structure like in the CFD analyses, and therefore the results for the Gregorian are comparable. The comparison is shown in Figure 20. The two sets of wind loads are generally consistent, considering that some of the wind tunnel test parameters are unknown and may differ from the CFD analyses.

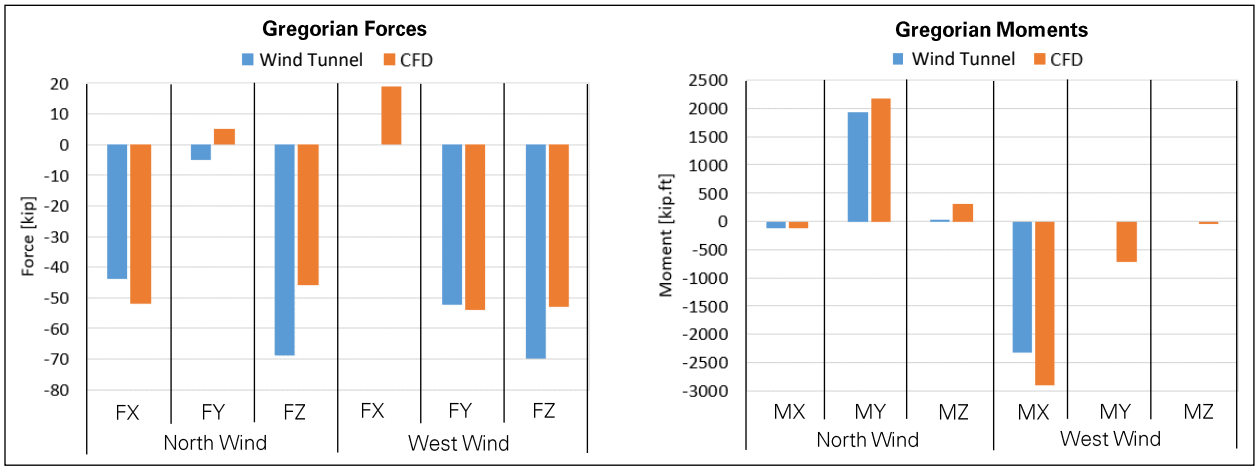

Figure 20: Comparison of Gregorian forces and moments from wind tunnel test and CFD analysis at 110 mph.

To verify that the CFD results can be scaled to higher wind speeds, we repeated the north wind analysis with the speed doubled to 44.8 mph (20 m/s) and compared the results with the original analysis at 22.4 mph (10 m/s). The comparison is shown in Figure 21 and Table 14 for the forces acting on the platform as an example. We observe that when the wind speed doubles, the average force and turbulence amplitude essentially quadruple, while the turbulence frequency essentially doubles. The same ratios were observed for the forces and moments on the platform, azimuth arm, and Gregorian. The behavior of the CFD model is therefore as expected and confirms that the flow is fully turbulent, such that the CFD results can be scaled instead of running the CFD model for more wind speeds.

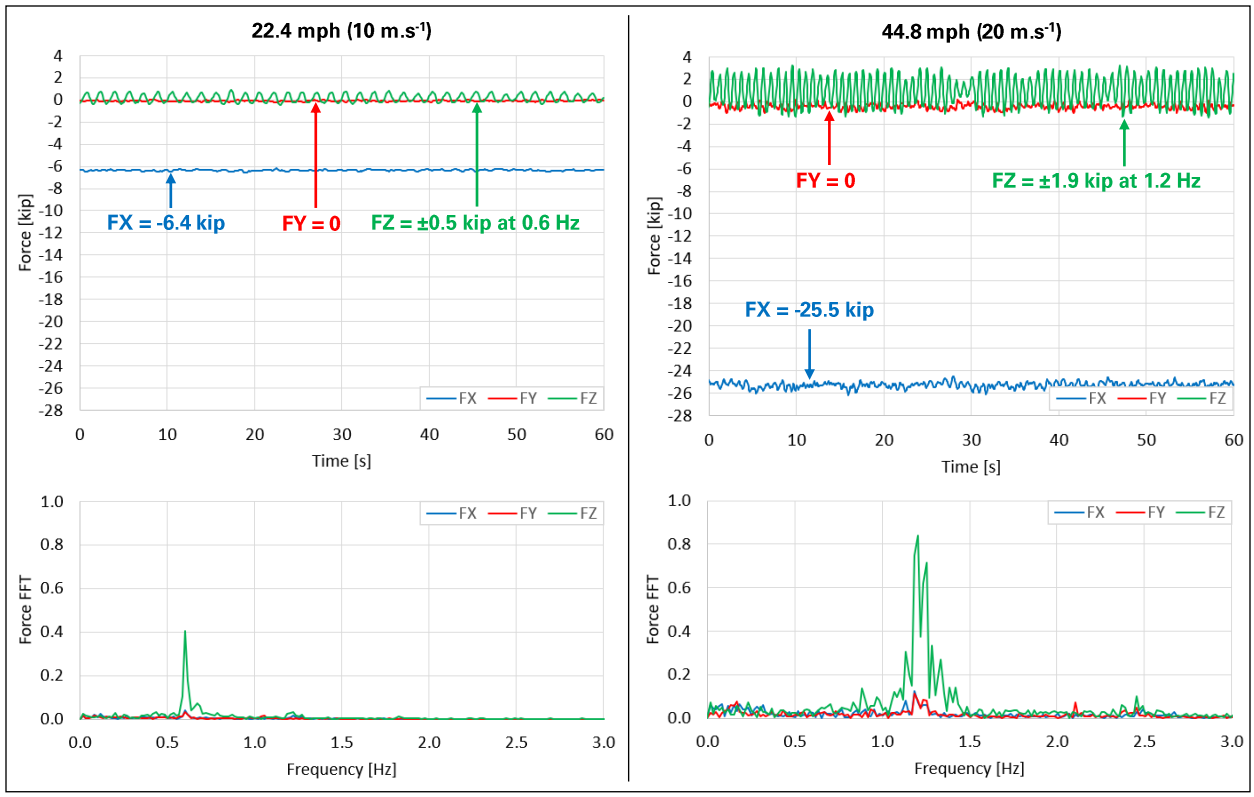

Figure 21: Resultant forces on platform in quasi-steady state for 22.4 mph (10 m/s) and 44.8 (20 m/s) north wind.

Table 14: Difference in resultant forces on platform between quasi-steady state for 22.4 mph (10 m/s) and 44.8 mph (20 m/s) north wind.

	FX Average [kip]	FZ Amplitude [kip]	FZ Frequency [Hz]
22.4 mph	-6.4	0.5	0.6
44.8 mph	-25.5	1.9	1.2
Ratio (44.8 mph) / (22.4 mph)	4.0	3.8	2.0

6.0 Dynamic Structural Response Analysis

We performed a series of dynamic analyses on the finite element (FE) models of the original and upgraded telescope to determine the structure's response to wind loads. This section describes the set-up of the analyses, which includes the construction of time-dependent wind loads from the CFD results, their application to the FE models, and the selection of simulated wind conditions. The results of the analyses are presented in section 0 below. The FE models of the telescope are described in Appendix F.

6.1 Wind Conditions and Directions

We analyzed the behavior of the telescope in two wind conditions: ambient wind and Hurricane Maria. For each condition, we extracted a 2.5-hour segment of the wind speed data recorded at one-second intervals on the telescope's platform (Figure 22).

The **ambient wind** speed was recorded at daytime on July 15, 2019 and is representative of the wind speed experienced on most summer days at the Observatory.

For **Hurricane Maria**, we combined the wind speed data recorded by two instruments: an anemometer, which recorded the instantaneous wind speed at one-second intervals but failed approximately one hour before the peak of the storm, and a doppler, which recorded the instantaneous wind speed at 15-second intervals for the entire duration of the storm (Section 3.1). The doppler data cannot be used directly in a dynamic analysis of the telescope because the 15-second interval is larger than the natural period of the structure. However, the doppler data captures the peak intensity of the storm, and we used it to scale the anemometer data to that peak intensity. The maximum 10-minute average speed is 69 mph and 50 mph in the doppler and anemometer data respectively. We therefore added the difference of 19 mph to the anemometer data, such that its maximum 10-minute average matches the actual maximum of 69 mph captured by the doppler. Every 10 minutes, the doppler also logged the peak instantaneous wind speed over the past 10 minutes (Section 3.1), and the maximum during Hurricane Maria is 108 mph. The scaled anemometer data has a peak instantaneous wind speed of 118 mph, and using it in the analysis is therefore slightly conservative.

For both wind conditions, we considered three wind directions corresponding the three tower-to-platform directions (Figure 23). For each wind direction, the load on the platform is most effectively resisted by the main cables connected to one of the towers, which maximizes the tension increase in those cables. Cable tension results will be reported as envelopes over the three wind directions for each wind condition.

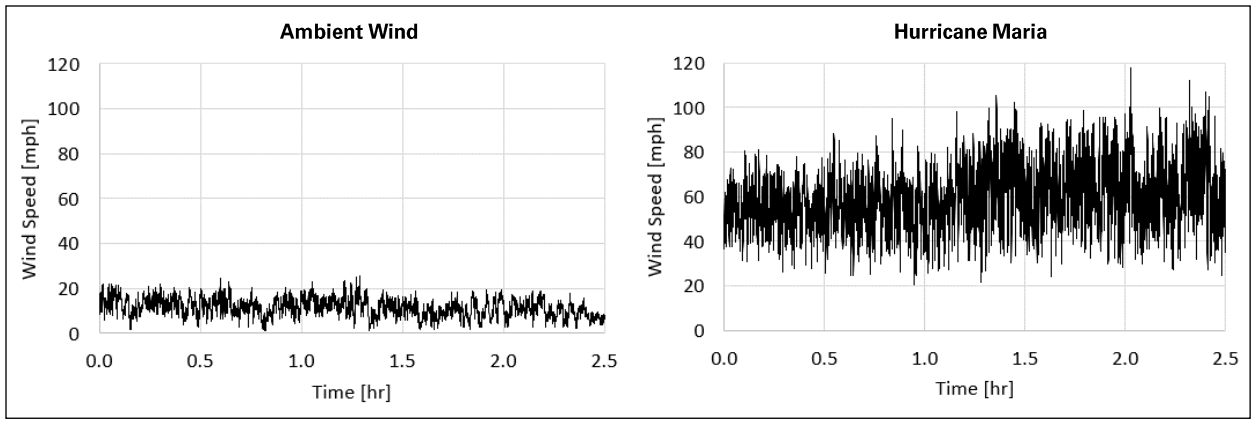

Figure 22: Wind speed time histories considered.

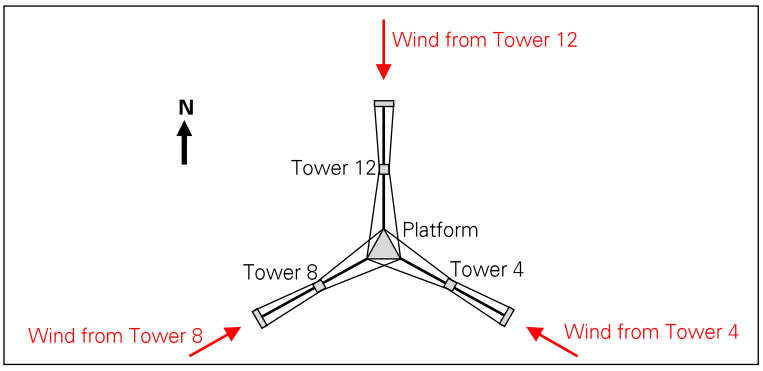

Figure 23: Wind directions considered.

6.2 Time-dependent Wind Loads

6.2.1 Suspended Structure

If the wind speed was constant, each wind load (force and moment on platform, azimuth arm, and Gregorian) could be idealized as a periodic load with three parameters: mean value, turbulence amplitude, and turbulence frequency. As described in Section 0, we determined these parameters through computational fluid dynamic (CFD) analysis for a constant wind speed of 22.4 mph (10 m/s).

The parameters of the periodic load induced by a constant wind speed on a given object are tied to the wind speed as follows: the turbulence frequency is directly proportional to the speed, while the mean value and turbulence amplitude are proportional to the square of the speed. To approximate the load induced by a time-varying wind speed, we considered a sinusoid function and varied its parameters over time based on the wind speed. This process is described in Table 15 and Figure 24.

Examples of wind load time histories on the platform, azimuth arm and Gregorian constructed from CFD results and wind speed time history are provided in Figure 25.

Table 15: Construction of wind load time history from CFD results and wind speed time history.

CFD Wind Speed	U_{CFD}
CFD Mean Load	$P_{CFD,mean}$
CFD Turbulence Amplitude	$P_{CFD,turb}$
CFD Turbulence Frequency	f_{CFD}
CFD Load Time History	$P_{CFD}(t) = P_{CFD,mean} + P_{CFD,turb}\sin(2\pi f_{CFD}t)$
Actual Velocity Time History	$U(t)$
Actual Turbulence Frequency	$f(t) = f_{CFD}\left(\frac{U(t)}{U_{CFD}}\right)$
Load Time Step	dt
Actual Turbulence Phase	$\phi(0) = 0$ $\phi(t) = \phi(t - dt) + 2\pi f(t)dt$
Actual Load Time History	$P(t) = \left(P_{CFD,mean} + P_{CFD,turb}\sin(\phi(t))\right)\left(\frac{U(t)}{U_{CFD}}\right)^2$

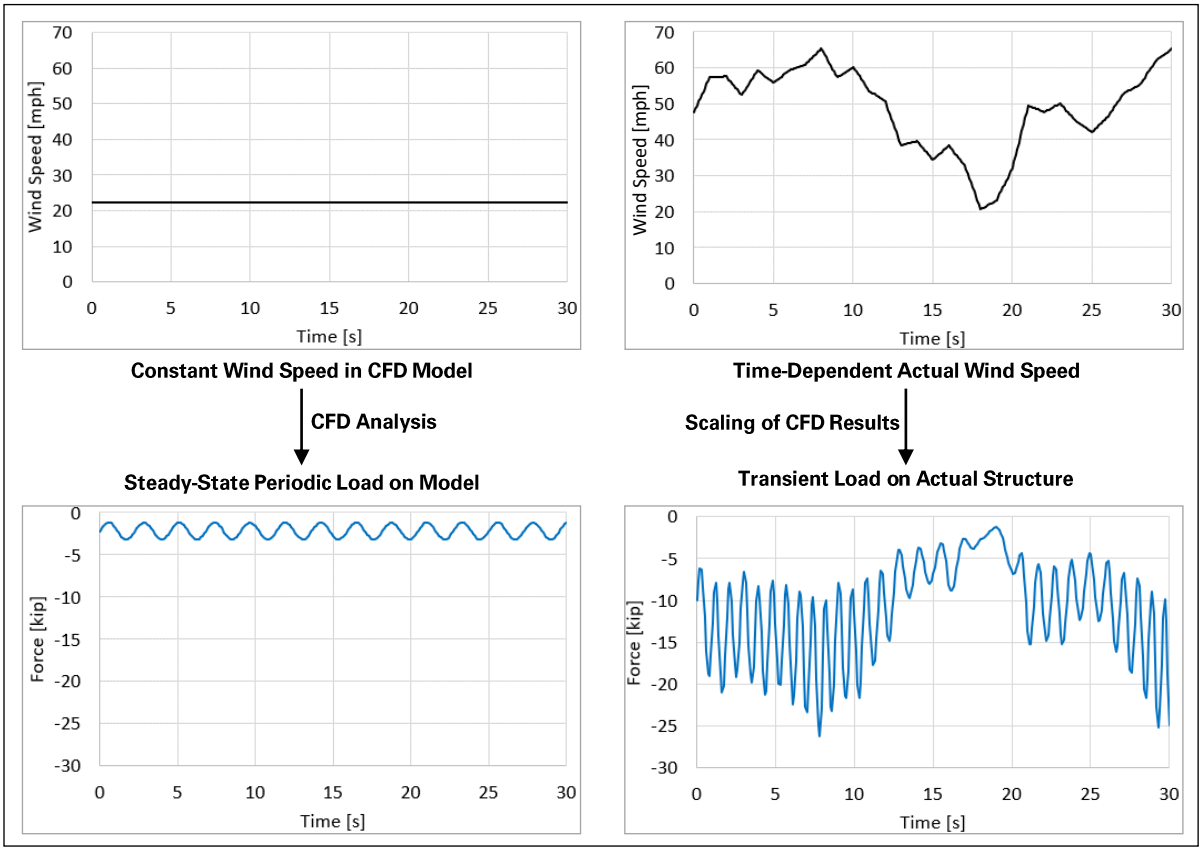

Figure 24: Construction of wind load time history from CFD results and wind speed time history.

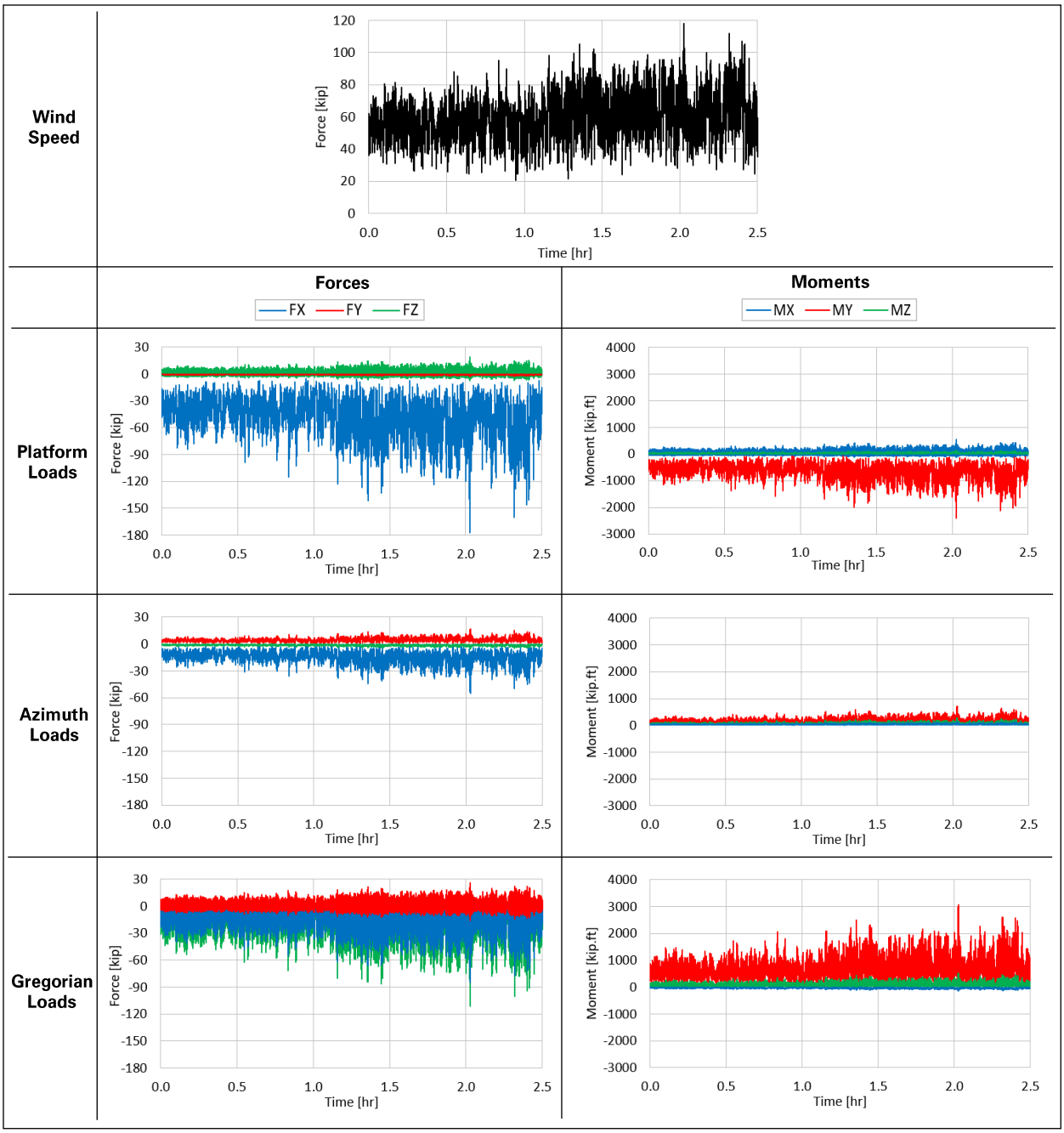

Figure 25: Wind loads on suspended structure under hurricane wind from Tower 12 (north-south).

6.2.2 Towers

For the three towers, we constructed the wind load time histories by scaling the calculated static wind loads (section 4.2 above) with the square of the wind speed. Examples of resulting wind load time histories are provided Figure 26.

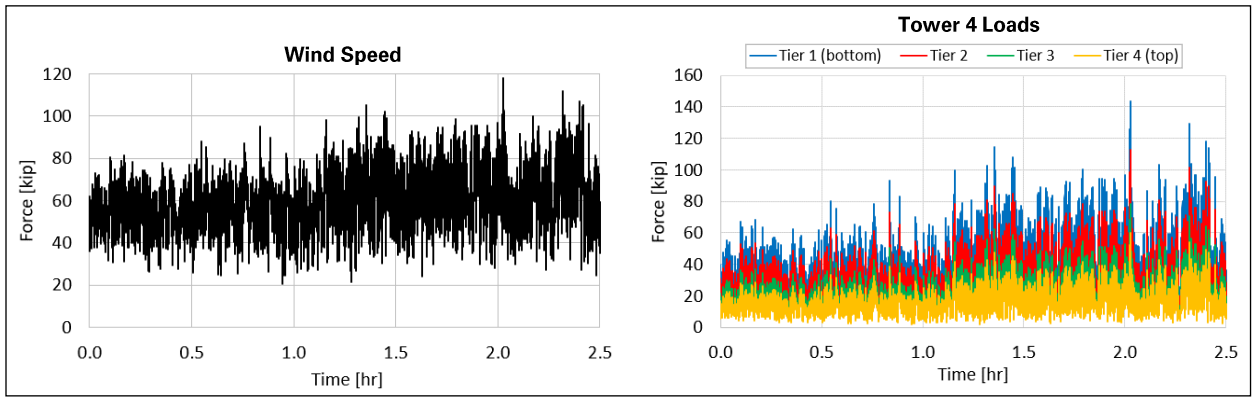

Figure 26: Wind loads on Tower 4 under hurricane wind from Tower 12.

6.3 Load Application

In the FE models, the wind loads are applied to the suspended structure as shown in Figure 27. For the platform and azimuth arm, multiple nodes are loaded to obtain the desired resultant force or moment. For the Gregorian, which is not modeled as elements, the resultant forces and moments are applied at the bottom of the azimuth arm where the Gregorian is located when the telescope is stowed. Finally, the wind loads on the towers are applied as line loads.

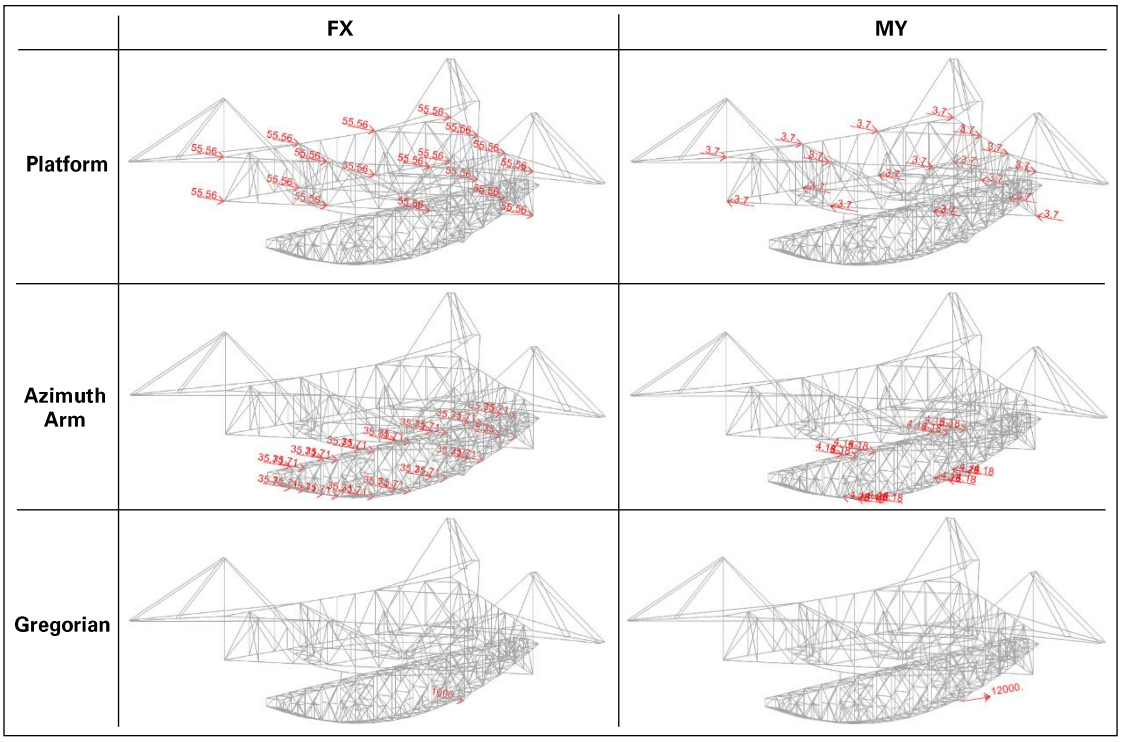

Figure 27: Examples of load application to suspended structure.

6.4 Wind Analyses Performed

As shown in Table 16, we performed total of 12 analyses considering two structures (original and upgraded), two wind conditions (ambient and Hurricane Maria) and three wind directions (from each of the three towers toward the platform). While the original structure (1964-1997) did not experience Hurricane Maria (2017), this storm is a conservative event to evaluate the potential impact of past hurricanes on the original structure. The tiedowns of the upgraded structure were released in the analysis of Hurricane Maria, consistently with the Observatory's practice of releasing the tiedowns before significant storms. Each analysis is a linear dynamic analysis simulating 2.5 hours of wind and solved through modal superposition, with a damping ratio of one percent on each mode.

Table 16: Wind analyses performed.

Analysis #	Structure	Tiedowns	Wind Condition	Wind Direction
1	Original	Taut	Ambient wind	Tower 4 → Platform
2	Original	Taut	Ambient wind	Tower 8 → Platform
3	Original	Taut	Ambient wind	Tower 12 → Platform
4	Original	Taut	Hurricane Maria	Tower 4 → Platform
5	Original	Taut	Hurricane Maria	Tower 8 → Platform
6	Original	Taut	Hurricane Maria	Tower 12 → Platform
7	Upgraded	Taut	Ambient wind	Tower 4 → Platform
8	Upgraded	Taut	Ambient wind	Tower 8 → Platform
9	Upgraded	Taut	Ambient wind	Tower 12 → Platform
10	Upgraded	Slack	Hurricane Maria	Tower 4 → Platform
11	Upgraded	Slack	Hurricane Maria	Tower 8 → Platform
12	Upgraded	Slack	Hurricane Maria	Tower 12 → Platform

7.0 Cable Tension Results

7.1 Original Structure

The cable tension time histories in the original structure are shown in Figure 28 for one wind direction of the ambient and hurricane conditions. For the ambient condition, the fluctuations of the cable tensions are minimal compared to the pre-existing tensions. The rest of the results presented in this section are therefore focused on the hurricane condition. The cable tension maps (Figure 29, Figure 30 and Figure 31) show the envelope of the hurricane results for the three wind directions considered.

Figure 29 shows the maximum tension increase in each cable during the hurricane as a percentage of the pre-hurricane tension. Excluding the tiedowns, the maximum tension increase is nine percent and occurs in the backstays of tower 8.

Figure 30 shows the lowest safety factor reached in each cable during the hurricane. The lowest safety factor is the ratio of the highest cable tension experienced during the hurricane to the cable's minimum breaking strength. The safety factors remain around two in all of the cables.

Figure 31 shows the maximum normalized stress range experienced by each cable during the hurricane. The maximum normalized stress range is the ratio of the maximum tension range (difference between

maximum and minimum tension experienced) to the cable's minimum breaking strength. The maximum normalized stress range is between three and five percent in the mains and backstays.

Table 17 indicates the number of stress cycles experienced by each cable per hour of hurricane wind condition, for different stress levels. The number of cycles were counted in the cable tension time history results using the rainflow method, and averaged over the three wind directions considered.

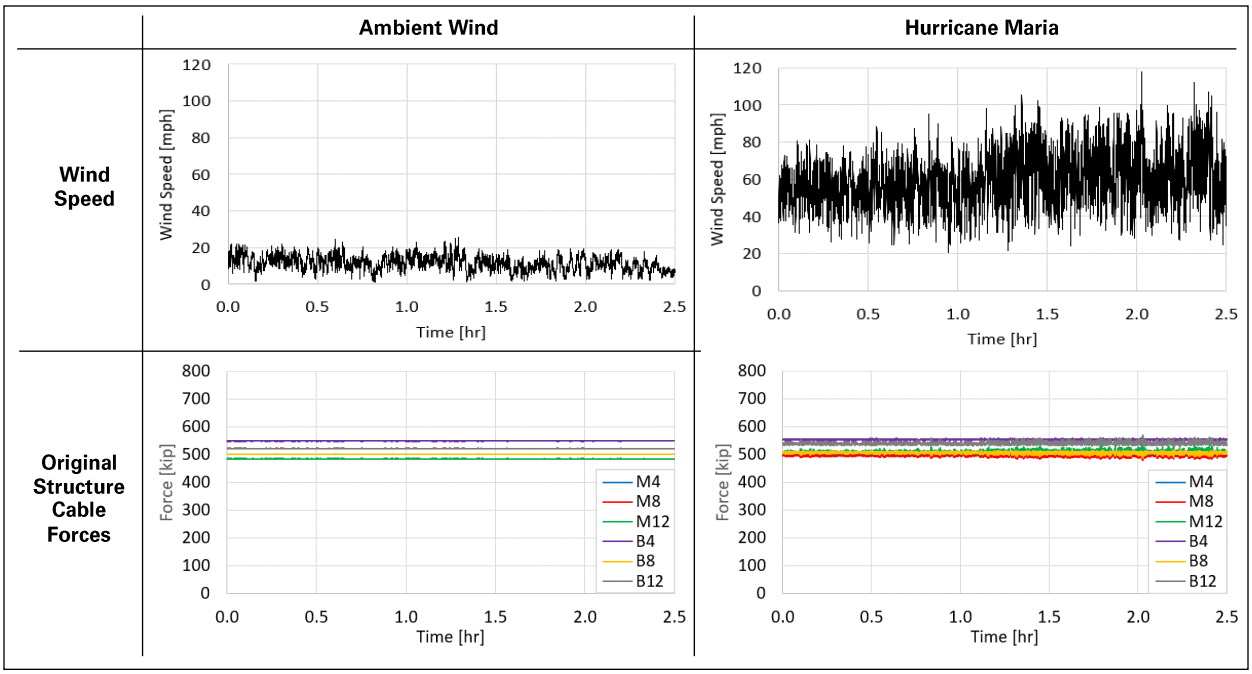

Figure 28: Cable tension time history in original structure under ambient and hurricane wind from Tower 12 (north-south).

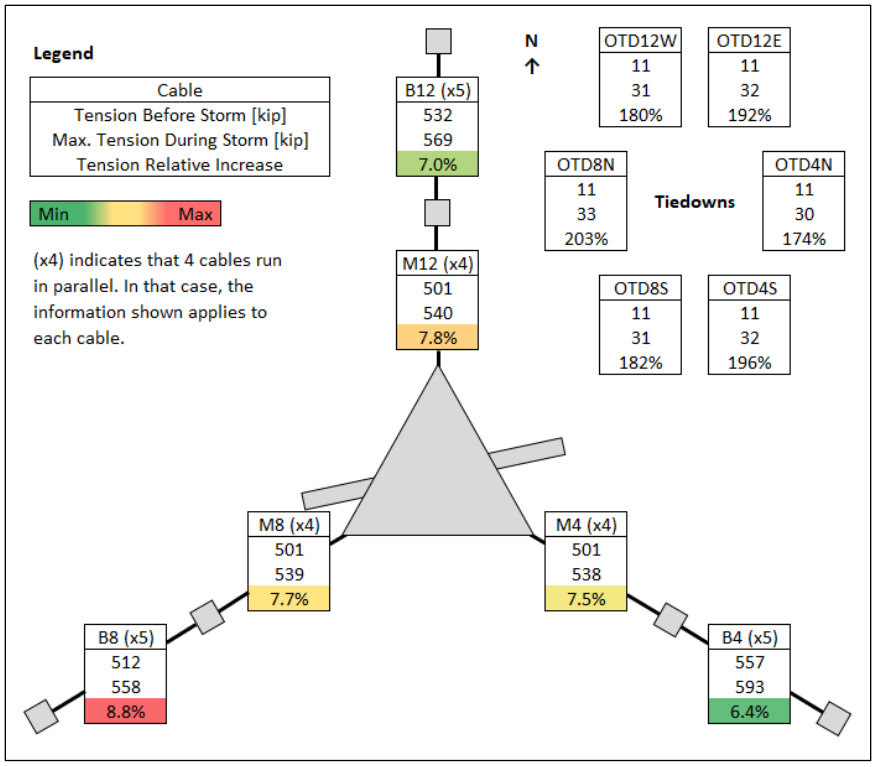

Figure 29: Maximum cable tension increase in original structure in hurricane conditions.

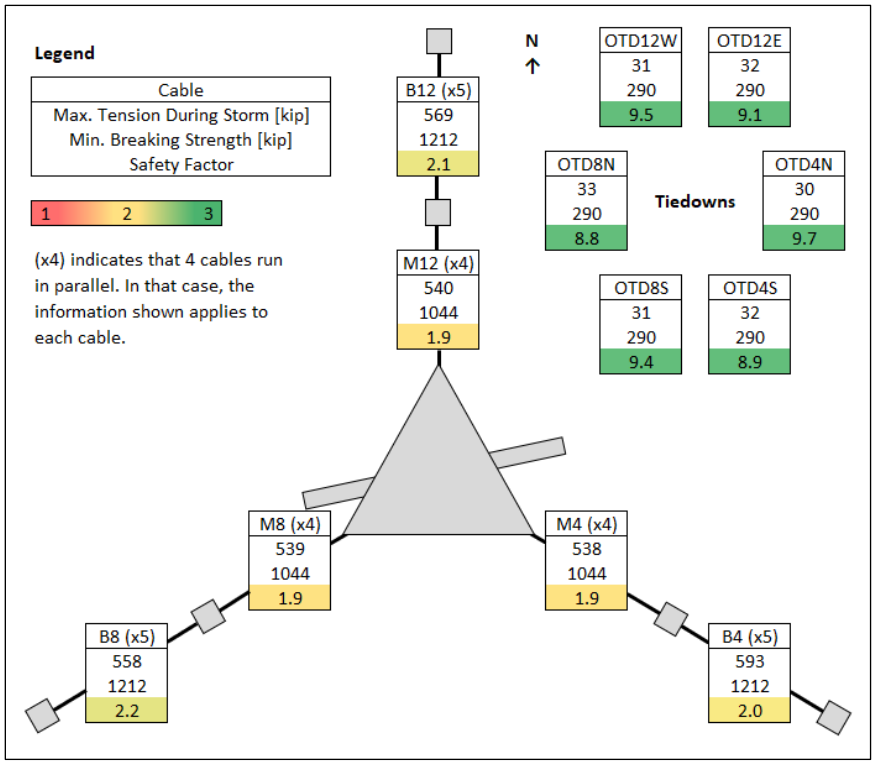

Figure 30: Maximum cable tension and corresponding safety factor in original structure in hurricane conditions.

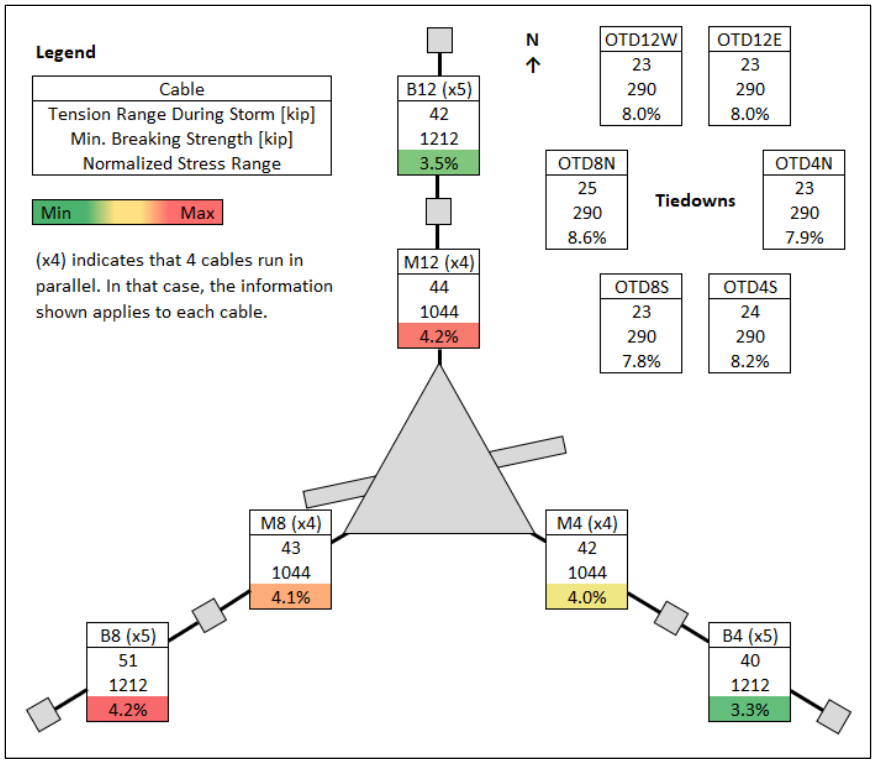

Figure 31: Maximum normalized stress range in cables of original structure in hurricane conditions.

Table 17: Number of stress cycles in cables of original structure per hour of peak hurricane conditions.

	Normalized stress range (= tension range / minimum breaking strength)			
	1-2%	**2-3%**	**3-4%**	**4-5%**
M4	66	6.1	0.3	0.1
M8	77	6.5	0.5	0.1
M12	71	5.3	0.3	0.1
B4	41	2.3	0.1	
B8	76	6.3	0.5	0.1
B12	44	2.4	0.1	

7.2 Upgraded Structure

The cable tension time histories in the upgraded structure are shown in Figure 32 for one wind direction of the ambient and hurricane conditions. For the ambient condition, the fluctuations of the cable tensions are minimal compared to the pre-existing tensions. The rest of the results presented in this section are therefore focused on the hurricane condition. The cable tension maps (Figure 33, Figure 34, Figure 35) show the envelope of the hurricane results for the three wind directions considered.

Figure 33 shows the maximum tension increase in each cable during the hurricane as a percentage of the pre-hurricane tension. The maximum tension increase is 14 percent and occurs in the three mains that support the corner of the platform where the Gregorian is stowed (M8, M4S, M12W). This is due to the significant drag-down force that the wind induces on the gregorian. The maximum tension increase in cable M4N (where the first failure occurred in August 2020) is 10 percent.

Figure 34 shows the lowest safety factor reached in each cable during the hurricane. The lowest safety factor is the ratio of the highest cable tension experienced during the hurricane to the cable's minimum breaking strength. The lowest safety factor in cable M4N is 2.1.

Figure 35 shows the maximum normalized stress range experienced by each cable during the hurricane. The maximum normalized stress range is the ratio of the maximum tension range (difference between maximum and minimum tension experienced) to the cable's minimum breaking strength. The maximum normalized stress range is around eight percent in the three cables that experience the maximum tension increase due to the drag-down force on the Gregorian.

Table 17 shows the number stress cycles experienced by each cable per hour of hurricane wind condition, for different stress levels. The number of cycles were counted in the cable tension time history results using the rainflow method, and averaged over the three wind directions considered.

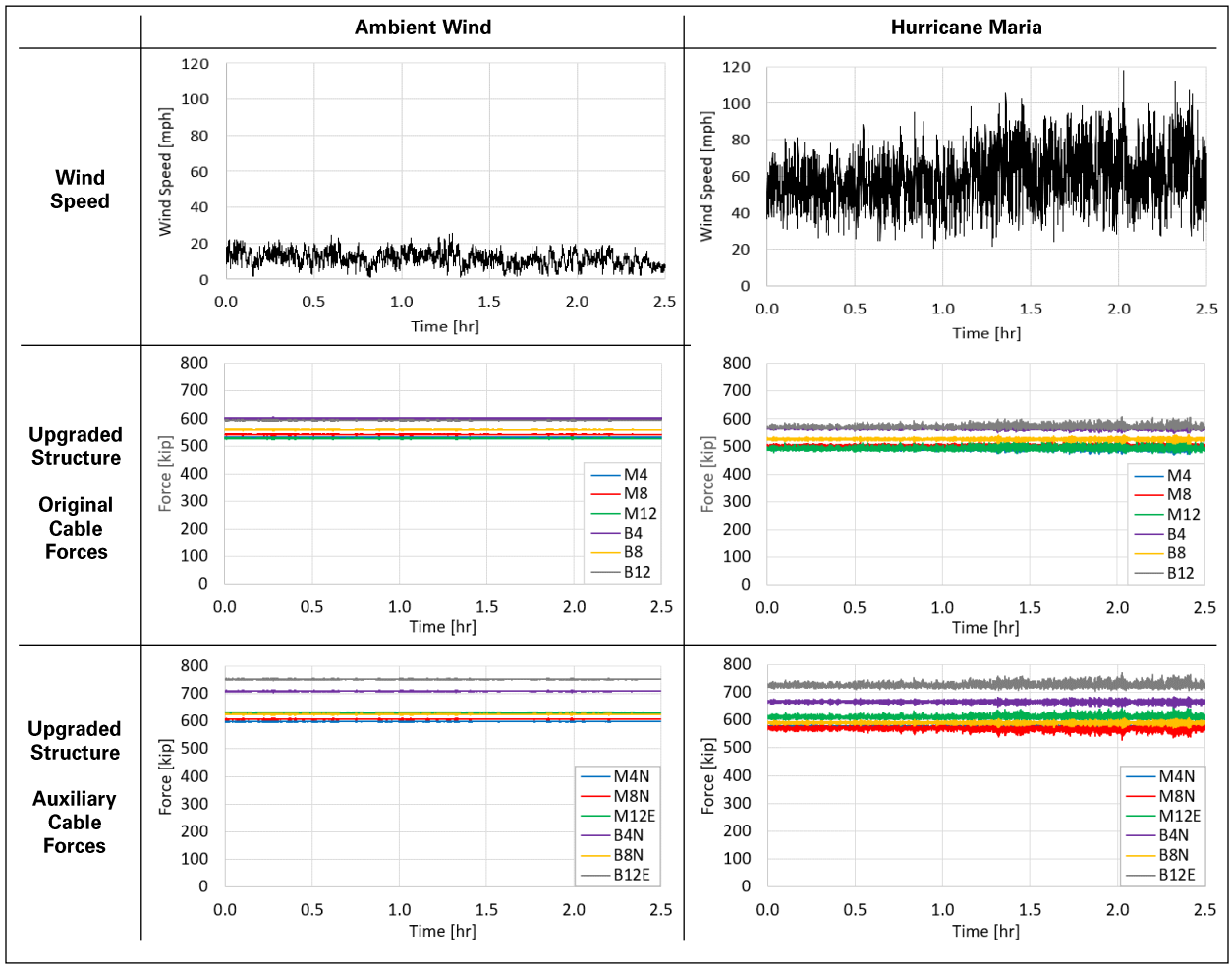

Figure 32: Cable tension time-history in original structure under ambient and hurricane wind from Tower 12 (north-south).

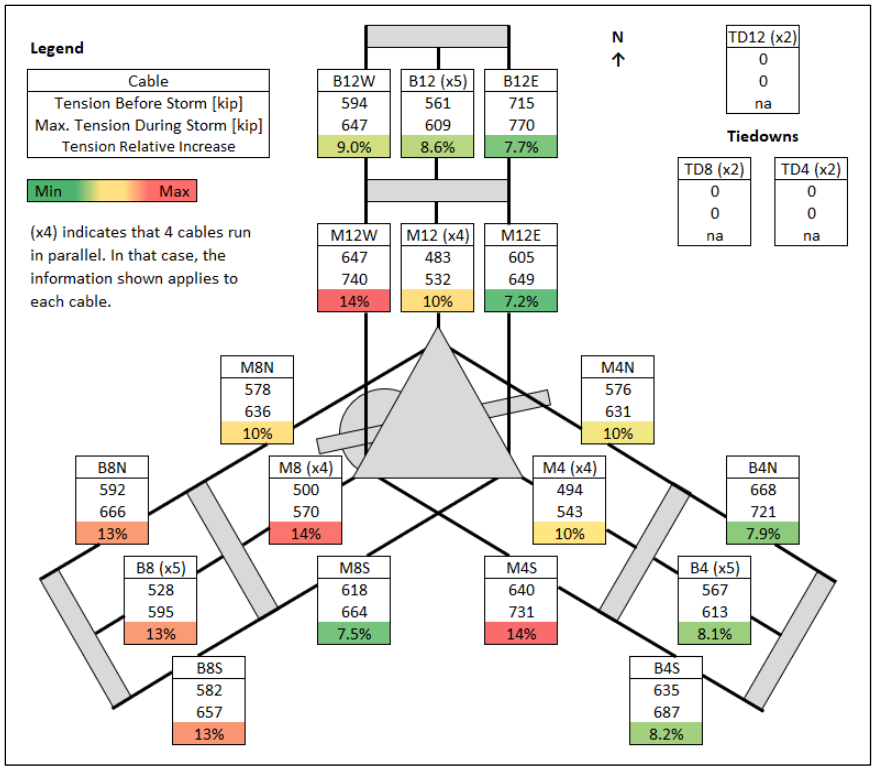

Figure 33: Maximum cable tension increase in upgraded structure in hurricane conditions.

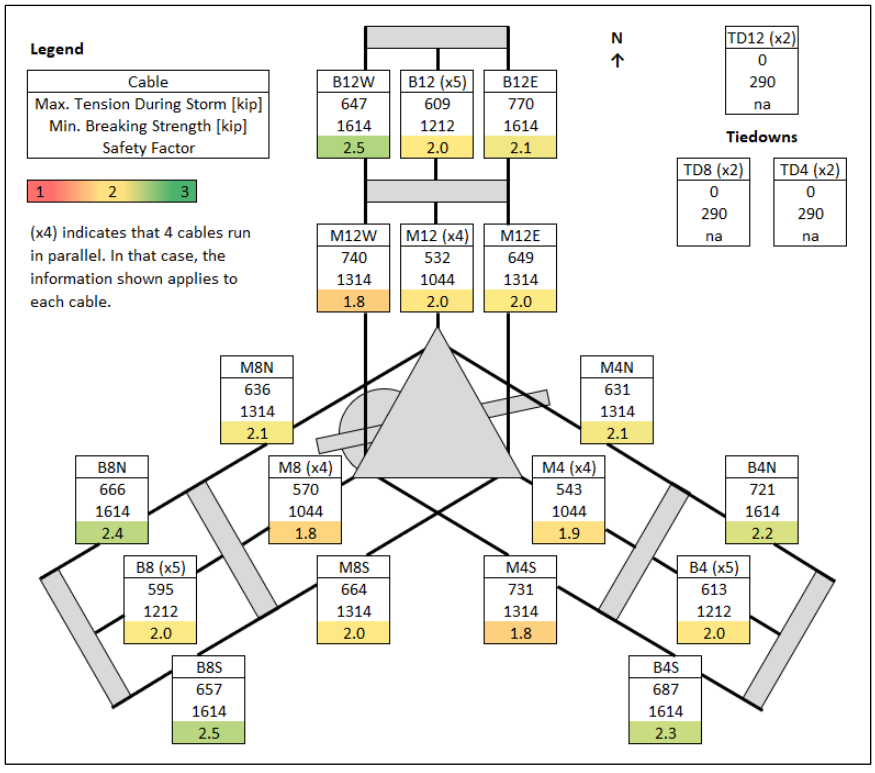

Figure 34: Maximum cable tension and corresponding safety factor in upgraded structure in hurricane conditions.

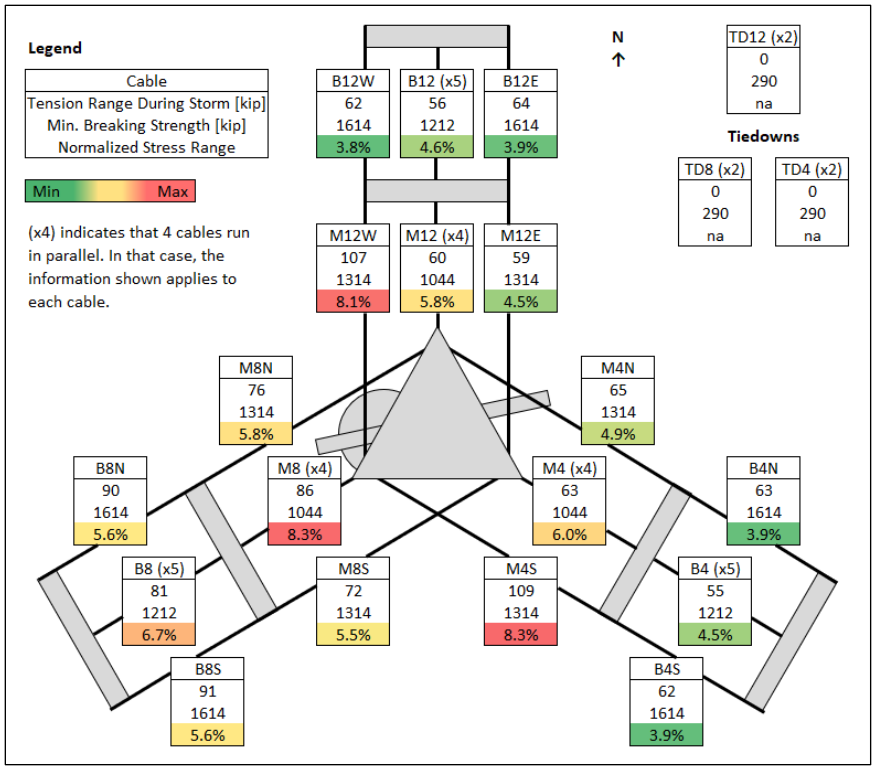

Figure 35: Maximum normalized stress range in cables of upgraded structure in hurricane conditions.

Table 18: Average number of stress cycles in cables of upgraded structure per hour of peak hurricane conditions.

	Normalized Stress Range (= Tension Range / Minimum Breaking Strength)							
	1-2%	**2-3%**	**3-4%**	**4-5%**	**5-6%**	**6-7%**	**7-8%**	**8-9%**
M4	368	101	18	3.4	0.9			
M4N	254	24	3.6	0.7				
M4S	489	114	25	7.8	1.9	1.1	0.1	0.1
M8	351	89	21	3.8	1.3	0.3	0.1	0.1
M8N	340	53	6.8	0.6	0.2			
M8S	438	96	15	1.7	0.3			
M12	352	88	19	1.9	0.7			
M12E	299	29	3.3	0.4				
M12W	473	110	20	5.7	1.5	0.3		0.1
B4	308	31	3.7	0.4				
B4N	227	16	1.6					
B4S	219	15	1.5					
B8	227	30	4.5	1.0	0.1	0.1		
B8N	158	16	1.9	0.3	0.1			
B8S	159	16	1.9	0.2	0.1			
B12	351	37	2.9	0.4				
B12E	258	14	1.3					
B12W	247	14	1.2					

Appendix K
Earthquakes' Impact on Cable Tensions

1.0 Introduction

The island of Puerto Rico is in a seismically active region between the North American and Caribbean tectonic plates. As a result, the telescope has experienced multiple earthquakes since construction in 1963. In January 2020, less than a year before the telescope's collapse, Puerto Rico was hit by a series of significant earthquakes with magnitudes up to 6.4 (January 7, 2020).

This appendix presents our analysis of the seismic effects on the telescope's cable system. The objective is to determine how much tension and how many tension cycles the cables and sockets experienced during representative earthquakes.

2.0 Background

Between the completion of the original telescope in 1964 to the first cable failure in August 2020, there was approximately 200 earthquakes of magnitude greater than 4.5 within 125 miles of Arecibo Observatory (AO).

The subsurface conditions at the site consist of surficial clay and silt layers underlain by limestone. Consequently, tower and anchor foundations are generally supported on competent limestone, which is consistent with a site class C per ASCE 7-16. Based on measurements at various locations in Puerto Rico, the shear wave velocity is estimated to be between 1,475 and 2,065 foot per second (ft/s) at the AO site.

A seismic monitoring station is located at AO. Designated as AOPR, the station is part of the Puerto Rico Seismic Network and is located on a hill of similar subsurface conditions and topography as the where the telescope's towers and cable anchors are build. Therefore, ground motion recorded by the AOPR station is used input for our seismic analysis.

In early 2020, a sequence of earthquakes took place in the southwest region of Puerto Rico, with 43 events magnitude greater than 4.5 recorded before the first cable failure. The strongest earthquake happened on January 7, 2020, with a magnitude of 6.4 and and epicenter 29 miles south of AO at a depth of 4.3 miles. The second-largest earthquake was an aftershock on January 11, 2020, with a magnitude of 5.9 and an epicenter 28 miles south of AO at a depth of 3.1 miles. Both earthquakes were strongly felt at AO. Due to the relatively short time (eight months) between the two earthquakes and the first cable failure, it is natural to evaluate the impact of those earthquakes on the telescope's cable system. The two earthquakes are referred to as M6.4 and M5.9 in this appendix.

Figure 1 shows the acceleration time histories at the AOPR station for M6.4 and M5.9, with the corresponding acceleration response spectra. Also shown in the figure is the Design Earthquake (DE) response spectrum per the ASCE 7-16 standard[1] at the AO site for an assumed site class C. All spectra are based on five percent damping. The DE spectrum is about two times larger at shorter periods and about five times larger at moderate to long periods than the M6.4 earthquake. The 2020 earthquakes were therefore significantly less severe than the current design earthquake for the AO site.

[1] American Society of Civil Engineers (ASCE). *ASCE 7-16. Minimum Design Loads and Associated Criteria for Buildings and Other Structures.* Chapters 26 and 29. 2016.

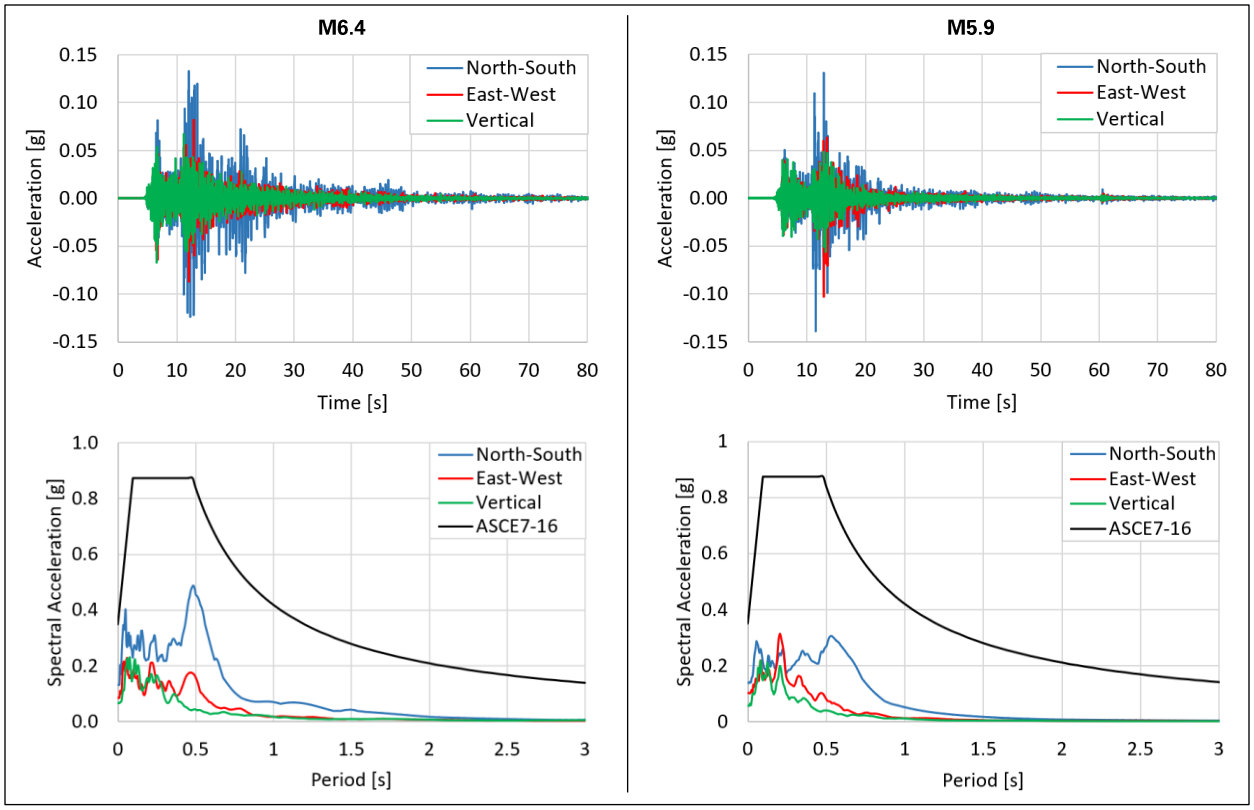

Figure 1: Ground acceleration time histories and five percent damping response spectra for M6.4 and M5.9 earthquakes.

3.0 Structural Response Analysis

To evaluate the potential impact of seismic activity on the telescope structure, we simulated the M6.4 and M5.9 earthquakes in finite element (FE) models of the original and upgraded telescope. The FE models are described in appendix F.

The ground accelerations of the M6.4 and M5.9 earthquakes were recorded by AO's seismic station (AOPR), and the towers and anchors of the telescope experienced similar accelerations. However, due to the distance between the different towers and cable anchors, the arrival time of the acceleration was slightly different at each tower and anchor location. The recorded ground accelerations were therefore applied to the FE models with time delays between towers and anchors calculated from the shear wave velocity at the site (Figure 2).

As shown in Table 1, a total of eight analyses were performed considering two structures (original and upgraded), two earthquakes (M6.4 and M5.9), and the two bounds of the shear wave velocity (1,475 ft/s and 2,065 ft/s).

The analyses use multi-support excitation to consider the propagation of ground motions to the different towers, anchorages, and tie-down cable supports. The acceleration times histories in three directions were converted to ground displacement time histories and applied to the FE models with time delays between towers and anchors calculated from the shear wave velocity at the site. Nonlinear direct integration time history was performed, with a Rayleigh damping model calibrated such that the effective damping ratio is one percent for the first two modes of the structure.

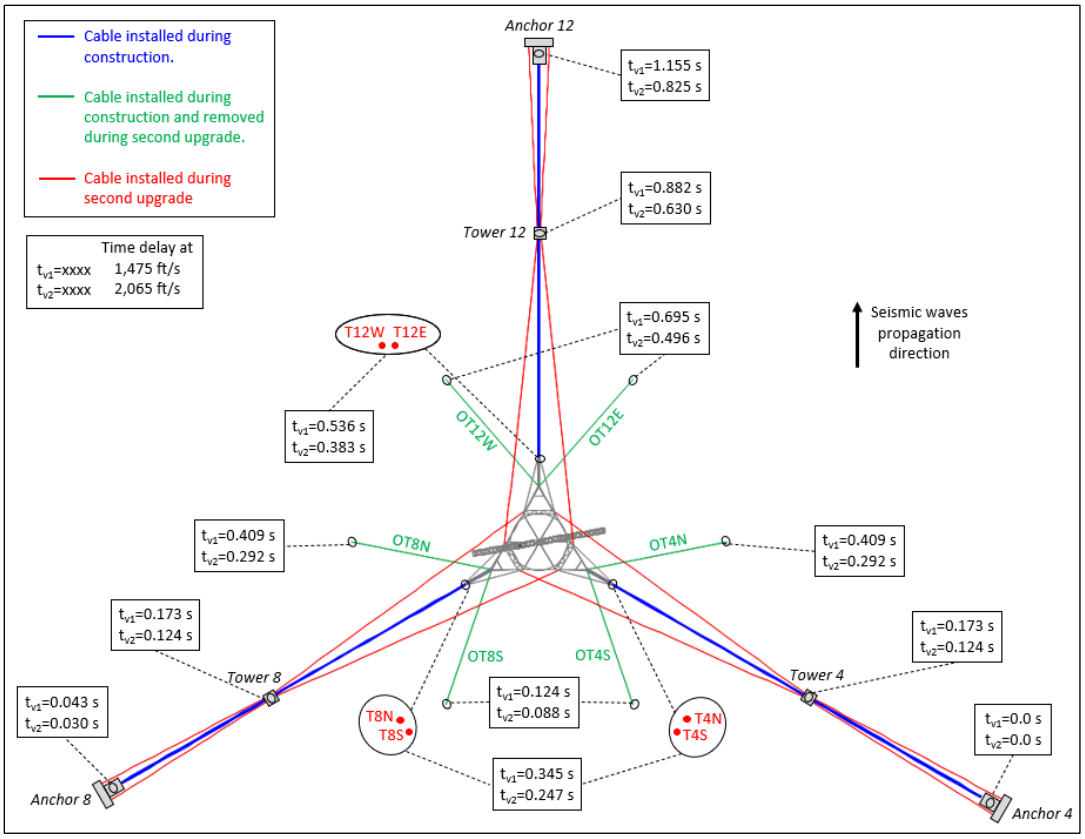

Figure 2: Ground motion time delay based on two shear wave velocities (1,475 and 2,065 ft/s).

Table 1: Earthquake analyses performed.

Analysis #	Telescope Model	Earthquake	Shear Wave Velocity [ft/s]
1	Upgraded	M6.4	1,475
2	Upgraded	M6.4	2,065
3	Upgraded	M5.9	1,475
4	Upgraded	M5.9	2,065
5	Original	M6.4	1,475
6	Original	M6.4	2,065
7	Original	M5.9	1,475
8	Original	M5.9	2,065

4.0 Cable Tension Results

4.1 Original Structure

The cable tension time histories in the original structure are shown in Figure 3 for the M6.4 and M5.9 earthquakes, with a shear wave velocity of 2,065 ft/s. The cable tension maps (Figure 4, Figure 5, and Figure 6) show the worst-case envelope over the four cases considered (M6.4 and M5.9 earthquakes, with 1,475 ft/s and 2,065 ft/s shear wave velocity).

Figure 4 shows the maximum tension increase in each cable during the earthquake as a percentage of the pre-earthquake tension. Excluding the tiedowns, the maximum tension increase is 10 percent and occurs in the backstays of Tower 8.

Figure 5 shows the lowest safety factor reached in each cable during the earthquake. The lowest safety factor is the ratio of the highest cable tension experienced during the earthquake to the cable's minimum breaking strength. The safety factors remain around two in all of the cables.

Figure 6 shows the maximum normalized stress range experienced by each cable during the earthquake. The maximum normalized stress range is the ratio of the maximum tension range (difference between the maximum and minimum tension experienced) to the cable's minimum breaking strength. The maximum normalized stress range is between two and nine percent in the mains and backstays.

Table 2 shows the number of stress cycles experienced by each cable during an earthquake for different stress levels. The number of cycles were counted in the cable tension time history results using the rainflow method, and averaged over the four cases considered (M6.4 and M5.9 earthquakes, with 1,475 ft/s and 2,065 ft/s shear wave velocity).

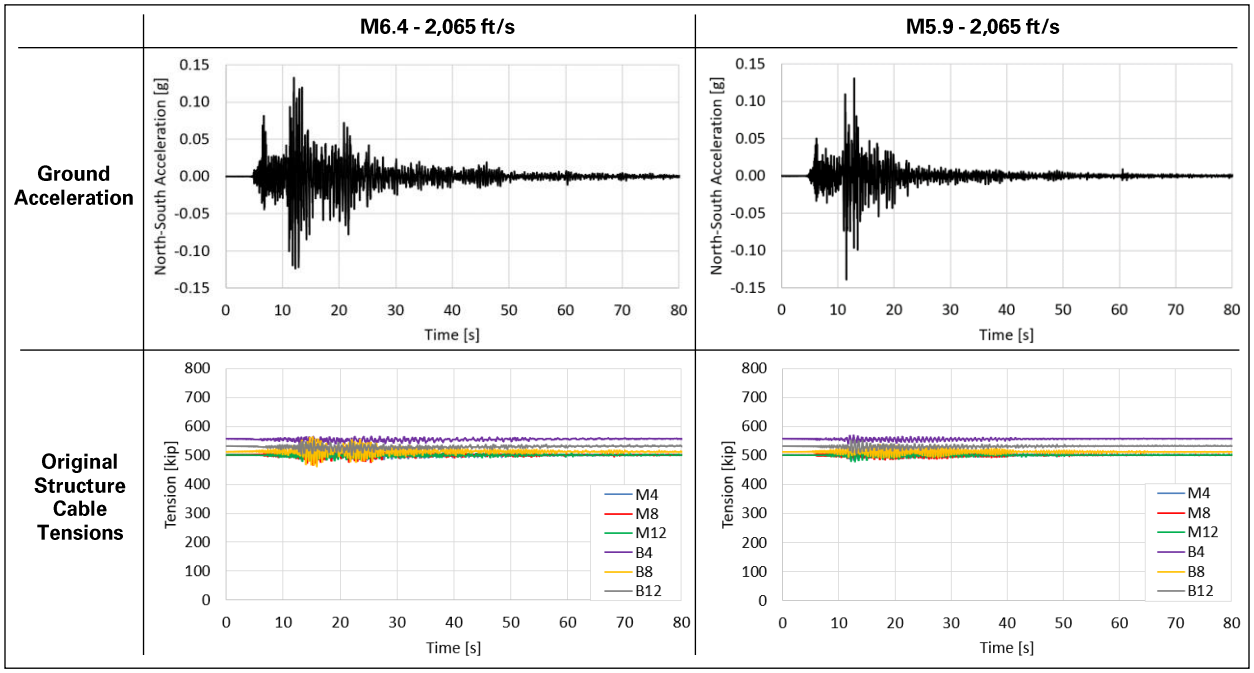

Figure 3: Cable tension time history in original structure during M6.4 and M5.9 earthquakes, with 2,065 ft/s shear wave velocity.

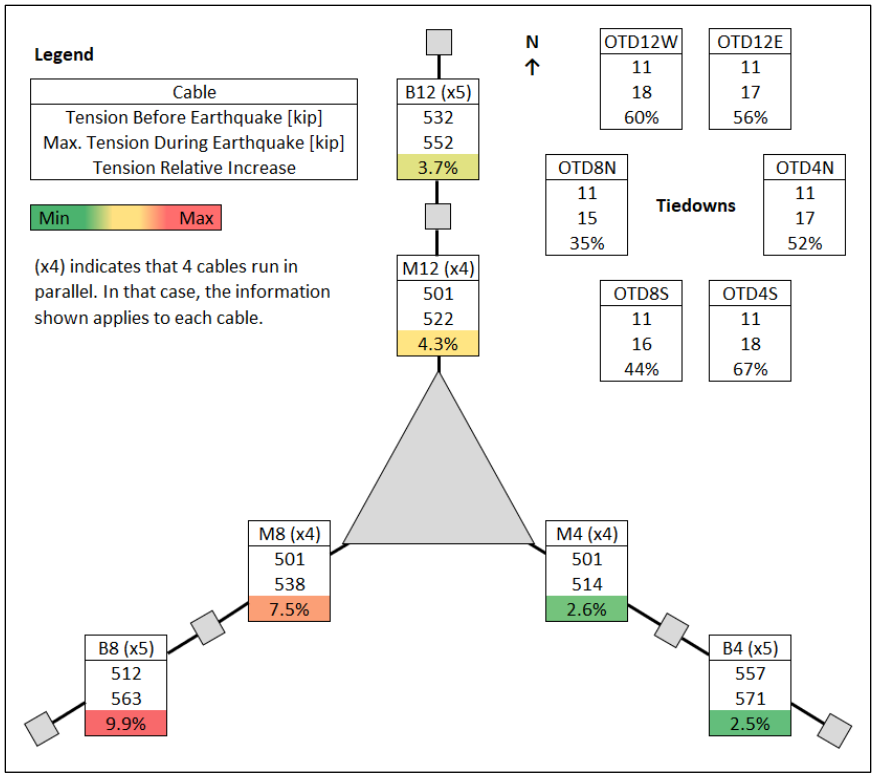

Figure 4: Maximum cable tension increase in original structure due to 2020 earthquakes.

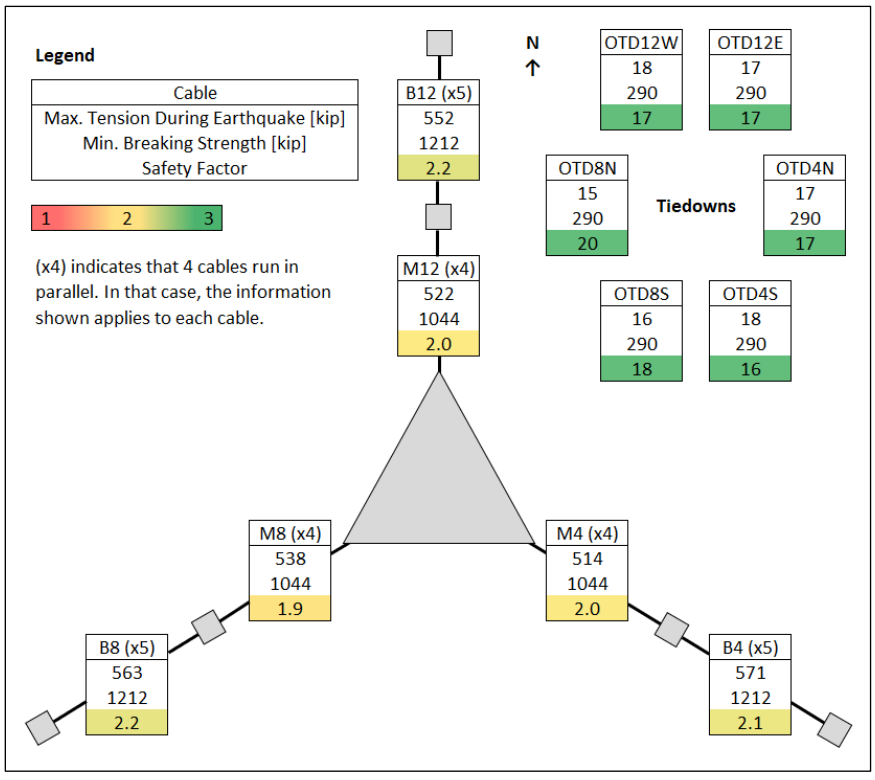

Figure 5: Maximum cable tension and corresponding safety factor in original structure due to 2020 earthquakes.

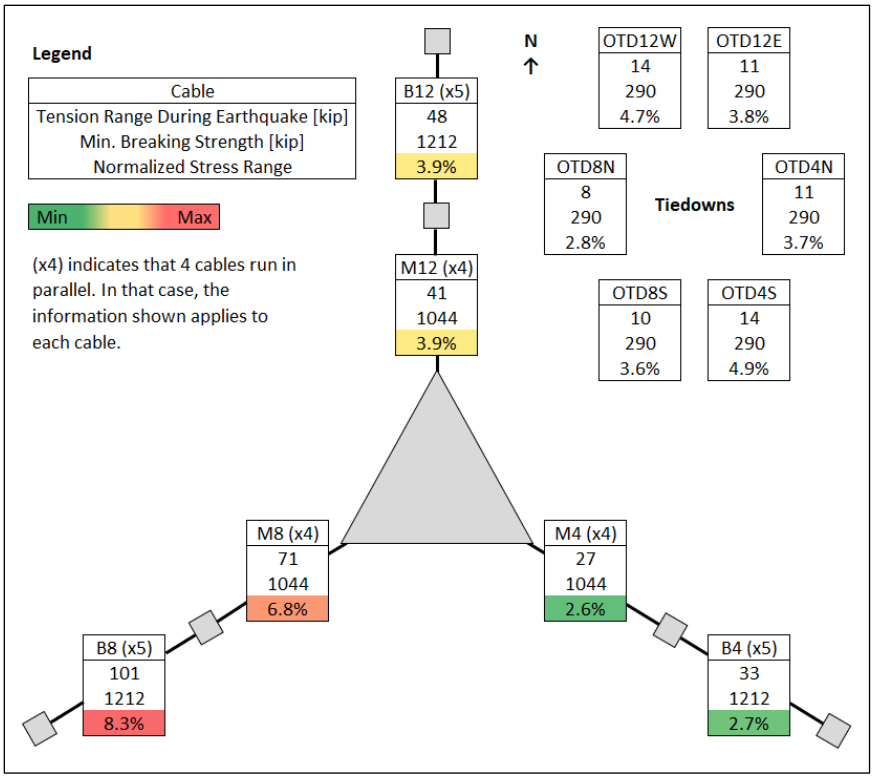

Figure 6: Maximum normalized stress range in cables of original structure due to 2020 earthquakes.

Table 2: Average number of stress cycles in cables of original structure during a 2020 earthquake.

	Normalized Stress Range (= Tension Range / Minimum Breaking Strength)							
	1-2%	**2-3%**	**3-4%**	**4-5%**	**5-6%**	**6-7%**	**7-8%**	**8-9%**
M4	21	2.3						
M8	16	8.5	7.0	4.5	1.3	0.5		
M12	17	6.8	1.8					
B4	17	1.3						
B8	21	11	7.5	4.8	3.3	2.3	1.5	0.3
B12	18	6.8	1.8					

4.2 Upgraded Structure

The cable tension time histories in the original structure are shown in Figure 7 for the M6.4 and M5.9 earthquakes with a shear wave velocity of 2,065 ft/s. The cable tension maps (Figure 8, Figure 9, and Figure 10) show the worst-case envelope over the four cases considered (M6.4 and M5.9 earthquakes, with 1,475 ft/s and 2,065 ft/s shear wave velocity).

Figure 8 shows the maximum tension increase in each cable during the earthquake as a percentage of the pre-earthquake tension. The maximum tension increase is five percent, occurring in the M12 main cables.

Figure 9 shows the lowest safety factor reached in each cable during the earthquake. The lowest safety factor is the ratio of the highest cable tension experienced during the earthquake to the cable's breaking strength. The safety factors in the mains and bactays are around or above two, and the safety factor in cable M4N (first cable failure) is 2.1.

Figure 10 shows the maximum normalized stress range experienced by each cable during the earthquake. The maximum normalized stress range is the ratio of the maximum tension range (difference between the maximum and minimum tension experienced) to the cable's breaking strength. The maximum normalized stress range is between two and five in the mains and backstays.

Table 3 shows the number of stress cycles experienced by each cable during the earthquake for different stress levels. The number of cycles were counted in the cable tension time history results using the rainflow method, and averaged over the four cases considered (M6.4 and M5.9 earthquakes, with 1,475 ft/s and 2,065 ft/s shear wave velocity).

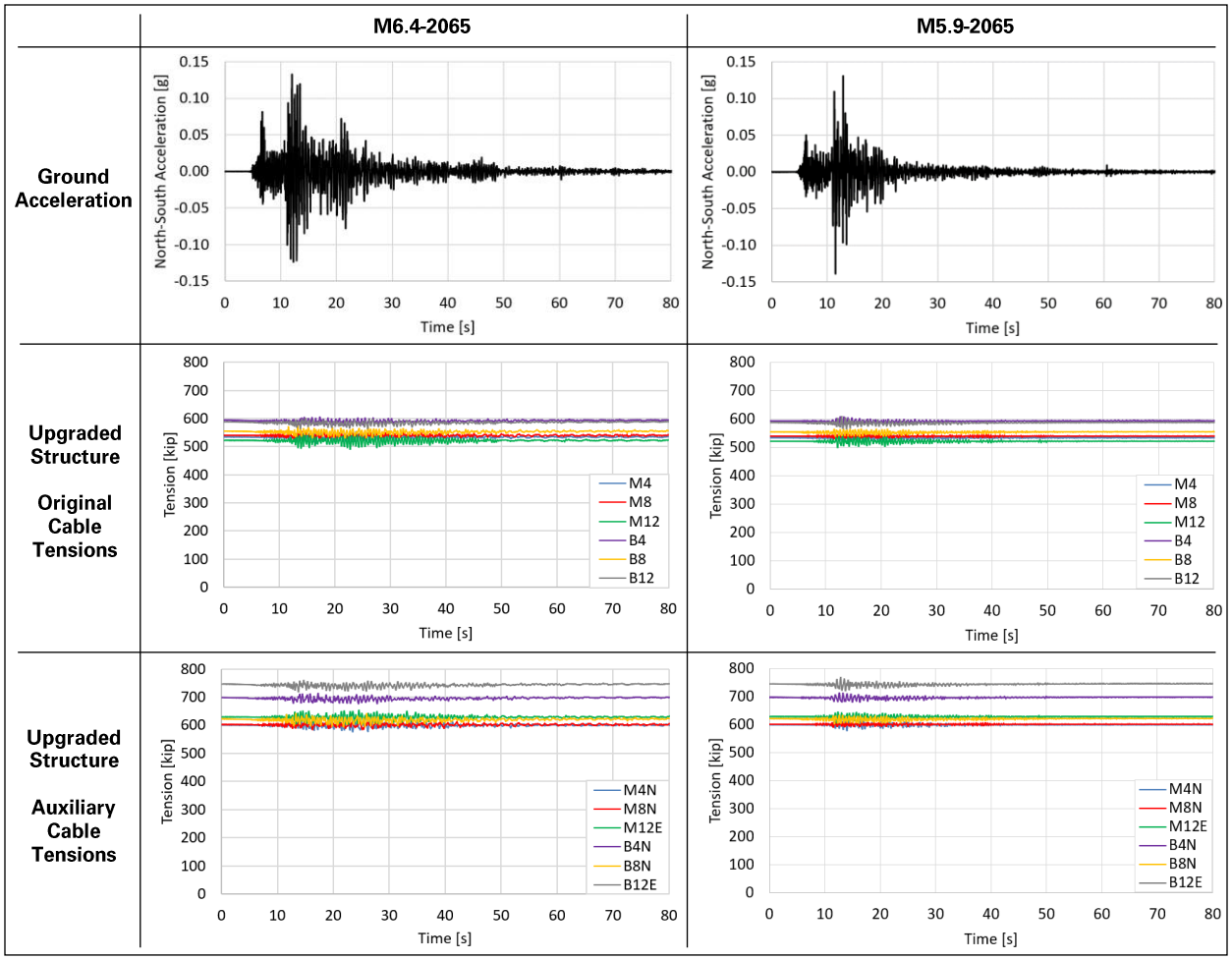

Figure 7: Cable tension time history in original structure during M6.4 and M5.9 earthquakes, with 2,065 ft/s shear wave velocity.

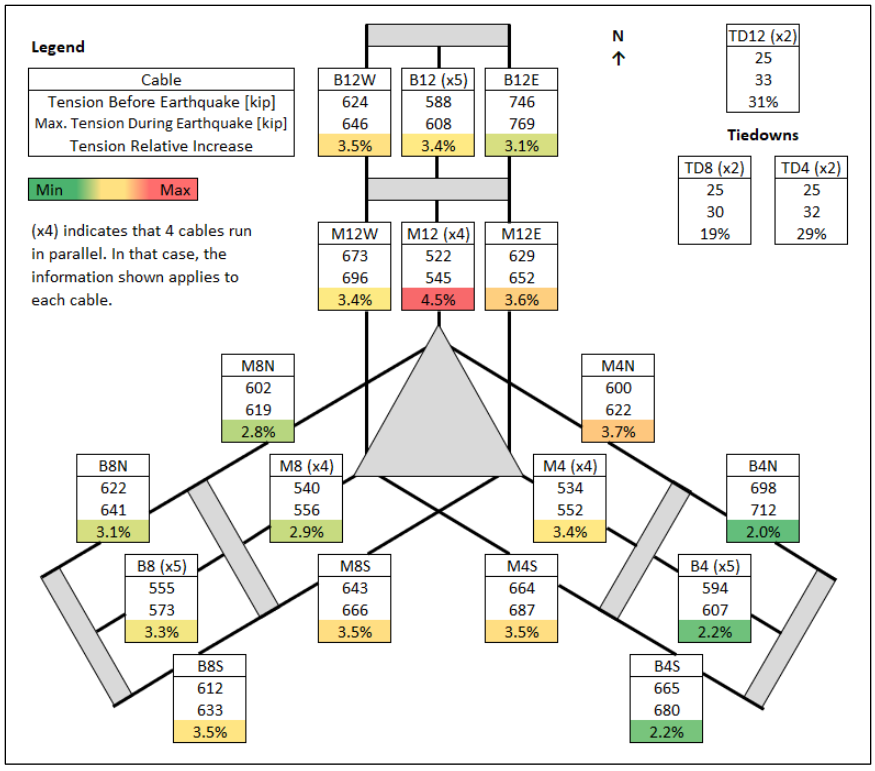

Figure 8: Maximum cable tension increase in upgraded structure due to 2020 earthquakes.

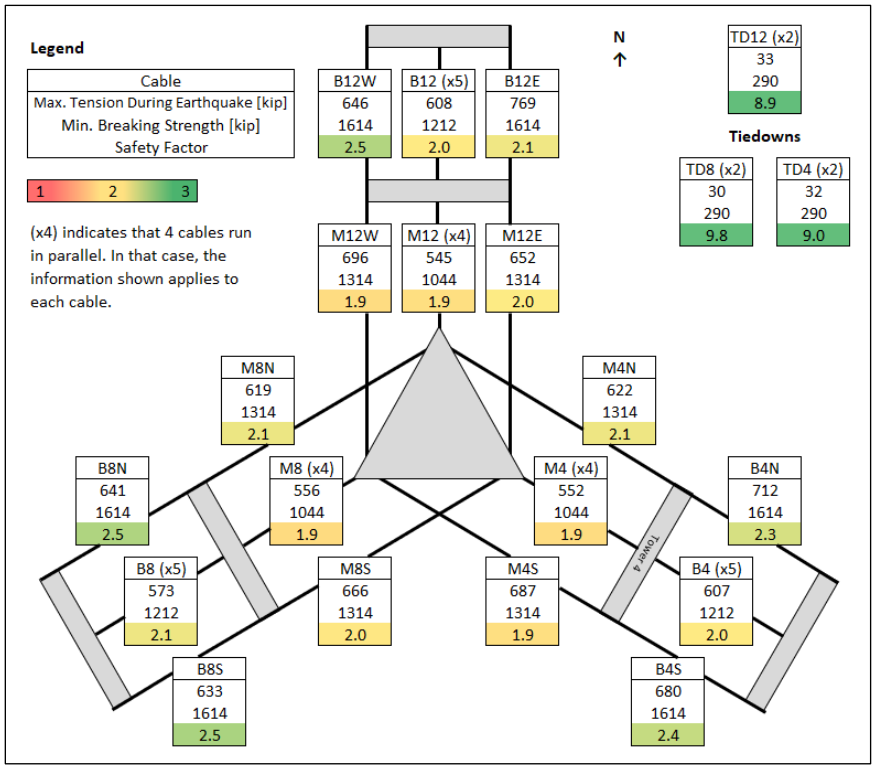

Figure 9: Maximum cable tension and corresponding safety factor in upgraded structure due to 2020 earthquakes.

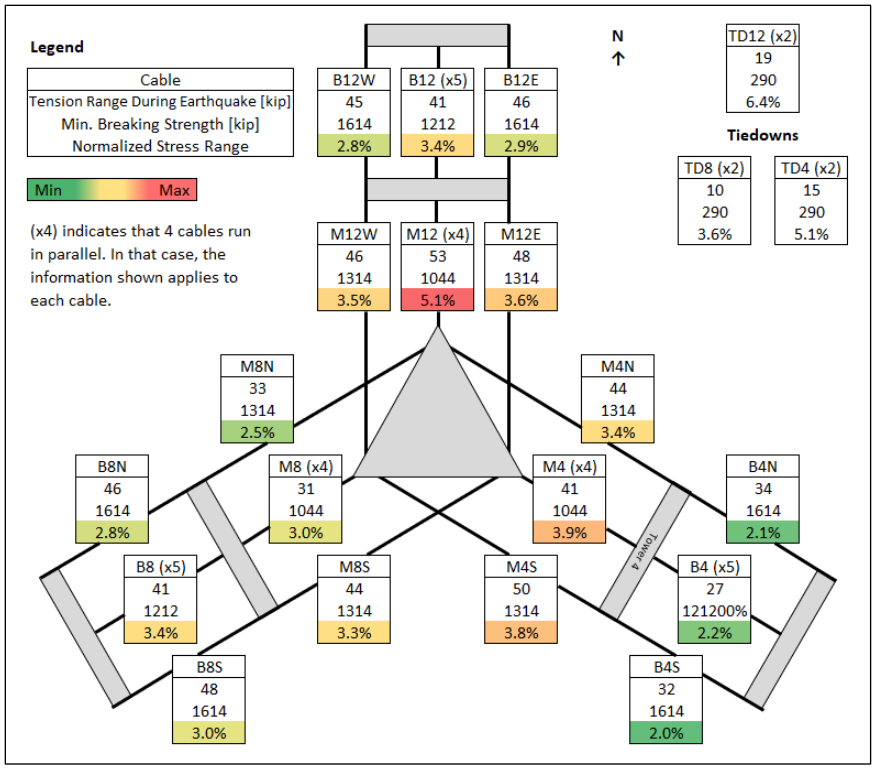

Figure 10: Maximum normalized stress range in cables of upgraded structure die to 2020 earthquakes.

Table 3: Average number of normalized stress cycles in cables of upgraded structure during a 2020 earthquake.

	Normalized Stress Range (= Tension Range / Breaking Strength)				
	1-2%	**2-3%**	**3-4%**	**4-5%**	**5-6%**
M4	22	8.0	0.8		
M4N	23	3.3	0.8		
M4S	16	3.3	0.8		
M8	19	4.0			
M8N	15	1.5			
M8S	15	5.8	0.5		
M12	28	14	8.3	2.3	0.3
M12E	21	10	2.8		
M12W	21	7.3	1.8		
B4	14	0.8			
B4N	11	0.3			
B4S	11				
B8	28	6.8	1.5		
B8N	22	4.5			
B8S	22	5.0			
B12	20	4.8	0.3		
B12E	18	2.3			
B12W	20	2.0			

Appendix L
Cable Laboratory Analysis

1.0 Introduction

After the telescope's collapse, samples were cut from the steel cables and sent to Socotec's laboratory for analysis. The objective was threefold: determine whether the cables satisfied the design requirements, evaluate the cables' condition after years of service, and investigate how some of the cables failed near the socket connections.

2.0 Cable Samples

On December 1, 2020, the telescope's platform lost stability and collapsed when the three remaining M4 cables failed in rapid succession at the top of Tower 4. After the collapse, the failed end of each cable was cut from the rest of the cable and sent to Socotec's laboratory for analysis (Figure 1). These samples are referred to as *failed cable end 11M*, *12M* and *13I* in this appendix.

Another M4 cable, M4-4, failed three weeks before the collapse. Some of the cable's wires fractured within socket M4-4_T, while others fractured outside of the socket. Socket M4-4_T was recovered and sent to Socotec's laboratory for analysis, and the fractured wires still attached to the socket are considered as *failed cable end M4-4* in this appendix (Figure 2).

An additional segment was cut from each of the four M4 cables and sent to Socotec's laboratory for analysis (Figure 3). Each segment was cut away from the cable failure point and had no visible wire break. These samples are referred to *intact cable segment 10H*, *11I*, *12G* and *13GH* in this appendix.

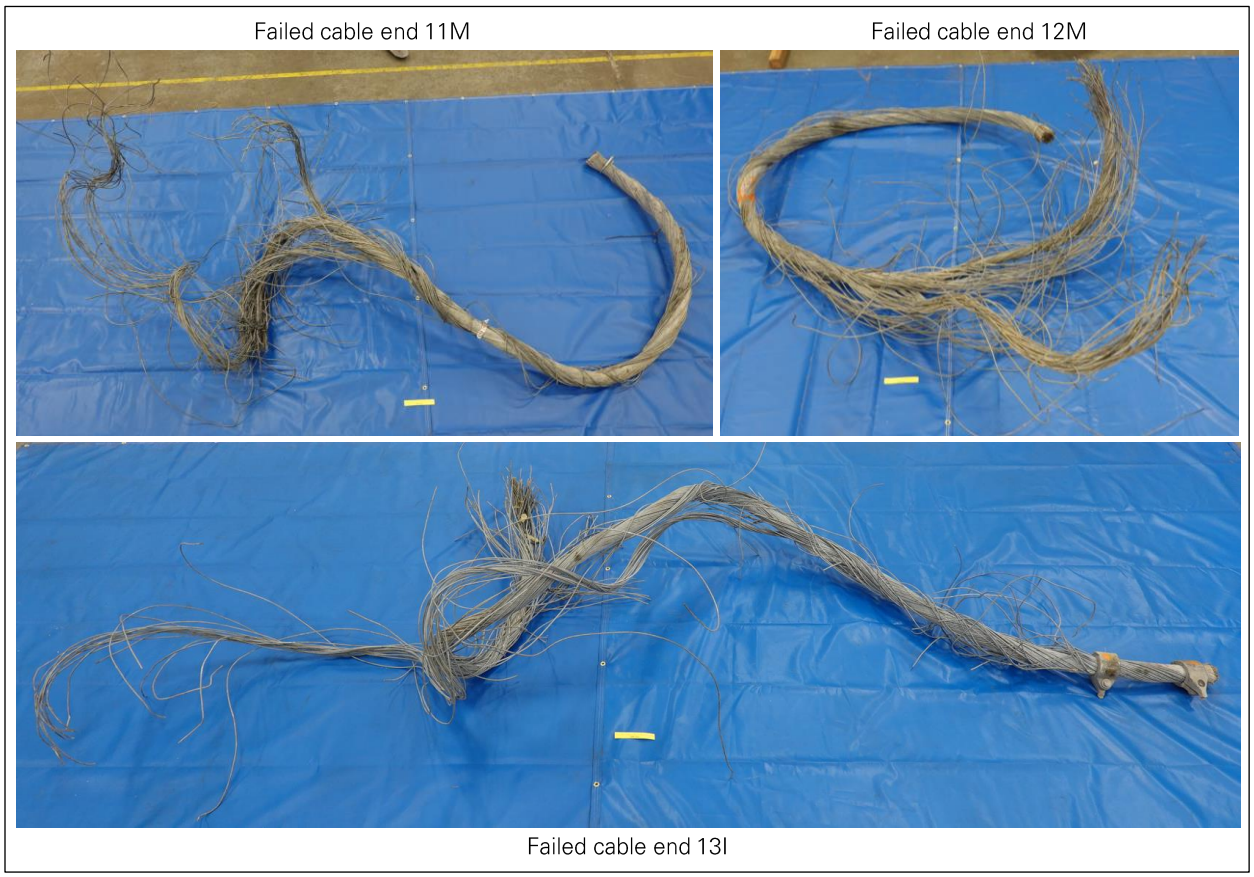

Figure 1: Failed ends of three M4 cables *(photos: Socotec).*

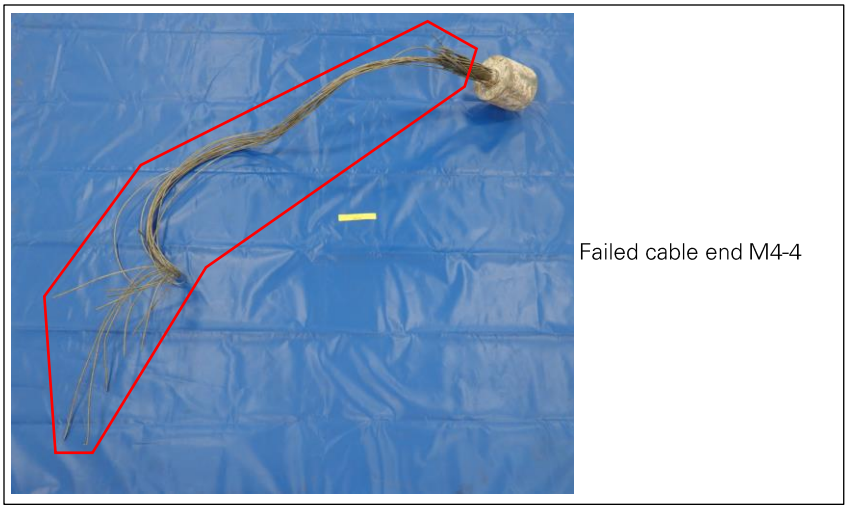

Figure 2: Socket M4-4_T with multiple M4-4 wires fractured outside of socket *(photo: Socotec).*

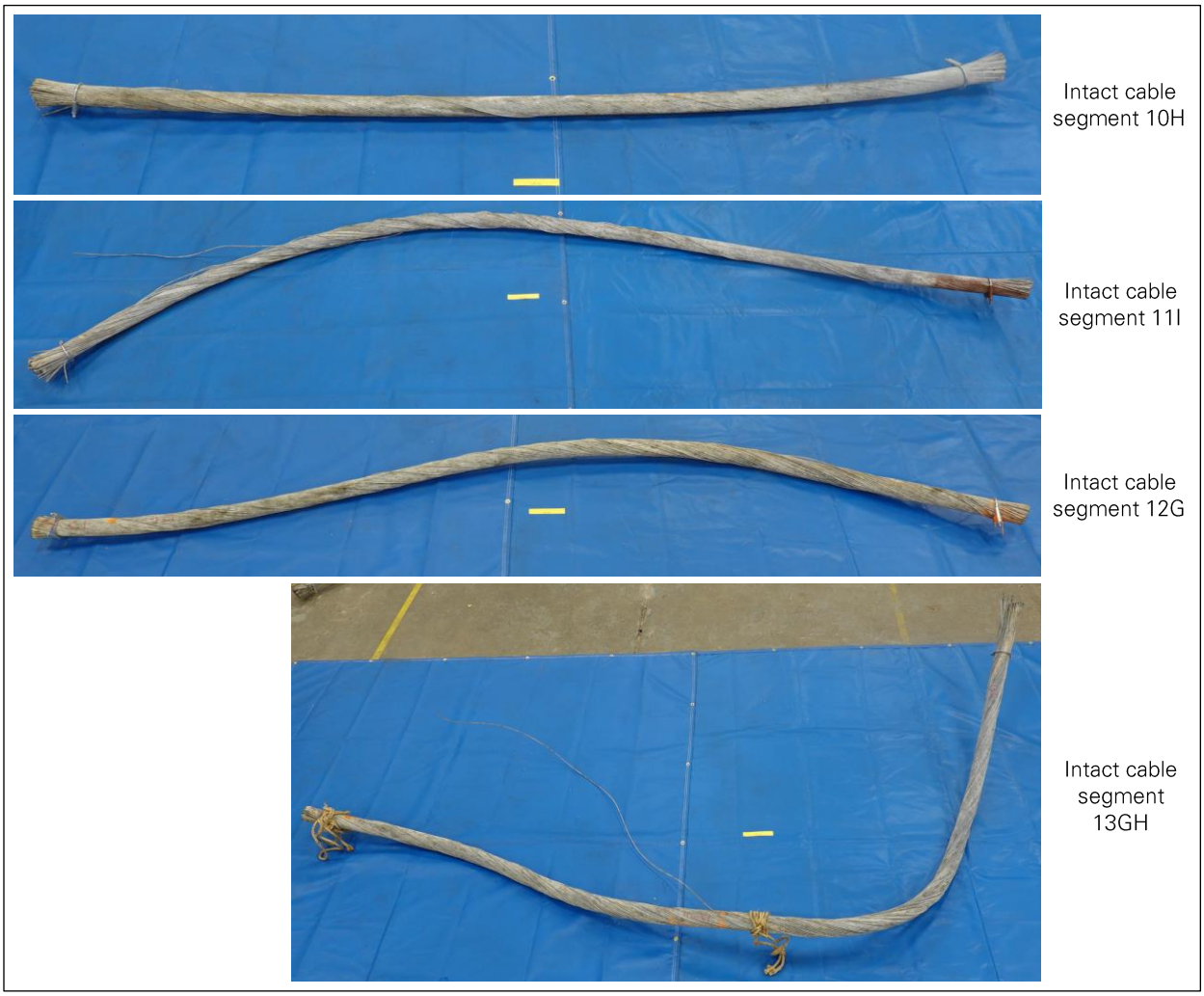

Figure 3: Intact segments of four M4 cables *(photos: Socotec).*

3.0 Cable Condition

3.1 Corrosion Deposits

Each M4 cable consists of 7 concentric layers of galvanized steel wires. The outermost layer is referred to as the first layer, while the innermost layer is the seventh layer. The four intact cable segments were taken apart layer by layer to observe the condition of each layer, and two types of corrosion deposits were observed in the first five layers (Figure 4). A white powdery deposit is generally present on the entire length of the cable segments and is characteristic of galvanizing zinc corrosion. Red/brown deposits are also present but more localized, and indicate that the steel of the wires started to corrode at some locations.

Four samples of corrosion deposits were analyzed with energy dispersive x-ray spectroscopy (EDS) to determine their chemical composition (Figure 5, Table 1). The white deposits consist primarily of oxygen of zinc, and contain very little iron. This confirms that the white deposits are due to corrosion of the galvanizing zinc, while the wires' steel remained protected. The red/brown deposits, however, consist primarily of oxygen, zinc, and iron. This confirms that at the locations of the red/brown deposits, the wires' steel started to corrode.

The other elements present in the deposits may have been part of the corroded steel or the paint(s) applied to the cable, or come from the environment.

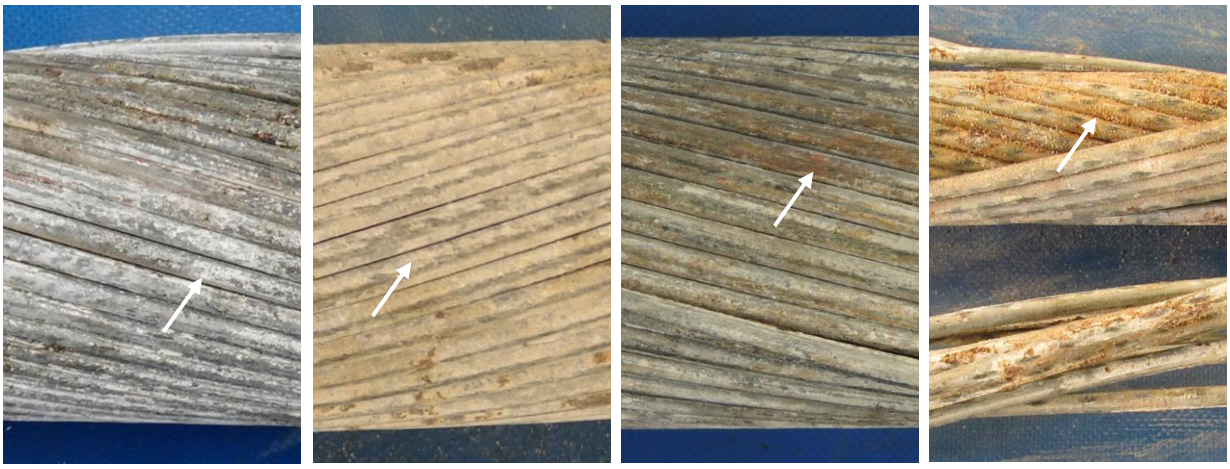

White deposit on first layer of intact cable segment 11I

White deposit on second layer of intact cable segment 12G

Red/brown deposit on first layer of intact cable segment 10H

Red/brown deposit on fourth layer of intact cable segment 10H

Figure 4: Corrosion deposits tested for chemical composition *(photos: Socotec).*

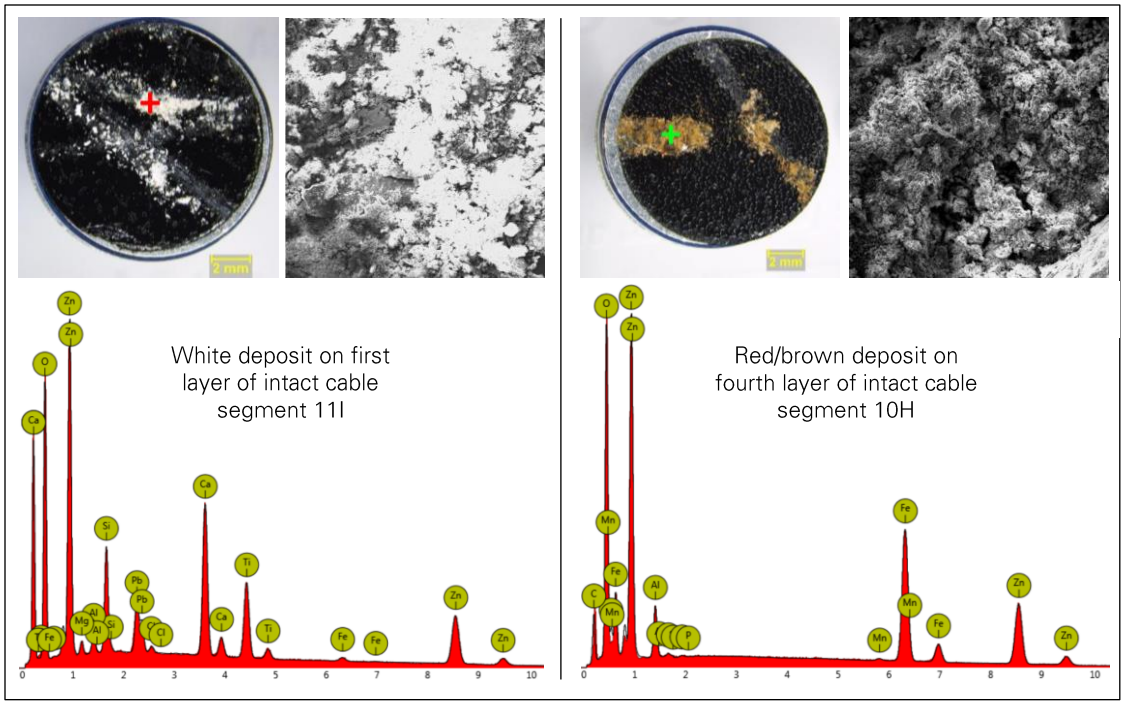

Figure 5: Representative EDS spectra from white and red/brown deposits *(photos and figures: Socotec).*

Table 1: Corrosion deposit composition by element weight.

			Intact Cable Segment 11I	Intact Cable Segment 12G	Intact Cable Segment 10H	
			Wire Layer 1[A]	Wire Layer 2[A]	Wire Layer 1[A]	Wire Layer 4[A]
Deposit Color			White	White	Red/brown	Red/brown
Weight Fraction [%]	**Oxygen**	**O**	34.2	22.3	24.7	24.3
	Zinc	**Zn**	30.6	75.4	52.6	42.1
	Iron	**Fe**	0.8	0.6	21.6	28.8
	Aluminum	**Al**	1.0	0.3	0.2	3.3
	Calcium	**Ca**	10.6	0.7	0.2	
	Carbon	**C**				1.0
	Chlorine	**Cl**	0.2			
	Lead	**Pb**	10.1			
	Magnesium	**Mg**	0.9			
	Manganese	**Mn**				0.3
	Phosphorus	**P**		0.3	0.2	0.1
	Silicon	**Si**	4.1	0.2	0.3	0.1
	Sulfur	**S**			0.3	
	Titanium	**Ti**	7.7	0.3		

[A] Layer 1 is the outermost layer.

3.2 Remaining Galvanizing Zinc

The galvanizing zinc weight was measured on 27 wires taken from the first two layers of three failed cable ends. The amount of galvanizing zinc on a steel surface is typically expressed as a weight of zinc per surface area, in this case in ounces per square foot (oz/ft^2). Measurements were performed according to the ASTM A90 standard[1] on wire lengths ranging from 18 to 27 inches.

The results are provided in Table 2, where five measurements are flagged for being less than one oz/ft^2. One oz/ft^2 is the minimum required for Class A wires in the ASTM A586 standard,[2] which was prescribed for the auxiliary cables of the telescope installed in 1997. The M4 cables tested at Socotec's laboratory are part of the original cables installed in 1964, and the requirement on galvanizing zinc weight is not known for those cables. Yet, after 57 years of service, over 80 percent of the wires tested still have more galvanizing zinc than required in a standard applicable to the fabrication of new cables. For the five wires that no longer meet that standard, the average and minimum galvanizing zinc weight are respectively 88 percent and 85 percent of the standard's requirement.

Table 2: Galvanizing zinc weight measured on cable wires.

		Failed Cable End 11M	Failed Cable End 12M	Failed Cable End 13I
Zinc Coating Weight [oz/ft^2]	**Wire 1**	1.11	0.85	0.85
	Wire 2	1.51	1.32	0.91
	Wire 3	1.45	1.35	0.87
	Wire 4	1.19	1.23	1.18
	Wire 5	1.11	1.20	1.24
	Wire 6	0.94	1.22	1.42
	Wire 7	1.19	1.06	1.21
	Wire 8	1.04	1.11	1.49
	Wire 9	1.04	1.10	1.17
Average Zinc Coating Weight [oz/ft^2]		1.18	1.16	1.15
Zinc Coating Weight CV		15%	12%	19%

3.3 Fractured Wires

Visual examination of the four intact cable segments revealed three fractured wires in the second layer of one segment (11I). The wire fracture surfaces are flat transverse planes with thumbnail-shaped regions covered with a dark layer of oxide deposit (Figure 6). Scanning electron microscopy (SEM) of the fracture surfaces shows a morphology with micro void coalescence indicative of ductile overstress fracture (Figure 7). Additional stereomicroscopic examination revealed multiple cracks on the surface of two of the fractured wires parallel to the fracture surface. Finally, a cross-section through the length of the wire cutting through the crack revealed multiple branched cracks parallel to the primary fractured surface (Figure 8). This indicates that the wires fractured to stress-corrosion cracking.

[1] American Society for Testing and Materials (ASTM). *ASTM A90/A90M-21. Standard Test Method for Weight [Mass] of Coating on Iron and Steel Articles with Zinc or Zinc-Alloy Coatings.* 2021.
[2] American Society for Testing and Materials (ASTM). *ASTM A586-18. Standard Specification for Metallic-Coated Parallel and Helical Steel Wire Structural Strand.* 2018.

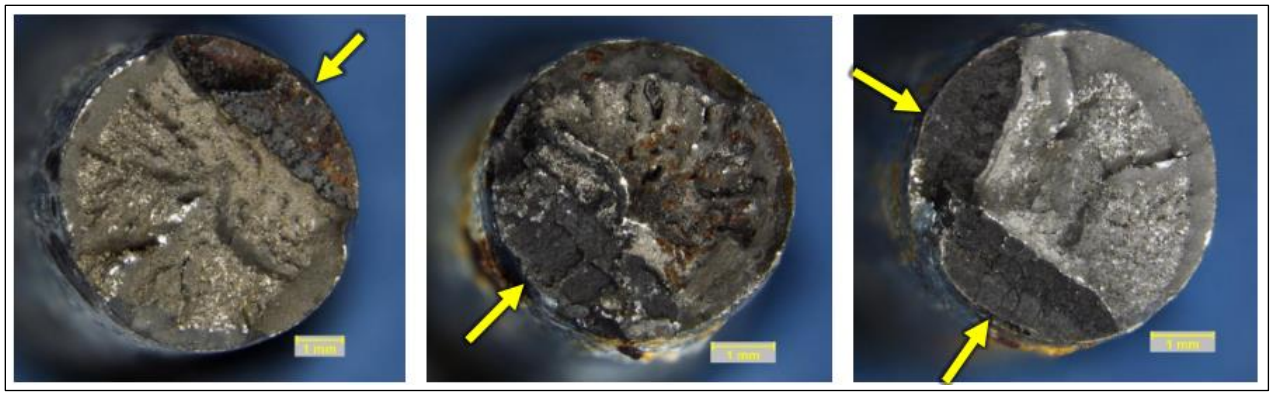

Figure 6: Stereomicroscopic images of three fractured wires of intact cable segment 11I, showing thumbnail-shaped areas covered with an oxide layer *(photos: Socotec).*

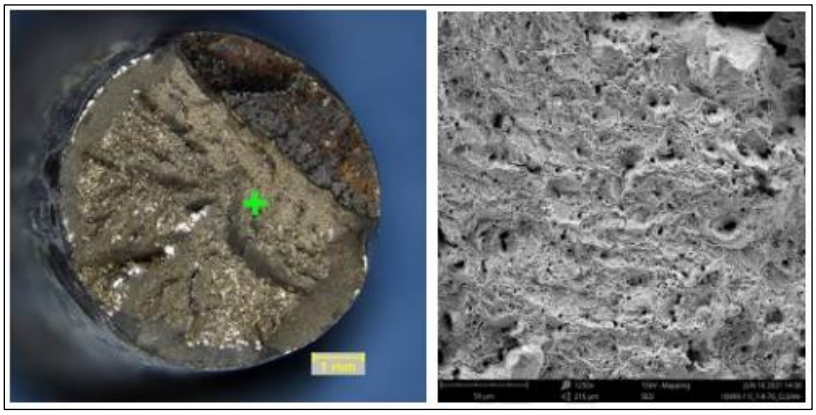

Figure 7: SEM image of a fractured wire of intact cable segment 11I, showing fracture morphology consistent with microvoid coalescence *(photos: Socotec).*

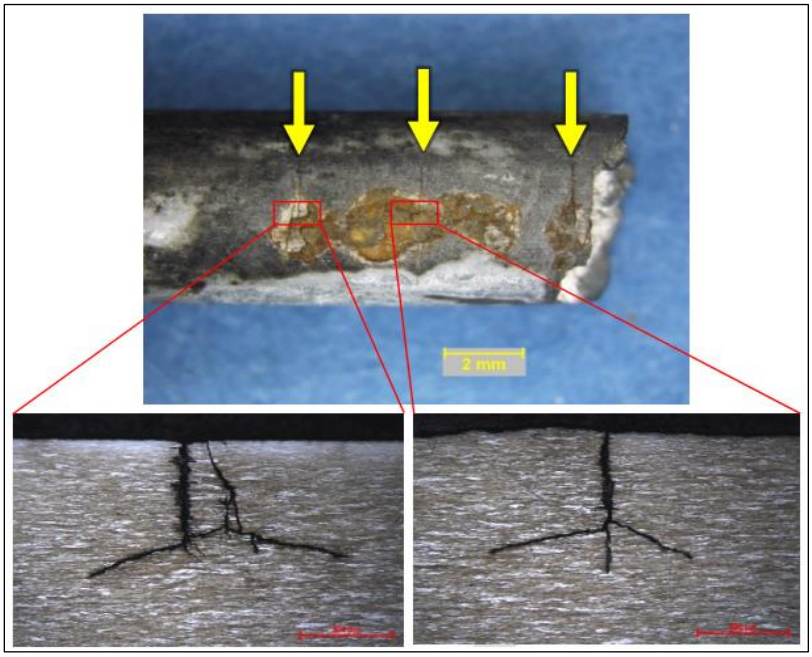

Figure 8: Metallographic images of branched cracks near fracture point of a wire of intact cable segment 11I *(photos: Socotec).*

4.0 Wire Properties

4.1 Wire Diameter

The diameter of 10 wires were measured on each of the three failed cable ends, which were part of three original main cables. Additional wire diameter were measured on two other cable types: an auxiliary main cable, and an auxiliary backstay cable. Segments of those cable types were still attached to the sockets sent to Socotec's laboratory for analysis (Appendix M).

The nominal wire diameter is 13/64 (= 0.2038) inch in the original main cables. It is 1/4 (= 0.25) inch in the auxiliary main and backstay cables, except for the fifth layer of the auxiliary backstay cables, which uses 3/16 (= 0.175) inch diameter wires. As shown in Table 3, the measured wire diameters are consistent with the nominal values.

Table 3: Cable wire diameter measurements.

		Failed Cable End 11M	Failed Cable End 12M	Failed Cable End 13I	Auxiliary Main Cable	Auxiliary Backstay Cable	
						Layers 1-4 and 6-7[A]	Layer 5[A]
Wire Diameter [in]	Wire 1	0.2045	0.2030	0.2035	0.2460	0.2505	0.1890
	Wire 2	0.2030	0.2025	0.2000	0.2455	0.2555	0.1890
	Wire 3	0.2060	0.2015	0.1985	0.2460	0.2510	
	Wire 4	0.2170	0.2000	0.1970	0.2435	0.2500	
	Wire 5	0.2045	0.2020	0.2010	0.2500	0.2515	
	Wire 6	0.1985	0.2020	0.2000	0.2450	0.2500	
	Wire 7	0.2025	0.1975	0.1975	0.2440		
	Wire 8	0.2010	0.2010	0.1965	0.2460		
	Wire 9	0.2045	0.1990	0.1985	0.2445		
	Wire 10	0.1965	0.1990	0.2005	0.2480		
Average Wire Diameter [in]		0.2038	0.2008	0.1993	0.2459	0.2514	0.1890
Wire Diameter CV		2.56%	0.85%	1.01%	0.74%	0.76%	0.00%
Nominal Wire Diameter [in]		0.2031	0.2031	0.2031	0.2500	0.2500	0.1875
Average / Nominal		100%	99%	98%	98%	101%	101%

[A] Layer 1 is the outermost layer.

4.2 Wire Chemical Composition

The steel's chemical composition was determined for nine wires taken from three failed cable ends using optical emission spectroscopy (OES). As shown in Table 4, the results indicate that the wires meet the requirements of 1080 carbon steel (AISI 1080, or UNS G10800).

The three failed cable ends whose chemical composition was tested are from cables installed in 1964 as part of the original structure. The original structural drawings only prescribe a minimum tensile strength on 220 kilopound per square inch (ksi) for the cables, with no reference to any specific material standard. However, a strength of 220 ksi is consistent with the requirements of ASTM A586, which requires the wires' steel to be carbon steel.

Table 4: Cable wire composition by element weight (iron excluded).

			AISI 1080 Limits	Failed Cable End 11M				Failed Cable End 12M		Failed Cable End 13I		
				Wire 1	Wire 2	Wire 3	Wire 4	Wire 1	Wire 2	Wire 1	Wire 2	Wire 3
Element Weight Fraction [%]	Carbon	C	0.75-0.88	0.80	0.82	0.81	0.82	0.81	0.82	0.79	0.79	0.82
	Chromium	Cr	-	0.036	0.026	0.045	0.032	0.029	0.027	0.026	0.027	0.030
	Manganese	Mn	0.60-0.90	0.82	0.69	0.75	0.75	0.63	0.65	0.60	0.60	0.74
	Phosphorus	P	0.030 max	0.024	0.020	0.025	0.027	0.016	0.016	0.011	0.014	0.019
	Sulfur	S	0.050 max	0.021	0.021	0.019	0.020	0.023	0.021	0.022	0.023	0.020
	Silico	Si	-	0.21	0.068	0.26	0.18	0.20	0.16	0.20	0.20	0.20
	Vanadium	V	-	0.005	0.003	0.005	0.004	0.003	0.003	0.002	0.003	0.003

4.3 Wire Strength

A total of 12 wire samples taken from three intact cable segments were tested to failure in conformance with the ASTM A586 standard.[3] Per the original structural drawings of the telescope, these wires were required to have an ultimate tensile strength of at least 220 ksi. The test results indicate that every tested wire meets this requirement (Table 5). Moreover, every tested wire meets the strength and ductility requirements of ASTM A586, which was prescribed for the auxiliary cables installed in 1997. Photographs of the fracture surface of each tested wire are provided in Figure 9.

Table 5: Wire tensile test results.

		Ultimate Tensile Strength [ksi]	Yield Strength [ksi]	Elongation in 10 inches [%]	Area Reduction [%]
Intact Cable Segment 11I	Wire 1	233	186	5	22
	Wire 2	221	170	5	15
	Wire 3	227	171	4	29
	Wire 4	222	166	5	29
Intact Cable Segment 12G	Wire 1	236	185	4	21
	Wire 2	227	176	4	25
	Wire 3	224	174	5	28
	Wire 4	231	177	5	21
Intact Cable Segment 13GH	Wire 1	233	179	5	26
	Wire 2	225	175	6	6
	Wire 3	233	179	4	30
	Wire 4	227	169	4	23
Average		228	176	5	23
CV		2.0%	3.3%	13.4%	28.8%
ASTM A586, Class A Limits		220 min.	160 min	4 min.	-
Average / ASTM A586		104%	110%	117%	-

[3] American Society for Testing and Materials (ASTM). *ASTM A586-18. Standard Specification for Metallic-Coated Parallel and Helical Steel Wire Structural Strand.* 2018.

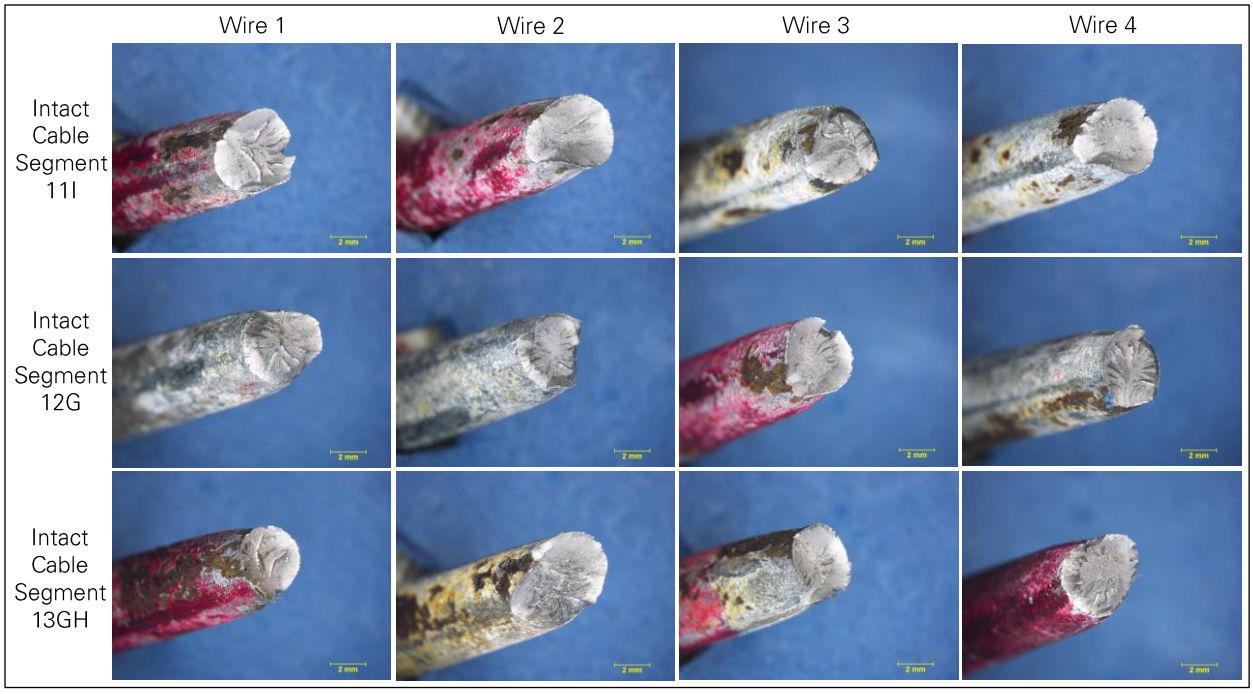

Figure 9: Fracture surfaces after wire tensile tests *(photos: Socotec).*

5.0 M4 Wires Failure Mode

On the four failed cable ends, each wire was examined to determine its fracture mode. Each wire was initially assigned a fracture mode based on the shape of the wire end and fracture surface: a "cup and cone" shape indicates axial overstress, a 45 degree slant indicates shear overstress, and a flat fracture surface indicates potential brittle fracture. Brittle fracture can be due to several causes, such as stress corrosion cracking, hydrogen embrittlement, or fatigue. For the wires categorized as potential brittle fractures, the fracture mode was verified through scanning electron microscopy (SEM) of the fracture surfaces after cleaning. This second examination revealed that many of these wires actually failed due to axial or shear overstress.

The final count of each fracture mode is provided in Table 6 and indicate that more than 90 percent of the wires fractured due to axial or shear overstress.

Each original main cable includes 168 wires arranged around a core made of seven smaller wires. Both the wires and core wires were examined in the failed cable ends, but the total number of wires examined varies between cables as some wires were missing or not examinable. The number of wires examined is significantly lower for M4-4, as many wires in that case failed within the socket.

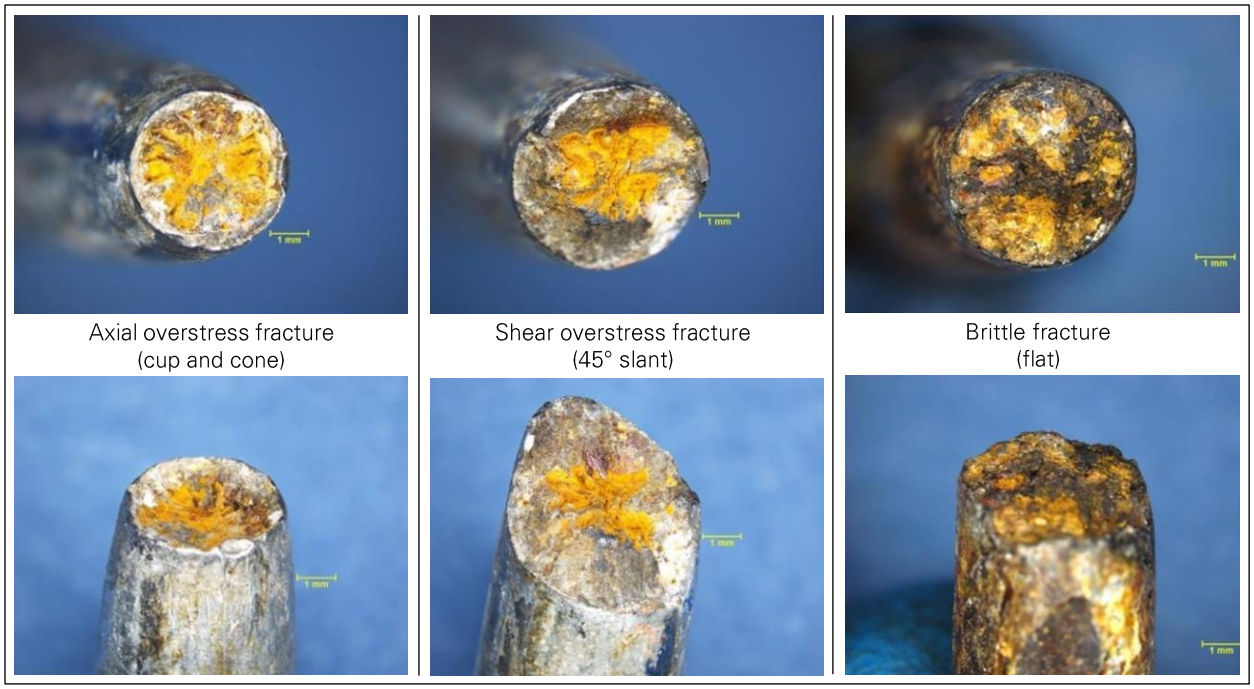

Figure 10: Representative images of axial overstress, shear overstress, and brittle fracture surfaces on wires of the failed cable ends *(photos: Socotec)*.

Table 6: Wire fracture mode counts on failed cable ends.

		Failed Cable End 11M	Failed Cable End 12M	Failed Cable End 13I	Failed Cable End M4-4
Number of Wires	**Axial Overstress Fracture**	133	130	154	34
	Shear Overstress Fracture	18	37	9	1
	Brittle Fracture	10	3	6	4
	Total Examined	161	170	169	39
Fraction of Wires	**Axial Overstress Fracture**	83%	76%	91%	87%
	Shear Overstress Fracture	11%	22%	5%	3%
	Brittle Fracture	6%	2%	4%	10%
	Total Examined	100%	100%	100%	100%

Appendix M
Socket Laboratory Analysis

1.0 Introduction

The cables of the telescope were terminated with zinc-filled spelter sockets, which are commonly used to connect large structural cables. The first and second cable failures in 2020 occurred near or within the sockets at the top of Tower 4, and significant cable slips were observed on other sockets before and after the cable failures. The behavior and failure of the sockets is therefore a focus of our investigation, and several sockets were recovered from the collapsed structure and analyzed in laboratories. The results of the laboratory analyses are presented in this appendix, which is organized by type of laboratory test.

2.0 Sockets Analyzed

Six of the telescope's sockets were analyzed in laboratories, including the two sockets that failed before the collapse and four other sockets selected based on cable slip and access in the early stages of site cleanup. The sockets considered and the cable slip observed at each socket are shown in Figure 1.

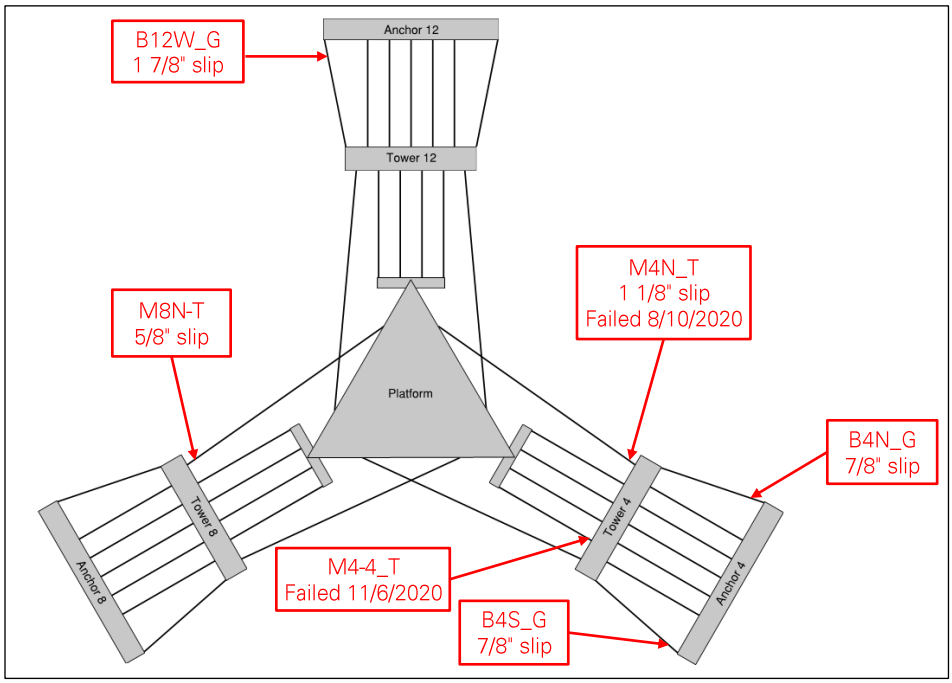

Figure 1: Map of sockets analyzed.

2.1 M4N_T Socket (WJE-NESC)

Socket M4N_T is where the first cable failure occurred on August 10, 2020. The socket was recovered from the top of tower 4 on September 23, 2020 (Figure 2), and shipped to Kennedy Space Center for analysis by the NASA Engineering and Safety Center (NESC) in collaboration with Wiss, Janney, Elstner Associates (WJE). The cable end that pulled out of M4N_T was recovered after the collapse (Figure 3) and also analyzed by WJE-NESC. The results of the WJE-NESC analysis are provided in a report,[1] and we

[1] Wiss, Janney, Elstner Associates (WJE). *Auxiliary Main Cable Socket Failure Investigation*. June 21, 2021. Draft report provided by WJE.

include some of the report's findings in this appendix as additional data points when comparing the properties and behavior of different sockets.

Figure 2: Socket M4N_T recovered from Tower 4 after M4N failure *(photo: WJE).*

Figure 3: Cable end pulled out of socket M4N_T.

2.2 Other Sockets (TT-Socotec)

We selected five additional sockets for laboratory analysis:

- M4-4_T (Figure 4), where the second cable failure occurred on November 6, 2020.
- B12W_G (Figure 5), which exhibits the largest cable slip (1.875 inch).
- M8N_T (Figure 6), which exhibits a relatively small cable slip (0.625 inch).
- B4N_G (Figure 7) and B4S_G (Figure 8), which exhibit intermediate cable slips (0.875 inch)

We worked with Socotec (formerly Lucius Pitkin Inc) to analyze these five sockets in Socotec's New York, NY laboratory. Except for the failed socket M4-4_T, each socket was shipped to Socotec with a segment of cable still attached. Pictures of the five sockets as received by Socotec are provided in Figure 4 to Figure 8.

Unless socket M4N_T is mentioned, the methods and results presented in this appendix apply to the five sockets listed above and analyzed by Socotec.

Figure 4: Socket M4-4_T *(photos: Socotec).*

Figure 5: Socket B12W_G *(photos: Socotec).*

Figure 6: Socket M8N_T *(photos: Socotec).*

Figure 7: Socket B4N_G *(photos: Socotec).*

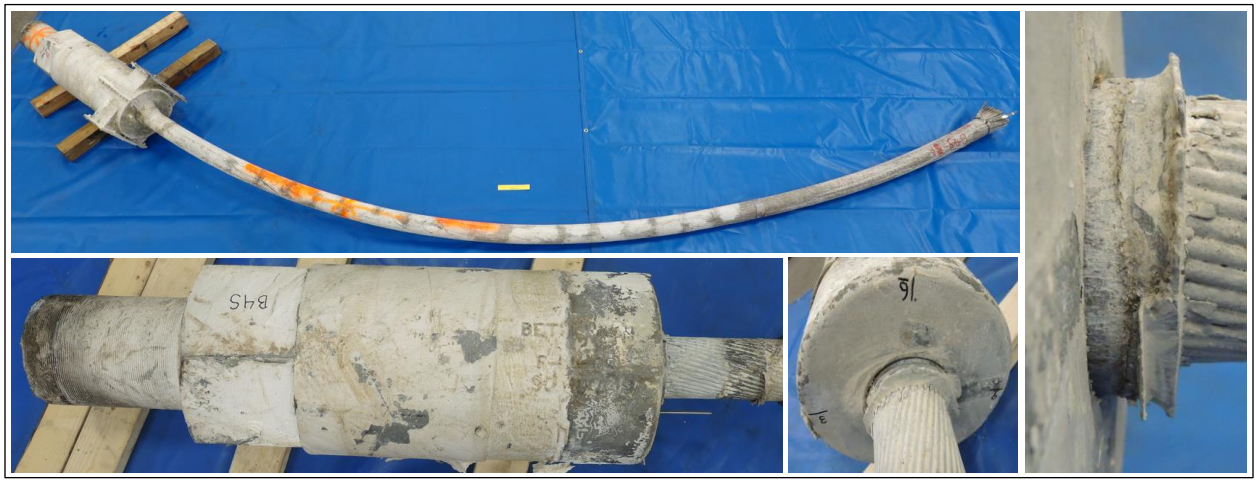

Figure 8: Socket B4S_G *(photos: Socotec).*

3.0 Cable Slips

The cable slip is the distance that a cable end shifted with respect to its socket, as measured outside of the socket. As shown in Figure 9, the cable slip can be measured as the length of zinc that was extruded out of the socket as the cable slipped. The cable slips at the sockets considered in laboratory studies are summarized in Table 1.

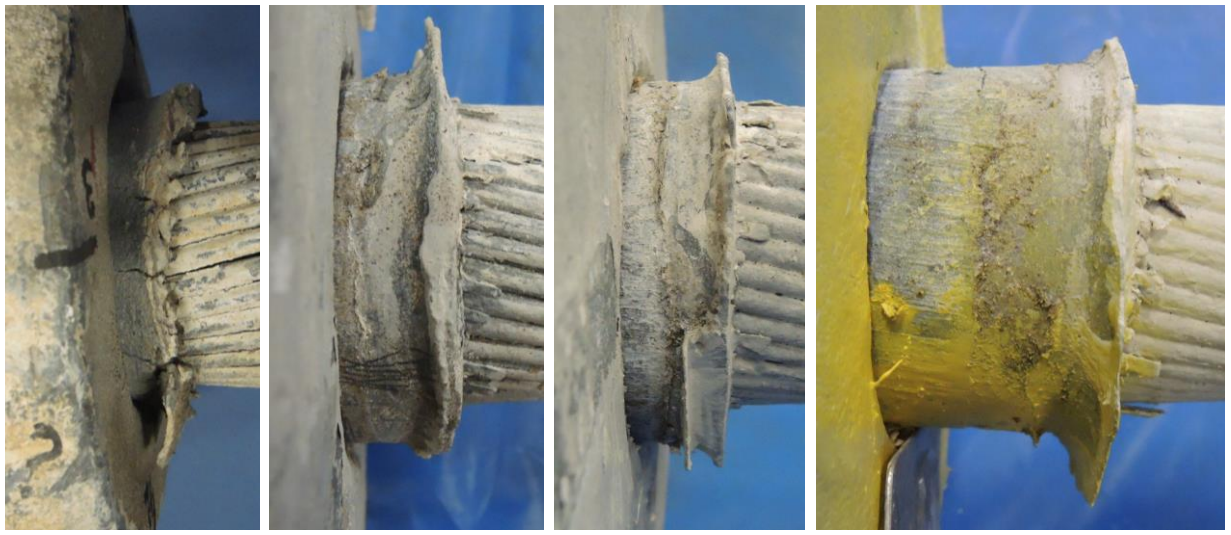

Figure 9: Cable slips observed on four auxiliary sockets *(photos: Socotec).*

Table 1: Cable slip of sockets considered in laboratory studies.

Socket	Cable slip	Notes
M4-4_T	Unknown	Not measurable before socket failure on November 6, 2020.
M4N_T	1.125	Measured on February 18, 2019. Socket failed on August 10, 2020.
M8N_T	0.625	Measured after collapse.
B4N_G	0.875	Measured on September 23, 2020, and after collapse.
B4S_G	0.875	Measured after collapse.
B12W_G	1.875	Measured on September 18, 2020, and after collapse.

4.0 Longitudinal Cuts and Macroetch

Each socket is a volume of cast steel with a cavity containing a zinc casting where the cable end is embedded. The steel of the sockets did not show any sign of damage or distress, and therefore the laboratory analysis focused on the zinc castings and embedded wires. To extract the zinc casting from each socket, the cast steel was sectioned and removed in steps as shown in Figure 10. After cutting away most of the socket's steel, two longitudinal cuts were made 180 degrees apart and the steel pieces were separated from the zinc casting by driving a wedge into one or both cuts.

After visual observation and measurements of the outside of the zinc casting, the first step to look inside the casting was to make a longitudinal cut. One of the cut surfaces was then macro-etched using hydrochloric acid. The macro-etched surfaces are shown in Figure 11 and key observations are as follows:

- The back surface of every casting is deformed, with a dip towards the socket's axis.
- In the castings of sockets B4S_G (failed during load test), B12W_G (maximum cable slip) and M4-4_T (failed on November 6, 2020), fracture planes developed at the back of the casting and a central core shifted in the direction of the cable pull.
- In the casting of socket B12W_G (maximum cable slip), several wires slipped with respect to the zinc outside of the displaced core.
- In the casting of M4-4_T (failed on November 6, 2020), several wires fractured inside the casting.

The core displacement and the fractured and slipped wires observed in the castings are relevant to the socket's failure modes and are further discussed in Appendix O.

1) Socket as received. 2) Solid steel is cut away around zinc casting. 3) Remaining steel is cut open to expose zinc casting 4) Zinc casting is split open, and surfaces are macro-etched.

Figure 10: Initial processing of socket B12W_G *(photos: Socotec).*

B4N_G
(0.875" slip)

B4S_G
(0.875" slip before load test,
section shown after load test)

B12W_G
(1.875" slip)

M4-4_T
(unknown slip before failure,
section shown after failure)

M8N_T
(0.625" slip)

Figure 11: Macro-etched transverse sections of socket zinc castings *(photos: Socotec).*

5.0 Radiography

The largest cable slip was observed on socket B12W_G, and the longitudinal sectioning of that socket's zinc casting revealed that several cable wires had slipped within the casting. To determine the extent of the wire slips, we performed a neutron radiography of a one inch-thick longitudinal slice of the casting (Figure 12). The radiograph is shown in Figure 13 and reveals that within the slice considered, every wire end located outside of the displaced casting core has slipped. The wire slip distances varies from 0.4 to 0.8 inch. For comparison, we performed the same radiography on a one inch-thick slice of casting of socket M8N_T, which exhibits the smallest cable slip among the sockets considered in the laboratory studies. The radiograph is shown in Figure 14, and we observe a wire slip on only two wires, with a slip distance of less than 0.05 inch.

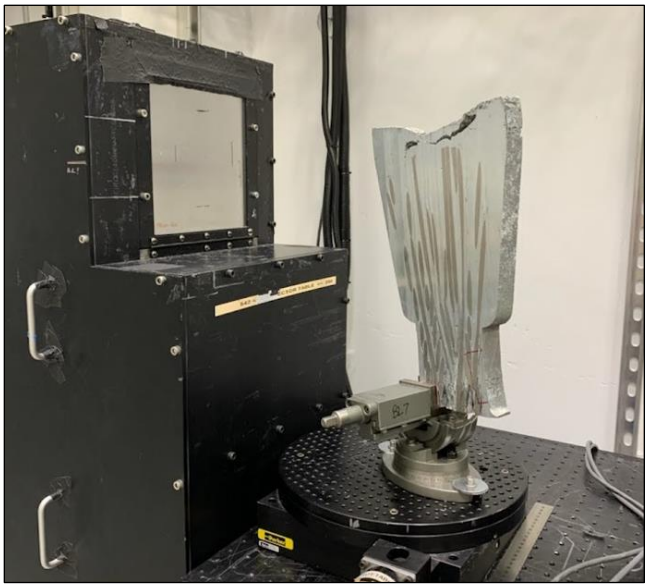

Figure 12: one inch-thick slide of B12W_G (1.875" slip) casting held in neutron imaging scanner
(photo: Adrian Brügger, Columbia University - Oak Ridge National Laboratory).

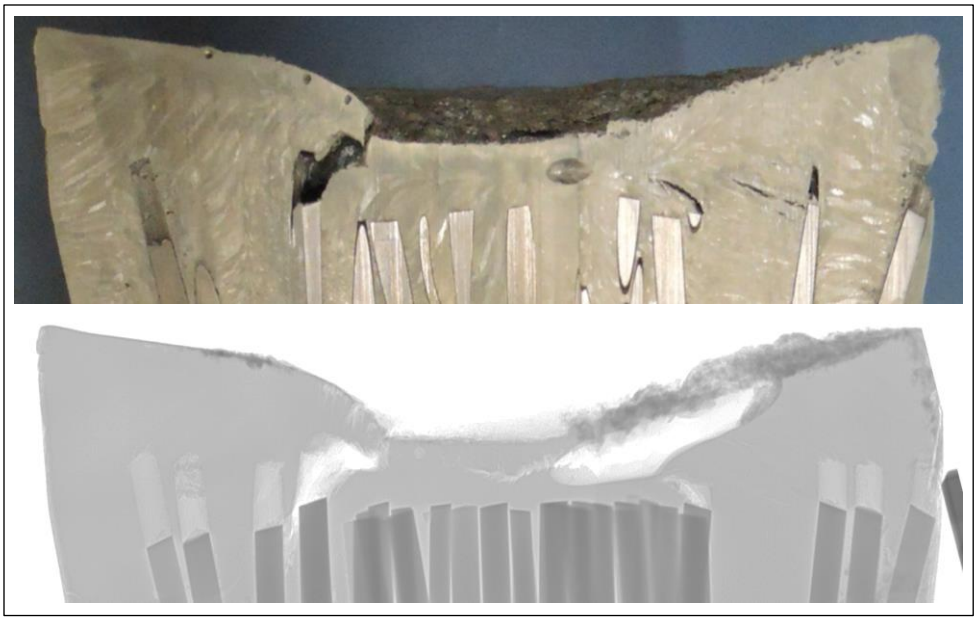

Figure 13: Neutron imaging of back of one inch-thick slice of B12W_G (1.875" slip) casting
(top photo: Socotec; bottom radiograph: Adrian Brügger, Columbia University - Oak Ridge National Laboratory).

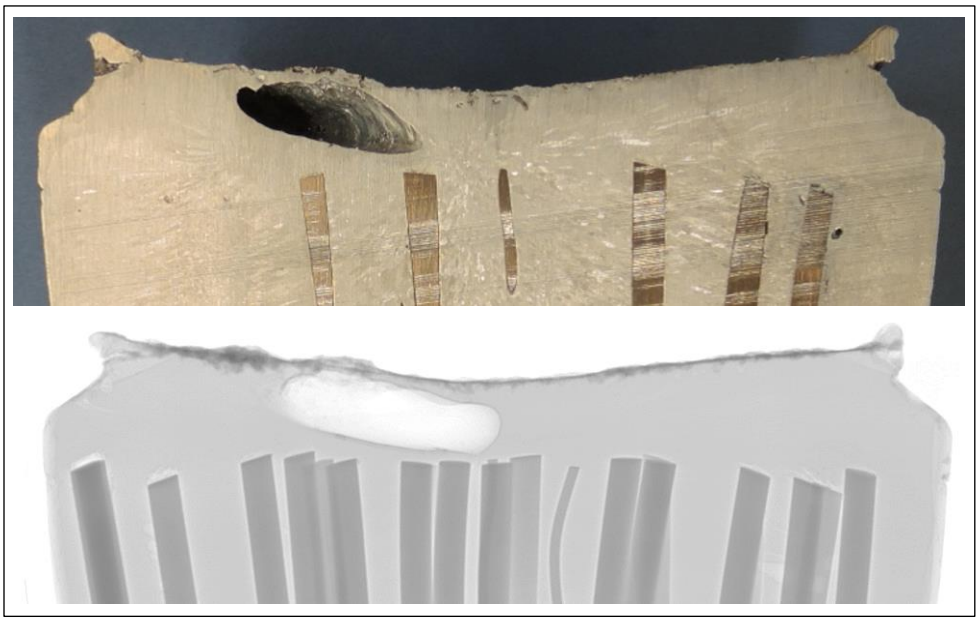

Figure 14: Neutron imaging of back of one inch-thick slice of M8N_T (0.625" slip) casting
(top photo: Socotec; bottom radiograph: Adrian Brügger, Columbia University - Oak Ridge National Laboratory).

6.0 Transverse Cuts and Wire Brooms

The zinc castings were sectioned in the transverse direction to observe the wire distribution within the casting, which is referred to as the wire broom. As shown in Figure 15, in some of the castings the wires were traced through multiple transverse sections and color-coded based by on the layer that they belonged to in the cable.

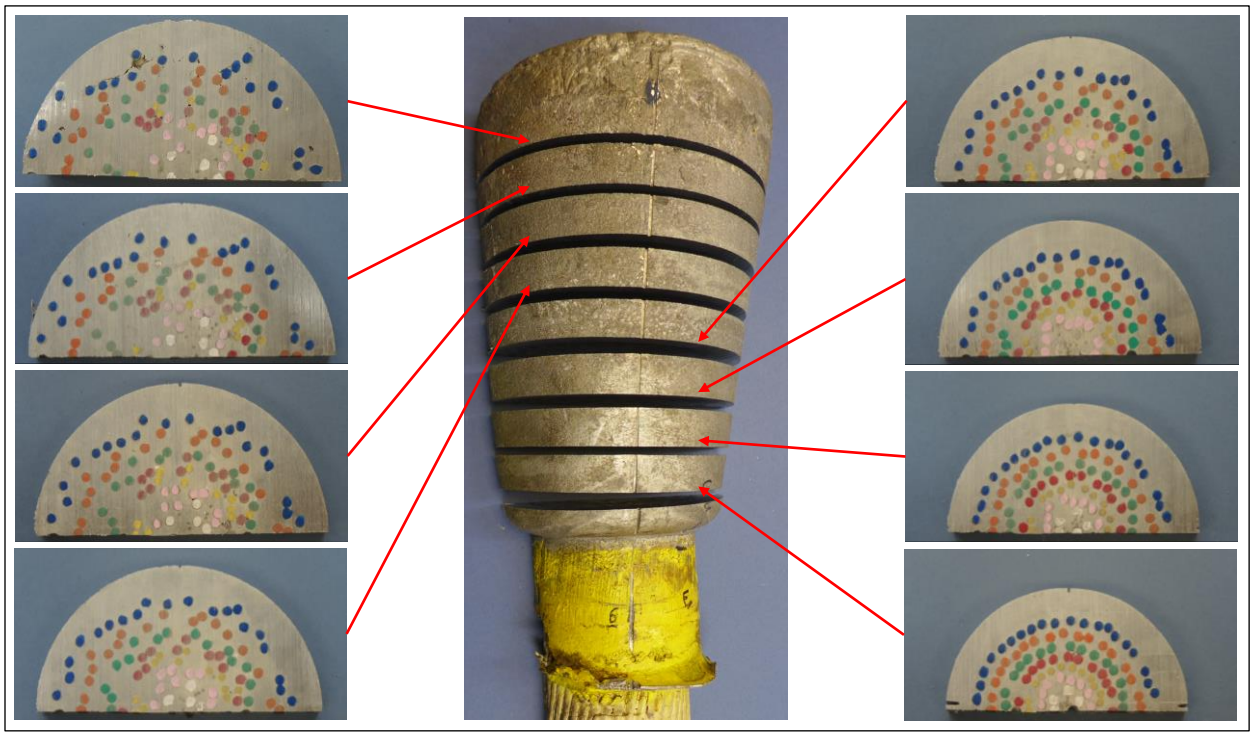

Figure 15: Transverse sections and wire layer tracing in B12W-G (1.875" slip) zinc casting *(photos: Socotec).*

Key transverse sections for the six sockets considered in the laboratory studies are shown in Figure 16 to Figure 21. For four of the sockets (M4-4_T, M8N_T, B4N_G and B12W_G), only one half of the casting was sectioned as the other half was preserved for other laboratory tests.

In every socket considered, the wire broom is irregular and does not follow any consistent pattern. General differences are immediately visible between the wire brooms in the sections close to the wire ends. For instance, most of the outer layer of wires is fully broomed out in socket M8N_T (Figure 17), while no wire is fully broomed-out in socket B12W_G (Figure 19). Then, the wire broom of M4-4_T (Figure 16) appears to be relatively uniform, while there is a significant zinc area with no embedded wire in socket B4N_G (Figure 18).

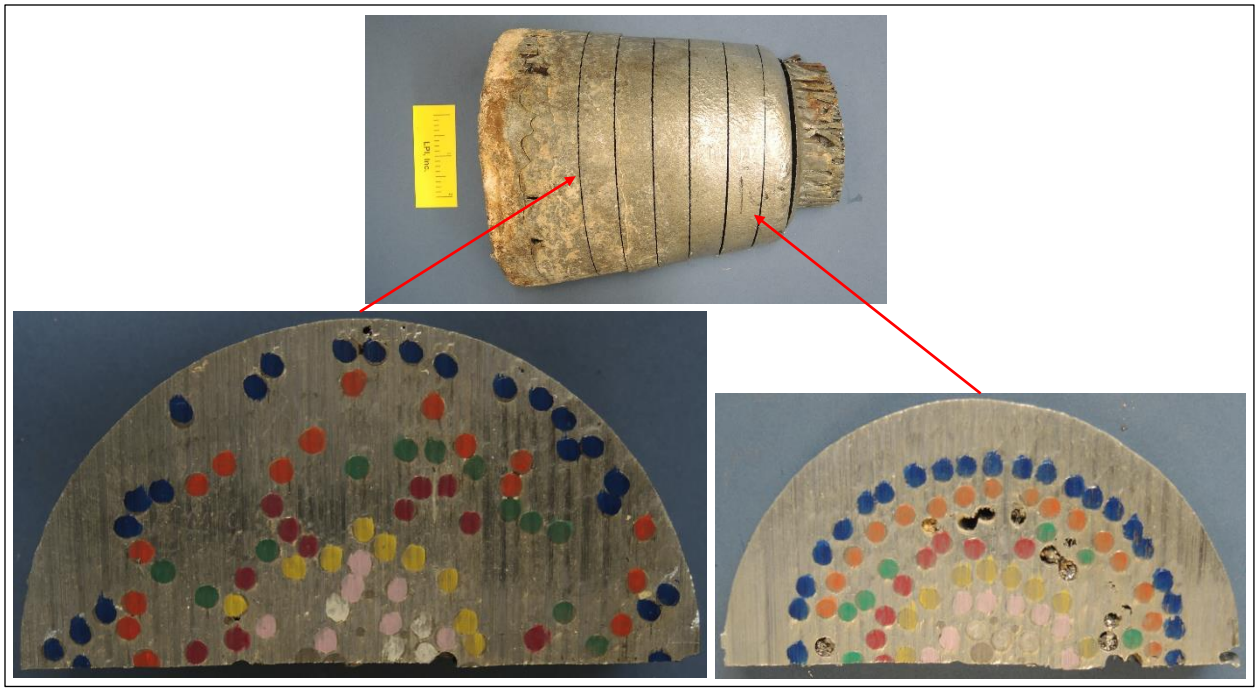

Figure 16: M4-4_T transverse sections *(photos: Socotec).*

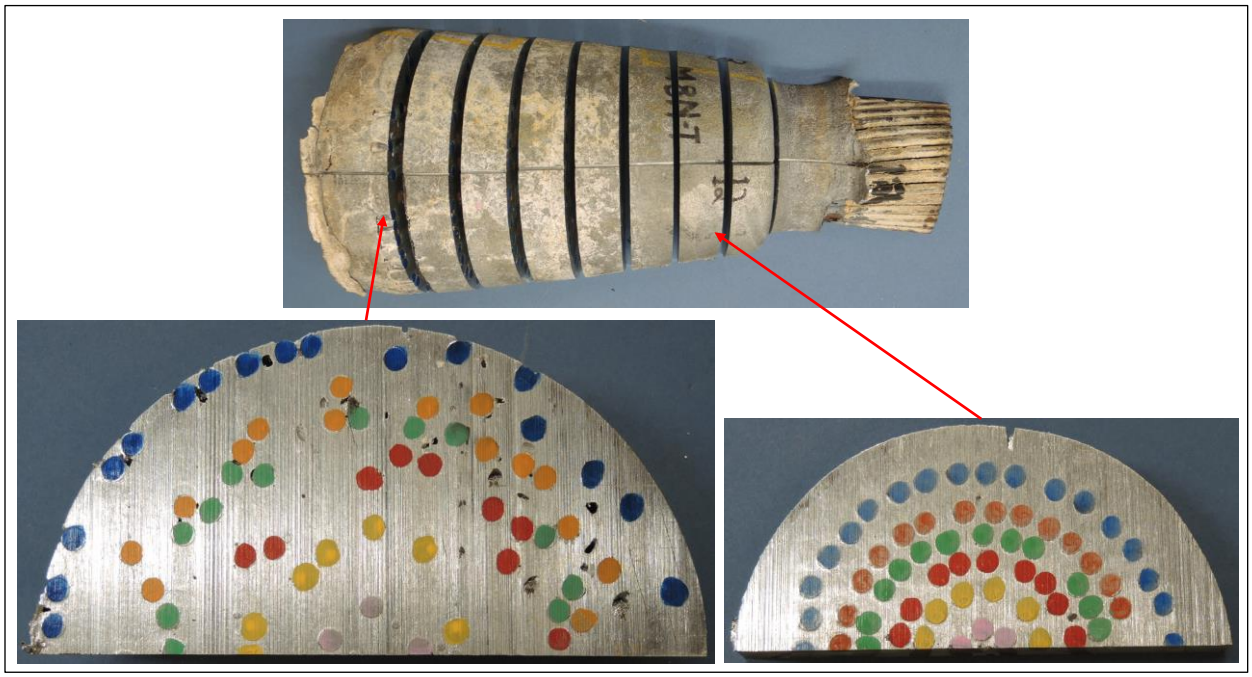

Figure 17: M8N_T (0.625" slip) transverse sections *(photos: Socotec).*

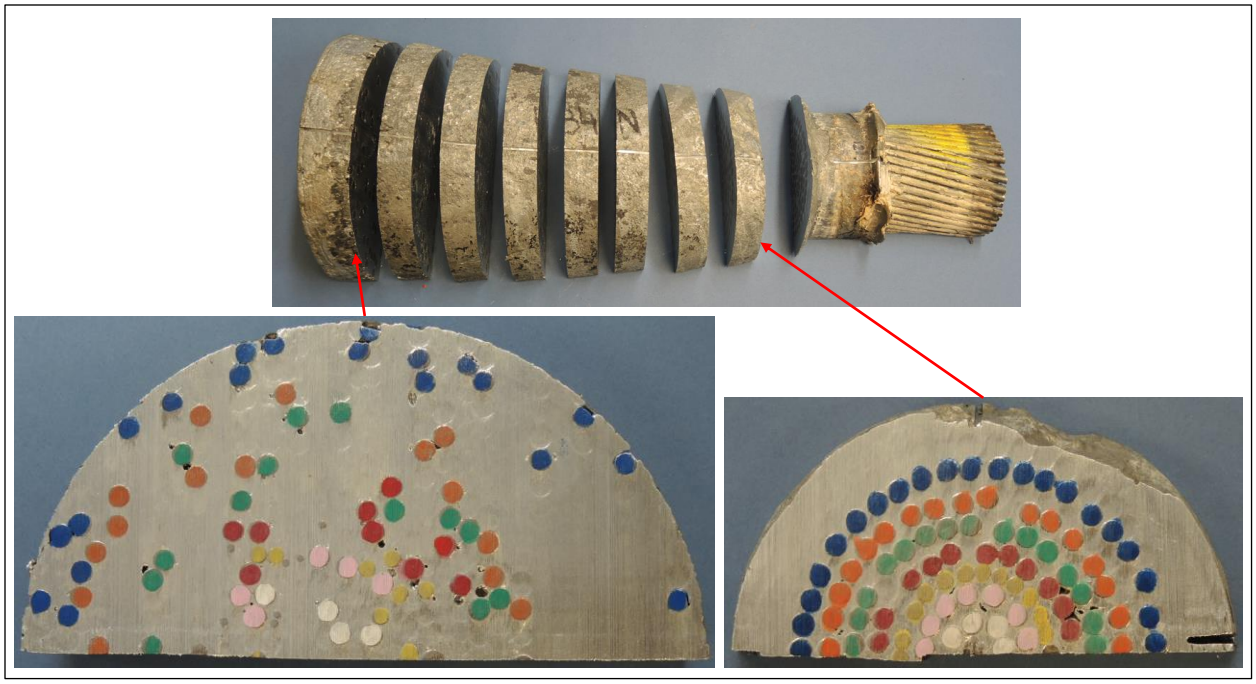

Figure 18: B4N_G (0.875" slip) transverse sections *(photos: Socotec).*

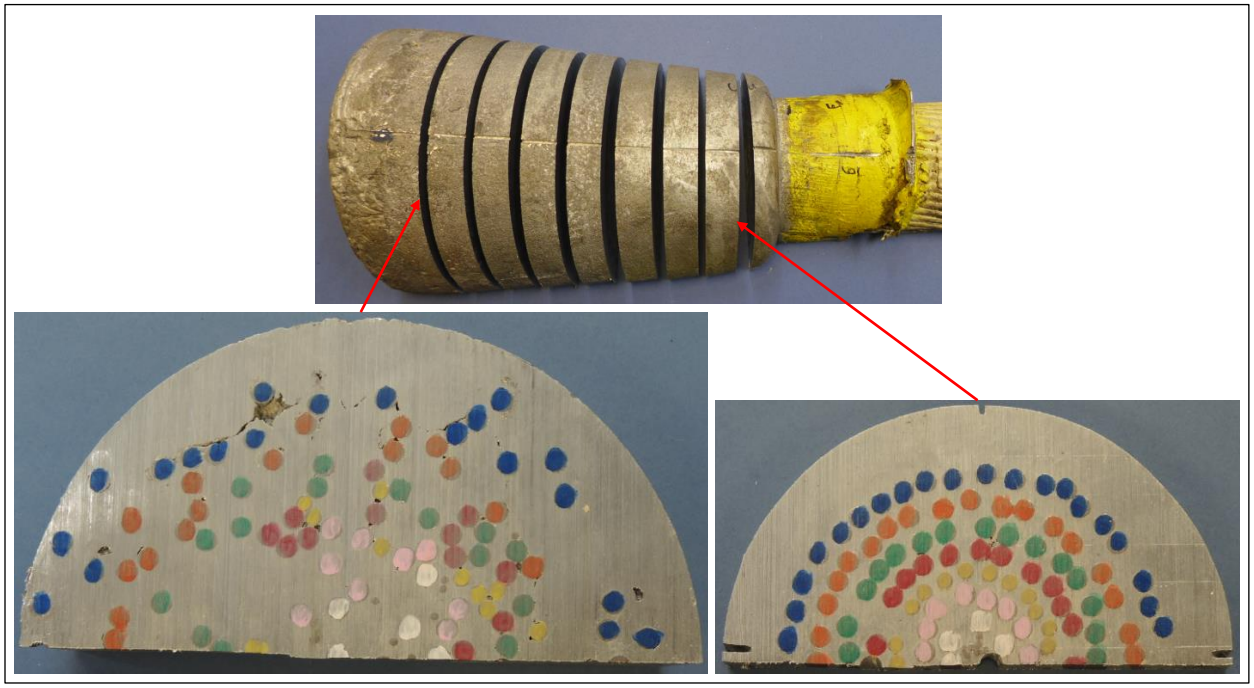

Figure 19: B12W_G (1.875" slip) transverse sections *(photos: Socotec).*

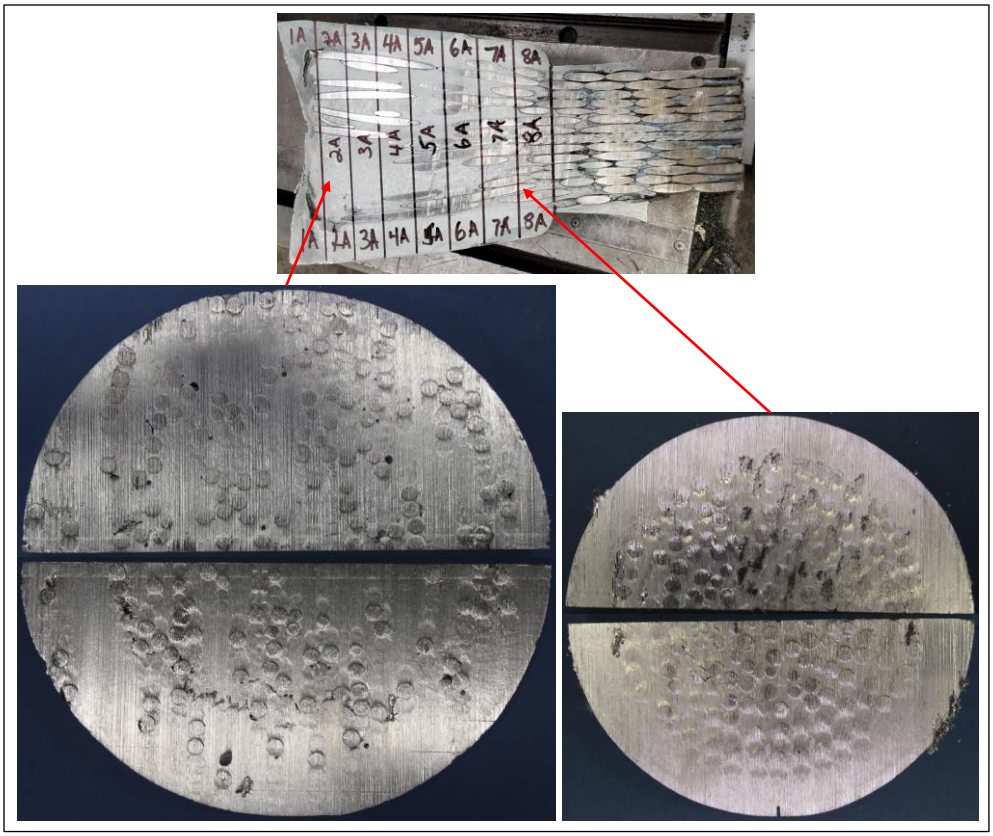

Figure 20: B4S_G (0.875" slip) transverse sections *(photos: Socotec).*

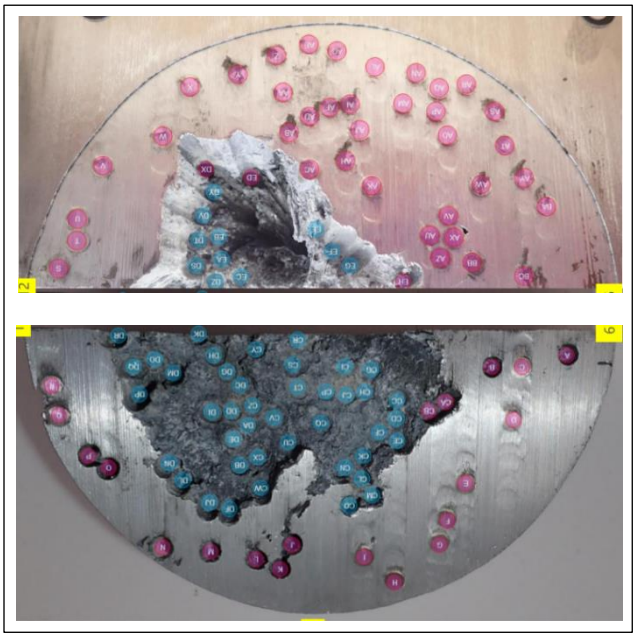

Figure 21: Wire locations at back of M4N_T (1.125" slip) *(photos: WJE[2]).*

[2] Wiss, Janney, Elstner Associates (WJE). *Auxiliary Main Cable Socket Failure Investigation.* June 21, 2021. Draft report provided by WJE.

The wire end distribution are shown in Figure 22 for the six socket castings considered. When the broom was observed on only half of the casting, the wire distribution was mirrored in the other half. For each type of socket, the actual brooms are compared to a hypothetical uniform broom where the wires are evenly-spaced in the radial and circumferential directions.

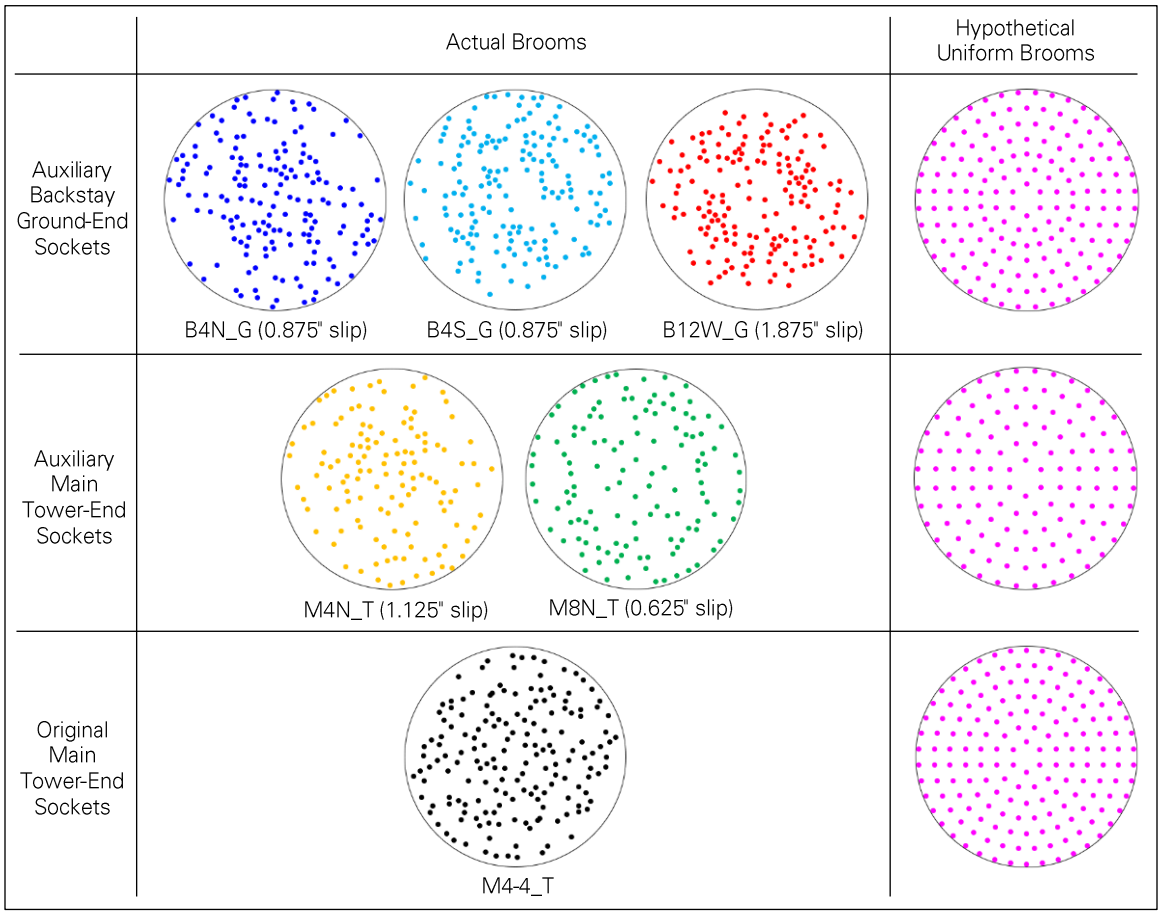

Figure 22: Wire end distribution at back of actual brooms and in hypothetical uniform brooms.

To compare the wire brooms quantitatively, we define a wire's brooming ratio and the wire's distance to the socket axis divided by the casting's radius at the wire ends (Figure 23). In a socket, the average brooming ratio is the average of the brooming ratios of all the wires.

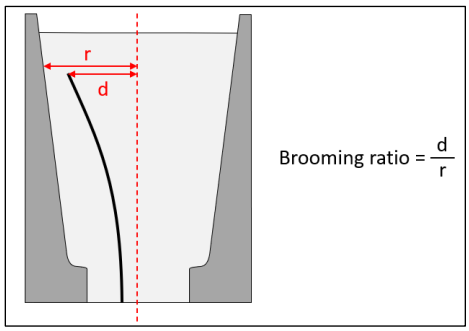

Figure 23: Definition of wire brooming ratio.

For the five sockets whose cable slips are known, the average brooming ratio is plotted against cable slip in Figure 24. We observe a general correlation, with the cable slip decreasing as the brooming ratio increases. Due to the limited number of data points, this correlation is not sufficient to draw a conclusion on the impact that the wire broom many have on the cable slips. The potential ties between wire broom and cable slip were further investigated through calculations presented in Appendix O. We also observe that socket M8N_T, which exhibits the smallest cable slip, is the only socket whose average brooming ratio is similar to the ones of the uniform brooms.

The cumulative distribution of the wire brooming ratios in each socket and in the uniform brooms are shown in Figure 25. For the uniform brooms, the distribution has discontinuities because the wires ends are assumed to remain in concentric layers.

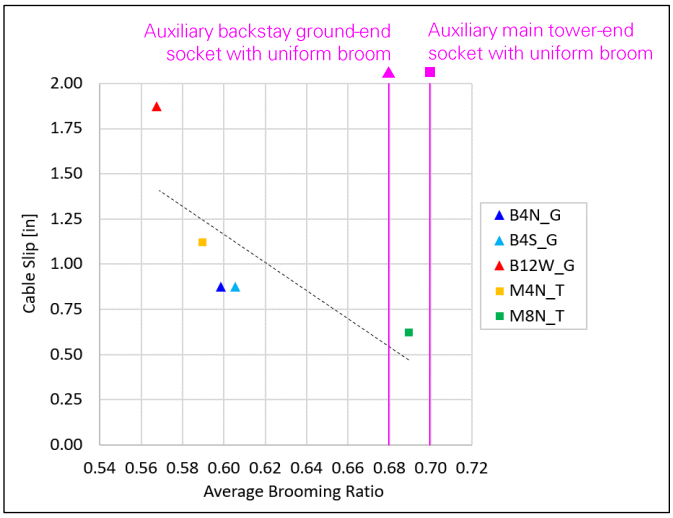

Figure 24: Wire average relative distance to center vs. cable slip.

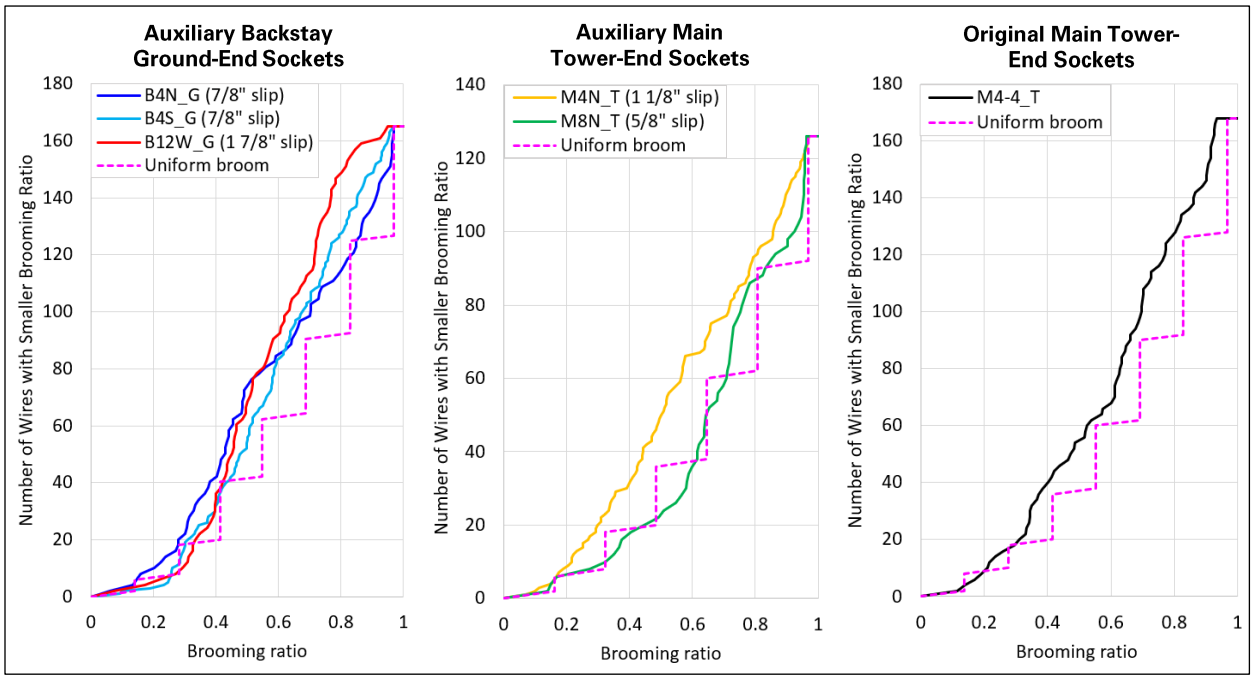

Figure 25: Cumulative distribution of wire brooming ratios.

7.0 Zinc Properties

7.1 Composition

The chemical composition of the zinc casting was tested through optical emission spectroscopy (OES) for one original and two auxiliary sockets. The results are shown in Table 2 and indicate that the three samples meet the high-grade requirements of the ASTM B6 standard.[3] The ASTM B6 standard for high-grade requires the zinc to be 99.5 percent pure and was prescribed for the socket castings in the structural drawings of the original structure. We did not find any similar requirement in the construction documents of the upgraded structure, but the composition tests indicate that the sockets installed during the second upgrade also used pure zinc.

Table 2: Zinc composition by element weight.

Element	ASTM B6 High-Grade Limits		Arecibo Socket Samples		
	Min	Max	B4N_G	B12W_G	M4-4_T
Al		0.01%	< 0.01%	< 0.01%	< 0.01%
Cd		0.01%	< 0.01%	< 0.01%	< 0.01%
Cu		0.20%	< 0.01%	< 0.01%	< 0.01%
Fe		0.05%	0.01%	0.04%	0.02%
Mg			< 0.001%	< 0.001%	< 0.001%
Mn			0.001%	0.002%	0.005%
Ni			0.005%	0.005%	0.001%
Pb		0.45%	< 0.01%	< 0.01%	< 0.01%
Sb			< 0.001%	< 0.001%	< 0.001%
Sn			0.004%	0.003%	0.003%
Total Non-Zn		0.5%	< 0.1%	< 0.1%	< 0.1%
Zn	99.5%		100.0%	99.9%	99.9%
	Meets ASTM B6 High Grade?		Yes	Yes	Yes

7.2 Tensile Properties

The ASTM B6 standard prescribed for the original cable sockets only covers the zinc's chemical composition, and it does not set any requirement on the zinc's mechanical properties. However, we performed a series of tensile tests to evaluate the mechanical behavior of the socket's zinc and their potential impact on cable slip and socket failure.

Ten miniaturized flat tensile specimens were machined from four socket castings. As shown in Figure 26, specimens were taken from the front (smaller diameter end) and back (larger diameter end) of each casting. The specimens had nominal cross-sectional dimensions of 0.2-inch x 0.2-inch, with a 0.625-inch gage length (Figure 27). Each specimen was tested at room temperature per ASTM E8. The specimens were taken from various locations of the casting.

[3] American Society for Testing and Materials (ASTM). *ASTM B6-18. Standard Specification for Zinc.* 2018.

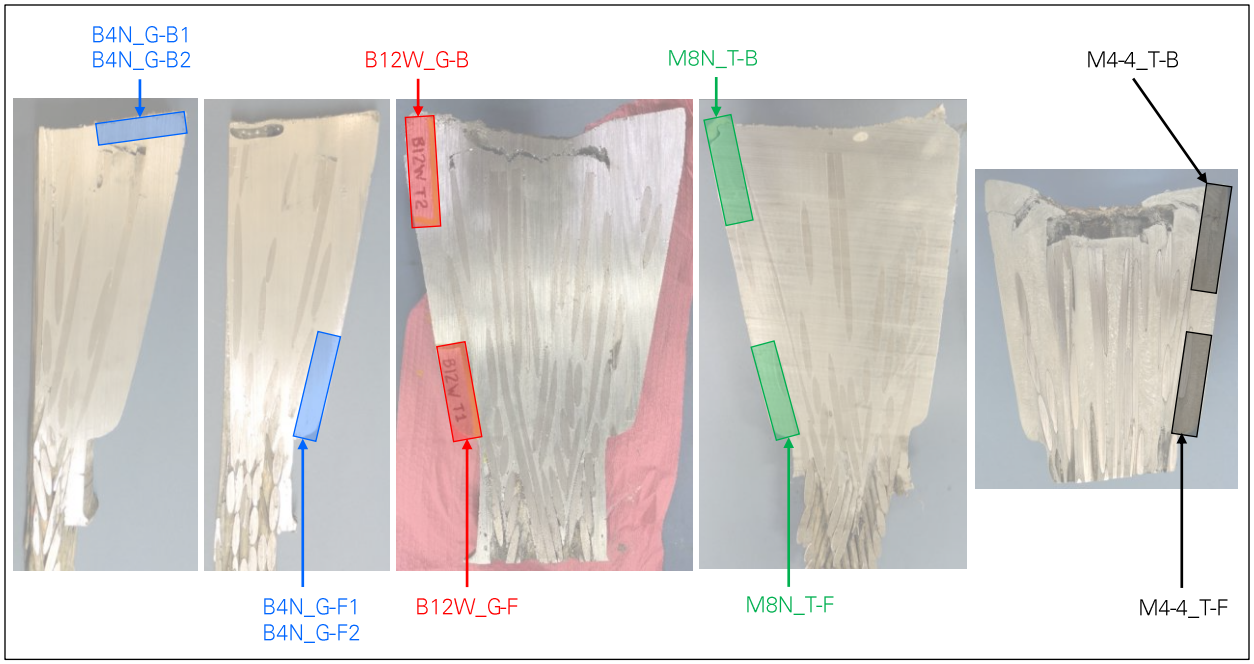

Figure 26: Tensile test sample locations in socket zinc castings *(photos: Socotec).*

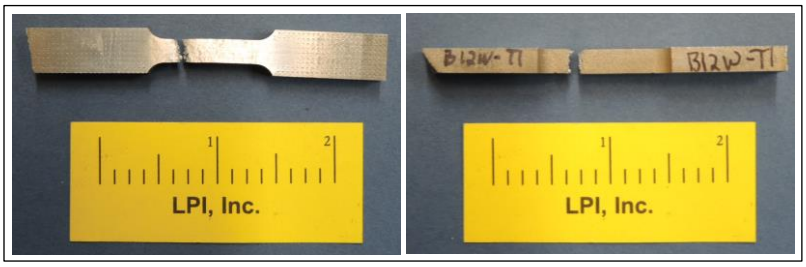

Figure 27: Zinc sample B12W_G-F after tensile testing to failure *(photos: Socotec).*

The results of the tensile tests are presented in Figure 28 as stress-strain curves up to the ultimate tensile stress reached. We first observe a wide range of ultimate tensile stress across the specimens, between three kilopound per square inch (ksi) and 12 ksi. The ultimate tensile stress is also reached for a wide range of strains. For every casting, the ultimate tensile stress is higher in the specimen(s) taken from the front of the casting than the specimen(s) taken from the back. This is consistent with the larger grain sizes observed at the back of the sockets, as described in (section 7.3 below).

For the three sockets whose cable slips are known, the tensile test results (yield stress, ultimate tensile stress, and strain at ultimate tensile stress) are plotted against cable slip in Figure 29. WJE-NESC performed tensile tests on the zinc of socket M4N_T, and the results provided in their report are added to the plots. We observe no correlation between cable slip and the tensile properties of the zinc.

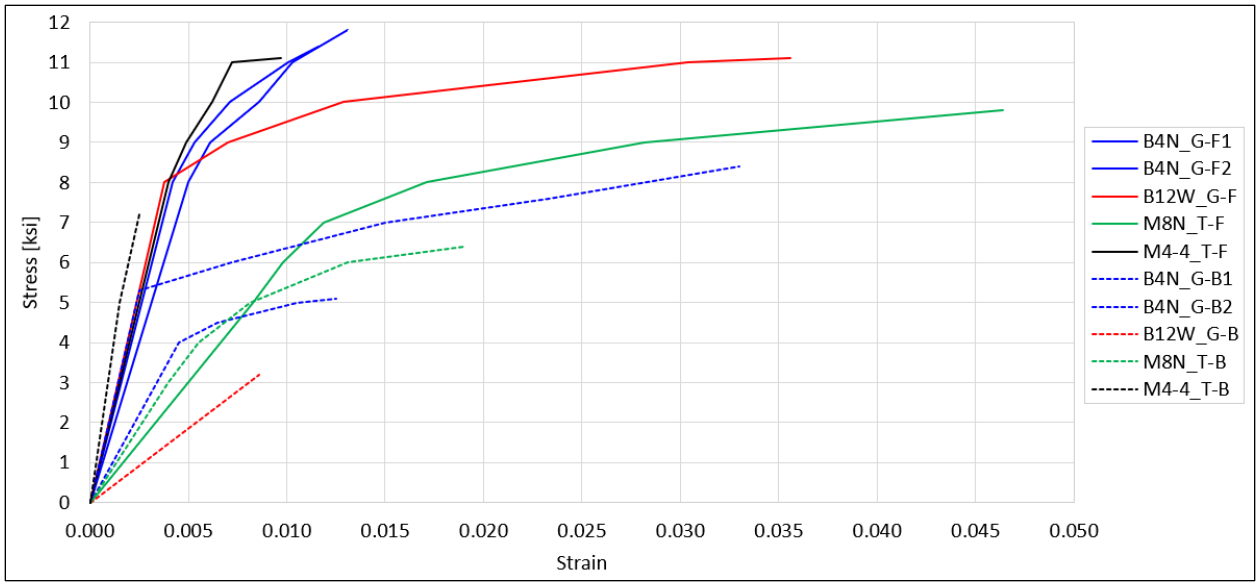

Figure 28: Strain-stress curves from tensile test results, up to ultimate stress.

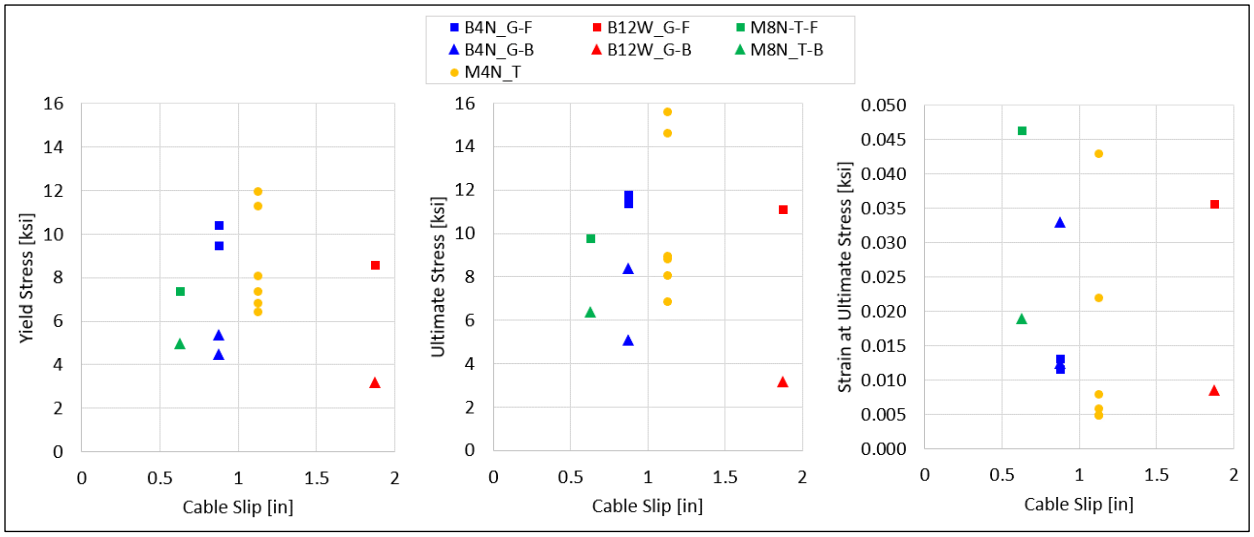

Figure 29: Zinc tensile test results vs. cable slip.

7.3 Grain Size

The zinc specimens cut from the socket castings and tested in tension were prepared for metallographic observation. The results are shown in Figure 30 to Figure 33, with each figure comparing the grain structure of the sample(s) taken at the front and back of a given casting. In every casting, the grains are smaller at the front of the casting and larger at the back. This is consistent with the tensile test results, where higher yield and ultimate tensile stresses were measured at the front of the casting. The smaller grain size is likely due to the faster cooling of the molten zinc at the front of the casting during the socketing process.

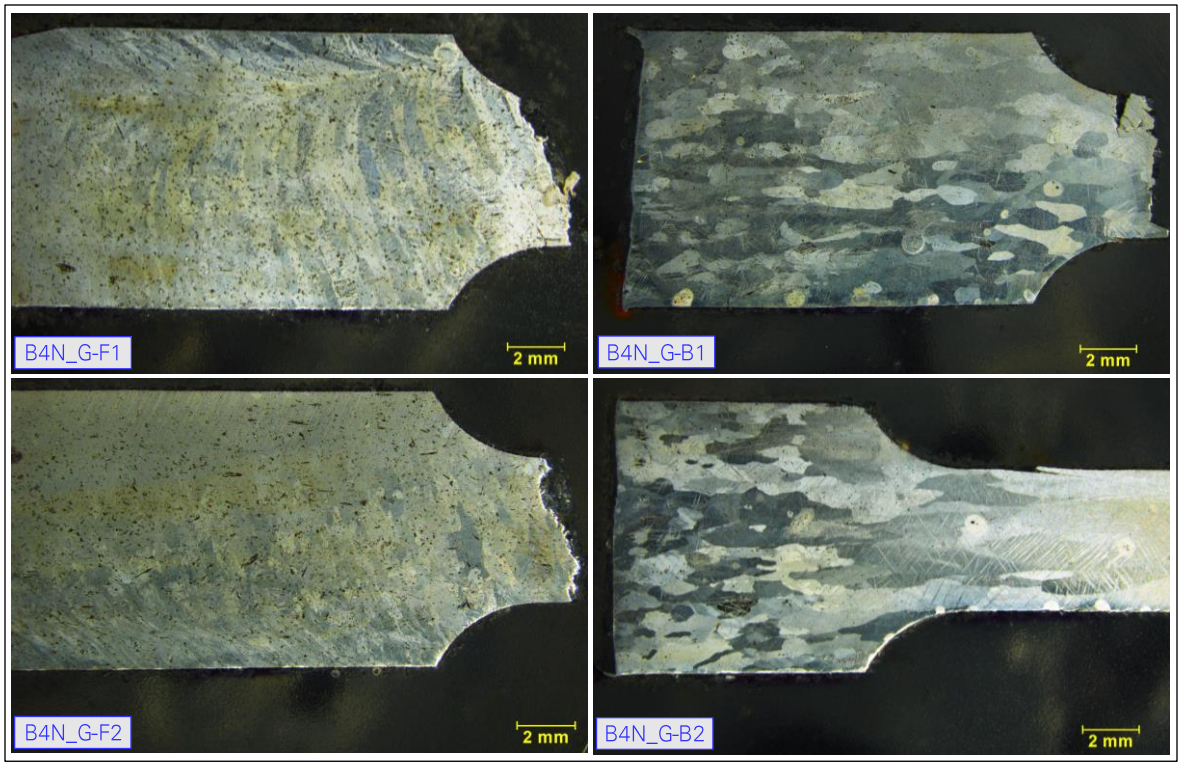

Figure 30: Grain size comparison between tensile specimens of socket B4N_G *(photos: Socotec).*

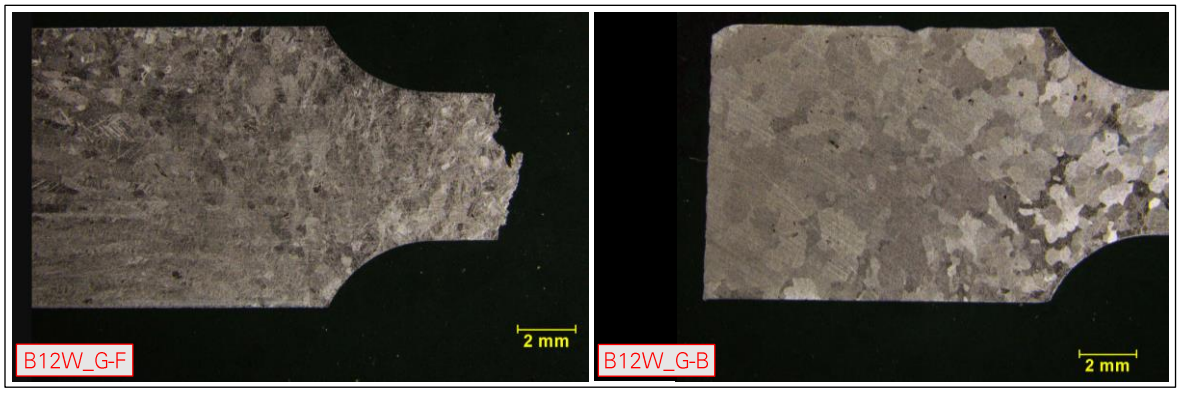

Figure 31: Grain size comparison between tensile specimens of socket B12W_G *(photos: Socotec).*

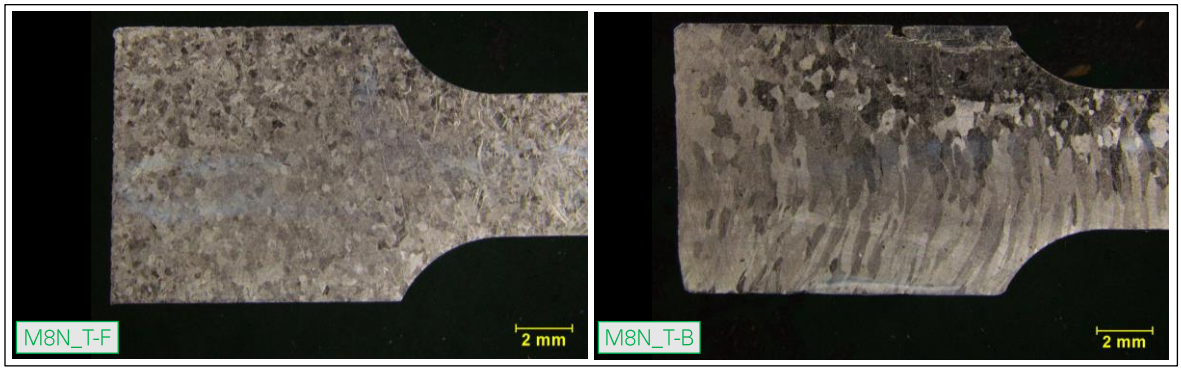

Figure 32: Grain size comparison between tensile specimens of socket M8N_T *(photos: Socotec).*

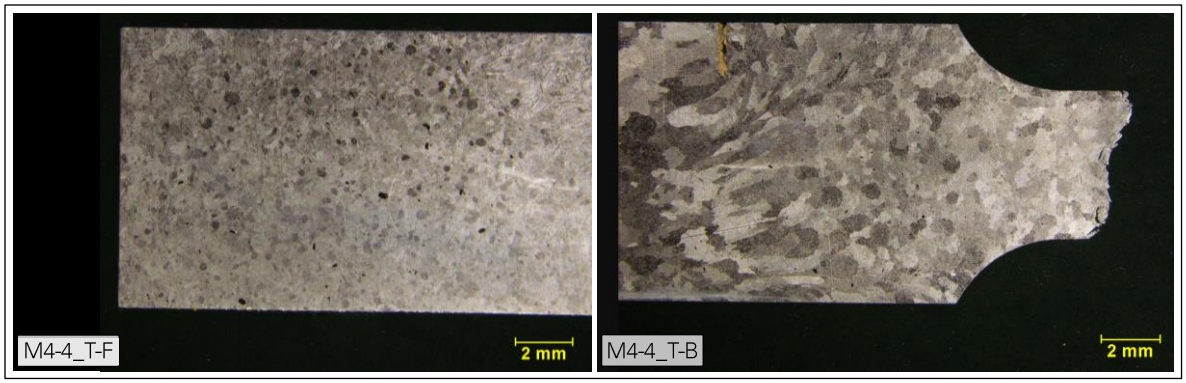

Figure 33: Grain size comparison between tensile specimens of socket M4-4_*T (photos: Socotec).*

8.0 Miscellaneous

8.1 No-Shoulder Socket Design

A socket is designed to terminate a cable of specific diameter, and to connect to the supporting structure with a specific detail. The six sockets considered in laboratory studies are of three different designs:

- Tower-end socket of original main cable: M4-4_T (failed November 6, 2020).
- Tower-end socket of auxiliary main cable: M4N_T (failed August 10, 2020) and M8N_T.
- Ground-end socket of auxiliary backstay cable: N4N_G, B4S_G and B12W_G (max. cable slip).

The laboratory studies revealed that these three socket designs featured a shoulder. As shown in Figure 34, the shoulder is a discontinuity in the slope of the socket's cavity near the front of the socket. However, as also shown in Figure 34, not all of the telescope's sockets had a shoulder design. The platform-end socket of an auxiliary main cable, M8N_P, was cut open by Socotec and found to not have a shoulder. The impact of the presence of a shoulder on the short-term and long-term behavior of the socket is studied in Appendix P.

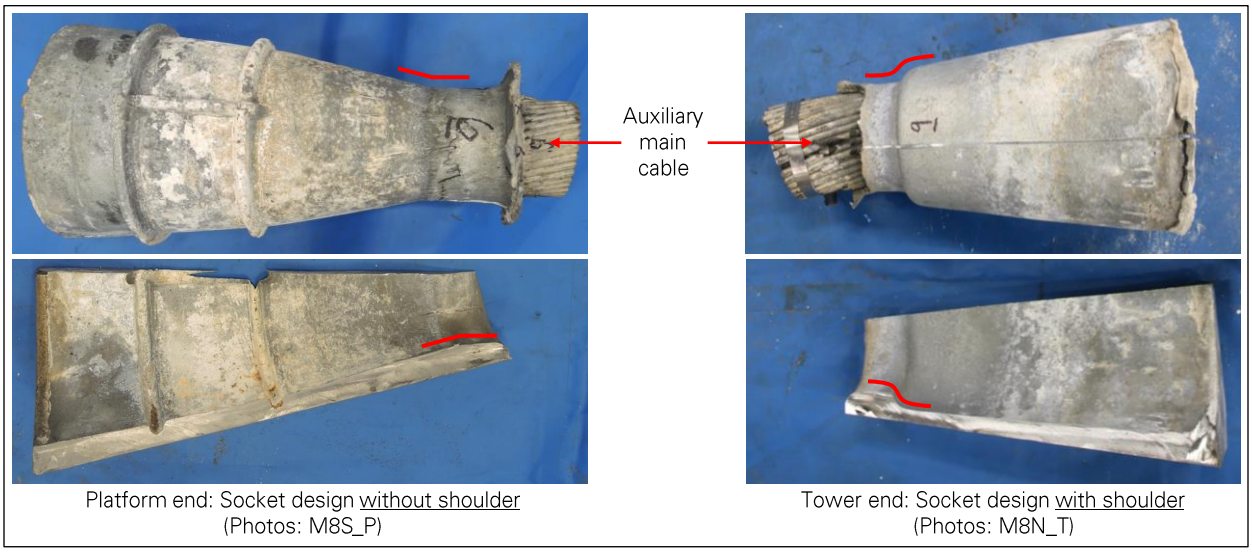

Figure 34: Socket designs with and without shoulder *(photos: Socotec).*

8.2 Wire Galvanizing Layer

The drawings specify the cables to be galvanized structural strands based on ASTM A586, class A which requires a minimum zinc coating weight of one ounce per square foot (equivalent to a thickness of 43 micrometer). During metallographic examination of the casting of socket B4N_G, it was observed that the zinc coating had not been removed from the wires prior to socketing (Figure 35). This observation is consistent with current socketing practice.

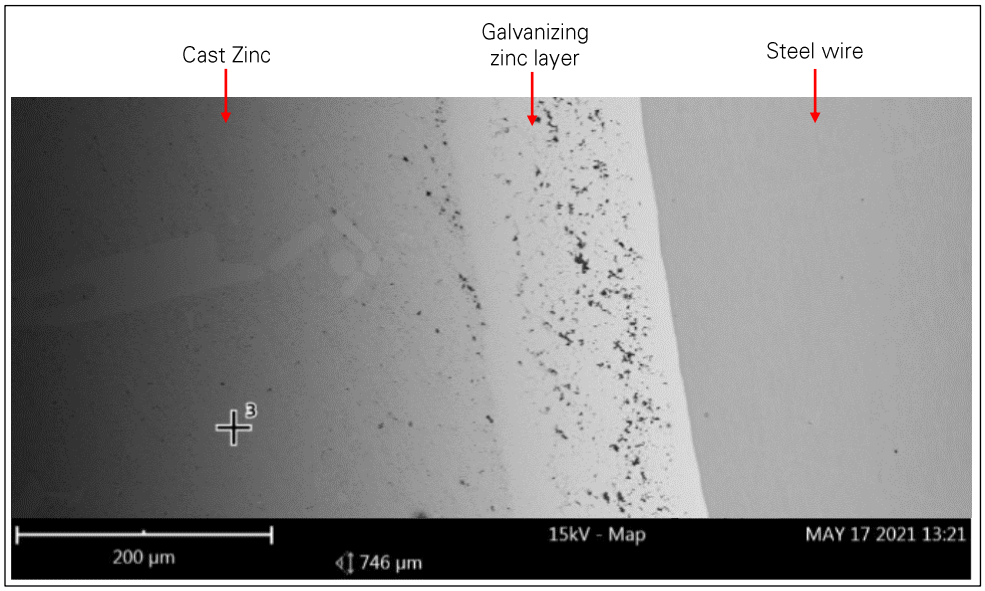

Figure 35: Galvanizing zinc layer on wires within zinc casting *(photo: Socotec).*

Appendix N
Socket Load Test

1.0 Introduction

The cables of the telescope are terminated at both ends with zinc-filled spelter sockets, which are commonly used to connect large structural cables. The first two cable failures in August and November 2020 occurred near or within their sockets at Tower 4. In addition, significant displacements of other cables with respect to their sockets (cable slips) were observed before the cable failures. As part of the investigation of the cable slips and socket failures, a socket recovered from the collapsed telescope was load-tested at Lehigh University's Fritz Laboratory. During the test, the socket-cable assembly was subjected to sustained and cyclic loads of different amplitudes, before being pulled to failure. The setup and results of the test are presented in this appendix. The laboratory analysis of the failed socket after the load test is covered in Appendix M.

2.0 Test Specimen

2.1 Socket B4S_G

The socket selected for the load test is B4S_G, which was recovered from the ground end of an auxiliary backstay stabilizing Tower 4. On December 1, 2020, the collapse started with with the failure of multiple main cables at the top of Tower 4, which caused an immediate force release in the Tower 4 backstays. As a result, socket B4S_G did not experience any impact loading during the collapse. The socket was in good general condition, had no visible wire breaks, and exhibited a cable slip of 0.875 inch. This cable slip is intermediate compared to the other auxiliary sockets of the telescope, where cable slips between 0.375 inch and 1.875 inch were observed. Like the first two sockets that failed (M4N_T and M4-4_T), socket B4S_G had a shoulder. B4S_G was recovered with 15 feet of cable B4S still attached (Figure 1).

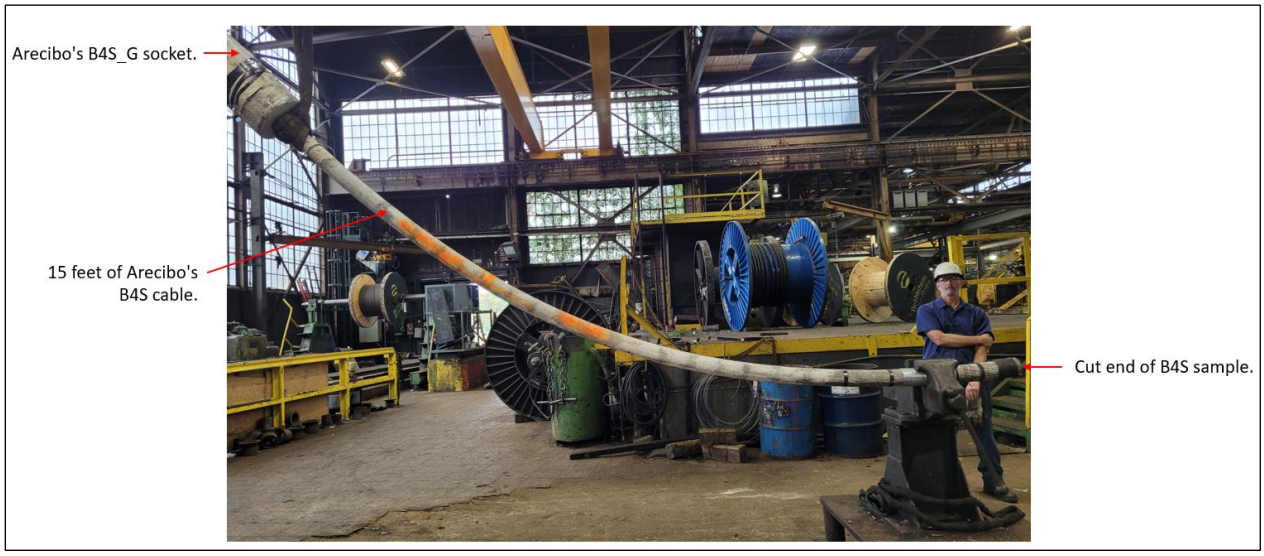

Figure 1: Recovered B4S_G cable-socket assembly.

2.2 Free End Socketing

The free end of the cable segment recovered with socket B4S_G was connected to a new socket, such that it could later be installed in the load testing fixture. Like the telescope's sockets, the new socket is a zinc-filled spelter socket. However, contrary to most of the telescope's sockets, the new socket is of a design without a shoulder. As shown in Figure 2, a spelter socket is a steel block with a cone-shaped cavity where the cable's wires are inserted and spread out before being filled with molten zinc.

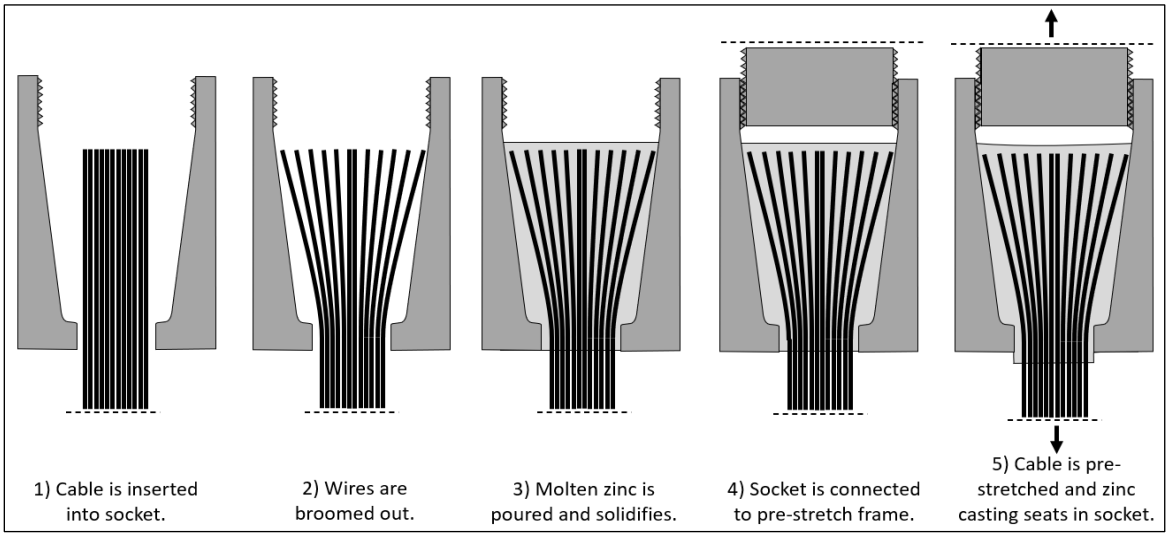

Figure 2: Cable socketing amd pre-stretching process.

The socketing procedure was performed by Wirerope Works in Williamsport, PA, and key steps are shown in Figure 3 to Figure 6. As a first step, wires are bent manually in a broom made wider to access and bend the inner wires (Figure 3). The wires are then chemically cleaned from paint and grease residues using the Tergo metal cleaning solution, and flux treatment is used to improve the wire-zinc bonding. The clean broom is then temporarily closed to allow socket installation (Figure 4). The broom is then released into the socket, and molten zinc is poured to fill the gaps between the wires (Figure 5). After initial solidification of the zinc, the socket is submerged in water to accelerate the cooling process (Figure 6).

Figure 3: Manual wire brooming.

Figure 4: Wire broom cleaning.

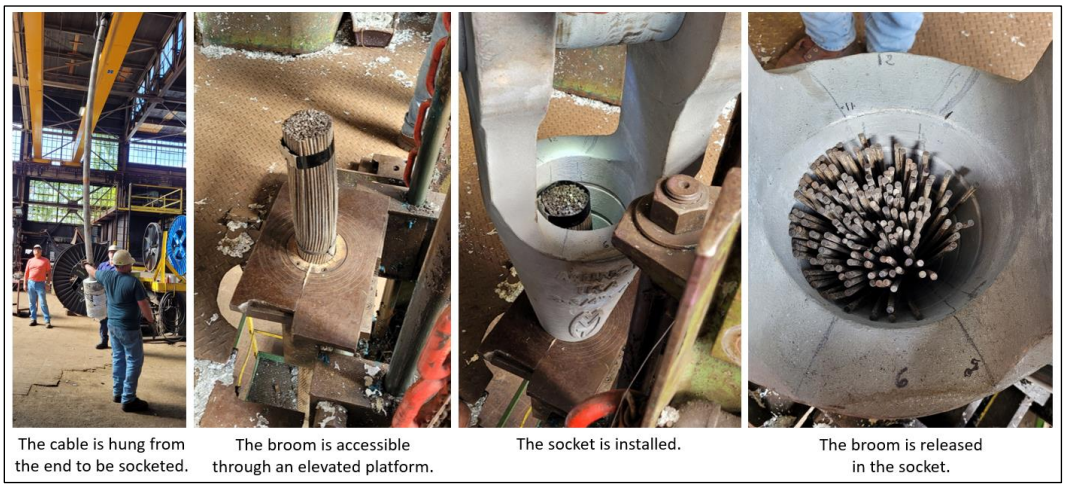

Figure 5: Socket installation.

Figure 6: Zinc casting and socket cooling.

3.0 Test Setup

3.1 Testing Machine

The cable test was conducted at Lehigh University's Fritz Laboratory using a 5,000-kip universal testing machine (Figure 7). The new socket was connected to the fixed top of the machine, and the B4S_G socket was connected to the moving table below. The load applied to the specimen is controlled by adjusting the vertical position of the moving table.

Figure 7: Cable test at Fritz Laboratory using a 5,000-kip universal testing machine.

3.2 Instrumentation

The ends of the specimen were instrumented as shown in Figure 8. At both ends, four displacement sensors (LVDTs - linear variable displacement transducers) were installed to measure the cable slip, and strain gages were installed on four of the cable's outer wires. Extensometers were also installed at the middle of the specimen to measure cable strain away from the sockets. The load applied to the cable is provided through a gage on the testing machine's control panel.

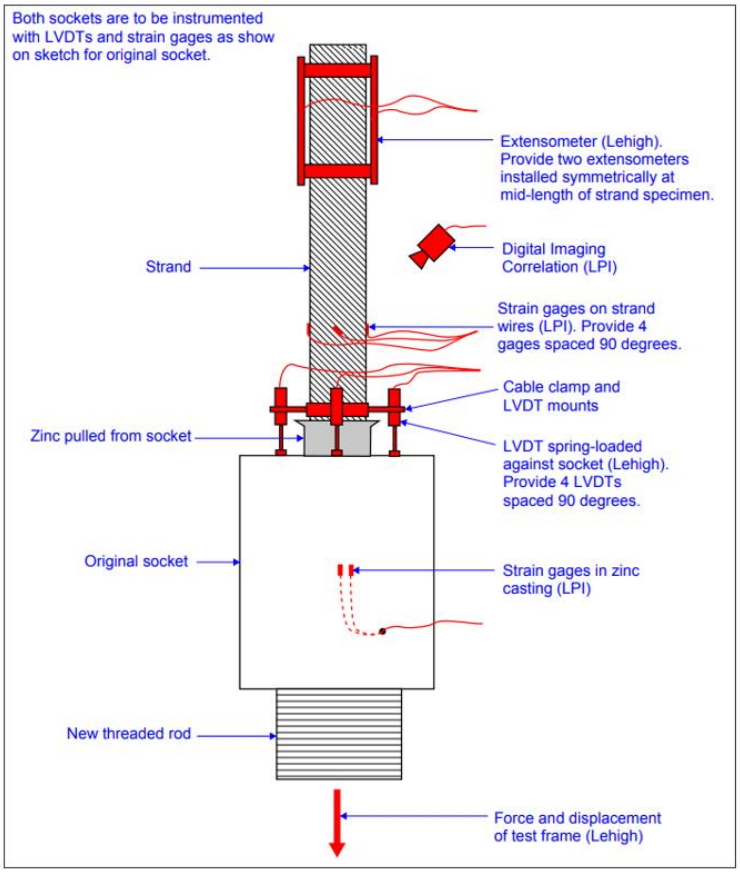

Figure 8: Instrumented cable assembly.

3.3 Load Sequence

The load test was performed over four days starting on October 18, 2021. With the objective to observe the specimen's response to sustained and cyclic loads of different magnitudes before loading to failure, the precise loading sequence was adjusted during the test based on the observed response. The time history of the applied load is shown in Figure 9.

The specimen was first loaded to the service load of 675 kip. This is the tension that cable B4S and socket B4S_G experienced during most of their lifetime, as determined through sag survey and analysis. After holding overnight, the load was cycled 150 times between 675 kip and 625 kip. This amplitude of 50 kip is similar to the largest tension cycle that the telescope experienced during hurricane Maria per our analysis (Appendix J). Each cycle was performed in approximately one minute. The load was then increased to 125 percent of the service load (825 kip), and the same 50-kip cyclic loading process was repeated before holding overnight. The load was then cycled three time between the service load (675 kip) and 150 percent of the service load (1000 kip), and that higher load was held overnight. Finally, after a few intermediate holds, the specimen was loaded to failure. We ended the test after seven outer wires had fractured in the B4S_G socket, while no wire fractures were observed at the new socket. The test was ended to avoid pulling the cable out of the socket completely, such that we could observe the condition of the socket on the brink of failure. Just before the last few wire failures, a maximum load of 1647 kip was reached. This load is two percent higher than the cable's minimum breaking strength.

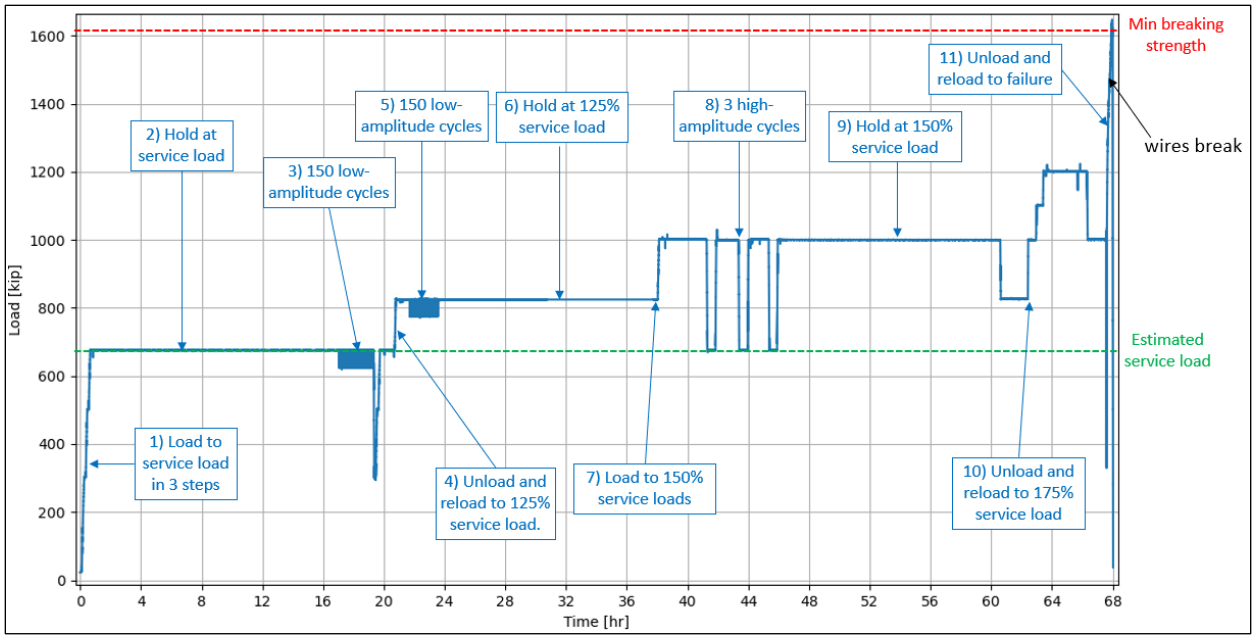

Figure 9: Loading time history.

4.0 Results

4.1 Cable Slip under Static Load

The average cable slip measured throughout the test is shown for both sockets and compared to the applied load in Figure 10. At each socket, the average cable slip is calculated by taking the average of the four displacement sensors installed between the cable end and the socket. The displacement sensors were zeroed at the start of the test, such that the pre-existing cable slip of socket B4S_G (0.875 inch) is not included in the average cable slip shown in Figure 10.

The specimen was loaded and held overnight at three different load levels corresponding to 100, 125 and 150 percent of the cable's service load. During the initial loading, the cable slipped by 0.35 inch at the new socket, an order of magnitude more than for the B4S_G socket. This is due to the zinc casting of the new socket experiencing some degree of elasting and plastic deformation as it is engaged and wedged into the socket for the first time. The cable slip increase caused by the next two load levels is also more significant at the new socket. For each of the three load levels, the cable continues to slip after the load is applied, at a rate that gradually decreases. This delayed response is observed at both sockets.

A close-up of the same data is shown in Figure 11 for the last 25 minutes of the test, when the specimen was loaded to failure. During this last step, the cable slip increases more at the B4S_G socket (+0.4 inch) than the new socket (+0.25 inch). This is consistent with the B4S_G socket failing first, with multiple wire fractures within the socket. The final cable slips at the BS_G socket is 0.53 inch, or 1.41 inch when including the pre-existing slip that occurred during the socket's service life on the telescope. The final cable slip at the new socket is 0.84 inch (Figure 12).

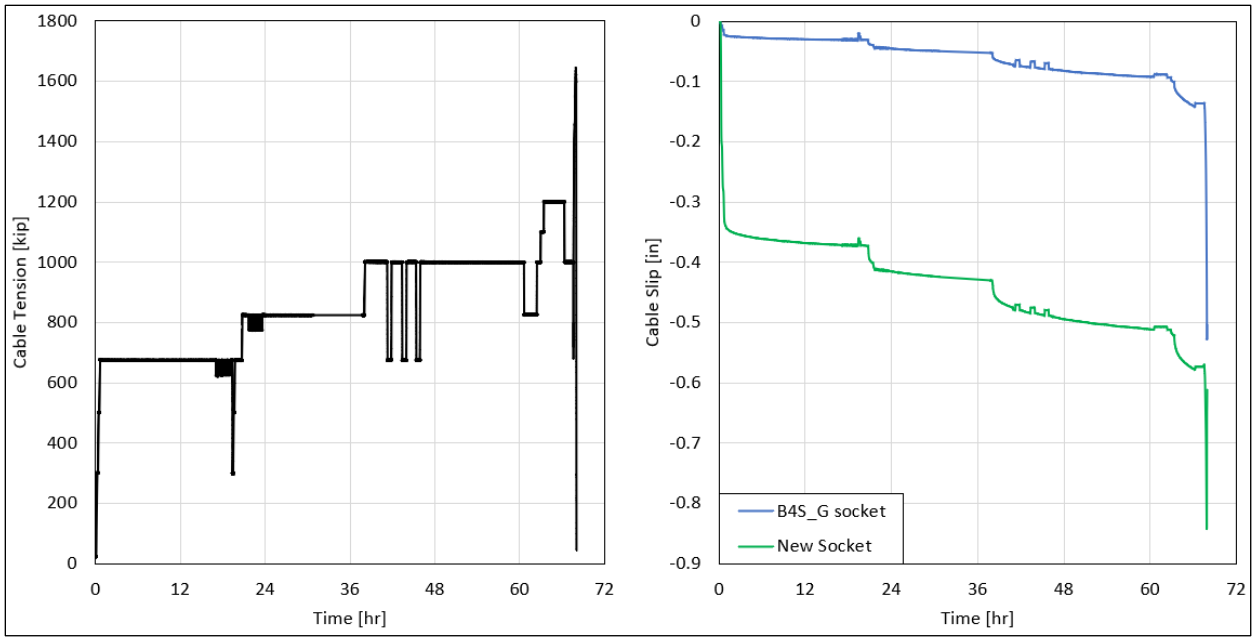

Figure 10: Cable tension and slip at both sockets during full load test.

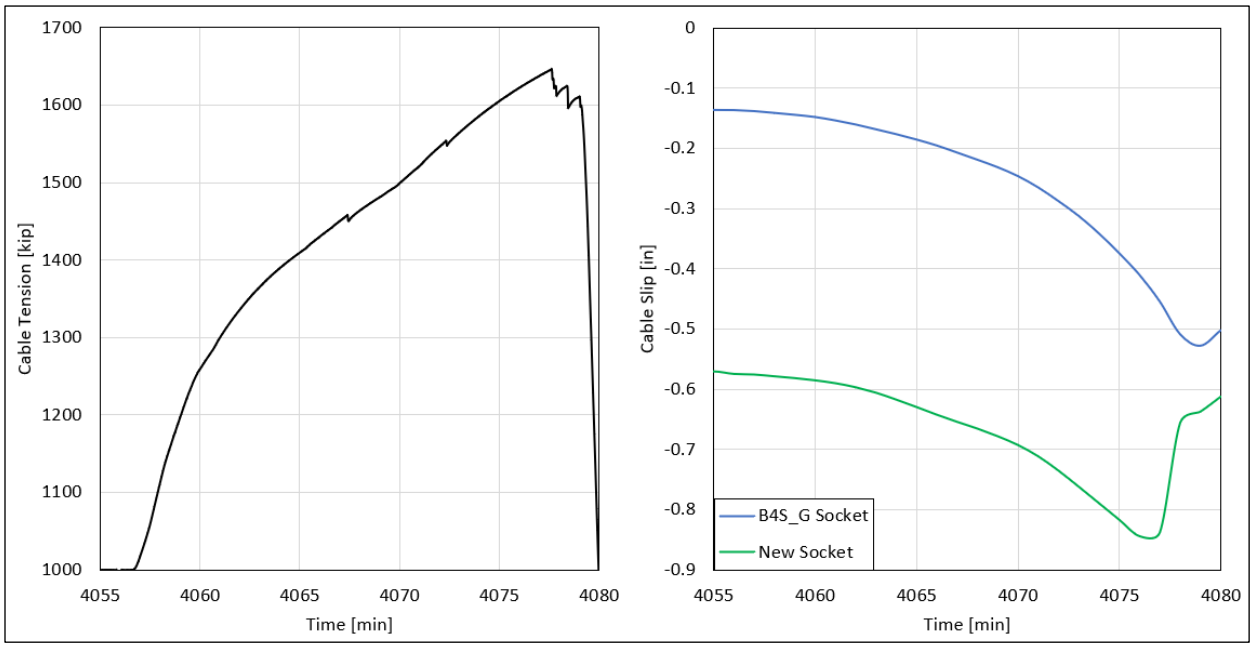

Figure 11: Cable tension and slip at both sockets during final loading to failure.

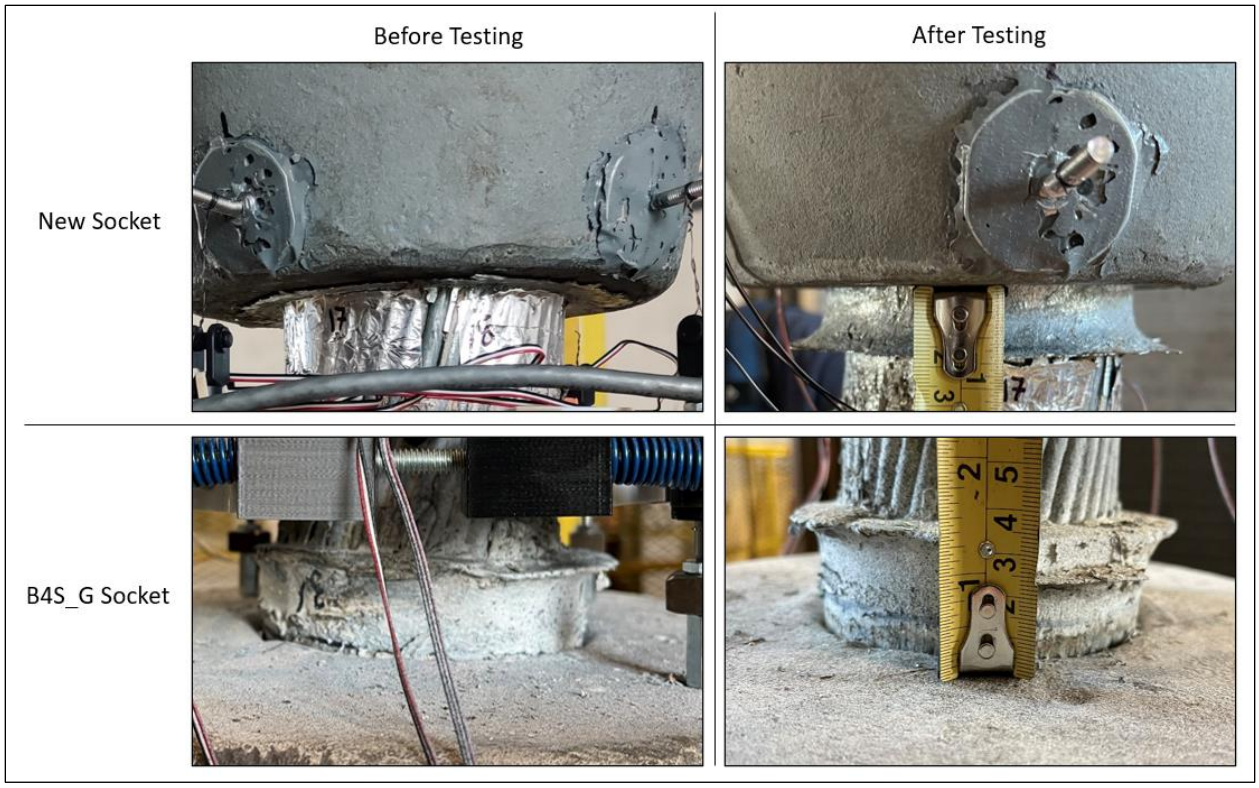

Figure 12: The cable slip for each socket before and after the test.

4.2 Cable Slip under Cyclic Load

The test sequence includes two series 50-kip load cycles, centered on 650 kip for the first series and 800 kip for the second series. Each series consists of 150 cycles performed at a rate of approximately one cycle per minute. The average cable slip at each socket is plotted against the load for the first and last cycle on Figure 13 (first series) and Figure 14 (second series). Similar observations are made for both series. First, the force-displacement loops are narrower for socket B4S_G and wider for the new socket. This indicates that the new socket is experiencing more plastic deformation during the load cycles. Then, for the same reason, the non-recovered cable slip increase between the first and last cycle is larger for the new socket.

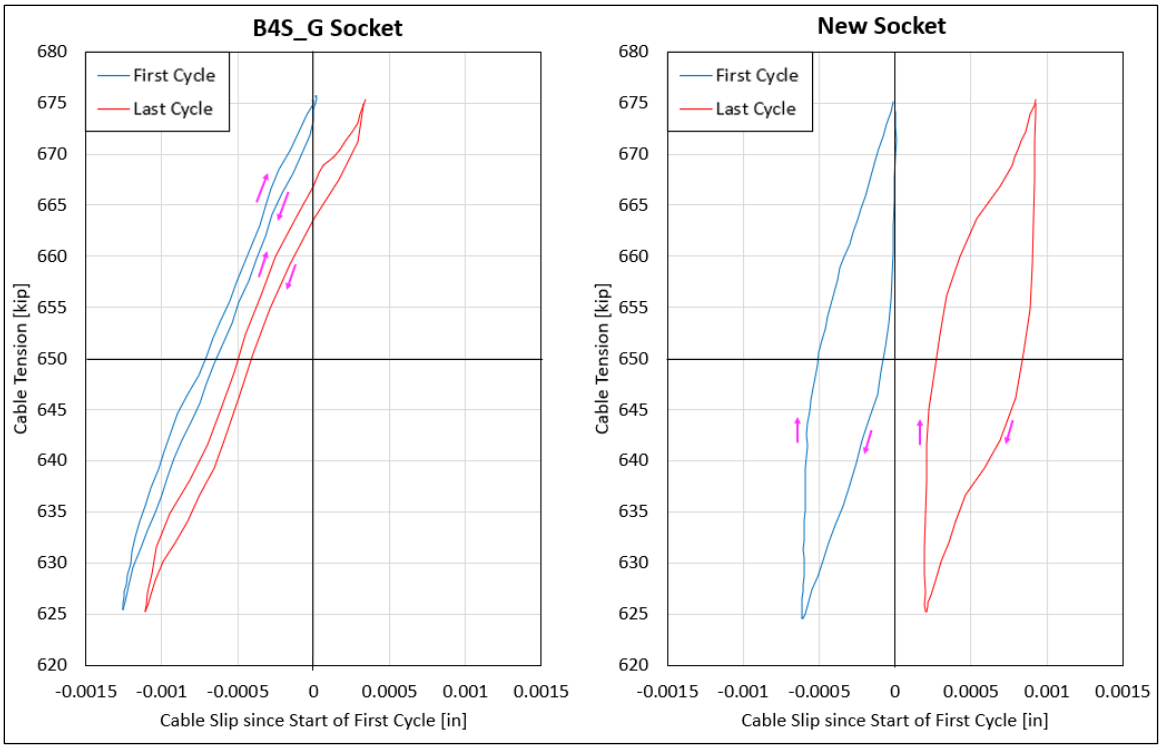

Figure 13: First and last of 150 cycles at 650 kip +/- 25kip.

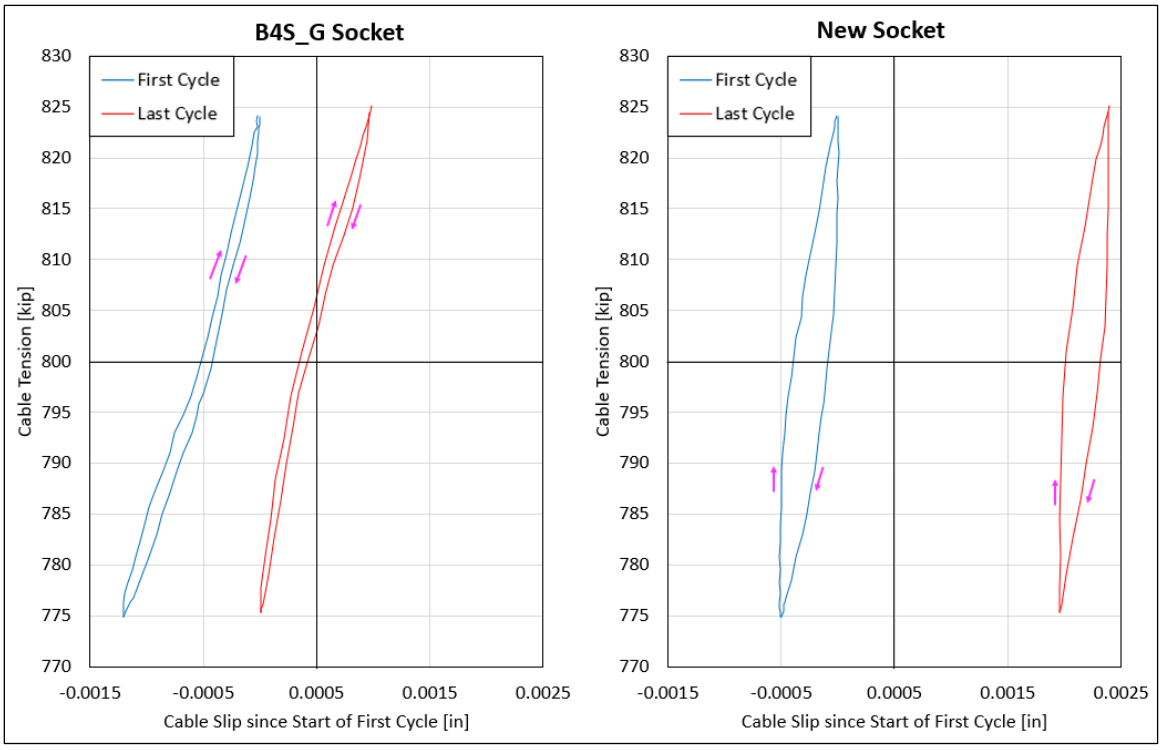

Figure 14: First and last of 150 cycles at 800 kip +/- 25kip.

4.3 Wire Stress Distribution

Figure 15 compares the outer wire stress near each socket with the average wire stress in the cable throughout the load test. The outer wire stress near a socket was calculated from the average of the four outer wire strains measured just outside of the socket with strain gages. The average wire stress in the cable is calculated directly from the known cable tension and metallic area.

The outer wire stress is higher that the average wire stress near both sockets, and the difference is more significant at the new socket. At both sockets, the relative difference between outer and average wire stress increases with the load. This indicates that as the sockets are experiencing cable slip, more load is transferred to the outer wires.

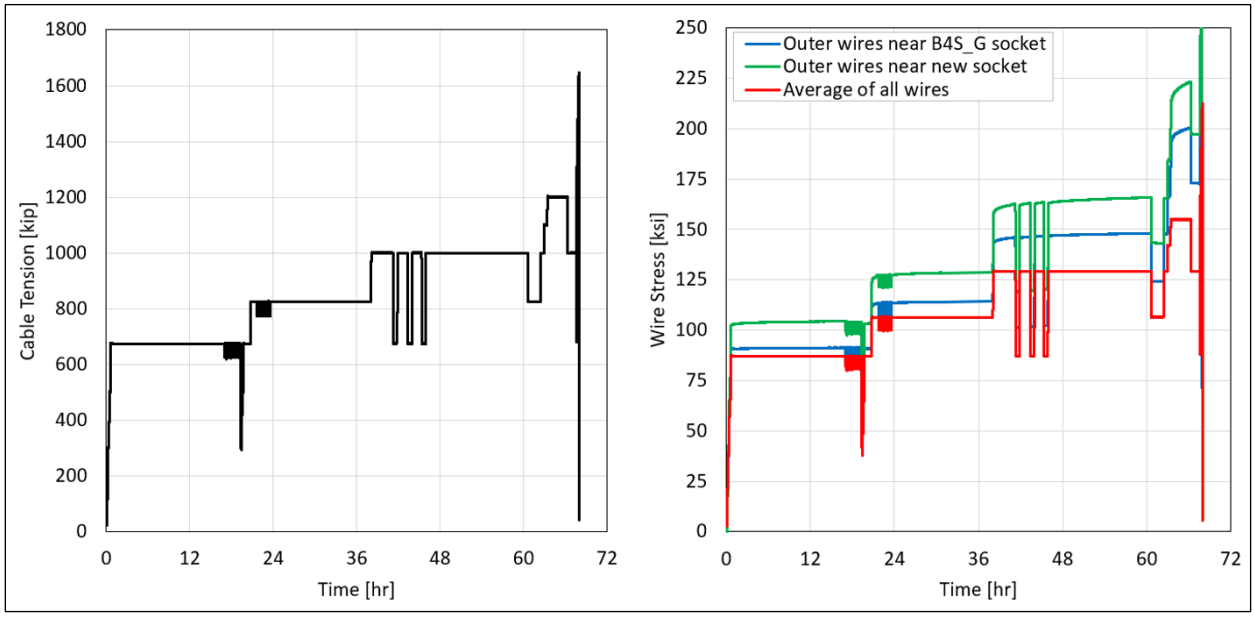

Figure 15: Loading and wire stress distribution time histories.

4.4 Socket Failure Mode

As the cable was being loaded to failure, several wires fractured inside the B4S_G socket. As shown in Figure 16, the first two fractures occurred at cable tensions of 1,454 kip and 1,552 kip. The cable tension was then increased past the minimum breaking strength of 1,614 kip, and reached a maximum of 1,647 kip before three wires fractured simultaneously. As the testing machine attempted to increase the load again, two more wires fractured at cable tensions lower than the maximum previously reached. This suggested that a complete failure of the cable-socket assembly was imminent, and the test was therefore terminated by rapidly unloading the cable.

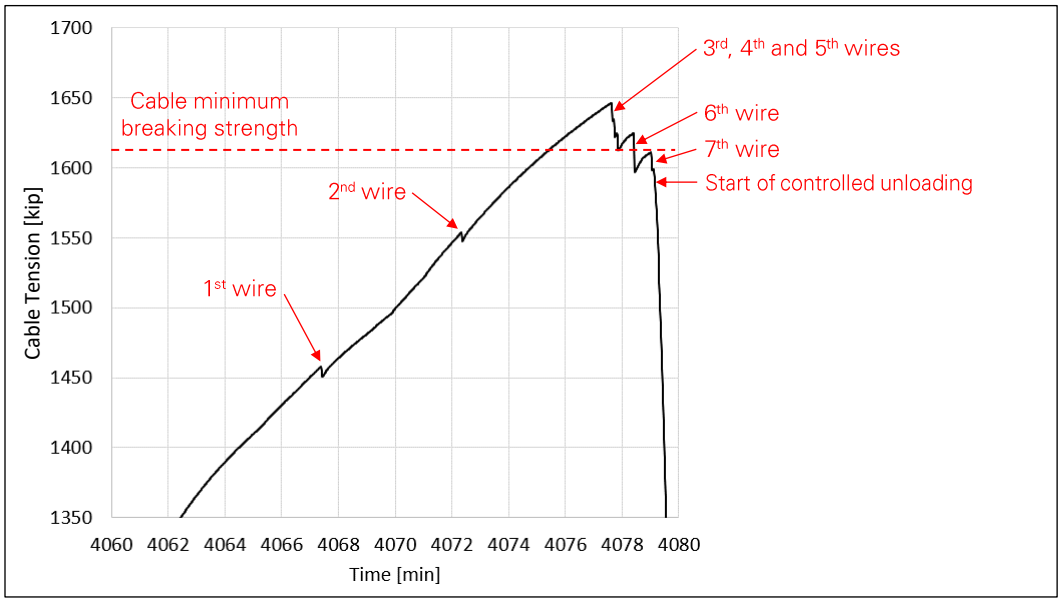

Figure 16: Cable tension drops due to wire fractures.

The condition of the specimen at the end of the test is shown in Figure 17. The seven fractured wires exhibit a cup-cone failure surface characteristic on tensile overload, and all of the fracture occurred within the B4S_G socket. The specimen was later moved to Socotec's laboratory, where the zinc casting of socket B4S_G was cut open for analysis. As shown in Figure 18, a central core has shifted with respect to the rest of the casting. The laboratory test results are covered in M.

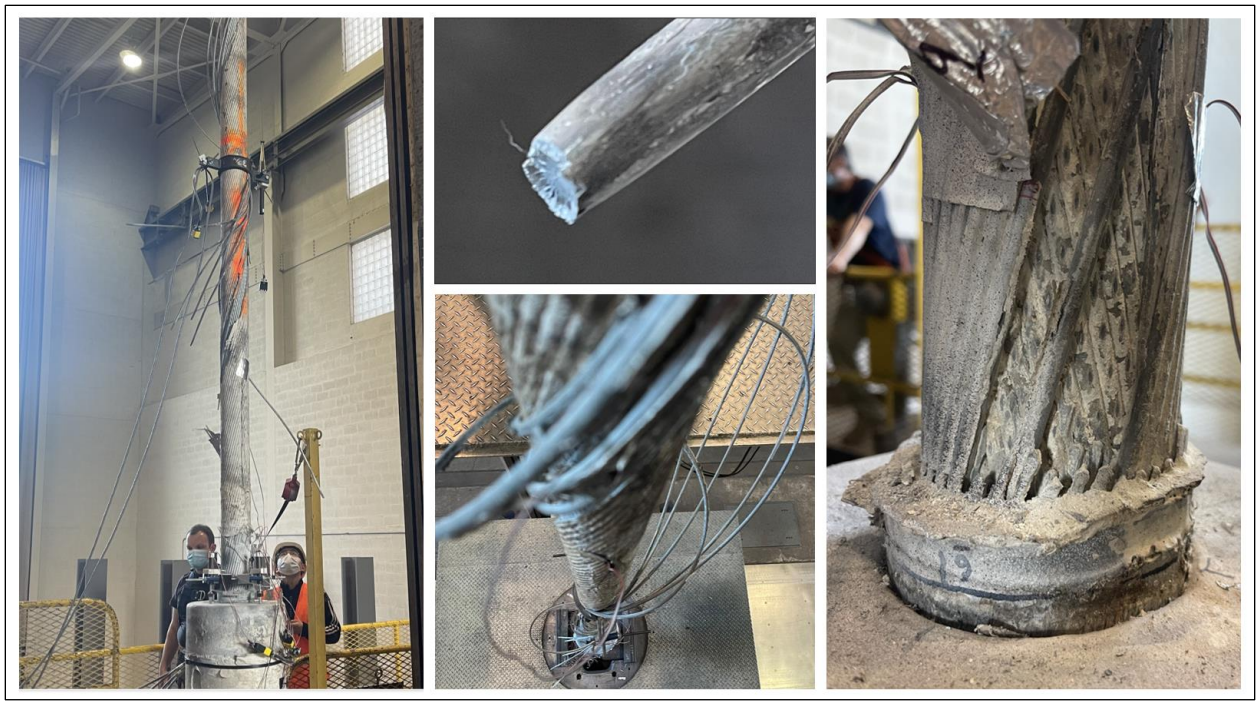

Figure 17: Specimen condition at end of load test.

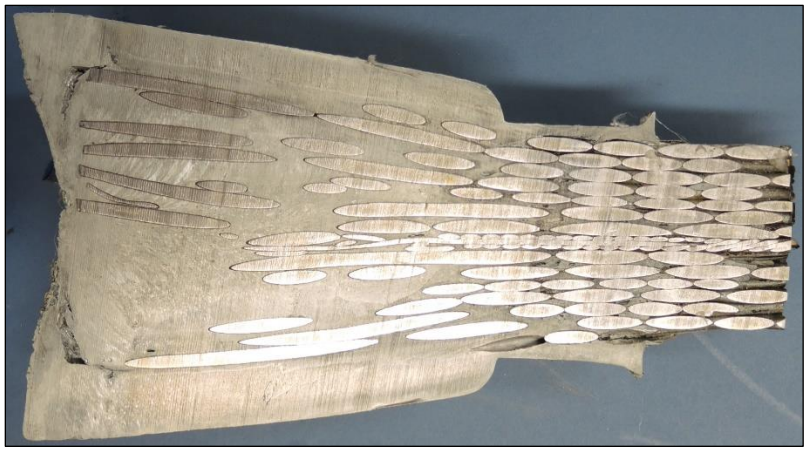

Figure 18: B4S_G casting cut open after load test to *(photo: Socotec).*

Appendix O
Socket Calculations

1.0 Introduction

The cables supporting the telescope were connected to the platform, towers, and anchors through zinc-filled spelter sockets. The telescope collapsed after three sockets failed at the top of Tower 4 (Appendix E), and significant cable slip was observed on other sockets before the collapse (Appendix D). After the collapse, six sockets were recovered from the site and tested to determine dimensions, material properties and wire broom geometry (Appendix M). One socket was also load-tested to failure (Appendix O).

To analyze how the socket properties may have caused or contributed to the observed cable slips and socket failures, we developed a mathematical model for the strength of zinc-filled spelter sockets. The model and its application to the telescope's sockets are presented in this appendix.

In a zinc-filled spelter socket, forces are transferred through a composite medium where a zinc continuum fills the gaps between discrete steel wires. This material has complex mechanical properties, and engineering assumptions were made to simplify the mathematical model. The model is not intended to predict any specific cable slip distance or socket failure load, but to analyze how a socket's property affects its mechanical behavior and strength.

In this appendix, the failure of a cable near a socket is referred to as a *socket failure* as long as multiple wires fractured inside the socket. The *cable slip* is the distance by which a cable moved longitudinally with respect to the socket before failure. The *socket casting* is the composite medium that includes the cast zinc and the enclosed steel wires.

2.0 Model Basis

The proposed model was developed to replicate the behavior of the telescope's sockets that failed or exhibited the most significant cable slips. These sockets are referred to as the *damaged sockets* in the following.

2.1 Observations

As shown in Figure 5 through Figure 1, three key features were observed on the damaged sockets: a displaced inner core, some ruptured outer wires, and/or some slipped outer wires.

Socket **M4N_T** (Figure 1) was the first socket to fail, on August 10, 2020. In this case, an inner core of the casting slipped out of the socket entirely, and multiple outer wires ruptured. The socket and slipped-out core and cable end were analyzed by Wiss, Janney, Elstner Associates (WJE) and the NASA Engineering and Safety Center (NESC), and their findings were provided in a report[1]. Among these findings, it was observed that some wire located outside the core had slipped with respect to the cast zinc.

[1] Wiss, Janney, Elstner Associates (WJE). *Auxiliary Main Cable Socket Failure Investigation*. June 21, 2021. Draft report provided by WJE.

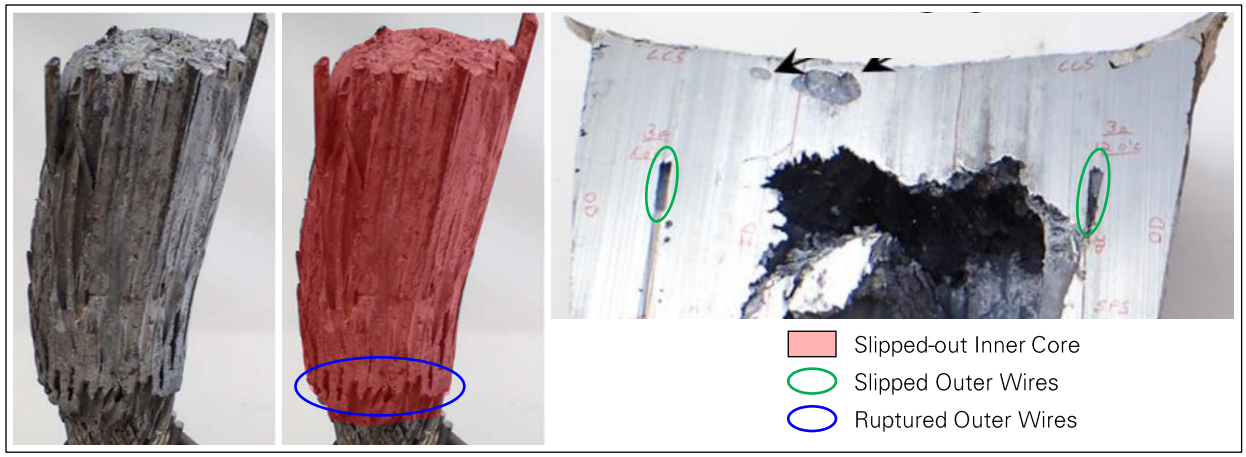

Figure 1: Slipped-out inner core, and ruptured and slipped outer wires in socket M4N_T
(photos: WJE[2]).

Socket **M4-4_T** (Figure 2) failed on November 6, 2020, approximately three months after the first socket failure (M4N_T). The first socket failure had caused four outer wires to rupture in M4-4_T. The socket's casting was cut open after the collapse, and on the cut surface we observe the significant displacement of an inner core.

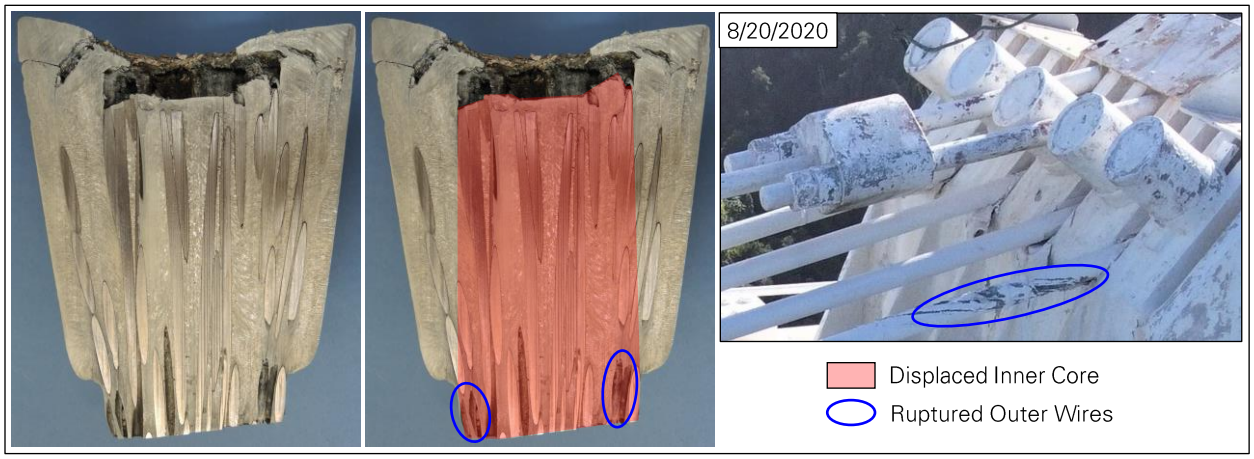

Figure 2: Displaced inner core and ruptured outer wires in socket M4-4_T
(left and center photos: Socotec, right photo: NAIC Arecibo Observatory, a facility of the NSF).

Socket **M4-2_T** (Figure 3) failed on December 1, 2020, which triggered the collapse of the telescope. At least seven outer wires had ruptured before the socket's failure: one wire ruptured after the first socket failed (M4N_T), another wire ruptured when the second socket failed (M4-4_T), and at least five additional wires ruptured in the three weeks preceding the collapse. Photographs of the back of the socket taken before and after the collapse show that an inner core of the socket's casting displaced before and possibly during the socket failure.

[2] Wiss, Janney, Elstner Associates (WJE). *Auxiliary Main Cable Socket Failure Investigation.* June 21, 2021. Draft report provided by WJE.

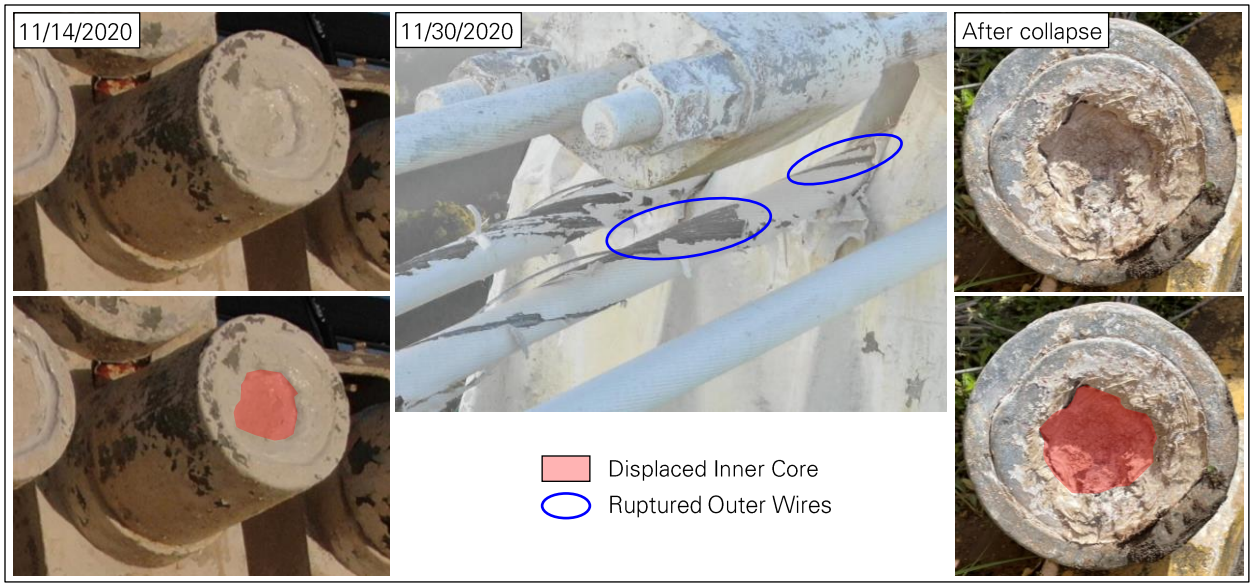

Figure 3: Displaced inner core and ruptured outer wires in socket M4-2_T
before failure (left and center) and after failure (right)
(left and center photos: NAIC Arecibo Observatory, a facility of the NSF).

Socket **B12W_G** (Figure 4) exhibited the largest cable slip among the telescope's sockets before the collapse. The casting was cut open after the collapse, and on the cut surface we observe that an inner core has displaced within the casting, with cracks opening at the back of the core. We also observe that the wire ends located outside of the core have slipped with respect to the cast zinc. A one-inch-thick slice of the casting was radiographed with neutron imaging, and the radiograph reveals that every wire end located outside of the core has slipped.

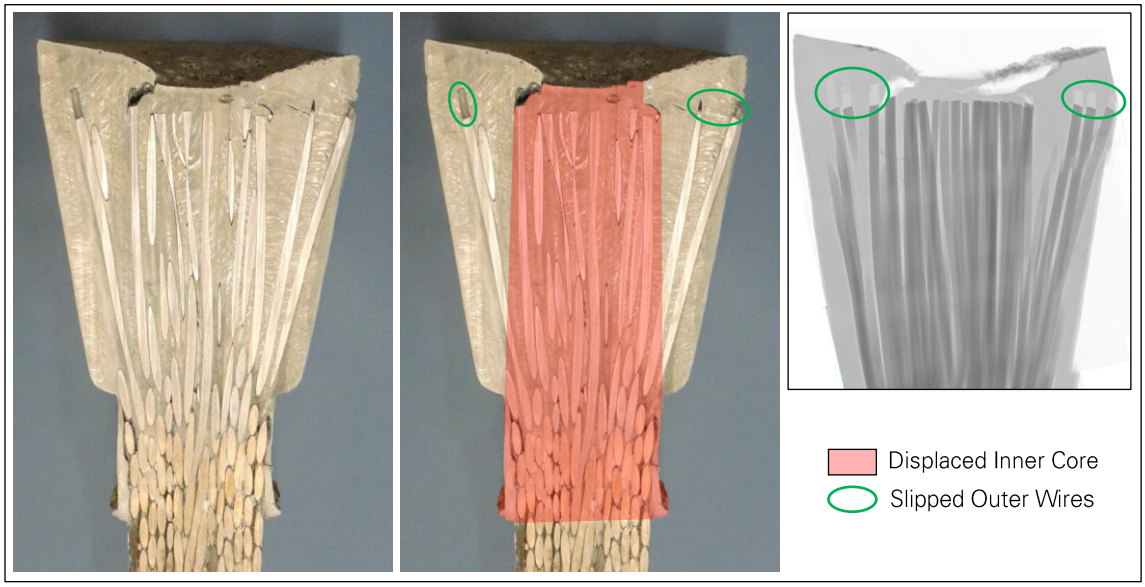

Figure 4: Displaced inner core and slipped outer wires in socket B12W_G
(left and center photos: Socotec; right photo: Adrian Brügger, Columbia University - Oak Ridge National Laboratory).

Socket **B4S_G** (Figure 5) did not fail before or during the telescope's collapse, but was recovered from the site and load-tested to failure as part of the investigation (Appendix O). The load test was ended after seven outer wires ruptured inside the socket. When the seventh wire ruptured, the cable tension was

two percent higher than the cable's Minimum Breaking Strength. The socket's casting was cut open after the test. On the cut surface, we observe that an inner core has displaced within the casting, with cracks opening at the back of the core. The seven ruptured wires are outer wires that used to extend across the core surface towards the socket wall.

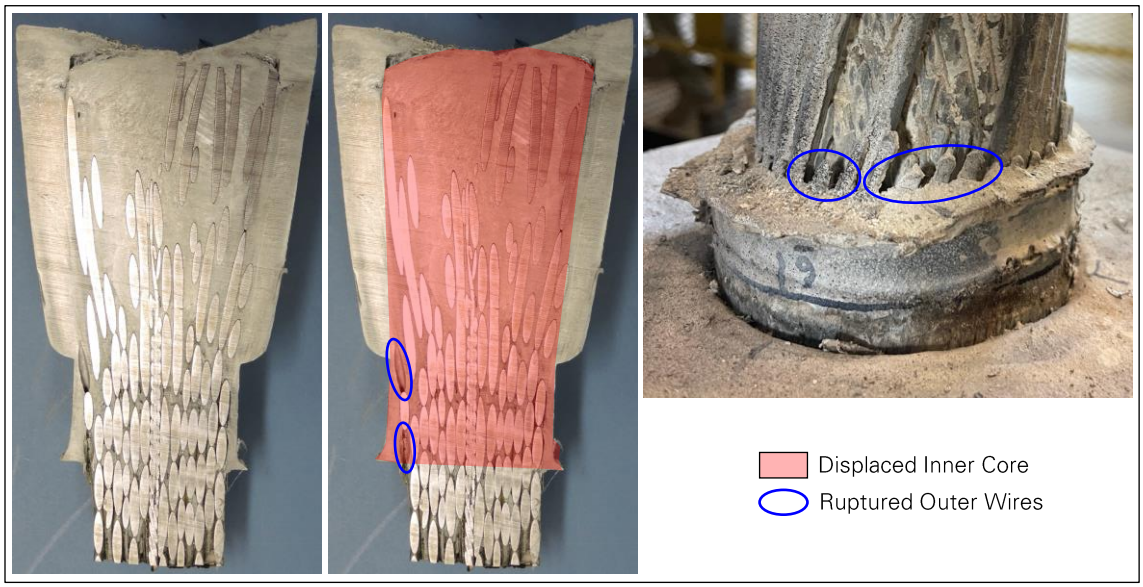

Figure 5: Displaced inner core slip and ruptured outer wire in socket B4S_G after tensile test to failure *(left and center photos: Socotec).*

Significant permanent deformation occurred within the zinc casting of the damaged sockets. As shown in Figure 6, the deformation is visible near the surface of the displaced core in some of the castings investigated. This indicates that at least some of the core displacement occurred through plastic deformation and/or creep of the zinc, which we refer to as zinc *flow*.

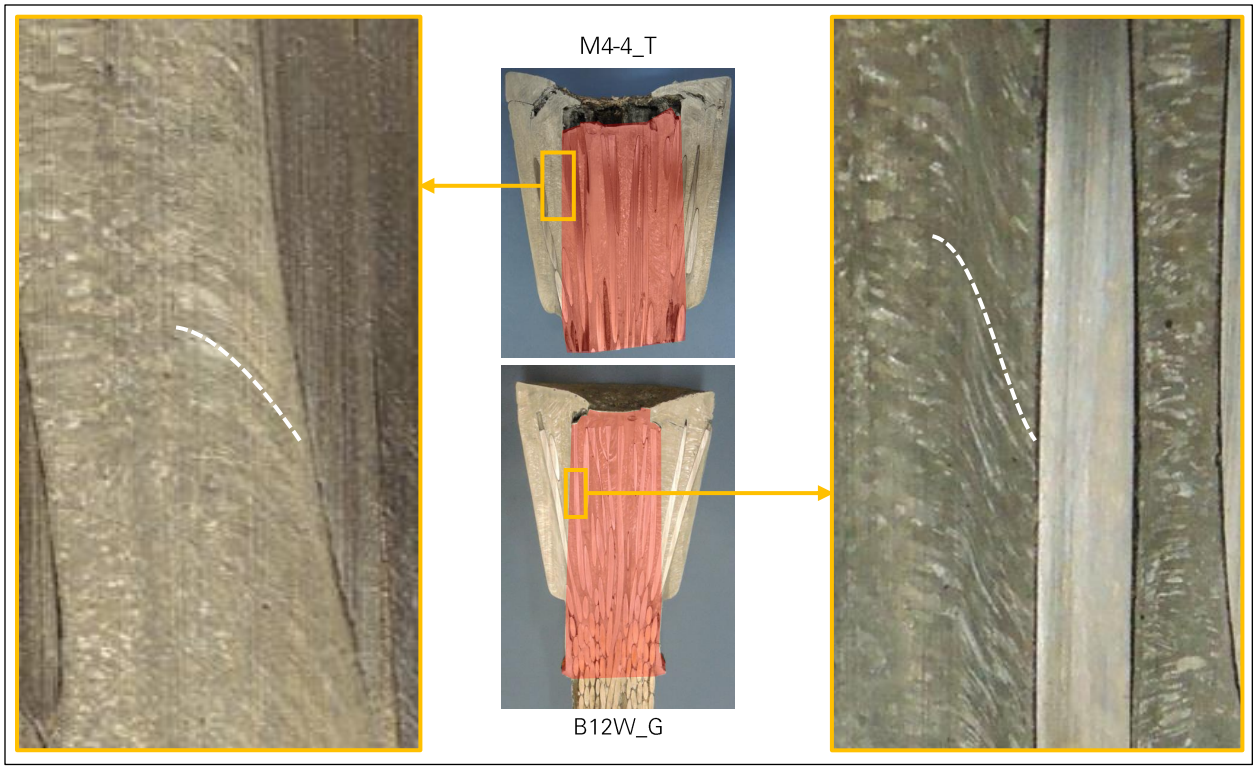

Figure 6: Zinc flow near surface of slipped core in sockets M4-4_T and B12W_G *(photos: Socotec).*

2.2 Idealization

The zinc casting is the interface that transfers the cable tension to the socket. As shown in Figure 7, the casting is held inside the socket by a combination of compression and shear on the casting surface, and bearing on the socket's shoulder if the socket has one.

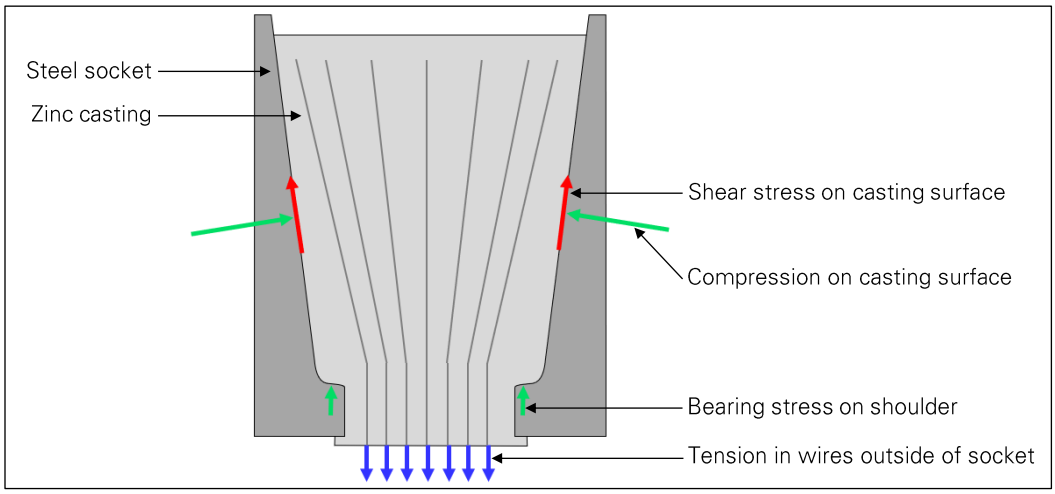

Figure 7: Zinc casting equilibrium.

In each of the fives damaged sockets considered above, the displacement of an inner core was observed within the socket's casting. We therefore propose to analyze the strength of zinc-filled spelter sockets with a model that distinguishes the core from the rest of the casting. As shown in Figure 8, the *core* is

idealized as a cylinder aligned with the cable direction and extending over the entire casting length. The casting outside the core is called the *perimeter*, and any wire that passes through the core surface is called a *crossing wire*. Figure 8 also shows the forces acting on the core. The cable tension tends to pull the core out of the socket, and the core is held in place by a combination of tension in the crossing wires and shear stress on the core surface. There is also a radial compressive stress field in the socket, which allows to develop friction on the core surface and between the wires and the zinc.

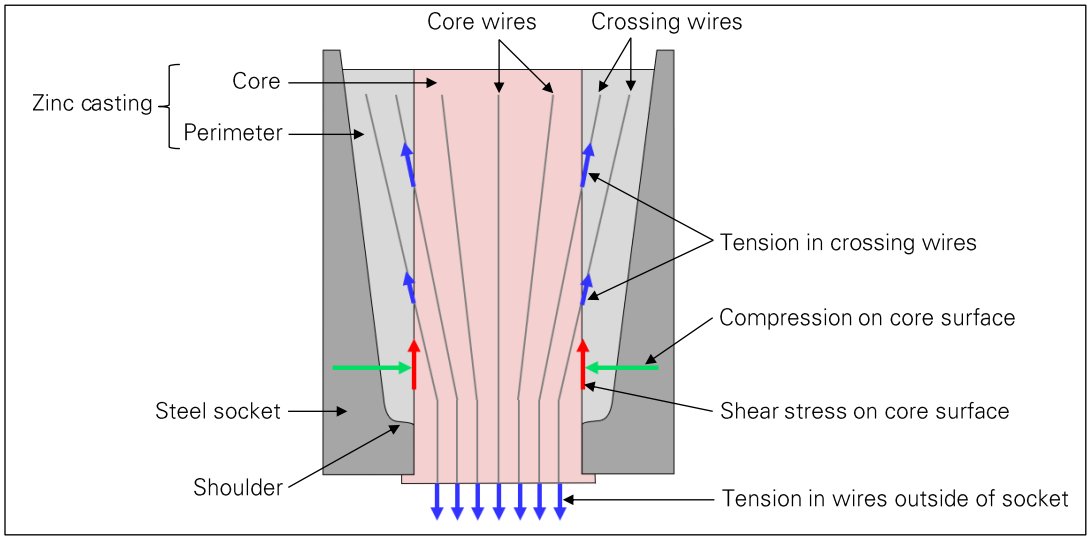

Figure 8: Casting core equilibrium and model nomenclature.

3.0 Model Formulation

A set of equations was derived to calculate the maximum force that can be transferred out of the core through tension in the crossing wires and shear on the core surface. The tension and shear load transfer mechanisms are considered separately in this section. Whether they can occur simultaneously is discussed in further sections, when applying the model to the telescope's sockets.

3.1 Applicability to Sockets with and without Shoulder

A spelter socket may or may not have a shoulder, which is a step in the diameter of the socket's cavity. All of the damaged sockets considered above have a shoulder, but some other sockets of the telescope, such as the platform-end sockets of the auxiliary main cables, do not have the shoulder. Spelter sockets with and without shoulder are also found in other existing structures. Our finite element analysis results (Appendix P) indicate that the presence of a shoulder does not affect the long-term behavior of the socket casting. Therefore, for those sockets that include a shoulder, our model consider a simplified casting geometry where the shoulder is bypassed (Figure 9). With this simplification, the proposed model is applicable to zinc-filled spelter sockets with and without shoulders.

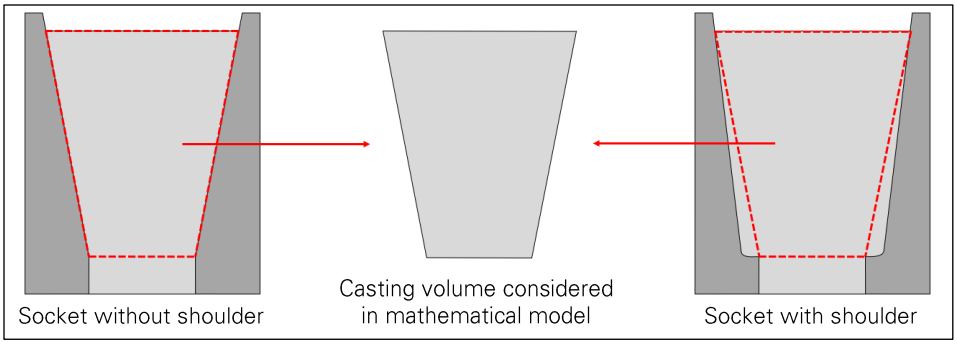

Figure 9: Casting volume considered in socket strength model.

3.2 Pressure on Casting Surface

The normal and tangential pressures acting on the casting surface are determined from the equilibrium of the entire casting (Figure 10).

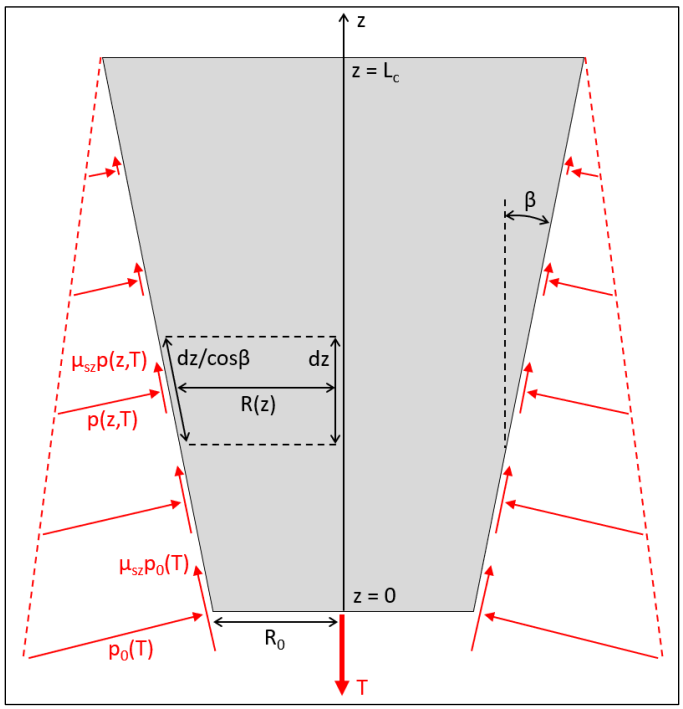

Figure 10: Zinc casting equilibrium under cable tension and stresses on casting surface.

The shape of the casting is defined by three dimensions: smaller diameter R_0, length L_c, and slope β. The variable z designates a position along the socket axis, and any quantity that varies with z is noted as such in the calculations (e.g. $R(z)$). The radius of the casting varies along the axis:

$$R(z) = R_0 + z\,tan\beta \quad [1]$$

The cable tension is noted T. The cable tension is a key parameter in the analysis of the socket failures, and any quantity that depends on the cable tension is noted as such in the calculations (e.g. $p_0(T)$). The normal pressure on the casting surface, noted $p(z,T)$, is assumed to vary linearly along the socket axis,

consistently with published experimental results.[3] With $p_0(T)$ its maximum value, the normal pressure distribution is as follows:

$$p(z,T) = p_0(T)\left(1 - \frac{z}{L_c}\right) \quad [2]$$

The friction coefficient between the steel socket and zinc casting is noted μ_{sz}. The cable tension is in equilibrium with the normal and tangential stresses on the casting surface:

$$T = \int_{z=0}^{L_c} (p(z,T)sin\beta + \mu_{sz}p(z,T)cos\beta)2\pi R(z)\frac{dz}{cos\beta}$$

Replacing with [1] and [2] in the equation above, and integrating along the casting's length:

$$T = 2\pi p_0(T)(tan\beta + \mu_{sz}) \int_{z=0}^{L_c} \left(1 - \frac{z}{L_c}\right)(R_0 + z\, tan\beta)dz$$

$$T = \pi p_0(T)(tan\beta + \mu_{sz})L_c\left(R_0 + \frac{tan\beta}{3}L_c\right)$$

The maximum pressure on the casting surface, which occurs at the front end of the socket, is therefore:

$$p_0(T) = \frac{3T}{\pi L_c(3R_0 + L_c tan\beta)(tan\beta + \mu_{sz})} \quad [3]$$

[3] Klaus Freyer. *Drahsteile*. Springer Vieweg Berlin. 1994.

3.3 Shear Capacity on Core Surface

In the castings of the damaged sockets, we observed that a central core had slipped with respect to the rest of the casting (section 2.0 above). The core is highlighted in Figure 11 and Figure 12, and its radius is considered as a variable noted *r*. Any quantity that depends on the core radius is noted as such in the calculations (e.g. $S_c(r)$).

In the following, we determine the maximum shear force that can be developed on the core surface to resist the cable pull. The maximum shear force is developed through zinc cohesion (Figure 11) and zinc-to-zinc friction (Figure 12).

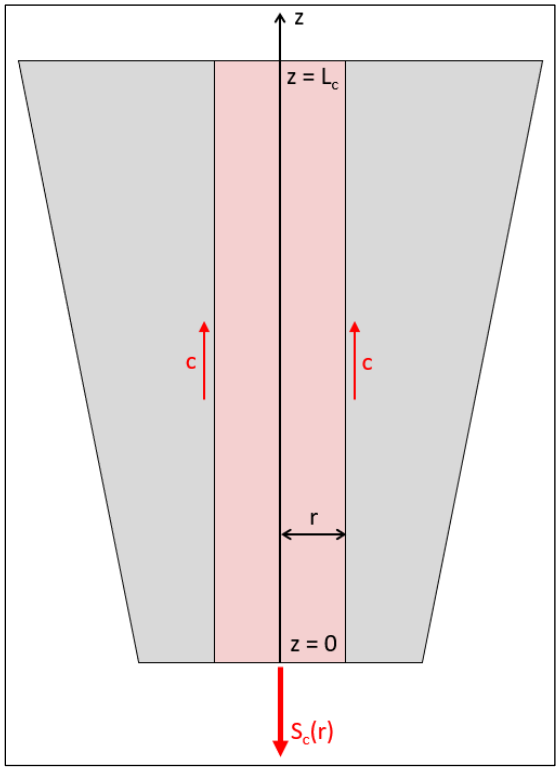

Figure 11: Core cohesion capacity.

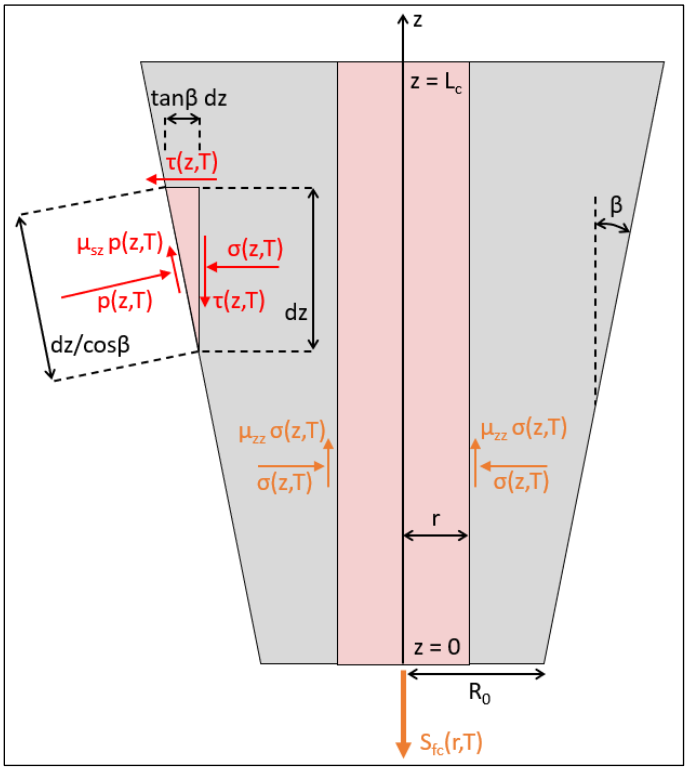

Figure 12: Core confinement friction capacity.

The maximum force that can be resisted through zinc cohesion on the core surface is called the *cohesion capacity* and noted $S_c(r)$. The cohesion capacity is the resultant of the zinc's cohesion stress *c* applied to the surface area of the core (Figure 11):

$$S_c(r) = 2\pi r L_c c \qquad [4]$$

As shown in Figure 12, the normal and tangential pressures on the casting surface induce a radial stress $\sigma(z,T)$ and a shear stress $\tau(z,T)$ in the casting volume. The equilibrium of an infinitesimal zinc volume near the casting surface is as follows:

$$\sigma(z,T)dz + \tau(z,T)tan\beta\, dz = p(z,T)(cos\beta - \mu_{sz}sin\beta)\frac{dz}{cos\beta}$$

$$\tau(z,T)dz = p(z,T)(sin\beta + \mu_{sz}cos\beta)\frac{dz}{cos\beta}$$

The above system can be solved to determine the radial and shear stresses in the casting:

$$\sigma(z,T) = p(z,T)(1 - 2\mu_{sz}tan\beta - tan^2\beta) \quad [5]$$

$$\tau(z,T) = p(z,T)(tan\beta + \mu_{sz})$$

The radial stress in the casting is compressive and acts as a confinement stress on the core, allowing to develop friction on the core surface. This friction is zinc-to-zinc, and the corresponding friction coefficient is noted μ_{zz}. The maximum force that can be resisted by this friction is called the *confinement friction capacity* and noted $S_{fc}(r,T)$. From the equilibrium of the core shown in Figure 12, the confinement friction capacity is as follows:

$$S_{fc}(r,T) = \int_{z=0}^{L_c} \mu_{zz}\sigma(z,T)\, 2\pi r dz$$

Replacing with [2] and [5] in the equation above, and integrating along the casting's length:

$$S_{fc}(r,T) = 2\pi r\mu_{zz}p_0(T)(1 - 2\mu_{sz}tan\beta - tan^2\beta) \int_{z=0}^{L_c} \left(1 - \frac{z}{L_c}\right) dz$$

$$S_{fc}(r,T) = \pi r\mu_{zz}L_c p_0(T)\,(1 - 2\mu_{sz}tan\beta - tan^2\beta) \quad [6]$$

3.4 Crossing Wires Capacity

A crossing wire is a wire that crosses through the surface of the core, as shown in Figure 13. Whether a wire is a crossing wire depends on the wire's geometry and the core's radius. The set of crossing wires for a given core radius *r* is note *I(r)*. The geometry of each crossing wire is described by two parameters that depend on the core radius: the position $z_i(r)$ of the crossing point along the socket axis, and the angle $\gamma_i(r)$ between the wire and socket axis at the crossing point. The length of wire inserted in the casting is assumed equal for all wires and noted L_w.

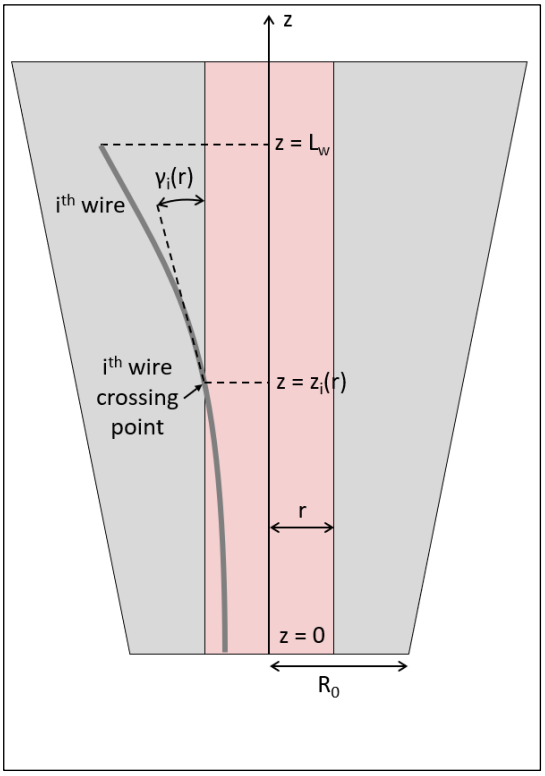

Figure 13: Crossing wire geometry.

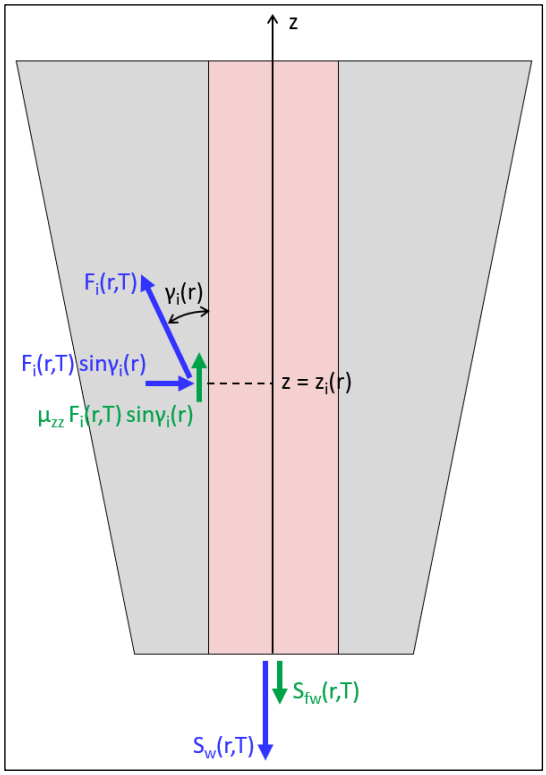

Figure 14: Crossing wire capacity

The maximum tension that a crossing wire can develop at the crossing point is noted $F_i(r,T)$. The longitudinal component of the crossing wire tension directly resists core pull-out, and the sum of this component over all crossing wires is called the *crossing wires capacity* and noted $S_w(r,T)$.

$$S_w(r,T) = \sum_{i \in I(r)} F_i(r,T) cos\gamma_i(r) \quad [7]$$

The radial component of the crossing wire tension induces an additional radial compressive stress on the core surface, which allows to develop additional friction on the core surface (Figure 14). The maximum force that can be resisted by this friction is called the *crossing wires friction capacity* and noted $S_{fw}(r,T)$.

$$S_{fw}(r,T) = \mu_{zz} \sum_{i \in I(r)} F_i(r,T)\ sin\gamma_i(r) \quad [8]$$

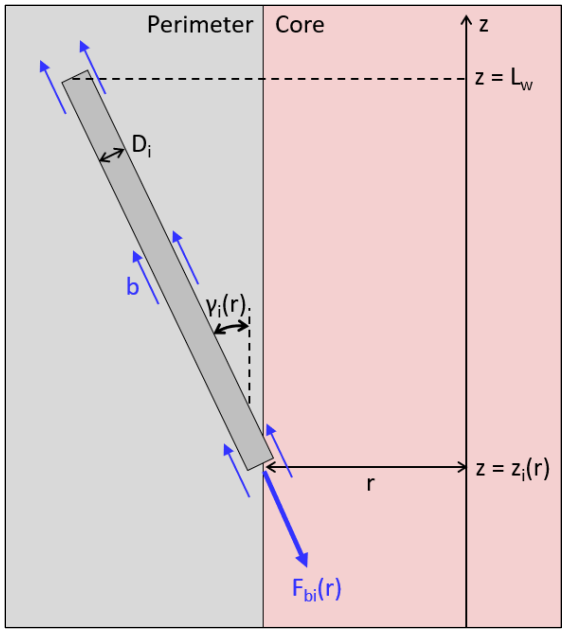

Figure 15: Wire slip resistance from bond with zinc.

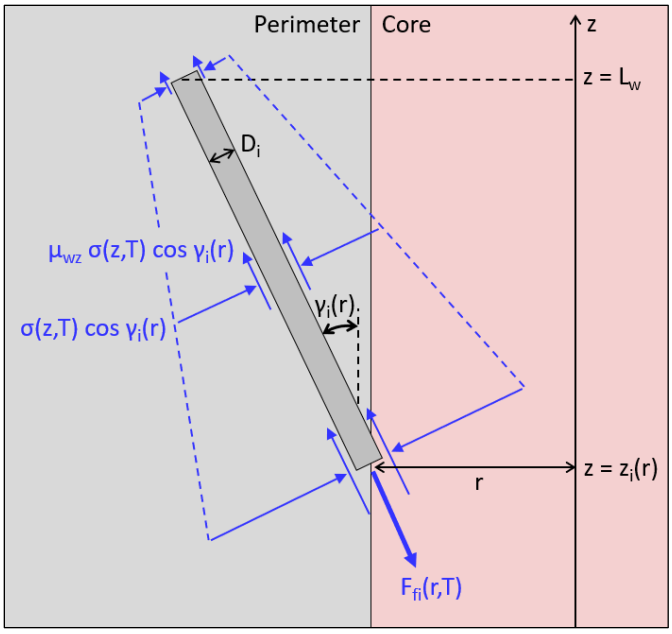

Figure 16: Wire slip resistance from friction with zinc.

The tensile behavior of the wires is assumed elastic-perfectly plastic. The maximum tension that a wire can develop before yielding and eventually rupturing is called the *nominal wire strength* and noted F_{ui}. With D_i the wire diameter and u a nominal critical stress, the nominal wire strength is as follows:

$$F_{ui} = \frac{\pi {D_i}^2 u}{4} \quad [9]$$

The end of each crossing wire is embedded in the perimeter zinc (zinc volume outside of core). As the core pulls out, the wire ends can slip in the perimeter zinc if the slip resistance is not sufficient. Wire slip is resisted by bonding and friction with the perimeter zinc.

A crossing wire's *bond capacity* $F_{bi}(r)$ is the maximum wire tension that can be resisted by the mechanical bond between the wire and perimeter zinc. With b the maximum bond stress in shear, the wire's bond capacity is as follows (Figure 15):

$$F_{bi}(r) = \pi D_i b \frac{L_w - z_i(r)}{cos\gamma_i(r)} \quad [10]$$

A crossing wire's *friction capacity* $F_{fi}(r,T)$ is the maximum wire tension that can be resisted in friction between the wire and perimeter zinc. This friction is developed based upon the radial compressive stress $\sigma(z,T)$ present in the casting and the friction coefficient μ_{wz} between wire and zinc. The wire's friction capacity is as follows (Figure 16):

$$F_{fi}(r,T) = \int_{z=z_i(r)}^{L_w} \mu_{wz}\sigma(z,T)cos\gamma_i(r)\pi D_i \frac{dz}{cos\gamma_i(r)}$$

Replacing with [2] and [5] in the equation above, and integrating along the wire length in the perimeter zinc:

$$F_{fi}(r,T) = \mu_{wz}\pi D_i(1 - 2\mu_{sz}tan\beta - tan^2\beta)p_0(T) \int_{z=z_i(r)}^{L_w} \left(1 - \frac{z}{L_c}\right) dz$$

$$F_{fi}(r,T) = \mu_{wz}\pi D_i p_0(T)(1 - 2\mu_{sz}tan\beta - tan^2\beta)\left(L_w - z_i(r)\right)\left(1 - \frac{L_w + z_i(r)}{2L_c}\right) \quad [11]$$

The maximum tension $F_i(r,T)$ that a crossing wire can develop to resist core pull-out is the least of either the wire's nominal strength or the sum of the wire's bond and friction capacities:

$$F_i(r,\ T) = min\ \left(F_{ui}(r),\ F_{bi}(r) + F_{fi}(r,T)\right) \quad [12]$$

A crossing wire is described as *fully developed* if it ruptures before slipping:

$$F_{bi}(r) + F_{fi}(r,T) > F_{ui}(r)$$

Conversely, a crossing wire is described as *partially developed* if it slips before rupturing:

$$F_{bi}(r)\ + F_{fi}(r,T) < F_{ui}(r)$$

3.5 Total Core Capacity

The *total core capacity* $S_t(r,T)$ is the maximum force that can be developed in the casting to resist core pull-out, considering shear on the core surface and tension in the crossing wires:

$$S_t(r,T) = S_c(r) + S_{fc}(r,T\ ) + S_w(r,T) + S_{fw}(r,T) \quad [13]$$

The total core capacity depends on the cable tension T because the friction components of the capacity depend on the radial compressive stress produced by squeezing casting into the cone-shaped socket under the cable tension.

When considering a core of smaller diameter than the cable, only part of the cable tension T is pulling on the core. This *core tension* is noted $S(r,T)$ and calculated based on the total wire area in the core section $A_S(r)$ and the total wire area in the cable section A_T:

$$S(r,T) = \frac{A_S(r)}{A_T}T \quad [14]$$

For a given core diameter, the *cable pullout tension* $T_p(r)$ is the cable tension for which the core tension is equal to the total core capacity:

$$S\left(r,T_p(r)\right) = S_t\left(r,T_p(r)\right) \quad [15]$$

Combining [14] and [15] provides an expression that can be solved numerically to calculate the cable pullout tension:

$$T_p(r) = \frac{A_T}{A_S(r)}S_t\left(r,T_p(r)\right) \quad [16]$$

When the pullout tension is reached in the cable, the core is expected to pull out of the socket. The cable-socket assembly is therefore expected to fail when the cable pullout tension is reached for any core diameter.

3.6 Full Model

The variables and equations of the proposed mathematical model are summarized as follows:

Socket casting geometry	R_0	Casting front radius [in]
	β	Casting slope [rad]
	L_c	Casting length [in]
	L_w	Wire length in casting's longitudinal direction [in]
Core and Cable Variables	r	Core radius [in]
	T	Cable tension [kip]
Crossing wires geometry	D_i	i^{th} crossing wire diameter [in]
	$\gamma_i(r)$	i^{th} crossing wire angle with core surface [rad]
	$z_i(r)$	i^{th} crossing wire crossing location [in]
Areas	A_T	Total wire area in cable section [in^2]
	$A_S(r)$	Total wire area in core section [in^2]
Material properties	c	Zinc cohesion [ksi]
	b	Wire-zinc bond strength [ksi]
	u	Wire nominal critical stress [ksi]
Friction coefficients	μ_{zz}	Zinc-zinc friction coefficient
	μ_{sz}	Socket-zinc friction coefficient
	μ_{wz}	Wire-zinc friction coefficient

Socket

Maximum pressure on socket surface:

$$p_0(T) = \frac{3T}{\pi L_c(3R_0 + L_c tan\beta)(tan\beta + \mu_{sz})}$$

Crossing wire

Nominal strength:

$$F_{ui}(r) = \frac{\pi {D_i}^2 u}{4}$$

Bond capacity with perimeter zinc:

$$F_{bi}(r) = \pi D_i b \frac{L_w - z_i(r)}{cos\gamma_i(r)}$$

Friction capacity with perimeter zinc:

$$F_{fi}(r,T) = \mu_{wz}\pi D_i p_0(T)(1 - 2\mu_{sz}tan\beta - tan^2\beta)\big(L_w - z_i(r)\big)\left(1 - \frac{L_w + z_i(r)}{2L_c}\right)$$

Maximum tension at crossing point:

$$F_i(r,\ T) = min\ \Big(F_{ui}(r),\ F_{bi}(r) + F_{fi}(r,T)\Big)$$

Core

Cohesion capacity	$S_c(r) = 2\pi r L_c c$
Confinement friction capacity	$S_{fc}(r,T) = \pi r \mu_{zz} L_c p_0(T)\ (1 - 2\mu_{sz} tan\beta - tan^2\beta)$
Crossing wires capacity:	$S_w(r,T) = \sum_{i \in I(r)} F_i(r,T) cos\gamma_i(r)$
Crossing wires friction capacity:	$S_{fw}(r,T) = \mu_{zz} \sum_{i \in I(r)} F_i(r,T)\ sin\gamma_i(r)$
Total capacity:	$S_t(r,T) = S_c(r) + S_{fc}(r,T\ ) + S_w(r,T) + S_{fw}(r,T)$

Cable

Cable pullout tension:	$T_p(r) = \frac{A_T}{A_S(r)} S_t\left(r, T_p(r)\right)$

4.0 Wire Brooms

The proposed model includes the contribution of the crossing wires to resist core pullout. To calculate this contribution, one must know which wires cross through the core surface and, for each crossing wire, the position of the crossing point and the angle between the wire and the socket axis at that point (Figure 13 above). These parameters depend on the core radius. In order to apply the proposed model to the sockets of interest, we extracted the wire broom geometry from laboratory observations. The wire broom is a description of the shape and position of each individual wire within the socket casting.

4.1 Method and Assumptions

For the six socket castings cut open in laboratories, we assembled the wire broom geometry as shown in Figure 17. The positions of the wire ends were measured on the transverse sections made at the back of each casting (Appendix M). For sockets M4-4_T, M8N_T, B4N_G and B12W_G, half of the casting was cut in the transverse direction for the wire broom study while the other half was used for other tests, such as mechanical testing of the zinc. In this case, the wire distribution was assumed to be symmetrical in the other half of the casting. At the front of the casting, the wires are assumed to remain tightly packed together up to socket's shoulder. Each wire position at the back of the socket was paired with a wire position at the front of the socket to obtain the wire broom. Each wire is assumed to be bent near the shoulder and to remain straight between the bend and the wire end. This is consistent with the wire shapes observed on the socket's longitudinal sections (section 2.1 above). This is also consistent with a cable socketing process where the wires are permanently (plastically) bent such that the wire broom remains open in the socket before casting the zinc.

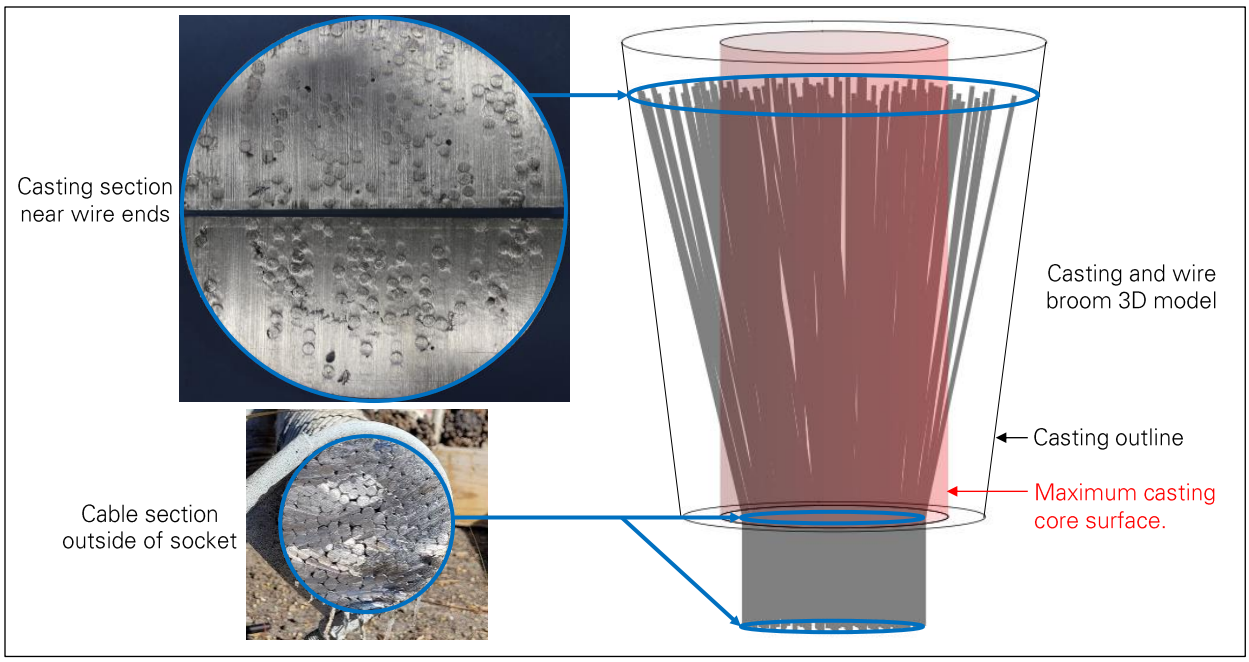

Figure 17: Broom geometry construction from cable and casting sections *(top photo: Socotec)*.

4.2 Results

We assembled the wire broom geometry of the six sockets that were cut open in laboratories. These sockets are of three different types, corresponding to three different cable diameters. For each socket type, we also assembled a uniform wire broom where the wires ends are evenly spaced in the radial and circumferential directions. The uniform wire brooms are hypothetical and considered for comparison purpose only.

The actual and uniform wire brooms of auxiliary backstay ground-end sockets are shown in Figure 18. Socket B4S_G was tested to failure at Lehigh University, and socket B12W_G exhibited the largest cable slip across the entire telescope structure, with 1.875 inch. The broom of socket B12W_G is visually narrower than for the other sockets, with wires crossing the core surface closer to the wire ends, resulting on relatively short embedment lengths in the perimeter zinc.

The actual and uniform wire brooms of auxiliary main tower-end sockets are shown in Figure 19. Socket M4N_T is where the first cable failure occurred on August 10, 2020, and socket M8N_T exhibited a relatively small cable slip of 0.625 inch.

The actual and uniform wire brooms of original main tower-end sockets are shown in Figure 20. Socket M4-4_T is where the second cable failure occurred on November 6, 2020.

For each wire broom, the start and end position of every wire were saved in a database and used as input parameters when applying the proposed model to the telescope's sockets (section 5.0 below).

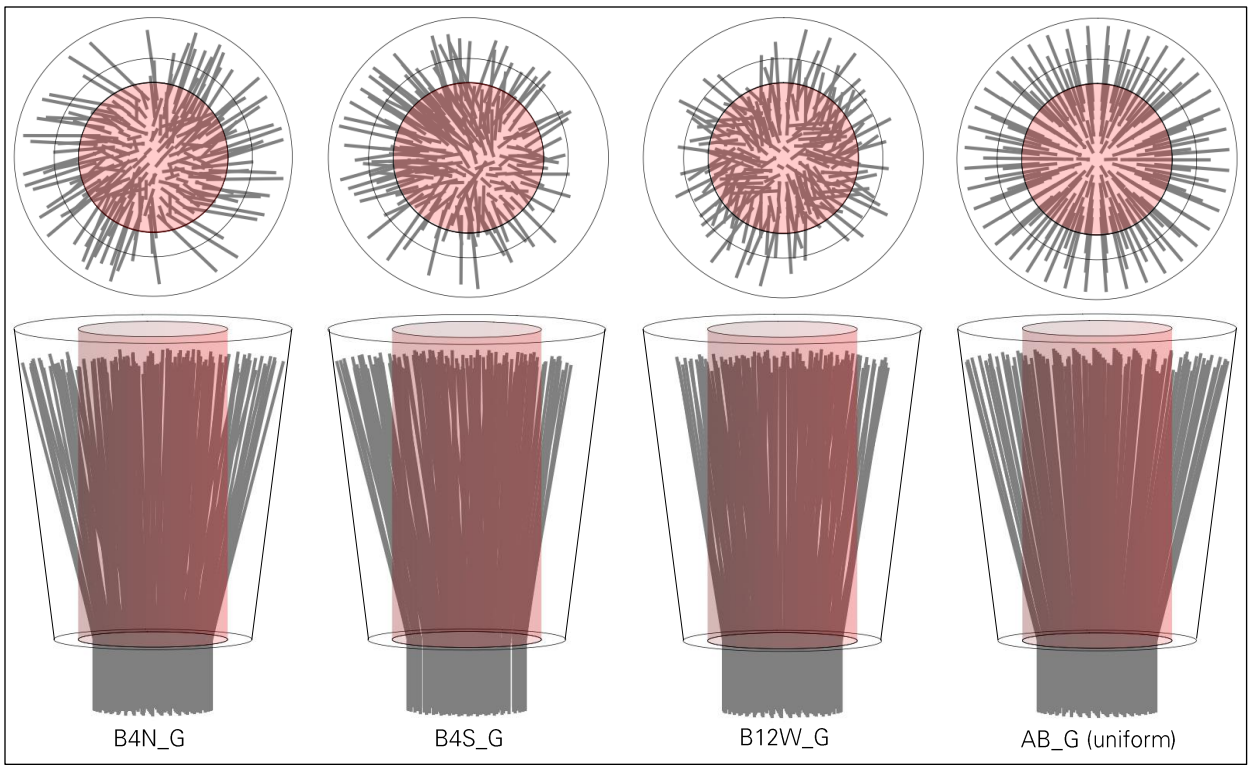

Figure 18: Auxiliary backstay ground-end socket brooms.
The maximum diameter core is highlighted in red.

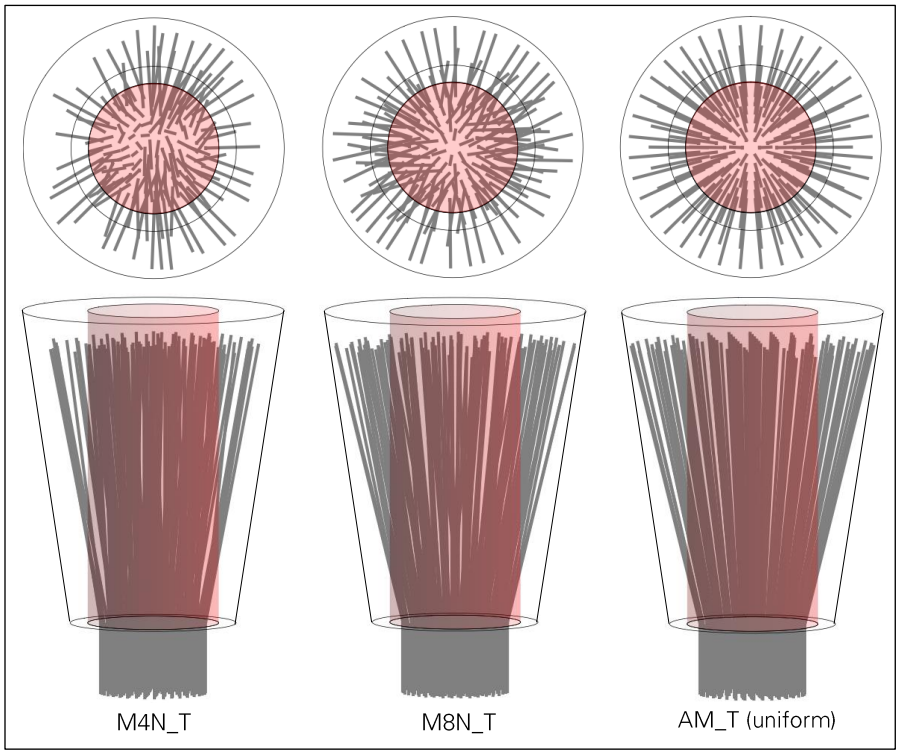

Figure 19: Auxiliary main tower-end socket brooms.
The maximum diameter core is highlighted in red.

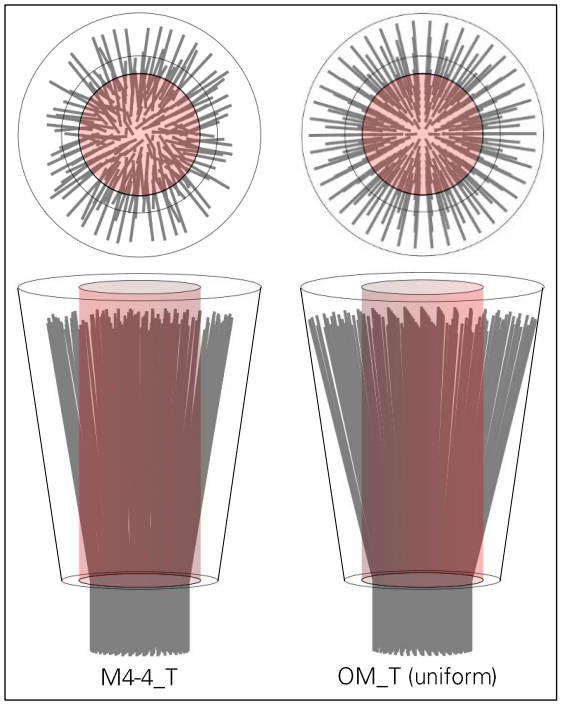

Figure 20: Original main tower-end socket brooms.

5.0 Model Application

5.1 Assumptions

The set of results presented below is based on the following material properties and friction coefficients:

- The wire nominal critical stress is taken as u = 202 kilopound per square inch (ksi). This is at mid-point between the yield stress of 169 ksi and the ultimate tensile stress of 227 ksi measured on average through testing of 12 wires of the telescope's cables (Appendix L).
- The zinc-to-zinc, socket-to-zinc and wire-to-zinc static friction coefficients are assumed to be 0.5. ($\mu_{zz} = \mu_{sz} = \mu_{wz} = 0.5$).
- The zinc's cohesion and the wire-to-zinc shear bond strength are assumed to be 1.02 ksi. ($b = c = 1.02$ ksi). This value was determined based on the results of the socket load test performed at Lehigh University (Appendix N), by equating the cable pullout tension predicted by the mathematical model with the actual failure load of 1,642 kip observed during the test. The wire-to-zinc shear bond strength was also measured experimentally by WJE-NESC as part of the investigation of the first socket failure[4], and the measured average strength was 1.07 ksi. This result is generally consistent with our cohesion and bond strength value derived from the socket load test.

[4] Wiss, Janney, Elstner Associates, *Arecibo Observatory - Auxiliary Main Cable Socket Failure Investigation*, 6/21/2021.

5.2 Results

5.2.1 Cable Pullout Tension and Critical Core

For a given core radius *r*, the cable pullout tension $T_p(r)$ is the tension in the entire cable when the core pulls out. The cable pullout tension is plotted in Figure 21 over a range of core radii for the six sockets of known wire broom geometry. The sockets are grouped by socket type and, for each socket type, a hypothetical socket with uniform wire broom is also included.

The cable pullout tension generally decreases as the core radius increases. A sharp drop in the cable pullout tension occurs each time the core radius increases past the radius of a wire layer at the front of the socket, where the wires are still tightly packed together in the cable section. As a new wire layer gets included in the enlarged core, the wire tension pulling on the core increases. For five of the six actual sockets, the cable pullout tension is minimum when the core radius is maximum. The only exception is socket M8N_T, but even in that case the minimum cable pullout tension is less than two percent lower than the cable pullout tension for the maximum core radius. This difference is negligible. To determine the minimum capacity of the cable pullout tension, we assume that the critical core is the largest possible core, whose radius is equal to the socket's front radius (i.e. $r = R_0$). The rest of results presented in this appendix are based on that assumption.

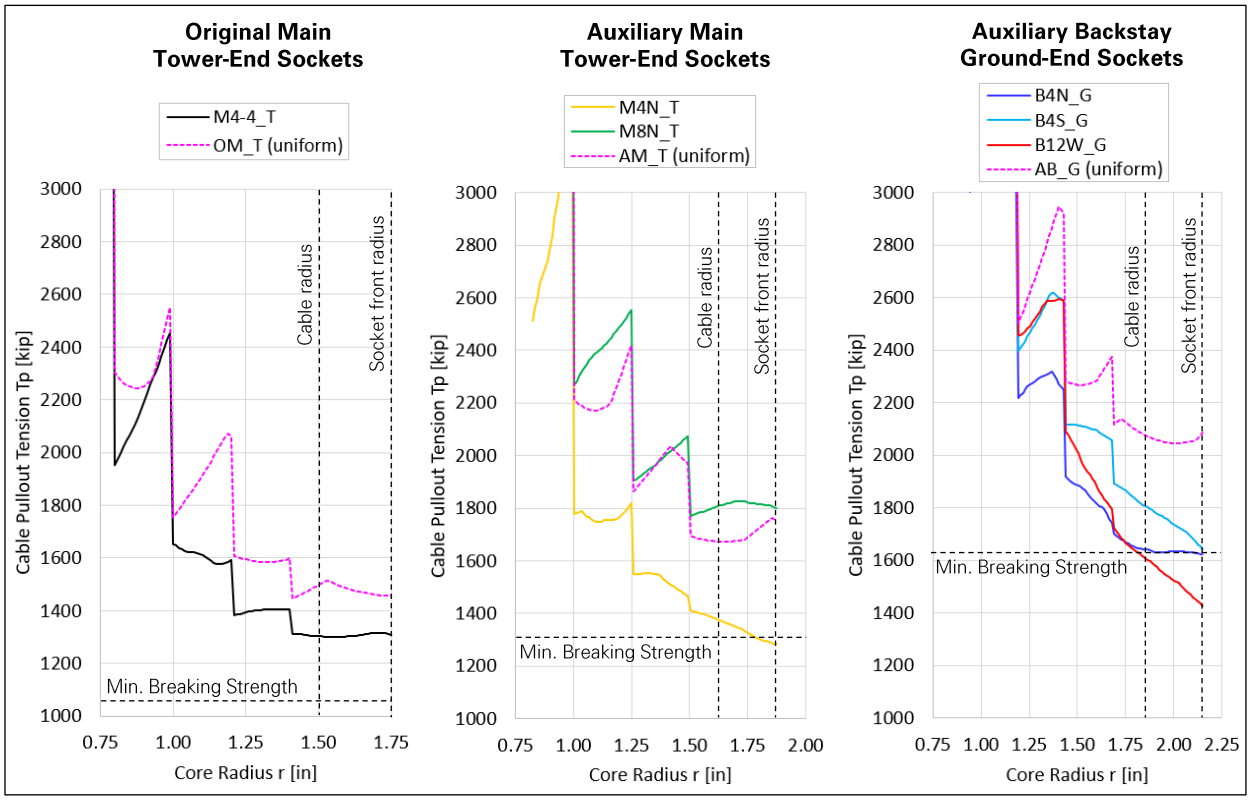

Figure 21: Cable pullout force vs core radius.

The cable pullout tension and Minimum Breaking Strength are compared in Table 1 for the sockets with uniform brooms. The pullout tension is 30 to 40 percent greater than the Minimum Breaking Strength, which is consistent with the expectation that a properly-installed spelter socket is stronger than the connected cable. Table 1 also compares the pullout tension and Minimum Breaking Strength for the

same sockets in the hypothetical case where there is no wire broom, such that the cable tension can only be resisted by zinc cohesion and friction on the core surface. In that case, the pullout tension is less than 15 percent of the Minimum Breaking Strength, which emphasizes the importance of the wire broom in spelter sockets.

The cable pullout tension and Minimum Breaking Strength are compared in Table 2 for the telescope's sockets, i.e. considering the actual wire brooms. The pullout tension is smaller than the Minimum Breaking Strength for sockets M4N_T and B12W_G. These are the two sockets where the maximum cable slips were measured prior to collapse. This result suggests a correlation between wire broom geometry and cable slip, which was further investigated.

Table 1: Cable Minimum Breaking Strength and pullout tension in sockets with uniform broom and no broom.

		OM_T **Original Main Tower-end Socket**	**AM_T** **Auxiliary Main Tower-end Socket**	**AB_G** **Auxiliary Backstay Ground-end Socket**
Cable Minimum Breaking Strength T_b [kip]		1,044	1,314	1,614
Uniform Broom	**Cable Pullout Tension $T_p = T_p(R_0)$ [kip]**	1,456	1,750	2,085
	Ratio T_p/T_b	1.39	1.33	1.29
No Broom	**Cable Pullout Tension $T_p = T_p(R_0)$ [kip]**	159	179	211
	Ratio T_p/T_b	0.15	0.14	0.13

Table 2: Cable Minimum Breaking Strength and pullout tension in actual sockets.

	M4-4_T	**M8N_T**	**B4S_G**	**B4N_G**	**M4N_T**	**B12W_G**
Cable Minimum Breaking Strength T_b [kip]	1,044	1,314	1,614	1,614	1,314	1,614
Cable Pullout Tension $T_p = T_p(R_0)$ [kip]	1,310	1,800	1,642	1,622	1,283	1,425
Ratio T_p/T_b	1.25	1.37	1.02	1.00	0.98	0.88
Cable Slip [in]	Unknown	0.625	0.875	0.875	1.125	1.875

5.2.2 Core Shear and Cable Slip

The large cable slips observed on some of the telescope's sockets are the result of two steps. First, the pre-stretching and/or initial loading of the cable caused the zinc casting to shift and deform to become tightly wedged into the socket. This is expected to occur in any zinc-filled spelter socket, and to result in a relatively small cable slip. Larger cable slips were observed in some of the sockets cut open in the laboratory. This increased slip was caused by the displacement of a core within the casting. This second step is the focus of our analysis.

For the core to displace within the casting, at least one of two mechanisms must occur. The first possible mechanism is a plastic deformation and/or creep of the zinc material near the core surface, which we refer to as *zinc flow*. Zinc flow is driven by a shear stress in the material in the flow direction. The second possible mechanism is the core slipping after the development of a fracture plane on the core surface. In that case, the core slips when a shear stress overcomes the bond and friction capacities on the core surface. Therefore, for either mechanism, the casting core can only displace if there is a shear stress acting on the core surface. Conversely, the core cannot displace when the full cable tension is resisted by the crossing wires, such that there is no shear stress on the core surface. The shear stress on the core surface is simply referred to *core shear* in the following.

We performed an analysis to evaluate the core shear in the telescope's sockets. When a socket is initially loaded, the cable tension is resisted by a combination of core shear and crossing wire tension.

The split between those two resisting forces depends on the relative stiffnesses of the zinc and wires, which is not considered in the socket strength model developed above. However, the model can be used to determine the minimum core shear needed to resist a cable tension. For a given cable tension T, and considering the maximum core radius R_0, the crossing wires capacity S_w is calculated first:

$$S_w = S_w(R_0, T)$$

The surface area of the core is as follows:

$$A_c = 2\pi R_0 L_c$$

If the crossing wires capacity S_w is less than the cable tension T, the difference must be resisted as core shear. We note τ_c the minimum core shear needed to resist the cable tension T:

$$\tau_c = max\left(\frac{T - S_w}{A_c}, 0\right)$$

The maximum cable tension that can be resisted without any core shear can also be calculated. Noted T_{ns}, it is calculated by solving the following equation numerically:

$$T_{ns} = S_w(R_0, T_{ns})$$

Results are provided in Table 3 for the sockets with uniform broom. When the cable safety factor is two, which is the approximate safety factor in the telescope's cables, no core shear is needed in any of the three sockets. The minimum safety factor to not need core shear ranges from 1.5 to 1.9.

Results are provided in Table 4 for the telescope's sockets, i.e. considering the actual wire brooms. The core shear needed was calculated for two loading conditions: gravity loads only, which the telescope experienced for most of its lifetime, and hurricane Maria as representative of an extreme event. The cable tensions for both conditions were determined through analysis (Appendix G and Appendix J). For the five auxiliary sockets, the cable slip increases with the core shear needed under gravity loads. This correlation is plotted in Figure 22. The hurricane condition can cause a significant increase in core shear needed, such that cable slip may have been activated or accelerated during significant windstorms. Socket M4-4_T experienced a 20 percent load increase when the first cable failed, and per our model this event increased the core shear needed from zero to the highest value among the sockets considered (0.70 ksi). The minimum safety factor to not need core shear ranges from 1.7 to 3.0, and those minimum and maximum values are for the sockets exhibiting the minimum and maximum cable slips, respectively.

Table 3: Core shear analysis results in sockets with uniform broom.

	OM_T **Original Main Tower-end Socket**	**AM_T** **Auxiliary Main Tower-end Socket**	**AB_G** **Auxiliary Backstay Ground-end Socket**
Cable Minimum Breaking Strength T_b [kip]	1,044	1,314	1,614
Cable Tension T = T_b/2.0[(1)] [kip]	522	657	807
Crossing Wires Capacity S_w [kip]	648	753	862
Core Shear Needed τ_c [ksi]	0	0	0
Cable Safety Factor T_b/T	2.0	2.0	2.0
Max. Cable Tension to Not Need Core Shear T_{ns} [kip]	674	763	869
Min. Cable Safety Factor to Not Need Core Shear T_b/T_{ns}	1.5	1.7	1.9

(1) 2.0 is the assumed cable safety factor.

Table 4: Core shear analysis results needed in telescope sockets.

		Before M4N Failure						After M4N Failure
		M4-4_T	M8N_T	B4S_G	B4N_G	M4N_T	B12W_G	M4-4_T
Cable Slip [in]		Unknown	0.625	0.875	0.875	1.125	1.875	Observed
Core Surface Area Ac [in^2]		93	106	122	122	106	122	93
Cable Minimum Breaking Strength T_b [kip]		1,044	1,314	1,614	1,614	1,314	1,614	1,044
Under Gravity Loads	**Cable Tension T [kip]**	534	602	665	698	600	624	646
	Crossing Wires Capacity S_w [kip]	565	752	659	671	554	561	581
	Core Shear Needed τ_c [ksi]	0	0	0.05	0.22	0.43	0.52	0.70
	Cable Safety Factor T_b/T	2.0	2.2	2.4	2.3	2.2	2.6	1.6
Maximum During Hurricane Maria	**Cable Tension T [kip]**	543	636	687	721	631	647	-
	Crossing Wires Capacity S_w [kip]	567	761	662	674	558	565	-
	Core Shear Needed τ_c [ksi]	0	0	0.20	0.39	0.69	0.67	-
	Shear Stress Increase vs. Gravity	-	-	+283%	+73%	+58%	+29%	-
	Cable Safety Factor T_b/T	1.9	2.1	2.3	2.2	2.1	2.5	-
Max. Cable Tension to Not Need Core Shear T_{ns} [kip]		571	796	657	666	547	540	571
Min. Cable Safety Factor to Not Need Core Shear T_b/T_{ns}		1.8	1.7	2.5	2.4	2.4	3.0	1.8

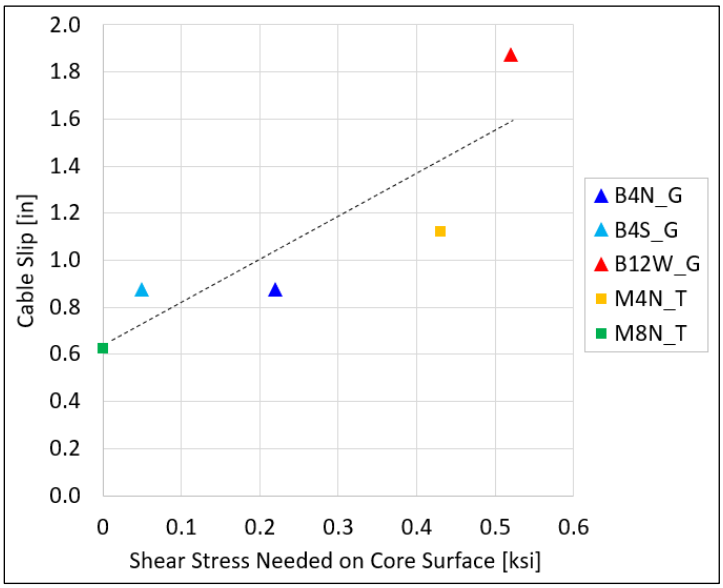

Figure 22: Cable slip vs. core shear needed in auxiliary sockets under gravity loads before M4N failure.

The above results are consistent with the socket behavior shown in Figure 23 and Figure 24, where the zinc material flows as long as it is subjected to shear stress. When the socket is initially loaded, the cable tension is partially resisted by core shear, which causes zinc flow. As zinc flows, the casting core displaces and the crossing wires stretch, causing an increase in crossing wire tension and therefore a decrease in core shear. If the crossing wires can resist the full cable tension (Figure 23), the core shear eventually drops to zero and zinc flow stops. But if the crossing wires cannot resist the full cable tension (Figure 24), zinc flows continues and leads to the large cable slips and eventual socket failures observed on the telescope.

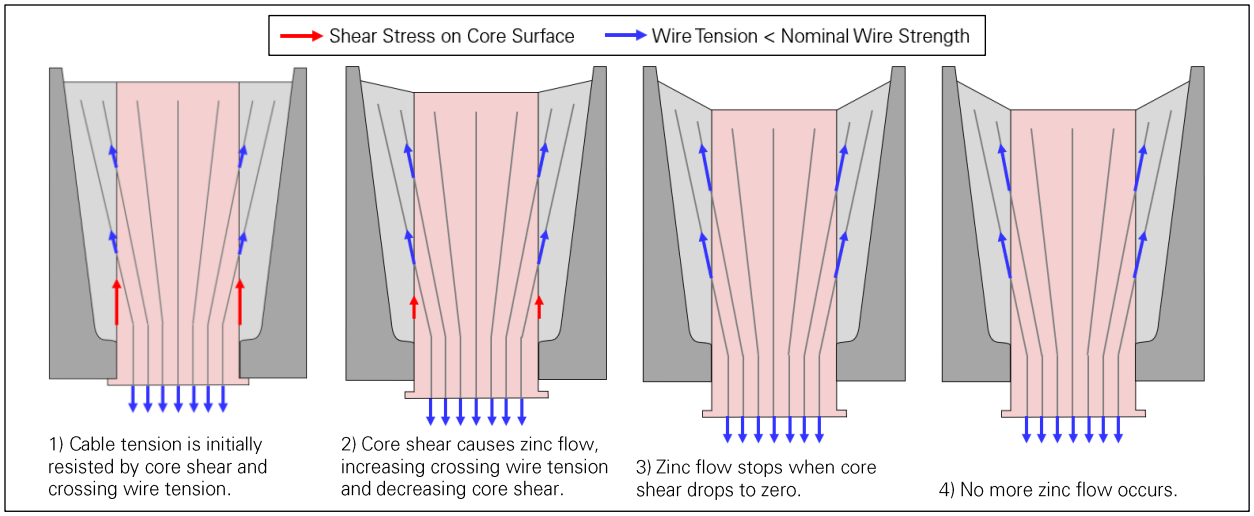

Figure 23: Limited cable slip in socket with crossing wire capacity sufficient to resist full cable tension.

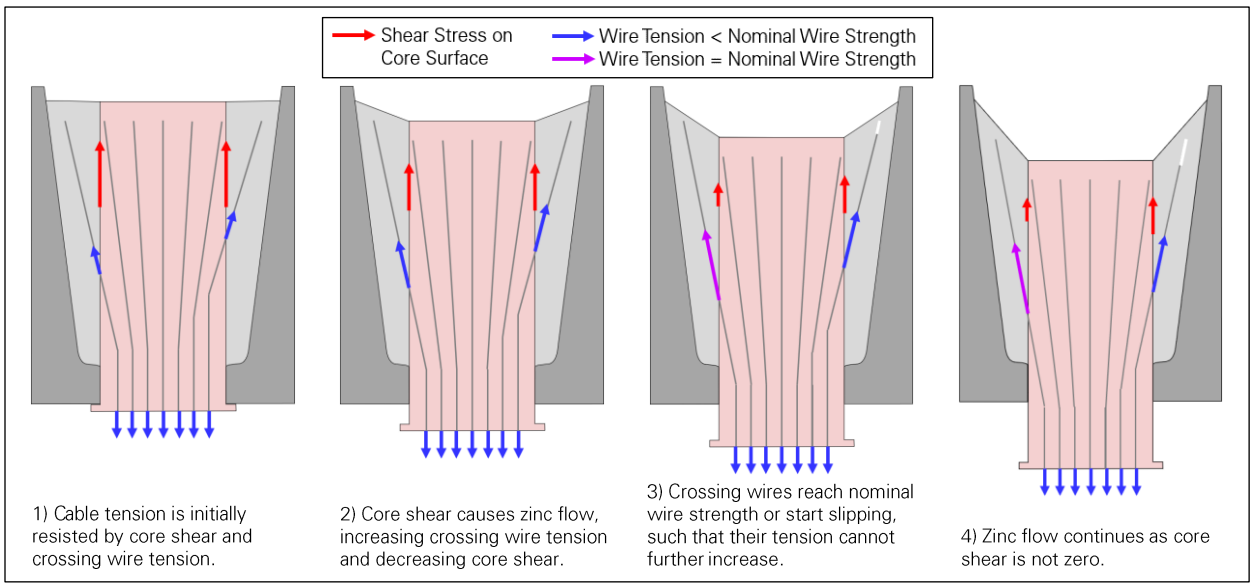

Figure 24: Continued zinc flow and cable slip in socket with crossing wire capacity insufficient to resist full cable tension.

5.2.3 Socket Failure Mode

Two general failure modes were observed on the telescope's sockets : *core rupture*, and *core flow-out*.

The failures of sockets M4N_T and M4-4_T in the field involved the rupture of multiple outer wires inside the socket and a significant displacement or complete pull-out of the casting core. We refer to this failure mode as *core rupture*. The load test of socket B4S_G was stopped after seven outer wires ruptured inside the socket, and the cable slip measurements and post-test laboratory analysis revealed that the casting core had displaced significantly. Socket B4S_G was therefore on the brink of experiencing core rupture like M4N_T and M4-4_T. Core rupture occurred when the cable slip was 1.125 inch and 1.375 inch in M4N_T and B4S_G, respectively. Cable slip could not be measured in M4-4_T as the socket's front was not visible at the top of Tower 4.

Socket B12W_G exhibited the largest cable slip among the telescope's sockets, with 1.875 inch. However, the socket did not fail or experience any wire rupture. The laboratory analysis revealed that in B12W_G, the crossing wire ends slipped with respect to the zinc outside of the core and moved towards the front of the socket in parallel with the core. It is evident that if the displacement of the core and crossing wires had continued, the socket would eventually have failed due to reduced contact area between cable and socket and/or extreme strain of the wires and zinc materials. This failure mode is referred to as *core flow-out*.

From the laboratory observations, it appears that B12W_G experienced core flow-out instead of core rupture due to its crossing wires' tendency to slip instead of rupturing. To test this hypothesis, we compared the number of fully developed wires (rupture before slipping) and partially developed wires (slip before rupturing) in the sockets analyzed. We define a socket's *wire development ratio* as the fraction of crossing wires that are fully developed. The wire development ratio is therefore a measure of the general tendency for the crossing wires to slip (low ratio) or rupture (high ratio) in a given socket. The wire development ratio depends on the cable tension, as a higher tension causes in a higher radial compressive stress in the socket, allowing to develop more friction between wires and zinc to resist wire slip.

Results are provided in Table 5 for the sockets with uniform wire brooms, assuming a cable tension equal to half of the cable's Minimum Breaking Strength. The wire development ratios range between 59 and 73 percent, such that a majority of the crossing wires would rupture before slipping in those sockets. However, since the crossing wires could have resisted the full cable tension (Table 3 page 21) zinc flow would have stopped, and the crossing wires would not have rupture nor slipped.

Results are provided in Table 6 for the telescope's sockets, i.e. considering the actual wire brooms. The wire development ratio was determined under gravity loads and, when applicable, for the failure load. Among the failed and failing sockets, the three sockets experiencing core rupture have a higher wire development ratio (59 to 66 percent) than the socket experiencing core flow-out (38 percent). The fully and partially developed crossing wires are shown in Figure 25 for those four sockets.

Table 5: Crossing wire development analysis results in sockets with uniform broom.

	OM_T **Original Main Tower-end Socket**	**AM_T** **Auxiliary Main Tower-end Socket**	**AB_G** **Auxiliary Backstay Tower-end Socket**
Cable Minimum Breaking Strength T_b [kip]	1,044	1,314	1,614
Cable Tension T/2.0 [kip]	522	657	807
Cable Safety Factor T_b/T	2.0	2.0	2.0
Number of Wires N	168	126	164
Number of Crossing Wires N_c	132	90	102
Number of Fully Developed Crossing Wires N_{cf}	78	66	74
Wire Development Ratio N_{cf}/N_c	59%	73%	73%

Table 6: Crossing wire development analysis results in telescope sockets.

	Gravity Loads Before M4N Failure						Gravity Loads After M4N Failure	End of Load Test
	M4-4_T	**M8N_T**	**B4S_G**	**B4N_G**	**M4N_T**	**B12W_G**	**M4-4_T**	**B4S_G**
Cable Slip [in]	Unknown	0.625	0.875	0.875	1.125	1.875	Observed	1.375
Number of Wires N	168	126	164	164	126	164	168	164
Number of Crossing Wires N_c	110	102	97	86	71	84	110	97
Number of Fully Developed Crossing Wires N_{cf}	64	44	46	52	42	32	72	64
Wire Development Ratio N_{cf}/N_c	58%	43%	47%	60%	59%	38%	65%	66%
Socket Failure Mode	None	None	None	None	Core Rupture	Core Flow-out	Core Rupture	Core Rupture

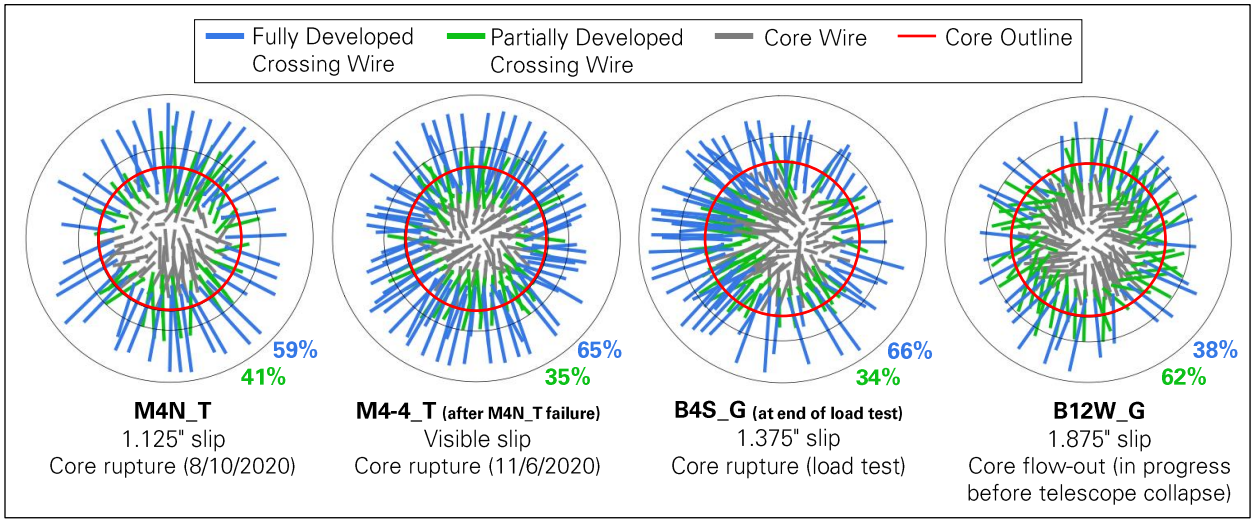

Figure 25: Fully and partially developed crossing wires in failed and failing sockets.

The above results are consistent with the socket behavior idealized in Figure 26 and Figure 27. In both cases, the crossing wires cannot resist the full cable tension, such that zinc flow cannot stop and the socket is bound to fail. The failure mode, however, depends on whether the crossing wires are fully or partially developed. If the crossing wires are fully developed (Figure 26), they continue to stretch near the core surface as the zinc continues to flow. Some of the wires rupture when they reach their ultimate tensile strain, which increases core shear and accelerates zinc flow, leading to more wire ruptures and, eventually, to core rupture. If the crossing wires are partially developed (Figure 27), they can slip in parallel with the cable instead of rupturing. In this case, the cable continues to gradually slip out of the socket. Complete slip-out or rupture will eventually occur as the contact length between cable and socket decreases and/or the zinc's strain becomes too large. Macroscopically, the socket failure is more brittle when the crossing wires are fully developed, and more ductile when the crossing wires are partially developed. Actual sockets include both fully and partially developed crossing wires and can therefore exhibit intermediate behaviors and failure modes.

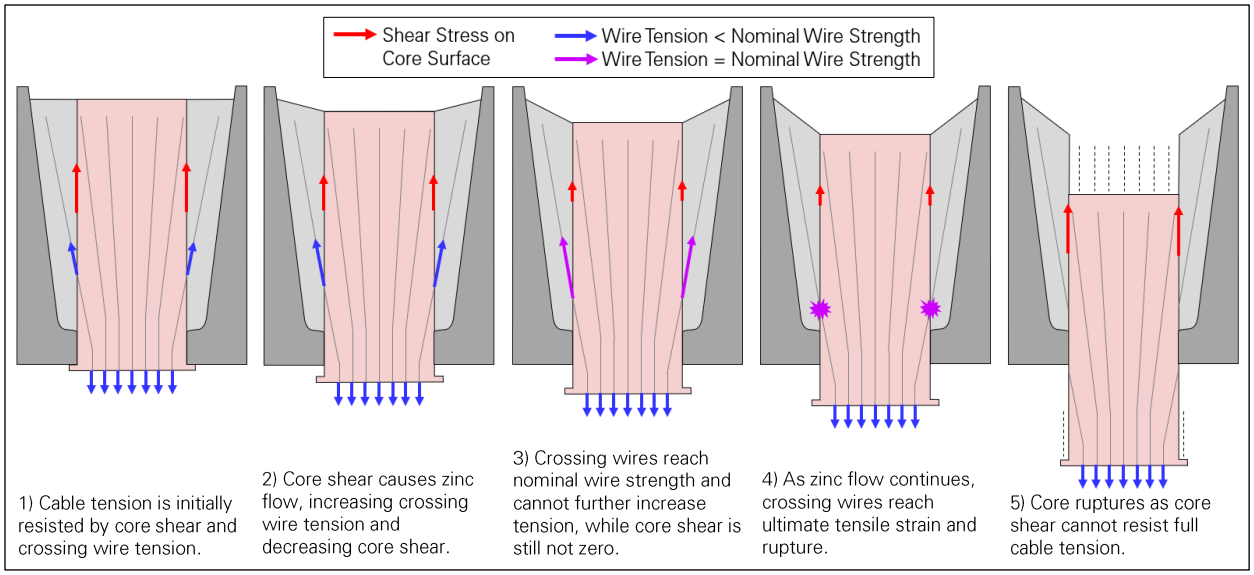

Figure 26: Core rupture in socket where crossing wires cannot resist full cable tension and are fully developed.

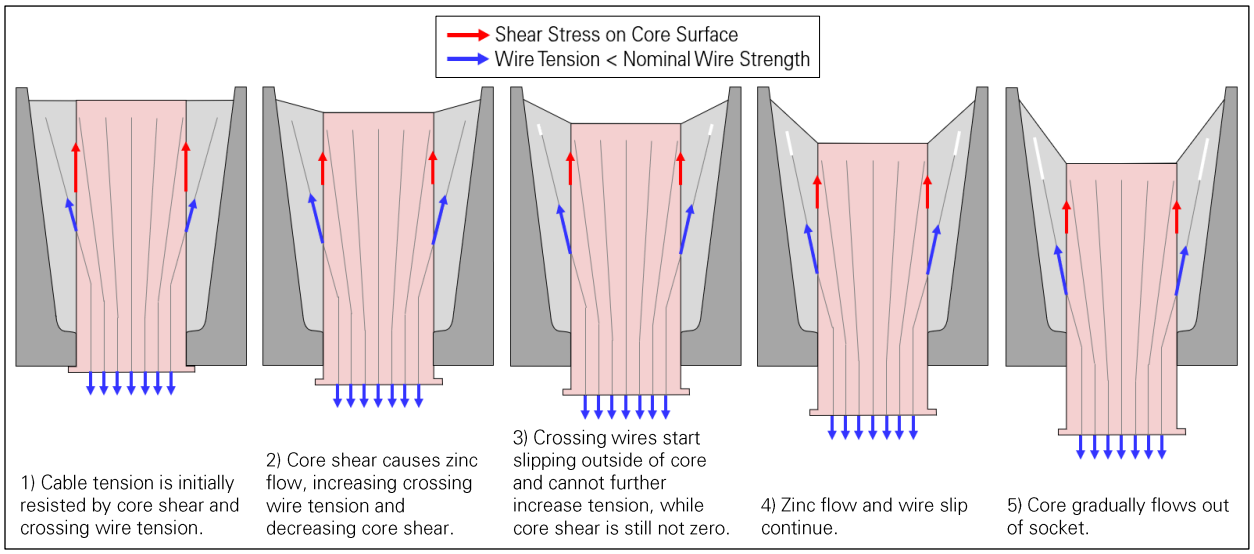

Figure 27: Core flow-out in socket where crossing wires cannot resist full cable tension and are partially developed.

5.2.4 Summary

By applying the proposed mathematical model to the six telescope sockets of known wire broom, we observed correlations between core shear, wire development ratio, cable slip and socket failure mode. These correlations are summarized in Figure 28 for the auxiliary sockets. The original socket (M4-4_T) is not included because its cable slip is not known. The left side of Figure 28 shows that the cable slip observed in the field increases with the core shear needed to resist the cable tension under gravity loads (same as Figure 22 page 22). This core shear depends on the collective capacity of the crossing wires to resist the cable tension: if the crossing wires capacity is lower, the core shear needed is higher. The right side of Figure 28 shows that failure occurs in the sockets exhibiting the largest cable slips, with a failure mode that depends on the wire development ratio: the socket experiences core rupture if its crossing wires tend to rupture before slipping (high ratio), and core flow-out if its wires tend to slip before

rupturing (low ratio). Both the cable slip and the socket failure mode are affected by the wire broom geometry, which is therefore key to the strength of a zinc-filled spelter socket. A summary of the cable safety factors, core shear needed, cable slip, wire development ratio and socket failure modes is provided in Table 7.

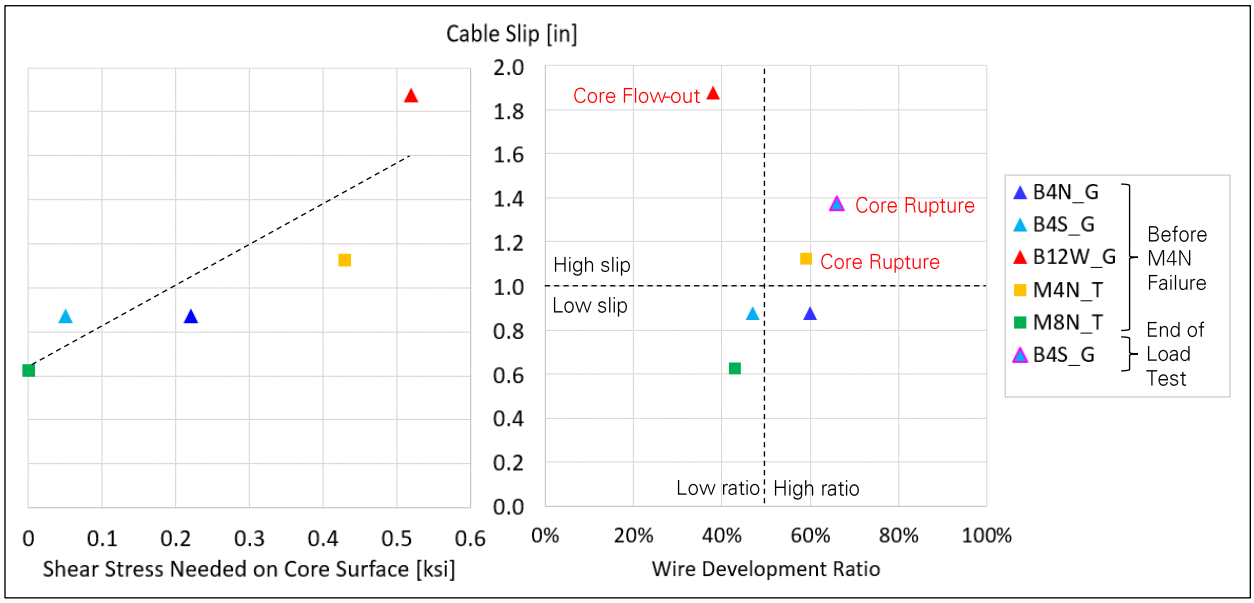

Figure 28: Correlation between core shear, wire development ratio, cable slip, and socket failure.

Table 7: Core shear, wire development ratio, cable slip, and socket failure mode.

	Under Gravity Before M4N Failure						Under Gravity After M4N Failure	At End of Load Test
	M4-4_T	**M8N_T**	**B4S_G**	**B4N_G**	**M4N_T**	**B12W_G**	**M4-4_T**	**B4S_G**
Min. Cable Safety Factor to Not Need Core Shear	1.8	1.7	2.5	2.4	2.4	3.0	1.8	2.5
Actual Cable Safety Factor	2.0	2.2	2.4	2.3	2.2	2.6	1.6	0.98
Core Shear Needed [ksi]	0	0	0.05	0.22	0.43	0.52	0.70	7.26
Cable Slip [in]	Unknown	0.625	0.875	0.875	1.125	1.875	Observed	1.375
Wire Development Ratio	58%	43%	47%	60%	59%	38%	65%	66%
Socket Failure Mode	None	None	None	None	Core Rupture	Core Flow-out	Core Rupture	Core Rupture

5.2.5 Illustration

Based on the above analysis results, the behavior of the six telescope sockets considered is described in the following through the lens of the proposed socket strength model (Figure 29 through Figure 34). It is understood that the proposed model simplifies and approximates the socket behavior.

Socket M4-4_T

1. As the socket is initially loaded, the cable tension is resisted by a combination of core shear and crossing wire tension.
2. Core shear causes zinc flow, which increases crossing wire tension and decreases core shear. The crossing wires capacity (565 kip) is greater than the cable tension (534 kip), so the core shear eventually drops to zero and zinc flow stops.
3. The first cable failure (M4N) on August 10, 2020 causes a 20 percent increase in cable tension, which reactivates zinc flow.
4. The new crossing wires capacity (581 kip) is less than the new cable tension (646 kip), so core shear (0.70 ksi) is still needed to resist the cable tension after the crossing wires reach their capacity. Most of the crossing wires (65 percent) are fully developed and reach their nominal strength.
5. As zinc flow continues, the fully developed crossing wires reach their ultimate tensile strain and rupture.
6. The core ruptures as core shear cannot resist the full cable tension, but the remaining wires rupture before the core fully slips out.

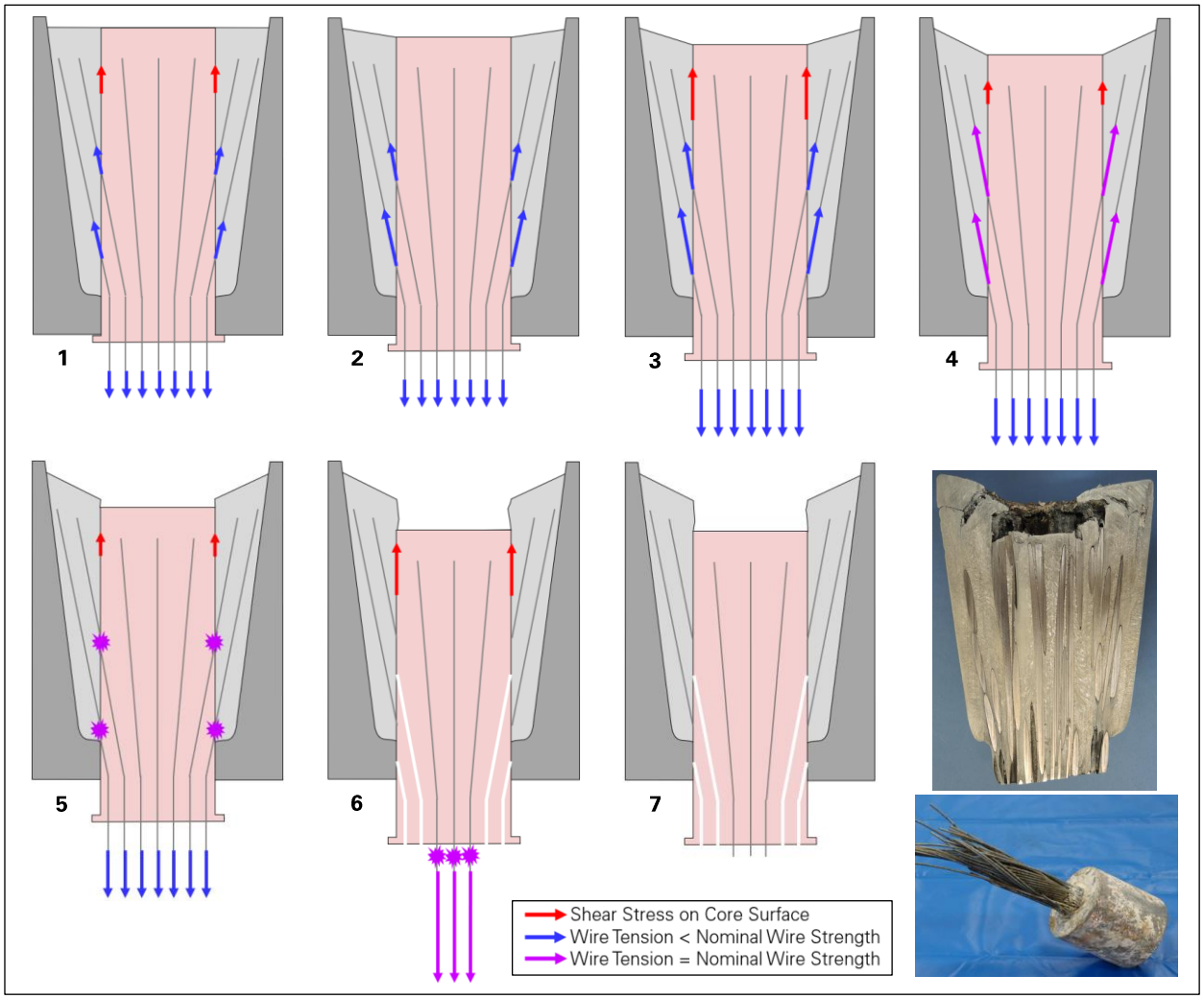

Figure 29: Behavior and failure of socket M4-4_T *(photos: Socotec).*

Socket M8N_T

1. As the socket is initially loaded, the cable tension is resisted by a combination of core shear and crossing wire tension.
2. Core shear causes zinc flow, which increases crossing wire tension and decreases core shear. The crossing wires capacity (752 kip) is greater than the cable tension (602 kip), so the core shear eventually drops to zero and zinc flow stops.

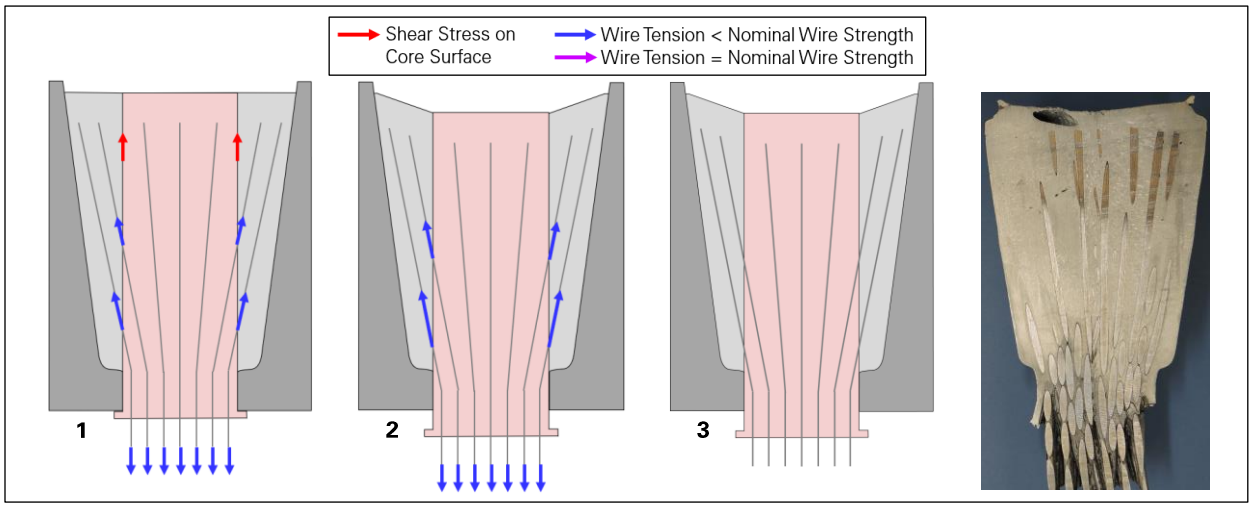

Figure 30: Behavior of socket M8N_T *(photo: Socotec).*

Socket B4N_G

1. As the socket is initially loaded, the cable tension is resisted by a combination of core shear and crossing wire tension.
2. Core shear causes zinc flow, which increases crossing wire tension and decreases core shear. The crossing wires capacity (671 kip) is less than the cable tension (698 kip), so core shear (0.22 ksi) is still needed to resist the cable tension after the crossing wires reach their capacity.
3. The core shear needed is relatively low, so zinc flow is slow, and the socket does not fail before the telescope's collapse.

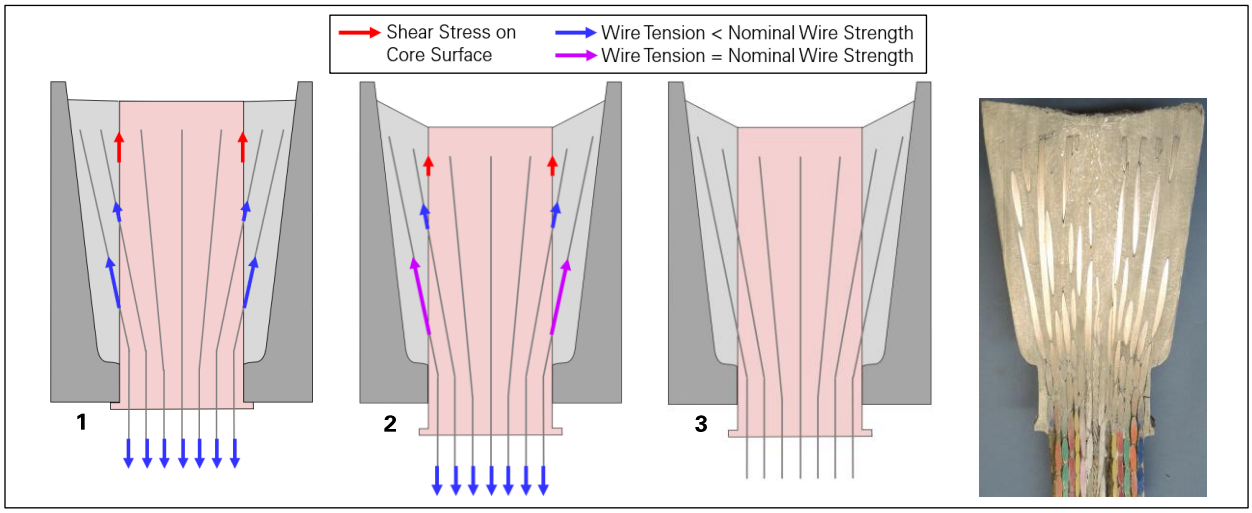

Figure 31: Behavior of socket B4N_G *(photo: Socotec).*

Socket B4S_G

1. As the socket is initially loaded, the cable tension is resisted by a combination of core shear and crossing wire tension.
2. Core shear causes zinc flow, which increases crossing wire tension and decreases core shear. The crossing wires capacity (659 kip) is less than the cable tension (665 kip), so core shear (0.05 ksi) is still needed to resist the cable tension after the crossing wires reach their capacity.
3. The core shear needed is relatively low, so zinc flow is slow, and the socket does not fail before the telescope's collapse.
4. As the socket is load-tested after the collapse, the maximum cable tension reached (1,647 kip) is higher than the cable's Minimum Breaking Strength (1,614 kip), and much higher than the crossing wires capacity. This activates a fast zinc flow and/or core fracture. Most of the crossing wires (66 percent) are fully developed and reach their nominal strength.
5. As zinc flow and/or core fracture continues to develop, some of the fully developed crossing wires rupture.
6. The test is ended by dropping the cable tension before the socket fails completely.

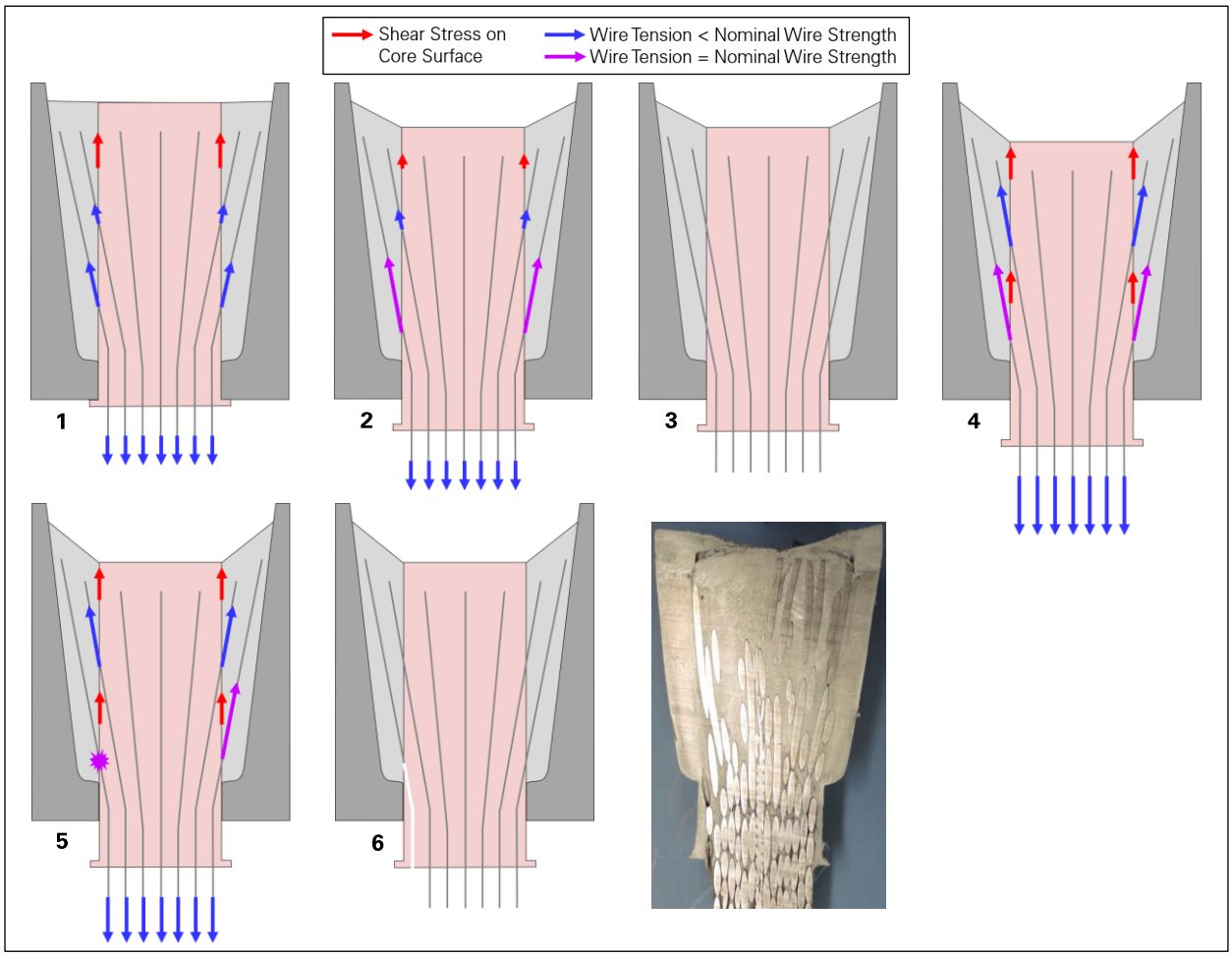

Figure 32: Behavior and failure of socket B4S_G *(photo: Socotec).*

Socket M4N_T

1. As the socket is initially loaded, the cable tension is resisted by a combination of core shear and crossing wire tension.
2. Core shear causes zinc flow, which increases crossing wire tension and decreases core shear. The crossing wires capacity (554 kip) is less than the cable tension (600 kip), so core shear (0.43 ksi) is still needed to resist the cable tension after the crossing wires reach their capacity. Most of the crossing wires (59 percent) are fully developed and reach their nominal strength.
3. As zinc flow continues, the fully developed crossing wires reach their ultimate tensile strain and rupture.
4. The core ruptures and slips out of the socket as core shear cannot resist the full cable tension.

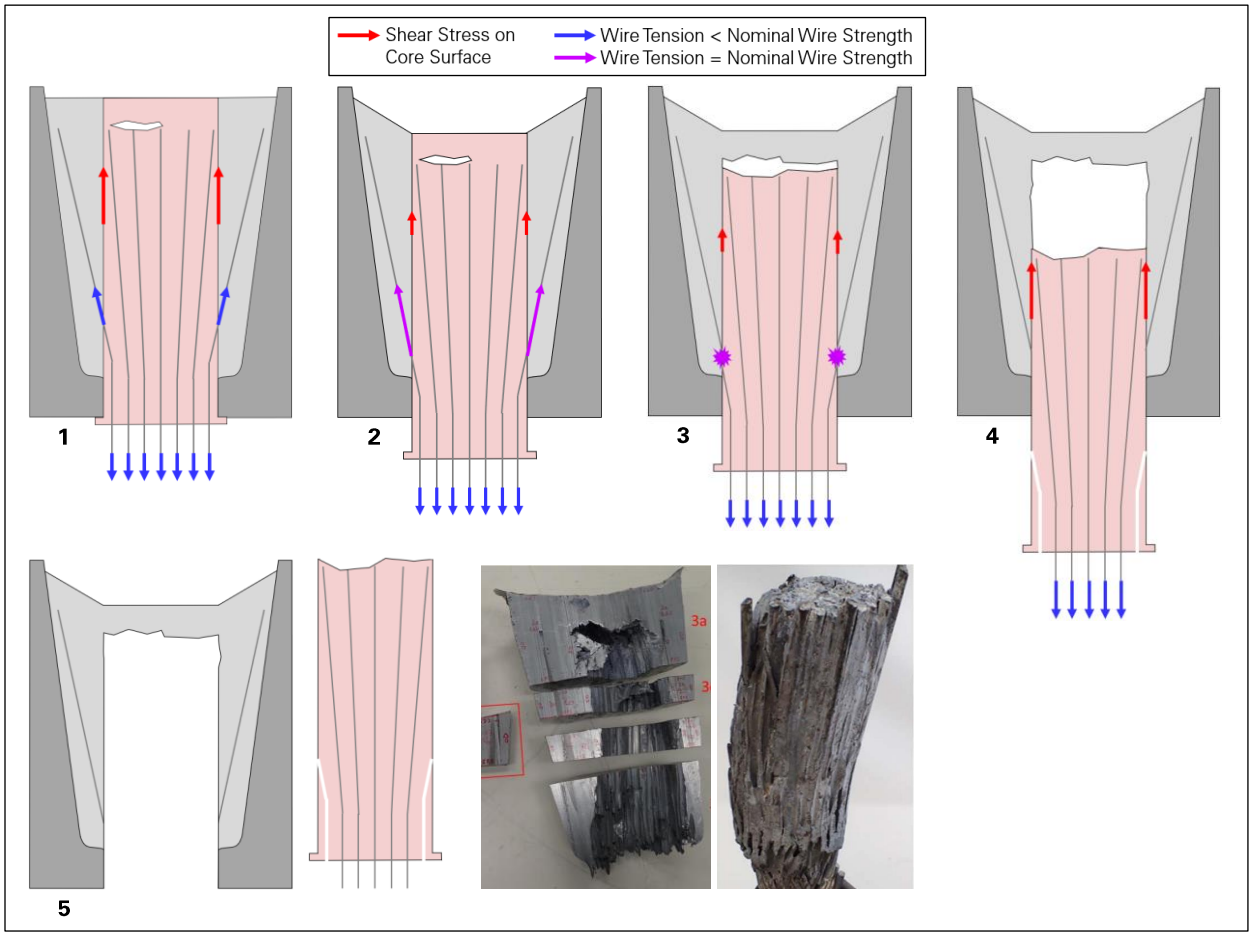

Figure 33: Behavior and failure of socket M4N_T *(photos: WJE[5]).*

[5] Wiss, Janney, Elstner Associates (WJE). *Auxiliary Main Cable Socket Failure Investigation.* June 21, 2021. Draft report provided by WJE.

Socket B12W_G

1. As the socket is initially loaded, the cable tension is resisted by a combination of core shear and crossing wire tension.
2. Core shear causes zinc flow, which increases crossing wire tension and decreases core shear. The crossing wires capacity (561 kip) is less than the cable tension (624 kip), so core shear (0.52 ksi) is still needed to resist the cable tension after the crossing wires reach their capacity. Most of the crossing wires (62 percent) are partially developed and start slipping before reaching their nominal strength.
3. As zinc flow continues, the partially developed crossing wires continue to slip as the core gradually flows out of the socket. This delays the socket failure, which does not occur before the telescope's collapse.

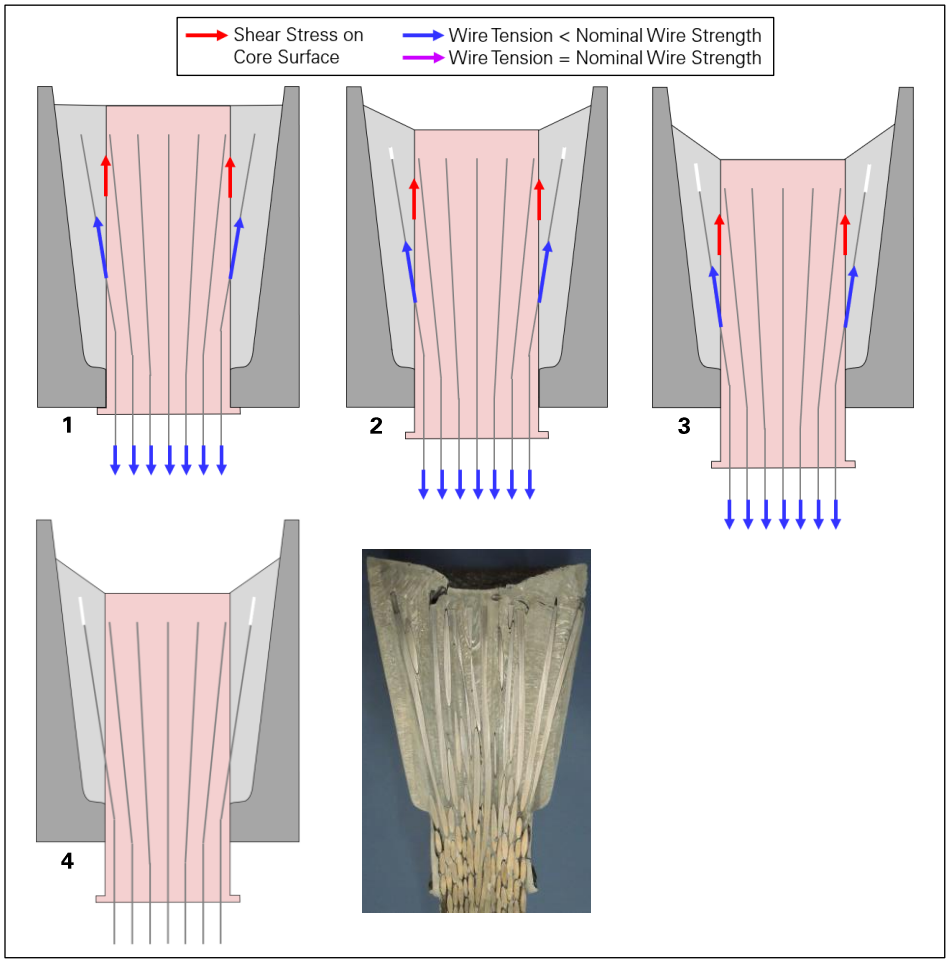

Figure 34: Behavior of socket B12W_G *(photo: Socotec).*

Appendix P
Socket Finite Element Analysis

1.0 Introduction

We performed a series of finite element (FE) analyses to simulate the behavior of zinc-filled spelter sockets under load and determine how this behavior varies with some of the socket's properties. The FE analyses are complementary to the other approaches taken to analyze the failures of the telescope's sockets, which include a laboratory study (Appendix M), and full-scale load test (Appendix N), and the development of a mathematical model for the strength of sockets (Appendix O).

2.0 Modeling Assumptions

The FE models are built in Abaqus, which is a general-purpose FE analysis program. The general modeling assumptions are presented in this section and apply to all of the models and results presented in this appendix, unless noted otherwise.

2.1 Baseline Model Geometry

The FE models are derived from a baseline model representing the ground-end socket of an auxiliary backstay. One of these sockets experienced the maximum cable slip (B12W_G), and its overall geometry is similar to the sockets where the first two cable failures occurred (M4N_T and M4-4_T).

The wire broom is assumed uniform in the baseline model. In the uniform broom, the wire ends are evenly spaced in the radial and tangential directions. The uniform broom has a 60-degree axisymmetry, and therefore a single representative 60-degree wedge is modeled (Figure 1).

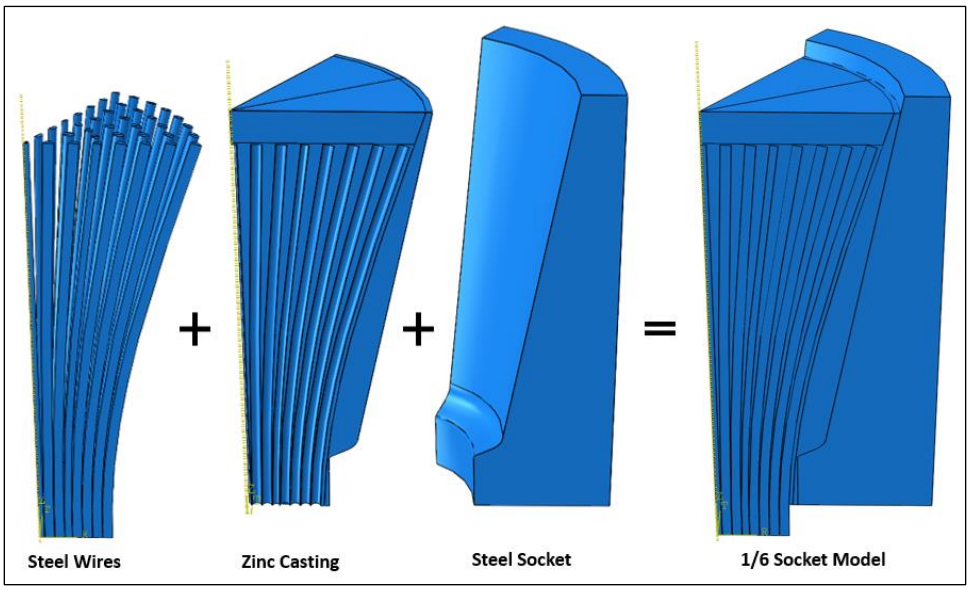

Figure 1: Finite element model of cable socket.

2.2 Material Properties

The steel wires and zinc casting are assigned nonlinear material properties to capture plastic deformation and load redistribution that may occur inside the socket (Table 1, Figure 2). The steel of the wires is modeled as an elastoplastic material with a yield stress of 175 ksi, which is the average yield stress measured on wires cut from the telescope's cables (Appendix L). The zinc is also modeled as an

elastoplastic material, with a stress-strain curve based on the results of a test performed by WJE[1] on the zinc of socket M4N_T (first cable failure). In addition, the zinc is assigned a creep behavior to model zinc flow. The creep model is a power law where the creep rate is proportional to the fourth power of the stress. The steel of the socket is modeled as an elastic material.

The zinc material is allowed to slip on the socket's surface, with a friction coefficient of 0.6. The zinc can also separate from the socket's surface, as was observed at the back of some of the telescope's sockets. The wires and the zinc are tied, and therefore the wires cannot slip with respect to the zinc. Wire slip was observed in the zinc of some of the telescope's sockets, but its impact on the socket behavior and strength is not the focus of the FE analyses.

Table 1: FE model material properties.

Material parameter	Wire Steel	Zinc
Young's modulus, E [ksi]	29,000	12,490
Yield strength, F_y [ksi]	175	12.0
Poisson's ratio	0.3	0.245

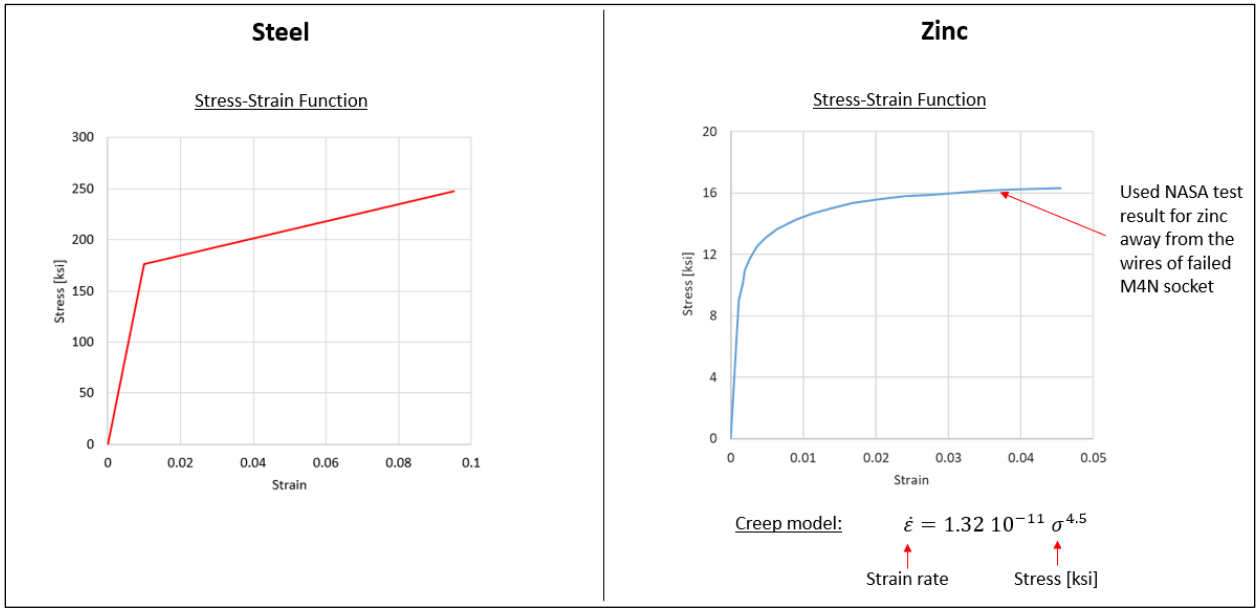

Figure 2: FE model material properties.

2.3 Mesh

The models are meshed (Figure 3) using a combination of linear hexahedral and tetrahedron elements (C3D8R and C3D4). The tetrahedron elements are used in the zinc material close to the wires to facilitate the meshing process. After performing a mesh sensitivity study, the maximum element size was selected at 0.2 inch.

[1] Wiss, Janney, Elstner Associates, Inc (WJE). *Auxiliary Main Cable Socket Failure Investigation*. June 21, 2021. Draft report provided by WJE.

2.4 Loading and Boundary Conditions

In the FE model, the socket is loaded by pulling on the back of the socket while fixing the cable end at the front of the socket (Figure 4). The socket is loaded to half of the cable's Minimum Breaking Strength, which is a stress level similar to what the telescope's sockets experienced. When analyzing the long-term behavior of a socket, the load is held for 25 years, which corresponds to the time between the installation of the auxiliary cables (started in 1995) and the telescope's collapse (2020). Additional boundary conditions are applied to the socket, zinc, and wires on the two sides of the 60-degree wedge to achieve axisymmetric behavior.

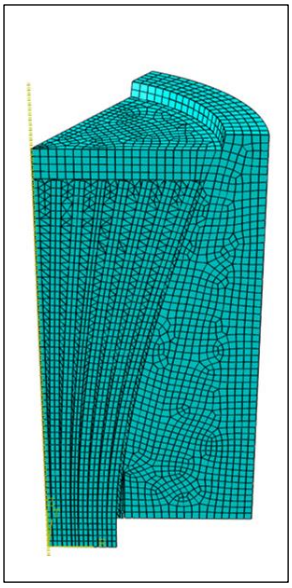

Figure 3: Finite element mesh.

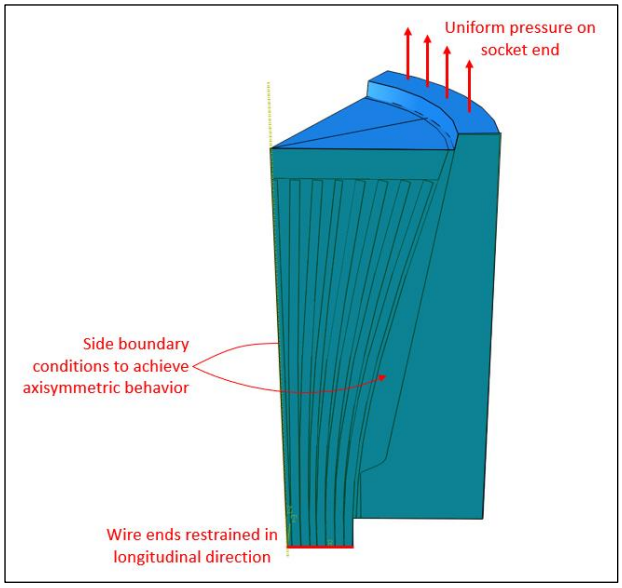

Figure 4: FE model loading and boundary conditions.

3.0 Analysis and Results

3.1 Baseline Model Behavior

The baseline model, whose wire broom is uniform, was first loaded to half of the cable's Minimum Breaking Strength and held at that load for 25 years to observe the evolution of the stress state in the socket casting over time.

The cone-shaped cavity of a spelter socket is expected to engage the zinc casting through wedging action, thus inducing a radial compressive stress in the casting. As shown in Figure 5, the radial stress in the zinc is close to zero when the socket is initially loaded. This is due to the casting bearing on the socket's shoulder instead of being wedged into the cone. However, a radial compressive stress gradually develops over time due to zinc flow. The zinc flow is driven by shear stress which, as shown in Figure 6, gradually decreases in the casting over time. When the shear stress is low, the casting is being held in the socket primarily through the intended wedging action. As shown in Figure 7, zinc flow also causes a stress redistribution among the cable's wires, with the outer wires picking up more tension than the inner wires. The cable slip after 25 years is negligible, at 0.07 inch. It is understood that even with a uniform wire broom, an actual zinc-filled spelter socket would likely exhibit a larger cable slip due to imperfections in the initial contact between the socket and zinc, which are not included in the FE model.

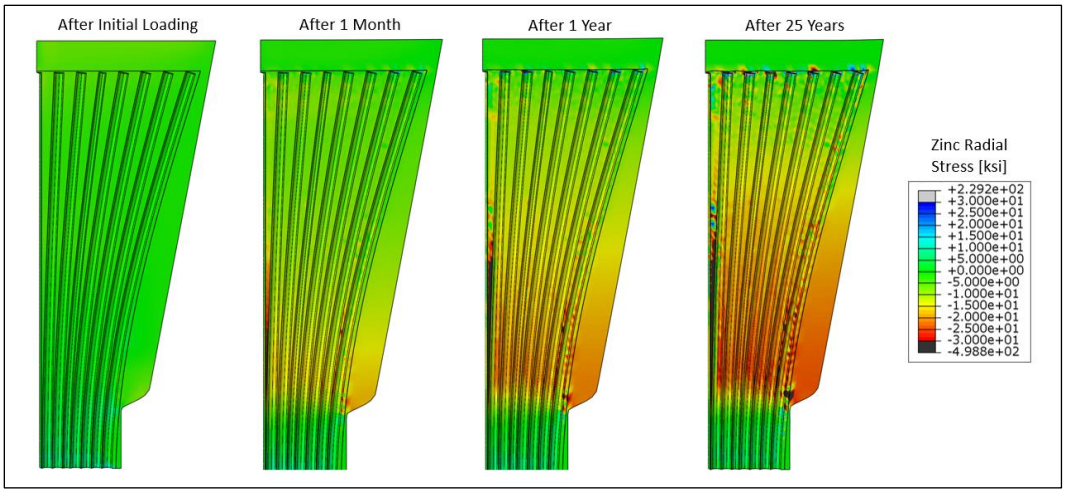

Figure 5: Radial stress evolution over time in zinc of baseline model.

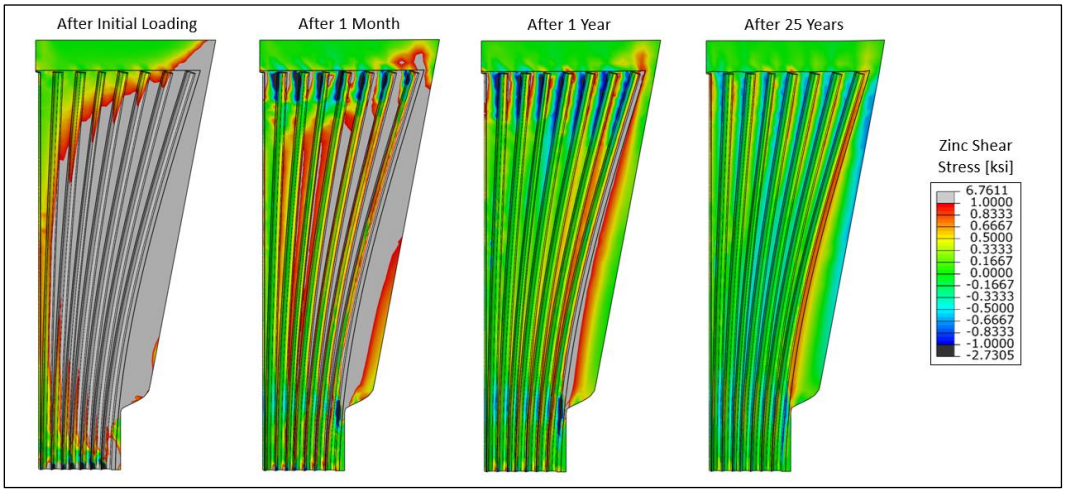

Figure 6: Shear stress evolution over time in zinc of baseline model.

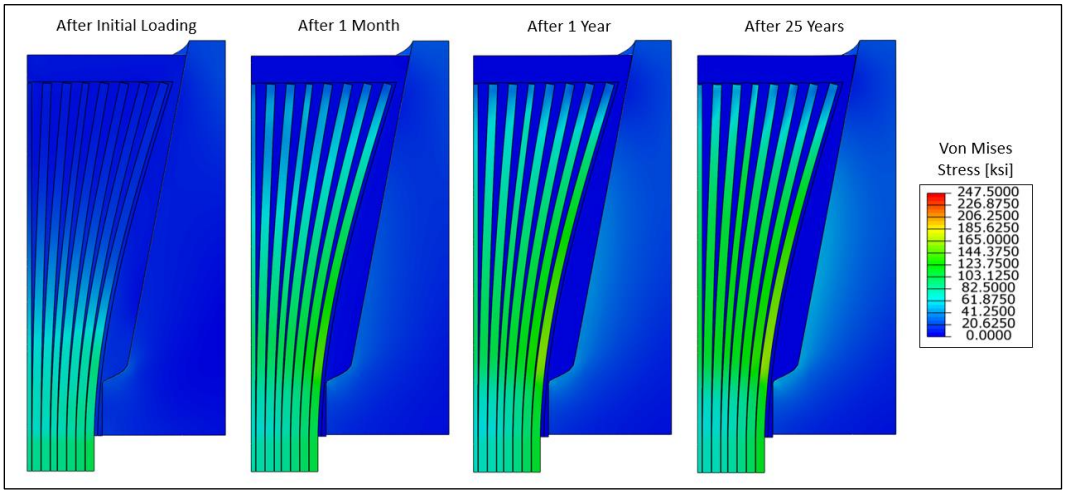

Figure 7: Von Mises stress evolution over time in wires of baseline model.

3.2 Effect of Socket Shoulder

The baseline model represents a socket design that includes a shoulder, which is a step in the profile of the socket's cavity near the front of the socket. Shoulders were present on most of the telescope's sockets, including the socket that experienced the largest cable slip (B12W_G) and where the first two cable failures occurred (M4N_T and M4-4_T). Zinc-filled spelter sockets, however, do not always have a shoulder. This was for example the case for the platform-end sockets of the telescope's auxiliary main cables. The presence of a shoulder can affect the load transfer mechanism between zinc casting and socket, as the casting can bear directly on the shoulder. Without a shoulder, the load transfer must occur through wedging action as the casting is squeezed in the cone-shaped cavity of the socket.

To study the effect of the shoulder on socket behavior, the FE model of a socket without a shoulder was derived from the baseline model by removing the shoulder (Figure 9, Figure 8). The front and back diameters of the socket's cavity is the same in both models, but the cavity's slope is steeper in the model with a shoulder. Both models were loaded to half of the cable's breaking strength, and the load was held for a year before comparing wire tension and zinc shear stress.

As shown in Figure 8, when the socket is initially loaded, the shoulder causes higher shear stress at the front of the zinc casting because the casting bears on the shoulder. However, after allowing the zinc to creep for a year, the shear stress distribution is similar in the models with and without a shoulder.

Similarly, the wire stress and cable slip are almost equivalent between the creep models with and without shoulders (Figure 9). The shoulder does not appear to have a significant impact on the long-term behavior of the socket.

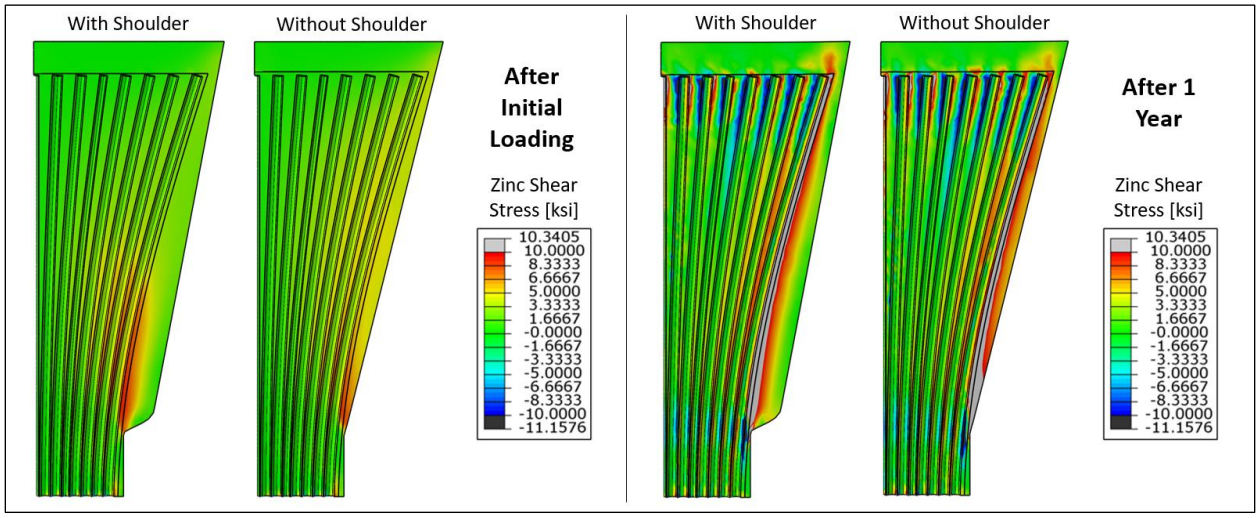

Figure 8: Zinc casting shear stress with and without shoulder.

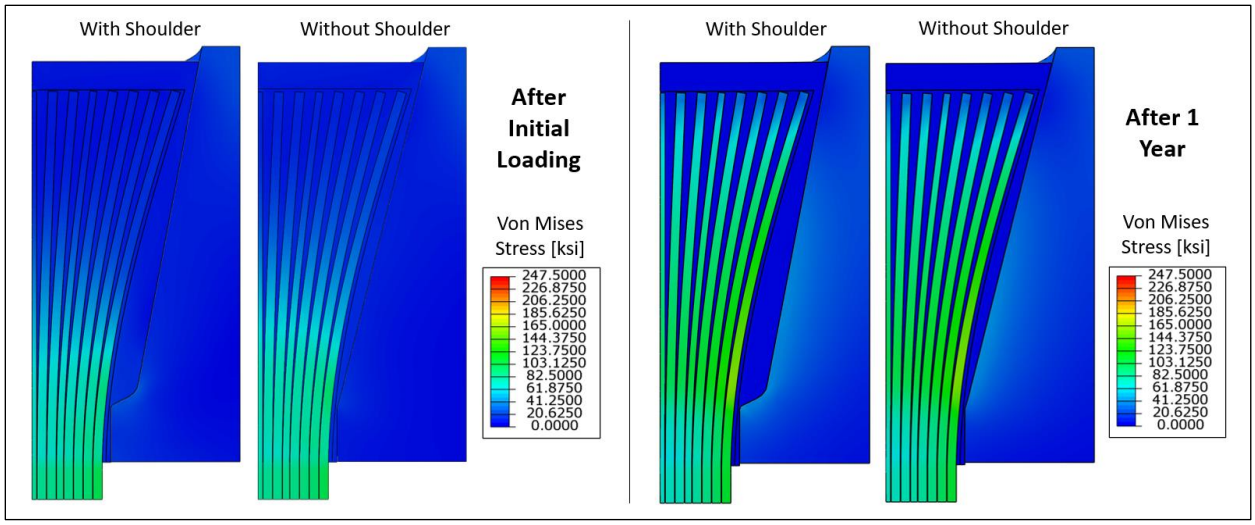

Figure 9: cable slip and wire stress with and without shoulder.

3.3 Effect of Wire Broom Extent

The cable wires are spread out inside the socket to fill the cone-shaped cavity and form a wire broom. The laboratory analysis of the socket samples indicates that the wire brooms vary between sockets, as they were shaped manually during the socket fabrication. Wire broom variations could cause or contribute to the different cable slips observed between sockets and the eventual failure of socket M4N_T. Therefore, we performed a series of FE analyses to investigate the effect of wire broom on socket behavior. As shown in Figure 10 to Figure 15, five wire brooms were considered.

The wire stresses and cable slips are equivalent in every broom when the socket is initially loaded (Figure 10), with the casting bearing on the shoulder. Zinc flow over time causes a stress redistribution resulting in the broomed-out wires carrying most of the cable's tension (Figure 11, Figure 12). In the socket with a single layer of wires broomed out, those wires rupture after just three years of zinc flow (Figure 11), causing failure of the socket. The sockets with at least two layers of wires broomed out do not fail after 25 years, and at that point the broomed-out layers carry most of the cable tension.

The shear stress in the zinc is also equivalent in every socket after the initial loading (Figure 13), and changes over time as zinc flows (Figure 14, Figure 15). The shear stress is higher within a zone located on the outer side of each wire layer, where the wires transfer their load to the zinc. For the socket with a single layer of wires broomed out, a broad zone of high shear stress is present around the central bundle of wires, which are not broomed out. This causes those un-broomed wires to gradually pull out of the socket, stretching and eventually rupturing the single layer of broomed-out wires.

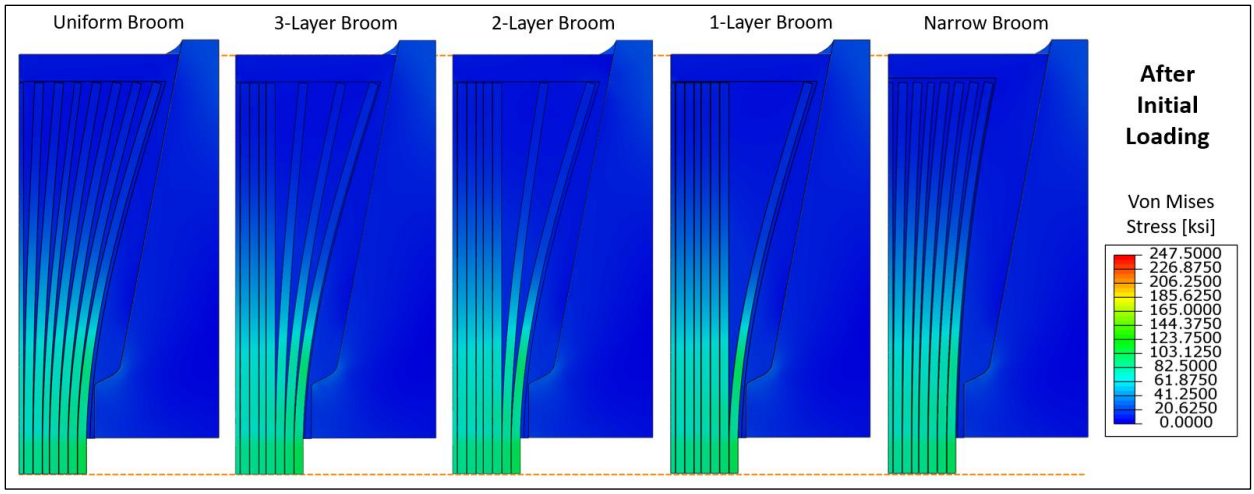

Figure 10: Wire tensile stress for different wire brooms after initial loading.

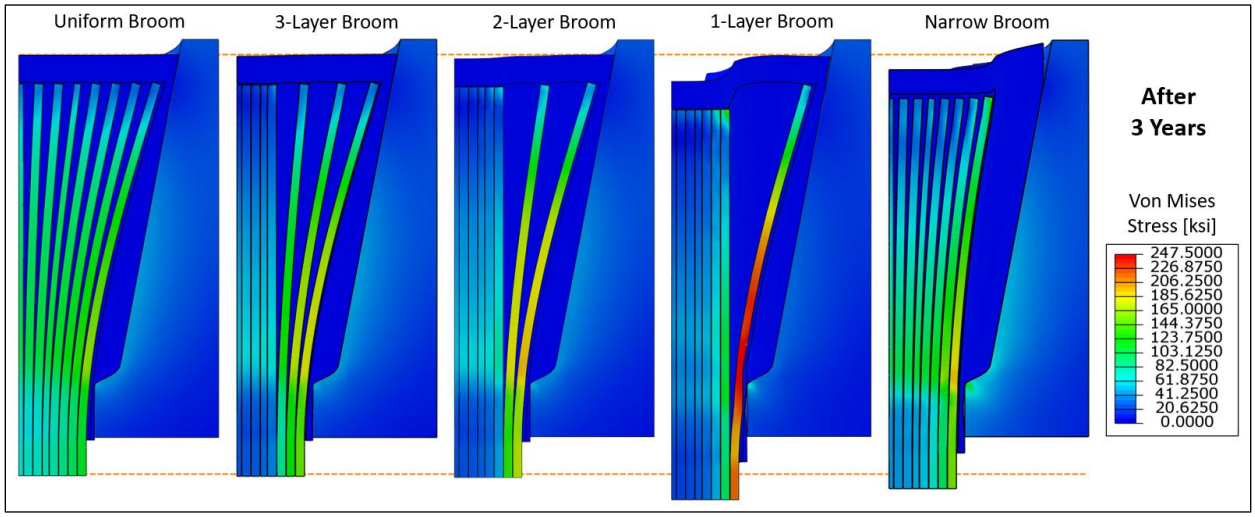

Figure 11: Wire tensile stress for different wire brooms after 3 years of zinc flow.

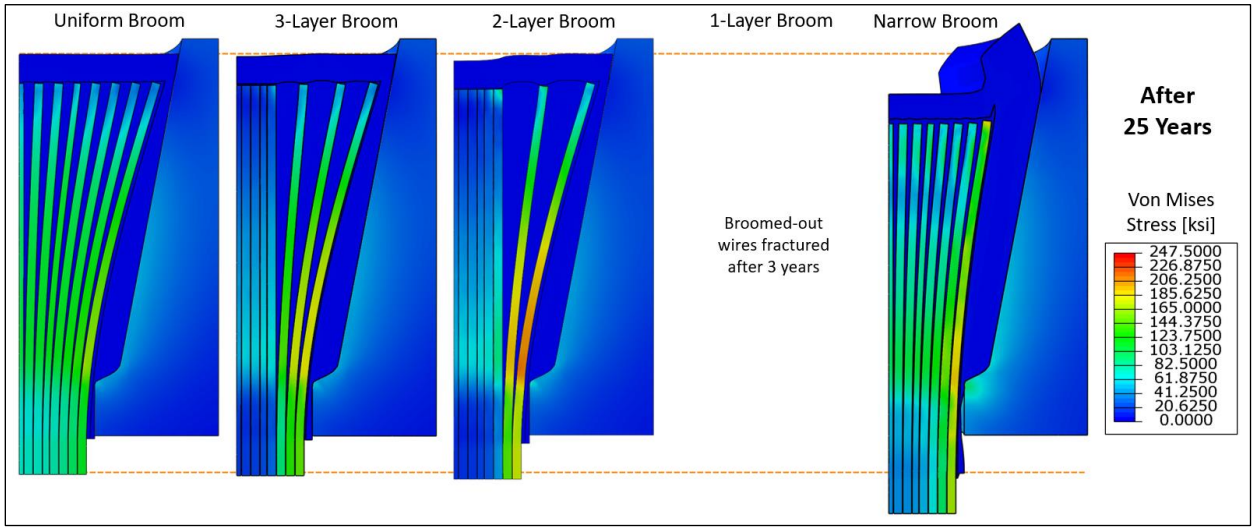

Figure 12: Wire tensile stress for different wire brooms after 25 years of zinc flow.

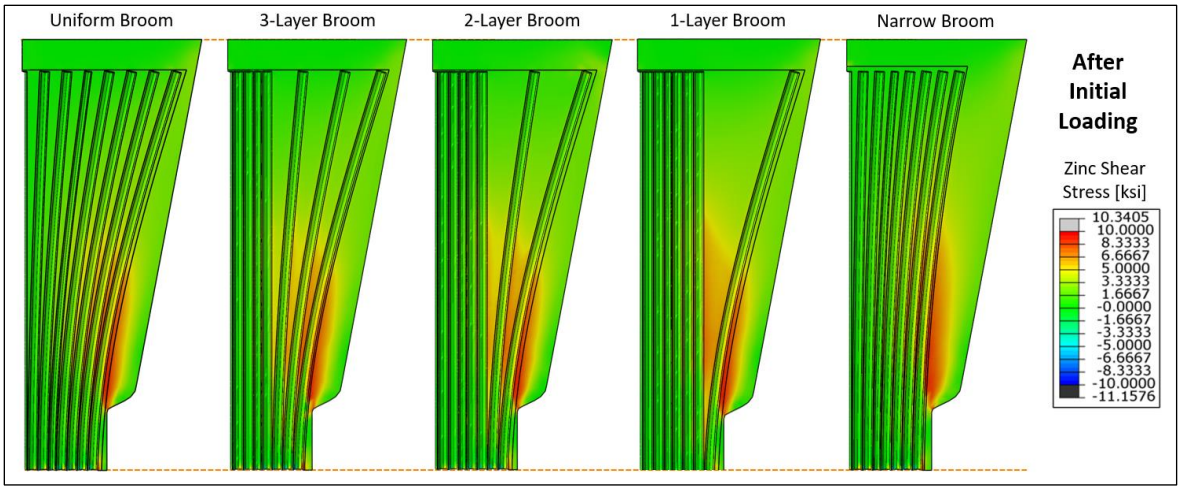

Figure 13: Zinc shear stress for different wire brooms after initial loading.

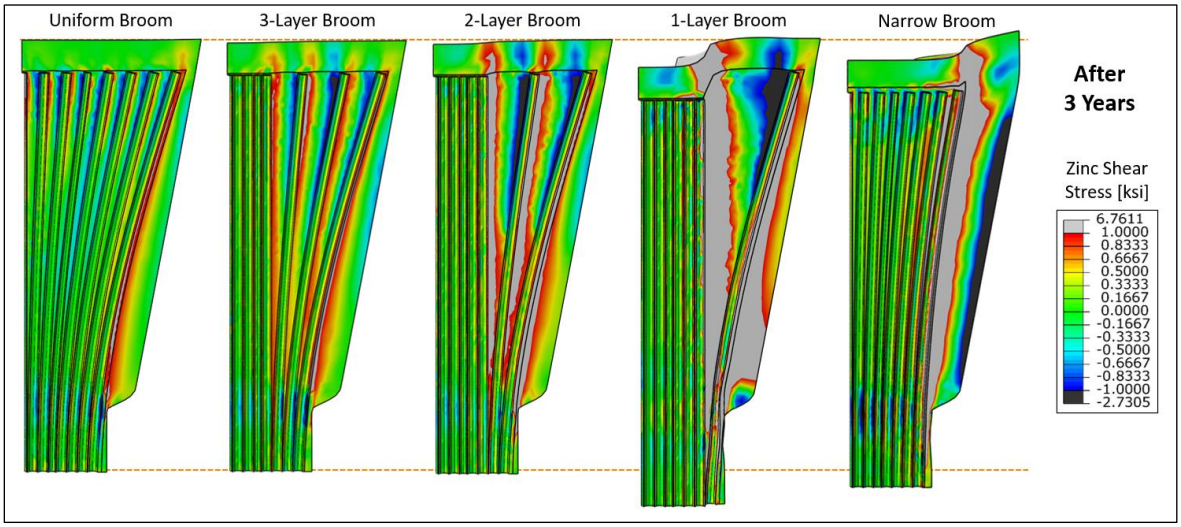

Figure 14: Zinc shear stress for different wire brooms after 3 years of zinc flow.

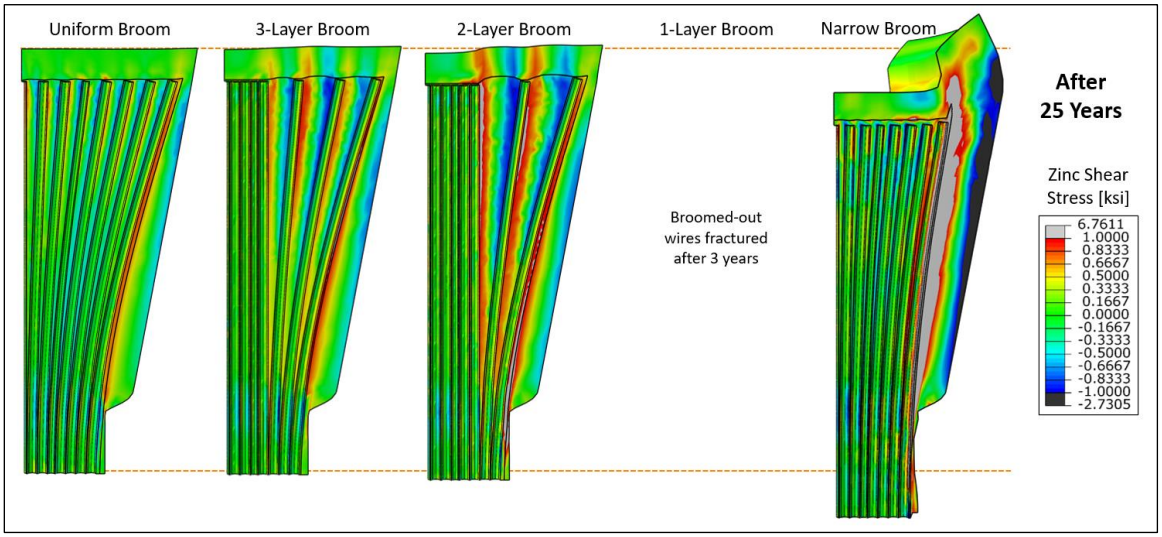

Figure 15: Zinc shear stress for different wire brooms after 25 years of zinc flow.

Appendix Q
Glossary

This glossary defines a number of terms used in this report. The definitions are specific to this report, and some of the terms may have a different or broader definition is other contexts.

Anchorage	Reinforced concrete block sitting on a hill and serving as anchor point for the ground-end sockets of backstay cables.
Auxiliary	(auxiliary cable, auxiliary main, auxiliary backstay) An auxiliary cable is a main or backstay cable installed during the second upgrade of the telescope, completed in 1997.
Azimuth Arm	Bow-shaped truss hung under the platform as part of the suspended structure. The azimuth arm can rotate about the platform's vertical axis to steer the telescope, and supports other moveable parts (Gregorian, line feed).
Back	(socket back) Socket end opposite to the connected cable.
Backstay	(backstay cable) Structural cable connecting the top of a tower to an anchorage on the ground.
Broom	(wire broom) Wires of a cable end splayed out inside a socket's cavity. The gaps between the wires of the broom are filled with zinc to form the socket's casting during cable socketing.
Cable	Single strand of high-strength galvanized steel wires, arranged in concentric layers woven helicoidally. The cables include the mains (between towers and platform) and backstays (between towers and anchorages).
Cable slip	Distance by which a cable end has displaced with respect to its socket, usually measurable as a zinc extrusion at the front of the socket.
Cable tension	Resultant in the cable's longitudinal direction of the wire stresses over the cable's cross-section, i.e. the cable's internal longitudinal force. The actual tension may vary along a cable. Any tension value provided in this report is the average over the cable length, unless noted otherwise.
Carriage house	Box-shaped enclosure containing equipment and serving as mount for some of the telescope's radio feeds. A carriage house can slide along the bottom of the azimuth arm. The original telescope had two carriage houses, one of which was replaced with the Gregorian during the second upgrade.
Casting	(socket zinc casting) Cone-shaped zinc block enclosing the broomed-out wires of a cable end, locking the cable end inside a socket cavity.
Cavity	(socket cavity) Cone-shaped volume inside a socket where the connected cable is broomed out before being filled with zinc to form a casting.
Core	(socket zinc casting core) Central part of a socket's casting, observed to have displaced towards the socket's front in the distressed sockets.
Core rupture	Socket failure mode where the crossing wires tend rupture as the cable slips.

Core shear	Resultant of the shear stresses acting on the surface of the core in a socket casting.
Core wire	Wire whose end is located inside the core in a socket casting.
Counterweight	Lead weight installed on the azimuth arm during the second upgrade of the telescope to balance the weight of the Gregorian. The counterweight was fixed on the azimuth arm, unlike the Gregorian.
Crossing wire	Wire located inside the core at the front of a socket, but whose end is located outside of the core. A crossing wire crosses the surface of the core between the front of the socket and the wire end.
Crossing wire tension	Total force that the crossing wires can develop to resist core pull-out.
Flow	(zinc flow) Large deformation of the zinc material in a socket casting due to plasticity and/or creep.
Flow-out	(core flow-out) Socket failure mode where the crossing wires tend to slip together with the core.
Front	(socket front) Socket end receiving through which the connected cable enters the socket.
Gregorian	Dome-shaped enclosure containing radio reflectors and receivers, installed as replacement for one of the two carriage houses during the second upgrade of the telescope. The Gregorian can slide along the bottom of the azimuth arm.
Ground screen	Inclined wire mesh wall built along the edge of the primary reflector to block off interference from surrounding terrain.
Layer	(wire layer) A cable is made on multiple wires arranged in concentric layers.
Line feed	Radio antenna mounted on a carriage house, which can slide along the bottom of the azimuth arm.
Main	(main cable) Structural cable supporting the suspended structure from the top of a tower.
Minimum Breaking Strength	Minimum tension that a brand new cable is expected to resist without rupturing.
Nominal wire strength	Maximum tension that a cable wire can resist before yielding and eventually fracturing, in the elastic-perfectly plastic idealized model of the wire behavior.
Normalized stress range	(cable normalized stress range, NSR) Measure of the fluctuation of a cable tension, calculated as the peak-to-peak amplitude of the fluctuation divided by the cable's Minimum Breaking Strength.
Original	(original cable, original main, original backstay) An original cable is a main or backstay cable installed during the original construction of the telescope, completed in 1963. Cable B12-3 was replaced in 1980, and the replacement cable is also considered an original.
Outrigger	Steel trusses and stay cables added to the platform during the second upgrade of the telescope, to connect the new vertical tiedowns
Primary reflector	see *Reflector*
Reflector	Large dish antenna located just above ground and below the telescope's suspended structure. The reflector is 1,000 feet in diameter and made of approximately 40,000 rectangular aluminum panels supported by a cable net.

Ring girder	Circular steel beam hung at the bottom of the platform and allowing the azimuth arm to rotate about the platform's vertical axis.
Rupture	see *Wire rupture* or *Core rupture*
Safety factor	(cable safety factor, SF) Measure of the stress level in a cable, calculated as the design, actual or estimated cable tension divided by the cable's minimum Breaking Strength.
Shoulder	(socket shoulder) Step in a socket's cavity shape between the front of the socket and the inclined wall forming the cone-shaped cavity.
Slip	see *Cable slip* or *Wire slip*
Socket	(zinc-filled spelter socket) Cable termination device allowing to connect a cable end to another structural element. A zinc-filled spelter socket contains a cone-shaped cavity where the cable end is inserted and broomed out, before filling the gaps with zinc.
Spelter socket	see *Socket*
Strand	see *Cable*
Suspended structure	Steel structure suspended above the reflector, comprised of the fixed platform and moveable azimuth arm, Gregorian and/or line feeds.
Tension	see *Cable tension* or *Crossing wire tension*
Tiedown	Cable or pair of cables tying the suspended structure directly to the ground. The original structure had six inclined tiedowns, which were replaced by three vertical tiedowns during the second upgrade of the telescope. Each vertical tiedown consists of two parallel cables.
Tower	Reinforced concrete tower from which the suspended structure is supported through main cables, and tied back to the ground with backstay cables.
Waveguide	Cable-supported structure used to carry personnel and radio waves to the suspended structure from the top of Tower 12.
Wire	(cable wire) High-strength steel wire composing a cable. A cable is made of several concentric layers of wire.
Wire rupture	Complete failure of a wire. Wire rupture can be ductile or brittle and due to tensions and/or shear stress.
Wire slip	Displacement of an individual cable wire with respect to the zinc outside of the casting's core.
Zinc-filled spelter socket	see *Socket*